UNIVERSITÉ DU LUXEMBOURG

PhD-FSTM-2022-106
The Faculty of Science, Technology and Medicine

DISSERTATION

Defense held on 28/09/2022 in Esch-sur-Alzette

to obtain the degree of

DOCTEUR DE L'UNIVERSITÉ DU LUXEMBOURG

EN BIOLOGIE

by

Semra SMAJIC
Born on 12. October 1991 in Tuzla (Bosnia and Herzegovina)

THE ROLE OF NEUROMELANIN IN DOPAMINERGIC NEURON DEMISE AND INFLAMMATION IN IDIOPATHIC PARKINSON'S DISEASE

Dissertation defense committee

Dr Anne Grünewald, Dissertation Supervisor
Professor, University of Luxembourg,

Dr Jens C. Schwamborn, Vice-Chair
Professor, University of Luxembourg,

Dr Alexander Skupin, Chair
Professor, University of Luxembourg

Dr Philip Seibler
Group Leader, University of Lübeck, Institute of Neurogenetics

Dr Katrin Frauenknecht
Deputy Head, Laboratoire National de Santé, Luxembourg Center of Neuropathology

UNIVERSITÉ DU LUXEMBOURG

University of Luxembourg

Doctoral Thesis

The role of neuromelanin in dopaminergic neuron demise and inflammation in idiopathic Parkinson's disease

Author:

Semra Smajić

Supervisors:

Prof Dr Anne Grünewald

Prof Dr Jens C. Schwamborn

A thesis submitted in fulfillment of the requirements for the

Doctoral Degree of the University of Luxembourg

in the

Molecular and Functional Neurobiology group

Developmental and Cellular Biology group

Luxembourg Centre for Systems Biomedicine

September 28, 2022

”It may be unfair, but what happens in a few days, sometimes even a single day, can change the course of a whole lifetime...”

– Khaled Hosseini, The Kite Runner

Abstract

For a very long time, the main focus in Parkinson's disease (PD) research was the loss of neuromelanin-containing dopaminergic neurons from the *substantia nigra* (SN) of the midbrain - the key pathological feature of the disease. However, the association of neuronal vulnerability and neuromelanin presence has not been a common study subject. Recently, cells other than neurons also gained attention as mediators of PD pathogenesis. There are indications that glial cells undergo disease-related changes, however, the exact mechanisms remain unknown.

In this thesis, I aimed to explore the contribution of every cell type of the midbrain to PD using single-nuclei RNA sequencing. Additionally, the goal was to explore their association to PD risk gene variants. As we identified microgliosis as a major mechanism in PD, we further extended our research to microglia. We sought to investigate the relation of microglia and neuromelanin. Thus, we aimed to, by means of immunohistochemical staining, imaging and laser-capture microdissection-based transcriptomics, elucidate this association on a single-cell level.

This work resulted in the first midbrain single-cell atlas from idiopathic PD subjects and age- and sex-matched controls. We revealed SN-specific microgliosis with GPNMB upregulation, which also seemed to be specific to the idiopathic form of the disease. We further observed an accumulation of (extraneuronal) neuromelanin particles in Parkinson's midbrain parenchyma, indicative of incomplete degradation. Moreover, we showed that *GPNMB* can be alleviated in microglia in contact with neuromelanin.

Taken together, we provide evidence of a GPNMB-related microglial state as a disease mechanism specific to idiopathic PD, and highlight neuromelanin as an important player in microglia disease pathology. Further investigations are needed to understand whether the modulation of neuromelanin levels could be relevant in the context of PD therapy.

Acknowledgements

Of all the chapters I have written so far, this one is by far the hardest. It is hard, because it marks the closure of a very special part of my life. It is hard, because all the words seem too small to express my gratitude to people who stood by me through three and a half years of my PhD journey.

First, my deepest gratitude goes to Prof. Dr. Anne Grünewald and Prof. Dr. Jens C. Schwamborn for the amazing opportunity to work in the field of neuroscience. Thank you for your mentorship, for the encouragement and endless trust you have put into my work. This endeavour would have not been possible without you.

I would, also, like to thank Prof. Dr. Alexander Skupin, for all the discussions and all the thought-stimulating questions during my CETs. Your invaluable advice helped me a lot on this journey, for which I will always be grateful.

I am much obliged to acknowledge all the members of my two groups, the Molecular and Functional Neurobiology group and the Developmental and Cellular Biology group. For all the chat, laughter, frustration, worries, work, food and coffee we shared... thank you. I will forever cherish these memories.

My time in LCSB would not be the same without Dr. Sandro Pereira, Dr. Carmen Venegas, Jenny Ghelfi, Dr. Sylvie Delcambre, Maria Tziortziou and Gideon Agyeah... thank you for everything. I also need to give much appreciation, to Dr. Kobi Wasner and Adelene Lai for reading my thesis. A very special thanks goes to Dr. Katja Badanjak and Patrycja Mulica. You selflessly shared your knowledge and help, and made the work more fun. For that, I am always grateful.

My deepest gratitude goes to my family and my friends. To my mom, my dad and my brother - I am forever grateful for the biggest support, and for being there in every difficulty I ever had.

Contents

List of Abbreviations

6 – OHDA	6-hydroxydopamine
A – syn	alpha synuclein
AADC	aromatic amino acid decarboxylase
ALS	amyotrophic lateral sclerosis
CADPS2	calcium-dependent activator of secretion 2
CC	crus cerebri
CO	control
D – NM	dark neuromelanin
DA	dopamine
DAM	damage-associated microglia
DAMP	damage-associated molecular pattern
DaNs	dopaminergic neurons
dNM	dark neuromelanin
FACS	fluorescence-activated cell-sorting
GWAS	genome-wide association study
hDA	human embryonic dopaminergic neuron 0-2
hNb/hNbML	human embryonic neuroblasts
hNProg	human embryonic neural progenitors
IPD	idiopathic Parkinson's disease
iPSC	induced pluripotent stem cell

L – NM	light neuromelanin
LB	Lewy body
LCM	laser-capture microdissection
lNM	light neuromelanin
MHC – II	major histocompatibility class II
MPTP	1-methyl-4-phenyl-1,2,3,6-tetrahydropyridine
NM	neuromelanin
noNM	neuromelanin-free area
NR	nucleus ruber
OPC	oligodendrocyte precursor cell
PAMP	pathogen-associated molecular pattern
PD	Parkinson's disease
PRR	pattern-recognition receptor
ROS	reactive oxygen species
smNPCs	small molecule neural precursor cells
SN	substantia nigra
snRNAseq	single-nuclei RNA-sequencing
T/T	tectum and tegmentum
TH	tyrosine hydroxylase
UPR	unfolded protein response

Chapter 1

Introduction

1.1 Parkinson's disease - definition and symptoms

Slow and progressive loss of dopaminergic neurons (DaNs) from the *substantia nigra* (SN) is the main hallmark of Parkinson's disease (PD). DaNs synthesise the neurotransmitter dopamine (DA) which is responsible for movement, pleasure, memory, learning, mood etc. However, with progressive loss of DaNs in PD, the consequential decline in DA leads to the manifestation of motor and non-motor symptoms, which affects the quality of patients' lives (Fig. 1.1). The most prominent motor features are tremor, muscle rigidity, brady- and hypo-kinesia and overall postural instability (Clarke, 2007). Of non-motor features, the most common are mental health disturbances such as dementia, depression, hallucinations and anxiety (Clarke, 2007). These are further accompanied with sleep and autonomic nervous system disturbances like dysphagia, constipation, salivation, bladder and sexual dysfunction (Clarke, 2007; Emamzadeh and Surguchov, 2018). The disease is considered to begin years before the actual diagnosis when the motor symptoms arise (Kalia and Lang, 2015).

These motor symptoms were first described in 1817 by James Parkinson in 'An Essay on the Shaking Palsy'. Despite all the research performed since, the exact aetiology and pathology remain obscure. Therefore, the existing therapy is still symptomatic and mainly focuses on DA replenishment with levodopa (Rizek, Kumar and Jog, 2016).

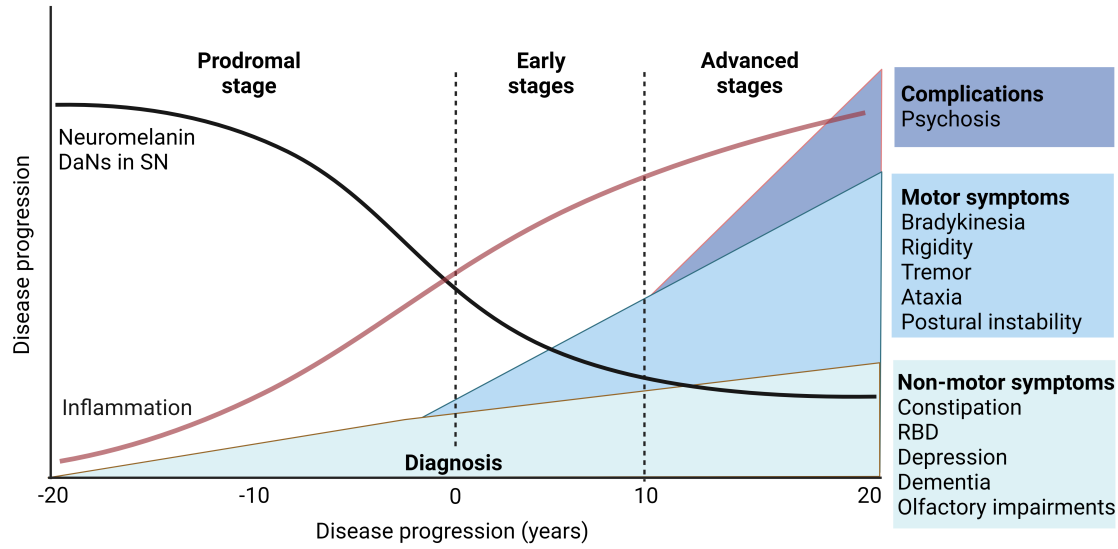

Figure 1.1: Symptoms and progression of PD. Before the diagnosis, in the prodromal phase, unspecific non-motor symptoms occur and intensify over time. At the time of diagnosis based on motor symptoms, ~50% of DaNs are lost. These symptoms worsen with advanced disease which ends with long-term complications of L-dopa therapy, psychosis or dyskinesia (adapted from Kalia and Lang, 2015).

1.2 IPD causes and risk factors

Currently, more than 1% of the world population above 60 years of age are affected by PD (Saikia *et al.*, 2020). The number of cases is likely to double by the year 2040, making PD the second most common neurodegenerative disease (GBD 2016 Parkinson's Disease Collaborators, 2018; Day and Mullin, 2021). The origin of PD is associated with genetic or environmental factors, or a combination of both. Among patients, only ~5% have a clear monogenic form of PD (Lang and Lozano, 1998). The most commonly-found mutations in these patients are located in *SNCA, LRRK2, PRKN, PINK1, DJ1* or the *ATP13A2* gene (Klein and Westenberger, 2012). While ~10% of the PD population has a positive family history of PD, the vast majority (around 90%) of PD cases are idiopathic (IPD) (Lang and Lozano, 1998). The term "idiopathic" denotes a sporadic disease case without known cause nor family history.

Knowing the genetic component of the disease, scientists can focus their research

on disease-causing genes. Therefore, the majority of PD research is performed with genetic cases, despite the larger number of IPD cases.

Multiple studies have shown that exposure to various environmental factors or toxins can also trigger PD. In 1982, seven individuals developed PD-like motor symptoms after injecting 1-methyl-4-phenyl-1,2,3,6-tetrahydropyridine (MPTP) (Ballard, Tetrud and Langston, 1985). In addition, constant exposure to herbicides and pesticides (Semchuk, Love and Lee, 1992; Gorell *et al.*, 1998; Paolini, Sapone and Gonzalez, 2004), heavy metals such as iron, manganese or copper (Gorell *et al.*, 1999), certain bacterial endotoxins (Niehaus and Lange, 2003; Murros *et al.*, 2021), head trauma (Jafari *et al.*, 2013) and brain tumours (Ye *et al.*, 2016) are implicated in the aetiology and pathology of PD.

Sex and aging are also inevitable risk factors for PD. Men are 1.5 times greater at risk for developing PD than women, but the underlying cause for the link between PD and male sex remains unknown (Wooten *et al.*, 2004). Further, ageing is one of the main risk factors to develop IPD. The SN region of the midbrain has been shown to be more susceptible to pathological changes with age than any other brain region. Around one third of elderly individuals without PD already show moderate to severe DaNs loss in the SN (Buchman *et al.*, 2012). This loss is even more pronounced in individuals with PD. Around 1% of the population above the age of 60 develops IPD, and this prevalence rises to 5% in the population above 85 years of age (Wood-Kaczmar, Gandhi and Wood, 2006). With advancing age, many fundamental cellular processes naturally decline in SN neurons. Dopamine metabolism dysregulation, iron and NM accumulation and mitochondrial dysfunction lead to an increase in oxidative stress levels (Reeve, Simcox and Turnbull, 2014). In addition, the functioning of protein degradation pathways in neurons also declines with age, leading to DaN vulnerability (Reeve, Simcox and Turnbull, 2014). The consequential decrease in ATP production, accumulation of undegraded proteins and production of reactive oxygen species (ROS) interfere with neuronal functioning. This cascade of stressors that appears with normal ageing impairs neurons in the SN and disables their adaptability and response to surrounding stimuli, ultimately resulting in neuronal death (Reeve, Simcox and Turnbull, 2014).

1.3 Disease pathology

With its multifactorial spectrum, PD affects multiple molecular mechanisms. The most studied molecular changes in PD involve protein aggregation and alpha synuclein (a-syn) accumulation, protein degradation failure, mitochondrial dysfunction, oxidative stress and neuroinflammation.

These PD-related changes have been mainly studied in nigral neurons of the midbrain. However, knowing the complex cellular diversity of the brain and cell-cell connectivity and support, the probability of non-neuronal cell types' contribution to PD became apparent. Only recently has the scientific focus been broadened to different cell types and brain regions other than DaNs in the SN.

1.3.1 Microglia and Parkinson's disease

Inflammation in the brain is mainly driven by microglia - the resident immune cells of the brain. They are specialised macrophages, which emerge by primitive hematopoiesis in the foetal yolk sack. In the early embryonic stages, they migrate to the central nervous system, where they reside permanently. In the developing brain, microglia govern the removal of stagnating neurons (Witting *et al.*, 2000). Moreover, they provide support and help with neuronal maturation and pruning. Various studies indicate the importance of microglia-secreted trophic factors for the control of neuronal precursor survival (Cunningham, Martínez-Cerdeño and Noctor, 2013; Ueno *et al.*, 2013; Tronnes *et al.*, 2016; Kierdorf and Prinz, 2017). Such microglia soluble products are, in addition, essential for the support of angiogenesis and the direction of vessel sprouting in the developing brain (Rymo *et al.*, 2011). *In vivo* experiments showed reduced vascularisation upon microglia depletion (Checchin *et al.*, 2006; Kubota *et al.*, 2009; Fantin *et al.*, 2010).

Similar to their importance for the developing brain, microglia also play an essential role in the adult brain by maintaining synaptic plasticity associated with learning (Biber

et al., 2007; Parkhurst *et al.*, 2013). In the adult brain, the microglia population size is constant and regulated by continuous apoptosis and proliferation (Bruttger *et al.*, 2015; Askew *et al.*, 2017; Tay *et al.*, 2017). Their cellular morphology is ramified, which is due to the outspreading of cellular processes that actively inspect the surroundings in the brain parenchyma (Nimmerjahn, Kirchhoff and Helmchen, 2005). Thus, microglia can sense the presence of any pathogen or a dying brain cell and initiate their phagocytosis and clearance, providing immune protection for the brain (Green, Oguin and Martinez, 2016; Wolf, Boddeke and Kettenmann, 2017).

However, the benefit of the immune processes in the brain can be deceptive. Contrary to immunoprotective roles, they can also promote cytotoxicity and neurodegeneration. It is recognised that the inflammation that occurs in neurodegenerative diseases is not only a mere coincidence of the disease, but has a much greater role in the disease progression. Upon ageing and constant exposure to stressors, especially in a disease like PD, microglia can develop a chronic inflammatory state defined by a dysbalance in pro- and anti-inflammatory activity, and undergo different structural and functional changes to promote neuropathologic processes. The first described characteristic of reactive microglia in the PD patient postmortem SN was a change in their morphology (McGeer *et al.*, 1988). When stimulated, microglia retract their processes to acquire an amoeboid morphology and are characterised by the expression of major histocompatibility class II (MHC-II) proteins important in immune signalling (McGeer *et al.*, 1988). Moreover, reactive microglia secrete pro-inflammatory cytokines, such as IL1ß, IL6 or TNFα, which are detrimental to neurons (Wang *et al.*, 2014; Cheng *et al.*, 2020; Badanjak *et al.*, 2021; de Araújo *et al.*, 2021).

These functional changes are triggered through microglia receptors. Microglia express pattern-recognition receptors (PRRs), which sense the presence of pathogen-associated molecular patterns (PAMPs) from microorganisms, or damage-associated molecular patterns (DAMPs) found as misfolded and aggregated proteins or nucleic acids (Wolf, Boddeke and Kettenmann, 2017). Once activated, these receptors can trigger a signalling cascade and the transcription of genes involved in inflammatory pathways (Lu *et al.*,

2018).

1.3.2 Neuromelanin and Parkinson's disease

A candidate that may contribute to microgliosis in PD is neuromelanin (NM). A reduction in the amount of NM pigment from the SN is the first apparent pathological hallmark associated with PD, described almost a hundred years ago (Foix *et al.*, 1925). More than a decade later, it was shown that the loss of pigmented neurons in the SN starts in the ventral zone and spreads dorsally (Hassler, 1938). Although the loss of NM has been the pioneering association with PD, there has not been much interest into its role, specifically in the context of PD.

The dark-colored brain pigment NM is the most apparent in the catecholaminergic neurons of the SN and the *locus coeruleus*, causing a noticeably darker appearance of these regions. NM contains a dense pheomelanin core surrounded by eumelanin, a protein matrix and lipid droplets (Zecca *et al.*, 2008). NM is absent at birth, but builds up through life and is first visible at the age of three (Fenichel and Bazelon, 1968). Nonetheless, the function and the origin of NM are baffling. Melanic pigments in the human body are formed through well-described enzymatic actions that involve tyrosinase. However, the biosynthesis of NM, whether it is formed through enzymatic or non-enzymatic processes, has long been debated. Currently, the commonly accepted hypothesis suggests that NM is a byproduct of DA oxidation (Zucca *et al.*, 2004, 2018; Fedorow *et al.*, 2006; Vila, 2019). Tyrosine hydroxylase (TH), a rate-limiting enzyme in DA production, converts the amino-acid tyrosine to L-dopa (Nagatsu, Levitt and Udenfriend, 1964). The DA-precursor L-dopa is then further metabolised to DA by aromatic amino acid decarboxylase (AADC) (Nagatsu, Levitt and Udenfriend, 1964). DaNs accumulate and package cytosolic DA together with recycled DA from the extracellular space. The excessive amounts of DA that are not packaged into vesicles are thought to later be oxidised to dopaquinone (Zucca *et al.*, 2018). Dopaquinone can be trapped by the cysteine residues of the polypeptide chains, thus forming cysteinyl-DA, a precursor

to NM pigment biosynthesis (Rosengren, Linder-Eliasson and Carlsson, 1985; Carstam *et al.*, 1991; Zecca *et al.*, 1992). The newly formed NM compound can then bind to aggregated cytosolic proteins and chelate metal ions (Zucca *et al.*, 2018). Such noxious NM material is believed to be engulfed by the double membrane of the phagophore, destined for macroautophagy (Zucca *et al.*, 2018). After fusing with the lysosome, the undegradable NM material can interact and neutralise lysosomal enzymes and activity. This appropriation of a lysosome culminates in the formation of the double membrane-bound NM organelle that, with age, continues to accumulate in the neuronal soma (Zucca *et al.*, 2018). This hypothesis is supported by a few sporadic studies which performed proteomic characterisations of NM granules. These analyses revealed that lysosomal and lysosomal membrane proteins constitute the majority of the protein part of NM (Tribl *et al.*, 2005; Plum *et al.*, 2016; Zucca *et al.*, 2018).

The NM organelle is considered to have an autophagic activity, since it binds drugs, toxins, metal ions or additional oxidised DA and misfolded proteins (Zucca *et al.*, 2018). If left unbound in the cytosol, these substances would have otherwise interfered and burdened the basic cellular processes, ultimately resulting in neuronal death. The ability to capture and retain these intruding molecules implicates a neuroprotective role for NM.

However, the pigmented DaNs in PD are more susceptible to degeneration than non-pigmented DaNs (Zecca *et al.*, 2003; Zucca *et al.*, 2017). In addition, the death of a neuron is directly linked to the amount of NM, where the darker-pigmented ones are most sensitive (Kastner *et al.*, 1992). A-syn-containing somatic inclusions appearing in PD DaNs, termed Lewy bodies (LBs), are usually formed in close proximity to NM accumulation (Braak and Del Tredici, 2011). Moreover, human brain studies showed that a-syn is sequestered and captured within NM during the early stages of PD (Fasano *et al.*, 2003; Halliday *et al.*, 2005).

Despite this intimate connection between PD pathogenesis and NM, NM has been surprisingly overlooked in the scientific community.

1.3.3 Neuromelanin and microglia interplay

Studies have shown that neuroinflammatory changes, such as microgliosis, occur in highly-melanized SN areas rather than in regions with lower pigmentation (Braak *et al.*, 2003). With the continuous death of DaNs in PD, NM content is released extracellularly (Zhang *et al.*, 2011, 2013; Viceconte *et al.*, 2015). Hence, all the life-long bound substances within the NM granule become exposed to the surrounding cells in the brain parenchyma. This sudden overload of detrimental molecules can be a trigger for microgliosis, and with progressive neuronal demise, this process becomes chronic (Zhang *et al.*, 2011, 2013; Viceconte *et al.*, 2015).

Analysis of rat mesencephalic cultures (including neurons, micro- and astroglia) after the exposure to human NM showed that NM has little to no impact on DaNs alone; contrarily, a significant neurotoxic effect of NM was demonstrated only in the presence of microglia (Zhang *et al.*, 2013). Multiple experiments in animals show that NM stimulates pro-inflammatory function and reactive morphology in microglia (Zhang *et al.*, 2011, 2013; Viceconte *et al.*, 2015; Carballo-Carbajal *et al.*, 2019; Vila, 2019). Upon NM exposure, microglia start to secrete cytokines like IL1ß, TNFα, IL6 and iNOS, and neurotoxic factors such as superoxide, nitric oxide and hydrogen peroxide (Zhang *et al.*, 2011). In addition, newborn rat microglia effectively phagocytosed and degraded NM particles *in vitro*. However, PD patient microglia are much more aged compared to those of young rats. Therefore, when rat microglia cultures were 'aged' for one month *in vitro* (microglia cultures were cultivated for a month prior to treatment), they could still rapidly engulf NM, but not degrade it (Zhang *et al.*, 2011).

Accordingly, *in vivo* study in rats showed phagocytic properties of microglia over NM aggregates, and that such NM-laden microglia tend to accumulate in perivascular areas (Carballo-Carbajal *et al.*, 2019). This migration towards the blood vessels might imply a clearance of excess NM from the brain through the bloodstream. In the adult human SN, microglia were found to surround and phagocytose extra-neuronal NM for degradation (Depboylu *et al.*, 2011). However, no evidence of complete degradation was reported to

date. Due to improper clearance, NM remains longer in the brain parenchyma, further increasing inflammation, and as a consequence, neurodegeneration (Depboylu *et al.*, 2011; Zhang *et al.*, 2013).

1.4 Parkinson's disease (neuromelanin) models

Current knowledge of pathological changes in PD largely emerges from experimental models such as cell cultures and animal models. However, these models do not recapitulate the complexity, nor the cellular diversity of the human brain (Fig. 1.2). With the advancement of induced pluripotent stem cell (iPSC) technology, various PD cellular models have emerged.

On the one hand, cultured 2D and 3D cells offer the advantages of having a patient-derived model, the ability to understand disease progression and to develop and test potential treatment options. However, these models limit the meticulous disease pathology, thus requiring targeting of specific known disease elements, while neglecting others. Even the multicellular 3D models fail to recapitulate the entire spectrum and distribution of brain cells. In addition, cell cultures are usually treated with exogenous stimulants, such as levodopa to induce NM production (Zecca *et al.*, 2001). However, this induced NM is rather innocuous since it does not contain proteinaceous or lipid parts as the adult human NM.

On the other hand, IPD animal models like monkeys, rats and mice, despite a more intricate structure and dynamics, are mostly toxin-induced (Blesa and Przedborski, 2014; Jagmag *et al.*, 2015). Most commonly used neurotoxins like rotenone, paraquat, 1-methyl-4-phenyl-1,2,3,6-tetrahydropyridine (MPTP) or 6-hydroxydopamine (6-OHDA), have similar effects (Bové *et al.*, 2005; El-Gamal *et al.*, 2021); they act by causing lesions in nigrostriatal DA neurons, mitochondrial dysfunction, ROS production or proteasome disturbances (El-Gamal *et al.*, 2021). However, these toxins act acutely, causing severe effects in a short period of time. Therefore, the slow years-long progression of PD is

not replicated. The animals neither exhibit typical LB pathology nor do they grasp the diversity of motor and non-motor symptoms (El-Gamal *et al.*, 2021).

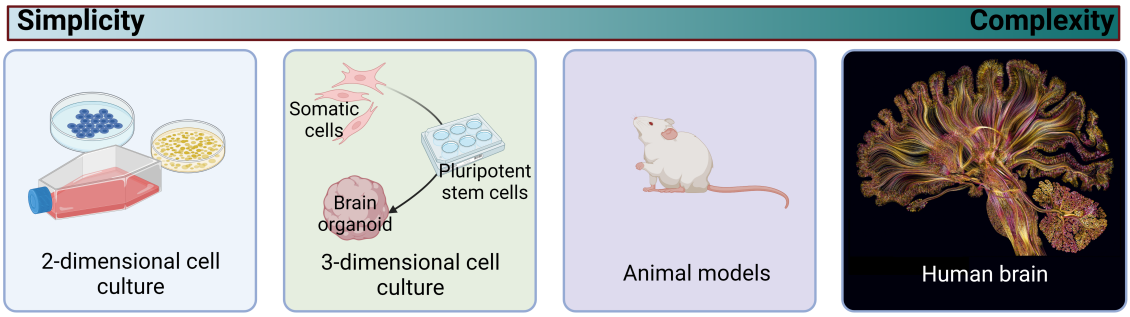

Figure 1.2: Parkinson's disease models ordered by complexity from left to right: simple 2D cultures, to the most complex human brain (Human brain drawing: *"Self Reflected"* by Greg Dunn, 2017, www.gregadunn.com).

More importantly, the high abundance of NM is inherent in humans alone (Zucca *et al.*, 2004). Only a few animal species like monkeys, frogs and dolphins produce NM, although at insignificant levels compared to humans (Kemali and Gioffré, 1985; Herrero *et al.*, 1993; Sacchini *et al.*, 2018; Vila, 2019). In addition, the most commonly used laboratory animal models completely lack the endogenous formation of the dark pigment. Therefore, the *in vivo* examination of the most obvious hallmark of PD, the loss of NM in SN, remains largely impossible. Thus, to elucidate the role of NM in neurodegenerative and neuroinflammatory processes, human postmortem brain samples are indispensable.

In conclusion, to date, there is no model that can fully recapitulate the entire cellular range of the human brain, nor the intricate NM structure and dynamics.

Chapter 2

Aims

Considering recent discoveries that implicate multiple cell types in PD pathology, it is important to investigate the underlying changes in these cells more thoroughly. Extending the focus to cells other than neurons would result in greater understanding of cellular mechanisms and processes that lead to neuronal demise.

One such process is neuroinflammation, which increasingly gains importance amongst the central mechanisms of PD. An obvious candidate for triggering inflammation in SN is NM released from dying neurons. NM contains years-long accumulation of toxic materials such as undegraded proteins, chemicals and lipids which, if left exposed in the brain, can be detrimental. The understanding of aforementioned processes could potentially serve as a starting point for novel (non-neuronal) therapeutic targets.

To address these questions, a multilevel approach was established:

- we used single-nuclei RNA-sequencing (snRNAseq) to unravel two major points:
  - identifying different cell types of the midbrain and understanding the disease-driven differences in their distribution
  - elucidation of PD-dependent perturbations in gene expression in each of the cell types
- we used immunohistochemistry labelling:
  - to store the findings into spatial context and
  - to elucidate the connection between NM and microgliosis

- we used laser-capture microdissection (LCM) to dissect the midbrain tissue:
  - to investigate the relation of microglial markers and NM

Chapter 3

Results

3.1 Manuscript I

Single-cell sequencing of human midbrain reveals glial activation and a Parkinson-specific neuronal state

Semra Smajić[1$], Cesar A. Prada-Medina[2$], Zied Landoulsi[1], Jenny Ghelfi[1], Sylvie Delcambre[1], Carola Dietrich[2], Javier Jarazo[1,7], Jana Henck[2], Saranya Balachandran[8], Sinthuja Pachchek[1], Christopher M. Morris[4], Paul Antony[1], Bernd Timmermann[2], Sascha Sauer[6], Sandro L. Pereira[1], Jens C. Schwamborn[1,7], Patrick May[1], Anne Grünewald[1,3,#,*], Malte Spielmann[2,5,8,#,*]

$These two authors share first-authorship.

#These two authors share last-authorship.

*Corresponding authors

Author affiliations:

[1]Luxembourg Centre for Systems Biomedicine, University of Luxembourg, Esch-sur-Alzette, Luxembourg

[2]Max Planck Institute for Molecular Genetics, Berlin, Germany

[3]Institute of Neurogenetics, University of Lübeck, Lübeck, Germany

[4]Newcastle Brain Tissue Resource, Translational and Clinical Research Institute, Faculty of Medical Sciences, Newcastle University, Newcastle upon Tyne, United Kingdom

[5]Institute of Human Genetics, University of Lübeck, Lübeck, Germany

[6]Max-Delbrück-Centrum für Molekulare Medizin, Genomics Group, Berlin, Germany

[7]OrganoTherapeutics SARL-S, Esch-sur-Alzette, Luxembourg

[8]Institute of Human Genetics, Kiel University, Kiel, Germany

This article has been published in the *Brain* journal.

3.1.1 Preface

Until recently, PD has been studied mainly in dopamine-producing neurons of the substantia nigra. Thus, the current scientific understanding of the aetiology, pathogenesis, resulting symptoms or potential therapeutic treatments is predominantly associated with DaNs. Therefore, the contribution of different cell types of the brain to the PD pathology is underexplored.

Here, we utilised single-cell transcriptomics to obtain the first snRNAseq dataset from postmortem human midbrain tissue of PD patients and healthy individuals. We identified the cell type distribution differences specific to IPD. Moreover, we identified the dysregulated gene expression in each of the main cell types in the midbrain of IPD individuals. We associated the risk genes to cell types, discovering that microglia have the most significant association with PD-risk genes. We also uncovered an IPD-specific neuronal cluster marked by high levels of *CADPS2* expression.

In this study, I developed a protocol for nuclei extraction for snRNAseq from frozen brain tissue sections with fluorescence-activated cell sorting (FACS-sorting). My contribution further includes experimental procedures regarding the processing of frozen (nuclei extraction, FACS-sorting, and initial steps of 10X library preparation, LCM, RNA extraction and cDNA preparation) and FFPE human postmortem midbrain samples (immunohistochemical staining, image acquisition) for sequencing and imaging. Moreover, I participated in sequencing and imaging data analysis and the preparation of the figures, tables and supplementary files. Lastly, I wrote the first draft of the manuscript and contributed to the editing of the draft throughout the review process.

3.1.2 Manuscript

https://doi.org/10.1093/brain/awab446 BRAIN 2022: 145; 964–978 | 964

BRAIN
ORIGINAL ARTICLE

Single-cell sequencing of human midbrain reveals glial activation and a Parkinson-specific neuronal state

Semra Smajić,[1,†] Cesar A. Prada-Medina,[2,†] Zied Landoulsi,[1] Jenny Ghelfi,[1] Sylvie Delcambre,[1] Carola Dietrich,[2] Javier Jarazo,[1,3] Jana Henck,[2] Saranya Balachandran,[4] Sinthuja Pachchek,[1] Christopher M. Morris,[5] Paul Antony,[1] Bernd Timmermann,[2] Sascha Sauer,[6] Sandro L. Pereira,[1] Jens C. Schwamborn,[1,3] Patrick May,[1] Anne Grünewald[1,7,‡] and Malte Spielmann[2,4,8,‡]

[†,‡]These authors contributed equally to this work.

See Lin and Narendra (https://doi.org/10.1093/brain/awac071) for a scientific commentary on this article.

Idiopathic Parkinson's disease is characterized by a progressive loss of dopaminergic neurons, but the exact disease aetiology remains largely unknown. To date, Parkinson's disease research has mainly focused on nigral dopaminergic neurons, although recent studies suggest disease-related changes also in non-neuronal cells and in midbrain regions beyond the substantia nigra. While there is some evidence for glial involvement in Parkinson's disease, the molecular mechanisms remain poorly understood. The aim of this study was to characterize the contribution of all cell types of the midbrain to Parkinson's disease pathology by single-nuclei RNA sequencing and to assess the cell type-specific risk for Parkinson's disease using the latest genome-wide association study.

We profiled >41 000 single-nuclei transcriptomes of post-mortem midbrain from six idiopathic Parkinson's disease patients and five age-/sex-matched controls. To validate our findings in a spatial context, we utilized immunolabelling of the same tissues. Moreover, we analysed Parkinson's disease-associated risk enrichment in genes with cell type-specific expression patterns. We discovered a neuronal cell cluster characterized by *CADPS2* overexpression and low *TH* levels, which was exclusively present in idiopathic Parkinson's disease midbrains. Validation analyses in laser-microdissected neurons suggest that this cluster represents dysfunctional dopaminergic neurons. With regard to glial cells, we observed an increase in nigral microglia in Parkinson's disease patients. Moreover, nigral idiopathic Parkinson's disease microglia were more amoeboid, indicating an activated state. We also discovered a reduction in idiopathic Parkinson's disease oligodendrocyte numbers with the remaining cells being characterized by a stress-induced upregulation of *S100B*. Parkinson's disease risk variants were associated with glia- and neuron-specific gene expression patterns in idiopathic Parkinson's disease cases. Furthermore, astrocytes and microglia presented idiopathic Parkinson's disease-specific cell proliferation and dysregulation of genes related to unfolded protein response and cytokine signalling. While reactive patient astrocytes showed *CD44* overexpression, idiopathic Parkinson's disease microglia revealed a pro-inflammatory trajectory characterized by elevated levels of *IL1B*, *GPNMB* and *HSP90AA1*.

Taken together, we generated the first single-nuclei RNA sequencing dataset from the idiopathic Parkinson's disease midbrain, which highlights a disease-specific neuronal cell cluster as well as 'pan-glial' activation as a central mechanism in the pathology of the movement disorder. This finding warrants further research into inflammatory signalling and immunomodulatory treatments in Parkinson's disease.

Received June 22, 2021. Revised September 21, 2021. Accepted November 18, 2021. Advance access publication December 17, 2021

1 Luxembourg Centre for Systems Biomedicine, University of Luxembourg, L-4362 Esch-sur-Alzette, Luxembourg
2 Max Planck Institute for Molecular Genetics, D-14195 Berlin, Germany
3 OrganoTherapeutics SARL-S, L-4362 Esch-sur-Alzette, Luxembourg
4 Institute of Human Genetics, Kiel University, D-42118 Kiel, Germany
5 Newcastle Brain Tissue Resource, Translational and Clinical Research Institute, Faculty of Medical Sciences, Newcastle University, NE1 7RU Newcastle upon Tyne, UK
6 Max-Delbrück-Centrum für Molekulare Medizin, Genomics Group, D-13125 Berlin, Germany
7 Institute of Neurogenetics, University of Lübeck, D-23562 Lübeck, Germany
8 Institute of Human Genetics, University of Lübeck, D-23562 Lübeck, Germany

Correspondence to: Malte Spielmann
Institute of Human Genetics
University of Lübeck
Ratzeburger Allee 160
23562 Lübeck, Germany
E-mail: malte.spielmann@uksh.de

Correspondence may also be addressed to: Anne Grünewald
Luxembourg Centre for Systems Biomedicine
University of Luxembourg
6 avenue du Swing
L-4367 Belvaux, Luxembourg
E-mail: anne.gruenewald@uni.lu

Keywords: Parkinson's disease; midbrain substantia nigra; single-cell sequencing; microglia; neuroinflammation

Abbreviations: DaNs = dopaminergic neurons; OPCs = oligodendrocyte precursor cells; SN = substantia nigra; SNP = single nucleotide polymorphism; snRNA-seq = single-nucleus RNA sequencing; UMAP = uniform manifold approximation and projection

Introduction

Parkinson's disease is a neurological disorder that is commonly characterized by a progressive loss of neuromelanin-containing dopaminergic neurons (DaNs) in the substantia nigra (SN).[1,2] Age, genetic and environmental factors contribute to Parkinson's disease pathogenesis, but disease pathology and aetiology remain mostly unknown.[3] Approximately 95% of Parkinson's disease patients do not harbour an interpretable genetic cause; therefore, they are classified as idiopathic Parkinson's disease.[4]

So far Parkinson's disease research has mainly focused on nigral dopaminergic neurons. By contrast, recent studies suggest disease-related changes also in non-neuronal cells and in brain regions beyond the SN. For instance, PET of drug-naive Parkinson's disease patients revealed microglial activation of the entire brain.[5] This finding is supported by histological analyses in post-mortem Parkinson's disease tissue, which indicate microglial activation in the nigra but also in the putamen, hippocampus, and cortex.[6] Reactive microglia can trigger the induction of neurotoxic reactive astrocytes,[7] which, in turn, interfere with oligodendrocyte survival.[8] Accordingly, glial pathology is suspected to drive neuroinflammatory processes throughout the brain, which contribute to neuronal demise in Parkinson's disease.

The current understanding of neuron-glia cellular perturbations in Parkinson's disease relies largely on experimental models that lack adequate representation of the disease complexity. For instance, toxin-induced animal models capture neither the nature of the human brain nor the multifactorial aspect of the disease.[9] Also, induced pluripotent stem cell (iPSC) models derived from idiopathic Parkinson's disease patients lack the complex cellular composition and dynamics found in a human brain. Several transcriptomic studies using human post-mortem midbrain tissue have investigated the transcriptional programs disrupted in idiopathic Parkinson's disease. However, these studies used either bulk RNA-seq approaches on midbrain tissue or on laser capture-microdissected dopaminergic neurons, thereby failing to disentangle cell-type-specific contributions to the disease pathology.[10] The recent development of single-cell sequencing technologies offers the possibility to overcome these challenges. In particular, transcriptional profiling of single cells (scRNA-seq) or nuclei (snRNA-seq) has proved itself to be an effective strategy to obtain a global view of disease-associated changes at an unprecedented resolution.[11] Moreover, this single-cell approach can be linked to known disease-specific genetic variants to reveal disease trait association in specific cell types.

To address the above-described knowledge gaps and technical limitations, we performed snRNA-seq of post-mortem adult human midbrain tissue of idiopathic Parkinson's disease patients and age-matched control subjects. Using this approach, we obtained an unbiased and global view of the cell type composition as well as the transcriptional programmes disrupted in idiopathic Parkinson's disease glia and neurons at single-cell resolution.

Materials and methods

Human brain tissue cryosectioning

Frozen human post-mortem midbrain tissue sections and the associated clinical and neuropathological data were supplied by the Parkinson's UK Brain Bank and the Newcastle Brain Tissue Resource. According to the neuropathological procedure, after removing the brainstem and cerebellum, the brain hemispheres were divided down the midline, with the hemi-midbrain associated

with each hemisphere. The left hemi-midbrain was removed with a transverse section by taking a line from just behind the mammillary body through the superior colliculus. This midbrain block was then snap-frozen at −120°C and cryosectioned at ∼15 μm thickness in the transverse plane. The resulting sections were stored at −80°C.

Patients and control subjects gave written informed consent with the brain banks, which, together with the ethics review panel of the University of Luxembourg, approved the study.

Sample preparation for nuclei isolation

Six to eight sections were combined from one individual for nuclei isolation. Nuclei were isolated by adapting the published 10X Genomics® protocol for 'Isolation of Nuclei for Single Cell RNA Sequencing'. In brief, the tissue was lysed in a chilled lysis buffer (10 mM Tris-HCl, 10 mM NaCl, 3 mM $MgCl_2$, 0,1% Nonidet™ P40). Then, the suspension was filtered and nuclei were pelleted by centrifugation. Nuclei-pellets were then washed in a 'nuclei wash and resuspension buffer' [1× PBS (phosphate-buffered saline), 1% BSA (bovine serum albumin), 0.2 U/μl RNase inhibitor], filtered, and pelleted again. Nuclei-pellets were suspended in the DAPI solution (1.5 μM DAPI in 1× PBS) and incubated for 5 min prior to FACS sorting. After dissociation, single DAPI-positive nuclei were filtered by size and granularity using a FACSDiva Cell Sorter (BD Biosciences) to minimize the amount of cell debris in the suspension. The resulting nuclei were inspected under the microscope. Only those that appeared intact were considered when adjusting the nuclei concentration prior to loading of the sequencer.

Library preparation and sequencing

Sorted nuclei were processed using the Chromium Next GEM Single Cell 3′ Kit v3.1 to generate the cDNA libraries. The quality of cDNA was assessed using the Agilent 2100 Bioanalyzer System. Sequencing was performed on Illumina NovaSeq 6000-S2.

Transcript quantification and filtering

FASTQ files were generated from the raw base call (BCL) outputs with the Cell Ranger (10× Genomics) *mkfastq* pipeline v.3.0. From this, we obtained a gene-barcode UMI count matrix per sample using the Cell Ranger (10× Genomics) count pipeline v.3.0 using default parameters. The Cell Ranger count pipeline only considers exon-mapping reads during UMI-counting. Also, single-nuclei sequencing readouts are enriched in intronic regions. To account for this, we used the Cell Ranger recommended variation of the human reference transcriptome (hg38), where introns are annotated as exons. The CellRanger pipeline predicted 51 929 barcodes to represent intact single nuclei across all samples, from which 10 494 were filtered out. We retained barcodes with >1500 UMIs and >1000 genes, as well as <10% of mitochondrial-encoded (mtDNA) and <10% of ribosomal gene counts. We only kept genes that were detected in at least three barcodes. Next, we removed ribosomal and mtDNA-encoded genes from the count matrix. We then used Scrublet[12] to identify potential multiplet-barcodes, and only kept barcodes with an estimated doublet score <0.15 for downstream analysis.

Normalization, sample integration and cell clustering

To identify the major cell types comprising the human midbrain, we combined the samples in a single embedding following the Seurat v3[13] CCA integration workflow. First, each sample was normalized using the SCTransform approach.[14] Cell-cycle phase assignment was performed based on this normalized expression matrix. We used the Seurat *CellCycleScoring* function and the Seurat v3 reference genes for the S and G2/M cell-cycle phases. To determine the inter-sample anchors for integration, we used the *FindIntegrationAnchors* Seurat function with the top 4000 consistent highly variable genes across the samples, identified with the *SelectIntegrationFeatures* function. We then used the *IntegrateData* Seurat function to obtain a combined and centred expression matrix. Principal component analysis was carried out on this centred expression matrix. The top 25 principal components were used to build a shared nearest neighbour (SNN) cell graph, which was then clustered using the Louvain algorithm (resolution = 1.5) implemented in the Seurat *FindClusters* function. The top 25 principal components were embedded onto two dimensions using the Uniform Manifold Approximation and Projection (UMAP) algorithm with the number of neighbours set to 30 and a minimum distance set to 0.3 following Seurat3 default implementation.[15] We identified marker genes for each cluster by using the ROC method of the Seurat *FindAllMarkers* function. The top marker genes were used to assign cell type annotations manually for each cell cluster. We compared the cell types by correlating their pseudo bulk profiles. The resulting gene-cell type matrix was normalized (transcript per million) and log2 transformed. The Pearson correlation estimates among the normalized cell type profiles were used as the input distance matrix for hierarchical clustering.

Machine learning cross-validation of cell-type annotation

To quantitatively validate the cell-cluster definition and annotation, we implemented a stratified cross-validation machine learning approach. Briefly, we removed the sample effects on the combined UMI count dataset using Harmony.[16] For normalization, we used the loess transform[17] to fit a smooth curve between mean and variance using the log-transformed data. We then scaled the data with the fitted mean and standard deviation (SD). The identified marker genes (Supplementary Table 3) were selected as the features of the model. We considered each cell type's median cell type to subsample the dataset as a few cell types (DaNs and CADPS2^{high}) were under-represented. To ensure similar label composition in the training and test sets, we split the data using scikit-learn[18] *StratifiedKFold* with 70% of the data as training and 30% as test dataset 5-fold cross-validation. We performed dimensionality reduction with *truncatedSVD* to 30 components. These 30 components were classified based on scikit-multilearn's ensemble classification,[19] which uses Louvain-based clustering[20,21] and a random forest classification to account for the clustered and sparse nature of the snRNA-seq data. The predicted cell types were then compared to the manually curated cell label assignments using a confusion matrix.

Differential cell-type composition

We estimated the differential cell type composition by comparing the UMAP embeddings and the cell type proportions between the idiopathic Parkinson's disease and control samples. We considered the two-dimensional kernel cell density of the idiopathic Parkinson's disease and control cells independently on the first two UMAP components using the *kde2d* function (bins = 100) implemented in the *MASS* R package.[22] The idiopathic Parkinson's

disease log2 differential UMAP density was calculated. Also, for each cell type, we compared the proportion of cells per sample between the idiopathic Parkinson's disease patients and control individuals. We assessed this difference with the Student's *t*-test implemented in the *t.test* function of the R stats package.[23] Furthermore, we used the beta-regression model to estimate the contribution of the sample clinical features [e.g. condition, post-mortem interval (PMI), age] on the cell proportion variation. We modelled the cell type proportion using the *betareg* R package.[24]

Sub-clustering, trajectory reconstruction, and differential gene expression in three glial cell types

We subset cell-type-specific UMI raw counts. To identify the glial subpopulations, we integrated cells from different samples following the Seurat3 reciprocal principal component analysis based protocol considering the top 1000 highly variable genes for astrocytes and oligodendrocytes and the top 500 highly variable genes for microglia. Then we used the unsupervised and network-based Louvain clustering approach based on the top 25 principal components of the integrated datasets. Marker genes were defined as described before. We reconstructed the cellular activation trajectories following the *monocle3* approach. Briefly, cells from different samples were integrated, and factor size normalized. The sample effect was removed using the Mutual Nearest Neighbor method.[25] Then the highly variable genes defined before were embedded in the first 25 principal components used for dimensionality reduction and trajectory inference using the DDR algorithm implemented in the *learn_graph* function of the *monocle3* R package.[11] Pseudotime ordering was done in a supervised manner by rooting the trajectory in the graph node that maximizes the distance to the known activated cell subpopulation. We identified cell type-specific perturbed genes in idiopathic Parkinson's disease using the Quasi-Poisson generalized linear model implemented in the *fit_models* function of the *monocle3* R package.[11] Idiopathic Parkinson's disease differential expression coefficient with $q < 0.05$ were considered as differentially expressed genes. Highly variable genes associated with the cell trajectories were identified using the spatial correlation analysis Moran's I approach implemented in the *graph_test* function of the *monocle3* R package.[11] Functional enrichment analysis of the differentially perturbed genes was done using Enrichr.[26]

CADPS2 expression validation in dopaminergic neurons

Midbrain tissues on PEN slides were fixed in ice-cold 75% ethanol for 3 min, then in 99% ethanol for 1 min and then air-dried for 5–10 min prior to dissection.[27] From the SN of each sample, 150 neuromelanin-positive neurons were captured with laser-microdissection using the PALM Microbeam (Zeiss) in 20 µl nuclease-free water with 0.2 U/µl RNase inhibitor (Roche). RNA was extracted with the NucleoSpin RNA XS purification kit (Macherey-Nagel) according to the manufacturer's protocol. The reverse-transcription into cDNA was performed with SuperScript III Reverse Transcriptase (ThermoFisher).

The *CADPS2* expression was quantified by means of digital PCR (dPCR) using the QuantStudio™ 3D Digital PCR System (Applied Biosystems). Samples were prepared following the manufacturer's instructions using SYBR™ Green (S5763, Life Technologies) and QuantStudio™ 3D digital Master Mix v2 (A26359, Life Technologies). Primer sequences for CADPS2 are: forward 3′-AAACTCTGTGCCCTGGATGG-5′ and reverse 3′-GACAACACGCC TTCCAACAC-5′. Primer sequences for Actin are: forward 3′-CGA GGACTTTGATTGCACATTGTT-5′ and reverse 3′-TGGGGTGGCTTTT AGGATGG-5′. Samples were loaded on a QuantStudio™ 3D digital PCR Chip v2 using the QuantStudio™ 3D Digital PCR Chip loader. The PCR was then performed on the ProFlex™ 2X Flat PCR System using the following parameters: 95°C for 5 min, 45 cycles of 95°C for 10 s, and 60°C for 10 s, 72°C for 10 s. The chips were read using the QuantStudio™ 3D Digital PCR instrument and the data were analysed using the QuantStudio™ 3D AnalysisSuite, version 3.1.6-PRC-build18.

Multi-fluorescence immunolabelling of the tissue

Paraffin-embedded PFA-fixed midbrain sections were deparaffinized by incubation at 60°C for 30 min. This was followed by washing with Histoclear (2 × 5 min) and ethanol gradient series (100%, 100%, 95%, 70% vol/vol, 5 min each), and finally in distilled water for 10 min. Antigen retrieval was performed in 1 mM EDTA, pH = 8, in a pressure cooker for 40 min. Next, the slides were washed in distilled water and 1% TBST and blocked with 10% NGS in 1% TBST for 1 h. The sections were then incubated in the primary antibody (anti-tyrosine hydroxylase MAB318, 1:100, Millipore; anti-myelin PLP, 1:100, Abcam; anti-IBA1 019-19741, 1:500, FUJIFILM Wako; anti-GFAP ab7260, 1:100, Abcam), diluted to a working concentration in 1% NGS in 0.1% TBST, at 4°C overnight. This was followed by washing 3 × 5 min in 1% TBST. Then, the midbrain sections were incubated with a secondary antibody (goat anti-mouse IgG1 Alexa Fluor 647, A21240; goat anti-mouse IgG2a Alexa Fluor 546, A-21133; goat anti-rabbit IgG Alexa Fluor 488, A-27034), diluted to a working concentration of 1:100 in 1% NGS in 0.1% TBST, for 1 h. Sections were rewashed 3 × 5 min in 1% TBST and incubated in Sudan black solution for 2 min. This was followed by three washes in 1% TBST and mounting in ProLong Gold mounting medium.

Automated image analysis

Immunofluorescence images of human post-mortem midbrain sections were acquired with Carl Zeiss Axio Observer Inverted Microscope Z1 with 20× objective and analysed in MATLAB (Version 2019B, Mathworks). Automated in-house developed image analysis algorithms segmented the fluorescent cell areas (neurons, astrocytes, microglia, oligodendrocyte) extracting features such as area and perimeter. The segmentation of dopaminergic neurons was computed by convolving the raw TH channel with a Gaussian filter. TH-positive cell areas were detected by setting a pixel threshold followed by *bwareaopen* to remove small connected components to generate a TH area mask. The neuromelanin mask was computed by identifying areas below the selected pixel threshold and subtracting the small connected components with *bwareaopen*. The segmentation of astrocytes and microglia was calculated by selecting a pixel threshold, followed by an *imfill* filter to generate the cell area masks for GFAP or IBA1, respectively. Further, the skeleton of the IBA1 mask was generated with a thinning function to identify the branching of the mask. Because of the massive oligodendrocyte population, we generated the mask by selecting a pixel threshold to identify all the PLP1 positive areas without segmentation. The mean area of each individual was calculated, and the groups were compared with an unpaired *t*-test. The results were visualized with ggplot2 in R 4.0.0.

Genotyping of Parkinson's disease cases using NeuroChip

DNA samples from all idiopathic Parkinson's disease cases underwent genotyping at the Institute of Human Genetics at the Helmholtz Zentrum München using the Illumina (San Diego, CA) NeuroChip.[28] Standard genotype data quality control (QC) steps were carried out.[29] Single nucleotide polymorphism (SNP) imputation was carried out on our NeuroChip data using the Michigan Imputation Server[30] to produce a final list of common (minor allele frequency ≥1%) variants for further analyses. Imputed SNP positions were based on Genome Reference Consortium Human 37/human genome version 19 (GRCh37/hg19). All cases were screened for disease-associated variants in known major Parkinson's disease genes (*SNCA*, *LRRK2*, *DJ-1*, *PRKN*, *GBA*, *PINK1*, *ATP13A2*, *VPS35*, *MAPT*, *DCTN1*, *DNAJC6*, *SYNJ1*, *VPS13C* and *MAPT*) covered by the NeuroChip.

Cell type association with genetic risk of Parkinson's disease

Association analysis of cell type-specific expressed genes with genetic risk of Parkinson's disease was performed using Multi-marker Analysis of GenoMic Annotation (MAGMA) v1.08, to identify idiopathic Parkinson's disease-relevant cell types in the midbrain. MAGMA is a gene-set enrichment analysis method that tests the joint association of all risk SNPs in a gene with the phenotype while accounting for the linkage disequilibrium (LD) structure between SNPs.[31] In our study, the SNPs and their *P*-values were taken from the summary statistics of the Parkinson's disease genome-wide association study (GWAS) from Nalls *et al.*[32] (excluding 23andMe). The publicly available European subset of 1000 Genomes Phase 3 was used as a reference panel to estimate LD between SNPs. MAGMA analysis consists of three steps. First, the annotation step, where SNPs were mapped to genes using the NCBI GRCh37 build (annotation release 105). Gene boundaries were defined as the transcribed region of each gene. An extended window of 35 kb upstream and 10 kb downstream of each gene was added to the gene boundaries.[33] Second, the gene analysis step computes gene-wise *P*-values based on SNP GWAS *P*-values. The third step is the competitive gene-set analysis implemented as a linear regression model on a gene-set data matrix. The gene-sets used here are the differentially expressed genes in every cell type or the cell-type-specific expressed genes [filtered for false discovery rate (FDR)-corrected *P*-values < 0.05, percentage of cells of the cluster where the expression was detected >0.5, and logFC > 0.25]. MAGMA gene-set analysis provides association results for every gene-set and for every gene in the gene-sets. The association of a gene with a cell type is quantified as a z-score. Z-scores will be close to zero if a gene is not differentially expressed, while high positive z-scores indicate most differentially expressed genes.

Data availability

Raw snRNA-seq data for the 11 samples presented in this study are available in the Gene Expression Omnibus (GEO) with accession number GSE157783. Imaging data are available upon request.

Results

We sampled adult human post-mortem midbrain tissue from five idiopathic Parkinson's disease cases, for which pathology reports described a severe neuronal loss in the SN without a family history of Parkinson's disease (Supplementary Table 1). We confirmed the idiopathic nature by SNP-Chip profiling of 179 467 known variants associated with neurological diseases, including Parkinson's disease,[34] which did not reveal a genetic aetiology (Supplementary Table 2). We sampled six control midbrains to match the idiopathic Parkinson's disease patient characteristics. The average age of idiopathic Parkinson's disease patients and control individuals were ∼77 [standard error of the mean (SEM = 3)] and ∼81 (SEM = 4) years, respectively, and both groups had similar post-mortem intervals (idiopathic Parkinson's disease ∼22 and controls ∼16 h) (Supplementary Table 1).

We sequenced single nuclei from frozen ventral sections of human post-mortem midbrains (Fig. 1A) and obtained ∼2000–6000 high-quality nuclei per sample with an average of ∼7600 transcripts and ∼2700 genes per nucleus after filtering out poorly sequenced nuclei and potential doublets (Fig. 1B). This dataset comprised 22 433 and 19 002 single nuclei from control individuals and patients with idiopathic Parkinson's disease, respectively (Fig. 1C).

We embedded the 41 435 nuclei transcriptomes into two dimensions using the UMAP algorithm. We found that the overall cluster structure was mostly driven by cell-type identity and inter-sample variability (Supplementary Fig. 1A and B). Of note, patient and control cells gathered together within the major cell clusters (Supplementary Fig. 1B). To account for this inter-individual variation during the cell-type identification, we followed the Seurat3 sample integration protocol (see 'Materials and methods' section) (Fig. 1D). Using this corrected principal component analysis embedding and the unsupervised, network-based Louvain clustering approach, we found that the human midbrain comprised 12 major cell types (Fig. 1D and E and Supplementary Fig. 1C).

The studied human midbrain tissue was composed of glial, neuronal, and vascular cells (Fig. 1D and E). We annotated most cell clusters by manually comparing well-known marker genes in the literature and the identified marker genes of each unsupervised cell cluster (Supplementary Fig. 1C–I and Supplementary Table 3). Oligodendrocytes, the most abundant cell type in the midbrain (Fig. 1F), were characterized by the expression of *MOBP*.[35] Oligodendrocyte precursor cells (OPCs) highly express *VCAN*.[36] Expression of *AQP4* was characteristic for astrocytes[37] and *FOXJ1* for ependymal cells (Fig. 1E–G and Supplementary Fig. 1C–I).[38] Also, immune and vascular cells displayed a highly specific expression of well-known marker genes; *CD74* in microglia,[39] *CLDN5* in endothelial cells,[40,41] and *GFRB* in pericytes[42] (Fig. 1E–G and Supplementary Fig. 1C). Regarding neuronal cells, we identified four cell types: excitatory (*SLC17A6*),[43] inhibitory (*GAD2*),[43] GABAergic (*GAD2*/*GRIK1*)[44,45] and, dopaminergic neurons (*TH*) (Fig. 1E–G and Supplementary Fig. 1C–I).[46]

A closer look at the number of profiled nuclei indicated that DaNs only comprised 0.18% of the total cell count limiting the comparison between the idiopathic Parkinson's disease and control DaNs (Fig. 1F). Therefore, we performed quantitative immunofluorescence imaging analysis of TH- or neuromelanin-positive cells in idiopathic Parkinson's disease and control tissues and confirmed a significant reduction in TH- or neuromelanin-positive nigral DaNs in the idiopathic Parkinson's disease midbrains compared to controls (Supplementary Fig. 2A–D).

Interestingly, we also found a neuronal cluster of 120 cells, which we could not annotate initially based on known marker genes, that was characterized by high expression of *CADPS2* (CADPS2^{high} cells) (Fig. 1E–F and H–I and Supplementary Fig. 1C and I). These cells almost exclusively originated from idiopathic

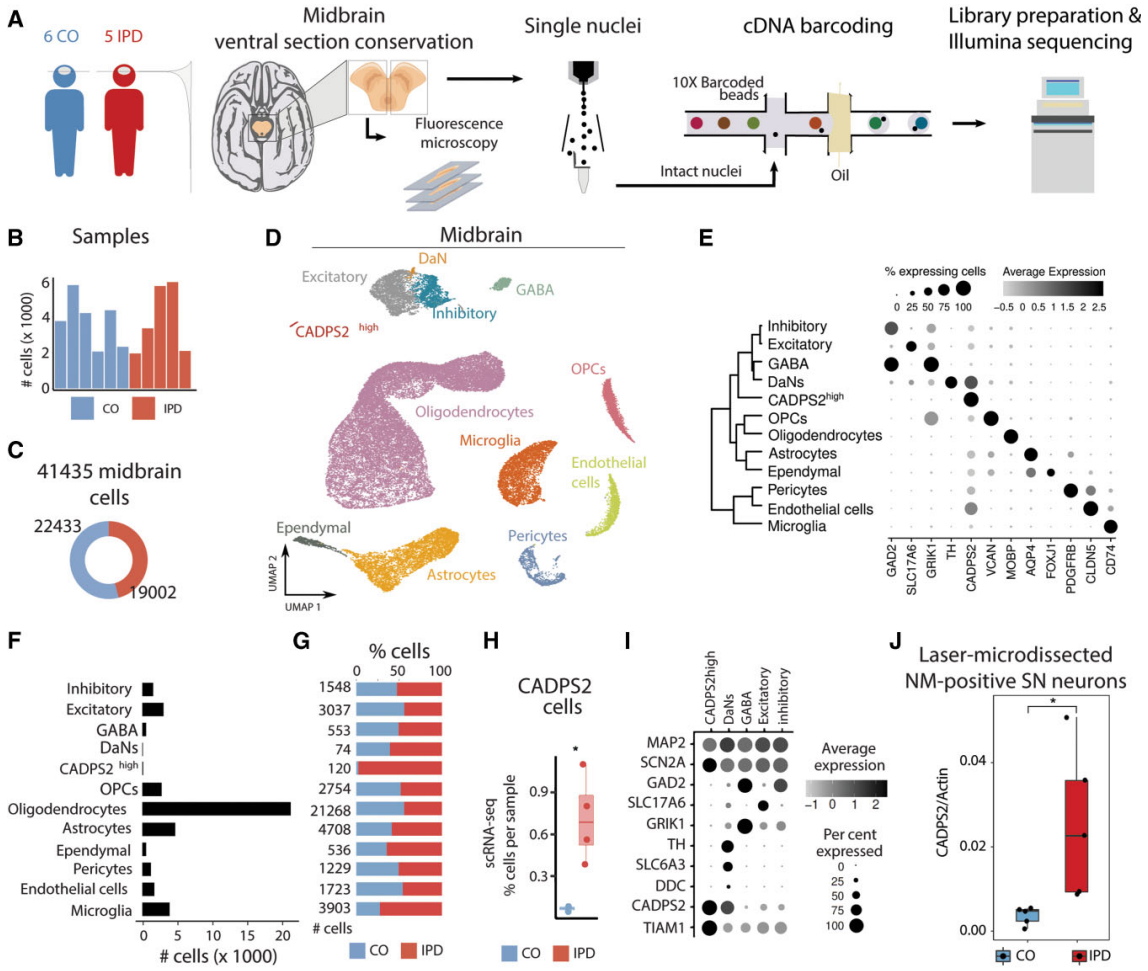

Figure 1 Cell type composition of human midbrain. (**A**) The experimental approach to midbrain tissue processing and nuclei extraction. Nuclei suspensions were processed with the 10× Genomics platform and sequenced with an Illumina sequencer. (**B**) Contribution of nuclei from idiopathic Parkinson's disease (IPD) patients or controls to each cell type. (**C**) The number of high-quality nuclei per sample. Overall, the population consists of 19 002 nuclei from idiopathic Parkinson's disease patients and 22 433 nuclei from controls. (**D**) UMAP embedding of the 41 435 human midbrain nuclei. Cells are coloured by cell type. (**E**) Cell type transcriptome similarity and representative marker genes. CADPS2^{high} cells cluster together with the neuronal cells. (**F**) The number of profiled nuclei per cell type. (**G**) The proportion of idiopathic Parkinson's disease and control profiled cells per cell type. (**H**) CADPS2^{high} cell proportion per sample, (*t*-test $P = 0.02$). (**I**) CADPS2^{high} cells are neurons. They express *MAP2*, *SCN2A*, and *TIAM1*, but have low levels of *TH*. (**J**) Digital PCR reveals significantly higher expression of *CADPS2* in neuromelanin-positive nigral neurons ($n = 150$ per person) dissected from idiopathic Parkinson's disease midbrain sections compared to those isolated from control tissue (*t*-test $P = 0.027$).

Parkinson's disease patients (idiopathic Parkinson's disease, 98.4%; control, 1.6%) (Fig. 1G). Quantitative assessment of the cell annotation assignment validated our cell-type annotation (Supplementary Fig. 1D). With regard to neuronal markers, these cells show a similar profile to DaNs, except for low *TH* abundance (Fig. 1I). Moreover, CADPS2^{high} cells express even higher levels of *TIAM1* than DaNs (Fig. 1I). TIAM1 has been identified as a regulator of the Wnt/Dvl/Rac1 pathway, which controls midbrain DaN differentiation.[47,48] Thus, we hypothesized that CADPS2^{high} cells might constitute degenerating DaNs.

In order to test this hypothesis, we applied laser-capture microdissection (LCM) to frozen midbrain sections from additional idiopathic Parkinson's disease patients and aged control subjects. Our 'validation cohort' included C1 and IPD4 from the original 'snRNA-seq cohort' as well as sections from four previously unstudied cases and four new controls (Supplementary Table 1). From each individual, we isolated 150 neuromelanin-containing neurons that were subjected to *CADPS2* gene expression analysis by means of digital PCR, whereby *Beta-actin* served as a house-keeping gene. This experiment indicated significantly higher *CADPS2*:*Beta-actin* ratios in idiopathic Parkinson's disease compared to control DaNs with neuromelanin deposits (Fig. 1J), suggesting that CADPS2^{high} cells are indeed of dopaminergic origin.

Next, we aimed to reveal cell-type composition changes of the midbrain associated with idiopathic Parkinson's disease and followed three approaches. We compared idiopathic Parkinson's disease and control cell density distributions in the 2D UMAP representation (Fig. 2A and B) and analysed the idiopathic

970 | BRAIN 2022: 145; 964–978 S. Smajić et al.

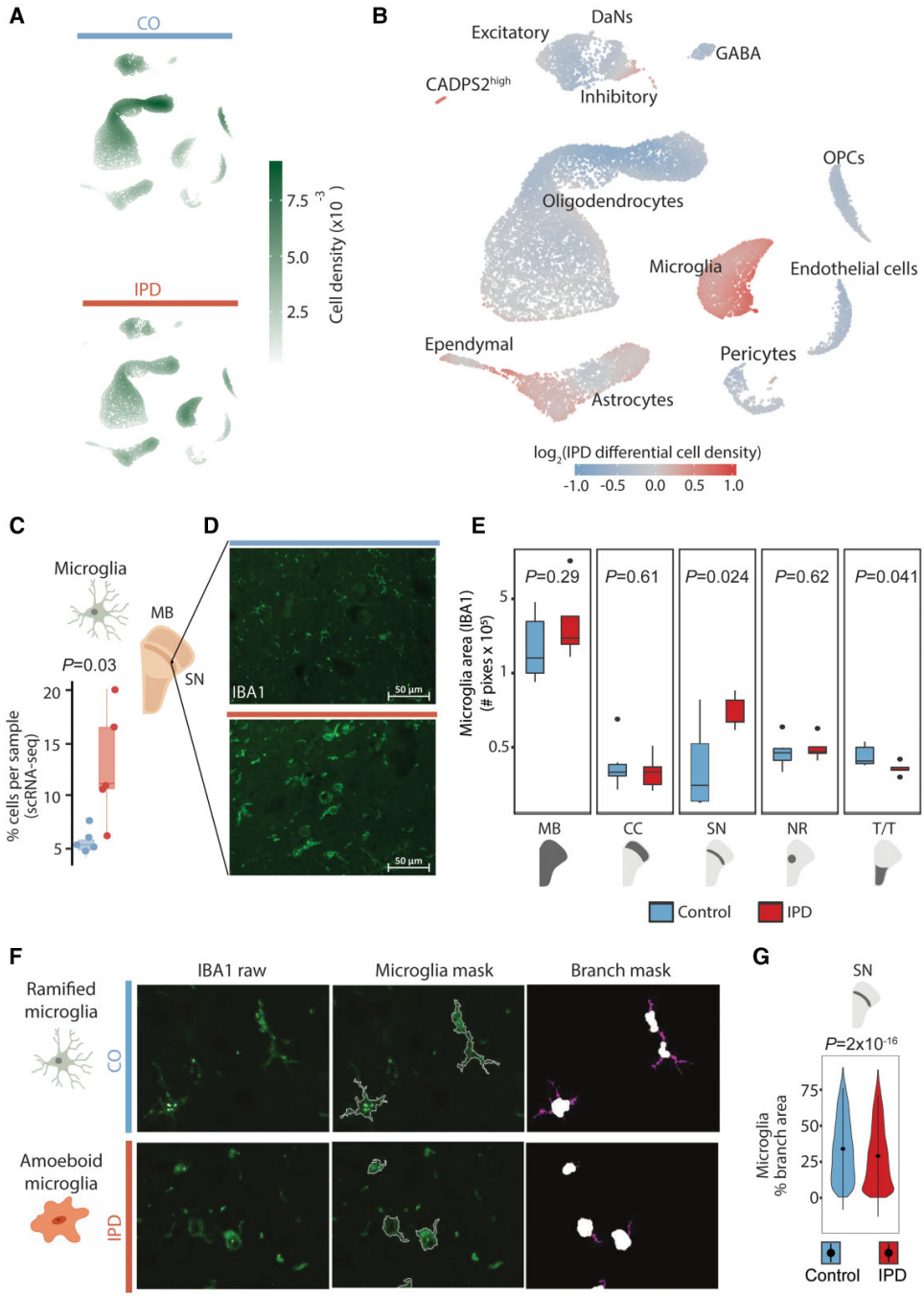

Figure 2 Idiopathic Parkinson's disease (IPD) midbrain is characterized by an increase in microglia. Differential cell type composition in idiopathic Parkinson's disease patients compared to age-matched control subjects. (**A**) Two-dimensional cell density in the first UMAP embeddings of the human midbrain for idiopathic Parkinson's disease patients and control subjects independently. (**B**) Differential 2D cell density in idiopathic Parkinson's disease midbrain. Idiopathic Parkinson's disease midbrain has a larger population of microglia and astrocytes than control midbrain tissue. (**C**) Microglia cell proportion per sample. Idiopathic Parkinson's disease patients display a higher proportion of microglia cells (*t*-test $P = 0.03$). (**D**) IBA1 immunofluorescence in idiopathic Parkinson's disease and control ventral midbrain sections. (**E**) IBA1-positive areas in the entire midbrain and individual regions of 11 individuals. The Parkinson's disease-associated increase of microglia is the most significant in the SN (*t*-test $P = 0.024$). (**F**) Microglia morphology analysis. (**G**) An idiopathic Parkinson's disease-associated reduction of microglia branching indicates less ramified microglia in the SN (*t*-test $P = 2 \times 10^{-16}$), which implies increased cell reactivity. MB = midbrain; PD = Parkinson's disease; NR = nucleus ruber; TT = tectum/tegmentum; CC = crus cerebri. IPD: red bar; control: blue bar; scale bar = 50 µm.

Parkinson's disease and control distributions of the cell type proportions per sample. Altogether, these results revealed an increase in the fraction of microglia and astrocytes and a decreased fraction of oligodendrocytes in idiopathic Parkinson's disease midbrains compared to controls (Fig. 2C, Supplementary Fig. 3A and D and Supplementary Table 6). To validate these results with an independent approach, we examined paraformaldehyde-fixed paraffin-embedded sections from the right hemi-midbrain of the same 11 individuals by performing multi-labelling immunofluorescence analysis.[49] First, we confirmed the increased fraction of microglia in idiopathic Parkinson's disease midbrains by labelling it with an antibody against the marker protein IBA1 (Fig. 2D). Automated image analysis demonstrated an increase in IBA1-positive areas in idiopathic Parkinson's disease midbrain tissue compared to control samples (Fig. 2E and Supplementary Table 7). This microglia increase was the most significant in the SN compared to other midbrain regions (Fig. 2E and Supplementary Table 7). Further image analysis of the microglia cellular shape in the SN of age- and sex-matched idiopathic Parkinson's disease and control cases (Fig. 2F) revealed an idiopathic Parkinson's disease-related decrease in microglial branching, indicating cellular activation (Fig. 2G and Supplementary Table 7).[50] Second, we validated the increased fraction of astrocytes and a decreased fraction of oligodendrocytes in idiopathic Parkinson's disease midbrains. We labelled astrocytes and oligodendrocytes with antibodies against their marker proteins GFAP and PLP1, respectively (Supplementary Fig. 3B and E). We observed a trend towards a higher abundance of GFAP-positive areas throughout all the regions in idiopathic Parkinson's disease midbrain tissue compared to control subjects (Supplementary Fig. 3C, Supplementary Table 7). Moreover, we detected a reduction of PLP1-positive areas in the idiopathic Parkinson's disease midbrain sections compared to controls with the highest significance in the SN (Supplementary Fig. 3F). In contrast, the other midbrain cell types, OPCs, pericytes, ependymal, excitatory, inhibitory, and GABAergic cells, did not display significant deviations associated with idiopathic Parkinson's disease (Supplementary Fig. 4 and Supplementary Table 6).

We also investigated how other clinical characteristics, in addition to the disease status (condition), affect the midbrain cellular composition. For this, we modelled the percentage of each cell type per sample as a function of age, post-mortem interval, and condition. We used beta-regression modelling to estimate the

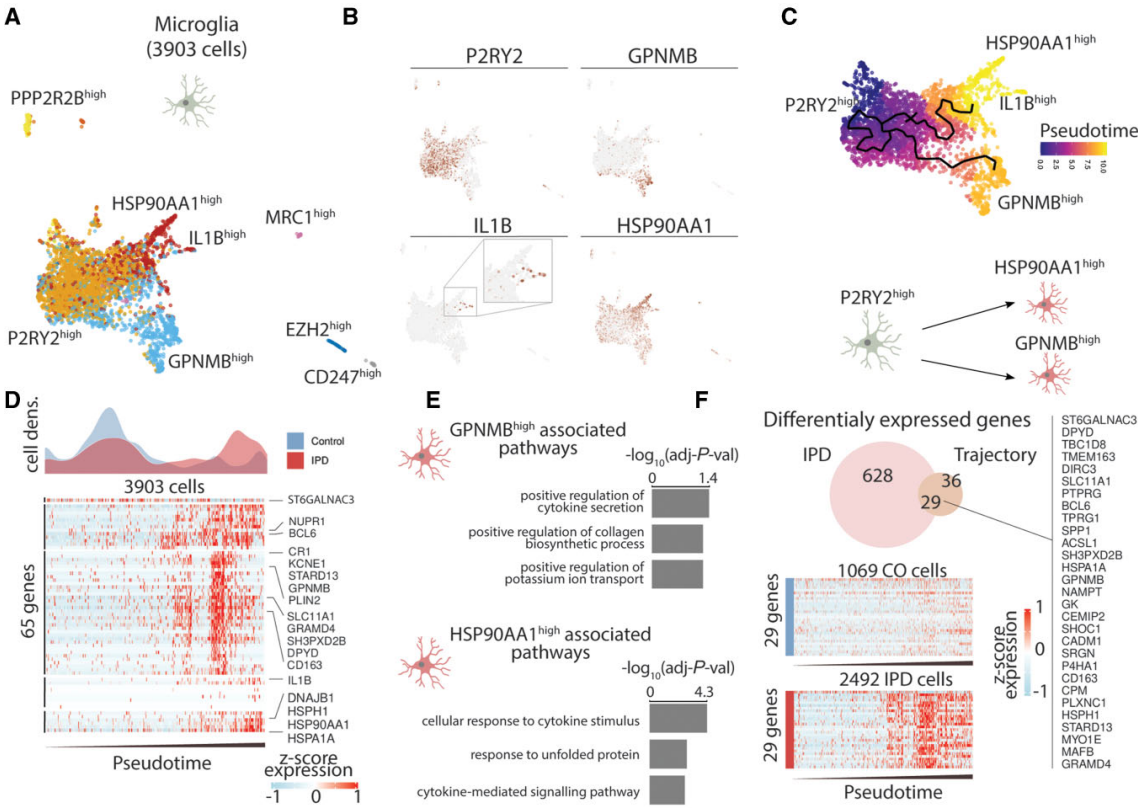

Figure 3 Trajectory reconstruction reveals microglia differential activation in idiopathic Parkinson's disease (IPD). (**A**) Microglia subpopulations labelled with a representative marker gene. (**B**) Expression of *P2RY12*, *GPNMB*, *IL1B* and *HSP90AA1* along the ~4000 microglia cells. These genes are characteristic of the major three microglia subpopulations. (**C**). Trajectory reconstruction and pseudotime representation based on the *P2RY1*^{high}, *GPNMB*^{high}, and *HSP90AA1B*^{high} subpopulations. This reveals a two-branches activation trajectory. (**D**) Differential cell-density distribution along pseudotime for idiopathic Parkinson's disease and control samples. Also, the expression of 65 genes, whose expression is associated with the microglia activation trajectory. *Z*-score normalized expression is presented for each gene over ~4000 microglia cells organized by their pseudotime. (**E**) Gene ontology (GO) molecular function enrichment of the genes associated with the *GPNMB* and *HSP90AA1* activation trajectories. (**F**) Twenty-nine idiopathic Parkinson's disease differentially expressed genes intersect with the differentially expressed genes along the microglia activation trajectory.

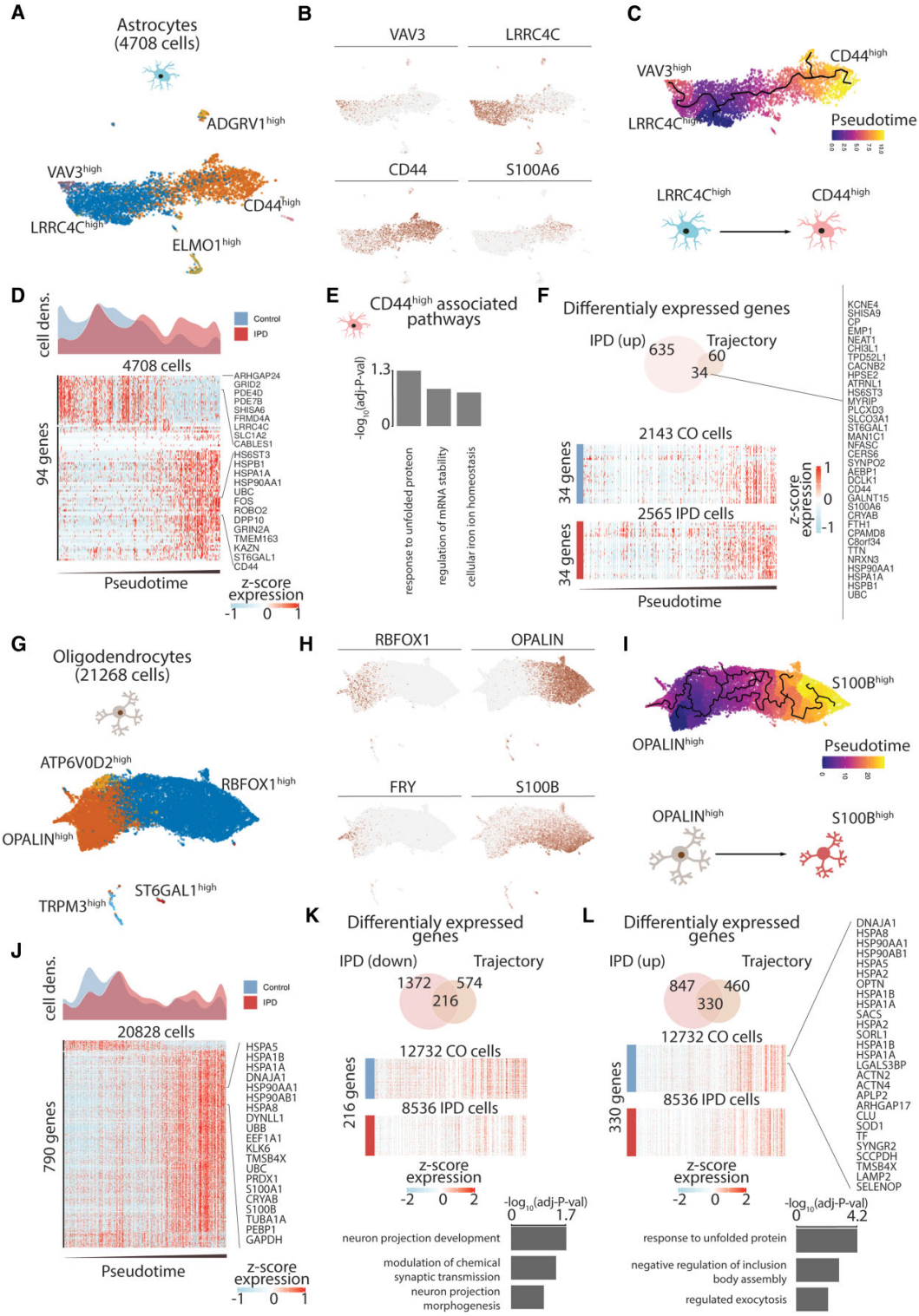

Figure 4 Trajectory reconstruction reveals astrocyte differential activation, loss of myelinating oligodendrocytes, and differential activation in idiopathic Parkinson's disease (IPD).

Continued

coefficients of these clinical features (Supplementary Fig. 5). Condition (idiopathic Parkinson's disease) appeared to be the sample characteristics with the highest impact on the midbrain cellular composition. For instance, the most significant coefficients were the loss of DaNs and the gain of CADPS2^{high} cells associated with idiopathic Parkinson's disease (Supplementary Fig. 5).

To reveal the transcriptional programmes and pathways associated with the increased fraction of microglia and astrocytes in idiopathic Parkinson's disease, we subclustered these cell types to identify glial subpopulations and reconstruct their activation trajectories. We identified seven microglia subpopulations characterized by the expression of a few marker genes (Fig. 3A). The three biggest subpopulations are defined by the high expression of *P2RY12*, *GPNMB*, and *HSP90AA1* (Fig. 3B). Given that these three subpopulations conform to a continuum in the UMAP projection and both *GPNMB* and *HSP90AA1* are microglia activation markers, we estimated a cell trajectory structure comprising these major subpopulations (Fig. 3C). We then organized cells along this trajectory (pseudotime), starting from the trajectory node that maximizes the distance to the *GPNMB* and *HSP70AA1* trajectory branch tips (Fig. 3C). This microglia activation trajectory spans from *P2RY12*^{high} cells towards two activation branches, one containing *GPNMB*^{high} cells and another with cells highly expressing *HSP90AA1* or *IL1B* (Fig. 3C). Idiopathic Parkinson's disease cells differentially distribute along the microglia activation trajectory being enriched towards the activated state compared (Fig. 3D and Supplementary Fig. 6). While P2RY12 is highly abundant in the resting microglia,[51] GPNMB,[52] HSP90,[53] and IL-1β[54] are involved in the inflammatory response and have previously been linked to neurodegeneration[53,55,56] supporting the notion that the idiopathic Parkinson's disease-specific upregulation of *GPNMB* and *HSP90AA1* are markers of microglial activation. To further characterize the molecular phenotype of these two activated microglia states, we identified genes whose expression was associated with the activation trajectory and functionally enriched them to gene-ontology molecular functions (Fig. 3D and E). This analysis revealed that these subpopulations are enriched in cytokine secretion and the stress response to unfolded protein pathways (Fig. 3E). Next, we identified the genes whose expression was differentially upregulated in idiopathic Parkinson's disease microglia across the activation trajectory. We intersected the upregulated genes in idiopathic Parkinson's disease and the activation-trajectory associated genes in microglia and identified 29 genes linked with the differential activation of the midbrain microglia in idiopathic Parkinson's disease (Fig. 3F and Supplementary Table 8), several of which have previously been associated with idiopathic Parkinson's disease.[57–59]

We also characterized the astrocyte and oligodendrocyte subpopulations, reconstructed their activation trajectories, and identified gene signatures associated with idiopathic Parkinson's disease differential activation (Fig. 4). First, we identified five astrocyte subpopulations characterized by high expression of *VAV3*, *LRRC4C*, *ELMO1*, *ADGRV1* and *CD44* (Fig. 4A and B). We recovered the astrocyte activation trajectory based on the main cell types comprising *VAV3*^{high}, *LRRC4C*^{high}, and *CD44/S100A6*^{high} subpopulations (Fig. 4C). Given that *CD44* expression implicates reactive astrogliosis,[60] we ordered cells on the activation trajectory by setting the root in the trajectory graph-node that maximizes the distance from the *CD44*^{high} branch end. These results implied an astrocyte activation transition from *LRRC4C*^{high} to *CD44*^{high} subpopulations (Fig. 4C). Indeed, idiopathic Parkinson's disease astrocytes were highly enriched at the end of the astrogliosis trajectory compared to control astrocytes (Fig. 4D and Supplementary Fig. 6). We further characterized the molecular phenotype of the *CD44*^{high} astrocyte activated state by enriching GO molecular functions to the highly upregulated genes across the astrocytes activation trajectory (Fig. 4D and E). The *CD44*^{high} subpopulation was related to the unfolded protein response (UPR) pathway, which has recently been linked to a specific astrocyte reactivity state that is detrimental to the survival of neurons (Fig. 4E).[61] Next, we calculated idiopathic Parkinson's disease-differentially upregulated genes, which were also highly expressed towards the end of the astrogliosis trajectory (Fig. 4F), and identified 34 genes associated with idiopathic Parkinson's disease differential astrogliosis (Fig. 4F and Supplementary Table 8). These genes include several heat-shock proteins that have previously been shown to co-localize with α-synuclein deposits in the human brain.[62] Similarly, we investigated the oligodendrocyte diversity and reconstructed its differentiation trajectory (Fig. 4G–L). We identified five subpopulations characterized by the expression of *ATP6V02*, *OPALIN*, *TRPM3*, *ST6GAL1*, and *RBFOX1* (Fig. 4G and H). The inferred trajectory based on subpopulations recovered differentiation trajectory spanning from *FRY/OPALIN*^{high} cells towards *RBFOX1/S100B*^{high} cells (Fig. 4H and I). *OPALIN* (also denominated as *Tmem*) is a marker of myelinating oligodendrocytes,[63] while *S100B* has been associated with glial stress response in Parkinson's disease post-mortem midbrain.[64] When comparing idiopathic Parkinson's disease oligodendrocyte density across this trajectory, we found a reduced fraction of myelinating *OPALIN*^{high} cells compared to controls (Fig. 4J and Supplementary Fig. 6). An overlay of the idiopathic Parkinson's disease-differentially expressed genes and of such genes defining the oligodendrocyte trajectory identified 216 and 330 downregulated and upregulated genes across the trajectory. Downregulated genes are associated with neuronal maintaining pathways, while upregulated genes are related to the response to unfolded protein pathways (Fig. 4K and L and Supplementary Table 8). We also investigated the idiopathic Parkinson's disease differential expression

Figure 4 Continued
(**A**) Astroglial subpopulations are named based on characteristic marker genes. (**B**) *VAV3*, *LRRC4C*, *CD44*, and *S100A6* expression across the ∼4700 astrocytes. (**C**) Inferred cell trajectory and pseudotime for the major astrocyte subpopulations, *VAV3*^{high}, *LRRC4C*^{high} and *CD44*^{high} cells. (**D**) Idiopathic Parkinson's disease and control differential cell-density distribution over pseudotime and the expression of the 94 genes highly associated with the astrogliosis trajectory in the ∼4700 astrocytes organized by pseudotime. (**E**) GO molecular function pathway enrichment of the upregulated genes in the *CD44*^{high} activated branch. (**F**) The 34 intersected genes between the upregulated genes in idiopathic Parkinson's disease and across the astrocyte activation trajectory. (**G**) Oligodendrocyte subpopulations are named based on representative marker genes. (**H**) Expression of *OPALIN*, *RBFOX1*, *FRY* and *S100B* in the ∼21 000 oligodendrocytes. (**I**) Inferred cell trajectory and pseudotime ordering of the major oligodendrocytes subpopulations, *OPALIN*^{high}, *ATP6V0D2*^{high}, and *S100B*^{high} cells. (**J**) Idiopathic Parkinson's disease and control differential cell density over pseudotime. Expression levels of 790 highly variable genes across the oligodendrocyte trajectory. Expression is presented for ∼21 000 oligodendrocytes organized by their pseudotime. (**K** and **L**) The intersection of idiopathic Parkinson's disease differentially expressed and trajectory-associated genes. Also, the GO molecular enrichment of the intersected genes is presented. (**K**) Two hundred and sixteen idiopathic Parkinson's disease downregulated genes across the trajectory are associated with pathways important for neuron projection and synaptic transmission. (**L**) Three hundred and thirty genes are idiopathic Parkinson's disease upregulated along the oligodendrocyte trajectory. These genes are mainly associated with the unfolded protein response.

974 | BRAIN 2022: 145; 964–978 S. Smajić et al.

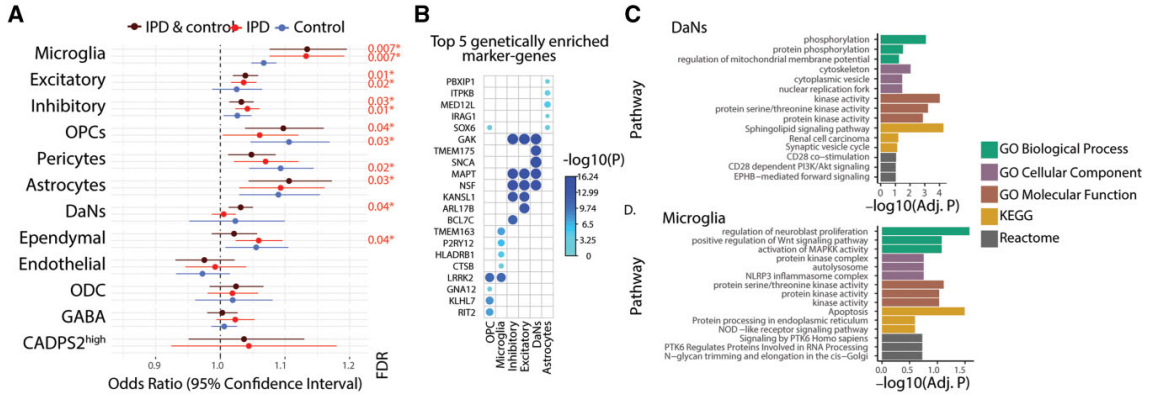

Figure 5 Idiopathic Parkinson's disease (IPD)-associated genetic variants enriched in microglia and neuron-specific genes. (**A**) Forest plots of the odds ratio (OR) and 95% confidence intervals for the association between the Parkinson's disease-associated variants and the marker genes of the midbrain cell types from idiopathic Parkinson's disease patients, control subjects and both conditions. This approach describes the enrichment of Parkinson's disease risk variants, taken from the latest Parkinson's disease GWAS, in genes with cell-type-specific patterns in order to identify idiopathic Parkinson's disease relevant cell types in the midbrain. Only significant association *P*-values were shown (*$P < 0.05$). (**B**) Top five enriched genes in six midbrain cell types. The association of a gene with a cell type is quantified and the most responsible genes for the genetic variant enrichment observed in (**A**) were shown. The *P*-values of genes association are colour coded from light to dark blue and the size of circles is inversely proportional to *P*-values. (**C** and **D**) Gene Ontology terms (GO) and molecular pathways (KEGG, Reactome) associated respectively with the DaNs and microglia marker genes responsible for the Parkinson's disease variant enrichment.

across all cell types in the human midbrain and evidenced that the unfolded protein pathways are also upregulated in the OPCs, and the vascular cells (Supplementary Table 8).

To gain cellular mechanistic insights into how the Parkinson's disease-associated genetic variants could affect the midbrain physiology, we evaluated the enrichment of midbrain cell-type marker genes with the Parkinson's disease-associated genetic variants. We found that Parkinson's disease risk variants are significantly associated with microglia, neurons, astrocytes, and OPCs (Fig. 5A and Supplementary Table 4). Having access to both control and idiopathic Parkinson's disease tissue, we tested whether these associations depend on the disease context. After analysing each condition separately, we found that the Parkinson's disease risk variants associate differently with patients and controls (Fig. 5A). Considering idiopathic Parkinson's disease samples alone, microglia and neurons remain significantly associated with Parkinson's disease risk variants (Fig. 5A and Supplementary Table 4). By contrast, in control subjects, disease variants are associated with pericytes and OPCs (Fig. 5A and Supplementary Table 4). These results show that the link between Parkinson's disease genetic risk and cell type is highly influenced by the disease status. When analysing the samples separately (Fig. 5A), the association of DaNs to risk variants is weaker, presumably due to the low number of DaNs. Therefore, we utilized the entire dataset (controls and idiopathic Parkinson's disease cases) for further analyses (Fig. 5B–D).

We prioritized the cell-type-specific and Parkinson's disease risk-associated genes based on their enrichment contribution for each cell type (Fig. 5B). We found that *LRRK2* showed the highest association with microglia and OPCs, and *SNCA* was the most prominent Parkinson's disease-associated gene in DaNs (Fig. 5B and Supplementary Table 5). These findings are in line with previous reports of Parkinson's disease-associated mutations in α-synuclein promoting Lewy body formation in DaNs[65] and with studies suggesting a role for *LRRK2* mutations in the activation of microglia in Parkinson's disease.[66] Lastly, we investigated which pathways are associated with the Parkinson's disease variant enrichment in DaNs and microglial differentially expressed genes (Fig. 5C and D). Among the key hits from GO, KEGG, and Reactome, we identified terms such as 'phosphorylation' and 'kinase activity' in DaNs and 'NLRP3 inflammasome complex' in microglia (Fig. 5D). In particular, the latter finding further supports a role for inflammatory signalling in Parkinson's disease.

Discussion

This study provides the first single-cell atlas of the human midbrain from idiopathic Parkinson's disease patients and age-matched control subjects to the best of our knowledge. Rather than exclusively focusing on nigral DaNs, the most studied cell type in Parkinson's disease, we aimed to characterize cell- and disease-specific molecular signatures associated with idiopathic Parkinson's disease in the entire midbrain. In addition, we associated Parkinson's disease risk variants to specific midbrain cell types in idiopathic Parkinson's disease patients and control subjects.

Our key observations include an increment in the astrocytes and microglia midbrain fractions, which coincided with a reduction of oligodendrocyte fraction in the idiopathic Parkinson's disease midbrain. Immunofluorescence analysis and pseudotime trajectory reconstructions revealed glial activation in idiopathic Parkinson's disease—a finding that was further supported by Parkinson's disease variant enrichment in the idiopathic Parkinson's disease microglia. Finally, we discovered a small CADPS2-positive neuronal cell cluster in idiopathic Parkinson's disease midbrain tissue, which warrants further investigations in a larger sample set.

When assessing DaNs in our snRNA-seq data, we did not observe a significant loss in idiopathic Parkinson's disease tissue. The low abundance of DaNs likely hampered this compared to other cell types in the midbrain. However, the automated image analysis of immunofluorescence-labelled idiopathic Parkinson's disease and control midbrain sections confirmed a significant loss of TH-positive DaNs and neuromelanin aggregates. This result was in line with the neuropathological reports, which described

severe DaN degeneration in all idiopathic Parkinson's disease patient samples (*cf.* Supplementary Table 1). Thus, technical limitations may have caused the under-representation of DaNs in the transcriptomic data. First, we used 15-µm thick midbrain slices, which are in the size range of the rather large DaN nuclei (10–20 µM). Hence, a considerable proportion of nuclei may not have remained intact during the sectioning process—a prerequisite for high-quality snRNA-seq results. Second, rather than sampling only SN cells, we extracted nuclei from the entire midbrain. This may have led to an under-representation of nigral neurons in our dataset. Despite these constraints, when combining the latest GWAS[32] with our snRNA-seq results from idiopathic Parkinson's disease and control midbrain sections, we observed an enrichment of Parkinson's disease variants in DaNs. Pathway analyses of differentially expressed DaN marker genes with Parkinson's disease variant enrichment identified processes such as 'mitochondrial function' and 'kinase activity' that have previously been associated with Parkinson's disease.

In addition, we identified a disease-specific cell type, consisting of only 120 cells, characterized by its transcriptional similarity to midbrain DaNs but with low *TH* levels and high *CADPS2* expression. CADPS2 has previously been linked to catecholamine uptake and genetic Parkinson's disease.[67–69] In addition, elevated levels of *TIAM1*, which is involved in Wnt/Dvl/Rac1 signalling,[47,48] made us wonder whether CADPS2^{high} cells constitute degenerating DaNs that have lost their dopaminergic identity. Aberrant dopamine function in metabolically impaired but viable neurons in the SN has previously been observed in Parkinson's disease post-mortem tissue.[70] Corroborating our hypothesis, *CADPS2* quantification in neuromelanin-positive DaNs isolated from midbrain tissue of two scRNA-sequenced samples (C1 and IPD4) and four additional idiopathic Parkinson's disease patients and four new control subjects revealed higher levels of *CADPS2* in the former cells. However, further mechanistic studies beyond the scope of the manuscript will be needed to uncover the physiological cause and consequence of *CADPS2* upregulation in DaNs.

In our dataset, glia made up ∼80% of all sequenced cells, enabling an in-depth analysis of their contribution to the pathogenesis of idiopathic Parkinson's disease. We identified a disease-specific upregulation of microglia, which mediates the innate immune defence in the brain. During microgliosis, microglia amplify, undergo morphological changes, and secrete cytokines, which can further engage surrounding microglia and astrocytes.[7,71] Suggestive of an activated state, we detected fewer ramified microglia in idiopathic Parkinson's disease post-mortem SN tissue using a quantitative immunofluorescence approach. Moreover, we identified a significant Parkinson's disease risk variant enrichment in microglia, showing the strongest association with the Parkinson's disease gene *LRRK2*. The kinase LRRK2 is most abundant in immune cells and may contribute to inflammasome formation via the phosphorylation of Rab GTPases.[72] In line with this finding, Parkinson's disease risk variant enrichment analysis in microglial differentially expressed genes highlighted the kinase activity and NLRP3 inflammasome pathways. By inferring the activation trajectories of the microglial subpopulations, we observed an increase in cells from resting into an activated state. Interestingly, our finding of *GPNMB* upregulation in activated microglia is supported by recent results in Alzheimer's disease brains. Reactive patient microglia, which presented an amoeboid shape, also showed higher GPNMB protein levels in this immunohistochemistry study.[55] Moreover, pathway analyses in the activated cell populations identified cytokine signalling and, likely upstream of this, induction of the UPR pathway in the microglia. We also found chaperones and heat-shock proteins to be overexpressed along the disease trajectory, which, when they are released from the cell, can act as damage-associated molecular patterns (DAMPs) that trigger an immune reaction.[73]

Astrocytes can equally act as immune effector cells in the brain by releasing proinflammatory cytokines.[74] When modelling astroglial activation trajectories, we detected reactive astrogliosis specifically in idiopathic Parkinson's disease patient cells.[60] As for microglia, pathway analysis along the trajectory identified the UPR pathway, which has recently been described to influence the astrocytic secretome.[61] Neurotrophic factors released from reactive astrocytes were shown to accelerate neuronal demise[61]—a disease mechanism that has not gained much attention in Parkinson's disease research so far. Besides neurons, reactive astrocytes can also affect oligodendrocyte function and survival.[7]

Accordingly, our snRNA-seq data also showed a trend towards decreased oligodendrocyte numbers in idiopathic Parkinson's disease midbrain tissue. Immunofluorescence analyses suggest that this reduction is the most profound in the SN. In the white matter, oligodendrocytes generate myelin sheets, which provide insulation of axons and ensure saltatory conduction.[75] However, since Parkinson's disease has long been considered a 'grey matter' disease, oligodendrocytes only recently gained attention in the field. A single-cell study[76] in nigral tissue from controls showed that common genetic Parkinson's disease risk variants are associated with oligodendrocyte-specific expression. Another study on the entire mouse nervous system also reported an association with oligodendrocytes.[77] By contrast, we did not observe an enrichment of Parkinson's disease risk variants in oligodendrocytes from control or idiopathic Parkinson's disease tissue. This may be explained by the fact that our data are based on nuclei from the entire midbrain, possibly masking nigra-specific genetic effects. However, a closer look into trajectory inference analysis in oligodendrocytes revealed a transition from high *OPALIN* to high *S100B* expression subpopulations. S100B was shown to control the maturation process of oligodendrocytes[78] and has previously been linked to neurodegeneration.[79] *S100B* overexpression in response to cytokine injections mediates dystrophic neurite formation in an Alzheimer rat model.[79] Accordingly, the oligodendrocyte-specific upregulation of *S100B* observed in the idiopathic Parkinson's disease midbrains may be the result of enhanced cytokine release from microglia and astrocytes. These results further implicate glial cells in the propagation of neuroinflammatory and neurodegenerative processes in idiopathic Parkinson's disease.

In summary, our study reinforces the relevance of neuroinflammation in idiopathic Parkinson's disease. Applying snRNA-seq for the first time to post-mortem midbrain tissue from patients and matched control subjects, we identified a disease-specific upregulation of microglia and astrocytes as well as a loss of oligodendrocytes. In addition, we discovered a small neuronal cell population that was almost exclusively identified in idiopathic Parkinson's disease midbrain tissue, likely representing degenerating DaNs. Disease trajectory analyses in the glial cell populations identified stress in response to misfolded proteins as the major trigger of inflammatory signalling in idiopathic Parkinson's disease, extending from microglia via astrocytes to oligodendrocytes. Further strengthening this finding, Parkinson's disease risk variants were specifically enriched in microglia from idiopathic Parkinson's disease patients.

Our study also has several limitations. Due to the precious nature of post-mortem brain tissue, our results are based on snRNA-seq of sections from 11 individuals and dPCR analysis of laser-capture microdissected DaNs from eight additional

individuals. Therefore, single-cell RNA analyses in independent cohorts will be needed to validate the key findings from our study. Moreover, additional *in vitro* and *in vivo* experiments are necessary to explore the role of CADPS2 in the pathogenesis of Parkinson's disease and to elucidate how the observed glial interplay perpetuates or induces DaN demise.

Despite these challenges, our unique human single-cell dataset provides the basis for new research approaches investigating the role of the different midbrain cell types in idiopathic Parkinson's disease and for translational programmes that aim to develop immunomodulatory Parkinson's disease therapies.

Acknowledgements

We thank the patients and their families for their generous participation.

Funding

S.Sm. and S.P. received funding from the Luxembourg National Research Fund (FNR) within the PARK-QC DTU (PRIDE17/12244779/PARK-QC). A.G. is supported by the FNR within the framework of the ATTRACT (Model-idiopathic Parkinson's disease, FNR9631103) career development program, and were generously funded by a donation from Le Foyer Assurances Luxembourg. Moreover, A.G., P.M. and Z.L. obtained FNR funding as part of the National Centre of Excellence in Research on Parkinson's disease (NCER-Parkinson's disease, FNR11264123). In addition, A.G. and P.M. received funding within the framework of the FNR CORE grant 'MiRisk-Parkinson's disease' (C17/BM/11676395) and FNR INTER grant 'ProtectMove' (INTER/DFG/19/14429377). M.S. is a DZHK principal investigator and is supported by grants from the Deutsche Forschungsgemeinschaft (DFG) (SP1532/3-1, SP1532/4-1, and SP1532/5-1) and the Deutsches Zentrum für Luft- und Raumfahrt (DLR 01GM1925). C.M.M. is supported by grants to the Newcastle Brain Tissue Resource from UK MRC (MR/L016451/1), the Alzheimer's Society and Alzheimer's Research Trust through the Brains for Dementia Research Initiative, and from National Institutes for Health Research Biomedical Research Centre Newcastle. The Parkinson's UK Brain Bank is funded by Parkinson's UK, a charity registered in England and Wales (258197) and in Scotland (SC037554).

Competing interests

The authors report no competing interests.

Supplementary material

Supplementary material is available at *Brain* online.

References

1. Grünewald A, Kumar KR, Sue CM. New insights into the complex role of mitochondria in Parkinson's disease. *Prog Neurobiol*. 2019;177:73–93.
2. Smolders S, Van Broeckhoven C. Genetic perspective on the synergistic connection between vesicular transport, lysosomal and mitochondrial pathways associated with Parkinson's disease pathogenesis. *Acta Neuropathol Commun*. 2020;8:63.
3. Inamdar NN, Arulmozhi DK, Tandon A, Bodhankar SL. Parkinson's disease: genetics and beyond. *Curr Neuropharmacol*. 2007;5:99–113.
4. Obeso JA, Stamelou M, Goetz CG, *et al*. Past, present, and future of Parkinson's disease: a special essay on the 200th Anniversary of the Shaking Palsy. *Mov Disord*. 2017;32:1264–1310.
5. Ouchi Y, Yagi S, Yokokura M, Sakamoto M. Neuroinflammation in the living brain of Parkinson's disease. *Parkinsonism Relat Disord*. 2009;15(Suppl 3):S200–S204.
6. Imamura K, Hishikawa N, Sawada M, Nagatsu T, Yoshida M, Hashizume Y. Distribution of major histocompatibility complex class II-positive microglia and cytokine profile of Parkinson's disease brains. *Acta Neuropathol*. 2003;106:518–526.
7. Liddelow SA, Guttenplan KA, Clarke L, *et al*. Neurotoxic reactive astrocytes are induced by activated microglia. *Nature*. 2017;541:481–487.
8. Kıray H, Lindsay SL, Hosseinzadeh S, Barnett SC. The multifaceted role of astrocytes in regulating myelination. *Exp Neurol*. 2016;283:541–549.
9. Blesa J, Przedborski S. Parkinson's disease: animal models and dopaminergic cell vulnerability. *Front Neuroanat*. 2014;8:155.
10. Borrageiro G, Haylett W, Seedat S, Kuivaniemi H, Bardien S. A review of genome-wide transcriptomics studies in Parkinson's disease. *Eur J Neurosci*. 2018;47:1–16.
11. Cao J, Spielmann M, Qiu X, *et al*. The single-cell transcriptional landscape of mammalian organogenesis. *Nature*. 2019;566:496–502.
12. Wolock SL, Lopez R, Klein AM. Scrublet: computational identification of cell doublets in single-cell transcriptomic data. *Cell Systems*. 2019;8:281–291.e9.
13. Stuart T, Butler A, Hoffman P, *et al*. Comprehensive integration of single-cell data. *Cell*. 2019;177:1888–1902.e21.
14. Hafemeister C, Satija R. Normalization and variance stabilization of single-cell RNA-seq data using regularized negative binomial regression. *Genome Biol*. 2019;20:296.
15. McInnes L, Healy J, Melville J. UMAP: Uniform manifold approximation and projection for dimension reduction. arXiv:1802.03426. https://doi.org/10.48550/arXiv.1802.03426
16. Korsunsky I, Millard N, Fan J, *et al*. Fast, sensitive and accurate integration of single-cell data with Harmony. *Nat Methods*. 2019;16:1289–1296.
17. Cleveland WS. Robust locally weighted regression and smoothing scatterplots. *J Am Stat Assoc Stat Assoc*. 1979;74:829–836.
18. Pedregosa F, Varoquaux G, Gramfort A, *et al*. Scikit-learn: machine learning in python. *J Mach Learn Res*. 2011;12:2825–2830.
19. Szymański P, Kajdanowicz T, Kersting K. How is a data-driven approach better than random choice in label space division for multi-label classification? *Entropy*. 2016;18:282.
20. Hagberg A, Swart P, S Chult, D. Exploring network structure, dynamics, and function using networkx. https://www.osti.gov/biblio/960616-exploring-network-structure-dynamics-function-using-networkx
21. Blondel VD, Guillaume J-L, Lambiotte R, Lefebvre E. Fast unfolding of communities in large networks. *J Stat Mech*. 2008;2008:P10008.
22. Venables WN, Ripley BD. *Modern Applied Statistics with S*. Springer; 2002. https://doi.org/10.1007/978-0-387-21706-2
23. R Development Core Team. R: A language and environment for statistical computing (ISBN 3-900051-07-0). https://www.scienceopen.com/document?vid=300a2dc0-3207-4383-818c-51eb0f49f561
24. Cribari-Neto F, Zeileis A. Beta regression in R. *J Stat Softw*. 2010;34:1–24.
25. Haghverdi L, Lun ATL, Morgan MD, Marioni, JC. Batch effects in single-cell RNA-sequencing data are corrected by matching mutual nearest neighbors. *Nat Biotechnol*. 2018;36:421–427.

26. Chen EY, Tan CM, Kou Y, *et al*. Enrichr: interactive and collaborative HTML5 gene list enrichment analysis tool. *BMC Bioinform*. 2013;14:128.
27. Clément-Ziza M, Munnich A, Lyonnet S, Jaubert F, Besmond C. Stabilization of RNA during laser capture microdissection by performing experiments under argon atmosphere or using ethanol as a solvent in staining solutions. *RNA*. 2008;14:2698–2704.
28. Maher MP, Pine J, Wright J, Tai YC. The neurochip: a new multi-electrode device for stimulating and recording from cultured neurons. *J Neurosci Methods*. 1999;87:45–56.
29. Reed E, Nunez S, Kulp D, Qian J, Reilly M, Foulkes AS A guide to genome-wide association analysis and post-analytic interrogation. *Stat Med*. 2015;34:3769–3792.
30. Das S, Forer L, Schönherr S, *et al*. Next-generation genotype imputation service and methods. *Nat Genet*. 2016;48:1284–1287.
31. de Leeuw CA, Mooij JM, Heskes T, Posthuma D. MAGMA: generalized gene-set analysis of GWAS data. *PLoS Comput Biol*. 2015; 11:e1004219.
32. Nalls MA, Blauwendraat C, Vallerga CL, *et al*. Identification of novel risk loci, causal insights, and heritable risk for Parkinson's disease: a meta-analysis of genome-wide association studies. *Lancet Neurol*. 2019;18:1091–1102.
33. Reynolds RH, Botía J, Nalls MA, *et al*. Moving beyond neurons: the role of cell type-specific gene regulation in Parkinson's disease heritability. *NPJ Parkinsons Dis*. 2019;5:6.
34. Blauwendraat C, Faghri F, Pihlstrom L, *et al*. NeuroChip, an updated version of the NeuroX genotyping platform to rapidly screen for variants associated with neurological diseases. *Neurobiol Aging*. 2017;57:247.e9–247.e13.
35. Mitkus SN, Hyde TM, Vakkalanka R, *et al*. Expression of oligodendrocyte-associated genes in dorsolateral prefrontal cortex of patients with schizophrenia. *Schizophr Res*. 2008;98:129–138.
36. van Bruggen D, Agirre E, Castelo-Branco G. Single-cell transcriptomic analysis of oligodendrocyte lineage cells. *Curr Opin Neurobiol*. 2017;47:168–175.
37. Ikeshima-Kataoka H. Neuroimmunological Implications of AQP4 in Astrocytes. *Int J Mol Sci*. 2016;17:1306.
38. Shah PT, Stratton JA., Stykel MG, *et al*. Single-cell transcriptomics and fate mapping of ependymal cells reveals an absence of neural stem cell function. *Cell*. 2018;173:1045–1057.e9.
39. Hwang IK, Park JH, Lee T-K, *et al*. CD74-immunoreactive activated M1 microglia are shown late in the gerbil hippocampal CA1 region following transient cerebral ischemia. *Mol Med Rep*. 2017;15:4148–4154.
40. Maher TJ, Ren Y, Li Q, *et al*. ATP-binding cassette transporter Abcg2 lineage contributes to the cardiac vasculature after oxidative stress. *Am J Physiol Heart Circ Physiol*. 2014;306:H1610–H1618.
41. Jang AS, Concel VJ, Bein K, *et al*. Endothelial dysfunction and claudin 5 regulation during acrolein-induced lung injury. *Am J Respir Cell Mol Biol*. 2011;44:483–490.
42. Bell RD, Winkler EA, Sagare AP, *et al*. Pericytes control key neurovascular functions and neuronal phenotype in the adult brain and during brain aging. *Neuron*. 2010;68:409–427.
43. Kodama T, Guerrero S, Shin M, Moghadam S, Faulstich M, du Lac S. Neuronal classification and marker gene identification via single-cell expression profiling of brainstem vestibular neurons subserving cerebellar learning. *J Neurosci*. 2012;32:7819–7831.
44. Merrill CB, Friend LN, Newton ST, Hopkins ZH, Edwards JG. Ventral tegmental area dopamine and GABA neurons: Physiological properties and expression of mRNA for endocannabinoid biosynthetic elements. *Sci Rep*. 2015;5:16176.
45. Wu L-J, Ko SW, Toyoda H, *et al*. Increased anxiety-like behavior and enhanced synaptic efficacy in the amygdala of GluR5 knockout mice. *PLoS One*. 2007;2:e167.
46. Thompson L, Barraud P, Andersson E, Kirik D, Björklund A. Identification of dopaminergic neurons of nigral and ventral tegmental area subtypes in grafts of fetal ventral mesencephalon based on cell morphology, protein expression, and efferent projections. *J Neurosci*. 2005;25:6467–6477.
47. Čajánek L, Ganji RS, Henriques-Oliveira C, *et al*. Tiam1 regulates the Wnt/Dvl/Rac1 signaling pathway and the differentiation of midbrain dopaminergic neurons. *Mol Cell Biol*. 2013;33:59–70.
48. Arenas E. Wnt signaling in midbrain dopaminergic neuron development and regenerative medicine for Parkinson's disease. *J Mol Cell Biol*. 2014;6:42–53.
49. Grünewald A, Lax NZ, Rocha MC, *et al*. Quantitative quadruple-label immunofluorescence of mitochondrial and cytoplasmic proteins in single neurons from human midbrain tissue. *J Neurosci Methods*. 2014;232:143–149.
50. Torres-Platas SG, Comeau S, Rachalski A, *et al*. Morphometric characterization of microglial phenotypes in human cerebral cortex. *J Neuroinflammation*. 2014;11:12.
51. Walker DG, Tang TM, Mendsaikhan A, *et al*. Patterns of expression of purinergic receptor p2ry12, a putative marker for non-activated microglia, in aged and Alzheimer's disease brains. *Int J Mol Sci*. 2020;21:678.
52. van der Poel M, Ulas T, Mizee MR, *et al*. Transcriptional profiling of human microglia reveals grey-white matter heterogeneity and multiple sclerosis-associated changes. *Nat Commun*. 2019; 10:1139.
53. Kakimura J-I, Kitamura Y, Takata K, *et al*. Microglial activation and amyloid-β clearance induced by exogenous heat-shock proteins. *FASEB J*. 2002;16:601–603.
54. Burm SM, Zuiderwijk-Sick EA, 't Jong AEJ, *et al*. Inflammasome-induced IL-1β secretion in microglia is characterized by delayed kinetics and is only partially dependent on inflammatory caspases. *J Neurosci*. 2015;35:678–687.
55. Hüttenrauch M, Ogorek I, Klafki H, *et al*. Glycoprotein NMB: a novel Alzheimer's disease associated marker expressed in a subset of activated microglia. *Acta Neuropathol Commun*. 2018;6:108.
56. Parajuli B, Sonobe Y, Horiuchi H, Takeuchi H, Mizuno T, Suzumura A. Oligomeric amyloid β induces IL-1β processing via production of ROS: implication in Alzheimer's disease. *Cell Death Dis*. 2013;4:e975.
57. Nalls MA, Pankratz N, Lill CM, *et al*. Large-scale meta-analysis of genome-wide association data identifies six new risk loci for Parkinson's disease. *Nat Genet*. 2014;46:989–993.
58. Wu K-C, Liou H-H, Kao Y-H, Lee C-Y, Lin C-J. The critical role of Nramp1 in degrading α-synuclein oligomers in microglia under iron overload condition. *Neurobiol Dis*. 2017;104:61–72.
59. Li S, Liu H, Bian S, Sha X, Li Y, Wang Y. The accelerated aging model reveals critical mechanisms of late-onset Parkinson's disease. *BioData Min*. 2020;13, 4.
60. Bradford BM, Wijaya CAW, Mabbott NA. Discrimination of prion strain targeting in the central nervous system via reactive astrocyte heterogeneity in CD44 expression. *Front Cell Neurosci*. 2019; 13, 411.
61. Smith HL, Freeman OJ, Butcher AJ, *et al*. Astrocyte unfolded protein response induces a specific reactivity state that causes non-cell-autonomous neuronal degeneration. *Neuron*. 2020; 105:855–866.e5.
62. Muchowski PJ, Wacker JL. Modulation of neurodegeneration by molecular chaperones. *Nat Rev Neurosci*. 2005;6:11–22.
63. Jiang W, Yang W, Yang W, *et al*. Identification of Tmem10 as a novel late-stage oligodendrocytes marker for detecting hypomyelination. *Int J Biol Sci*. 2013;10:33–42.
64. Sathe K, Maetzler W, Lang JD, *et al*. S100B is increased in Parkinson's disease and ablation protects against MPTP-induced

toxicity through the RAGE and TNF-α pathway. *Brain*. 2012;135: 3336–3347.
65. Spillantini MG, Schmidt ML, Lee VMY, Trojanowski JQ, Jakes R, Goedert M. Alpha-synuclein in Lewy bodies. *Nature*. 1997;388: 839–840.
66. Schapansky J, Nardozzi JD, LaVoie MJ. The complex relationships between microglia, alpha-synuclein, and LRRK2 in Parkinson's disease. *Neuroscience*. 2015;302:74–88.
67. Tsuda L, Lim Y-M. Regulatory system for the G1-arrest during neuronal development in *Drosophila*. *Dev Growth Differ*. 2014; 56:358–367.
68. Brunk I, Blex C, Speidel D, Brose N, Ahnert-Hilger G. Ca2+-dependent activator proteins of secretion promote vesicular monoamine uptake. *J Biol Chem*. 2009;284: 1050–1056.
69. Reinhardt P, Schmid B, Burbulla LF, *et al*. Genetic correction of a LRRK2 mutation in human iPSCs links parkinsonian neurodegeneration to ERK-dependent changes in gene expression. *Cell Stem Cell*. 2013;12:354–367.
70. Kordower JH, Olanow CW, Dodiya HB, *et al*. Disease duration and the integrity of the nigrostriatal system in Parkinson's disease. *Brain*. 2013;136:2419–2431.
71. Joers V, Tansey MG, Mulas G, Carta AR. Microglial phenotypes in Parkinson's disease and animal models of the disease. *Prog Neurobiol*. 2017;155:57–75.
72. Alessi DR, Sammler E. LRRK2 kinase in Parkinson's disease. *Science*. 2018;360:36–37.
73. Smith JA. Regulation of cytokine production by the unfolded protein response; implications for infection and autoimmunity. *Front Immunol*. 2018;9:422.
74. Dong Y, Benveniste EN. Immune function of astrocytes. *Glia*. 2001;36:180–190.
75. Hamanaka G, Ohtomo R, Takase H, Lok J, Arai K. White-matter repair: Interaction between oligodendrocytes and the neurovascular unit. *Brain Circ*. 2018;4:118–123.
76. Agarwal D, Sandor C, Volpato V, *et al*. A single-cell atlas of the human substantia nigra reveals cell-specific pathways associated with neurological disorders. *Nat Commun*. 2020;11:4183.
77. Bryois J, Skene NG, Hansen TF, *et al*. Genetic identification of cell types underlying brain complex traits yields insights into the etiology of Parkinson's disease. *Nat Genet*. 2020;52:482–493.
78. Deloulme JC, Raponi E, Gentil BJ, *et al*. Nuclear expression of S100B in oligodendrocyte progenitor cells correlates with differentiation toward the oligodendroglial lineage and modulates oligodendrocytes maturation. *Mol Cell Neurosci*. 2004;27: 453–465.
79. Sheng JG, Ito K, Skinner RD, *et al*. In vivo and in vitro evidence supporting a role for the inflammatory cytokine interleukin-1 as a driving force in Alzheimer pathogenesis. *Neurobiol Aging*. 1996;17:761–766.

3.1.3 Supplementary data to Manuscript I

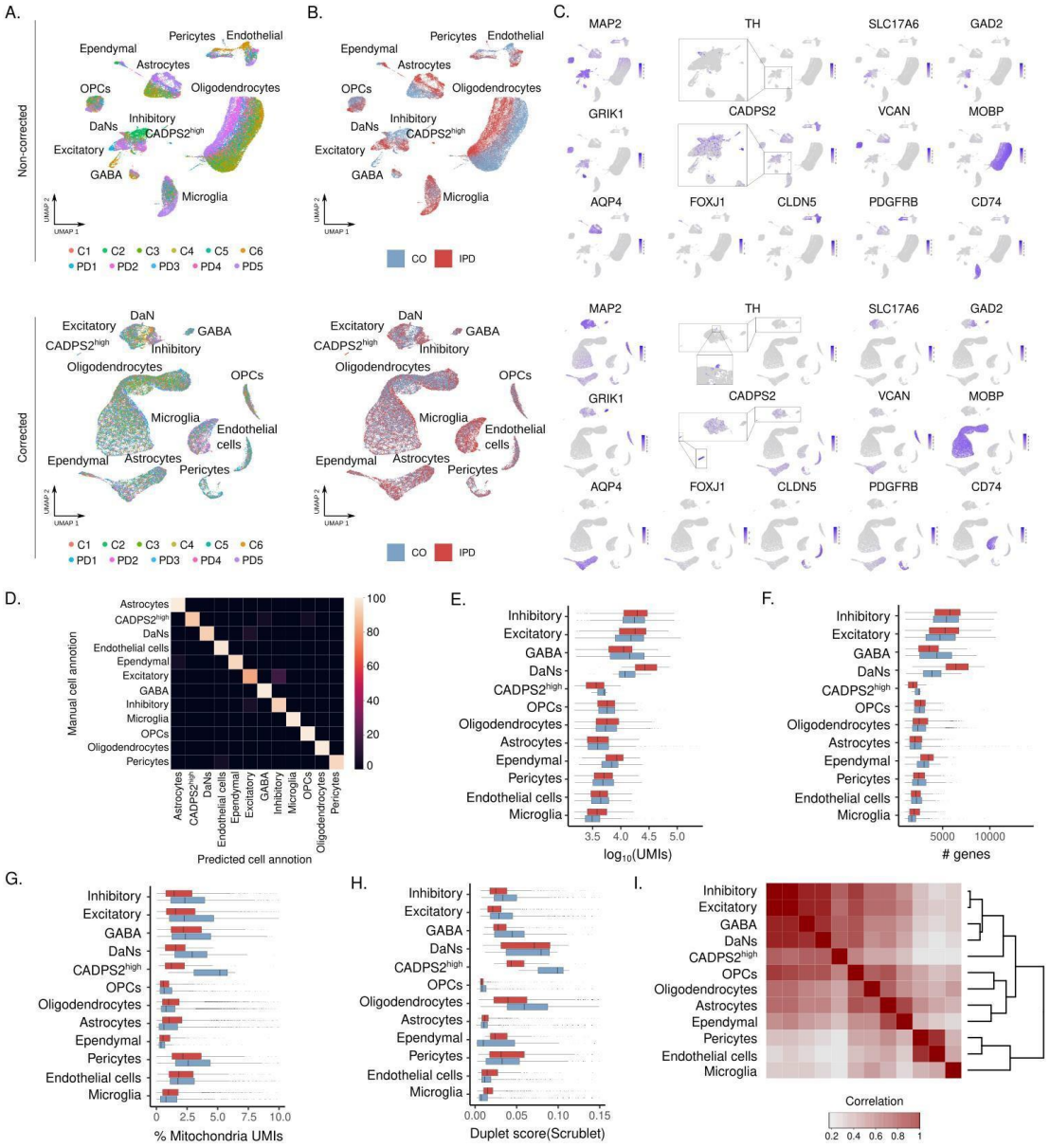

Supplementary Fig. 1 Midbrain cell UMAP embedding and cell type-specific snRNA-seq quality control metrics and similarity. (**A**-**B**) Midbrain single-cell atlas UMAP embedding colored by sample and condition. Top panels display UMAP embeddings based on the top 25 non-corrected principal components. Bottom panels show the UMAP embeddings based on the top 25 principal components after removing the inter-individual variability using the Seurat3 Canonical Correlation Analysis based integration protocol. (**C**) Expression distribution of cell type marker genes on the ~41,000 midbrain cells. (**D**) Confusion matrix results of the machine learning cross-validation approach to validate the cell type definition. (**E**) UMI count distribution. (**F**) Number of detected genes. (**G**) Percentage of mtDNA-encoded transcripts per cell. (**H**) Scrublet duplet score. (**I**) Unsupervised clustering of the midbrain cell-types based on their transcriptional pseudo-bulk profile correlation. CADPS2^{high} transcriptome profile clusters together with the neuronal cells.

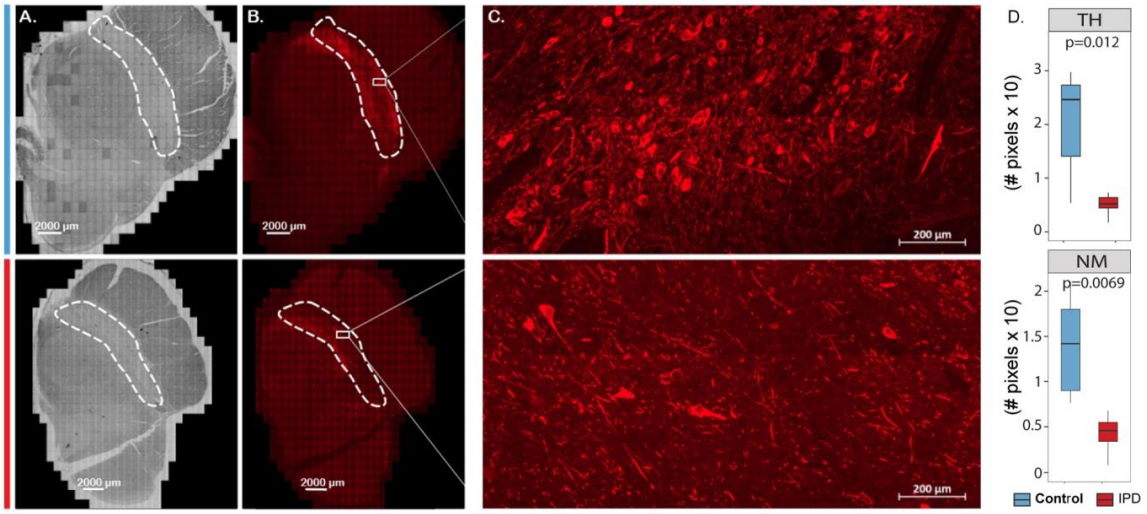

Supplementary Fig. 2 Immunofluorescent labelling of idiopathic Parkinson's disease (IPD) and control midbrain tissue with TH. (**A**) Representative control (top) and IPD (bottom) sections in brightfield reveal midbrain sub-areas. (**B**) Representative control (top) and IPD (bottom) sections stained for TH show a dopaminergic neuron reduction in IPD patients. (**C**) SN area of the control (top) and IPD (bottom) midbrain stained for TH. (**D**) Quantification of TH-positive and neuromelanin-containing neurons. Immunofluorescence analysis with an antibody targeting TH revealed loss of nigral DaNs in IPD samples compared to controls. Similarly, the number of DaNs with NM deposits was reduced in the SN of IPD patients. Scale bar = 2000µm (**A**, **B**); scale bar = 200µm (**C**). DaNs, dopaminergic neurons; IPD, idiopathic Parkinson's disease; NM, neuromelanin; SN, substantia nigra; TH, tyrosine hydroxylase.

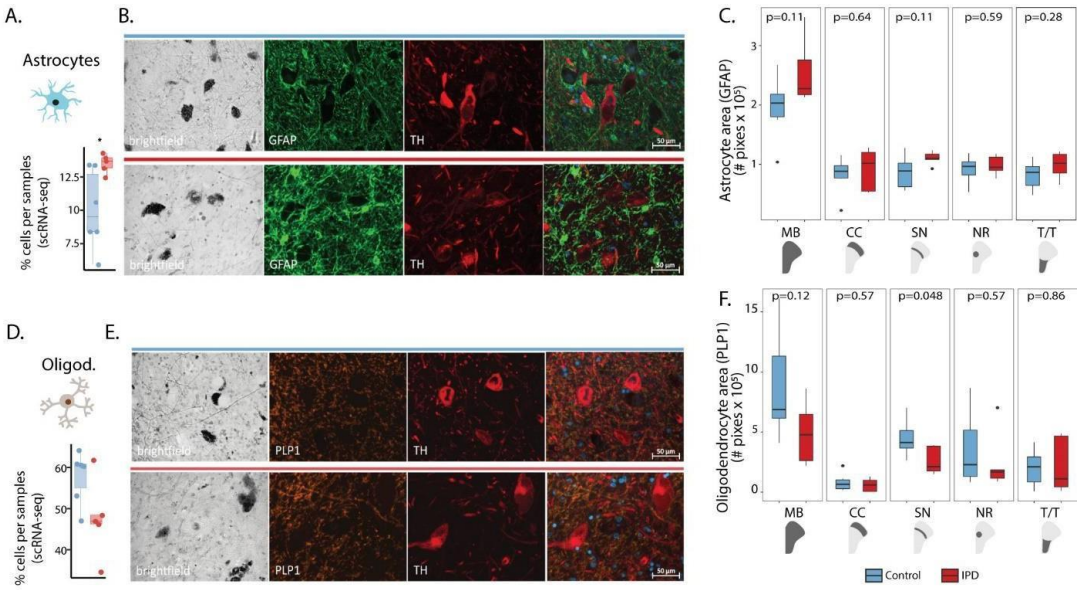

Supplementary Fig. 3 Quantitative immunofluorescence analysis of control and idiopathic Parkinson's disease (IPD) midbrain astrocytes and oligodendrocytes. (**A**) Astrocyte cell proportion per sample. IPD patients display a higher proportion of astrocyte cells (t-test p = 0.03). (**B**) Representative control and IPD sections in brightfield (neuromelanin deposits) or stained for GFAP (astrocytes) and TH (DaNs). (**C**) GFAP astrocyte area quantification. (**D**) Oligodendrocytecell proportion per sample. IPD patients display a lower proportion of oligodendrocyte cells (t-test p = 0.08). (**E**) Representative control and IPD sections in brightfield (neuromelanin deposits) or stained for PLP1 (oligodendrocytes) and TH (DaNs). (**F**) PLP1 oligodendrocyte area quantification. MB, midbrain; SN, substantia nigra; NR, nucleus ruber; T/T, tectum/tegmentum; CC, crus cerebri; PD, red bar; control, blue bar; scale bar = 50µm

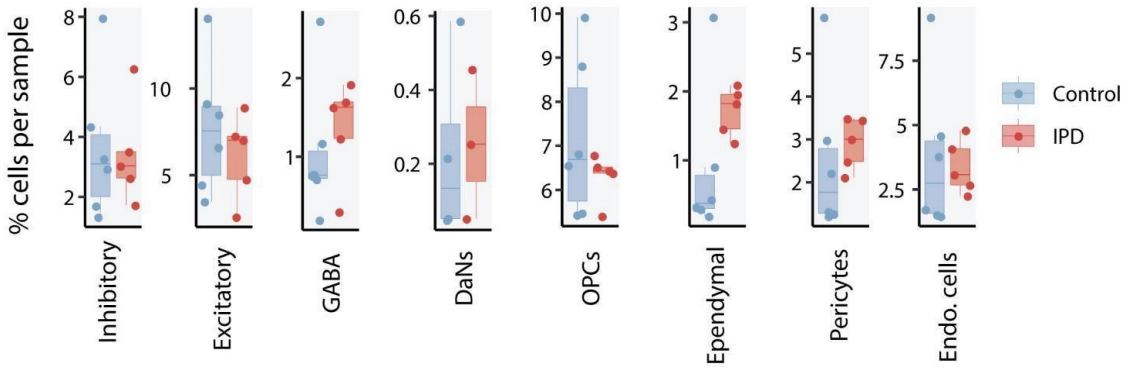

Supplementary Fig. 4 Idiopathic Parkinson's disease (IPD) differential cell-type composition. The percentage of cells per sample is presented for control individuals and IPD patients. The percentage of inhibitory, excitatory, GABA and dopaminergic (DaNs) neurons is given alongside the proportion of Oligodendrocyte precursor cells (OPCs), ependymal, pericytes and endothelial cells.

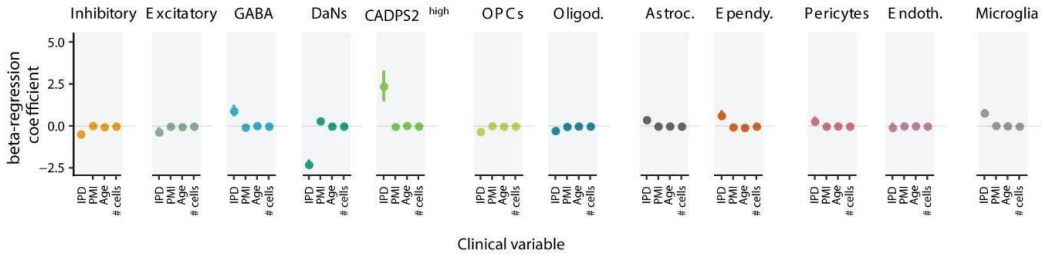

Supplementary Fig. 5 Cell type proportion beta-regression modeling estimates for the clinical variables: disease condition (IPD), PMI, age and number of cells detected.

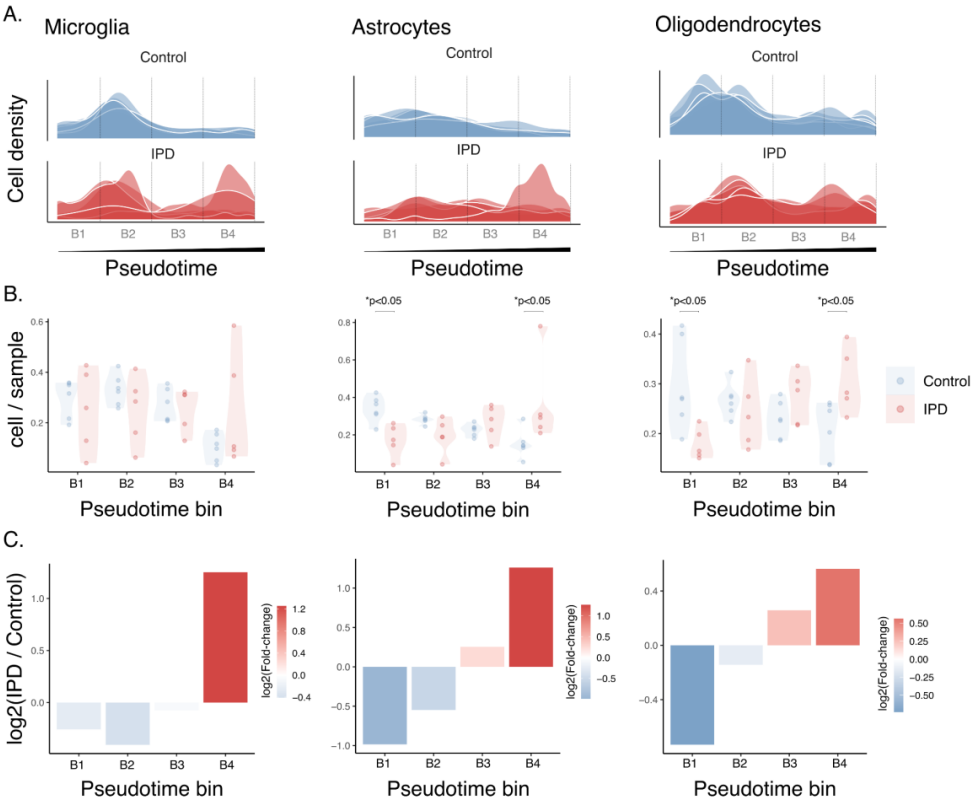

Supplementary Figure 6. Sample heterogeneity of microglia, astrocyte, and oligodendrocyte distribution along their respective activation trajectories. (**A**) Cellular density distribution along the activation trajectory per sample for controls and IPD patients. Four pseudotime bins are indicated. (**B**) Fraction of cells per sample for each pseudotime bin. IPD patient and control distributions per bin were compared using the Wilcoxon test. (**C**) Differential distribution of the IPD cells along the four pseudotime bins of the activation trajectory. Bar plots represent the log2 IPD fold-change of the mean fraction of cells per sample for each pseudotime bin.

Supplementary Table 1 Patient Information

Patient	Sex	Age at onset (years)	Age at death (years)	Disease duration (years)	PMI (h)	Lewy body Braak stage	Non-motor features	Profiled nuclei	SN neuron loss
Single-cell RNA sequenced cohort									
IPD1	F	71	84	13	25	5	Depression, visual hallucinations	1943	severe
IPD2	M	57	66	10	24	6	Hallucinations, paranoia	5925	severe
IPD3	M	71	77	7	24	6	Stroke, cognitive impairment, dementia	3345	severe
IPD4	M	69	81	12	13	6	Cognitive impairment, hallucinations, depression	2083	severe
IPD5	M	71	79	8	25	5	Blindness, memory impairment	5706	severe
	Mean	**67,8**	**77,4**	**10**	**22,2**			**3800,4**	
	SEM	**2,7**	**3**	**1,1**	**2,3**			**858,8**	
C1	F	-	93	-	29	-	-	3753	mild
C2	M	-	66	-	16	-	-	4358	none
C3	M	-	77	-	22	-	-	2047	none
C4	M	-	84	-	5	-	-	4199	none
C5	M	-	88	-	8	-	-	2318	none
C6	M	-	90	-	12	-	-	5758	none
	Mean		**83**		**15,3**			**3738,8**	
	SEM		**4**		**3,6**			**564,3**	
Patient	**Sex**	**Age at onset (years)**	**Age at death (years)**	**Disease duration (years)**	**PMI (h)**	**Lewy body Braak stage**	**Non-motor features**	**Dissected DaNs**	**SN neuron loss**
LCM validation cohort									
IPD4	M	69	81	12	13	6	Cognitive impairment, hallucinations, depression	150	severe
IPD6	M	56	61	5	90	4	hypophonia	150	severe
IPD7	M	70	80	10	34	6	Impaired memory, hallucinations	150	severe
IPD8	M	67	72	5	41	4	No cognitive impairments	150	severe
IPD9	F	66	81	15	35	6	dementia, impaired consciousness, auditory and visual hallucinations	150	severe
C1	F	-	93	-	29	-	-	150	mild
C7	M	-	81	-	34	-	Cognitive decline	150	none
C8	M	-	90	-	80	-	-	150	none

C9	M	-	96	-	16	-	-	150	none
C10	M	-	92	-	9	-		150	none

IPD: idiopathic Parkinson's disease
C: control
PMI: post-mortem interval
SN: substantia nigra
LCM: laser capture microdissection

Supplementary Table 2 Genotyping results in IPD patients

Sample	Genomic position Zygosity	Gene	Exonic variant type	Aminoacid change	GnomAD Exon NFE	GnomAD Genome NFE	ClinVar
IPD4	1:153066050A>C het	SPRR2E	nonsyn	p.S60A (NM_001024209)	0.0021	0.0011	
IPD1	2:40653336G>T het	LRRK2	nonsyn	p.M4911 (NM_198578)	8.99E-05	6.67E-05	
IPD5	115:62261612T>C het	VPS13C	nonsyn	p.T890A (NM_017684)	0.0053	0.009	
IPD5	16:12798607A>G het	CPPED1	nonsyn	p.C197R (NM_018340)	0.0045	0.0043	
IPD2	5:121786403C>T het	SNCAIP	nonsyn	p.R255C (NM_001242935)	0.0054	0.0051	PD late onset
IPD2	5:141694021G>T het	SPRY4	nonsyn	p.S218Y (NM_001127496)	0.0061	0.0078	Hypogonado-tropic hypogonadism
IPD2	6:136882715C>T het	MAP3K5	nonsyn	p.D1315N (NM_005923)	0.0084	0.0069	

gnomAD: genome annotation databse
NFE: non-Finish European ethnic group

Supplementary Table 3 Gene expression markers of the midbrain comprising cell types

Cell type	Gene name	Gene ensembl ID	myAUC	avg_diff	Power	pct.1	pct.2
Oligodendrocytes	ENPP2	ENSG00000136960	0.977	2.235075586	0.954	0.967	0.098
Oligodendrocytes	ST18	ENSG00000147488	0.994	3.294565969	0.988	0.996	0.139
Oligodendrocytes	MOBP	ENSG00000168314	0,967	2,58678107	0,934	0,95	0,1
Oligodendrocytes	MOG	ENSG00000204655	0,933	1,776167992	0,866	0,88	0,04
Oligodendrocytes	PCSK6	ENSG00000140479	0,947	2,347402667	0,894	0,92	0,11
Oligodendrocytes	SLC5A11	ENSG00000158865	0,929	2,441596733	0,858	0,88	0,07
Oligodendrocytes	UGT8	ENSG00000174607	0,947	1,932001447	0,894	0,92	0,12
Oligodendrocytes	ANLN	ENSG00000011426	0,928	1,798336266	0,856	0,88	0,08
Oligodendrocytes	SYNJ2	ENSG00000078269	0,955	2,138356041	0,91	0,93	0,14
Oligodendrocytes	CNTN2	ENSG00000184144	0,952	1,873124432	0,904	0,93	0,15
Oligodendrocytes	MAG	ENSG00000105695	0,904	1,757176387	0,808	0,83	0,05
Oligodendrocytes	CNDP1	ENSG00000150656	0,9	1,757811884	0,8	0,82	0,04
Oligodendrocytes	CDK18	ENSG00000117266	0,954	2,078721588	0,908	0,93	0,16
Oligodendrocytes	FA2H	ENSG00000103089	0,913	1,590872312	0,826	0,87	0,09
Oligodendrocytes	SLCO1A2	ENSG00000084453	0,912	1,646108064	0,824	0,87	0,1
Oligodendrocytes	C10orf90	ENSG00000154493	0,963	2,037208564	0,926	0,97	0,19
Oligodendrocytes	MYRF	ENSG00000124920	0,898	1,480018545	0,796	0,82	0,04
Oligodendrocytes	ABCA8	ENSG00000141338	0,898	1,535561375	0,796	0,83	0,06
Oligodendrocytes	FAM107B	ENSG00000065809	0,943	1,81357168	0,886	0,93	0,16
Oligodendrocytes	AC026316.4	ENSG00000285218	0,928	2,278849715	0,856	0,89	0,13
Oligodendrocytes	CLMN	ENSG00000165959	0,94	1,825492906	0,88	0,95	0,19
Oligodendrocytes	TMEM144	ENSG00000164124	0,981	2,339162961	0,962	0,98	0,22
Oligodendrocytes	CD22	ENSG00000012124	0,884	1,430435733	0,768	0,79	0,03
Oligodendrocytes	CERCAM	ENSG00000167123	0,924	1,733621005	0,848	0,89	0,14
Oligodendrocytes	TF	ENSG00000091513	0,981	2,47039125	0,962	0,98	0,23
Oligodendrocytes	ZNF536	ENSG00000198597	0,957	1,926078139	0,914	0,96	0,21
Oligodendrocytes	SH3TC2	ENSG00000169247	0,882	1,452266349	0,764	0,78	0,03
Oligodendrocytes	LRP2	ENSG00000081479	0,887	1,809192526	0,774	0,79	0,05
Oligodendrocytes	PIEZO2	ENSG00000154864	0,884	1,69566892	0,768	0,79	0,05
Oligodendrocytes	BCAS1	ENSG00000064787	0,901	1,473374593	0,802	0,91	0,17
Oligodendrocytes	HAPLN2	ENSG00000132702	0,897	1,644242222	0,794	0,83	0,09
Oligodendrocytes	LINC00639	ENSG00000259070	0,878	1,569803014	0,756	0,79	0,05
Oligodendrocytes	SHROOM4	ENSG00000158352	0,899	1,593097624	0,798	0,87	0,14
Oligodendrocytes	FGFR2	ENSG00000066468	0,917	1,709726887	0,834	0,89	0,16
Oligodendrocytes	PLEKHH1	ENSG00000054690	0,953	1,884696908	0,906	0,94	0,21
Oligodendrocytes	NKX6-2	ENSG00000148826	0,87	1,416415787	0,74	0,76	0,04
Oligodendrocytes	LDB3	ENSG00000122367	0,867	1,465226066	0,734	0,75	0,04
Oligodendrocytes	PDE1C	ENSG00000154678	0,927	2,049363969	0,854	0,93	0,22
Oligodendrocytes	FOLH1	ENSG00000086205	0,863	1,466844663	0,726	0,74	0,03
Oligodendrocytes	PLD1	ENSG00000075651	0,895	1,519277677	0,79	0,87	0,16
Oligodendrocytes	COL4A5	ENSG00000188153	0,896	1,477472114	0,792	0,88	0,17
Oligodendrocytes	CTNNA3	ENSG00000183230	0,993	3,118061362	0,986	1	0,29
Oligodendrocytes	LINC00609	ENSG00000257585	0,902	2,066476511	0,804	0,85	0,15
Oligodendrocytes	ERMN	ENSG00000136541	0,863	1,416798769	0,726	0,75	0,05
Oligodendrocytes	CARNS1	ENSG00000172508	0,863	1,482623168	0,726	0,76	0,06
Oligodendrocytes	AC009063.2	ENSG00000260788	0,856	1,465175447	0,712	0,73	0,03
Oligodendrocytes	RAPGEF5	ENSG00000136237	0,94	1,819136703	0,88	0,95	0,25
Oligodendrocytes	ATP10B	ENSG00000118322	0,873	1,446988424	0,746	0,82	0,13
Oligodendrocytes	LPAR1	ENSG00000198121	0,869	1,387648352	0,738	0,84	0,14
Oligodendrocytes	CNP	ENSG00000173786	0,924	1,894812941	0,848	0,9	0,21
Oligodendrocytes	CREB5	ENSG00000146592	0,907	1,598161312	0,814	0,92	0,23

Oligodendrocytes	RNF220	ENSG00000187147	0,99	2,725357556	0,98	1	0,31
Oligodendrocytes	SH3GL3	ENSG00000140600	0,936	1,78129152	0,872	0,94	0,27
Oligodendrocytes	GRM3	ENSG00000198822	0,883	1,375437478	0,766	0,9	0,23
Oligodendrocytes	KCNH8	ENSG00000183960	0,872	1,599133366	0,744	0,85	0,18
Oligodendrocytes	SCD	ENSG00000099194	0,893	1,673034222	0,786	0,86	0,19
Oligodendrocytes	GPR37	ENSG00000170775	0,845	1,23923656	0,69	0,73	0,06
Oligodendrocytes	ABCA2	ENSG00000107331	0,946	1,719217176	0,892	0,95	0,28
Oligodendrocytes	PEX5L	ENSG00000114757	0,976	2,303625915	0,952	0,99	0,33
Oligodendrocytes	CNTNAP4	ENSG00000152910	0,888	1,768043796	0,776	0,86	0,2
Oligodendrocytes	FAM124A	ENSG00000150510	0,865	1,349130653	0,73	0,79	0,13
Oligodendrocytes	TTYH2	ENSG00000141540	0,861	1,218440429	0,722	0,82	0,17
Oligodendrocytes	APLP1	ENSG00000105290	0,927	1,793199921	0,854	0,91	0,26
Oligodendrocytes	PLP1	ENSG00000123560	0,985	3,030458567	0,97	0,99	0,34
Oligodendrocytes	QDPR	ENSG00000151552	0,922	1,908551315	0,844	0,91	0,26
Oligodendrocytes	PRR5L	ENSG00000135362	0,853	1,355347897	0,706	0,78	0,14
Oligodendrocytes	ITGA2	ENSG00000164171	0,831	1,331130911	0,662	0,72	0,08
Oligodendrocytes	CLDND1	ENSG00000080822	0,904	1,627655436	0,808	0,88	0,24
Oligodendrocytes	SLC24A2	ENSG00000155886	0,975	2,242823775	0,95	0,99	0,36
Oligodendrocytes	PRUNE2	ENSG00000106772	0,975	2,162611024	0,95	0,98	0,35
Oligodendrocytes	TMEM63A	ENSG00000196187	0,836	1,174947996	0,672	0,75	0,13
Oligodendrocytes	SELENOP	ENSG00000250722	0,854	1,587808346	0,708	0,79	0,16
Oligodendrocytes	MYO1D	ENSG00000176658	0,895	1,500390789	0,79	0,89	0,27
Oligodendrocytes	AL359091.1	ENSG00000207955	0,819	1,417318225	0,638	0,68	0,06
Oligodendrocytes	AK5	ENSG00000154027	0,866	1,435338775	0,732	0,84	0,23
Oligodendrocytes	NKAIN2	ENSG00000188580	0,917	1,727126438	0,834	0,96	0,35
Oligodendrocytes	NDRG1	ENSG00000104419	0,866	1,253531713	0,732	0,85	0,24
Oligodendrocytes	EDIL3	ENSG00000164176	0,978	2,077058104	0,956	0,99	0,39
Oligodendrocytes	KIRREL3	ENSG00000149571	0,837	1,443408156	0,674	0,85	0,24
Oligodendrocytes	EFHD1	ENSG00000115468	0,835	1,174909083	0,67	0,8	0,19
Oligodendrocytes	COBL	ENSG00000106078	0,849	1,16188646	0,698	0,89	0,28
Oligodendrocytes	MAL	ENSG00000172005	0,811	1,160629111	0,622	0,67	0,07
Oligodendrocytes	DAAM2	ENSG00000146122	0,826	0,990998099	0,652	0,9	0,3
Oligodendrocytes	SRCIN1	ENSG00000277363	0,873	1,3377086	0,746	0,83	0,23
Oligodendrocytes	DOCK5	ENSG00000147459	0,943	1,720383305	0,886	0,98	0,38
Oligodendrocytes	PLAAT3	ENSG00000176485	0,851	1,187239936	0,702	0,82	0,23
Oligodendrocytes	NECAB1	ENSG00000123119	0,818	1,183300194	0,636	0,73	0,14
Oligodendrocytes	PXK	ENSG00000168297	0,949	1,723215631	0,898	0,96	0,37
Oligodendrocytes	FRMD4B	ENSG00000114541	0,937	1,680495014	0,874	0,98	0,39
Oligodendrocytes	PPP1R14A	ENSG00000167641	0,805	1,124545912	0,61	0,69	0,1
Oligodendrocytes	SEMA3B	ENSG00000012171	0,804	1,046146446	0,608	0,69	0,1
Oligodendrocytes	AATK	ENSG00000181409	0,86	1,218118025	0,72	0,81	0,22
Oligodendrocytes	LRRC63	ENSG00000173988	0,805	1,25838343	0,61	0,64	0,05
Oligodendrocytes	KCNMB4	ENSG00000135643	0,822	1,477257384	0,644	0,72	0,14
Oligodendrocytes	MEGF10	ENSG00000145794	0,829	1,083061943	0,658	0,82	0,24
Oligodendrocytes	POLR2F	ENSG00000100142	0,864	1,56208217	0,728	0,82	0,23
Oligodendrocytes	DSCAML1	ENSG00000177103	0,858	1,231309362	0,716	0,92	0,33
Oligodendrocytes	HHIP	ENSG00000164161	0,807	1,454279321	0,614	0,66	0,08
Oligodendrocytes	CRYAB	ENSG00000109846	0,859	1,657299097	0,718	0,84	0,26
Oligodendrocytes	HDAC2-AS2	ENSG00000228624	0,834	1,541394988	0,668	0,76	0,18
Oligodendrocytes	AC016597.1	ENSG00000261329	0,793	1,08451799	0,586	0,61	0,03
Oligodendrocytes	SPOCK3	ENSG00000196104	0,924	1,580612112	0,848	0,98	0,41
Oligodendrocytes	NDE1	ENSG00000072864	0,804	1,059343866	0,608	0,7	0,14
Oligodendrocytes	HS3ST5	ENSG00000249853	0,808	1,230152296	0,616	0,74	0,18
Oligodendrocytes	GLDN	ENSG00000186417	0,793	0,773659929	0,586	0,77	0,21
Oligodendrocytes	TTLL7	ENSG00000137941	0,963	1,876115312	0,926	0,98	0,42

Oligodendrocytes	ARHGAP23	ENSG00000275832	0,826	1,096360027	0,652	0,75	0,19
Oligodendrocytes	AMER2	ENSG00000165566	0,843	1,299817317	0,686	0,81	0,25
Oligodendrocytes	ATP8A1	ENSG00000124406	0,957	1,688477577	0,914	0,98	0,42
Oligodendrocytes	SEC14L5	ENSG00000103184	0,785	1,015275926	0,57	0,59	0,04
Oligodendrocytes	AC096564.1	ENSG00000245293	0,801	1,125418638	0,602	0,65	0,1
Oligodendrocytes	LANCL1	ENSG00000115365	0,892	1,437643125	0,784	0,88	0,33
Oligodendrocytes	VRK2	ENSG00000028116	0,8	1,170662791	0,6	0,74	0,19
Oligodendrocytes	COLGALT2	ENSG00000198756	0,844	1,239225585	0,688	0,82	0,27
Oligodendrocytes	SLAIN1	ENSG00000139737	0,942	1,77001968	0,884	0,96	0,42
Oligodendrocytes	PPP1R16B	ENSG00000101445	0,822	1,114420225	0,644	0,76	0,22
Oligodendrocytes	UNC5C	ENSG00000182168	0,906	1,571654934	0,812	0,97	0,42
Oligodendrocytes	GNAI1	ENSG00000127955	0,844	1,203692556	0,688	0,81	0,27
Oligodendrocytes	KIF6	ENSG00000164627	0,813	1,219756066	0,626	0,74	0,2
Oligodendrocytes	ASPA	ENSG00000108381	0,774	1,002238372	0,548	0,58	0,04
Oligodendrocytes	AC079352.1	ENSG00000226994	0,778	1,370024902	0,556	0,63	0,09
Oligodendrocytes	LAMP2	ENSG00000005893	0,872	1,305184289	0,744	0,88	0,35
Oligodendrocytes	TMEFF2	ENSG00000144339	0,809	1,083986066	0,618	0,86	0,32
Oligodendrocytes	SHTN1	ENSG00000187164	0,933	1,527112743	0,866	0,98	0,45
Oligodendrocytes	ANK3	ENSG00000151150	0,776	0,896115701	0,552	0,96	0,43
Oligodendrocytes	RAB40B	ENSG00000141542	0,802	1,021236158	0,604	0,69	0,16
Oligodendrocytes	DPYSL5	ENSG00000157851	0,831	1,434099493	0,662	0,75	0,22
Oligodendrocytes	IGSF11	ENSG00000144847	0,811	1,037731149	0,622	0,81	0,29
Oligodendrocytes	IL1RAPL1	ENSG00000169306	0,961	1,946994182	0,922	1	0,47
Oligodendrocytes	ZCCHC24	ENSG00000165424	0,777	0,768666012	0,554	0,8	0,27
Oligodendrocytes	MAN2A1	ENSG00000112893	0,975	2,284350655	0,95	0,99	0,46
Oligodendrocytes	AC004690.2	ENSG00000241345	0,764	1,035420366	0,528	0,54	0,01
Oligodendrocytes	LINC01630	ENSG00000227115	0,771	1,172694213	0,542	0,58	0,06
Oligodendrocytes	LINC01170	ENSG00000253807	0,774	1,445932272	0,548	0,61	0,08
Oligodendrocytes	CDKN1C	ENSG00000129757	0,773	1,051779249	0,546	0,6	0,08
Oligodendrocytes	TMEM98	ENSG00000006042	0,766	1,094707955	0,532	0,56	0,03
Oligodendrocytes	RASGRF2	ENSG00000113319	0,813	1,180286982	0,626	0,79	0,26
Oligodendrocytes	SEMA4D	ENSG00000187764	0,857	1,242445304	0,714	0,85	0,32
Oligodendrocytes	TMTC4	ENSG00000125247	0,783	0,997477597	0,566	0,65	0,13
Oligodendrocytes	TMTC2	ENSG00000179104	0,961	1,963585141	0,922	0,99	0,47
Oligodendrocytes	PLCL1	ENSG00000115896	0,962	2,082854055	0,924	0,99	0,47
Oligodendrocytes	JAM3	ENSG00000166086	0,843	1,152162546	0,686	0,83	0,31
Oligodendrocytes	RFTN2	ENSG00000162944	0,79	0,878673306	0,58	0,84	0,32
Oligodendrocytes	MYO1E	ENSG00000157483	0,778	0,744198428	0,556	0,82	0,3
Oligodendrocytes	PLLP	ENSG00000102934	0,765	0,89557781	0,53	0,67	0,16
Oligodendrocytes	TUBB4A	ENSG00000104833	0,796	1,177604079	0,592	0,69	0,18
Oligodendrocytes	KLHL4	ENSG00000102271	0,763	1,112117239	0,526	0,58	0,07
Oligodendrocytes	FRMD5	ENSG00000171877	0,961	1,816705997	0,922	0,99	0,49
Oligodendrocytes	RASGRP3	ENSG00000152689	0,761	0,872813977	0,522	0,63	0,12
Oligodendrocytes	CDH19	ENSG00000071991	0,756	1,02366294	0,512	0,55	0,04
Oligodendrocytes	FEZ1	ENSG00000149557	0,823	1,133435376	0,646	0,77	0,27
Oligodendrocytes	PHLDB1	ENSG00000019144	0,812	1,011449098	0,624	0,82	0,31
Oligodendrocytes	HSPA2	ENSG00000126803	0,76	0,932416537	0,52	0,6	0,09
Oligodendrocytes	HECW2	ENSG00000138411	0,807	1,047625145	0,614	0,82	0,32
Oligodendrocytes	ATP1B1	ENSG00000143153	0,816	0,985549819	0,632	0,86	0,36
Oligodendrocytes	DNAJC6	ENSG00000116675	0,932	1,582815259	0,864	0,96	0,46
Oligodendrocytes	MAP7	ENSG00000135525	0,979	1,860411091	0,958	0,99	0,5
Oligodendrocytes	NCKAP5	ENSG00000176771	0,947	1,875974997	0,894	0,98	0,48
Oligodendrocytes	KLK6	ENSG00000167755	0,749	0,886875454	0,498	0,51	0,02
Oligodendrocytes	TFEB	ENSG00000112561	0,759	0,802523725	0,518	0,67	0,18
Oligodendrocytes	RYBP	ENSG00000163602	0,85	1,169200721	0,7	0,86	0,37

Oligodendrocytes	SUN2	ENSG00000100242	0,78	0,947686832	0,56	0,73	0,24
Oligodendrocytes	GPRC5B	ENSG00000167191	0,811	0,944577709	0,622	0,87	0,38
Oligodendrocytes	KIF13B	ENSG00000197892	0,826	1,087681268	0,652	0,82	0,34
Oligodendrocytes	SLCO3A1	ENSG00000176463	0,879	1,239982407	0,758	0,94	0,45
Oligodendrocytes	TP53TG5	ENSG00000124251	0,752	0,956400273	0,504	0,54	0,05
Oligodendrocytes	TMEM165	ENSG00000134851	0,975	1,914374779	0,95	0,99	0,5
Oligodendrocytes	LIPA	ENSG00000107798	0,82	1,042001169	0,64	0,8	0,32
Oligodendrocytes	MBP	ENSG00000197971	0,994	2,48223528	0,988	1	0,52
Oligodendrocytes	AC090015.1	ENSG00000251138	0,746	1,243884593	0,492	0,51	0,02
Oligodendrocytes	CPOX	ENSG00000080819	0,774	1,026471899	0,548	0,63	0,15
Oligodendrocytes	RNASE1	ENSG00000129538	0,737	0,772262506	0,474	0,59	0,11
Oligodendrocytes	CDK19	ENSG00000155111	0,875	1,313022314	0,75	0,92	0,44
Oligodendrocytes	SPOCK1	ENSG00000152377	0,849	1,363458675	0,698	0,93	0,45
Oligodendrocytes	LINC01608	ENSG00000253877	0,742	1,625079096	0,484	0,5	0,03
Oligodendrocytes	KIAA1755	ENSG00000149633	0,737	0,663066822	0,474	0,68	0,21
Oligodendrocytes	MEIS1	ENSG00000143995	0,755	0,902440096	0,51	0,64	0,17
Oligodendrocytes	BIN1	ENSG00000136717	0,804	0,944210946	0,608	0,81	0,34
Oligodendrocytes	BOK	ENSG00000176720	0,747	0,879314996	0,494	0,55	0,07
Oligodendrocytes	SLC31A2	ENSG00000136867	0,739	0,801517376	0,478	0,52	0,05
Oligodendrocytes	PTPRD	ENSG00000153707	0,869	0,985826092	0,738	1	0,53
Oligodendrocytes	SLC12A2	ENSG00000064651	0,808	0,891376898	0,616	0,83	0,37
Oligodendrocytes	SEPTIN4	ENSG00000108387	0,757	0,877815185	0,514	0,61	0,14
Oligodendrocytes	RASSF2	ENSG00000101265	0,743	0,773041448	0,486	0,64	0,17
Oligodendrocytes	RHOU	ENSG00000116574	0,745	0,810202188	0,49	0,6	0,13
Oligodendrocytes	PSEN1	ENSG00000080815	0,845	1,107038208	0,69	0,86	0,39
Oligodendrocytes	RETREG1	ENSG00000154153	0,795	0,999037711	0,59	0,76	0,3
Oligodendrocytes	NFIX	ENSG00000008441	0,765	0,782787122	0,53	0,77	0,31
Oligodendrocytes	PTPRK	ENSG00000152894	0,891	1,207539923	0,782	0,98	0,51
Oligodendrocytes	AGPAT4	ENSG00000026652	0,842	1,35117944	0,684	0,82	0,35
Oligodendrocytes	ENOX1	ENSG00000120658	0,818	1,087198196	0,636	0,9	0,44
Oligodendrocytes	LINC00320	ENSG00000224924	0,739	1,01286454	0,478	0,54	0,07
Oligodendrocytes	C12orf76	ENSG00000174456	0,771	0,865882586	0,542	0,68	0,22
Oligodendrocytes	ARAP2	ENSG00000047365	0,875	1,290576066	0,75	0,95	0,49
Oligodendrocytes	FAM13C	ENSG00000148541	0,825	1,118116254	0,65	0,82	0,36
Oligodendrocytes	SOX10	ENSG00000100146	0,733	0,727668798	0,466	0,56	0,1
Oligodendrocytes	YPEL2	ENSG00000175155	0,789	0,982841403	0,578	0,76	0,3
Oligodendrocytes	LPGAT1	ENSG00000123684	0,844	1,189576015	0,688	0,86	0,4
Oligodendrocytes	GAS7	ENSG00000007237	0,772	0,851453281	0,544	0,75	0,29
Oligodendrocytes	ATG4C	ENSG00000125703	0,808	0,983771307	0,616	0,81	0,35
Oligodendrocytes	NINJ2	ENSG00000171840	0,733	0,894346052	0,466	0,51	0,05
Oligodendrocytes	ZEB2	ENSG00000169554	0,879	1,179753946	0,758	0,98	0,52
Oligodendrocytes	ENPP6	ENSG00000164303	0,733	0,902168463	0,466	0,48	0,02
Oligodendrocytes	PLEKHB1	ENSG00000021300	0,746	0,808490325	0,492	0,62	0,16
Oligodendrocytes	ARFGEF3	ENSG00000112379	0,803	0,901138773	0,606	0,85	0,4
Oligodendrocytes	NT5DC1	ENSG00000178425	0,813	1,093752987	0,626	0,8	0,35
Oligodendrocytes	CPB2-AS1	ENSG00000235903	0,76	0,990436905	0,52	0,63	0,18
Oligodendrocytes	GLTP	ENSG00000139433	0,754	0,846808514	0,508	0,62	0,17
Oligodendrocytes	KIAA1324L	ENSG00000164659	0,787	0,995889837	0,574	0,74	0,29
Oligodendrocytes	KLHL32	ENSG00000186231	0,862	1,288793	0,724	0,92	0,47
Oligodendrocytes	INF2	ENSG00000203485	0,738	0,741793393	0,476	0,59	0,14
Oligodendrocytes	SLC22A23	ENSG00000137266	0,839	1,103996677	0,678	0,87	0,42
Oligodendrocytes	PRIMA1	ENSG00000175785	0,728	0,800902306	0,456	0,48	0,04
Oligodendrocytes	HEPACAM	ENSG00000165478	0,725	0,5936985	0,45	0,68	0,23
Oligodendrocytes	HIP1	ENSG00000127946	0,759	0,700305694	0,518	0,87	0,42
Oligodendrocytes	PIP4K2A	ENSG00000150867	0,988	2,153074657	0,976	1	0,55

Oligodendrocytes	LRRC1	ENSG00000137269	0,779	0,932150092	0,558	0,75	0,3
Oligodendrocytes	PPM1H	ENSG00000111110	0,79	1,017618978	0,58	0,77	0,33
Oligodendrocytes	CSRP1	ENSG00000159176	0,731	0,682572134	0,462	0,69	0,25
Oligodendrocytes	MARCKSL1	ENSG00000175130	0,765	1,060498795	0,53	0,67	0,23
Oligodendrocytes	PMP22	ENSG00000109099	0,73	0,700725158	0,46	0,63	0,19
Oligodendrocytes	SEMA6A	ENSG00000092421	0,797	0,921193661	0,594	0,81	0,37
Oligodendrocytes	TPPP	ENSG00000171368	0,76	0,909393253	0,52	0,64	0,21
Oligodendrocytes	DOCK10	ENSG00000135905	0,928	1,453964029	0,856	0,99	0,55
Oligodendrocytes	RNF144A	ENSG00000151692	0,812	0,983740398	0,624	0,83	0,39
Oligodendrocytes	LSS	ENSG00000160285	0,778	0,928789184	0,556	0,72	0,28
Oligodendrocytes	AL033523.1	ENSG00000228793	0,72	0,878490094	0,44	0,46	0,03
Oligodendrocytes	CA2	ENSG00000104267	0,724	0,841463202	0,448	0,52	0,09
Oligodendrocytes	P2RX7	ENSG00000089041	0,75	0,733216591	0,5	0,75	0,32
Oligodendrocytes	S100B	ENSG00000160307	0,766	1,201064948	0,532	0,72	0,28
Oligodendrocytes	ARHGEF2	ENSG00000116584	0,736	0,721761792	0,472	0,63	0,19
Oligodendrocytes	EPCAM-DT	ENSG00000234690	0,724	0,836302569	0,448	0,51	0,08
Oligodendrocytes	FAXDC2	ENSG00000170271	0,731	0,742912814	0,462	0,65	0,22
Oligodendrocytes	GAB1	ENSG00000109458	0,908	1,391257593	0,816	0,96	0,53
Oligodendrocytes	PDE1A	ENSG00000115252	0,726	0,926212937	0,452	0,59	0,16
Oligodendrocytes	DOCK1	ENSG00000150760	0,785	0,802619261	0,57	0,92	0,49
Oligodendrocytes	ZDHHC20	ENSG00000180776	0,86	1,583938221	0,72	0,85	0,42
Oligodendrocytes	NCOA7	ENSG00000111912	0,829	1,055080642	0,658	0,86	0,43
Oligodendrocytes	ADIPOR2	ENSG00000006831	0,813	0,880621801	0,626	0,88	0,45
Oligodendrocytes	GPM6B	ENSG00000046653	0,934	1,620537198	0,868	0,99	0,56
Oligodendrocytes	CCP110	ENSG00000103540	0,763	1,029349175	0,526	0,66	0,24
Oligodendrocytes	TMC7	ENSG00000170537	0,723	0,746526892	0,446	0,51	0,08
Oligodendrocytes	USP31	ENSG00000103404	0,779	1,032323482	0,558	0,71	0,28
Oligodendrocytes	SEMA3C	ENSG00000075223	0,717	0,816009981	0,434	0,51	0,08
Oligodendrocytes	CPNE2	ENSG00000140848	0,727	0,716747843	0,454	0,57	0,14
Oligodendrocytes	MARCH1	ENSG00000145416	0,782	0,805826498	0,564	0,97	0,54
Oligodendrocytes	GNAO1	ENSG00000087258	0,816	1,095853451	0,632	0,89	0,47
Oligodendrocytes	B3GAT1	ENSG00000109956	0,753	0,811107304	0,506	0,65	0,23
Oligodendrocytes	CORO2B	ENSG00000103647	0,763	0,895538394	0,526	0,7	0,28
Oligodendrocytes	FBXL7	ENSG00000183580	0,765	0,828315963	0,53	0,88	0,46
Oligodendrocytes	TRIM2	ENSG00000109654	0,903	1,307918774	0,806	0,97	0,55
Oligodendrocytes	ELMO1	ENSG00000155849	0,884	1,19386876	0,768	0,99	0,57
Oligodendrocytes	SLC44A1	ENSG00000070214	0,992	2,258648496	0,984	1	0,58
Oligodendrocytes	CBR1	ENSG00000159228	0,721	0,770493724	0,442	0,53	0,12
Oligodendrocytes	ERBB3	ENSG00000065361	0,709	0,684595519	0,418	0,46	0,05
Oligodendrocytes	TSPAN15	ENSG00000099282	0,709	0,656436481	0,418	0,49	0,08
Oligodendrocytes	OTUD7A	ENSG00000169918	0,862	1,176053423	0,724	0,93	0,52
Oligodendrocytes	SORCS2	ENSG00000184985	0,731	0,797627619	0,462	0,65	0,24
Oligodendrocytes	CHADL	ENSG00000100399	0,711	0,683868551	0,422	0,48	0,07
Oligodendrocytes	IQGAP1	ENSG00000140575	0,78	0,8455834	0,56	0,81	0,4
Oligodendrocytes	PACS2	ENSG00000179364	0,827	1,10999264	0,654	0,83	0,42
Oligodendrocytes	TTLL11	ENSG00000175764	0,77	0,94726702	0,54	0,7	0,29
Oligodendrocytes	SH3TC2-DT	ENSG00000250072	0,705	0,793168704	0,41	0,42	0,01
Oligodendrocytes	MVB12B	ENSG00000196814	0,872	1,247406856	0,744	0,91	0,5
Oligodendrocytes	FGF1	ENSG00000113578	0,716	0,693082144	0,432	0,6	0,2
Oligodendrocytes	LIMCH1	ENSG00000064042	0,896	1,215625936	0,792	0,98	0,57
Oligodendrocytes	NFASC	ENSG00000163531	0,795	0,968051538	0,59	0,89	0,48
Oligodendrocytes	DNM3	ENSG00000197959	0,922	1,269940908	0,844	0,99	0,59
Oligodendrocytes	LGR5	ENSG00000139292	0,715	0,876885981	0,43	0,51	0,11
Oligodendrocytes	AKAP6	ENSG00000151320	0,854	0,997524059	0,708	0,97	0,56
Oligodendrocytes	FBXO32	ENSG00000156804	0,724	0,990142708	0,448	0,56	0,16

Oligodendrocytes	LIPE	ENSG00000079435	0,712	0,723326433	0,424	0,49	0,09
Oligodendrocytes	GATM	ENSG00000171766	0,714	0,648280927	0,428	0,6	0,19
Oligodendrocytes	STMN1	ENSG00000117632	0,75	0,98342884	0,5	0,65	0,25
Oligodendrocytes	PIK3C2B	ENSG00000133056	0,731	0,779270748	0,462	0,61	0,21
Oligodendrocytes	NPC1	ENSG00000141458	0,748	0,729239453	0,496	0,74	0,34
Oligodendrocytes	SEPTIN8	ENSG00000164402	0,76	0,883235343	0,52	0,7	0,3
Oligodendrocytes	SECISBP2L	ENSG00000138593	0,817	0,963817803	0,634	0,83	0,44
Oligodendrocytes	DPYD	ENSG00000188641	0,89	1,224369852	0,78	0,98	0,58
Oligodendrocytes	GRID1	ENSG00000182771	0,817	0,962111698	0,634	0,92	0,53
Oligodendrocytes	ZNF708	ENSG00000182141	0,761	0,86484406	0,522	0,71	0,31
Oligodendrocytes	FAM102A	ENSG00000167106	0,721	0,710152594	0,442	0,58	0,18
Oligodendrocytes	APBB2	ENSG00000163697	0,831	0,920908209	0,662	0,95	0,56
Oligodendrocytes	SGK1	ENSG00000118515	0,793	1,08844688	0,586	0,86	0,47
Oligodendrocytes	OLMALINC	ENSG00000235823	0,721	0,787928994	0,442	0,65	0,25
Oligodendrocytes	ELOVL1	ENSG00000066322	0,702	0,670083375	0,404	0,48	0,09
Oligodendrocytes	PHACTR3	ENSG00000087495	0,76	0,720419701	0,52	0,86	0,47
Oligodendrocytes	DUBR	ENSG00000243701	0,746	0,825238972	0,492	0,69	0,3
Oligodendrocytes	NEO1	ENSG00000067141	0,8	0,869323968	0,6	0,88	0,49
Oligodendrocytes	SLC22A15	ENSG00000163393	0,76	0,830441678	0,52	0,75	0,36
Oligodendrocytes	SLC48A1	ENSG00000211584	0,714	0,687496637	0,428	0,57	0,18
Oligodendrocytes	KIF5C	ENSG00000168280	0,764	0,835417045	0,528	0,77	0,38
Oligodendrocytes	FAM95C	ENSG00000283486	0,714	0,976287771	0,428	0,49	0,1
Oligodendrocytes	CAMK2N1	ENSG00000162545	0,736	0,739027312	0,472	0,7	0,31
Oligodendrocytes	SAMD12	ENSG00000177570	0,824	1,047900204	0,648	0,89	0,51
Oligodendrocytes	TUBA1A	ENSG00000167552	0,784	1,161217668	0,568	0,77	0,39
Oligodendrocytes	SGK3	ENSG00000104205	0,817	0,99580427	0,634	0,86	0,48
Oligodendrocytes	LINC00877	ENSG00000241163	0,702	0,851328337	0,404	0,45	0,06
Oligodendrocytes	USP54	ENSG00000166348	0,836	0,943643411	0,672	0,93	0,54
Oligodendrocytes	RHOBTB1	ENSG00000072422	0,704	0,775109889	0,408	0,53	0,15
Oligodendrocytes	AGTPBP1	ENSG00000135049	0,818	1,00189802	0,636	0,87	0,49
Oligodendrocytes	FOXN2	ENSG00000170802	0,728	0,66218979	0,456	0,72	0,34
Oligodendrocytes	CPEB2	ENSG00000137449	0,776	0,869895756	0,552	0,78	0,4
Oligodendrocytes	MIR181A1HG	ENSG00000229989	0,73	0,738415306	0,46	0,75	0,37
Oligodendrocytes	ACTN2	ENSG00000077522	0,703	0,786133395	0,406	0,5	0,12
Oligodendrocytes	FUT8	ENSG00000033170	0,884	1,273133709	0,768	0,94	0,56
Oligodendrocytes	TMEM151A	ENSG00000179292	0,705	0,744498373	0,41	0,47	0,09
Oligodendrocytes	TECPR2	ENSG00000196663	0,747	0,798332733	0,494	0,71	0,33
Oligodendrocytes	SIRT2	ENSG00000068903	0,742	0,772678991	0,484	0,67	0,29
Oligodendrocytes	PDE8A	ENSG00000073417	0,883	1,228590709	0,766	0,96	0,58
Oligodendrocytes	GSN	ENSG00000148180	0,775	0,767931408	0,55	0,87	0,49
Oligodendrocytes	NXPE3	ENSG00000144815	0,732	0,757110903	0,464	0,63	0,25
Oligodendrocytes	MOB3B	ENSG00000120162	0,779	0,910308392	0,558	0,82	0,44
Oligodendrocytes	ZDHHC9	ENSG00000188706	0,707	0,700857051	0,414	0,52	0,14
Oligodendrocytes	BTBD3	ENSG00000132640	0,732	0,737966527	0,464	0,67	0,3
Oligodendrocytes	FAM222A	ENSG00000139438	0,702	0,669818201	0,404	0,5	0,13
Oligodendrocytes	ELAVL3	ENSG00000196361	0,741	0,735932332	0,482	0,75	0,38
Oligodendrocytes	TMCC2	ENSG00000133069	0,707	0,693814482	0,414	0,51	0,14
Oligodendrocytes	OTUD7B	ENSG00000264522	0,74	0,706152748	0,48	0,73	0,36
Oligodendrocytes	PHLPP1	ENSG00000081913	0,93	1,531048738	0,86	0,98	0,61
Oligodendrocytes	C1QTNF3-AMACR	ENSG00000273294	0,741	0,821489233	0,482	0,7	0,33
Oligodendrocytes	PKP4	ENSG00000144283	0,834	1,090120238	0,668	0,91	0,55
Oligodendrocytes	SORT1	ENSG00000134243	0,862	1,064848854	0,724	0,94	0,58
Oligodendrocytes	RAB30	ENSG00000137502	0,77	0,938148927	0,54	0,75	0,39
Oligodendrocytes	TARSL2	ENSG00000185418	0,743	0,748215552	0,486	0,72	0,35

Oligodendrocytes	KNOP1	ENSG00000103550	0,707	0,702670275	0,414	0,58	0,22
Oligodendrocytes	BRMS1L	ENSG00000100916	0,716	0,754772285	0,432	0,57	0,2
Oligodendrocytes	NALCN	ENSG00000102452	0,754	0,698176765	0,508	0,88	0,52
Oligodendrocytes	STMN4	ENSG00000015592	0,707	0,828192207	0,414	0,51	0,15
Oligodendrocytes	DNAJB2	ENSG00000135924	0,728	0,732258275	0,456	0,66	0,3
Oligodendrocytes	REPS2	ENSG00000169891	0,727	0,777220189	0,454	0,66	0,29
Oligodendrocytes	DLC1	ENSG00000164741	0,817	0,700290791	0,634	0,9	0,54
Oligodendrocytes	SLC25A13	ENSG00000004864	0,801	1,019273897	0,602	0,82	0,46
Oligodendrocytes	MTUS1	ENSG00000129422	0,805	0,889200899	0,61	0,89	0,53
Oligodendrocytes	ANKRD18A	ENSG00000180071	0,705	0,948339672	0,41	0,5	0,14
Oligodendrocytes	LRRC8B	ENSG00000197147	0,705	0,657746604	0,41	0,58	0,22
Oligodendrocytes	BACE1	ENSG00000186318	0,72	0,752364487	0,44	0,59	0,23
Oligodendrocytes	SH3D19	ENSG00000109686	0,74	0,734989235	0,48	0,81	0,45
Oligodendrocytes	SVIP	ENSG00000198168	0,706	0,730017576	0,412	0,53	0,18
Oligodendrocytes	JAKMIP3	ENSG00000188385	0,723	0,835176881	0,446	0,58	0,23
Oligodendrocytes	STK39	ENSG00000198648	0,762	0,757694069	0,524	0,81	0,45
Oligodendrocytes	TSPAN5	ENSG00000168785	0,761	0,802742604	0,522	0,83	0,47
Oligodendrocytes	OSBPL1A	ENSG00000141447	0,817	0,948271314	0,634	0,89	0,54
Oligodendrocytes	HBS1L	ENSG00000112339	0,726	0,729957172	0,452	0,66	0,31
Oligodendrocytes	NCAM2	ENSG00000154654	0,77	0,816219315	0,54	0,98	0,64
Oligodendrocytes	ALCAM	ENSG00000170017	0,762	0,703980075	0,524	0,93	0,58
Oligodendrocytes	FRYL	ENSG00000075539	0,942	1,489876748	0,884	0,98	0,64
Oligodendrocytes	LMCD1-AS1	ENSG00000227110	0,739	0,887871375	0,478	0,78	0,43
Oligodendrocytes	GNG7	ENSG00000176533	0,766	0,888155617	0,532	0,82	0,47
Oligodendrocytes	LHPP	ENSG00000107902	0,707	0,698179587	0,414	0,58	0,23
Oligodendrocytes	ABHD17B	ENSG00000107362	0,703	0,699726269	0,406	0,56	0,22
Oligodendrocytes	TBC1D12	ENSG00000108239	0,734	0,774706084	0,468	0,72	0,38
Oligodendrocytes	NCAM1	ENSG00000149294	0,846	0,886840911	0,692	0,99	0,65
Oligodendrocytes	RCAN2	ENSG00000172348	0,701	0,642622746	0,402	0,69	0,34
Oligodendrocytes	SLC13A3	ENSG00000158296	0,712	0,724011854	0,424	0,63	0,28
Oligodendrocytes	RASGRF1	ENSG00000058335	0,715	1,002505646	0,43	0,57	0,22
Oligodendrocytes	SNX30	ENSG00000148158	0,702	0,628214183	0,404	0,61	0,26
Oligodendrocytes	SEPTIN7	ENSG00000122545	0,904	1,30400155	0,808	0,96	0,62
Oligodendrocytes	CLIP4	ENSG00000115295	0,746	0,744179586	0,492	0,77	0,43
Oligodendrocytes	CDC14B	ENSG00000081377	0,758	0,774915599	0,516	0,82	0,48
Oligodendrocytes	CUEDC1	ENSG00000180891	0,703	0,635838361	0,406	0,64	0,3
Oligodendrocytes	AMD1	ENSG00000123505	0,709	0,681085651	0,418	0,63	0,3
Oligodendrocytes	PPP2R2B	ENSG00000156475	0,834	1,066980836	0,668	0,98	0,65
Oligodendrocytes	KCTD8	ENSG00000183783	0,714	0,74630307	0,428	0,73	0,4
Oligodendrocytes	MICAL3	ENSG00000243156	0,737	0,683403651	0,474	0,81	0,49
Oligodendrocytes	PPP1R21	ENSG00000162869	0,716	0,644079612	0,432	0,71	0,38
Oligodendrocytes	LINC01505	ENSG00000234323	0,703	1,355969048	0,406	0,57	0,25
Oligodendrocytes	WDR20	ENSG00000140153	0,721	0,668190704	0,442	0,7	0,38
Oligodendrocytes	DIP2C	ENSG00000151240	0,849	0,976274771	0,698	0,96	0,64
Oligodendrocytes	ZNF652	ENSG00000198740	0,772	0,853704121	0,544	0,82	0,5
Oligodendrocytes	HIPK2	ENSG00000064393	0,794	0,849679266	0,588	0,9	0,59
Oligodendrocytes	NTM	ENSG00000182667	0,738	0,651586708	0,476	0,96	0,65
Oligodendrocytes	TULP4	ENSG00000130338	0,771	0,798632265	0,542	0,88	0,57
Oligodendrocytes	DLG1	ENSG00000075711	0,926	1,407204503	0,852	0,97	0,66
Oligodendrocytes	CPQ	ENSG00000104324	0,71	0,649420106	0,42	0,78	0,48
Oligodendrocytes	DICER1	ENSG00000100697	0,779	0,763579468	0,558	0,85	0,54
Oligodendrocytes	AOPEP	ENSG00000148120	0,791	0,808913079	0,582	0,91	0,6
Oligodendrocytes	PTBP2	ENSG00000117569	0,795	0,838513672	0,59	0,89	0,59
Oligodendrocytes	TLE4	ENSG00000106829	0,72	0,731285247	0,44	0,75	0,45
Oligodendrocytes	ZFYVE16	ENSG00000039319	0,784	0,875845366	0,568	0,84	0,53

Oligodendrocytes	MAP4K5	ENSG00000012983	0,853	1,042664131	0,706	0,93	0,63
Oligodendrocytes	RNF13	ENSG00000082996	0,781	0,765764039	0,562	0,86	0,56
Oligodendrocytes	SAMD4B	ENSG00000179134	0,709	0,625239339	0,418	0,69	0,39
Oligodendrocytes	SCARB2	ENSG00000138760	0,726	0,651662939	0,452	0,75	0,45
Oligodendrocytes	DIP2B	ENSG00000066084	0,889	1,117085671	0,778	0,97	0,68
Oligodendrocytes	MYO6	ENSG00000196586	0,755	0,680106694	0,51	0,86	0,57
Oligodendrocytes	NLK	ENSG00000087095	0,715	0,585190818	0,43	0,79	0,51
Oligodendrocytes	RDX	ENSG00000137710	0,726	0,684629385	0,452	0,79	0,51
Oligodendrocytes	AGAP1	ENSG00000157985	0,854	0,915601403	0,708	0,99	0,71
Oligodendrocytes	ANKIB1	ENSG00000001629	0,772	0,746064392	0,544	0,89	0,61
Oligodendrocytes	RBPJ	ENSG00000168214	0,743	0,632309062	0,486	0,85	0,57
Oligodendrocytes	ITCH	ENSG00000078747	0,738	0,627380579	0,476	0,82	0,55
Oligodendrocytes	FAM171A1	ENSG00000148468	0,706	0,605276798	0,412	0,74	0,47
Oligodendrocytes	MAPRE2	ENSG00000166974	0,746	0,789525876	0,492	0,8	0,53
Oligodendrocytes	DLG2	ENSG00000150672	0,865	0,947550418	0,73	1	0,73
Oligodendrocytes	MBNL2	ENSG00000139793	0,846	0,900099393	0,692	0,95	0,68
Oligodendrocytes	PCDH9	ENSG00000184226	0,909	1,252405655	0,818	1	0,73
Oligodendrocytes	PDE4B	ENSG00000184588	0,933	1,416483973	0,866	0,99	0,73
Oligodendrocytes	PEBP1	ENSG00000089220	0,714	0,691660185	0,428	0,75	0,49
Oligodendrocytes	USP32	ENSG00000170832	0,717	0,642879223	0,434	0,79	0,53
Oligodendrocytes	ERBIN	ENSG00000112851	0,919	1,452307659	0,838	0,99	0,73
Oligodendrocytes	PPP1R12B	ENSG00000077157	0,752	0,644077208	0,504	0,87	0,61
Oligodendrocytes	UBE4B	ENSG00000130939	0,713	0,588049146	0,426	0,8	0,54
Oligodendrocytes	ARHGAP21	ENSG00000107863	0,884	1,069305358	0,768	0,97	0,71
Oligodendrocytes	ZKSCAN1	ENSG00000106261	0,714	0,606848265	0,428	0,77	0,51
Oligodendrocytes	FAR1	ENSG00000197601	0,727	0,647424041	0,454	0,77	0,52
Oligodendrocytes	APP	ENSG00000142192	0,751	0,599609948	0,502	0,94	0,69
Oligodendrocytes	MAGI2	ENSG00000187391	0,854	0,869720437	0,708	1	0,75
Oligodendrocytes	TJP1	ENSG00000104067	0,817	0,812279	0,634	0,96	0,72
Oligodendrocytes	CCDC88A	ENSG00000115355	0,837	0,845714661	0,674	0,96	0,73
Oligodendrocytes	RNF130	ENSG00000113269	0,758	0,628888482	0,516	0,91	0,69
Oligodendrocytes	RTN4	ENSG00000115310	0,902	1,093217859	0,804	0,98	0,75
Oligodendrocytes	CLASP2	ENSG00000163539	0,903	1,013594326	0,806	0,99	0,77
Oligodendrocytes	MAP4K4	ENSG00000071054	0,897	1,096173591	0,794	0,98	0,76
Oligodendrocytes	FMNL2	ENSG00000157827	0,915	1,311774904	0,83	0,99	0,8
Oligodendrocytes	FTH1	ENSG00000167996	0,725	0,776894145	0,45	0,85	0,66
Oligodendrocytes	PTK2	ENSG00000169398	0,756	0,639409331	0,512	0,96	0,8
Oligodendrocytes	SIK3	ENSG00000160584	0,881	1,11310599	0,762	0,99	0,83
Oligodendrocytes	ZNF638	ENSG00000075292	0,767	0,628759385	0,534	0,95	0,8
Oligodendrocytes	DST	ENSG00000151914	0,801	0,612109476	0,602	0,99	0,86
Oligodendrocytes	TCF12	ENSG00000140262	0,801	0,743308943	0,602	0,98	0,85
Oligodendrocytes	QKI	ENSG00000112531	0,948	1,29071784	0,896	1	0,88
Excitatory	MYT1L	ENSG00000186487	0,949	1,836078745	0,898	0,97	0,12
Excitatory	CELF4	ENSG00000101489	0,935	1,528801414	0,87	0,94	0,09
Excitatory	GRIN1	ENSG00000176884	0,925	1,291753069	0,85	0,92	0,08
Excitatory	SYT1	ENSG00000067715	0,938	2,003479071	0,876	0,96	0,12
Excitatory	PAK3	ENSG00000077264	0,93	1,532454893	0,86	0,94	0,1
Excitatory	ANKRD30BL	ENSG00000163046	0,943	1,68275509	0,886	0,95	0,12
Excitatory	SRRM3	ENSG00000177679	0,922	1,30050477	0,844	0,92	0,09
Excitatory	GRIN2B	ENSG00000273079	0,921	1,480829437	0,842	0,92	0,1
Excitatory	CACNA1B	ENSG00000148408	0,939	1,69432504	0,878	0,94	0,13
Excitatory	RIMS2	ENSG00000176406	0,952	2,108544744	0,904	0,97	0,16
Excitatory	LINGO2	ENSG00000174482	0,911	2,030034091	0,822	0,88	0,08
Excitatory	SYN2	ENSG00000157152	0,907	1,279209628	0,814	0,91	0,1
Excitatory	GABBR2	ENSG00000136928	0,904	1,238230212	0,808	0,89	0,08

Excitatory	ATP8A2	ENSG00000132932	0,934	1,697861983	0,868	0,95	0,15
Excitatory	SLC4A10	ENSG00000144290	0,908	1,313190073	0,816	0,9	0,1
Excitatory	CDH18	ENSG00000145526	0,929	2,194823648	0,858	0,92	0,13
Excitatory	GABRB3	ENSG00000166206	0,918	1,445003669	0,836	0,93	0,14
Excitatory	STMN2	ENSG00000104435	0,896	1,226738928	0,792	0,85	0,06
Excitatory	TENM2	ENSG00000145934	0,935	2,415074547	0,87	0,94	0,15
Excitatory	CELF5	ENSG00000161082	0,895	1,01373918	0,79	0,86	0,08
Excitatory	KCNB2	ENSG00000182674	0,9	1,896723618	0,8	0,83	0,05
Excitatory	FGF12	ENSG00000114279	0,924	1,713846524	0,848	0,97	0,18
Excitatory	SCN2A	ENSG00000136531	0,917	1,298722359	0,834	0,93	0,15
Excitatory	KSR2	ENSG00000171435	0,908	1,323234624	0,816	0,91	0,13
Excitatory	RAB3C	ENSG00000152932	0,897	1,292268148	0,794	0,89	0,11
Excitatory	MEG8	ENSG00000225746	0,901	1,38890458	0,802	0,89	0,11
Excitatory	LRFN5	ENSG00000165379	0,915	1,667067659	0,83	0,92	0,14
Excitatory	CHD5	ENSG00000116254	0,89	0,917338143	0,78	0,83	0,06
Excitatory	HECW1	ENSG00000002746	0,894	1,421957646	0,788	0,89	0,11
Excitatory	CAMK2B	ENSG00000058404	0,892	1,027051732	0,784	0,9	0,13
Excitatory	PTPRN2	ENSG00000155093	0,939	1,695309514	0,878	0,95	0,18
Excitatory	MIAT	ENSG00000225783	0,894	1,129147242	0,788	0,87	0,1
Excitatory	CADPS	ENSG00000163618	0,924	1,528831659	0,848	0,96	0,2
Excitatory	KCNC2	ENSG00000166006	0,888	1,488853556	0,776	0,81	0,05
Excitatory	NMNAT2	ENSG00000157064	0,891	1,128094288	0,782	0,88	0,12
Excitatory	DNM1	ENSG00000106976	0,892	1,029215195	0,784	0,89	0,13
Excitatory	OPCML	ENSG00000183715	0,872	1,214176777	0,744	0,94	0,18
Excitatory	NRG1	ENSG00000157168	0,898	2,343329129	0,796	0,86	0,1
Excitatory	XKR4	ENSG00000206579	0,884	1,34563042	0,768	0,9	0,14
Excitatory	DLGAP2	ENSG00000198010	0,89	1,51240628	0,78	0,86	0,1
Excitatory	RALYL	ENSG00000184672	0,937	2,116987122	0,874	0,97	0,21
Excitatory	SCN3A	ENSG00000153253	0,884	1,135297746	0,768	0,88	0,12
Excitatory	GABRB2	ENSG00000145864	0,883	1,436990823	0,766	0,82	0,07
Excitatory	GABRG2	ENSG00000113327	0,881	1,020336251	0,762	0,81	0,06
Excitatory	SHANK2	ENSG00000162105	0,879	1,044400357	0,758	0,88	0,13
Excitatory	ARHGAP44	ENSG00000006740	0,899	1,190827121	0,798	0,9	0,15
Excitatory	CACNA1E	ENSG00000198216	0,894	1,447986247	0,788	0,86	0,11
Excitatory	GRM7	ENSG00000196277	0,905	1,714651557	0,81	0,93	0,18
Excitatory	SCN1A	ENSG00000144285	0,876	1,141052593	0,752	0,91	0,16
Excitatory	WNK2	ENSG00000165238	0,876	0,973004115	0,752	0,88	0,13
Excitatory	UNC80	ENSG00000144406	0,88	1,064584128	0,76	0,93	0,18
Excitatory	GRM5	ENSG00000168959	0,886	1,458644988	0,772	0,91	0,16
Excitatory	SYN3	ENSG00000185666	0,883	1,394021221	0,766	0,85	0,11
Excitatory	GRIA1	ENSG00000155511	0,881	1,570289931	0,762	0,83	0,09
Excitatory	SNAP25	ENSG00000132639	0,892	1,211348459	0,784	0,93	0,19
Excitatory	GALNT17	ENSG00000185274	0,876	1,174919952	0,752	0,85	0,1
Excitatory	SEZ6L	ENSG00000100095	0,875	1,265310919	0,75	0,87	0,13
Excitatory	ROBO2	ENSG00000185008	0,908	2,165191603	0,816	0,92	0,17
Excitatory	MTUS2	ENSG00000132938	0,879	1,593867698	0,758	0,82	0,08
Excitatory	DNAH14	ENSG00000185842	0,886	1,279983337	0,772	0,85	0,12
Excitatory	EPHA6	ENSG00000080224	0,879	1,792841387	0,758	0,82	0,08
Excitatory	FGF14	ENSG00000102466	0,899	1,467022799	0,798	0,98	0,24
Excitatory	DCLK1	ENSG00000133083	0,886	1,148501274	0,772	0,94	0,2
Excitatory	KCNH7	ENSG00000184611	0,881	1,789290423	0,762	0,81	0,07
Excitatory	JPH4	ENSG00000092051	0,867	0,83685635	0,734	0,81	0,08
Excitatory	SUSD4	ENSG00000143502	0,87	0,952958051	0,74	0,82	0,09
Excitatory	MIR137HG	ENSG00000225206	0,875	1,361739271	0,75	0,79	0,06
Excitatory	AGBL4	ENSG00000186094	0,922	1,668228178	0,844	0,95	0,22

Excitatory	SYT16	ENSG00000139973	0,87	1,018537288	0,74	0,85	0,12
Excitatory	DOK6	ENSG00000206052	0,868	1,163711512	0,736	0,86	0,13
Excitatory	GRIP1	ENSG00000155974	0,908	1,639839567	0,816	0,92	0,19
Excitatory	AMPH	ENSG00000078053	0,871	1,033369364	0,742	0,84	0,11
Excitatory	RUNDC3B	ENSG00000105784	0,863	0,927942945	0,726	0,84	0,11
Excitatory	STXBP5L	ENSG00000145087	0,897	1,454810751	0,794	0,92	0,19
Excitatory	HS6ST3	ENSG00000185352	0,881	1,679383108	0,762	0,88	0,16
Excitatory	MAST1	ENSG00000105613	0,862	0,81628926	0,724	0,8	0,07
Excitatory	SPTBN4	ENSG00000160460	0,903	1,220484949	0,806	0,93	0,2
Excitatory	PCSK2	ENSG00000125851	0,872	1,409402138	0,744	0,8	0,07
Excitatory	CALY	ENSG00000130643	0,863	1,172618244	0,726	0,8	0,08
Excitatory	TENM3	ENSG00000218336	0,885	1,473352618	0,77	0,89	0,17
Excitatory	SRRM4	ENSG00000139767	0,859	0,976623481	0,718	0,78	0,06
Excitatory	GALNTL6	ENSG00000174473	0,872	1,967340051	0,744	0,82	0,1
Excitatory	PRKAR1B	ENSG00000188191	0,872	0,94370321	0,744	0,85	0,13
Excitatory	NELL2	ENSG00000184613	0,871	1,359528813	0,742	0,82	0,1
Excitatory	SNTG1	ENSG00000147481	0,867	1,656986759	0,734	0,87	0,15
Excitatory	KCNJ3	ENSG00000162989	0,861	1,129524508	0,722	0,83	0,11
Excitatory	UNC5D	ENSG00000156687	0,868	1,894736163	0,736	0,81	0,1
Excitatory	SYBU	ENSG00000147642	0,854	0,887320735	0,708	0,85	0,14
Excitatory	CCSER1	ENSG00000184305	0,913	1,632873222	0,826	0,96	0,25
Excitatory	TMEM130	ENSG00000166448	0,854	0,822758753	0,708	0,77	0,06
Excitatory	SORBS2	ENSG00000154556	0,859	1,035307352	0,718	0,9	0,2
Excitatory	PRICKLE1	ENSG00000139174	0,852	1,023419127	0,704	0,79	0,09
Excitatory	CACNA1A	ENSG00000141837	0,87	1,135196683	0,74	0,94	0,24
Excitatory	FRRS1L	ENSG00000260230	0,864	0,905900448	0,728	0,85	0,14
Excitatory	PLXNA4	ENSG00000221866	0,861	1,106433386	0,722	0,82	0,11
Excitatory	TUSC3	ENSG00000104723	0,851	0,845664185	0,702	0,81	0,1
Excitatory	SCN8A	ENSG00000196876	0,875	1,042393312	0,75	0,88	0,18
Excitatory	IQSEC3	ENSG00000120645	0,849	0,75312042	0,698	0,76	0,06
Excitatory	CNTN5	ENSG00000149972	0,872	2,307335272	0,744	0,81	0,1
Excitatory	BASP1	ENSG00000176788	0,857	0,953951943	0,714	0,88	0,17
Excitatory	GAP43	ENSG00000172020	0,854	0,946470331	0,708	0,78	0,08
Excitatory	GRIK2	ENSG00000164418	0,908	1,672820045	0,816	0,96	0,26
Excitatory	FRMPD4	ENSG00000169933	0,857	1,429255679	0,714	0,83	0,13
Excitatory	PTPRR	ENSG00000153233	0,852	1,069248841	0,704	0,75	0,05
Excitatory	ADD2	ENSG00000075340	0,849	0,763813784	0,698	0,78	0,08
Excitatory	KIAA1549L	ENSG00000110427	0,848	0,93457727	0,696	0,8	0,1
Excitatory	GABRG3	ENSG00000182256	0,852	1,570330139	0,704	0,75	0,05
Excitatory	ATRNL1	ENSG00000107518	0,838	0,937164967	0,676	0,87	0,18
Excitatory	ADAM23	ENSG00000114948	0,866	1,045191576	0,732	0,87	0,18
Excitatory	RIMS1	ENSG00000079841	0,91	1,500775303	0,82	0,93	0,24
Excitatory	KLHL29	ENSG00000119771	0,849	0,95856309	0,698	0,8	0,11
Excitatory	CNTNAP5	ENSG00000155052	0,859	1,628956776	0,718	0,84	0,15
Excitatory	SHISA9	ENSG00000237515	0,849	1,242819669	0,698	0,83	0,13
Excitatory	CACNB2	ENSG00000165995	0,877	1,238990006	0,754	0,94	0,24
Excitatory	GABRB1	ENSG00000163288	0,874	1,279647708	0,748	0,91	0,22
Excitatory	FHOD3	ENSG00000134775	0,851	1,010443778	0,702	0,81	0,11
Excitatory	FAM155A	ENSG00000204442	0,931	1,827240861	0,862	0,98	0,29
Excitatory	OLFM3	ENSG00000118733	0,855	1,296724951	0,71	0,79	0,1
Excitatory	KHDRBS2	ENSG00000112232	0,877	1,379594484	0,754	0,89	0,2
Excitatory	SLC8A1	ENSG00000183023	0,843	1,006918401	0,686	0,95	0,26
Excitatory	CAP2	ENSG00000112186	0,842	0,769229262	0,684	0,78	0,09
Excitatory	STXBP5-AS1	ENSG00000233452	0,856	1,228167931	0,712	0,81	0,12
Excitatory	REEP1	ENSG00000068615	0,843	0,810928791	0,686	0,78	0,1

Excitatory	NSG2	ENSG00000170091	0,837	0,818427178	0,674	0,78	0,1
Excitatory	ATCAY	ENSG00000167654	0,834	0,694109058	0,668	0,78	0,1
Excitatory	VSNL1	ENSG00000163032	0,842	0,956971125	0,684	0,75	0,06
Excitatory	RIMBP2	ENSG00000060709	0,846	0,815682256	0,692	0,8	0,11
Excitatory	SNRPN	ENSG00000128739	0,898	1,45028026	0,796	0,91	0,22
Excitatory	NEXMIF	ENSG00000050030	0,839	0,912110641	0,678	0,79	0,1
Excitatory	DSCAM	ENSG00000171587	0,844	0,700617852	0,688	0,95	0,27
Excitatory	CNTN4	ENSG00000144619	0,853	1,63310446	0,706	0,82	0,14
Excitatory	SLC2A13	ENSG00000151229	0,853	1,140690754	0,706	0,88	0,2
Excitatory	OSBPL6	ENSG00000079156	0,837	0,876932624	0,674	0,88	0,2
Excitatory	BICDL1	ENSG00000135127	0,843	0,798265564	0,686	0,77	0,1
Excitatory	ELAVL2	ENSG00000107105	0,838	0,971176942	0,676	0,73	0,05
Excitatory	DLGAP1	ENSG00000170579	0,867	1,342557138	0,734	0,92	0,25
Excitatory	NOL4	ENSG00000101746	0,826	0,822378014	0,652	0,85	0,18
Excitatory	PPM1E	ENSG00000175175	0,869	1,137385809	0,738	0,91	0,24
Excitatory	KCND2	ENSG00000184408	0,835	1,053742766	0,67	0,92	0,25
Excitatory	SLC41A2	ENSG00000136052	0,833	0,736811469	0,666	0,79	0,12
Excitatory	C11orf80	ENSG00000173715	0,839	0,797455118	0,678	0,79	0,12
Excitatory	SORCS3	ENSG00000156395	0,834	1,131425557	0,668	0,78	0,11
Excitatory	RAP1GAP2	ENSG00000132359	0,826	0,704166669	0,652	0,79	0,13
Excitatory	KCNIP4	ENSG00000185774	0,87	1,662495086	0,74	0,91	0,25
Excitatory	ZNF804A	ENSG00000170396	0,833	1,278761936	0,666	0,77	0,1
Excitatory	PLPPR4	ENSG00000117600	0,83	0,733983102	0,66	0,75	0,08
Excitatory	MYH10	ENSG00000133026	0,833	0,78160054	0,666	0,83	0,16
Excitatory	ELAVL4	ENSG00000162374	0,828	0,774086371	0,656	0,75	0,09
Excitatory	LRRC7	ENSG00000033122	0,885	1,562509689	0,77	0,94	0,27
Excitatory	CNTN1	ENSG00000018236	0,82	0,836436071	0,64	0,96	0,3
Excitatory	ANKRD34C-AS1	ENSG00000259234	0,83	0,861308332	0,66	0,7	0,04
Excitatory	PAM	ENSG00000145730	0,849	1,093142325	0,698	0,9	0,24
Excitatory	EPB41L4B	ENSG00000095203	0,832	0,812998394	0,664	0,75	0,09
Excitatory	SLC8A3	ENSG00000100678	0,824	0,78096972	0,648	0,77	0,11
Excitatory	TMEM132B	ENSG00000139364	0,83	0,95646704	0,66	0,79	0,13
Excitatory	KIAA0319	ENSG00000137261	0,823	0,74534728	0,646	0,77	0,11
Excitatory	RPH3A	ENSG00000089169	0,83	1,007261376	0,66	0,72	0,06
Excitatory	EFNA5	ENSG00000184349	0,827	1,093537905	0,654	0,78	0,12
Excitatory	CCDC85A	ENSG00000055813	0,823	0,916644115	0,646	0,77	0,12
Excitatory	CA10	ENSG00000154975	0,811	0,883974304	0,622	0,78	0,12
Excitatory	SLC24A3	ENSG00000185052	0,821	1,013047169	0,642	0,78	0,12
Excitatory	CHL1	ENSG00000134121	0,81	0,723794249	0,62	0,87	0,22
Excitatory	MDGA2	ENSG00000139915	0,874	1,332851979	0,748	0,96	0,31
Excitatory	AC073050.1	ENSG00000228222	0,833	1,1309326	0,666	0,8	0,15
Excitatory	ASIC2	ENSG00000108684	0,836	1,470915231	0,672	0,76	0,11
Excitatory	SLC17A6	ENSG00000091664	0,826	0,893899526	0,652	0,66	0,01
Excitatory	ANO5	ENSG00000171714	0,819	0,683252033	0,638	0,77	0,12
Excitatory	CAMK2A	ENSG00000070808	0,829	0,787996719	0,658	0,73	0,07
Excitatory	ATP2B2	ENSG00000157087	0,808	0,697245836	0,616	0,84	0,19
Excitatory	FGF13	ENSG00000129682	0,829	1,377968328	0,658	0,7	0,05
Excitatory	BASP1-AS1	ENSG00000215196	0,824	0,825243582	0,648	0,73	0,08
Excitatory	GUCY1A2	ENSG00000152402	0,826	0,968680079	0,652	0,81	0,17
Excitatory	LHFPL3	ENSG00000187416	0,82	0,819534017	0,64	0,83	0,18
Excitatory	LHFPL4	ENSG00000156959	0,82	0,633440714	0,64	0,75	0,1
Excitatory	LRRTM4	ENSG00000176204	0,862	1,528318444	0,724	0,91	0,26
Excitatory	MGAT4C	ENSG00000182050	0,839	1,61907205	0,678	0,81	0,16
Excitatory	CNKSR2	ENSG00000149970	0,822	0,953792643	0,644	0,8	0,15

Excitatory	DGKB	ENSG00000136267	0,838	1,373394197	0,676	0,82	0,17
Excitatory	CACNA1C	ENSG00000151067	0,895	1,386221178	0,79	0,96	0,31
Excitatory	NHS	ENSG00000188158	0,819	0,8770928	0,638	0,77	0,12
Excitatory	JAKMIP1	ENSG00000152969	0,819	0,699214629	0,638	0,72	0,07
Excitatory	SNAP91	ENSG00000065609	0,885	1,156963894	0,77	0,94	0,29
Excitatory	FAM189A1	ENSG00000104059	0,825	0,999919421	0,65	0,72	0,08
Excitatory	DENND1B	ENSG00000213047	0,817	0,727840433	0,634	0,78	0,14
Excitatory	KCNB1	ENSG00000158445	0,815	0,647498744	0,63	0,75	0,11
Excitatory	AC092683.1	ENSG00000230606	0,903	1,312822413	0,806	0,94	0,29
Excitatory	PRR16	ENSG00000184838	0,821	1,17195109	0,642	0,71	0,07
Excitatory	ZFR2	ENSG00000105278	0,82	0,654272762	0,64	0,73	0,09
Excitatory	CSMD3	ENSG00000164796	0,883	1,414820943	0,766	0,95	0,31
Excitatory	KCTD16	ENSG00000183775	0,836	1,208624592	0,672	0,82	0,18
Excitatory	EPHA5	ENSG00000145242	0,821	1,083273597	0,642	0,71	0,07
Excitatory	SLC44A5	ENSG00000137968	0,823	1,144364276	0,646	0,75	0,12
Excitatory	PTPRN	ENSG00000054356	0,818	0,678477827	0,636	0,69	0,05
Excitatory	CACNG2	ENSG00000166862	0,817	0,764329389	0,634	0,71	0,08
Excitatory	DPY19L2	ENSG00000177990	0,812	0,672751812	0,624	0,77	0,13
Excitatory	KCNQ3	ENSG00000184156	0,819	0,783981609	0,638	0,88	0,25
Excitatory	KCNJ6	ENSG00000157542	0,818	0,877572017	0,636	0,71	0,07
Excitatory	TENM1	ENSG00000009694	0,823	1,102615228	0,646	0,74	0,11
Excitatory	ABLIM2	ENSG00000163995	0,824	0,779732725	0,648	0,8	0,17
Excitatory	PCDH15	ENSG00000150275	0,816	1,322109856	0,632	0,79	0,16
Excitatory	RBFOX3	ENSG00000167281	0,817	0,836916621	0,634	0,69	0,06
Excitatory	PCLO	ENSG00000186472	0,912	1,364846243	0,824	0,96	0,33
Excitatory	CIT	ENSG00000122966	0,825	0,910154873	0,65	0,81	0,17
Excitatory	SIDT1	ENSG00000072858	0,812	0,699453418	0,624	0,71	0,08
Excitatory	PLCB4	ENSG00000101333	0,81	0,853859756	0,62	0,84	0,21
Excitatory	ANK1	ENSG00000029534	0,818	0,977515239	0,636	0,7	0,07
Excitatory	CLSTN3	ENSG00000139182	0,811	0,598520179	0,622	0,7	0,07
Excitatory	NYAP2	ENSG00000144460	0,812	0,722761919	0,624	0,68	0,05
Excitatory	BTBD11	ENSG00000151136	0,807	0,769904445	0,614	0,72	0,09
Excitatory	SCN9A	ENSG00000169432	0,816	0,933997796	0,632	0,74	0,11
Excitatory	SH3GL2	ENSG00000107295	0,809	0,776771703	0,618	0,76	0,13
Excitatory	MAP7D2	ENSG00000184368	0,812	0,612354704	0,624	0,69	0,06
Excitatory	SLC35F1	ENSG00000196376	0,803	0,7214571	0,606	0,82	0,2
Excitatory	SCN7A	ENSG00000136546	0,813	0,768899758	0,626	0,68	0,05
Excitatory	FP700111.1	ENSG00000224363	0,835	0,887797684	0,67	0,86	0,23
Excitatory	CSMD2	ENSG00000121904	0,82	0,902853503	0,64	0,86	0,23
Excitatory	PAK5	ENSG00000101349	0,807	0,690005836	0,614	0,72	0,1
Excitatory	GNB5	ENSG00000069966	0,806	0,588016683	0,612	0,74	0,11
Excitatory	RNF175	ENSG00000145428	0,811	0,641274999	0,622	0,69	0,06
Excitatory	CAMK4	ENSG00000152495	0,811	0,836164933	0,622	0,73	0,1
Excitatory	CNNM1	ENSG00000119946	0,809	0,598975289	0,618	0,69	0,06
Excitatory	NRG3	ENSG00000185737	0,847	1,091130079	0,694	0,98	0,35
Excitatory	NRSN1	ENSG00000152954	0,808	0,627838611	0,616	0,69	0,07
Excitatory	NEK10	ENSG00000163491	0,808	0,726295483	0,616	0,74	0,12
Excitatory	TMTC1	ENSG00000133687	0,804	0,809569524	0,608	0,82	0,2
Excitatory	CACNA1D	ENSG00000157388	0,823	0,787050455	0,646	0,87	0,25
Excitatory	GABRA2	ENSG00000151834	0,811	0,858549639	0,622	0,7	0,08
Excitatory	AKAP12	ENSG00000131016	0,798	0,599141329	0,596	0,77	0,14
Excitatory	RAD9A	ENSG00000172613	0,808	0,672622797	0,616	0,82	0,2
Excitatory	STXBP1	ENSG00000136854	0,836	0,800427893	0,672	0,88	0,27
Excitatory	GRM1	ENSG00000152822	0,812	1,130297904	0,624	0,68	0,06
Excitatory	PNMA2	ENSG00000240694	0,806	0,737984639	0,612	0,7	0,08

Excitatory	CLVS1	ENSG00000177182	0,803	0,659677241	0,606	0,76	0,15
Excitatory	KIAA1211	ENSG00000109265	0,807	0,76748139	0,614	0,81	0,19
Excitatory	MAP2	ENSG00000078018	0,916	1,374052122	0,832	0,98	0,37
Excitatory	SVOP	ENSG00000166111	0,809	0,632237755	0,618	0,66	0,05
Excitatory	ELMOD1	ENSG00000110675	0,799	0,718535119	0,598	0,74	0,12
Excitatory	GABRA1	ENSG00000022355	0,808	0,833291803	0,616	0,66	0,04
Excitatory	RGS17	ENSG00000091844	0,805	0,675179585	0,61	0,69	0,07
Excitatory	ERC2	ENSG00000187672	0,859	1,130196124	0,718	0,93	0,32
Excitatory	SV2A	ENSG00000159164	0,802	0,663787494	0,604	0,76	0,15
Excitatory	LINC01250	ENSG00000234423	0,808	0,781233333	0,616	0,66	0,05
Excitatory	CERS6	ENSG00000172292	0,809	0,788253946	0,618	0,86	0,25
Excitatory	MAP6	ENSG00000171533	0,804	0,604492318	0,608	0,77	0,16
Excitatory	SYT14	ENSG00000143469	0,818	0,776569162	0,636	0,86	0,25
Excitatory	SGCZ	ENSG00000185053	0,819	1,884327589	0,638	0,76	0,15
Excitatory	LINC01122	ENSG00000233723	0,808	0,960402425	0,616	0,78	0,17
Excitatory	LRFN2	ENSG00000156564	0,796	0,647541801	0,592	0,69	0,09
Excitatory	BRINP3	ENSG00000162670	0,803	1,096082874	0,606	0,78	0,17
Excitatory	RALGPS2	ENSG00000116191	0,791	0,636296593	0,582	0,76	0,16
Excitatory	PACRG	ENSG00000112530	0,803	0,774222071	0,606	0,8	0,2
Excitatory	HCN1	ENSG00000164588	0,803	1,188319502	0,606	0,66	0,06
Excitatory	FBXO16	ENSG00000214050	0,797	0,607220275	0,594	0,69	0,09
Excitatory	ADGRL2	ENSG00000117114	0,805	1,191564701	0,61	0,72	0,11
Excitatory	RAPGEF4	ENSG00000091428	0,816	0,775917868	0,632	0,91	0,31
Excitatory	PCDH7	ENSG00000169851	0,812	1,165839958	0,624	0,85	0,25
Excitatory	TMEM108	ENSG00000144868	0,81	0,993381197	0,62	0,84	0,24
Excitatory	KIF5A	ENSG00000155980	0,798	0,594320767	0,596	0,7	0,1
Excitatory	ASTN1	ENSG00000152092	0,804	0,74538418	0,608	0,85	0,25
Excitatory	RYR2	ENSG00000198626	0,852	1,526882085	0,704	0,85	0,26
Excitatory	VAT1L	ENSG00000171724	0,8	0,78347056	0,6	0,72	0,12
Excitatory	ME3	ENSG00000151376	0,792	0,623551302	0,584	0,77	0,17
Excitatory	TAFA2	ENSG00000198673	0,814	1,291586578	0,628	0,78	0,18
Excitatory	CSMD1	ENSG00000183117	0,877	1,378165766	0,754	0,96	0,36
Excitatory	LONRF2	ENSG00000170500	0,806	0,68797031	0,612	0,82	0,23
Excitatory	SYN1	ENSG00000008056	0,796	0,596585291	0,592	0,66	0,07
Excitatory	AFF3	ENSG00000144218	0,852	1,018109051	0,704	0,94	0,34
Excitatory	THY1	ENSG00000154096	0,794	0,760651957	0,588	0,68	0,09
Excitatory	KIAA0825	ENSG00000185261	0,806	0,782522262	0,612	0,85	0,26
Excitatory	ICA1	ENSG00000003147	0,791	0,616689343	0,582	0,69	0,1
Excitatory	KLHL1	ENSG00000150361	0,805	1,484632939	0,61	0,67	0,07
Excitatory	BRINP1	ENSG00000078725	0,788	0,791646927	0,576	0,73	0,14
Excitatory	RAB27B	ENSG00000041353	0,795	0,729729654	0,59	0,64	0,05
Excitatory	SPTAN1	ENSG00000197694	0,799	0,681993052	0,598	0,88	0,29
Excitatory	XKR6	ENSG00000171044	0,864	1,124997188	0,728	0,93	0,34
Excitatory	PATJ	ENSG00000132849	0,82	0,833271619	0,64	0,87	0,28
Excitatory	CLVS2	ENSG00000146352	0,792	0,610768487	0,584	0,65	0,06
Excitatory	LINC00937	ENSG00000226091	0,792	0,697979737	0,584	0,73	0,14
Excitatory	HMGCLL1	ENSG00000146151	0,791	0,644024712	0,582	0,75	0,16
Excitatory	SYP	ENSG00000102003	0,789	0,604378687	0,578	0,77	0,18
Excitatory	GNG2	ENSG00000186469	0,786	0,598771585	0,572	0,69	0,1
Excitatory	LINC01414	ENSG00000253554	0,795	1,007812523	0,59	0,66	0,07
Excitatory	NRXN1	ENSG00000179915	0,898	1,459646505	0,796	0,99	0,4
Excitatory	CACNG8	ENSG00000142408	0,792	0,60503273	0,584	0,65	0,07
Excitatory	CPNE4	ENSG00000196353	0,796	1,282271087	0,592	0,65	0,06
Excitatory	EML6	ENSG00000214595	0,789	0,735582378	0,578	0,79	0,2
Excitatory	TRERF1	ENSG00000124496	0,78	0,588678119	0,56	0,73	0,15

Excitatory	TMEM178B	ENSG00000261115	0,852	1,042136586	0,704	0,93	0,35
Excitatory	TMEM59L	ENSG00000105696	0,786	0,616464258	0,572	0,69	0,1
Excitatory	LINC02389	ENSG00000255693	0,79	0,69188611	0,58	0,64	0,06
Excitatory	ARPP21	ENSG00000172995	0,804	1,139646417	0,608	0,79	0,2
Excitatory	SCG2	ENSG00000171951	0,789	0,878328183	0,578	0,65	0,07
Excitatory	FRY	ENSG00000073910	0,793	0,70799437	0,586	0,9	0,32
Excitatory	VWC2L	ENSG00000174453	0,79	0,955024546	0,58	0,62	0,04
Excitatory	RIT2	ENSG00000152214	0,787	1,02852121	0,574	0,65	0,08
Excitatory	KIF9-AS1	ENSG00000227398	0,797	0,698827545	0,594	0,87	0,29
Excitatory	FBXL2	ENSG00000153558	0,791	0,661318018	0,582	0,8	0,22
Excitatory	GLRA3	ENSG00000145451	0,788	0,814399317	0,576	0,6	0,03
Excitatory	NDRG4	ENSG00000103034	0,778	0,587031564	0,556	0,68	0,11
Excitatory	KCND3	ENSG00000171385	0,776	0,702939115	0,552	0,74	0,17
Excitatory	CNTN3	ENSG00000113805	0,779	0,82224751	0,558	0,71	0,14
Excitatory	AC120193.1	ENSG00000253535	0,787	0,999331119	0,574	0,66	0,09
Excitatory	BAIAP3	ENSG00000007516	0,784	0,788894676	0,568	0,64	0,07
Excitatory	DPP10	ENSG00000175497	0,798	0,816658569	0,596	0,85	0,28
Excitatory	LIN7A	ENSG00000111052	0,777	0,661327948	0,554	0,67	0,11
Excitatory	CHRM3	ENSG00000133019	0,789	1,699494622	0,578	0,61	0,05
Excitatory	LINC00632	ENSG00000203930	0,862	1,021573588	0,724	0,91	0,34
Excitatory	TENM4	ENSG00000149256	0,834	1,027264622	0,668	0,9	0,33
Excitatory	UCHL1	ENSG00000154277	0,794	0,777212271	0,588	0,82	0,25
Excitatory	TAFA1	ENSG00000183662	0,79	1,401507084	0,58	0,69	0,12
Excitatory	WDR17	ENSG00000150627	0,788	0,628537077	0,576	0,81	0,24
Excitatory	FAT3	ENSG00000165323	0,763	0,642412388	0,526	0,75	0,19
Excitatory	GPR158	ENSG00000151025	0,779	0,667117542	0,558	0,85	0,28
Excitatory	SGSM1	ENSG00000167037	0,799	0,711052531	0,598	0,84	0,28
Excitatory	KCNH5	ENSG00000140015	0,784	1,003493176	0,568	0,61	0,05
Excitatory	TMEM232	ENSG00000186952	0,798	0,655461411	0,596	0,85	0,29
Excitatory	EPHB1	ENSG00000154928	0,788	0,880278767	0,576	0,72	0,15
Excitatory	CSRNP3	ENSG00000178662	0,846	0,948721257	0,692	0,92	0,35
Excitatory	TRMT9B	ENSG00000250305	0,778	0,660789787	0,556	0,67	0,11
Excitatory	HSPA4L	ENSG00000164070	0,775	0,588928437	0,55	0,73	0,17
Excitatory	PTPRO	ENSG00000151490	0,783	1,037009212	0,566	0,65	0,09
Excitatory	FSTL4	ENSG00000053108	0,78	1,235969541	0,56	0,61	0,06
Excitatory	VPS13A	ENSG00000197969	0,78	0,606632072	0,56	0,81	0,26
Excitatory	RUNX1T1	ENSG00000079102	0,776	0,744100114	0,552	0,82	0,26
Excitatory	EML5	ENSG00000165521	0,771	0,649556142	0,542	0,73	0,18
Excitatory	AFF2	ENSG00000155966	0,776	0,789599095	0,552	0,61	0,05
Excitatory	FOCAD	ENSG00000188352	0,844	0,979061284	0,688	0,91	0,36
Excitatory	MCF2L2	ENSG00000053524	0,825	0,831936796	0,65	0,89	0,34
Excitatory	LINC01322	ENSG00000244128	0,78	0,960582207	0,56	0,69	0,13
Excitatory	FAAH2	ENSG00000165591	0,774	0,626962687	0,548	0,69	0,14
Excitatory	MAGI3	ENSG00000081026	0,786	0,704044808	0,572	0,84	0,29
Excitatory	GNAL	ENSG00000141404	0,773	0,694525923	0,546	0,67	0,11
Excitatory	AC025159.1	ENSG00000257815	0,803	0,936177995	0,606	0,83	0,28
Excitatory	DAB1	ENSG00000173406	0,854	1,480675026	0,708	0,9	0,35
Excitatory	HSPA12A	ENSG00000165868	0,829	0,832447529	0,658	0,91	0,36
Excitatory	FAM135B	ENSG00000147724	0,765	0,613476019	0,53	0,75	0,2
Excitatory	AC092691.1	ENSG00000239268	0,783	0,878955425	0,566	0,88	0,33
Excitatory	RGS7	ENSG00000182901	0,825	1,02865025	0,65	0,93	0,39
Excitatory	PLCB1	ENSG00000182621	0,756	0,734305634	0,512	0,86	0,31
Excitatory	SLC25A12	ENSG00000115840	0,806	0,738874313	0,612	0,88	0,33
Excitatory	PWRN1	ENSG00000259905	0,771	0,701509028	0,542	0,78	0,24
Excitatory	CTNNA2	ENSG00000066032	0,817	0,906328657	0,634	0,97	0,43

Excitatory	CHSY3	ENSG00000198108	0,773	1,073318359	0,546	0,69	0,15
Excitatory	MCTP1	ENSG00000175471	0,766	0,77074091	0,532	0,68	0,14
Excitatory	INPP4B	ENSG00000109452	0,798	1,244364223	0,596	0,8	0,26
Excitatory	CACNA2D3	ENSG00000157445	0,764	0,770858598	0,528	0,8	0,26
Excitatory	RERG	ENSG00000134533	0,768	0,79459871	0,536	0,6	0,06
Excitatory	PCNX2	ENSG00000135749	0,805	0,682580313	0,61	0,91	0,37
Excitatory	NDST3	ENSG00000164100	0,77	0,925298996	0,54	0,6	0,06
Excitatory	ADGRV1	ENSG00000164199	0,767	0,704787038	0,534	0,64	0,1
Excitatory	NTNG1	ENSG00000162631	0,781	1,506315859	0,562	0,7	0,16
Excitatory	SLC35F4	ENSG00000151812	0,771	1,151471163	0,542	0,59	0,05
Excitatory	PLA2R1	ENSG00000153246	0,767	0,65616471	0,534	0,6	0,06
Excitatory	PLEKHA5	ENSG00000052126	0,805	0,791295148	0,61	0,93	0,4
Excitatory	NCDN	ENSG00000020129	0,764	0,628390783	0,528	0,67	0,14
Excitatory	DGKI	ENSG00000157680	0,824	0,981883833	0,648	0,9	0,37
Excitatory	CELF2	ENSG00000048740	0,768	0,76394756	0,536	0,93	0,4
Excitatory	EPHA7	ENSG00000135333	0,767	0,876818486	0,534	0,6	0,07
Excitatory	KALRN	ENSG00000160145	0,817	0,935837942	0,634	0,92	0,39
Excitatory	ABCA10	ENSG00000154263	0,762	0,597089307	0,524	0,64	0,11
Excitatory	FLRT2	ENSG00000185070	0,752	0,660096874	0,504	0,71	0,18
Excitatory	CEP112	ENSG00000154240	0,757	0,743111564	0,514	0,76	0,24
Excitatory	NSF	ENSG00000073969	0,839	0,9046371	0,678	0,94	0,42
Excitatory	UNC79	ENSG00000133958	0,839	0,9154308	0,678	0,93	0,42
Excitatory	KIAA1217	ENSG00000120549	0,755	0,878280107	0,51	0,74	0,22
Excitatory	LY6H	ENSG00000176956	0,756	0,603860476	0,512	0,57	0,06
Excitatory	PCSK1N	ENSG00000102109	0,765	0,968172785	0,53	0,71	0,2
Excitatory	CNTN6	ENSG00000134115	0,757	0,780801791	0,514	0,58	0,06
Excitatory	AC024901.1	ENSG00000255910	0,757	0,772679046	0,514	0,56	0,05
Excitatory	CDK14	ENSG00000058091	0,78	0,73357449	0,56	0,88	0,37
Excitatory	PRKG1	ENSG00000185532	0,763	1,051663566	0,526	0,74	0,23
Excitatory	UNC13C	ENSG00000137766	0,754	0,995550963	0,508	0,57	0,06
Excitatory	RBFOX1	ENSG00000078328	0,859	1,620097143	0,718	0,94	0,43
Excitatory	ZNF804B	ENSG00000182348	0,759	1,581423634	0,518	0,57	0,06
Excitatory	C8orf34	ENSG00000165084	0,754	0,929688567	0,508	0,61	0,1
Excitatory	DCC	ENSG00000187323	0,778	1,369498828	0,556	0,73	0,22
Excitatory	ZNF385B	ENSG00000144331	0,755	1,14541846	0,51	0,59	0,08
Excitatory	CLSTN2	ENSG00000158258	0,756	0,985087838	0,512	0,61	0,11
Excitatory	CUX2	ENSG00000111249	0,754	0,954978986	0,508	0,56	0,06
Excitatory	SLIT2	ENSG00000145147	0,766	1,085610814	0,532	0,68	0,17
Excitatory	ADAM22	ENSG00000008277	0,775	0,626500222	0,55	0,87	0,37
Excitatory	GRIN2A	ENSG00000183454	0,754	0,98884788	0,508	0,63	0,12
Excitatory	KIFAP3	ENSG00000075945	0,778	0,625127966	0,556	0,86	0,35
Excitatory	IDS	ENSG00000010404	0,776	0,702901831	0,552	0,83	0,33
Excitatory	GRIN3A	ENSG00000198785	0,751	0,698924684	0,502	0,54	0,04
Excitatory	KCNQ5	ENSG00000185760	0,754	1,524685706	0,508	0,57	0,07
Excitatory	VWC2	ENSG00000188730	0,748	0,824389002	0,496	0,58	0,08
Excitatory	AL033504.1	ENSG00000227681	0,748	0,943003264	0,496	0,55	0,05
Excitatory	OXR1	ENSG00000164830	0,786	0,68650776	0,572	0,91	0,41
Excitatory	LINC02223	ENSG00000249937	0,744	0,703037366	0,488	0,56	0,07
Excitatory	AC013652.1	ENSG00000259345	0,745	0,646949274	0,49	0,53	0,04
Excitatory	APBA1	ENSG00000107282	0,765	0,595928592	0,53	0,88	0,38
Excitatory	ST6GALNAC5	ENSG00000117069	0,747	1,33216422	0,494	0,53	0,04
Excitatory	FRMD4A	ENSG00000151474	0,854	0,956834809	0,708	0,97	0,48
Excitatory	CDH7	ENSG00000081138	0,746	0,749365149	0,492	0,52	0,03
Excitatory	SLIT1	ENSG00000187122	0,743	0,592372295	0,486	0,53	0,05
Excitatory	SAMD5	ENSG00000203727	0,742	0,945721374	0,484	0,54	0,06

Excitatory	AC090578.1	ENSG00000253553	0,739	0,595753742	0,478	0,57	0,08
Excitatory	ZNF385D	ENSG00000151789	0,744	1,288219651	0,488	0,6	0,11
Excitatory	ZMAT4	ENSG00000165061	0,738	0,823941456	0,476	0,54	0,06
Excitatory	PTPRT	ENSG00000196090	0,747	1,332493771	0,494	0,61	0,12
Excitatory	PLCXD3	ENSG00000182836	0,735	0,659226862	0,47	0,56	0,08
Excitatory	LRRTM3	ENSG00000198739	0,784	0,846756169	0,568	0,85	0,38
Excitatory	LUZP2	ENSG00000187398	0,725	0,709136919	0,45	0,7	0,23
Excitatory	HTR2C	ENSG00000147246	0,743	1,632985965	0,486	0,53	0,06
Excitatory	GLRA2	ENSG00000101958	0,737	0,692056935	0,474	0,52	0,05
Excitatory	CALB2	ENSG00000172137	0,736	0,681037951	0,472	0,51	0,03
Excitatory	SLIT3	ENSG00000184347	0,734	0,922183069	0,468	0,52	0,05
Excitatory	CDH4	ENSG00000179242	0,74	0,827390213	0,48	0,66	0,2
Excitatory	UBA6-AS1	ENSG00000248049	0,744	0,625575442	0,488	0,84	0,37
Excitatory	THSD7A	ENSG00000005108	0,724	0,59975237	0,448	0,72	0,25
Excitatory	LDB2	ENSG00000169744	0,732	0,843851719	0,464	0,62	0,16
Excitatory	FRAS1	ENSG00000138759	0,73	1,022381345	0,46	0,51	0,06
Excitatory	PCDH11X	ENSG00000102290	0,733	1,305678073	0,466	0,54	0,09
Excitatory	DYNC1I1	ENSG00000158560	0,79	0,738654251	0,58	0,94	0,48
Excitatory	GPC6	ENSG00000183098	0,735	1,171395302	0,47	0,64	0,19
Excitatory	MACROD2	ENSG00000172264	0,839	1,071580447	0,678	0,96	0,51
Excitatory	TMEM132D	ENSG00000151952	0,718	0,653899313	0,436	0,57	0,11
Excitatory	BRINP2	ENSG00000198797	0,722	0,595434879	0,444	0,56	0,11
Excitatory	NLGN1	ENSG00000169760	0,808	0,898108532	0,616	0,98	0,53
Excitatory	BMPER	ENSG00000164619	0,723	0,623640584	0,446	0,53	0,08
Excitatory	CNGB1	ENSG00000070729	0,724	0,63948134	0,448	0,46	0,02
Excitatory	COL25A1	ENSG00000188517	0,725	1,10022274	0,45	0,51	0,07
Excitatory	CHRM2	ENSG00000181072	0,718	0,810744439	0,436	0,49	0,04
Excitatory	CDH12	ENSG00000154162	0,741	1,542966866	0,482	0,6	0,16
Excitatory	DANT2	ENSG00000235244	0,775	0,696169659	0,55	0,91	0,47
Excitatory	GRID2	ENSG00000152208	0,82	1,240362595	0,64	0,92	0,49
Excitatory	CDH8	ENSG00000150394	0,735	0,799329387	0,47	0,73	0,29
Excitatory	ZFHX3	ENSG00000140836	0,743	0,881253572	0,486	0,83	0,4
Excitatory	CDH9	ENSG00000113100	0,718	0,862094171	0,436	0,45	0,02
Excitatory	PEG10	ENSG00000242265	0,714	0,655707276	0,428	0,56	0,13
Excitatory	CNTNAP2	ENSG00000174469	0,888	1,52535048	0,776	0,99	0,56
Excitatory	PREPL	ENSG00000138078	0,759	0,604019217	0,518	0,88	0,46
Excitatory	AEBP2	ENSG00000139154	0,751	0,641024171	0,502	0,88	0,45
Excitatory	GRM8	ENSG00000179603	0,714	0,903570044	0,428	0,52	0,1
Excitatory	PPP3CA	ENSG00000138814	0,775	0,709292737	0,55	0,94	0,52
Excitatory	DENND5B	ENSG00000170456	0,766	0,627826811	0,532	0,91	0,49
Excitatory	IQCJ-SCHIP1	ENSG00000283154	0,838	1,686951886	0,676	0,89	0,47
Excitatory	OPRM1	ENSG00000112038	0,708	0,711749325	0,416	0,46	0,04
Excitatory	PPFIA2	ENSG00000139220	0,808	0,878461858	0,616	0,96	0,54
Excitatory	RGS6	ENSG00000182732	0,701	0,779907724	0,402	0,59	0,17
Excitatory	PDE10A	ENSG00000112541	0,701	0,722805971	0,402	0,65	0,24
Excitatory	NXPH1	ENSG00000122584	0,702	1,131691449	0,404	0,51	0,1
Excitatory	SORCS1	ENSG00000108018	0,705	0,952499259	0,41	0,53	0,12
Excitatory	GRIA2	ENSG00000120251	0,799	0,827304681	0,598	0,95	0,54
Excitatory	SYNE1	ENSG00000131018	0,789	0,610206934	0,578	0,94	0,54
Excitatory	TTTY14	ENSG00000176728	0,738	0,723949619	0,476	0,79	0,39
Excitatory	LRRC4C	ENSG00000148948	0,79	0,794762065	0,58	0,92	0,53
Excitatory	CDH13	ENSG00000140945	0,702	0,867530136	0,404	0,57	0,18
Excitatory	NBEA	ENSG00000172915	0,865	1,09910362	0,73	0,95	0,57
Excitatory	NAV3	ENSG00000067798	0,822	0,971316584	0,644	0,96	0,59
Excitatory	AC124312.1	ENSG00000214265	0,859	0,916117105	0,718	0,96	0,58

Excitatory	ROBO1	ENSG00000169855	0,87	1,686411152	0,74	0,93	0,57
Excitatory	SMYD3	ENSG00000185420	0,812	0,833410591	0,624	0,95	0,59
Excitatory	NEGR1	ENSG00000172260	0,852	1,341992696	0,704	0,96	0,61
Excitatory	PHACTR1	ENSG00000112137	0,718	0,783172764	0,436	0,87	0,54
Excitatory	KAZN	ENSG00000189337	0,854	1,177578693	0,708	0,97	0,65
Excitatory	MAP1B	ENSG00000131711	0,788	0,747328116	0,576	0,97	0,65
Excitatory	DPP6	ENSG00000130226	0,751	0,675215046	0,502	0,97	0,66
Excitatory	GNAS	ENSG00000087460	0,788	0,969645586	0,576	0,93	0,62
Excitatory	AHI1	ENSG00000135541	0,88	0,982902942	0,76	0,98	0,67
Excitatory	PDE4D	ENSG00000113448	0,777	0,939199183	0,554	0,95	0,68
Excitatory	ERC1	ENSG00000082805	0,785	0,665695794	0,57	0,95	0,68
Excitatory	CACNA2D1	ENSG00000153956	0,744	0,795670263	0,488	0,91	0,66
Excitatory	ANKS1B	ENSG00000185046	0,808	0,842650867	0,616	0,98	0,74
Excitatory	ADGRL3	ENSG00000150471	0,744	0,605768288	0,488	0,98	0,77
Excitatory	LSAMP	ENSG00000185565	0,761	0,683076006	0,522	0,98	0,78
Excitatory	ADGRB3	ENSG00000135298	0,807	0,853239615	0,614	0,98	0,8
Excitatory	TNRC6A	ENSG00000090905	0,813	0,682118171	0,626	0,98	0,82
Excitatory	FTX	ENSG00000230590	0,804	0,635611403	0,608	0,98	0,93
Microglia	DOCK8	ENSG00000107099	0,98	2,991624235	0,96	0,96	0,02
Microglia	APBB1IP	ENSG00000077420	0,975	2,916228268	0,95	0,95	0,02
Microglia	ARHGAP15	ENSG00000075884	0,973	2,784046645	0,946	0,95	0,04
Microglia	FYB1	ENSG00000082074	0,962	2,650321886	0,924	0,93	0,02
Microglia	TBXAS1	ENSG00000059377	0,966	2,560827197	0,932	0,94	0,06
Microglia	PTPRC	ENSG00000081237	0,943	2,294188806	0,886	0,89	0,02
Microglia	ADAM28	ENSG00000042980	0,945	2,400703456	0,89	0,9	0,03
Microglia	INPP5D	ENSG00000168918	0,943	2,245567531	0,886	0,91	0,06
Microglia	CD74	ENSG00000019582	0,941	2,546984329	0,882	0,9	0,06
Microglia	DOCK2	ENSG00000134516	0,94	2,277365709	0,88	0,89	0,05
Microglia	CSF1R	ENSG00000182578	0,923	2,058760159	0,846	0,85	0,02
Microglia	SYK	ENSG00000165025	0,914	2,092685014	0,828	0,83	0,01
Microglia	ARHGAP24	ENSG00000138639	0,978	3,03249252	0,956	0,97	0,16
Microglia	RUNX1	ENSG00000159216	0,949	2,658780849	0,898	0,92	0,13
Microglia	SLCO2B1	ENSG00000137491	0,909	2,028970077	0,818	0,85	0,06
Microglia	C3	ENSG00000125730	0,907	2,02029567	0,814	0,84	0,05
Microglia	RIN3	ENSG00000100599	0,907	1,957166864	0,814	0,83	0,05
Microglia	ST6GAL1	ENSG00000073849	0,957	2,447245806	0,914	0,95	0,17
Microglia	PALD1	ENSG00000107719	0,913	2,03668727	0,826	0,85	0,08
Microglia	RHBDF2	ENSG00000129667	0,898	1,878199507	0,796	0,81	0,03
Microglia	ATP8B4	ENSG00000104043	0,909	2,210551197	0,818	0,83	0,06
Microglia	LYN	ENSG00000254087	0,891	1,906069396	0,782	0,79	0,03
Microglia	MEF2C	ENSG00000081189	0,947	2,327815541	0,894	0,94	0,18
Microglia	MYO1F	ENSG00000142347	0,885	1,751114265	0,77	0,78	0,04
Microglia	IKZF1	ENSG00000185811	0,875	1,946197231	0,75	0,75	0,01
Microglia	DENND3	ENSG00000105339	0,897	2,11884716	0,794	0,82	0,08
Microglia	HS3ST4	ENSG00000182601	0,899	2,644210094	0,798	0,84	0,1
Microglia	FLI1	ENSG00000151702	0,858	1,430993199	0,716	0,79	0,07
Microglia	TLR2	ENSG00000137462	0,855	1,813714723	0,71	0,71	0,01
Microglia	SP100	ENSG00000067066	0,873	1,683212851	0,746	0,79	0,09
Microglia	LY86	ENSG00000112799	0,854	1,741972888	0,708	0,71	0,01
Microglia	SLC8A1	ENSG00000183023	0,919	1,905218075	0,838	0,94	0,24
Microglia	SRGAP2B	ENSG00000196369	0,916	2,049174758	0,832	0,87	0,17
Microglia	RBM47	ENSG00000163694	0,86	1,966218079	0,72	0,73	0,03
Microglia	WDFY4	ENSG00000128815	0,852	1,653206346	0,704	0,71	0,01
Microglia	C1QB	ENSG00000173369	0,854	1,924511404	0,708	0,72	0,02
Microglia	HCLS1	ENSG00000180353	0,852	1,655153782	0,704	0,71	0,01

Microglia	ABCC4	ENSG00000125257	0,887	1,992210963	0,774	0,82	0,12
Microglia	CHST11	ENSG00000171310	0,961	2,288254222	0,922	0,97	0,28
Microglia	BNC2	ENSG00000173068	0,867	1,923883022	0,734	0,78	0,1
Microglia	LRRK1	ENSG00000154237	0,849	1,764846044	0,698	0,71	0,03
Microglia	PIK3R5	ENSG00000141506	0,841	1,682510896	0,682	0,68	0,01
Microglia	ALOX5	ENSG00000012779	0,846	1,651069443	0,692	0,7	0,02
Microglia	LINC02232	ENSG00000250125	0,844	1,970611868	0,688	0,7	0,02
Microglia	LHFPL2	ENSG00000145685	0,913	2,184610538	0,826	0,87	0,2
Microglia	SH3RF3	ENSG00000172985	0,894	2,211992046	0,788	0,83	0,16
Microglia	PIK3AP1	ENSG00000155629	0,838	1,69928445	0,676	0,68	0,01
Microglia	SLC11A1	ENSG00000018280	0,838	1,883122611	0,676	0,68	0,02
Microglia	LAPTM5	ENSG00000162511	0,836	1,553939161	0,672	0,68	0,01
Microglia	AOAH	ENSG00000136250	0,871	1,867537164	0,742	0,8	0,14
Microglia	CD53	ENSG00000143119	0,827	1,484041867	0,654	0,66	0,01
Microglia	SKAP2	ENSG00000005020	0,885	1,819423585	0,77	0,82	0,17
Microglia	FAM149A	ENSG00000109794	0,842	1,850049457	0,684	0,71	0,06
Microglia	DISC1	ENSG00000162946	0,896	1,847156953	0,792	0,87	0,22
Microglia	CYFIP1	ENSG00000273749	0,896	1,862848611	0,792	0,84	0,2
Microglia	RUNX2	ENSG00000124813	0,857	1,813395669	0,714	0,75	0,11
Microglia	NFATC2	ENSG00000101096	0,838	1,600902307	0,676	0,71	0,07
Microglia	ENTPD1	ENSG00000138185	0,84	1,686762748	0,68	0,71	0,07
Microglia	IRAK3	ENSG00000090376	0,827	1,519302322	0,654	0,71	0,07
Microglia	LPCAT2	ENSG00000087253	0,885	1,816989683	0,77	0,82	0,18
Microglia	SLC2A5	ENSG00000142583	0,821	1,547159605	0,642	0,65	0,01
Microglia	ABR	ENSG00000159842	0,932	1,940609586	0,864	0,93	0,3
Microglia	LRMDA	ENSG00000148655	0,974	2,497914773	0,948	0,98	0,35
Microglia	CPED1	ENSG00000106034	0,82	1,794816778	0,64	0,65	0,02
Microglia	SLA	ENSG00000155926	0,815	1,517044208	0,63	0,64	0,01
Microglia	MS4A6A	ENSG00000110077	0,812	1,580368368	0,624	0,63	0,01
Microglia	SCIN	ENSG00000006747	0,814	1,697402472	0,628	0,64	0,02
Microglia	CIITA	ENSG00000179583	0,814	1,489005445	0,628	0,64	0,02
Microglia	CD86	ENSG00000114013	0,808	1,549058316	0,616	0,62	0,01
Microglia	BLNK	ENSG00000095585	0,809	1,600734286	0,618	0,62	0,01
Microglia	RCSD1	ENSG00000198771	0,811	1,507638668	0,622	0,65	0,04
Microglia	IL18	ENSG00000150782	0,808	1,405192389	0,616	0,62	0,01
Microglia	TGFBR2	ENSG00000163513	0,812	1,377885529	0,624	0,69	0,08
Microglia	FOXP2	ENSG00000128573	0,82	1,549252241	0,64	0,74	0,13
Microglia	ETV6	ENSG00000139083	0,92	1,9326664	0,84	0,91	0,31
Microglia	TGFBR1	ENSG00000106799	0,85	1,831817715	0,7	0,75	0,14
Microglia	AKAP13	ENSG00000170776	0,916	1,722789308	0,832	0,91	0,31
Microglia	ARHGAP25	ENSG00000163219	0,808	1,531404485	0,616	0,63	0,02
Microglia	TFEC	ENSG00000105967	0,801	1,43294111	0,602	0,61	0,01
Microglia	KCNQ3	ENSG00000184156	0,866	2,005959664	0,732	0,83	0,24
Microglia	MGAT4A	ENSG00000071073	0,909	1,879303376	0,818	0,88	0,28
Microglia	SAMSN1	ENSG00000155307	0,801	1,638422058	0,602	0,61	0,01
Microglia	CSF3R	ENSG00000119535	0,798	1,381205627	0,596	0,6	0,01
Microglia	CELF2	ENSG00000048740	0,936	1,726446767	0,872	0,98	0,38
Microglia	OSBPL3	ENSG00000070882	0,813	1,505809217	0,626	0,67	0,09
Microglia	IFI16	ENSG00000163565	0,829	1,35587177	0,658	0,75	0,16
Microglia	FGD2	ENSG00000146192	0,792	1,379754504	0,584	0,59	0
Microglia	SMAP2	ENSG00000084070	0,881	1,768458537	0,762	0,82	0,24
Microglia	NCKAP1L	ENSG00000123338	0,792	1,315757829	0,584	0,59	0,01
Microglia	HLA-DRA	ENSG00000204287	0,794	1,63686405	0,588	0,6	0,02
Microglia	FMN1	ENSG00000248905	0,862	1,999122279	0,724	0,8	0,22
Microglia	SRGAP2	ENSG00000266028	0,963	2,286365841	0,926	0,96	0,38

Microglia	C1QC	ENSG00000159189	0,79	1,512496267	0,58	0,58	0,01
Microglia	CTSB	ENSG00000164733	0,864	1,7463214	0,728	0,8	0,22
Microglia	IPCEF1	ENSG00000074706	0,813	1,944637659	0,626	0,67	0,1
Microglia	APOE	ENSG00000130203	0,836	1,532531989	0,672	0,83	0,26
Microglia	TRPM2	ENSG00000142185	0,808	1,434552452	0,616	0,65	0,09
Microglia	HCK	ENSG00000101336	0,785	1,353694801	0,57	0,57	0,01
Microglia	ALPK1	ENSG00000073331	0,792	1,420848197	0,584	0,62	0,05
Microglia	SAT1	ENSG00000130066	0,831	1,646518128	0,662	0,75	0,19
Microglia	ZFP36L1	ENSG00000185650	0,805	1,299365749	0,61	0,74	0,19
Microglia	RREB1	ENSG00000124782	0,792	1,343782014	0,584	0,65	0,1
Microglia	DIAPH2	ENSG00000147202	0,868	1,650818968	0,736	0,84	0,29
Microglia	KCNIP1	ENSG00000182132	0,806	1,578030803	0,612	0,72	0,17
Microglia	ITGAX	ENSG00000140678	0,774	1,377008747	0,548	0,55	0,01
Microglia	LAT2	ENSG00000086730	0,779	1,257262732	0,558	0,57	0,03
Microglia	CSF2RA	ENSG00000198223	0,778	1,374454065	0,556	0,56	0,02
Microglia	IL13RA1	ENSG00000131724	0,785	1,29574741	0,57	0,62	0,08
Microglia	BMP2K	ENSG00000138756	0,94	2,042906063	0,88	0,94	0,4
Microglia	CPVL	ENSG00000106066	0,779	1,50446665	0,558	0,58	0,04
Microglia	SRGAP2C	ENSG00000171943	0,846	1,556141456	0,692	0,77	0,24
Microglia	DOCK11	ENSG00000147251	0,809	1,415515786	0,618	0,69	0,15
Microglia	CSGALNACT1	ENSG00000147408	0,807	1,558860677	0,614	0,77	0,23
Microglia	ZFHX3	ENSG00000140836	0,875	1,362510706	0,75	0,91	0,38
Microglia	LINC02798	ENSG00000227082	0,799	1,612452384	0,598	0,66	0,13
Microglia	ARHGAP26	ENSG00000145819	0,929	1,75554517	0,858	0,97	0,44
Microglia	LRCH1	ENSG00000136141	0,834	1,372662333	0,668	0,78	0,26
Microglia	LPAR6	ENSG00000139679	0,772	1,249563229	0,544	0,57	0,04
Microglia	PLA2G4A	ENSG00000116711	0,766	1,262369463	0,532	0,56	0,03
Microglia	C1QA	ENSG00000173372	0,765	1,349367523	0,53	0,54	0,01
Microglia	IL17RA	ENSG00000177663	0,798	1,332936598	0,596	0,66	0,14
Microglia	NCK2	ENSG00000071051	0,823	1,676258603	0,646	0,72	0,2
Microglia	GNB4	ENSG00000114450	0,779	1,2784887	0,558	0,61	0,09
Microglia	TMEM156	ENSG00000121895	0,763	1,376262434	0,526	0,53	0,01
Microglia	ITPR2	ENSG00000123104	0,928	1,862913817	0,856	0,96	0,44
Microglia	POU2F2	ENSG00000028277	0,781	1,351327429	0,562	0,61	0,09
Microglia	ST8SIA4	ENSG00000113532	0,774	1,407790343	0,548	0,59	0,07
Microglia	TLR1	ENSG00000174125	0,759	1,182164824	0,518	0,53	0,02
Microglia	FRMD4A	ENSG00000151474	0,943	2,057261328	0,886	0,98	0,47
Microglia	RGS10	ENSG00000148908	0,756	1,193518603	0,512	0,52	0,01
Microglia	SUSD6	ENSG00000100647	0,825	1,367238615	0,65	0,75	0,24
Microglia	TNFRSF1B	ENSG00000028137	0,76	1,254772607	0,52	0,55	0,04
Microglia	HLA-DRB1	ENSG00000196126	0,758	1,336991308	0,516	0,53	0,03
Microglia	TNS3	ENSG00000136205	0,792	1,373226346	0,584	0,68	0,18
Microglia	FMNL3	ENSG00000161791	0,793	1,213680497	0,586	0,71	0,2
Microglia	CAMK1D	ENSG00000183049	0,814	1,326609312	0,628	0,78	0,28
Microglia	P2RY12	ENSG00000169313	0,757	1,591758509	0,514	0,53	0,03
Microglia	PAG1	ENSG00000076641	0,846	1,529138978	0,692	0,8	0,31
Microglia	VAV1	ENSG00000141968	0,751	1,166102644	0,502	0,51	0,01
Microglia	SLC25A37	ENSG00000147454	0,838	1,636744651	0,676	0,77	0,27
Microglia	CYBA	ENSG00000051523	0,752	1,162501011	0,504	0,54	0,05
Microglia	MAML3	ENSG00000196782	0,894	1,720040365	0,788	0,91	0,41
Microglia	SLC4A7	ENSG00000033867	0,802	1,392943884	0,604	0,7	0,21
Microglia	SH3TC1	ENSG00000125089	0,748	1,151262051	0,496	0,51	0,01
Microglia	FCGR2A	ENSG00000143226	0,747	1,245371062	0,494	0,5	0,01
Microglia	PRKAG2	ENSG00000106617	0,797	1,361323778	0,594	0,71	0,22
Microglia	MTHFD1L	ENSG00000120254	0,853	1,531701506	0,706	0,82	0,34

Microglia	ZFP36L2	ENSG00000152518	0,778	1,394766116	0,556	0,65	0,17
Microglia	GPRIN3	ENSG00000185477	0,767	1,280220887	0,534	0,6	0,12
Microglia	LRMP	ENSG00000118308	0,743	1,195411115	0,486	0,5	0,02
Microglia	A2M	ENSG00000175899	0,742	0,973158151	0,484	0,59	0,11
Microglia	SRGN	ENSG00000122862	0,741	1,501584414	0,482	0,54	0,06
Microglia	KCTD12	ENSG00000178695	0,746	1,082458037	0,492	0,55	0,07
Microglia	PDE3B	ENSG00000152270	0,773	1,537728023	0,546	0,64	0,17
Microglia	MSR1	ENSG00000038945	0,742	1,347371604	0,484	0,51	0,04
Microglia	PLXDC2	ENSG00000120594	0,986	2,760625668	0,972	0,99	0,52
Microglia	ANOS1	ENSG00000011201	0,753	1,233937156	0,506	0,57	0,1
Microglia	CCND3	ENSG00000112576	0,783	1,347771065	0,566	0,67	0,21
Microglia	ZNF710	ENSG00000140548	0,79	1,284211053	0,58	0,68	0,22
Microglia	ARHGAP6	ENSG00000047648	0,754	1,256213996	0,508	0,59	0,13
Microglia	ADCY7	ENSG00000121281	0,738	1,068470546	0,476	0,49	0,03
Microglia	REL	ENSG00000162924	0,759	1,185587612	0,518	0,58	0,12
Microglia	CTSC	ENSG00000109861	0,738	1,135853001	0,476	0,5	0,04
Microglia	BACH1	ENSG00000156273	0,818	1,548030126	0,636	0,77	0,3
Microglia	KCNK13	ENSG00000152315	0,736	1,326069528	0,472	0,49	0,03
Microglia	CARD11	ENSG00000198286	0,736	1,234611736	0,472	0,48	0,02
Microglia	TBC1D1	ENSG00000065882	0,782	1,223728938	0,564	0,69	0,23
Microglia	GAB3	ENSG00000160219	0,733	1,085603466	0,466	0,48	0,02
Microglia	RAB31	ENSG00000168461	0,776	1,123323566	0,552	0,72	0,26
Microglia	TM6SF1	ENSG00000136404	0,738	1,119147549	0,476	0,51	0,05
Microglia	PRAM1	ENSG00000133246	0,733	1,073653661	0,466	0,48	0,03
Microglia	IGSF21	ENSG00000117154	0,747	1,362204614	0,494	0,57	0,11
Microglia	MYOF	ENSG00000138119	0,729	0,95437921	0,458	0,53	0,08
Microglia	MIR646HG	ENSG00000228340	0,753	1,41106182	0,506	0,6	0,15
Microglia	TSPAN14	ENSG00000108219	0,762	1,129541146	0,524	0,63	0,19
Microglia	MAP3K5	ENSG00000197442	0,751	0,852399873	0,502	0,74	0,3
Microglia	CMTM7	ENSG00000153551	0,724	1,054956396	0,448	0,47	0,03
Microglia	RAPGEF1	ENSG00000107263	0,833	1,376964036	0,666	0,81	0,37
Microglia	KCNMA1	ENSG00000156113	0,823	1,537017014	0,646	0,85	0,41
Microglia	LINC00278	ENSG00000231535	0,725	1,315511745	0,45	0,49	0,05
Microglia	FCGR3A	ENSG00000203747	0,719	1,088982338	0,438	0,44	0,01
Microglia	RYR1	ENSG00000196218	0,744	1,147445409	0,488	0,57	0,13
Microglia	MAF	ENSG00000178573	0,737	1,129975854	0,474	0,54	0,11
Microglia	ITGAM	ENSG00000169896	0,718	1,044379594	0,436	0,44	0,01
Microglia	PGM5	ENSG00000154330	0,738	1,158382515	0,476	0,55	0,11
Microglia	LCP2	ENSG00000043462	0,721	1,095063523	0,442	0,46	0,03
Microglia	HLA-DPA1	ENSG00000231389	0,72	1,13041294	0,44	0,46	0,02
Microglia	RUBCNL	ENSG00000102445	0,727	1,101716806	0,454	0,49	0,06
Microglia	KYNU	ENSG00000115919	0,717	1,116219804	0,434	0,44	0,01
Microglia	ITGB2	ENSG00000160255	0,717	0,975283265	0,434	0,44	0,01
Microglia	OXR1	ENSG00000164830	0,838	1,760907387	0,676	0,84	0,41
Microglia	ARRB2	ENSG00000141480	0,736	1,018595462	0,472	0,53	0,1
Microglia	CD14	ENSG00000170458	0,715	1,243688221	0,43	0,44	0,01
Microglia	GRB2	ENSG00000177885	0,822	1,416770315	0,644	0,76	0,33
Microglia	NIBAN1	ENSG00000135842	0,717	1,391780769	0,434	0,45	0,03
Microglia	TYROBP	ENSG00000011600	0,714	1,000309901	0,428	0,43	0,01
Microglia	SORL1	ENSG00000137642	0,945	2,010540699	0,89	0,96	0,53
Microglia	PELI1	ENSG00000197329	0,786	1,32984157	0,572	0,71	0,29
Microglia	BHLHE41	ENSG00000123095	0,786	1,247212406	0,572	0,7	0,28
Microglia	LINC01094	ENSG00000251442	0,712	0,956779842	0,424	0,5	0,07
Microglia	CLEC7A	ENSG00000172243	0,711	1,012244942	0,422	0,42	0
Microglia	MIS18BP1	ENSG00000129534	0,729	1,130552421	0,458	0,52	0,1

Microglia	CTSS	ENSG00000163131	0,718	1,011300085	0,436	0,46	0,04
Microglia	LRRK2	ENSG00000188906	0,735	1,172909021	0,47	0,57	0,15
Microglia	ETS2	ENSG00000157557	0,719	0,988927568	0,438	0,52	0,1
Microglia	APOC1	ENSG00000130208	0,713	1,226499974	0,426	0,45	0,03
Microglia	PRKCH	ENSG00000027075	0,712	0,873643554	0,424	0,53	0,11
Microglia	PARVG	ENSG00000138964	0,71	0,997973253	0,42	0,43	0,01
Microglia	PARP14	ENSG00000173193	0,713	0,896764288	0,426	0,51	0,1
Microglia	CHST15	ENSG00000182022	0,723	1,149603477	0,446	0,52	0,11
Microglia	NHSL1	ENSG00000135540	0,73	1,580479973	0,46	0,59	0,18
Microglia	RGS1	ENSG00000090104	0,705	1,46116494	0,41	0,41	0
Microglia	VSIG4	ENSG00000155659	0,705	1,09357028	0,41	0,41	0
Microglia	UTRN	ENSG00000152818	0,707	0,613724677	0,414	0,7	0,29
Microglia	PCNX2	ENSG00000135749	0,793	1,172970085	0,586	0,78	0,37
Microglia	SPI1	ENSG00000066336	0,706	0,942054632	0,412	0,43	0,02
Microglia	OLR1	ENSG00000173391	0,702	1,163325255	0,404	0,41	0
Microglia	MSN	ENSG00000147065	0,731	1,012083727	0,462	0,58	0,18
Microglia	ADGRG1	ENSG00000205336	0,719	0,967377366	0,438	0,54	0,14
Microglia	OTULINL	ENSG00000145569	0,704	1,017119428	0,408	0,42	0,02
Microglia	FGD4	ENSG00000139132	0,895	1,552486407	0,79	0,92	0,52
Microglia	PLCL2	ENSG00000154822	0,734	1,077305733	0,468	0,6	0,2
Microglia	B3GNT5	ENSG00000176597	0,702	1,037580377	0,404	0,42	0,03
Microglia	SLC1A3	ENSG00000079215	0,935	1,971717822	0,87	0,96	0,57
Microglia	PARP8	ENSG00000151883	0,73	1,089421882	0,46	0,62	0,23
Microglia	MAN1A1	ENSG00000111885	0,711	1,096519076	0,422	0,51	0,12
Microglia	IFNGR2	ENSG00000159128	0,735	1,077901283	0,47	0,57	0,19
Microglia	TBC1D2B	ENSG00000167202	0,731	1,011204508	0,462	0,57	0,19
Microglia	CARD8	ENSG00000105483	0,716	0,908379721	0,432	0,53	0,15
Microglia	GALNT2	ENSG00000143641	0,806	1,289949058	0,612	0,77	0,38
Microglia	COTL1	ENSG00000103187	0,711	1,022057924	0,422	0,5	0,12
Microglia	MERTK	ENSG00000153208	0,709	1,345796531	0,418	0,5	0,12
Microglia	GRK3	ENSG00000100077	0,75	1,002859311	0,5	0,69	0,31
Microglia	ARHGAP22	ENSG00000128805	0,85	1,346968455	0,7	0,88	0,5
Microglia	PLEKHA2	ENSG00000169499	0,717	0,955196489	0,434	0,54	0,16
Microglia	IFNGR1	ENSG00000027697	0,759	1,082718859	0,518	0,67	0,29
Microglia	KCNQ1	ENSG00000053918	0,726	1,093858092	0,452	0,55	0,17
Microglia	USP6NL	ENSG00000148429	0,74	1,06332604	0,48	0,63	0,26
Microglia	STK4	ENSG00000101109	0,745	1,062140042	0,49	0,63	0,25
Microglia	TBC1D14	ENSG00000132405	0,75	1,366911545	0,5	0,62	0,25
Microglia	CMIP	ENSG00000153815	0,838	1,259739477	0,676	0,84	0,47
Microglia	SOAT1	ENSG00000057252	0,708	0,953651644	0,416	0,5	0,13
Microglia	SFMBT2	ENSG00000198879	0,918	1,73622818	0,836	0,95	0,58
Microglia	LRRFIP1	ENSG00000124831	0,736	0,950251691	0,472	0,65	0,29
Microglia	SSH1	ENSG00000084112	0,742	1,037670808	0,484	0,62	0,26
Microglia	ST3GAL6	ENSG00000064225	0,717	0,892423548	0,434	0,59	0,23
Microglia	FCHSD2	ENSG00000137478	0,796	0,978554564	0,592	0,88	0,52
Microglia	EML4	ENSG00000143924	0,735	1,064778792	0,47	0,61	0,25
Microglia	GALNT10	ENSG00000164574	0,736	1,119266033	0,472	0,63	0,26
Microglia	SDK1	ENSG00000146555	0,715	1,184720479	0,43	0,6	0,24
Microglia	EPB41	ENSG00000159023	0,706	0,9641749	0,412	0,54	0,18
Microglia	PPARD	ENSG00000112033	0,746	1,225046629	0,492	0,64	0,28
Microglia	ITPR1	ENSG00000150995	0,716	1,018476966	0,432	0,57	0,22
Microglia	SKI	ENSG00000157933	0,741	1,061048743	0,482	0,63	0,28
Microglia	FOXN3	ENSG00000053254	0,932	1,719614776	0,864	0,96	0,61
Microglia	APMAP	ENSG00000101474	0,702	0,971531406	0,404	0,49	0,14
Microglia	HIF1A	ENSG00000100644	0,758	1,270050602	0,516	0,69	0,34

Microglia	SIPA1L2	ENSG00000116991	0,708	0,985184871	0,416	0,55	0,2
Microglia	TAB2	ENSG00000055208	0,82	1,283212162	0,64	0,81	0,47
Microglia	MEF2A	ENSG00000068305	0,965	2,000732047	0,93	0,98	0,64
Microglia	JAK2	ENSG00000096968	0,746	1,031028017	0,492	0,67	0,33
Microglia	SOCS6	ENSG00000170677	0,72	1,1869071	0,44	0,56	0,22
Microglia	SYNDIG1	ENSG00000101463	0,822	1,781592107	0,644	0,81	0,48
Microglia	SKIL	ENSG00000136603	0,707	0,966248412	0,414	0,54	0,21
Microglia	VOPP1	ENSG00000154978	0,75	1,047289753	0,5	0,67	0,34
Microglia	ACSL1	ENSG00000151726	0,765	1,492772902	0,53	0,69	0,36
Microglia	NUMB	ENSG00000133961	0,786	1,086667056	0,572	0,76	0,43
Microglia	PACSIN2	ENSG00000100266	0,721	0,94298667	0,442	0,6	0,27
Microglia	FAM49B	ENSG00000153310	0,921	1,46713839	0,842	0,96	0,63
Microglia	AP1B1	ENSG00000100280	0,709	0,935404872	0,418	0,55	0,22
Microglia	PTPRE	ENSG00000132334	0,789	1,285397828	0,578	0,78	0,45
Microglia	LIMS1	ENSG00000169756	0,758	1,140250436	0,516	0,72	0,39
Microglia	CTTNBP2NL	ENSG00000143079	0,707	0,928113482	0,414	0,56	0,24
Microglia	TBC1D22A	ENSG00000054611	0,878	1,378514437	0,756	0,91	0,58
Microglia	MAML2	ENSG00000184384	0,854	1,268994258	0,708	0,94	0,62
Microglia	USP15	ENSG00000135655	0,81	1,168973896	0,62	0,81	0,49
Microglia	SH3BGRL	ENSG00000131171	0,753	1,096147836	0,506	0,69	0,38
Microglia	MANBA	ENSG00000109323	0,732	1,007890723	0,464	0,64	0,33
Microglia	LPIN2	ENSG00000101577	0,72	0,946754406	0,44	0,61	0,3
Microglia	IL6ST	ENSG00000134352	0,764	1,108267993	0,528	0,73	0,42
Microglia	NCOA3	ENSG00000124151	0,729	0,956187184	0,458	0,65	0,34
Microglia	SUCLG2	ENSG00000172340	0,706	0,880775369	0,412	0,61	0,3
Microglia	RGS12	ENSG00000159788	0,705	0,929496577	0,41	0,58	0,27
Microglia	EPB41L2	ENSG00000079819	0,921	1,688127021	0,842	0,95	0,65
Microglia	STX7	ENSG00000079950	0,763	1,024777149	0,526	0,73	0,42
Microglia	TNRC18	ENSG00000182095	0,718	0,897591928	0,436	0,63	0,33
Microglia	TMSB4X	ENSG00000205542	0,762	1,025207735	0,524	0,78	0,48
Microglia	SH3KBP1	ENSG00000147010	0,801	1,063579091	0,602	0,84	0,54
Microglia	PTPN2	ENSG00000175354	0,718	1,083675411	0,436	0,59	0,3
Microglia	SRGAP1	ENSG00000196935	0,794	1,308351214	0,588	0,8	0,51
Microglia	FAM13A	ENSG00000138640	0,712	0,975423688	0,424	0,63	0,34
Microglia	LDLRAD4	ENSG00000168675	0,927	1,745138903	0,854	0,96	0,67
Microglia	RB1	ENSG00000139687	0,777	1,099851621	0,554	0,77	0,48
Microglia	B2M	ENSG00000166710	0,708	0,723862668	0,416	0,68	0,39
Microglia	CAB39	ENSG00000135932	0,74	1,004495693	0,48	0,68	0,39
Microglia	RNF213	ENSG00000173821	0,727	0,89005906	0,454	0,67	0,38
Microglia	FNDC3B	ENSG00000075420	0,705	0,945284186	0,41	0,64	0,35
Microglia	ARL15	ENSG00000185305	0,72	0,733012094	0,44	0,73	0,44
Microglia	NAV3	ENSG00000067798	0,761	0,907891347	0,522	0,87	0,59
Microglia	ANKRD44	ENSG00000065413	0,91	1,549504284	0,82	0,95	0,67
Microglia	JAZF1	ENSG00000153814	0,847	1,365777895	0,694	0,89	0,61
Microglia	PACS1	ENSG00000175115	0,718	0,870856955	0,436	0,69	0,4
Microglia	FKBP5	ENSG00000096060	0,898	1,452187578	0,796	0,96	0,67
Microglia	PADI2	ENSG00000117115	0,726	1,171572972	0,452	0,69	0,4
Microglia	RNF149	ENSG00000163162	0,744	1,107011528	0,488	0,68	0,4
Microglia	PTPRJ	ENSG00000149177	0,819	1,170126429	0,638	0,87	0,59
Microglia	PREX1	ENSG00000124126	0,82	1,050740289	0,64	0,9	0,62
Microglia	SPP1	ENSG00000118785	0,79	1,769240397	0,58	0,87	0,59
Microglia	ABI1	ENSG00000136754	0,705	0,811257636	0,41	0,64	0,37
Microglia	H2AFY	ENSG00000113648	0,714	0,890614404	0,428	0,61	0,34
Microglia	ANKS1A	ENSG00000064999	0,756	0,947595871	0,512	0,76	0,49
Microglia	RASAL2	ENSG00000075391	0,731	0,896414871	0,462	0,77	0,5

Microglia	P4HA1	ENSG00000122884	0,707	1,062655212	0,414	0,63	0,38
Microglia	AFF1	ENSG00000172493	0,727	0,851398281	0,454	0,73	0,49
Microglia	HDAC9	ENSG00000048052	0,723	1,163463972	0,446	0,72	0,48
Microglia	RAP1A	ENSG00000116473	0,769	0,942391193	0,538	0,81	0,57
Microglia	ATF6	ENSG00000118217	0,73	0,878982789	0,46	0,71	0,48
Microglia	RASSF8	ENSG00000123094	0,714	1,187375144	0,428	0,68	0,45
Microglia	ATM	ENSG00000149311	0,792	0,983398621	0,584	0,83	0,6
Microglia	PIAS1	ENSG00000033800	0,769	0,87729274	0,538	0,81	0,58
Microglia	CAPZB	ENSG00000077549	0,757	0,903791128	0,514	0,77	0,54
Microglia	TTC7A	ENSG00000068724	0,703	0,900815802	0,406	0,67	0,46
Microglia	SPRED1	ENSG00000166068	0,72	0,88193229	0,44	0,72	0,51
Microglia	NAIP	ENSG00000249437	0,757	0,953786002	0,514	0,78	0,57
Microglia	WASF2	ENSG00000158195	0,704	0,745998545	0,408	0,69	0,49
Microglia	PLCG2	ENSG00000197943	0,701	0,611388045	0,402	0,79	0,59
Microglia	SSH2	ENSG00000141298	0,938	1,503862219	0,876	0,98	0,79
Microglia	PHC2	ENSG00000134686	0,721	0,839523287	0,442	0,72	0,52
Microglia	ATP2C1	ENSG00000017260	0,717	0,850015409	0,434	0,72	0,52
Microglia	SPTLC2	ENSG00000100596	0,707	0,840289658	0,414	0,71	0,52
Microglia	SLC9A9	ENSG00000181804	0,785	0,948358412	0,57	0,89	0,7
Microglia	STAG1	ENSG00000118007	0,749	0,768175026	0,498	0,84	0,69
Microglia	PKN2	ENSG00000065243	0,717	0,754431145	0,434	0,76	0,61
Microglia	MED13L	ENSG00000123066	0,851	1,092969494	0,702	0,94	0,79
Microglia	GAB2	ENSG00000033327	0,721	0,734857787	0,442	0,85	0,71
Microglia	LPP	ENSG00000145012	0,74	0,762475111	0,48	0,85	0,72
Microglia	MBNL1	ENSG00000152601	0,844	1,037904047	0,688	0,95	0,82
Microglia	ANKRD11	ENSG00000167522	0,739	0,750230556	0,478	0,82	0,69
Microglia	MYCBP2	ENSG00000005810	0,74	0,702479701	0,48	0,86	0,73
Microglia	UBE2E2	ENSG00000182247	0,747	0,737444781	0,494	0,92	0,79
Microglia	SDCCAG8	ENSG00000054282	0,75	0,777068546	0,5	0,85	0,73
Microglia	PICALM	ENSG00000073921	0,836	1,003711625	0,672	0,96	0,84
Microglia	DOCK4	ENSG00000128512	0,956	1,750929775	0,912	0,99	0,9
Microglia	GNAQ	ENSG00000156052	0,838	0,934364541	0,676	0,95	0,87
Microglia	ZFAND3	ENSG00000156639	0,753	0,705351092	0,506	0,9	0,82
Microglia	NIPBL	ENSG00000164190	0,703	0,591850269	0,406	0,83	0,76
Microglia	FOXP1	ENSG00000114861	0,72	0,729857423	0,44	0,86	0,81
OPCs	MEGF11	ENSG00000157890	0,983	2,621750837	0,966	0,97	0,06
OPCs	VCAN	ENSG00000038427	0,994	2,941497108	0,988	0,99	0,09
OPCs	CA10	ENSG00000154975	0,962	2,319424768	0,924	0,96	0,12
OPCs	PCDH15	ENSG00000150275	0,975	2,486761309	0,95	0,99	0,15
OPCs	NXPH1	ENSG00000122584	0,925	1,934946985	0,85	0,91	0,08
OPCs	SNTG1	ENSG00000147481	0,939	1,899191889	0,878	0,98	0,15
OPCs	TNR	ENSG00000116147	0,998	3,375104408	0,996	1	0,17
OPCs	MMP16	ENSG00000156103	0,977	2,578156823	0,954	0,97	0,15
OPCs	OPCML	ENSG00000183715	0,979	2,510720776	0,958	0,99	0,18
OPCs	LHFPL3	ENSG00000187416	0,986	2,894139696	0,972	0,99	0,18
OPCs	GRIK1	ENSG00000171189	0,922	1,525092041	0,844	0,92	0,11
OPCs	ATRNL1	ENSG00000107518	0,97	2,311314838	0,94	0,98	0,17
OPCs	TMEM132D	ENSG00000151952	0,926	1,850847178	0,852	0,89	0,09
OPCs	COL11A1	ENSG00000060718	0,929	1,869221927	0,858	0,9	0,1
OPCs	PTPRZ1	ENSG00000106278	0,99	2,517146329	0,98	1	0,2
OPCs	SOX6	ENSG00000110693	0,971	2,271712733	0,942	0,98	0,19
OPCs	BRINP3	ENSG00000162670	0,945	1,96996274	0,89	0,96	0,16
OPCs	CHST9	ENSG00000154080	0,904	1,836818823	0,808	0,83	0,04
OPCs	COL9A1	ENSG00000112280	0,898	1,621103344	0,796	0,8	0,02
OPCs	SLC35F1	ENSG00000196376	0,96	2,140495779	0,92	0,97	0,19

OPCs	ADAMTS17	ENSG00000140470	0,911	1,826406835	0,822	0,85	0,08
OPCs	GRM7	ENSG00000196277	0,921	1,691065421	0,842	0,96	0,19
OPCs	FGF12	ENSG00000114279	0,907	1,593568017	0,814	0,95	0,19
OPCs	GRM5	ENSG00000168959	0,892	1,416298645	0,784	0,93	0,17
OPCs	LUZP2	ENSG00000187398	0,935	1,820654593	0,87	0,96	0,21
OPCs	TMEM132C	ENSG00000181234	0,95	1,950322053	0,9	0,96	0,21
OPCs	BCAN	ENSG00000132692	0,893	1,527816538	0,786	0,83	0,08
OPCs	FGF14	ENSG00000102466	0,948	1,983511926	0,896	0,99	0,25
OPCs	DCC	ENSG00000187323	0,913	1,577760314	0,826	0,95	0,21
OPCs	HIF3A	ENSG00000124440	0,881	1,213466135	0,762	0,94	0,19
OPCs	SCN1A	ENSG00000144285	0,896	1,43741716	0,792	0,91	0,16
OPCs	KCNIP4	ENSG00000185774	0,93	1,645571584	0,86	0,99	0,25
OPCs	DGKG	ENSG00000058866	0,958	1,984514884	0,916	0,98	0,24
OPCs	KCND2	ENSG00000184408	0,942	1,877548565	0,884	0,99	0,25
OPCs	LRRTM4	ENSG00000176204	0,947	1,95640539	0,894	0,99	0,26
OPCs	CHL1	ENSG00000134121	0,932	1,706888956	0,864	0,95	0,22
OPCs	LINC00511	ENSG00000227036	0,938	1,754459933	0,876	0,95	0,22
OPCs	NRCAM	ENSG00000091129	0,983	2,256571231	0,966	1	0,27
OPCs	DSCAM	ENSG00000171587	0,991	2,79017089	0,982	1	0,27
OPCs	FERMT1	ENSG00000101311	0,862	1,479737071	0,724	0,73	0,02
OPCs	UNC80	ENSG00000144406	0,89	1,416669453	0,78	0,9	0,19
OPCs	GRIK2	ENSG00000164418	0,909	1,425559135	0,818	0,97	0,26
OPCs	ARPP21	ENSG00000172995	0,898	1,429050286	0,796	0,91	0,2
OPCs	ZFPM2	ENSG00000169946	0,942	2,139775344	0,884	0,96	0,25
OPCs	CNTNAP5	ENSG00000155052	0,857	1,135780529	0,714	0,86	0,15
OPCs	SLC1A2	ENSG00000110436	0,875	1,000087503	0,75	0,92	0,22
OPCs	PCDH7	ENSG00000169851	0,893	1,444196743	0,786	0,95	0,25
OPCs	HS6ST3	ENSG00000185352	0,86	1,331689479	0,72	0,87	0,16
OPCs	SORCS3	ENSG00000156395	0,864	1,384938605	0,728	0,81	0,11
OPCs	PLPP4	ENSG00000203805	0,882	1,506936232	0,764	0,82	0,12
OPCs	MYT1	ENSG00000196132	0,868	1,385383934	0,736	0,76	0,06
OPCs	SLC24A3	ENSG00000185052	0,868	1,462547442	0,736	0,82	0,13
OPCs	UST	ENSG00000111962	0,879	1,424565427	0,758	0,86	0,17
OPCs	CSMD2	ENSG00000121904	0,907	1,535903505	0,814	0,92	0,23
OPCs	CACNA1A	ENSG00000141837	0,879	1,25186385	0,758	0,93	0,24
OPCs	PDZRN4	ENSG00000165966	0,863	1,587353366	0,726	0,82	0,14
OPCs	HECW1	ENSG00000002746	0,849	1,240789497	0,698	0,81	0,12
OPCs	FAM155A	ENSG00000204442	0,872	1,199190208	0,744	0,98	0,3
OPCs	SEZ6L	ENSG00000100095	0,86	1,487873791	0,72	0,82	0,13
OPCs	DLGAP1	ENSG00000170579	0,871	1,037708659	0,742	0,93	0,25
OPCs	NTRK3	ENSG00000140538	0,887	1,254639321	0,774	0,95	0,27
OPCs	SULF2	ENSG00000196562	0,855	1,299239131	0,71	0,77	0,09
OPCs	PID1	ENSG00000153823	0,881	1,445274894	0,762	0,87	0,19
OPCs	KCNIP1	ENSG00000182132	0,86	1,277973697	0,72	0,85	0,18
OPCs	SORCS1	ENSG00000108018	0,849	1,32487608	0,698	0,78	0,1
OPCs	AC004852.2	ENSG00000278254	0,837	1,844784452	0,674	0,68	0,01
OPCs	CSMD3	ENSG00000164796	0,939	1,736324337	0,878	0,98	0,31
OPCs	MDGA2	ENSG00000139915	0,916	1,520815274	0,832	0,98	0,32
OPCs	STK32A	ENSG00000169302	0,838	1,106038091	0,676	0,8	0,13
OPCs	SMOC1	ENSG00000198732	0,96	1,944753885	0,92	0,97	0,31
OPCs	CNTN3	ENSG00000113805	0,859	1,40952387	0,718	0,81	0,14
OPCs	XKR4	ENSG00000206579	0,846	1,389903403	0,692	0,81	0,15
OPCs	SOX5	ENSG00000134532	0,894	1,391110845	0,788	0,98	0,32
OPCs	PTPRG	ENSG00000144724	0,86	0,971610987	0,72	0,95	0,29
OPCs	SHISA9	ENSG00000237515	0,84	1,381418625	0,68	0,79	0,14

OPCs	GPM6A	ENSG00000150625	0,843	0,962555376	0,686	0,96	0,31
OPCs	GSG1L	ENSG00000169181	0,845	1,273355132	0,69	0,74	0,08
OPCs	CHST11	ENSG00000171310	0,879	1,202847507	0,758	0,95	0,3
OPCs	CNTN1	ENSG00000018236	0,868	1,237233793	0,736	0,96	0,31
OPCs	NOL4	ENSG00000101746	0,848	1,206828232	0,696	0,83	0,18
OPCs	ALK	ENSG00000171094	0,876	1,668154573	0,752	0,84	0,19
OPCs	APCDD1	ENSG00000154856	0,846	1,276587207	0,692	0,78	0,14
OPCs	AMZ1	ENSG00000174945	0,838	1,28709037	0,676	0,72	0,08
OPCs	LINC01322	ENSG00000244128	0,846	1,459728585	0,692	0,77	0,13
OPCs	CSMD1	ENSG00000183117	0,97	2,305673515	0,94	1	0,36
OPCs	LRRK2	ENSG00000188906	0,838	1,13518151	0,676	0,79	0,15
OPCs	RNF150	ENSG00000170153	0,857	1,292896627	0,714	0,84	0,21
OPCs	CDH10	ENSG00000040731	0,842	1,312630768	0,684	0,78	0,15
OPCs	SCN9A	ENSG00000169432	0,83	1,140260212	0,66	0,75	0,12
OPCs	CSGALNACT1	ENSG00000147408	0,828	0,955877876	0,656	0,87	0,24
OPCs	STK32B	ENSG00000152953	0,823	1,333123878	0,646	0,7	0,07
OPCs	SCN3A	ENSG00000153253	0,822	1,074392342	0,644	0,76	0,14
OPCs	PLCB1	ENSG00000182621	0,827	0,892829671	0,654	0,94	0,31
OPCs	POU6F2	ENSG00000106536	0,821	1,369037632	0,642	0,7	0,08
OPCs	AC092691.1	ENSG00000239268	0,855	1,159477162	0,71	0,95	0,33
OPCs	STXBP5L	ENSG00000145087	0,804	0,84414313	0,608	0,83	0,21
OPCs	KIAA1217	ENSG00000120549	0,823	1,095516424	0,646	0,83	0,22
OPCs	PLEKHH2	ENSG00000152527	0,82	1,10705455	0,64	0,71	0,09
OPCs	SEMA3E	ENSG00000170381	0,821	1,301502062	0,642	0,7	0,09
OPCs	TOX	ENSG00000198846	0,818	1,106050729	0,636	0,77	0,16
OPCs	OPHN1	ENSG00000079482	0,937	1,783127479	0,874	0,95	0,34
OPCs	RAB31	ENSG00000168461	0,861	1,233854048	0,722	0,88	0,26
OPCs	CACNG4	ENSG00000075461	0,82	1,196422653	0,64	0,67	0,05
OPCs	SLC22A3	ENSG00000146477	0,811	1,242234019	0,622	0,65	0,03
OPCs	CSPG4	ENSG00000173546	0,805	1,061066642	0,61	0,63	0,02
OPCs	ATP13A4	ENSG00000127249	0,836	1,132752753	0,672	0,81	0,2
OPCs	ZEB1	ENSG00000148516	0,856	1,141916074	0,712	0,92	0,31
OPCs	AC007563.2	ENSG00000236886	0,812	1,502134699	0,624	0,67	0,06
OPCs	KIF26B	ENSG00000162849	0,832	1,245719855	0,664	0,78	0,18
OPCs	NLGN4X	ENSG00000146938	0,9	1,572748331	0,8	0,9	0,3
OPCs	CDH13	ENSG00000140945	0,816	1,087141023	0,632	0,77	0,17
OPCs	IGSF21	ENSG00000117154	0,804	0,937286988	0,608	0,71	0,11
OPCs	LRRN1	ENSG00000175928	0,828	1,196380931	0,656	0,74	0,14
OPCs	TAFA1	ENSG00000183662	0,809	1,360035609	0,618	0,71	0,12
OPCs	PRRX1	ENSG00000116132	0,793	1,026790704	0,586	0,69	0,1
OPCs	NTN1	ENSG00000065320	0,802	1,070793247	0,604	0,66	0,07
OPCs	NRXN1	ENSG00000179915	0,917	1,531849618	0,834	0,99	0,4
OPCs	CRISPLD2	ENSG00000103196	0,797	1,199003818	0,594	0,62	0,04
OPCs	MAP2	ENSG00000078018	0,88	1,270113266	0,76	0,96	0,37
OPCs	MPPED2	ENSG00000066382	0,823	1,206892975	0,646	0,75	0,17
OPCs	PDZD2	ENSG00000133401	0,979	2,352019131	0,958	0,99	0,41
OPCs	TNK2	ENSG00000061938	0,864	1,273514614	0,728	0,84	0,26
OPCs	SHC3	ENSG00000148082	0,817	1,142888696	0,634	0,72	0,14
OPCs	LINC02588	ENSG00000257842	0,803	1,37314315	0,606	0,65	0,07
OPCs	C1orf21	ENSG00000116667	0,82	1,082412586	0,64	0,78	0,2
OPCs	PARD3	ENSG00000148498	0,847	1,021239183	0,694	0,96	0,39
OPCs	CALCRL	ENSG00000064989	0,788	1,098418445	0,576	0,62	0,05
OPCs	LRP1	ENSG00000123384	0,822	0,995192186	0,644	0,82	0,25
OPCs	EGFR	ENSG00000146648	0,782	0,907309503	0,564	0,73	0,16
OPCs	SEMA5A	ENSG00000112902	0,888	1,439629577	0,776	0,93	0,37

OPCs	ETV1	ENSG00000006468	0,787	1,04532403	0,574	0,63	0,07
OPCs	CCSER1	ENSG00000184305	0,779	0,804425878	0,558	0,82	0,26
OPCs	PTPRT	ENSG00000196090	0,784	0,996319266	0,568	0,68	0,12
OPCs	TAFA2	ENSG00000198673	0,794	1,075021796	0,588	0,75	0,19
OPCs	PHLDA1	ENSG00000139289	0,789	1,05418305	0,578	0,61	0,05
OPCs	AFAP1L2	ENSG00000169129	0,782	0,984930048	0,564	0,6	0,05
OPCs	TMEM108	ENSG00000144868	0,805	1,036161213	0,61	0,8	0,25
OPCs	PDGFRA	ENSG00000134853	0,775	0,985623489	0,55	0,55	0
OPCs	ASIC2	ENSG00000108684	0,777	0,867705781	0,554	0,67	0,12
OPCs	MEG8	ENSG00000225746	0,766	0,810825507	0,532	0,68	0,14
OPCs	MGLL	ENSG00000074416	0,802	1,140165804	0,604	0,73	0,19
OPCs	RAMP1	ENSG00000132329	0,797	0,988554303	0,594	0,72	0,18
OPCs	FAM110B	ENSG00000169122	0,799	1,03910985	0,598	0,73	0,19
OPCs	MTSS2	ENSG00000132613	0,805	0,969738269	0,61	0,76	0,22
OPCs	GRAMD1C	ENSG00000178075	0,776	0,916970221	0,552	0,67	0,13
OPCs	XYLT1	ENSG00000103489	0,929	1,815419323	0,858	0,96	0,42
OPCs	DAB1	ENSG00000173406	0,815	0,884036724	0,63	0,89	0,36
OPCs	ASTN1	ENSG00000152092	0,804	0,976545896	0,608	0,79	0,26
OPCs	ARHGAP31	ENSG00000031081	0,766	0,814271586	0,532	0,73	0,2
OPCs	KCNMA1	ENSG00000156113	0,833	0,880628422	0,666	0,95	0,42
OPCs	CTNNA2	ENSG00000066032	0,806	0,814806999	0,612	0,96	0,43
OPCs	MARCKS	ENSG00000277443	0,807	1,068166661	0,614	0,76	0,23
OPCs	GRIK3	ENSG00000163873	0,77	0,961641663	0,54	0,61	0,09
OPCs	CCDC50	ENSG00000152492	0,829	1,056002212	0,658	0,81	0,3
OPCs	RHBDL3	ENSG00000141314	0,766	0,909360877	0,532	0,63	0,11
OPCs	OLIG1	ENSG00000184221	0,81	1,08743951	0,62	0,8	0,29
OPCs	RAPGEF4	ENSG00000091428	0,794	0,885945421	0,588	0,83	0,32
OPCs	NCALD	ENSG00000104490	0,78	1,177522359	0,56	0,67	0,16
OPCs	KCNMB2-AS1	ENSG00000237978	0,768	1,018500011	0,536	0,64	0,13
OPCs	KLF12	ENSG00000118922	0,808	1,00304597	0,616	0,84	0,33
OPCs	RGS7	ENSG00000182901	0,799	0,865352029	0,598	0,9	0,39
OPCs	OLIG2	ENSG00000205927	0,766	0,93889797	0,532	0,62	0,11
OPCs	C1orf61	ENSG00000125462	0,774	0,778845352	0,548	0,75	0,25
OPCs	PRKG2	ENSG00000138669	0,761	1,004005704	0,522	0,56	0,05
OPCs	CMYA5	ENSG00000164309	0,762	0,917293389	0,524	0,6	0,1
OPCs	GRID2	ENSG00000152208	0,885	1,184504473	0,77	0,98	0,48
OPCs	KHDRBS3	ENSG00000131773	0,833	1,154604814	0,666	0,84	0,34
OPCs	TNS3	ENSG00000136205	0,758	0,81484995	0,516	0,69	0,19
OPCs	LRRC7	ENSG00000033122	0,747	0,658071167	0,494	0,79	0,29
OPCs	SLC44A5	ENSG00000137968	0,752	0,900278436	0,504	0,63	0,13
OPCs	KCNT2	ENSG00000162687	0,751	0,83377697	0,502	0,61	0,11
OPCs	BEST3	ENSG00000127325	0,747	1,037704116	0,494	0,5	0
OPCs	GRIA3	ENSG00000125675	0,797	0,887793682	0,594	0,81	0,32
OPCs	ITGA9	ENSG00000144668	0,758	0,932852898	0,516	0,61	0,11
OPCs	PALLD	ENSG00000129116	0,769	0,875110907	0,538	0,69	0,2
OPCs	NTNG1	ENSG00000162631	0,745	0,744022542	0,49	0,66	0,17
OPCs	CST3	ENSG00000101439	0,778	0,919144394	0,556	0,81	0,32
OPCs	SERPINE2	ENSG00000135919	0,751	0,715407613	0,502	0,67	0,18
OPCs	LRRTM3	ENSG00000198739	0,826	1,101004242	0,652	0,87	0,38
OPCs	ARHGAP10	ENSG00000071205	0,746	0,771955524	0,492	0,59	0,11
OPCs	ARHGAP42	ENSG00000165895	0,738	0,677719093	0,476	0,61	0,13
OPCs	KCND3	ENSG00000171385	0,761	0,889806597	0,522	0,66	0,18
OPCs	IL1RAP	ENSG00000196083	0,746	0,862711327	0,492	0,58	0,1
OPCs	ARHGEF4	ENSG00000136002	0,77	0,697066794	0,54	0,77	0,29
OPCs	AL133346.1	ENSG00000227220	0,752	1,044589996	0,504	0,58	0,1

OPCs	GALNT13	ENSG00000144278	0,911	1,529046966	0,822	0,96	0,48
OPCs	SCN2A	ENSG00000136531	0,735	0,681974115	0,47	0,66	0,18
OPCs	LINC02223	ENSG00000249937	0,747	1,027435167	0,494	0,55	0,07
OPCs	GUCY1A2	ENSG00000152402	0,741	0,733460701	0,482	0,66	0,18
OPCs	RIT2	ENSG00000152214	0,741	0,937406621	0,482	0,56	0,09
OPCs	AFAP1	ENSG00000196526	0,756	0,94891714	0,512	0,58	0,11
OPCs	RUNX1T1	ENSG00000079102	0,747	0,742829283	0,494	0,74	0,27
OPCs	RALYL	ENSG00000184672	0,743	0,924897331	0,486	0,71	0,24
OPCs	RIMS1	ENSG00000079841	0,739	0,658577654	0,478	0,73	0,26
OPCs	LRRC4C	ENSG00000148948	0,985	2,346357992	0,97	1	0,53
OPCs	NLGN1	ENSG00000169760	0,949	1,582617007	0,898	1	0,53
OPCs	CABLES1	ENSG00000134508	0,733	0,788176446	0,466	0,61	0,14
OPCs	ABHD2	ENSG00000140526	0,812	1,025709429	0,624	0,81	0,35
OPCs	GRIA4	ENSG00000152578	0,949	1,720371038	0,898	0,99	0,52
OPCs	CD82	ENSG00000085117	0,738	0,786327001	0,476	0,58	0,12
OPCs	SYT17	ENSG00000103528	0,734	0,660504826	0,468	0,65	0,18
OPCs	DGKI	ENSG00000157680	0,783	0,822271157	0,566	0,84	0,38
OPCs	SLC1A1	ENSG00000106688	0,745	0,802968893	0,49	0,59	0,13
OPCs	ASCL1	ENSG00000139352	0,734	0,84091111	0,468	0,48	0,01
OPCs	THSD7A	ENSG00000005108	0,743	0,694299155	0,486	0,72	0,26
OPCs	KCNAB1	ENSG00000169282	0,739	0,744151111	0,478	0,66	0,2
OPCs	ATCAY	ENSG00000167654	0,744	0,785063813	0,488	0,58	0,12
OPCs	TRIM9	ENSG00000100505	0,879	1,22641127	0,758	0,95	0,49
OPCs	ATP2B4	ENSG00000058668	0,815	0,955196664	0,63	0,86	0,41
OPCs	TACC2	ENSG00000138162	0,75	0,835339484	0,5	0,59	0,14
OPCs	SPSB4	ENSG00000175093	0,73	0,839250929	0,46	0,47	0,02
OPCs	ADARB2	ENSG00000185736	0,874	1,16177107	0,748	0,95	0,5
OPCs	SLC2A13	ENSG00000151229	0,722	0,622069041	0,444	0,67	0,22
OPCs	SAMHD1	ENSG00000101347	0,742	0,816994951	0,484	0,64	0,19
OPCs	NKAIN3	ENSG00000185942	0,722	0,708987914	0,444	0,64	0,19
OPCs	FIGN	ENSG00000182263	0,738	0,670187833	0,476	0,78	0,34
OPCs	BMP7	ENSG00000101144	0,737	0,735869776	0,474	0,6	0,15
OPCs	SGCZ	ENSG00000185053	0,722	0,85556654	0,444	0,61	0,17
OPCs	ST8SIA1	ENSG00000111728	0,739	0,79390635	0,478	0,67	0,23
OPCs	SEMA3D	ENSG00000153993	0,725	0,826621036	0,45	0,5	0,06
OPCs	CDK14	ENSG00000058091	0,778	0,840905568	0,556	0,82	0,38
OPCs	AL445250.1	ENSG00000225096	0,749	1,140350013	0,498	0,65	0,21
OPCs	LMO3	ENSG00000048540	0,724	0,753352241	0,448	0,56	0,13
OPCs	CSPG5	ENSG00000114646	0,732	0,85367895	0,464	0,52	0,08
OPCs	NFIB	ENSG00000147862	0,775	0,696631397	0,55	0,92	0,49
OPCs	RORA	ENSG00000069667	0,829	0,880220684	0,658	0,98	0,55
OPCs	TMEM132B	ENSG00000139364	0,727	0,788436254	0,454	0,59	0,15
OPCs	ATP2C2	ENSG00000064270	0,72	0,823421301	0,44	0,46	0,03
OPCs	COL4A3	ENSG00000169031	0,72	0,781138628	0,44	0,5	0,07
OPCs	GFRA1	ENSG00000151892	0,721	0,856195829	0,442	0,47	0,04
OPCs	PRKD1	ENSG00000184304	0,757	0,780366365	0,514	0,81	0,38
OPCs	TNIK	ENSG00000154310	0,763	0,625519204	0,526	0,91	0,48
OPCs	ADCY1	ENSG00000164742	0,726	0,760362433	0,452	0,57	0,14
OPCs	C1QL1	ENSG00000131094	0,716	0,899952217	0,432	0,45	0,02
OPCs	PLPPR1	ENSG00000148123	0,748	0,81362709	0,496	0,73	0,31
OPCs	GNPTAB	ENSG00000111670	0,75	0,838008734	0,5	0,66	0,23
OPCs	THRB	ENSG00000151090	0,756	0,823048072	0,512	0,77	0,34
OPCs	LRFN5	ENSG00000165379	0,701	0,600787062	0,402	0,6	0,17
OPCs	ITGA8	ENSG00000077943	0,713	0,942861017	0,426	0,46	0,04
OPCs	SNAP91	ENSG00000065609	0,716	0,593147336	0,432	0,73	0,31

OPCs	GPR37L1	ENSG00000170075	0,72	0,685725127	0,44	0,6	0,18
OPCs	SPRED2	ENSG00000198369	0,737	0,77870847	0,474	0,68	0,26
OPCs	GRIA2	ENSG00000120251	0,867	1,06819506	0,734	0,95	0,54
OPCs	TENM1	ENSG00000009694	0,706	0,61536445	0,412	0,54	0,13
OPCs	PTN	ENSG00000105894	0,734	0,695298192	0,468	0,72	0,31
OPCs	DZIP1	ENSG00000134874	0,725	0,689010963	0,45	0,59	0,18
OPCs	WSCD1	ENSG00000179314	0,728	0,803124625	0,456	0,56	0,15
OPCs	PLAAT1	ENSG00000127252	0,711	0,843524196	0,422	0,45	0,04
OPCs	NSG2	ENSG00000170091	0,71	0,679638028	0,42	0,53	0,12
OPCs	KANK1	ENSG00000107104	0,757	0,673759464	0,514	0,87	0,47
OPCs	VIPR2	ENSG00000106018	0,703	0,810125069	0,406	0,41	0,01
OPCs	GLCCI1	ENSG00000106415	0,77	0,923507852	0,54	0,77	0,37
OPCs	FGFR1	ENSG00000077782	0,732	0,749303155	0,464	0,65	0,25
OPCs	ADRA1A	ENSG00000120907	0,704	0,740807847	0,408	0,5	0,1
OPCs	GPC6	ENSG00000183098	0,705	0,73167646	0,41	0,59	0,19
OPCs	OLFM2	ENSG00000105088	0,71	0,682123531	0,42	0,54	0,14
OPCs	CSRNP3	ENSG00000178662	0,739	0,718604448	0,478	0,77	0,37
OPCs	SNX22	ENSG00000157734	0,705	0,73768128	0,41	0,47	0,07
OPCs	MAP3K1	ENSG00000095015	0,715	0,736549372	0,43	0,59	0,19
OPCs	HS3ST1	ENSG00000002587	0,702	0,783310883	0,404	0,43	0,03
OPCs	ANO6	ENSG00000177119	0,712	0,665111447	0,424	0,61	0,22
OPCs	SDC3	ENSG00000162512	0,71	0,703737745	0,42	0,53	0,13
OPCs	DPY19L2	ENSG00000177990	0,708	0,650843319	0,416	0,55	0,15
OPCs	ZNF462	ENSG00000148143	0,844	1,109162412	0,688	0,9	0,51
OPCs	CPNE5	ENSG00000124772	0,704	0,726147952	0,408	0,47	0,08
OPCs	APOD	ENSG00000189058	0,763	0,868344521	0,526	0,85	0,46
OPCs	ILDR2	ENSG00000143195	0,708	0,689745852	0,416	0,51	0,12
OPCs	GPR158	ENSG00000151025	0,721	0,776154644	0,442	0,68	0,3
OPCs	HIP1R	ENSG00000130787	0,823	0,952432072	0,646	0,9	0,51
OPCs	BAALC	ENSG00000164929	0,703	0,657681218	0,406	0,58	0,19
OPCs	RXRA	ENSG00000186350	0,71	0,685552913	0,42	0,56	0,17
OPCs	SOX8	ENSG00000005513	0,716	0,730776654	0,432	0,63	0,24
OPCs	U91319.1	ENSG00000262801	0,702	0,935875385	0,404	0,47	0,09
OPCs	PLPPR5	ENSG00000117598	0,701	0,719726546	0,402	0,46	0,08
OPCs	GRIK4	ENSG00000149403	0,709	0,623965478	0,418	0,69	0,33
OPCs	USP24	ENSG00000162402	0,822	0,97147449	0,644	0,88	0,52
OPCs	CTNND2	ENSG00000169862	0,797	0,68155909	0,594	0,98	0,62
OPCs	SGCD	ENSG00000170624	0,74	0,796069144	0,48	0,81	0,45
OPCs	CASK	ENSG00000147044	0,732	0,666974521	0,464	0,79	0,44
OPCs	ASTN2	ENSG00000148219	0,789	0,766109164	0,578	0,94	0,59
OPCs	SAMD4A	ENSG00000020577	0,727	0,619420455	0,454	0,82	0,48
OPCs	CYFIP2	ENSG00000055163	0,704	0,623097362	0,408	0,65	0,3
OPCs	KAT2B	ENSG00000114166	0,877	1,161821727	0,754	0,95	0,61
OPCs	DNER	ENSG00000187957	0,787	0,759458751	0,574	0,91	0,57
OPCs	DPP6	ENSG00000130226	0,951	1,52357438	0,902	0,99	0,66
OPCs	ADAM22	ENSG00000008277	0,704	0,587166521	0,408	0,72	0,38
OPCs	TRIO	ENSG00000038382	0,826	0,910052656	0,652	0,95	0,62
OPCs	DMD	ENSG00000198947	0,811	0,902773478	0,622	0,94	0,61
OPCs	NBEA	ENSG00000172915	0,764	0,652546936	0,528	0,9	0,58
OPCs	NAV1	ENSG00000134369	0,868	1,137041711	0,736	0,95	0,63
OPCs	KAZN	ENSG00000189337	0,833	0,934025237	0,666	0,98	0,65
OPCs	RIN2	ENSG00000132669	0,73	0,672652446	0,46	0,81	0,49
OPCs	NOVA1	ENSG00000139910	0,899	1,256159349	0,798	0,97	0,66
OPCs	MTSS1	ENSG00000170873	0,745	0,689289718	0,49	0,85	0,54
OPCs	PIK3R1	ENSG00000145675	0,832	1,008605363	0,664	0,92	0,61

OPCs	HIP1	ENSG00000127946	0,788	0,862751612	0,576	0,93	0,63
OPCs	ZDHHC14	ENSG00000175048	0,807	0,898773308	0,614	0,93	0,62
OPCs	MAML2	ENSG00000184384	0,749	0,597160805	0,498	0,94	0,63
OPCs	PHYHIPL	ENSG00000165443	0,738	0,678912588	0,476	0,85	0,55
OPCs	ARNT2	ENSG00000172379	0,726	0,616769085	0,452	0,81	0,51
OPCs	ERBB4	ENSG00000178568	0,83	0,864088932	0,66	0,99	0,7
OPCs	EPN2	ENSG00000072134	0,895	1,359761412	0,79	0,96	0,68
OPCs	NAV2	ENSG00000166833	0,788	0,777345358	0,576	0,96	0,68
OPCs	NLGN4Y	ENSG00000165246	0,74	1,030594788	0,48	0,74	0,46
OPCs	PHACTR3	ENSG00000087495	0,744	0,65857457	0,488	0,91	0,65
OPCs	ASAP1	ENSG00000153317	0,787	0,745337837	0,574	0,94	0,69
OPCs	KIF13A	ENSG00000137177	0,814	0,929573604	0,628	0,94	0,7
OPCs	SCD5	ENSG00000145284	0,84	0,89403382	0,68	0,98	0,74
OPCs	PRKCA	ENSG00000154229	0,829	0,82299835	0,658	0,98	0,75
OPCs	ADGRL3	ENSG00000150471	0,893	1,030822425	0,786	0,99	0,77
OPCs	LSAMP	ENSG00000185565	0,851	0,930199912	0,702	1	0,78
OPCs	ZHX2	ENSG00000178764	0,713	0,609677772	0,426	0,87	0,65
OPCs	LRP1B	ENSG00000168702	0,909	1,137687638	0,818	0,99	0,78
OPCs	ADGRB3	ENSG00000135298	0,821	0,76188164	0,642	0,99	0,8
OPCs	ZSWIM6	ENSG00000130449	0,737	0,593003858	0,474	0,97	0,88
Astrocytes	OBI1-AS1	ENSG00000234377	0,951	2,736114088	0,902	0,91	0,05
Astrocytes	RFX4	ENSG00000111783	0,955	2,396612762	0,91	0,92	0,06
Astrocytes	HPSE2	ENSG00000172987	0,959	3,328073605	0,918	0,93	0,07
Astrocytes	SLC14A1	ENSG00000141469	0,936	2,627401325	0,872	0,88	0,03
Astrocytes	AQP4	ENSG00000171885	0,934	2,198522936	0,868	0,88	0,06
Astrocytes	RYR3	ENSG00000198838	0,963	2,49723103	0,926	0,95	0,13
Astrocytes	TRPM3	ENSG00000083067	0,986	2,941241796	0,972	0,99	0,18
Astrocytes	LINC01088	ENSG00000249307	0,953	2,814103486	0,906	0,93	0,12
Astrocytes	ATP1A2	ENSG00000018625	0,934	1,784140078	0,868	0,93	0,13
Astrocytes	ADCY2	ENSG00000078295	0,968	2,416138821	0,936	0,96	0,16
Astrocytes	TNC	ENSG00000041982	0,893	2,284663774	0,786	0,79	0,01
Astrocytes	GLIS3	ENSG00000107249	0,95	2,248201841	0,9	0,95	0,17
Astrocytes	HIF3A	ENSG00000124440	0,92	1,757852621	0,84	0,93	0,15
Astrocytes	MAPK4	ENSG00000141639	0,913	2,068757784	0,826	0,85	0,08
Astrocytes	GJA1	ENSG00000152661	0,896	1,944073055	0,792	0,82	0,06
Astrocytes	RGMA	ENSG00000182175	0,893	1,798417354	0,786	0,8	0,05
Astrocytes	GPC5	ENSG00000179399	0,939	2,311162187	0,878	0,95	0,21
Astrocytes	FAM189A2	ENSG00000135063	0,891	1,938869812	0,782	0,8	0,06
Astrocytes	SDC4	ENSG00000124145	0,872	1,714830508	0,744	0,76	0,03
Astrocytes	WDR49	ENSG00000174776	0,867	1,623923044	0,734	0,77	0,04
Astrocytes	PTCHD1-AS	ENSG00000233067	0,89	1,998057609	0,78	0,83	0,11
Astrocytes	SLC4A4	ENSG00000080493	0,88	1,95809425	0,76	0,79	0,07
Astrocytes	PTPRZ1	ENSG00000106278	0,865	1,045668638	0,73	0,89	0,17
Astrocytes	EFEMP1	ENSG00000115380	0,862	1,697939471	0,724	0,74	0,03
Astrocytes	SLC25A18	ENSG00000182902	0,884	1,723803384	0,768	0,8	0,09
Astrocytes	SLC1A2	ENSG00000110436	0,914	2,339001231	0,828	0,89	0,19
Astrocytes	MGST1	ENSG00000008394	0,866	1,686291455	0,732	0,76	0,06
Astrocytes	AC073941.1	ENSG00000259255	0,852	1,900075379	0,704	0,71	0,01
Astrocytes	BMPR1B	ENSG00000138696	0,859	1,635364897	0,718	0,74	0,05
Astrocytes	GPM6A	ENSG00000150625	0,929	1,828722317	0,858	0,97	0,27
Astrocytes	SOX5	ENSG00000134532	0,919	1,667328543	0,838	0,97	0,28
Astrocytes	SPON1	ENSG00000262655	0,865	1,635082724	0,73	0,79	0,1
Astrocytes	PAMR1	ENSG00000149090	0,851	1,605223282	0,702	0,72	0,03
Astrocytes	FMN2	ENSG00000155816	0,951	1,97231427	0,902	0,95	0,27
Astrocytes	MGAT4C	ENSG00000182050	0,851	1,366257916	0,702	0,81	0,13

Astrocytes	NRG3	ENSG00000185737	0,963	2,082791891	0,926	1	0,32
Astrocytes	NEBL	ENSG00000078114	0,936	1,784006973	0,872	0,97	0,3
Astrocytes	RANBP3L	ENSG00000164188	0,846	1,826604486	0,692	0,71	0,04
Astrocytes	GFAP	ENSG00000131095	0,93	2,178838532	0,86	0,93	0,26
Astrocytes	PITPNC1	ENSG00000154217	0,965	2,251227336	0,93	0,98	0,31
Astrocytes	ADCY8	ENSG00000155897	0,872	1,634481984	0,744	0,81	0,14
Astrocytes	KCNN3	ENSG00000143603	0,884	1,734348874	0,768	0,82	0,15
Astrocytes	SLC24A4	ENSG00000140090	0,849	1,634306229	0,698	0,72	0,06
Astrocytes	CNTN1	ENSG00000018236	0,875	1,385205023	0,75	0,94	0,27
Astrocytes	ABLIM1	ENSG00000099204	0,901	1,620993618	0,802	0,89	0,24
Astrocytes	APOE	ENSG00000130203	0,881	1,663126404	0,762	0,89	0,24
Astrocytes	ANKFN1	ENSG00000153930	0,853	1,474960654	0,706	0,78	0,13
Astrocytes	TSHZ2	ENSG00000182463	0,843	1,484877038	0,686	0,78	0,13
Astrocytes	NTRK3	ENSG00000140538	0,865	1,311641617	0,73	0,89	0,24
Astrocytes	ACSBG1	ENSG00000103740	0,843	1,370814277	0,686	0,78	0,14
Astrocytes	ACOT11	ENSG00000162390	0,86	1,512399423	0,72	0,78	0,14
Astrocytes	NRCAM	ENSG00000091129	0,834	0,904096303	0,668	0,89	0,25
Astrocytes	EYA2	ENSG00000064655	0,833	1,47256884	0,666	0,7	0,06
Astrocytes	SORBS1	ENSG00000095637	0,968	2,187876208	0,936	0,98	0,35
Astrocytes	BOC	ENSG00000144857	0,831	1,511641789	0,662	0,69	0,05
Astrocytes	AC092691.1	ENSG00000239268	0,871	1,377153617	0,742	0,93	0,3
Astrocytes	WWC1	ENSG00000113645	0,839	1,511462404	0,678	0,72	0,09
Astrocytes	CARMIL1	ENSG00000079691	0,856	1,59462575	0,712	0,79	0,16
Astrocytes	STK32A	ENSG00000169302	0,83	1,434924529	0,66	0,73	0,11
Astrocytes	NHSL1	ENSG00000135540	0,826	1,132918485	0,652	0,77	0,14
Astrocytes	FGFR3	ENSG00000068078	0,822	1,476616242	0,644	0,67	0,05
Astrocytes	FAT3	ENSG00000165323	0,839	1,46916525	0,678	0,78	0,16
Astrocytes	NKAIN3	ENSG00000185942	0,837	1,480427525	0,674	0,77	0,15
Astrocytes	CD44	ENSG00000026508	0,828	1,969816778	0,656	0,69	0,08
Astrocytes	PLCB1	ENSG00000182621	0,855	1,337713073	0,71	0,9	0,28
Astrocytes	ATP1B2	ENSG00000129244	0,845	1,504547461	0,69	0,76	0,14
Astrocytes	SERPINI2	ENSG00000114204	0,81	1,324252675	0,62	0,64	0,03
Astrocytes	ARHGEF4	ENSG00000136002	0,892	1,664189467	0,784	0,86	0,25
Astrocytes	AQP1	ENSG00000240583	0,811	1,842175799	0,622	0,64	0,03
Astrocytes	RGS6	ENSG00000182732	0,823	1,571644835	0,646	0,75	0,14
Astrocytes	PARD3	ENSG00000148498	0,919	1,603329353	0,838	0,97	0,36
Astrocytes	GRAMD2B	ENSG00000155324	0,886	1,523491372	0,772	0,88	0,27
Astrocytes	SLC7A11	ENSG00000151012	0,843	1,560308875	0,686	0,77	0,17
Astrocytes	DGKG	ENSG00000058866	0,831	1,211901226	0,662	0,82	0,22
Astrocytes	CDHR3	ENSG00000128536	0,82	1,373431355	0,64	0,7	0,1
Astrocytes	IQCA1	ENSG00000132321	0,83	1,524617771	0,66	0,72	0,12
Astrocytes	ITGB4	ENSG00000132470	0,81	1,35730368	0,62	0,66	0,07
Astrocytes	WLS	ENSG00000116729	0,827	1,324632322	0,654	0,73	0,14
Astrocytes	ALDH1L1	ENSG00000144908	0,805	1,323376211	0,61	0,64	0,05
Astrocytes	ADGRA3	ENSG00000152990	0,82	1,352441016	0,64	0,69	0,1
Astrocytes	NPL	ENSG00000135838	0,849	1,499434483	0,698	0,79	0,2
Astrocytes	SOX6	ENSG00000110693	0,792	0,797108775	0,584	0,76	0,17
Astrocytes	PRKG1	ENSG00000185532	0,802	1,078190314	0,604	0,78	0,2
Astrocytes	MAP3K5	ENSG00000197442	0,853	1,334536512	0,706	0,85	0,28
Astrocytes	SLC6A11	ENSG00000132164	0,805	1,661729589	0,61	0,64	0,07
Astrocytes	UTRN	ENSG00000152818	0,806	0,968274077	0,612	0,84	0,26
Astrocytes	SPARCL1	ENSG00000152583	0,814	1,242558849	0,628	0,79	0,22
Astrocytes	SERPINE2	ENSG00000135919	0,82	1,353579634	0,64	0,72	0,15
Astrocytes	RFX2	ENSG00000087903	0,808	1,266469458	0,616	0,69	0,12
Astrocytes	ACACB	ENSG00000076555	0,859	1,538639475	0,718	0,81	0,25

Astrocytes	LGI1	ENSG00000108231	0,81	1,394567011	0,62	0,67	0,11
Astrocytes	CPE	ENSG00000109472	0,876	1,497618354	0,752	0,87	0,3
Astrocytes	COL5A3	ENSG00000080573	0,785	1,39538187	0,57	0,61	0,05
Astrocytes	ARHGEF26	ENSG00000114790	0,807	1,303460832	0,614	0,67	0,11
Astrocytes	CAMK2G	ENSG00000148660	0,848	1,492643191	0,696	0,79	0,23
Astrocytes	LHFPL6	ENSG00000183722	0,856	1,386920828	0,712	0,88	0,33
Astrocytes	CTNNA2	ENSG00000066032	0,869	1,37871502	0,738	0,96	0,41
Astrocytes	DCLK2	ENSG00000170390	0,889	1,611444284	0,778	0,88	0,33
Astrocytes	MED12L	ENSG00000144893	0,826	1,356830241	0,652	0,77	0,22
Astrocytes	ATP13A4	ENSG00000127249	0,808	1,191663774	0,616	0,73	0,18
Astrocytes	GMPR	ENSG00000137198	0,781	1,24448954	0,562	0,59	0,05
Astrocytes	EGFR	ENSG00000146648	0,784	1,155428618	0,568	0,68	0,14
Astrocytes	LINC01748	ENSG00000226476	0,776	1,304526178	0,552	0,57	0,02
Astrocytes	GLI3	ENSG00000106571	0,777	1,317242984	0,554	0,58	0,03
Astrocytes	FRMPD2	ENSG00000170324	0,771	1,127254621	0,542	0,57	0,02
Astrocytes	PRRX1	ENSG00000116132	0,777	1,238466155	0,554	0,62	0,08
Astrocytes	NTRK2	ENSG00000148053	0,941	1,78894997	0,882	0,97	0,43
Astrocytes	AHCYL1	ENSG00000168710	0,939	1,898526446	0,878	0,93	0,39
Astrocytes	PCDH7	ENSG00000169851	0,752	0,66849013	0,504	0,77	0,23
Astrocytes	YAP1	ENSG00000137693	0,774	1,094831828	0,548	0,61	0,07
Astrocytes	CACNA2D3	ENSG00000157445	0,811	1,562850759	0,622	0,77	0,24
Astrocytes	CACHD1	ENSG00000158966	0,798	1,208384168	0,596	0,71	0,17
Astrocytes	ETNPPL	ENSG00000164089	0,77	1,314193124	0,54	0,55	0,01
Astrocytes	NPAS2	ENSG00000170485	0,8	1,301360439	0,6	0,72	0,18
Astrocytes	GABRB1	ENSG00000163288	0,78	1,082387962	0,56	0,74	0,21
Astrocytes	PCSK5	ENSG00000099139	0,791	1,221497402	0,582	0,68	0,15
Astrocytes	BCL6	ENSG00000113916	0,844	1,411112451	0,688	0,81	0,28
Astrocytes	TCF7L1	ENSG00000152284	0,771	1,177806378	0,542	0,59	0,06
Astrocytes	KALRN	ENSG00000160145	0,86	1,312482901	0,72	0,9	0,37
Astrocytes	LRIG1	ENSG00000144749	0,853	1,541096098	0,706	0,81	0,28
Astrocytes	C1orf61	ENSG00000125462	0,82	1,368678963	0,64	0,75	0,22
Astrocytes	ABCA1	ENSG00000165029	0,828	1,38256521	0,656	0,79	0,26
Astrocytes	ADAMTS9-AS2	ENSG00000241684	0,772	1,249401605	0,544	0,64	0,12
Astrocytes	PDE7B	ENSG00000171408	0,784	1,054438899	0,568	0,73	0,21
Astrocytes	LINC00299	ENSG00000236790	0,767	1,290589335	0,534	0,55	0,03
Astrocytes	MRVI1	ENSG00000072952	0,764	1,271008346	0,528	0,54	0,02
Astrocytes	AGT	ENSG00000135744	0,771	1,257201718	0,542	0,59	0,07
Astrocytes	MCC	ENSG00000171444	0,786	1,122086602	0,572	0,69	0,17
Astrocytes	COL27A1	ENSG00000196739	0,772	1,308038973	0,544	0,6	0,08
Astrocytes	LAMA1	ENSG00000101680	0,764	1,160199521	0,528	0,55	0,03
Astrocytes	NR2F1-AS1	ENSG00000237187	0,782	1,132506005	0,564	0,67	0,15
Astrocytes	CABLES1	ENSG00000134508	0,781	1,714689351	0,562	0,63	0,11
Astrocytes	RASL12	ENSG00000103710	0,759	1,126040051	0,518	0,53	0,02
Astrocytes	PRDM16	ENSG00000142611	0,761	1,126990913	0,522	0,55	0,04
Astrocytes	PSD2	ENSG00000146005	0,782	1,172829678	0,564	0,63	0,12
Astrocytes	SFXN5	ENSG00000144040	0,851	1,416851492	0,702	0,81	0,3
Astrocytes	NRXN1	ENSG00000179915	0,771	0,822554189	0,542	0,89	0,39
Astrocytes	EYA1	ENSG00000104313	0,752	1,182442959	0,504	0,55	0,05
Astrocytes	ACSS3	ENSG00000111058	0,759	1,142241679	0,518	0,57	0,07
Astrocytes	ZNRF3	ENSG00000183579	0,798	1,258796473	0,596	0,71	0,21
Astrocytes	PHF21B	ENSG00000056487	0,764	1,109693225	0,528	0,6	0,11
Astrocytes	LUZP2	ENSG00000187398	0,751	0,906738883	0,502	0,7	0,21
Astrocytes	GRAMD1C	ENSG00000178075	0,761	1,121926444	0,522	0,6	0,11
Astrocytes	OGFRL1	ENSG00000119900	0,801	1,180112982	0,602	0,75	0,26
Astrocytes	SYTL4	ENSG00000102362	0,758	1,094126304	0,516	0,57	0,08

Astrocytes	ATP2B2	ENSG00000157087	0,766	1,050660963	0,532	0,67	0,18
Astrocytes	CSGALNACT1	ENSG00000147408	0,744	0,709422674	0,488	0,72	0,23
Astrocytes	TOGARAM2	ENSG00000189350	0,75	1,13395865	0,5	0,55	0,06
Astrocytes	PBXIP1	ENSG00000163346	0,751	1,063078889	0,502	0,54	0,06
Astrocytes	DAPK1	ENSG00000196730	0,766	1,107702638	0,532	0,62	0,15
Astrocytes	ZFP36L1	ENSG00000185650	0,742	0,832891104	0,484	0,66	0,18
Astrocytes	BCAR3	ENSG00000137936	0,767	1,102746247	0,534	0,64	0,17
Astrocytes	EDNRB	ENSG00000136160	0,741	1,08599258	0,482	0,5	0,03
Astrocytes	TNIK	ENSG00000154310	0,874	1,383844992	0,748	0,93	0,46
Astrocytes	DOCK7	ENSG00000116641	0,841	1,312862152	0,682	0,81	0,34
Astrocytes	RORA	ENSG00000069667	0,923	1,576514852	0,846	0,99	0,52
Astrocytes	FARP1	ENSG00000152767	0,774	1,051990659	0,548	0,71	0,24
Astrocytes	KIAA1671	ENSG00000197077	0,763	1,081945016	0,526	0,62	0,15
Astrocytes	SLC39A12	ENSG00000148482	0,736	1,15099676	0,472	0,49	0,02
Astrocytes	SOX9	ENSG00000125398	0,74	1,073078401	0,48	0,52	0,05
Astrocytes	BAALC	ENSG00000164929	0,762	1,157282085	0,524	0,63	0,17
Astrocytes	ITPKB	ENSG00000143772	0,885	1,393128482	0,77	0,92	0,45
Astrocytes	MARCH3	ENSG00000173926	0,757	1,164860916	0,514	0,65	0,19
Astrocytes	AQP4-AS1	ENSG00000260372	0,746	1,449654037	0,492	0,54	0,08
Astrocytes	LINC00461	ENSG00000245526	0,786	1,128906359	0,572	0,72	0,25
Astrocytes	OPHN1	ENSG00000079482	0,788	0,980905679	0,576	0,78	0,33
Astrocytes	PHYHD1	ENSG00000175287	0,731	1,061904599	0,462	0,48	0,02
Astrocytes	CHL1	ENSG00000134121	0,727	0,686653796	0,454	0,67	0,22
Astrocytes	ARHGAP26	ENSG00000145819	0,787	0,709034397	0,574	0,89	0,44
Astrocytes	MIR4300HG	ENSG00000245832	0,75	1,50402946	0,5	0,57	0,12
Astrocytes	ARHGEF10L	ENSG00000074964	0,763	1,094574406	0,526	0,63	0,18
Astrocytes	AC099792.1	ENSG00000231252	0,729	1,127280698	0,458	0,47	0,02
Astrocytes	PTCHD1	ENSG00000165186	0,737	1,088115754	0,474	0,51	0,06
Astrocytes	RBPMS	ENSG00000157110	0,726	0,919378042	0,452	0,53	0,08
Astrocytes	CLU	ENSG00000120885	0,929	2,018319861	0,858	0,95	0,5
Astrocytes	ECHDC2	ENSG00000121310	0,771	1,075353371	0,542	0,66	0,21
Astrocytes	IGFBP7	ENSG00000163453	0,719	0,750070547	0,438	0,55	0,1
Astrocytes	CDH23	ENSG00000107736	0,739	1,150025564	0,478	0,55	0,1
Astrocytes	COLEC12	ENSG00000158270	0,726	0,98154504	0,452	0,52	0,07
Astrocytes	PLEKHA5	ENSG00000052126	0,809	1,28757527	0,618	0,83	0,39
Astrocytes	C1orf21	ENSG00000116667	0,75	1,025868482	0,5	0,64	0,19
Astrocytes	DNAH7	ENSG00000118997	0,733	1,043529881	0,466	0,53	0,08
Astrocytes	FGF2	ENSG00000138685	0,745	1,038473696	0,49	0,56	0,12
Astrocytes	FLRT2	ENSG00000185070	0,739	1,024297385	0,478	0,61	0,17
Astrocytes	LINC01094	ENSG00000251442	0,722	1,167564215	0,444	0,5	0,06
Astrocytes	DPP10	ENSG00000175497	0,781	2,139438944	0,562	0,71	0,28
Astrocytes	SYT17	ENSG00000103528	0,735	0,909040894	0,47	0,6	0,16
Astrocytes	CHPT1	ENSG00000111666	0,78	1,118007825	0,56	0,71	0,27
Astrocytes	ABR	ENSG00000159842	0,747	0,612361948	0,494	0,74	0,31
Astrocytes	MRAS	ENSG00000158186	0,78	1,304820214	0,56	0,67	0,24
Astrocytes	CST3	ENSG00000101439	0,764	1,135807461	0,528	0,74	0,31
Astrocytes	SNTA1	ENSG00000101400	0,735	0,995597284	0,47	0,53	0,09
Astrocytes	CPAMD8	ENSG00000160111	0,721	1,566456592	0,442	0,46	0,03
Astrocytes	NWD1	ENSG00000188039	0,72	1,06713276	0,44	0,46	0,03
Astrocytes	BBOX1	ENSG00000129151	0,718	1,000317873	0,436	0,45	0,02
Astrocytes	STON2	ENSG00000140022	0,745	1,086015197	0,49	0,58	0,15
Astrocytes	DCLK1	ENSG00000133083	0,742	1,350035078	0,484	0,64	0,21
Astrocytes	MT1E	ENSG00000169715	0,723	0,982330743	0,446	0,54	0,12
Astrocytes	ARHGAP42	ENSG00000165895	0,714	0,76752919	0,428	0,53	0,11
Astrocytes	COL21A1	ENSG00000124749	0,722	1,071171067	0,444	0,5	0,08

Astrocytes	LPIN1	ENSG00000134324	0,823	1,311436582	0,646	0,78	0,36
Astrocytes	TMTC1	ENSG00000133687	0,727	0,866859669	0,454	0,62	0,2
Astrocytes	LINC00836	ENSG00000280809	0,713	1,174086461	0,426	0,43	0,01
Astrocytes	WFS1	ENSG00000109501	0,721	0,94990066	0,442	0,49	0,07
Astrocytes	MT2A	ENSG00000125148	0,769	0,989867021	0,538	0,75	0,33
Astrocytes	PLSCR4	ENSG00000114698	0,716	0,829569238	0,432	0,52	0,1
Astrocytes	ALDH1A1	ENSG00000165092	0,711	1,258211464	0,422	0,44	0,02
Astrocytes	PARD3B	ENSG00000116117	0,848	1,193626253	0,696	0,9	0,48
Astrocytes	MAOB	ENSG00000069535	0,726	1,163723155	0,452	0,52	0,1
Astrocytes	RNF19A	ENSG00000034677	0,797	1,236547037	0,594	0,75	0,33
Astrocytes	PAPLN	ENSG00000100767	0,708	0,917979386	0,416	0,42	0,01
Astrocytes	PLEC	ENSG00000178209	0,737	0,974580581	0,474	0,59	0,18
Astrocytes	CHI3L1	ENSG00000133048	0,709	1,760233603	0,418	0,45	0,05
Astrocytes	PHKA1	ENSG00000067177	0,719	0,994921707	0,438	0,49	0,08
Astrocytes	ANTXR1	ENSG00000169604	0,73	1,01871846	0,46	0,58	0,17
Astrocytes	TCF7L2	ENSG00000148737	0,777	0,946496037	0,554	0,79	0,39
Astrocytes	AL160272.2	ENSG00000285082	0,706	0,947138596	0,412	0,44	0,03
Astrocytes	ASPH	ENSG00000198363	0,811	1,15399267	0,622	0,79	0,39
Astrocytes	NTNG1	ENSG00000162631	0,706	0,677878826	0,412	0,56	0,16
Astrocytes	SLC16A9	ENSG00000165449	0,711	0,925143369	0,422	0,45	0,05
Astrocytes	ANGPTL4	ENSG00000167772	0,709	1,444962314	0,418	0,46	0,05
Astrocytes	PFKP	ENSG00000067057	0,722	1,073705831	0,444	0,51	0,11
Astrocytes	NDRG2	ENSG00000165795	0,782	1,024134897	0,564	0,81	0,41
Astrocytes	KIAA1217	ENSG00000120549	0,713	0,932646694	0,426	0,61	0,21
Astrocytes	AC027117.2	ENSG00000253944	0,732	1,006873797	0,464	0,6	0,2
Astrocytes	TIMP3	ENSG00000100234	0,705	0,693264037	0,41	0,55	0,15
Astrocytes	MTSS2	ENSG00000132613	0,732	0,893040736	0,464	0,6	0,21
Astrocytes	GPR37L1	ENSG00000170075	0,719	0,894181677	0,438	0,56	0,16
Astrocytes	STK33	ENSG00000130413	0,732	0,9078295	0,464	0,62	0,23
Astrocytes	SHROOM3	ENSG00000138771	0,706	1,04113941	0,412	0,46	0,06
Astrocytes	OSBPL11	ENSG00000144909	0,729	0,965265465	0,458	0,58	0,19
Astrocytes	NFIB	ENSG00000147862	0,765	0,775927535	0,53	0,86	0,47
Astrocytes	DDR2	ENSG00000162733	0,704	1,032656004	0,408	0,46	0,07
Astrocytes	CTNND2	ENSG00000169862	0,925	1,441852914	0,85	0,99	0,6
Astrocytes	PRKD1	ENSG00000184304	0,739	0,778243668	0,478	0,75	0,36
Astrocytes	CACNB2	ENSG00000165995	0,718	1,09978946	0,436	0,63	0,25
Astrocytes	PALLD	ENSG00000129116	0,72	0,943827207	0,44	0,57	0,19
Astrocytes	LINC00511	ENSG00000227036	0,711	0,880967681	0,422	0,61	0,23
Astrocytes	GAN	ENSG00000261609	0,744	0,980005702	0,488	0,64	0,26
Astrocytes	ZBTB7C	ENSG00000184828	0,701	0,895863201	0,402	0,48	0,11
Astrocytes	LRP1	ENSG00000123384	0,714	0,734618291	0,428	0,62	0,25
Astrocytes	MICALL2	ENSG00000164877	0,703	0,874796087	0,406	0,48	0,11
Astrocytes	TTYH1	ENSG00000167614	0,761	0,953454281	0,522	0,74	0,37
Astrocytes	ST8SIA1	ENSG00000111728	0,714	0,893384984	0,428	0,59	0,22
Astrocytes	SAMD4A	ENSG00000020577	0,804	1,302964445	0,608	0,83	0,46
Astrocytes	SPARC	ENSG00000113140	0,731	1,008286559	0,462	0,68	0,32
Astrocytes	ANKDD1A	ENSG00000166839	0,705	0,898681644	0,41	0,5	0,14
Astrocytes	RAMP1	ENSG00000132329	0,701	0,78207011	0,402	0,54	0,18
Astrocytes	FUT9	ENSG00000172461	0,813	1,017406787	0,626	0,88	0,51
Astrocytes	CTDSPL	ENSG00000144677	0,753	0,965801275	0,506	0,7	0,35
Astrocytes	NAV3	ENSG00000067798	0,782	0,773334059	0,564	0,93	0,57
Astrocytes	CNN3	ENSG00000117519	0,706	0,861572391	0,412	0,55	0,19
Astrocytes	ACSS1	ENSG00000154930	0,702	0,89607762	0,404	0,53	0,18
Astrocytes	GABBR1	ENSG00000204681	0,715	0,869592084	0,43	0,57	0,21
Astrocytes	PFKFB3	ENSG00000170525	0,735	0,868057364	0,47	0,67	0,32

Astrocytes	PDLIM5	ENSG00000163110	0,709	0,728049049	0,418	0,64	0,29
Astrocytes	DKK3	ENSG00000050165	0,708	0,833904869	0,416	0,56	0,22
Astrocytes	ACADVL	ENSG00000072778	0,722	0,933471045	0,444	0,6	0,26
Astrocytes	BCL2	ENSG00000171791	0,796	0,976107359	0,592	0,87	0,53
Astrocytes	EGLN3	ENSG00000129521	0,718	1,31622593	0,436	0,59	0,25
Astrocytes	ASTN2	ENSG00000148219	0,8	0,972645927	0,6	0,9	0,58
Astrocytes	ATP2B4	ENSG00000058668	0,726	0,771716959	0,452	0,72	0,4
Astrocytes	PALM	ENSG00000099864	0,703	0,834517498	0,406	0,56	0,25
Astrocytes	TEAD1	ENSG00000187079	0,745	0,826327977	0,49	0,76	0,45
Astrocytes	NAV2	ENSG00000166833	0,881	1,251127605	0,762	0,97	0,66
Astrocytes	PLXNB1	ENSG00000164050	0,706	0,816874155	0,412	0,63	0,33
Astrocytes	MAPK10	ENSG00000109339	0,892	1,225806367	0,784	0,96	0,66
Astrocytes	LIFR	ENSG00000113594	0,828	1,07515354	0,656	0,9	0,6
Astrocytes	SRGAP1	ENSG00000196935	0,735	0,64965647	0,47	0,8	0,5
Astrocytes	TRPS1	ENSG00000104447	0,87	1,203471496	0,74	0,94	0,64
Astrocytes	CDH20	ENSG00000101542	0,801	0,911911321	0,602	0,97	0,67
Astrocytes	ERBB4	ENSG00000178568	0,782	0,735505171	0,564	0,98	0,68
Astrocytes	APC2	ENSG00000115266	0,707	0,857403516	0,414	0,61	0,32
Astrocytes	MAML2	ENSG00000184384	0,752	0,721075865	0,504	0,91	0,62
Astrocytes	PDE4DIP	ENSG00000178104	0,897	1,308717416	0,794	0,96	0,67
Astrocytes	RHOBTB3	ENSG00000164292	0,723	0,833810741	0,446	0,7	0,42
Astrocytes	APC	ENSG00000134982	0,766	0,946905067	0,532	0,78	0,5
Astrocytes	MSI2	ENSG00000153944	0,927	1,365474652	0,854	0,98	0,7
Astrocytes	DTNA	ENSG00000134769	0,977	1,829188811	0,954	1	0,73
Astrocytes	FYN	ENSG00000010810	0,83	1,079625317	0,66	0,9	0,63
Astrocytes	BCKDHB	ENSG00000083123	0,738	0,840614427	0,476	0,76	0,5
Astrocytes	GLUD1	ENSG00000148672	0,711	0,826502511	0,422	0,66	0,4
Astrocytes	SLC39A11	ENSG00000133195	0,775	0,911307466	0,55	0,93	0,68
Astrocytes	ZHX3	ENSG00000174306	0,764	0,85024105	0,528	0,82	0,57
Astrocytes	REPS1	ENSG00000135597	0,703	0,741952139	0,406	0,66	0,41
Astrocytes	KIAA0930	ENSG00000100364	0,703	0,673826753	0,406	0,73	0,49
Astrocytes	CLEC16A	ENSG00000038532	0,753	0,913479465	0,506	0,79	0,55
Astrocytes	ARNT2	ENSG00000172379	0,709	0,713087418	0,418	0,74	0,5
Astrocytes	LSAMP	ENSG00000185565	0,928	1,397229682	0,856	1	0,77
Astrocytes	CKB	ENSG00000166165	0,715	0,785043969	0,43	0,76	0,54
Astrocytes	SASH1	ENSG00000111961	0,784	0,863777122	0,568	0,92	0,7
Astrocytes	TRAK1	ENSG00000182606	0,706	0,73562172	0,412	0,71	0,48
Astrocytes	LRP1B	ENSG00000168702	0,818	0,848525891	0,636	0,99	0,77
Astrocytes	PRKCA	ENSG00000154229	0,816	0,922006164	0,632	0,95	0,74
Astrocytes	REV3L	ENSG00000009413	0,73	0,77201734	0,46	0,81	0,62
Astrocytes	NPAS3	ENSG00000151322	0,845	0,874976655	0,69	0,99	0,82
Astrocytes	MIR99AHG	ENSG00000215386	0,892	1,156373342	0,784	0,98	0,8
Astrocytes	NFIA	ENSG00000162599	0,828	0,876962256	0,656	0,97	0,8
Astrocytes	TNRC6A	ENSG00000090905	0,856	0,978881535	0,712	0,97	0,82
Astrocytes	SSBP2	ENSG00000145687	0,737	0,707813636	0,474	0,88	0,74
Astrocytes	AC245297.3	ENSG00000274265	0,702	0,698096865	0,404	0,8	0,66
Astrocytes	NEAT1	ENSG00000245532	0,806	1,070522977	0,612	1	0,87
Astrocytes	MKLN1	ENSG00000128585	0,838	0,858508804	0,676	0,96	0,87
Astrocytes	MACF1	ENSG00000127603	0,91	1,048599585	0,82	0,99	0,9
Endothelial cells	CLDN5	ENSG00000184113	0,987	3,171582047	0,974	0,98	0,04
Endothelial cells	FLT1	ENSG00000102755	0,99	3,542137792	0,98	0,99	0,06
Endothelial cells	ATP10A	ENSG00000206190	0,979	3,213763802	0,958	0,97	0,04
Endothelial cells	ABCB1	ENSG00000085563	0,983	3,329673439	0,966	0,97	0,05
Endothelial cells	VWF	ENSG00000110799	0,983	3,088698552	0,966	0,97	0,05
Endothelial cells	EPAS1	ENSG00000116016	0,979	2,717071709	0,958	0,98	0,07

Endothelial cells	ERG	ENSG00000157554	0,954	2,367403183	0,908	0,92	0,02
Endothelial cells	ANO2	ENSG00000047617	0,958	2,909174449	0,916	0,93	0,05
Endothelial cells	COBLL1	ENSG00000082438	0,951	2,511059011	0,902	0,93	0,06
Endothelial cells	ADGRL4	ENSG00000162618	0,936	2,181629371	0,872	0,88	0,02
Endothelial cells	PODXL	ENSG00000128567	0,948	2,198738402	0,896	0,91	0,05
Endothelial cells	EGFL7	ENSG00000172889	0,944	2,16155874	0,888	0,9	0,05
Endothelial cells	HLA-E	ENSG00000204592	0,964	2,301178019	0,928	0,96	0,11
Endothelial cells	IFITM3	ENSG00000142089	0,94	2,198961462	0,88	0,92	0,08
Endothelial cells	FLI1	ENSG00000151702	0,935	2,078844055	0,87	0,92	0,1
Endothelial cells	TGM2	ENSG00000198959	0,916	2,094136474	0,832	0,84	0,02
Endothelial cells	PECAM1	ENSG00000261371	0,934	2,043588868	0,868	0,89	0,07
Endothelial cells	MECOM	ENSG00000085276	0,964	2,804102615	0,928	0,95	0,13
Endothelial cells	PTPRB	ENSG00000127329	0,941	2,344455769	0,882	0,9	0,09
Endothelial cells	IFI27	ENSG00000165949	0,913	2,344182971	0,826	0,84	0,04
Endothelial cells	BTNL9	ENSG00000165810	0,907	2,033572357	0,814	0,82	0,02
Endothelial cells	SYNE2	ENSG00000054654	0,936	1,974373788	0,872	0,91	0,12
Endothelial cells	ADGRF5	ENSG00000069122	0,899	1,880431431	0,798	0,81	0,03
Endothelial cells	ARHGAP29	ENSG00000137962	0,928	1,998917035	0,856	0,9	0,11
Endothelial cells	ABCG2	ENSG00000118777	0,899	2,187659149	0,798	0,81	0,02
Endothelial cells	THSD4	ENSG00000187720	0,935	2,883039223	0,87	0,9	0,11
Endothelial cells	PRKCH	ENSG00000027075	0,928	2,047408372	0,856	0,9	0,12
Endothelial cells	A2M	ENSG00000175899	0,921	1,947483353	0,842	0,9	0,12
Endothelial cells	TMSB10	ENSG00000034510	0,965	2,667374806	0,93	0,96	0,19
Endothelial cells	ITGA1	ENSG00000213949	0,901	1,944969911	0,802	0,83	0,06
Endothelial cells	SLC7A5	ENSG00000103257	0,937	2,470558572	0,874	0,91	0,14
Endothelial cells	SLCO4A1	ENSG00000101187	0,892	1,933027003	0,784	0,8	0,03
Endothelial cells	ENG	ENSG00000106991	0,896	1,873483692	0,792	0,82	0,06
Endothelial cells	IGFBP7	ENSG00000163453	0,899	1,765797173	0,798	0,88	0,12
Endothelial cells	CMTM8	ENSG00000170293	0,88	2,006984157	0,76	0,77	0,03
Endothelial cells	CGNL1	ENSG00000128849	0,891	1,817559967	0,782	0,83	0,09
Endothelial cells	CD34	ENSG00000174059	0,871	1,797393396	0,742	0,75	0,01
Endothelial cells	ST8SIA6	ENSG00000148488	0,884	1,977330008	0,768	0,79	0,06
Endothelial cells	SLC2A1	ENSG00000117394	0,915	2,027083075	0,83	0,87	0,14
Endothelial cells	TAGLN2	ENSG00000158710	0,879	1,696329337	0,758	0,79	0,07
Endothelial cells	TBC1D4	ENSG00000136111	0,93	2,123052116	0,86	0,91	0,18
Endothelial cells	HLA-B	ENSG00000234745	0,898	1,809352509	0,796	0,86	0,14
Endothelial cells	ITM2A	ENSG00000078596	0,872	1,893568732	0,744	0,77	0,05
Endothelial cells	IFITM2	ENSG00000185201	0,864	1,627786756	0,728	0,76	0,04
Endothelial cells	SPARCL1	ENSG00000152583	0,927	1,763342735	0,854	0,97	0,25
Endothelial cells	ITGA6	ENSG00000091409	0,89	1,983521311	0,78	0,82	0,11
Endothelial cells	GALNT18	ENSG00000110328	0,945	2,376696322	0,89	0,94	0,23
Endothelial cells	RNF144B	ENSG00000137393	0,872	1,960926789	0,744	0,79	0,08
Endothelial cells	PAPSS2	ENSG00000198682	0,859	1,743648911	0,718	0,74	0,03
Endothelial cells	ID1	ENSG00000125968	0,859	1,963298288	0,718	0,74	0,03
Endothelial cells	IL4R	ENSG00000077238	0,864	1,676472827	0,728	0,77	0,07
Endothelial cells	EMP2	ENSG00000213853	0,863	1,585936347	0,726	0,76	0,06
Endothelial cells	NXN	ENSG00000167693	0,896	1,851863793	0,792	0,84	0,15
Endothelial cells	SLC9A3R2	ENSG00000065054	0,861	1,694958562	0,722	0,75	0,05
Endothelial cells	LEF1	ENSG00000138795	0,861	1,792360534	0,722	0,76	0,07
Endothelial cells	VIM	ENSG00000026025	0,857	1,555039173	0,714	0,77	0,08
Endothelial cells	IRAK3	ENSG00000090376	0,852	1,44090473	0,704	0,79	0,1
Endothelial cells	NOSTRIN	ENSG00000163072	0,847	1,624011616	0,694	0,71	0,02
Endothelial cells	NEDD9	ENSG00000111859	0,864	1,685217132	0,728	0,77	0,09
Endothelial cells	SRGN	ENSG00000122862	0,845	1,403444168	0,69	0,76	0,08
Endothelial cells	CRIM1	ENSG00000150938	0,928	2,381640445	0,856	0,91	0,23

Endothelial cells	ICAM2	ENSG00000108622	0,841	1,528116736	0,682	0,69	0,02
Endothelial cells	LIMS2	ENSG00000072163	0,844	1,480284712	0,688	0,7	0,03
Endothelial cells	SORBS2	ENSG00000154556	0,904	1,98549362	0,808	0,89	0,22
Endothelial cells	CDYL2	ENSG00000166446	0,871	1,755625482	0,742	0,78	0,11
Endothelial cells	TM4SF1	ENSG00000169908	0,838	1,582744048	0,676	0,69	0,02
Endothelial cells	ID3	ENSG00000117318	0,841	1,65584821	0,682	0,72	0,05
Endothelial cells	SLCO2B1	ENSG00000137491	0,827	1,147634641	0,654	0,77	0,11
Endothelial cells	TIE1	ENSG00000066056	0,833	1,454577999	0,666	0,68	0,02
Endothelial cells	PTPRG	ENSG00000144724	0,948	2,257232525	0,896	0,97	0,31
Endothelial cells	STOM	ENSG00000148175	0,875	1,520990488	0,75	0,83	0,17
Endothelial cells	PALMD	ENSG00000099260	0,836	1,679680134	0,672	0,69	0,03
Endothelial cells	CPNE8	ENSG00000139117	0,865	1,656543818	0,73	0,79	0,14
Endothelial cells	FAM107A	ENSG00000168309	0,857	1,560756937	0,714	0,79	0,13
Endothelial cells	TGFBR2	ENSG00000163513	0,836	1,37025601	0,672	0,77	0,11
Endothelial cells	ETS2	ENSG00000157557	0,849	1,629742196	0,698	0,76	0,11
Endothelial cells	CADPS2	ENSG00000081803	0,872	1,643784171	0,744	0,84	0,19
Endothelial cells	OSMR	ENSG00000145623	0,839	1,504222109	0,678	0,72	0,08
Endothelial cells	RGS5	ENSG00000143248	0,84	1,656157275	0,68	0,74	0,1
Endothelial cells	HLA-C	ENSG00000204525	0,862	1,627774362	0,724	0,79	0,15
Endothelial cells	ELOVL7	ENSG00000164181	0,971	2,49835492	0,942	0,97	0,33
Endothelial cells	SLC1A1	ENSG00000106688	0,858	1,728428935	0,716	0,77	0,13
Endothelial cells	JCAD	ENSG00000165757	0,826	1,40853077	0,652	0,67	0,03
Endothelial cells	WWTR1	ENSG00000018408	0,883	1,723457092	0,766	0,85	0,21
Endothelial cells	XAF1	ENSG00000132530	0,829	1,398008273	0,658	0,71	0,07
Endothelial cells	SLC7A1	ENSG00000139514	0,877	2,06497787	0,754	0,8	0,17
Endothelial cells	S100A10	ENSG00000197747	0,826	1,577376079	0,652	0,68	0,04
Endothelial cells	UTRN	ENSG00000152818	0,883	1,40802982	0,766	0,93	0,3
Endothelial cells	CRIP2	ENSG00000182809	0,843	1,444447494	0,686	0,74	0,11
Endothelial cells	CYYR1	ENSG00000166265	0,82	1,621069684	0,64	0,65	0,02
Endothelial cells	RBMS2	ENSG00000076067	0,848	1,389983319	0,696	0,76	0,13
Endothelial cells	ANXA3	ENSG00000138772	0,818	1,550601685	0,636	0,65	0,02
Endothelial cells	PLXNA2	ENSG00000076356	0,862	1,680392639	0,724	0,8	0,18
Endothelial cells	SGPP2	ENSG00000163082	0,839	1,665615316	0,678	0,72	0,09
Endothelial cells	EMCN	ENSG00000164035	0,815	1,65702389	0,63	0,64	0,02
Endothelial cells	SRARP	ENSG00000183888	0,81	1,375284899	0,62	0,63	0,01
Endothelial cells	CEMIP2	ENSG00000135048	0,841	1,616012461	0,682	0,75	0,13
Endothelial cells	MRTFB	ENSG00000186260	0,931	2,084390837	0,862	0,92	0,31
Endothelial cells	LRRC32	ENSG00000137507	0,806	1,44808985	0,612	0,63	0,02
Endothelial cells	ADAMTS9	ENSG00000163638	0,814	2,145084682	0,628	0,68	0,08
Endothelial cells	ESAM	ENSG00000149564	0,805	1,29613925	0,61	0,63	0,02
Endothelial cells	NAMPT	ENSG00000105835	0,849	1,675427787	0,698	0,77	0,17
Endothelial cells	BSG	ENSG00000172270	0,948	2,497179755	0,896	0,96	0,36
Endothelial cells	ITIH5	ENSG00000123243	0,799	1,430999738	0,598	0,65	0,06
Endothelial cells	PARP14	ENSG00000173193	0,81	1,301828504	0,62	0,7	0,11
Endothelial cells	APOLD1	ENSG00000178878	0,846	1,369004914	0,692	0,82	0,23
Endothelial cells	CAVIN2	ENSG00000168497	0,794	1,443722658	0,588	0,6	0,02
Endothelial cells	EBF1	ENSG00000164330	0,798	1,187433123	0,596	0,71	0,13
Endothelial cells	RPGR	ENSG00000156313	0,843	1,522940217	0,686	0,76	0,18
Endothelial cells	MYRIP	ENSG00000170011	0,881	2,015033567	0,762	0,85	0,27
Endothelial cells	AHNAK	ENSG00000124942	0,801	1,115003822	0,602	0,69	0,11
Endothelial cells	ZNF366	ENSG00000178175	0,791	1,613239201	0,582	0,59	0,02
Endothelial cells	BST2	ENSG00000130303	0,792	1,29691963	0,584	0,62	0,04
Endothelial cells	GIMAP7	ENSG00000179144	0,789	1,300356638	0,578	0,59	0,02
Endothelial cells	ADGRL2	ENSG00000117114	0,801	1,32318412	0,602	0,71	0,13
Endothelial cells	PTPN14	ENSG00000152104	0,802	1,249873302	0,604	0,68	0,11

Endothelial cells	ARHGAP31	ENSG00000031081	0,814	1,198763534	0,628	0,78	0,21
Endothelial cells	ACSL5	ENSG00000197142	0,787	1,230690803	0,574	0,59	0,02
Endothelial cells	GNG11	ENSG00000127920	0,784	1,254502536	0,568	0,59	0,03
Endothelial cells	HLA-A	ENSG00000206503	0,843	1,513684904	0,686	0,78	0,22
Endothelial cells	MT2A	ENSG00000125148	0,899	2,171978902	0,798	0,91	0,35
Endothelial cells	GGT5	ENSG00000099998	0,78	1,083395128	0,56	0,61	0,05
Endothelial cells	FN1	ENSG00000115414	0,798	1,409446836	0,596	0,66	0,1
Endothelial cells	ACER2	ENSG00000177076	0,797	1,551197214	0,594	0,63	0,07
Endothelial cells	YBX3	ENSG00000060138	0,792	1,302118874	0,584	0,65	0,09
Endothelial cells	RUNDC3B	ENSG00000105784	0,807	1,411601913	0,614	0,7	0,14
Endothelial cells	CFH	ENSG00000000971	0,781	1,734162634	0,562	0,58	0,03
Endothelial cells	ANGPT2	ENSG00000091879	0,798	2,684612869	0,596	0,63	0,08
Endothelial cells	ST6GAL1	ENSG00000073849	0,789	0,933453895	0,578	0,78	0,22
Endothelial cells	EPB41L4A	ENSG00000129595	0,834	1,46175371	0,668	0,77	0,21
Endothelial cells	SP100	ENSG00000067066	0,782	1,093029658	0,564	0,68	0,13
Endothelial cells	TIMP3	ENSG00000100234	0,804	1,301225372	0,608	0,72	0,17
Endothelial cells	LY6E	ENSG00000160932	0,789	1,310077682	0,578	0,61	0,06
Endothelial cells	PAM	ENSG00000145730	0,825	1,271382607	0,65	0,82	0,26
Endothelial cells	ACVRL1	ENSG00000139567	0,777	1,130664335	0,554	0,56	0,01
Endothelial cells	SMAD6	ENSG00000137834	0,781	1,623825405	0,562	0,59	0,04
Endothelial cells	NOTCH4	ENSG00000204301	0,775	1,142628776	0,55	0,56	0,01
Endothelial cells	ETS1	ENSG00000134954	0,784	1,209650115	0,568	0,63	0,08
Endothelial cells	PARVB	ENSG00000188677	0,816	1,357638402	0,632	0,71	0,16
Endothelial cells	GALNT15	ENSG00000131386	0,855	1,438197361	0,71	0,84	0,3
Endothelial cells	CDH5	ENSG00000179776	0,773	1,114642302	0,546	0,55	0,01
Endothelial cells	B2M	ENSG00000166710	0,922	1,896244497	0,844	0,94	0,39
Endothelial cells	DIPK2B	ENSG00000147113	0,805	1,321213124	0,61	0,7	0,16
Endothelial cells	LGALS3	ENSG00000131981	0,776	1,215933392	0,552	0,58	0,03
Endothelial cells	MYOF	ENSG00000138119	0,781	1,256870279	0,562	0,64	0,1
Endothelial cells	ROBO4	ENSG00000154133	0,772	1,14052962	0,544	0,55	0,01
Endothelial cells	NFKBIA	ENSG00000100906	0,818	1,442210431	0,636	0,73	0,19
Endothelial cells	MFSD2A	ENSG00000168389	0,776	1,375516769	0,552	0,57	0,03
Endothelial cells	C22orf34	ENSG00000188511	0,776	1,304894161	0,552	0,6	0,06
Endothelial cells	HIF1A-AS3	ENSG00000258667	0,786	1,88547011	0,572	0,63	0,1
Endothelial cells	SLC16A1	ENSG00000155380	0,797	1,782931914	0,594	0,65	0,12
Endothelial cells	DOCK6	ENSG00000130158	0,776	1,147627709	0,552	0,6	0,07
Endothelial cells	PDE10A	ENSG00000112541	0,824	1,430451043	0,648	0,78	0,25
Endothelial cells	INPP5D	ENSG00000168918	0,755	0,744362704	0,51	0,65	0,12
Endothelial cells	SLC2A3	ENSG00000059804	0,79	1,574128932	0,58	0,66	0,13
Endothelial cells	TEK	ENSG00000120156	0,776	1,269242851	0,552	0,59	0,06
Endothelial cells	PPFIBP1	ENSG00000110841	0,92	1,786420814	0,84	0,93	0,4
Endothelial cells	SPOCK2	ENSG00000107742	0,812	1,314115549	0,624	0,73	0,2
Endothelial cells	TFRC	ENSG00000072274	0,795	1,441857488	0,59	0,66	0,13
Endothelial cells	FGD5	ENSG00000154783	0,766	1,094428866	0,532	0,55	0,02
Endothelial cells	DEPP1	ENSG00000165507	0,769	1,617427409	0,538	0,56	0,04
Endothelial cells	SLC39A10	ENSG00000196950	0,86	1,815087034	0,72	0,82	0,3
Endothelial cells	PLSCR1	ENSG00000188313	0,783	1,173834047	0,566	0,65	0,13
Endothelial cells	SEC14L1	ENSG00000129657	0,916	1,74706784	0,832	0,91	0,39
Endothelial cells	CHSY1	ENSG00000131873	0,834	1,465939962	0,668	0,79	0,27
Endothelial cells	HERPUD1	ENSG00000051108	0,819	1,390055661	0,638	0,74	0,22
Endothelial cells	CCDC85A	ENSG00000055813	0,785	1,490280014	0,57	0,66	0,14
Endothelial cells	PLSCR4	ENSG00000114698	0,778	1,207749016	0,556	0,65	0,13
Endothelial cells	EPHA4	ENSG00000116106	0,778	1,314423309	0,556	0,62	0,1
Endothelial cells	HYAL2	ENSG00000068001	0,765	1,188813578	0,53	0,55	0,03
Endothelial cells	CP	ENSG00000047457	0,775	1,95218664	0,55	0,6	0,08

Endothelial cells	MEF2C	ENSG00000081189	0,768	0,734464007	0,536	0,75	0,23
Endothelial cells	KANK3	ENSG00000186994	0,762	1,029622962	0,524	0,55	0,04
Endothelial cells	ESYT2	ENSG00000117868	0,923	1,806800913	0,846	0,93	0,41
Endothelial cells	ZEB1	ENSG00000148516	0,8	0,993972298	0,6	0,85	0,33
Endothelial cells	TPM1	ENSG00000140416	0,807	1,187144168	0,614	0,73	0,22
Endothelial cells	DUSP1	ENSG00000120129	0,772	1,255170713	0,544	0,62	0,12
Endothelial cells	TMEM123	ENSG00000152558	0,828	1,330151745	0,656	0,78	0,28
Endothelial cells	SAT1	ENSG00000130066	0,794	1,403456665	0,588	0,73	0,22
Endothelial cells	GRASP	ENSG00000161835	0,755	1,104817955	0,51	0,52	0,02
Endothelial cells	LMO2	ENSG00000135363	0,76	1,060242851	0,52	0,57	0,06
Endothelial cells	RHOC	ENSG00000155366	0,76	1,065944787	0,52	0,57	0,06
Endothelial cells	LHFPL6	ENSG00000183722	0,832	1,352608752	0,664	0,87	0,37
Endothelial cells	SVIL	ENSG00000197321	0,78	1,326495258	0,56	0,63	0,13
Endothelial cells	TPST2	ENSG00000128294	0,766	1,185154447	0,532	0,58	0,07
Endothelial cells	FOSL2	ENSG00000075426	0,757	1,147011312	0,514	0,55	0,04
Endothelial cells	RBMS3	ENSG00000144642	0,778	1,222939575	0,556	0,67	0,17
Endothelial cells	RELL1	ENSG00000181826	0,792	1,254123642	0,584	0,68	0,18
Endothelial cells	ABLIM1	ENSG00000099204	0,79	1,036041003	0,58	0,79	0,29
Endothelial cells	MYH9	ENSG00000100345	0,82	1,192065106	0,64	0,78	0,27
Endothelial cells	RAMP2	ENSG00000131477	0,753	1,16912527	0,506	0,52	0,02
Endothelial cells	SCARB1	ENSG00000073060	0,819	1,47602711	0,638	0,75	0,26
Endothelial cells	MCC	ENSG00000171444	0,789	1,462361878	0,578	0,71	0,21
Endothelial cells	MYO10	ENSG00000145555	0,795	1,2858151	0,59	0,71	0,21
Endothelial cells	PLEKHG1	ENSG00000120278	0,866	1,500788953	0,732	0,88	0,39
Endothelial cells	ANXA2	ENSG00000182718	0,752	1,073928002	0,504	0,55	0,05
Endothelial cells	HEG1	ENSG00000173706	0,814	1,321423719	0,628	0,76	0,27
Endothelial cells	EDN1	ENSG00000078401	0,749	1,863044192	0,498	0,51	0,02
Endothelial cells	SPARC	ENSG00000113140	0,82	1,100299861	0,64	0,83	0,34
Endothelial cells	NEBL	ENSG00000078114	0,751	0,718886283	0,502	0,84	0,35
Endothelial cells	DGKH	ENSG00000102780	0,782	1,186743198	0,564	0,67	0,18
Endothelial cells	SULF2	ENSG00000196562	0,758	1,036946762	0,516	0,61	0,12
Endothelial cells	SLC19A3	ENSG00000135917	0,751	1,101623798	0,502	0,52	0,04
Endothelial cells	NPAS2	ENSG00000170485	0,776	1,215182186	0,552	0,71	0,22
Endothelial cells	RBPMS	ENSG00000157110	0,747	1,005722863	0,494	0,6	0,11
Endothelial cells	PCAT19	ENSG00000267107	0,745	1,109286918	0,49	0,5	0,01
Endothelial cells	SLC39A8	ENSG00000138821	0,752	1,113142012	0,504	0,54	0,05
Endothelial cells	UACA	ENSG00000137831	0,809	1,172979811	0,618	0,77	0,29
Endothelial cells	SLC38A5	ENSG00000017483	0,742	1,18392068	0,484	0,49	0,01
Endothelial cells	LRCH1	ENSG00000136141	0,798	1,143699279	0,596	0,76	0,29
Endothelial cells	KCTD12	ENSG00000178695	0,747	1,03993489	0,494	0,58	0,1
Endothelial cells	SDCBP	ENSG00000137575	0,778	1,089972957	0,556	0,67	0,19
Endothelial cells	CAVIN1	ENSG00000177469	0,758	1,043061864	0,516	0,59	0,12
Endothelial cells	KLF2	ENSG00000127528	0,739	1,190432358	0,478	0,5	0,02
Endothelial cells	SLC30A1	ENSG00000170385	0,745	1,018520658	0,49	0,53	0,06
Endothelial cells	ACVR1	ENSG00000115170	0,788	1,334634449	0,576	0,68	0,21
Endothelial cells	TSPAN14	ENSG00000108219	0,772	0,997117525	0,544	0,68	0,21
Endothelial cells	CEP112	ENSG00000154240	0,773	1,035524235	0,546	0,73	0,26
Endothelial cells	RASIP1	ENSG00000105538	0,739	0,988883238	0,478	0,49	0,02
Endothelial cells	SORBS1	ENSG00000095637	0,795	0,793634869	0,59	0,87	0,4
Endothelial cells	PON2	ENSG00000105854	0,858	1,416025579	0,716	0,86	0,39
Endothelial cells	FOXC1	ENSG00000054598	0,736	0,979725068	0,472	0,49	0,02
Endothelial cells	TM4SF18	ENSG00000163762	0,736	1,091154179	0,472	0,48	0,01
Endothelial cells	MAP3K20	ENSG00000091436	0,753	1,032501066	0,506	0,61	0,15
Endothelial cells	SNED1	ENSG00000162804	0,753	1,122366342	0,506	0,62	0,15
Endothelial cells	S1PR1	ENSG00000170989	0,732	0,980010552	0,464	0,49	0,03

Endothelial cells	CEBPD	ENSG00000221869	0,741	1,053979699	0,482	0,6	0,14
Endothelial cells	PTPRM	ENSG00000173482	0,914	1,88520418	0,828	0,94	0,48
Endothelial cells	MT1E	ENSG00000169715	0,743	1,244729372	0,486	0,6	0,14
Endothelial cells	ARL15	ENSG00000185305	0,881	1,887434772	0,762	0,9	0,45
Endothelial cells	GPCPD1	ENSG00000125772	0,76	1,222133542	0,52	0,64	0,19
Endothelial cells	S100A11	ENSG00000163191	0,729	0,962078544	0,458	0,51	0,06
Endothelial cells	CFLAR	ENSG00000003402	0,853	1,314734464	0,706	0,85	0,39
Endothelial cells	VAMP5	ENSG00000168899	0,73	1,046431419	0,46	0,49	0,05
Endothelial cells	EPSTI1	ENSG00000133106	0,728	1,11718168	0,456	0,51	0,06
Endothelial cells	PDXK	ENSG00000160209	0,795	1,233750605	0,59	0,73	0,28
Endothelial cells	PTTG1IP	ENSG00000183255	0,794	1,065214304	0,588	0,74	0,29
Endothelial cells	RBMS1	ENSG00000153250	0,773	1,026878708	0,546	0,73	0,28
Endothelial cells	MYL12B	ENSG00000118680	0,758	1,111476083	0,516	0,61	0,16
Endothelial cells	EGFR	ENSG00000146648	0,734	0,970563932	0,468	0,63	0,18
Endothelial cells	NET1	ENSG00000173848	0,733	1,207283768	0,466	0,5	0,06
Endothelial cells	USP6NL	ENSG00000148429	0,777	1,040931516	0,554	0,72	0,27
Endothelial cells	TMEM132C	ENSG00000181234	0,754	1,176706078	0,508	0,69	0,24
Endothelial cells	UNC13B	ENSG00000198722	0,79	1,264605051	0,58	0,71	0,26
Endothelial cells	TMEM204	ENSG00000131634	0,723	0,938082652	0,446	0,46	0,02
Endothelial cells	MGLL	ENSG00000074416	0,748	0,952755492	0,496	0,65	0,2
Endothelial cells	PLAT	ENSG00000104368	0,727	1,197332667	0,454	0,48	0,04
Endothelial cells	TSPAN9	ENSG00000011105	0,735	0,979724814	0,47	0,53	0,09
Endothelial cells	THSD7A	ENSG00000005108	0,772	1,401447077	0,544	0,71	0,27
Endothelial cells	GBP4	ENSG00000162654	0,719	1,406470974	0,438	0,45	0,02
Endothelial cells	DAB2IP	ENSG00000136848	0,744	1,038861882	0,488	0,59	0,15
Endothelial cells	MSRB3	ENSG00000174099	0,739	1,060483706	0,478	0,57	0,14
Endothelial cells	LSR	ENSG00000105699	0,719	0,906778035	0,438	0,45	0,01
Endothelial cells	RAPGEF4	ENSG00000091428	0,773	1,04745858	0,546	0,76	0,33
Endothelial cells	GPR85	ENSG00000164604	0,725	1,242988213	0,45	0,48	0,05
Endothelial cells	BMPR2	ENSG00000204217	0,893	1,468382511	0,786	0,93	0,5
Endothelial cells	SLC52A3	ENSG00000101276	0,714	0,937419278	0,428	0,43	0,01
Endothelial cells	TMOD3	ENSG00000138594	0,76	0,992262291	0,52	0,66	0,23
Endothelial cells	CLIC1	ENSG00000213719	0,715	0,861014506	0,43	0,46	0,04
Endothelial cells	YES1	ENSG00000176105	0,733	0,988364306	0,466	0,55	0,13
Endothelial cells	BMP6	ENSG00000153162	0,717	1,712003479	0,434	0,45	0,03
Endothelial cells	CST3	ENSG00000101439	0,739	0,733381076	0,478	0,76	0,34
Endothelial cells	LEPR	ENSG00000116678	0,744	1,036343476	0,488	0,61	0,19
Endothelial cells	ADIRF	ENSG00000148671	0,713	1,040423974	0,426	0,47	0,05
Endothelial cells	ITPR3	ENSG00000096433	0,712	0,899599528	0,424	0,43	0,01
Endothelial cells	WWC2	ENSG00000151718	0,808	1,268318988	0,616	0,78	0,36
Endothelial cells	RIMKLB	ENSG00000166532	0,755	1,378807418	0,51	0,63	0,22
Endothelial cells	JAM2	ENSG00000154721	0,723	1,03242282	0,446	0,53	0,11
Endothelial cells	TINAGL1	ENSG00000142910	0,71	0,832104169	0,42	0,43	0,02
Endothelial cells	AKAP12	ENSG00000131016	0,737	1,245145476	0,474	0,59	0,17
Endothelial cells	TCN2	ENSG00000185339	0,715	0,893561419	0,43	0,46	0,04
Endothelial cells	CNOT8	ENSG00000155508	0,736	0,94623393	0,472	0,56	0,14
Endothelial cells	CNTNAP3B	ENSG00000154529	0,735	1,121518738	0,47	0,6	0,18
Endothelial cells	TUBB6	ENSG00000176014	0,711	0,874988158	0,422	0,45	0,03
Endothelial cells	MT1M	ENSG00000205364	0,716	1,114499293	0,432	0,5	0,09
Endothelial cells	SLC3A2	ENSG00000168003	0,744	1,073482563	0,488	0,61	0,19
Endothelial cells	RHOJ	ENSG00000126785	0,71	0,947956171	0,42	0,48	0,06
Endothelial cells	NES	ENSG00000132688	0,713	0,896465609	0,426	0,47	0,05
Endothelial cells	MYL12A	ENSG00000101608	0,716	0,927899779	0,432	0,48	0,07
Endothelial cells	SHE	ENSG00000169291	0,708	0,869740079	0,416	0,42	0,01
Endothelial cells	CCDC85B	ENSG00000175602	0,735	0,952874695	0,47	0,57	0,16

Endothelial cells	LAMA5	ENSG00000130702	0,715	0,888763895	0,43	0,47	0,06
Endothelial cells	IFI16	ENSG00000163565	0,722	0,863341009	0,444	0,61	0,2
Endothelial cells	RAPGEF1	ENSG00000107263	0,795	1,07248656	0,59	0,8	0,39
Endothelial cells	LMBR1	ENSG00000105983	0,823	1,172838978	0,646	0,81	0,4
Endothelial cells	VSIR	ENSG00000107738	0,723	0,912399711	0,446	0,58	0,17
Endothelial cells	PXN	ENSG00000089159	0,728	0,948851235	0,456	0,56	0,15
Endothelial cells	LAMA3	ENSG00000053747	0,712	1,149026295	0,424	0,46	0,05
Endothelial cells	AP3S1	ENSG00000177879	0,777	1,154367591	0,554	0,7	0,29
Endothelial cells	HMCN1	ENSG00000143341	0,707	1,208872993	0,414	0,44	0,03
Endothelial cells	KLF6	ENSG00000067082	0,729	0,93016606	0,458	0,58	0,18
Endothelial cells	PRSS23	ENSG00000150687	0,714	1,150193819	0,428	0,47	0,07
Endothelial cells	TSC22D1	ENSG00000102804	0,889	1,604183134	0,778	0,92	0,52
Endothelial cells	TPT1	ENSG00000133112	0,802	1,155021151	0,604	0,8	0,4
Endothelial cells	ARHGAP26	ENSG00000145819	0,772	0,808599201	0,544	0,87	0,47
Endothelial cells	WARS	ENSG00000140105	0,731	1,324949149	0,462	0,55	0,15
Endothelial cells	PTMS	ENSG00000159335	0,714	0,876511071	0,428	0,51	0,11
Endothelial cells	MSN	ENSG00000147065	0,724	0,860749317	0,448	0,6	0,2
Endothelial cells	CTNNB1	ENSG00000168036	0,812	1,143357328	0,624	0,81	0,41
Endothelial cells	CLEC14A	ENSG00000176435	0,701	0,863731333	0,402	0,42	0,03
Endothelial cells	PERP	ENSG00000112378	0,701	0,871121511	0,402	0,42	0,03
Endothelial cells	TMEM87B	ENSG00000153214	0,73	0,978430179	0,46	0,58	0,18
Endothelial cells	NEDD4	ENSG00000069869	0,727	0,980577398	0,454	0,58	0,2
Endothelial cells	PRICKLE2	ENSG00000163637	0,752	1,231382622	0,504	0,69	0,3
Endothelial cells	MCTP1	ENSG00000175471	0,719	1,396973486	0,438	0,55	0,16
Endothelial cells	CNOT6L	ENSG00000138767	0,792	1,152849901	0,584	0,76	0,37
Endothelial cells	PDZRN3	ENSG00000121440	0,716	1,31270756	0,432	0,56	0,18
Endothelial cells	GNAI2	ENSG00000114353	0,798	1,055105003	0,596	0,79	0,41
Endothelial cells	OCLN	ENSG00000197822	0,712	0,903917689	0,424	0,5	0,12
Endothelial cells	NFIB	ENSG00000147862	0,803	1,120520597	0,606	0,89	0,5
Endothelial cells	SYNE1	ENSG00000131018	0,88	1,546591985	0,76	0,94	0,55
Endothelial cells	SHANK3	ENSG00000251322	0,741	0,932569103	0,482	0,63	0,25
Endothelial cells	TDRP	ENSG00000180190	0,713	0,957461617	0,426	0,51	0,13
Endothelial cells	EEF1A1	ENSG00000156508	0,82	1,195585662	0,64	0,84	0,47
Endothelial cells	KLHL5	ENSG00000109790	0,754	0,972863887	0,508	0,71	0,34
Endothelial cells	CCDC50	ENSG00000152492	0,747	0,887058268	0,494	0,69	0,32
Endothelial cells	SWAP70	ENSG00000133789	0,715	0,829114397	0,43	0,58	0,21
Endothelial cells	TMSB4X	ENSG00000205542	0,822	1,137556506	0,644	0,87	0,5
Endothelial cells	ITGB1	ENSG00000150093	0,777	0,969729144	0,554	0,75	0,38
Endothelial cells	CD2AP	ENSG00000198087	0,731	0,926590839	0,462	0,61	0,24
Endothelial cells	ACTN1	ENSG00000072110	0,707	0,936093007	0,414	0,51	0,14
Endothelial cells	PRKD3	ENSG00000115825	0,701	0,804435549	0,402	0,54	0,17
Endothelial cells	GFAP	ENSG00000131095	0,703	0,636374964	0,406	0,69	0,32
Endothelial cells	KIAA1549	ENSG00000122778	0,706	0,884697985	0,412	0,51	0,14
Endothelial cells	FAT4	ENSG00000196159	0,704	0,990298282	0,408	0,53	0,16
Endothelial cells	ETV6	ENSG00000139083	0,717	0,68085918	0,434	0,71	0,35
Endothelial cells	BACE2	ENSG00000182240	0,711	1,130396952	0,422	0,59	0,23
Endothelial cells	TPM3	ENSG00000143549	0,722	0,874594696	0,444	0,59	0,23
Endothelial cells	CTTNBP2NL	ENSG00000143079	0,721	0,88999629	0,442	0,61	0,25
Endothelial cells	FNDC3B	ENSG00000075420	0,729	0,799952281	0,458	0,72	0,36
Endothelial cells	RAC1	ENSG00000136238	0,795	1,010758264	0,59	0,81	0,46
Endothelial cells	SPTAN1	ENSG00000197694	0,714	0,747185309	0,428	0,67	0,32
Endothelial cells	SERPINB6	ENSG00000124570	0,775	0,980103386	0,55	0,76	0,41
Endothelial cells	GMDS	ENSG00000112699	0,741	0,981775819	0,482	0,7	0,36
Endothelial cells	SUSD6	ENSG00000100647	0,709	0,786281943	0,418	0,62	0,28
Endothelial cells	ARHGEF12	ENSG00000196914	0,754	0,819125955	0,508	0,79	0,45

Endothelial cells	HIVEP1	ENSG00000095951	0,706	1,061386869	0,412	0,57	0,23
Endothelial cells	NPIPB5	ENSG00000243716	0,741	1,263472767	0,482	0,65	0,32
Endothelial cells	GFOD1	ENSG00000145990	0,723	1,048114151	0,446	0,61	0,29
Endothelial cells	STAT3	ENSG00000168610	0,76	0,854926595	0,52	0,78	0,46
Endothelial cells	SERF2	ENSG00000140264	0,758	0,916454921	0,516	0,76	0,44
Endothelial cells	TACC1	ENSG00000147526	0,932	1,584014363	0,864	0,97	0,66
Endothelial cells	ANKS1A	ENSG00000064999	0,796	1,186122411	0,592	0,82	0,5
Endothelial cells	ARFGEF2	ENSG00000124198	0,749	0,936985783	0,498	0,72	0,4
Endothelial cells	HIPK3	ENSG00000110422	0,759	1,101773836	0,518	0,74	0,42
Endothelial cells	PDLIM5	ENSG00000163110	0,702	0,839056854	0,404	0,63	0,32
Endothelial cells	SH3BP4	ENSG00000130147	0,702	0,797347234	0,404	0,6	0,29
Endothelial cells	EXOC6	ENSG00000138190	0,738	0,96637052	0,476	0,7	0,39
Endothelial cells	PPP3CC	ENSG00000120910	0,743	0,936165683	0,486	0,7	0,39
Endothelial cells	RBM17	ENSG00000134453	0,708	0,857562506	0,416	0,59	0,28
Endothelial cells	MCF2L	ENSG00000126217	0,749	0,879107175	0,498	0,74	0,43
Endothelial cells	TPM4	ENSG00000167460	0,703	0,771922811	0,406	0,6	0,29
Endothelial cells	DSTN	ENSG00000125868	0,712	0,834503872	0,424	0,61	0,31
Endothelial cells	UBC	ENSG00000150991	0,788	1,035214075	0,576	0,85	0,55
Endothelial cells	TNS1	ENSG00000079308	0,715	0,816802144	0,43	0,71	0,41
Endothelial cells	RASAL2	ENSG00000075391	0,763	0,96802948	0,526	0,81	0,51
Endothelial cells	GRB10	ENSG00000106070	0,766	1,085536084	0,532	0,78	0,48
Endothelial cells	CD46	ENSG00000117335	0,734	0,905249818	0,468	0,68	0,38
Endothelial cells	ST6GALNAC3	ENSG00000184005	0,94	1,696170693	0,88	0,98	0,69
Endothelial cells	AGFG1	ENSG00000173744	0,8	1,024297362	0,6	0,82	0,52
Endothelial cells	FLNB	ENSG00000136068	0,728	0,901920933	0,456	0,67	0,37
Endothelial cells	H3F3B	ENSG00000132475	0,74	0,773010209	0,48	0,77	0,47
Endothelial cells	RBFOX2	ENSG00000100320	0,779	0,891825917	0,558	0,84	0,55
Endothelial cells	TUBA1B	ENSG00000123416	0,711	0,756843747	0,422	0,68	0,39
Endothelial cells	NR3C2	ENSG00000151623	0,756	1,08553587	0,512	0,78	0,49
Endothelial cells	FCHO2	ENSG00000157107	0,714	0,865106496	0,428	0,65	0,36
Endothelial cells	ACTG1	ENSG00000184009	0,76	0,93149781	0,52	0,8	0,51
Endothelial cells	AFF1	ENSG00000172493	0,74	0,843361834	0,48	0,78	0,5
Endothelial cells	PIK3C2A	ENSG00000011405	0,744	0,856264985	0,488	0,74	0,46
Endothelial cells	PTPN12	ENSG00000127947	0,731	0,806343441	0,462	0,72	0,43
Endothelial cells	KIAA0355	ENSG00000166398	0,703	0,811330393	0,406	0,62	0,34
Endothelial cells	PPP3CA	ENSG00000138814	0,716	0,727966848	0,432	0,81	0,54
Endothelial cells	RAP1B	ENSG00000127314	0,712	0,762575833	0,424	0,68	0,41
Endothelial cells	HERC2	ENSG00000128731	0,922	1,705746009	0,844	0,95	0,68
Endothelial cells	ADIPOR2	ENSG00000006831	0,79	0,925645015	0,58	0,93	0,66
Endothelial cells	FEZ2	ENSG00000171055	0,706	0,763026251	0,412	0,66	0,39
Endothelial cells	DOCK9	ENSG00000088387	0,892	1,305233956	0,784	0,97	0,71
Endothelial cells	RAPGEF2	ENSG00000109756	0,821	1,103897525	0,642	0,88	0,63
Endothelial cells	TRIO	ENSG00000038382	0,77	0,829651418	0,54	0,89	0,63
Endothelial cells	TANC1	ENSG00000115183	0,752	0,814627813	0,504	0,84	0,59
Endothelial cells	RIN2	ENSG00000132669	0,711	0,780892578	0,422	0,75	0,5
Endothelial cells	LDLRAD3	ENSG00000179241	0,735	0,900122704	0,47	0,79	0,54
Endothelial cells	EIF1	ENSG00000173812	0,725	0,766214438	0,45	0,77	0,53
Endothelial cells	IGF1R	ENSG00000140443	0,856	1,27269968	0,712	0,93	0,69
Endothelial cells	ACTN4	ENSG00000130402	0,736	0,733864953	0,472	0,81	0,58
Endothelial cells	ASAP1	ENSG00000153317	0,801	0,925225655	0,602	0,91	0,69
Endothelial cells	TTC28	ENSG00000100154	0,729	0,802530557	0,458	0,82	0,6
Endothelial cells	ZBTB38	ENSG00000177311	0,708	0,712043331	0,416	0,73	0,52
Endothelial cells	MEF2A	ENSG00000068305	0,741	0,596746983	0,482	0,87	0,66
Endothelial cells	PTMA	ENSG00000187514	0,741	0,803397725	0,482	0,86	0,66
Endothelial cells	SPTBN1	ENSG00000115306	0,847	1,053559229	0,694	0,94	0,74

Endothelial cells	GAPDH	ENSG00000111640	0,735	0,694219085	0,47	0,87	0,7
Endothelial cells	SMCHD1	ENSG00000101596	0,708	0,783131586	0,416	0,74	0,57
Endothelial cells	ADD1	ENSG00000087274	0,762	0,815775663	0,524	0,85	0,68
Endothelial cells	AFDN	ENSG00000130396	0,718	0,722865105	0,436	0,82	0,65
Endothelial cells	CCNY	ENSG00000108100	0,828	1,124076879	0,656	0,93	0,76
Endothelial cells	KAT6A	ENSG00000083168	0,718	0,687498049	0,436	0,78	0,61
Endothelial cells	ACTB	ENSG00000075624	0,753	0,754994248	0,506	0,92	0,77
Endothelial cells	KTN1	ENSG00000126777	0,702	0,619467061	0,404	0,79	0,64
Endothelial cells	INSR	ENSG00000171105	0,717	0,970673537	0,434	0,8	0,66
Endothelial cells	TCF4	ENSG00000196628	0,806	0,895752074	0,612	0,96	0,84
Endothelial cells	CSNK1A1	ENSG00000113712	0,712	0,60404674	0,424	0,84	0,73
Endothelial cells	FOXP1	ENSG00000114861	0,725	0,636648476	0,45	0,91	0,81
Endothelial cells	RALGAPA1	ENSG00000174373	0,713	0,801664277	0,426	0,85	0,76
Pericytes	PDGFRB	ENSG00000113721	0,961	2,339882991	0,922	0,94	0,08
Pericytes	COBLL1	ENSG00000082438	0,941	1,99810348	0,882	0,93	0,07
Pericytes	PTH1R	ENSG00000160801	0,944	2,446474131	0,888	0,9	0,04
Pericytes	DCN	ENSG00000011465	0,933	2,249121022	0,866	0,87	0,02
Pericytes	NDUFA4L2	ENSG00000185633	0,931	2,436985004	0,862	0,87	0,03
Pericytes	NOTCH3	ENSG00000074181	0,921	2,129174017	0,842	0,85	0,01
Pericytes	EBF1	ENSG00000164330	0,961	2,44401493	0,922	0,96	0,13
Pericytes	MYO1B	ENSG00000128641	0,926	2,011191797	0,852	0,87	0,05
Pericytes	IFITM3	ENSG00000142089	0,93	2,090321944	0,86	0,91	0,09
Pericytes	GGT5	ENSG00000099998	0,914	1,836593641	0,828	0,86	0,05
Pericytes	SLC6A12	ENSG00000111181	0,91	2,304409469	0,82	0,83	0,02
Pericytes	RGS5	ENSG00000143248	0,938	2,463966182	0,876	0,9	0,1
Pericytes	ITIH5	ENSG00000123243	0,914	2,021194478	0,828	0,86	0,06
Pericytes	IGFBP7	ENSG00000163453	0,938	2,23398022	0,876	0,93	0,13
Pericytes	SLC38A11	ENSG00000169507	0,901	2,185125767	0,802	0,8	0,01
Pericytes	EPAS1	ENSG00000116016	0,902	1,757601673	0,804	0,87	0,08
Pericytes	ARHGAP29	ENSG00000137962	0,927	1,85985594	0,854	0,91	0,12
Pericytes	RBPMS	ENSG00000157110	0,91	1,863850017	0,82	0,88	0,11
Pericytes	NID1	ENSG00000116962	0,897	1,833652478	0,794	0,81	0,04
Pericytes	PRELP	ENSG00000188783	0,885	1,896307632	0,77	0,78	0,02
Pericytes	BGN	ENSG00000182492	0,886	1,902660268	0,772	0,79	0,03
Pericytes	GJC1	ENSG00000182963	0,88	1,745315843	0,76	0,77	0,01
Pericytes	HES4	ENSG00000188290	0,889	1,910801169	0,778	0,8	0,06
Pericytes	TIMP3	ENSG00000100234	0,92	2,050179382	0,84	0,9	0,17
Pericytes	ARHGAP10	ENSG00000071205	0,9	1,821159034	0,8	0,85	0,12
Pericytes	ARHGAP42	ENSG00000165895	0,902	1,817070182	0,804	0,87	0,14
Pericytes	MYL9	ENSG00000101335	0,868	1,740806178	0,736	0,75	0,01
Pericytes	SYNE2	ENSG00000054654	0,891	1,563994762	0,782	0,85	0,13
Pericytes	LAMA2	ENSG00000196569	0,934	2,330059004	0,868	0,95	0,23
Pericytes	NR2F2-AS1	ENSG00000247809	0,883	1,778252792	0,766	0,84	0,12
Pericytes	NR2F2	ENSG00000185551	0,88	1,601655402	0,76	0,79	0,07
Pericytes	SLC30A10	ENSG00000196660	0,882	1,794722117	0,764	0,79	0,08
Pericytes	CARMN	ENSG00000249669	0,857	1,759181624	0,714	0,72	0
Pericytes	ATP1A2	ENSG00000018625	0,901	2,095947337	0,802	0,91	0,2
Pericytes	TFPI	ENSG00000003436	0,856	1,652987272	0,712	0,72	0,01
Pericytes	FN1	ENSG00000115414	0,883	1,846996816	0,766	0,81	0,11
Pericytes	RBMS3	ENSG00000144642	0,898	1,69621362	0,796	0,87	0,17
Pericytes	LZTS1	ENSG00000061337	0,856	1,572996396	0,712	0,72	0,01
Pericytes	MIR4435-2HG	ENSG00000172965	0,885	2,165707558	0,77	0,81	0,11
Pericytes	PRKG1	ENSG00000185532	0,915	1,904190267	0,83	0,94	0,25
Pericytes	RHOJ	ENSG00000126785	0,854	1,677253254	0,708	0,75	0,06
Pericytes	SPARCL1	ENSG00000152583	0,925	1,939554268	0,85	0,95	0,26

Pericytes	RIPOR3	ENSG00000042062	0,849	1,644118815	0,698	0,71	0,03
Pericytes	COLEC12	ENSG00000158270	0,86	1,966114718	0,72	0,78	0,1
Pericytes	ITGA1	ENSG00000213949	0,848	1,455318357	0,696	0,75	0,07
Pericytes	PDE7B	ENSG00000171408	0,92	2,185156834	0,84	0,92	0,25
Pericytes	PLXDC1	ENSG00000161381	0,846	1,575173583	0,692	0,71	0,04
Pericytes	COL5A3	ENSG00000080573	0,839	1,382268353	0,678	0,76	0,09
Pericytes	HIGD1B	ENSG00000131097	0,835	1,572186887	0,67	0,68	0,02
Pericytes	CFH	ENSG00000000971	0,831	1,463712764	0,662	0,69	0,03
Pericytes	COL1A2	ENSG00000164692	0,831	1,430815902	0,662	0,66	0
Pericytes	COL4A2	ENSG00000134871	0,849	1,827888779	0,698	0,74	0,08
Pericytes	AC092957.1	ENSG00000243620	0,835	1,847297301	0,67	0,7	0,04
Pericytes	FRMD3	ENSG00000172159	0,886	1,981649999	0,772	0,83	0,17
Pericytes	CEBPD	ENSG00000221869	0,863	1,78864675	0,726	0,8	0,14
Pericytes	UTRN	ENSG00000152818	0,919	1,619731605	0,838	0,96	0,31
Pericytes	C11orf96	ENSG00000187479	0,838	2,010205619	0,676	0,7	0,05
Pericytes	SLC12A7	ENSG00000113504	0,832	1,488145995	0,664	0,69	0,04
Pericytes	KCNT2	ENSG00000162687	0,847	1,597972849	0,694	0,78	0,13
Pericytes	PTPRG	ENSG00000144724	0,903	1,565141098	0,806	0,96	0,32
Pericytes	ZIC1	ENSG00000152977	0,848	1,453562857	0,696	0,78	0,14
Pericytes	FLNA	ENSG00000196924	0,844	1,505333234	0,688	0,75	0,11
Pericytes	RNF152	ENSG00000176641	0,885	2,135966664	0,77	0,83	0,19
Pericytes	LAMC3	ENSG00000050555	0,82	1,446904582	0,64	0,65	0,02
Pericytes	VIM	ENSG00000026025	0,821	1,239307774	0,642	0,72	0,09
Pericytes	TRPC4	ENSG00000133107	0,833	1,763201987	0,666	0,71	0,08
Pericytes	PLCB4	ENSG00000101333	0,856	1,398153024	0,712	0,86	0,24
Pericytes	PTMS	ENSG00000159335	0,838	1,368602023	0,676	0,73	0,11
Pericytes	COL4A1	ENSG00000187498	0,823	1,909486632	0,646	0,67	0,04
Pericytes	SLC19A1	ENSG00000173638	0,824	1,459258168	0,648	0,67	0,05
Pericytes	ZEB1	ENSG00000148516	0,914	1,695229522	0,828	0,96	0,34
Pericytes	COL4A3	ENSG00000169031	0,83	1,581376316	0,66	0,7	0,08
Pericytes	SMOC2	ENSG00000112562	0,817	1,492448558	0,634	0,65	0,03
Pericytes	DOCK6	ENSG00000130158	0,822	1,313103891	0,644	0,69	0,07
Pericytes	TAGLN2	ENSG00000158710	0,818	1,276608993	0,636	0,7	0,08
Pericytes	RBMS1	ENSG00000153250	0,897	1,513887188	0,794	0,9	0,28
Pericytes	P2RY14	ENSG00000174944	0,822	1,654021685	0,644	0,67	0,05
Pericytes	COL4A4	ENSG00000081052	0,822	1,546376049	0,644	0,68	0,06
Pericytes	AXL	ENSG00000167601	0,818	1,225586264	0,636	0,71	0,09
Pericytes	GRM8	ENSG00000179603	0,832	2,047637433	0,664	0,72	0,11
Pericytes	IFITM2	ENSG00000185201	0,81	1,319133974	0,62	0,67	0,05
Pericytes	TMSB10	ENSG00000034510	0,854	1,706311196	0,708	0,82	0,2
Pericytes	LEF1	ENSG00000138795	0,814	1,345157107	0,628	0,69	0,08
Pericytes	ABCC9	ENSG00000069431	0,813	1,477072212	0,626	0,66	0,05
Pericytes	GNG11	ENSG00000127920	0,805	1,188803255	0,61	0,64	0,03
Pericytes	ETS1	ENSG00000134954	0,812	1,193594436	0,624	0,69	0,09
Pericytes	C1QTNF1	ENSG00000173918	0,804	1,244932179	0,608	0,62	0,02
Pericytes	FLT1	ENSG00000102755	0,799	1,329009137	0,598	0,68	0,08
Pericytes	ADIRF	ENSG00000148671	0,808	1,550403776	0,616	0,65	0,05
Pericytes	LGALS1	ENSG00000100097	0,863	1,648428692	0,726	0,82	0,22
Pericytes	ADAMTS9-AS2	ENSG00000241684	0,824	1,642072858	0,648	0,76	0,16
Pericytes	ADGRF5	ENSG00000069122	0,798	1,170088755	0,596	0,64	0,04
Pericytes	CACNA1C	ENSG00000151067	0,909	1,807501478	0,818	0,94	0,34
Pericytes	MGLL	ENSG00000074416	0,842	1,321423786	0,684	0,8	0,2
Pericytes	A2M	ENSG00000175899	0,809	1,16115623	0,618	0,73	0,14
Pericytes	TIMP1	ENSG00000102265	0,805	2,065761923	0,61	0,64	0,04
Pericytes	CASC15	ENSG00000272168	0,844	1,538581169	0,688	0,77	0,17

Pericytes	EHD2	ENSG00000024422	0,799	1,164014684	0,598	0,63	0,03
Pericytes	SNTB1	ENSG00000172164	0,808	1,404564089	0,616	0,69	0,1
Pericytes	JAG1	ENSG00000101384	0,806	1,356303968	0,612	0,65	0,06
Pericytes	GPC5	ENSG00000179399	0,828	1,305407381	0,656	0,86	0,28
Pericytes	CDH6	ENSG00000113361	0,812	1,501308264	0,624	0,67	0,09
Pericytes	PLCE1	ENSG00000138193	0,82	1,389706205	0,64	0,73	0,15
Pericytes	LINC02147	ENSG00000249797	0,791	1,904490248	0,582	0,6	0,03
Pericytes	PDE3A	ENSG00000172572	0,801	1,55812963	0,602	0,69	0,12
Pericytes	COL6A2	ENSG00000142173	0,789	1,153296255	0,578	0,59	0,02
Pericytes	HLA-E	ENSG00000204592	0,791	1,157605029	0,582	0,69	0,13
Pericytes	KCNE4	ENSG00000152049	0,788	1,55761556	0,576	0,6	0,03
Pericytes	KANK3	ENSG00000186994	0,787	1,062119181	0,574	0,61	0,04
Pericytes	CLDN5	ENSG00000184113	0,781	1,383390528	0,562	0,63	0,06
Pericytes	LHFPL6	ENSG00000183722	0,886	1,546003975	0,772	0,94	0,37
Pericytes	TBX2	ENSG00000121068	0,785	1,23893374	0,57	0,57	0,01
Pericytes	CYTH3	ENSG00000008256	0,82	1,296620692	0,64	0,74	0,17
Pericytes	SLC6A13	ENSG00000010379	0,787	1,469601849	0,574	0,58	0,02
Pericytes	ADAMTS9	ENSG00000163638	0,794	2,173499218	0,588	0,65	0,09
Pericytes	MAP3K20	ENSG00000091436	0,801	1,116716415	0,602	0,71	0,15
Pericytes	PAPSS2	ENSG00000198682	0,78	1,166956492	0,56	0,61	0,05
Pericytes	RHOC	ENSG00000155366	0,785	1,080777123	0,57	0,62	0,07
Pericytes	SOX5	ENSG00000134532	0,782	0,801725414	0,564	0,9	0,34
Pericytes	MSC-AS1	ENSG00000235531	0,779	1,347306446	0,558	0,56	0,01
Pericytes	YBX3	ENSG00000060138	0,787	1,149854035	0,574	0,65	0,1
Pericytes	PCBP3	ENSG00000183570	0,846	1,90998112	0,692	0,79	0,23
Pericytes	PARD3	ENSG00000148498	0,844	1,128095909	0,688	0,96	0,41
Pericytes	SPARC	ENSG00000113140	0,878	1,470331588	0,756	0,89	0,34
Pericytes	PLAC9	ENSG00000189129	0,774	1,104403217	0,548	0,55	0,01
Pericytes	GRK5	ENSG00000198873	0,811	1,343866741	0,622	0,72	0,17
Pericytes	ARHGAP6	ENSG00000047648	0,789	1,25648784	0,578	0,7	0,16
Pericytes	CNTN4	ENSG00000144619	0,771	0,89892499	0,542	0,71	0,17
Pericytes	PHLDB2	ENSG00000144824	0,773	1,084432056	0,546	0,57	0,03
Pericytes	TESC	ENSG00000088992	0,774	1,113596951	0,548	0,56	0,03
Pericytes	IFI27	ENSG00000165949	0,769	1,274750094	0,538	0,59	0,06
Pericytes	TRPC3	ENSG00000138741	0,776	1,290303933	0,552	0,57	0,04
Pericytes	TNS2	ENSG00000111077	0,807	1,105775842	0,614	0,73	0,19
Pericytes	ISYNA1	ENSG00000105655	0,775	1,263004452	0,55	0,57	0,03
Pericytes	SNRK	ENSG00000163788	0,817	1,303841668	0,634	0,74	0,21
Pericytes	ARHGEF17	ENSG00000110237	0,79	1,123962549	0,58	0,65	0,12
Pericytes	ADGRD1	ENSG00000111452	0,767	1,298842132	0,534	0,55	0,02
Pericytes	VWF	ENSG00000110799	0,764	1,317763846	0,528	0,6	0,07
Pericytes	AC012409.2	ENSG00000275443	0,769	1,426883627	0,538	0,55	0,03
Pericytes	MYOF	ENSG00000138119	0,764	0,971672767	0,528	0,63	0,1
Pericytes	MYH9	ENSG00000100345	0,835	1,201675879	0,67	0,8	0,28
Pericytes	GPER1	ENSG00000164850	0,762	1,161302228	0,524	0,53	0,01
Pericytes	PID1	ENSG00000153823	0,792	1,292353497	0,584	0,74	0,22
Pericytes	EPS8	ENSG00000151491	0,957	2,061150168	0,914	0,97	0,45
Pericytes	DACH1	ENSG00000276644	0,772	1,256352681	0,544	0,63	0,11
Pericytes	UACA	ENSG00000137831	0,832	1,250887875	0,664	0,81	0,3
Pericytes	HSPB1	ENSG00000106211	0,786	1,130402138	0,572	0,71	0,2
Pericytes	VCL	ENSG00000035403	0,788	1,102539071	0,576	0,68	0,17
Pericytes	RAPH1	ENSG00000173166	0,818	1,281003589	0,636	0,76	0,25
Pericytes	ECE1	ENSG00000117298	0,802	1,042840862	0,604	0,77	0,26
Pericytes	TMTC1	ENSG00000133687	0,784	1,141396742	0,568	0,74	0,23
Pericytes	STOM	ENSG00000148175	0,779	0,986030926	0,558	0,69	0,18

Pericytes	BSG	ENSG00000172270	0,877	1,568101709	0,754	0,88	0,37
Pericytes	RRAS	ENSG00000126458	0,759	1,029121063	0,518	0,54	0,03
Pericytes	PLOD1	ENSG00000083444	0,78	1,072298997	0,56	0,64	0,13
Pericytes	TGFBR2	ENSG00000163513	0,752	0,925902613	0,504	0,63	0,12
Pericytes	ZBTB46	ENSG00000130584	0,776	1,057565606	0,552	0,65	0,14
Pericytes	S100A11	ENSG00000163191	0,754	0,984800533	0,508	0,57	0,06
Pericytes	GJA4	ENSG00000187513	0,753	1,154313346	0,506	0,51	0
Pericytes	MFGE8	ENSG00000140545	0,774	1,043650764	0,548	0,64	0,13
Pericytes	AHNAK	ENSG00000124942	0,76	0,966276517	0,52	0,63	0,12
Pericytes	SLC9A3R2	ENSG00000065054	0,758	1,075991333	0,516	0,57	0,07
Pericytes	APOLD1	ENSG00000178878	0,792	1,114396043	0,584	0,74	0,24
Pericytes	CRIP2	ENSG00000182809	0,766	0,994736544	0,532	0,62	0,12
Pericytes	ZFHX3	ENSG00000140836	0,84	1,17715434	0,68	0,92	0,42
Pericytes	HLA-B	ENSG00000234745	0,759	0,989126184	0,518	0,65	0,15
Pericytes	DGKB	ENSG00000136267	0,761	1,01743441	0,522	0,7	0,21
Pericytes	KIRREL1	ENSG00000183853	0,756	1,054044601	0,512	0,55	0,05
Pericytes	EDNRA	ENSG00000151617	0,748	1,161094948	0,496	0,51	0,02
Pericytes	HLA-C	ENSG00000204525	0,768	1,037435321	0,536	0,65	0,16
Pericytes	BCAM	ENSG00000187244	0,747	0,941295139	0,494	0,52	0,03
Pericytes	KANK2	ENSG00000197256	0,749	0,9752534	0,498	0,53	0,04
Pericytes	EVA1B	ENSG00000142694	0,745	0,932554788	0,49	0,51	0,03
Pericytes	CYSLTR2	ENSG00000152207	0,743	1,304641751	0,486	0,49	0,01
Pericytes	NR2F1	ENSG00000175745	0,757	1,03812448	0,514	0,61	0,12
Pericytes	ITGA10	ENSG00000143127	0,747	0,969303321	0,494	0,52	0,03
Pericytes	FBLN1	ENSG00000077942	0,745	1,213624124	0,49	0,52	0,03
Pericytes	MEF2C	ENSG00000081189	0,745	0,588903279	0,49	0,72	0,24
Pericytes	EGFR	ENSG00000146648	0,741	0,819929978	0,482	0,67	0,19
Pericytes	TPM1	ENSG00000140416	0,788	1,151346812	0,576	0,71	0,23
Pericytes	GRAMD2B	ENSG00000155324	0,781	0,96673839	0,562	0,81	0,33
Pericytes	LAMA4	ENSG00000112769	0,75	1,104034318	0,5	0,6	0,12
Pericytes	CDC42EP4	ENSG00000179604	0,747	0,877995703	0,494	0,58	0,1
Pericytes	ESAM	ENSG00000149564	0,738	0,834166844	0,476	0,51	0,03
Pericytes	ZFP36L1	ENSG00000185650	0,734	0,667907714	0,468	0,7	0,22
Pericytes	S1PR3	ENSG00000213694	0,739	0,973886018	0,478	0,49	0,01
Pericytes	CD151	ENSG00000177697	0,747	0,941571202	0,494	0,54	0,06
Pericytes	SERPING1	ENSG00000149131	0,744	0,926476879	0,488	0,54	0,06
Pericytes	TRIB2	ENSG00000071575	0,747	0,925667702	0,494	0,54	0,07
Pericytes	CYBA	ENSG00000051523	0,736	0,835502407	0,472	0,55	0,08
Pericytes	PDE5A	ENSG00000138735	0,779	1,125111645	0,558	0,66	0,19
Pericytes	CSPG4	ENSG00000173546	0,738	0,920757965	0,476	0,52	0,05
Pericytes	BTG1	ENSG00000133639	0,766	1,037141379	0,532	0,64	0,16
Pericytes	EMP2	ENSG00000213853	0,737	0,87849916	0,474	0,54	0,07
Pericytes	SVIL	ENSG00000197321	0,757	1,184854557	0,514	0,6	0,13
Pericytes	CPE	ENSG00000109472	0,788	1,06933841	0,576	0,82	0,35
Pericytes	TNS1	ENSG00000079308	0,846	1,188194942	0,692	0,87	0,4
Pericytes	HEYL	ENSG00000163909	0,734	1,091222987	0,468	0,48	0,01
Pericytes	FAM107A	ENSG00000168309	0,746	1,057480788	0,492	0,61	0,15
Pericytes	SMIM3	ENSG00000256235	0,733	0,848795083	0,466	0,5	0,04
Pericytes	PDZD2	ENSG00000133401	0,816	0,899380345	0,632	0,89	0,43
Pericytes	CALD1	ENSG00000122786	0,97	2,148469232	0,94	0,98	0,52
Pericytes	DGKH	ENSG00000102780	0,757	0,978968745	0,514	0,65	0,19
Pericytes	LPL	ENSG00000175445	0,737	1,150014987	0,474	0,52	0,06
Pericytes	RGL3	ENSG00000205517	0,732	1,010323512	0,464	0,51	0,05
Pericytes	VAMP5	ENSG00000168899	0,731	0,877412899	0,462	0,51	0,05
Pericytes	FRY	ENSG00000073910	0,777	1,012831322	0,554	0,8	0,35

Pericytes	MAOA	ENSG00000189221	0,737	0,945495707	0,474	0,55	0,09
Pericytes	FSTL1	ENSG00000163430	0,735	0,975639363	0,47	0,53	0,08
Pericytes	B2M	ENSG00000166710	0,833	1,248150847	0,666	0,86	0,4
Pericytes	ANXA2	ENSG00000182718	0,728	0,867929933	0,456	0,51	0,06
Pericytes	TBX3	ENSG00000135111	0,725	0,92302553	0,45	0,47	0,02
Pericytes	TGM2	ENSG00000198959	0,722	0,965239893	0,444	0,49	0,04
Pericytes	WWTR1	ENSG00000018408	0,751	0,8817815	0,502	0,68	0,23
Pericytes	PAWR	ENSG00000177425	0,729	0,899084518	0,458	0,54	0,1
Pericytes	LAMB2	ENSG00000172037	0,726	0,835832485	0,452	0,49	0,05
Pericytes	GUCY1B1	ENSG00000061918	0,746	0,983967884	0,492	0,57	0,13
Pericytes	PMEPA1	ENSG00000124225	0,755	1,010268371	0,51	0,63	0,18
Pericytes	TMEM204	ENSG00000131634	0,722	0,798875335	0,444	0,47	0,03
Pericytes	EGFL7	ENSG00000172889	0,723	0,871308105	0,446	0,51	0,07
Pericytes	TXNIP	ENSG00000265972	0,827	1,396517566	0,654	0,85	0,4
Pericytes	UST	ENSG00000111962	0,732	0,922899031	0,464	0,65	0,2
Pericytes	GSTP1	ENSG00000084207	0,782	1,070324536	0,564	0,72	0,28
Pericytes	LRRC32	ENSG00000137507	0,718	0,888185038	0,436	0,47	0,03
Pericytes	SLC2A3	ENSG00000059804	0,733	1,030130237	0,466	0,57	0,13
Pericytes	NBL1	ENSG00000158747	0,727	0,885131592	0,454	0,49	0,05
Pericytes	CST3	ENSG00000101439	0,741	0,648708641	0,482	0,78	0,34
Pericytes	FARP1	ENSG00000152767	0,735	0,751442228	0,47	0,71	0,28
Pericytes	MT2A	ENSG00000125148	0,788	1,201829884	0,576	0,8	0,36
Pericytes	YAP1	ENSG00000137693	0,714	0,702611755	0,428	0,55	0,12
Pericytes	NTRK3	ENSG00000140538	0,739	1,18572231	0,478	0,73	0,3
Pericytes	PTEN	ENSG00000171862	0,904	1,575694807	0,808	0,94	0,51
Pericytes	ACSS3	ENSG00000111058	0,721	0,894162525	0,442	0,55	0,12
Pericytes	INPP4B	ENSG00000109452	0,755	0,999949142	0,51	0,71	0,28
Pericytes	CLIC1	ENSG00000213719	0,716	0,816689618	0,432	0,47	0,04
Pericytes	CPM	ENSG00000135678	0,82	1,396510717	0,64	0,83	0,4
Pericytes	LIN7A	ENSG00000111052	0,732	0,990400536	0,464	0,56	0,13
Pericytes	COL6A1	ENSG00000142156	0,729	0,900431285	0,458	0,54	0,12
Pericytes	FOXD1	ENSG00000251493	0,714	0,842356106	0,428	0,43	0
Pericytes	ABCB1	ENSG00000085563	0,713	1,103636554	0,426	0,5	0,07
Pericytes	RHOB	ENSG00000143878	0,788	1,111238458	0,576	0,76	0,33
Pericytes	IL1R1	ENSG00000115594	0,713	0,889719408	0,426	0,44	0,02
Pericytes	ID3	ENSG00000117318	0,71	0,837830511	0,42	0,49	0,07
Pericytes	HLA-A	ENSG00000206503	0,747	0,950039819	0,494	0,65	0,23
Pericytes	KLF6	ENSG00000067082	0,735	0,867144169	0,47	0,6	0,18
Pericytes	CAV1	ENSG00000105974	0,715	0,833510992	0,43	0,47	0,05
Pericytes	FOXC1	ENSG00000054598	0,71	0,777861541	0,42	0,44	0,02
Pericytes	MYL6	ENSG00000092841	0,758	0,991106852	0,516	0,66	0,24
Pericytes	SMTN	ENSG00000183963	0,711	0,745276964	0,422	0,49	0,07
Pericytes	FRMD6	ENSG00000139926	0,724	0,964496827	0,448	0,53	0,11
Pericytes	SORBS3	ENSG00000120896	0,725	0,865386514	0,45	0,55	0,13
Pericytes	CPT1A	ENSG00000110090	0,718	0,849001363	0,436	0,52	0,1
Pericytes	LAMC1	ENSG00000135862	0,725	1,049094864	0,45	0,54	0,12
Pericytes	PDE8B	ENSG00000113231	0,72	0,87320983	0,44	0,5	0,09
Pericytes	RBMS2	ENSG00000076067	0,718	0,755277463	0,436	0,56	0,14
Pericytes	AC002546.1	ENSG00000267653	0,706	0,839008445	0,412	0,42	0,01
Pericytes	KLHL23	ENSG00000213160	0,749	1,008819776	0,498	0,64	0,22
Pericytes	AL138828.1	ENSG00000237596	0,713	0,983633373	0,426	0,46	0,05
Pericytes	PODXL	ENSG00000128567	0,708	0,863633553	0,416	0,49	0,08
Pericytes	NXN	ENSG00000167693	0,725	0,95214352	0,45	0,58	0,17
Pericytes	CD63	ENSG00000135404	0,748	0,902117152	0,496	0,66	0,25
Pericytes	ARHGEF12	ENSG00000196914	0,816	1,024846294	0,632	0,86	0,45

Pericytes	RBMS3-AS3	ENSG00000235904	0,71	0,862028551	0,42	0,46	0,05
Pericytes	CERS6	ENSG00000172292	0,731	0,851336554	0,462	0,69	0,28
Pericytes	RORA	ENSG00000069667	0,822	1,089941873	0,644	0,97	0,57
Pericytes	JAK1	ENSG00000162434	0,785	0,930308066	0,57	0,78	0,37
Pericytes	PARVA	ENSG00000197702	0,716	0,843646641	0,432	0,5	0,1
Pericytes	CRISPLD2	ENSG00000103196	0,709	1,293821653	0,418	0,47	0,06
Pericytes	KALRN	ENSG00000160145	0,753	0,841838107	0,506	0,82	0,42
Pericytes	ADGRL2	ENSG00000117114	0,702	0,66351076	0,404	0,55	0,15
Pericytes	NOSTRIN	ENSG00000163072	0,701	0,79449528	0,402	0,44	0,04
Pericytes	PACSIN2	ENSG00000100266	0,756	0,953907575	0,512	0,7	0,29
Pericytes	ENG	ENSG00000106991	0,702	0,78240275	0,404	0,49	0,08
Pericytes	SEPTIN11	ENSG00000138758	0,734	0,879137146	0,468	0,63	0,23
Pericytes	TAGLN	ENSG00000149591	0,727	2,032769944	0,454	0,52	0,12
Pericytes	GUCY1A1	ENSG00000164116	0,712	0,920522461	0,424	0,5	0,09
Pericytes	MYO1C	ENSG00000197879	0,706	0,760531837	0,412	0,46	0,06
Pericytes	OSMR	ENSG00000145623	0,705	0,844281784	0,41	0,5	0,09
Pericytes	CEBPB	ENSG00000172216	0,704	0,739602812	0,408	0,48	0,08
Pericytes	MRC2	ENSG00000011028	0,701	0,75897503	0,402	0,46	0,06
Pericytes	AGRN	ENSG00000188157	0,717	0,936807688	0,434	0,53	0,13
Pericytes	SELENOM	ENSG00000198832	0,725	0,853485045	0,45	0,57	0,17
Pericytes	CACHD1	ENSG00000158966	0,714	0,881292336	0,428	0,62	0,22
Pericytes	NT5DC2	ENSG00000168268	0,702	0,790494509	0,404	0,44	0,04
Pericytes	MSN	ENSG00000147065	0,716	0,736508408	0,432	0,6	0,21
Pericytes	C2CD2	ENSG00000157617	0,767	1,062376422	0,534	0,73	0,33
Pericytes	CYTOR	ENSG00000222041	0,702	0,90107519	0,404	0,44	0,04
Pericytes	JUNB	ENSG00000171223	0,703	1,193365385	0,406	0,47	0,07
Pericytes	CNN3	ENSG00000117519	0,72	0,742899884	0,44	0,61	0,22
Pericytes	MECOM	ENSG00000085276	0,711	0,99902004	0,422	0,54	0,15
Pericytes	MYL12A	ENSG00000101608	0,702	0,780545082	0,404	0,47	0,08
Pericytes	HIF1A-AS3	ENSG00000258667	0,702	1,034233369	0,404	0,5	0,11
Pericytes	PRKCH	ENSG00000027075	0,701	0,850977259	0,402	0,53	0,14
Pericytes	NR2F1-AS1	ENSG00000237187	0,706	0,86998222	0,412	0,59	0,2
Pericytes	PPFIBP1	ENSG00000110841	0,773	0,890170481	0,546	0,8	0,41
Pericytes	KLF9	ENSG00000119138	0,756	0,940833501	0,512	0,71	0,33
Pericytes	PAG1	ENSG00000076641	0,754	0,997138697	0,508	0,73	0,34
Pericytes	RUNX1T1	ENSG00000079102	0,707	0,732801826	0,414	0,67	0,29
Pericytes	MSRB3	ENSG00000174099	0,703	0,753020065	0,406	0,53	0,14
Pericytes	FNDC3B	ENSG00000075420	0,736	0,816688616	0,472	0,75	0,37
Pericytes	MYL12B	ENSG00000118680	0,715	0,811764687	0,43	0,55	0,17
Pericytes	CAVIN1	ENSG00000177469	0,703	0,793176296	0,406	0,51	0,13
Pericytes	TMOD3	ENSG00000138594	0,725	0,797005743	0,45	0,62	0,24
Pericytes	ROCK2	ENSG00000134318	0,802	1,001160884	0,604	0,82	0,44
Pericytes	SLC25A6	ENSG00000169100	0,713	0,743169942	0,426	0,56	0,18
Pericytes	PDZRN3	ENSG00000121440	0,702	1,019199853	0,404	0,56	0,18
Pericytes	TLN1	ENSG00000137076	0,713	0,725952928	0,426	0,57	0,19
Pericytes	CRIM1	ENSG00000150938	0,723	1,023145503	0,446	0,63	0,25
Pericytes	ITGB5	ENSG00000082781	0,708	0,815516355	0,416	0,56	0,19
Pericytes	CYB5R3	ENSG00000100243	0,734	0,847771287	0,468	0,63	0,26
Pericytes	AKAP13	ENSG00000170776	0,717	0,598644718	0,434	0,73	0,36
Pericytes	PTN	ENSG00000105894	0,728	0,859674486	0,456	0,7	0,33
Pericytes	KLF12	ENSG00000118922	0,722	0,802452514	0,444	0,73	0,36
Pericytes	STK24	ENSG00000102572	0,714	0,749467453	0,428	0,59	0,21
Pericytes	RELL1	ENSG00000181826	0,706	0,735269731	0,412	0,56	0,19
Pericytes	ITGB1	ENSG00000150093	0,767	0,892735406	0,534	0,75	0,38
Pericytes	TPT1	ENSG00000133112	0,764	0,935406667	0,528	0,77	0,4

Pericytes	SEPTIN9	ENSG00000184640	0,701	0,72823818	0,402	0,54	0,19
Pericytes	PFN1	ENSG00000108518	0,709	0,796185581	0,418	0,57	0,22
Pericytes	MAST4	ENSG00000069020	0,752	0,911129152	0,504	0,79	0,44
Pericytes	DENND2A	ENSG00000146966	0,721	0,885820314	0,442	0,67	0,32
Pericytes	SERF2	ENSG00000140264	0,778	0,997454292	0,556	0,78	0,44
Pericytes	BACH1	ENSG00000156273	0,71	0,725606386	0,42	0,68	0,34
Pericytes	TMSB4X	ENSG00000205542	0,794	1,088113558	0,588	0,84	0,5
Pericytes	RASAL2	ENSG00000075391	0,785	0,937653521	0,57	0,86	0,52
Pericytes	SLC6A1	ENSG00000157103	0,791	1,264738865	0,582	0,82	0,48
Pericytes	TLE5	ENSG00000104964	0,726	0,765780216	0,452	0,68	0,35
Pericytes	RHOA	ENSG00000067560	0,736	0,806804044	0,472	0,7	0,37
Pericytes	TPM4	ENSG00000167460	0,715	0,848953149	0,43	0,62	0,29
Pericytes	H3F3B	ENSG00000132475	0,774	0,923238759	0,548	0,8	0,48
Pericytes	NBEAL1	ENSG00000144426	0,821	1,034906515	0,642	0,88	0,56
Pericytes	SH3RF1	ENSG00000154447	0,725	0,833659813	0,45	0,75	0,43
Pericytes	TUBA1B	ENSG00000123416	0,713	0,718759255	0,426	0,7	0,39
Pericytes	TSC22D1	ENSG00000102804	0,77	0,915204099	0,54	0,83	0,53
Pericytes	CFLAR	ENSG00000003402	0,711	0,653658941	0,422	0,7	0,4
Pericytes	SLC38A2	ENSG00000134294	0,753	0,903779535	0,506	0,81	0,52
Pericytes	UBA2	ENSG00000126261	0,706	0,726337355	0,412	0,65	0,36
Pericytes	CD81	ENSG00000110651	0,735	0,73331625	0,47	0,8	0,52
Pericytes	TACC1	ENSG00000147526	0,866	1,16267375	0,732	0,94	0,66
Pericytes	EEF1A1	ENSG00000156508	0,732	0,851414064	0,464	0,75	0,48
Pericytes	TXNRD1	ENSG00000198431	0,714	0,727460591	0,428	0,7	0,43
Pericytes	PTPN12	ENSG00000127947	0,709	0,664534797	0,418	0,71	0,44
Pericytes	PTPRM	ENSG00000173482	0,72	0,792923412	0,44	0,76	0,5
Pericytes	CAST	ENSG00000153113	0,704	0,655608614	0,408	0,7	0,43
Pericytes	ESYT2	ENSG00000117868	0,705	0,76208513	0,41	0,69	0,42
Pericytes	DLC1	ENSG00000164741	0,935	1,915572047	0,87	0,97	0,71
Pericytes	RAC1	ENSG00000136238	0,708	0,662855641	0,416	0,72	0,46
Pericytes	ZBTB38	ENSG00000177311	0,736	0,765365753	0,472	0,77	0,52
Pericytes	EIF1	ENSG00000173812	0,718	0,686179259	0,436	0,78	0,53
Pericytes	SLC20A2	ENSG00000168575	0,738	1,022555412	0,476	0,81	0,57
Pericytes	UBC	ENSG00000150991	0,715	0,645400165	0,43	0,79	0,55
Pericytes	NCKAP1	ENSG00000061676	0,701	0,592175291	0,402	0,75	0,52
Pericytes	LPP	ENSG00000145012	0,855	1,193702009	0,71	0,95	0,72
Pericytes	SLC12A2	ENSG00000064651	0,724	0,840523695	0,448	0,81	0,6
Pericytes	PTPRK	ENSG00000152894	0,725	0,655706151	0,45	0,95	0,75
Pericytes	BTBD9	ENSG00000183826	0,72	0,890933455	0,44	0,81	0,61
Pericytes	PTMA	ENSG00000187514	0,724	0,67728879	0,448	0,86	0,66
Pericytes	SPTBN1	ENSG00000115306	0,824	0,862875255	0,648	0,94	0,75
Pericytes	SGIP1	ENSG00000118473	0,718	0,906342271	0,436	0,87	0,7
Pericytes	GAPDH	ENSG00000111640	0,747	0,796488991	0,494	0,87	0,7
Pericytes	KIAA1109	ENSG00000138688	0,753	0,802901763	0,506	0,87	0,7
Pericytes	ACTB	ENSG00000075624	0,797	1,124369314	0,594	0,92	0,77
Pericytes	MALAT1	ENSG00000251562	0,858	0,799895867	0,716	1	1
Inhibitory	GAD2	ENSG00000136750	0,923	1,397908849	0,846	0,88	0,03
Inhibitory	SRRM3	ENSG00000177679	0,918	1,103087194	0,836	0,96	0,12
Inhibitory	GRIN1	ENSG00000176884	0,921	1,161657744	0,842	0,95	0,11
Inhibitory	PAK3	ENSG00000077264	0,935	1,501764919	0,87	0,97	0,13
Inhibitory	CELF4	ENSG00000101489	0,93	1,446027046	0,86	0,96	0,12
Inhibitory	MYT1L	ENSG00000186487	0,936	1,615282481	0,872	0,98	0,15
Inhibitory	SYT1	ENSG00000067715	0,935	1,876918171	0,87	0,97	0,15
Inhibitory	ANKRD30BL	ENSG00000163046	0,925	1,424473661	0,85	0,96	0,15
Inhibitory	SYN2	ENSG00000157152	0,907	1,189138171	0,814	0,94	0,13

Inhibitory	GRIN2B	ENSG00000273079	0,901	1,170996221	0,802	0,94	0,14
Inhibitory	ATP8A2	ENSG00000132932	0,935	1,588379993	0,87	0,98	0,18
Inhibitory	LINGO2	ENSG00000174482	0,909	1,842833173	0,818	0,91	0,11
Inhibitory	MEG8	ENSG00000225746	0,916	1,382592735	0,832	0,94	0,14
Inhibitory	CACNA1B	ENSG00000148408	0,915	1,350261751	0,83	0,96	0,16
Inhibitory	SLC4A10	ENSG00000144290	0,907	1,240655264	0,814	0,93	0,13
Inhibitory	RIMS2	ENSG00000176406	0,934	1,717285279	0,868	0,99	0,19
Inhibitory	GRIA1	ENSG00000155511	0,908	1,629677278	0,816	0,91	0,11
Inhibitory	GABBR2	ENSG00000136928	0,896	1,071317696	0,792	0,91	0,11
Inhibitory	RAB3C	ENSG00000152932	0,907	1,293398766	0,814	0,93	0,14
Inhibitory	STMN2	ENSG00000104435	0,9	1,214506105	0,8	0,88	0,09
Inhibitory	GAD1	ENSG00000128683	0,899	1,273719137	0,798	0,85	0,07
Inhibitory	SCN2A	ENSG00000136531	0,914	1,180738096	0,828	0,96	0,18
Inhibitory	CELF5	ENSG00000161082	0,891	0,903235428	0,782	0,89	0,11
Inhibitory	KSR2	ENSG00000171435	0,905	1,217203155	0,81	0,94	0,16
Inhibitory	CALY	ENSG00000130643	0,898	1,300353501	0,796	0,88	0,1
Inhibitory	GABRB3	ENSG00000166206	0,899	1,185011986	0,798	0,95	0,17
Inhibitory	NMNAT2	ENSG00000157064	0,895	1,074049043	0,79	0,92	0,15
Inhibitory	DLGAP2	ENSG00000198010	0,894	1,375908015	0,788	0,9	0,13
Inhibitory	CHD5	ENSG00000116254	0,884	0,798762583	0,768	0,86	0,08
Inhibitory	GABRG2	ENSG00000113327	0,885	0,927703919	0,77	0,86	0,08
Inhibitory	DNM1	ENSG00000106976	0,901	1,020386023	0,802	0,93	0,16
Inhibitory	LRFN5	ENSG00000165379	0,904	1,439328787	0,808	0,94	0,17
Inhibitory	CDH18	ENSG00000145526	0,907	1,741167107	0,814	0,93	0,16
Inhibitory	SCN3A	ENSG00000153253	0,882	0,992108952	0,764	0,92	0,15
Inhibitory	CAMK2B	ENSG00000058404	0,877	0,85566681	0,754	0,92	0,16
Inhibitory	SYN3	ENSG00000185666	0,891	1,359065841	0,782	0,9	0,13
Inhibitory	FGF12	ENSG00000114279	0,908	1,497652419	0,816	0,97	0,21
Inhibitory	XKR4	ENSG00000206579	0,88	1,206421068	0,76	0,92	0,16
Inhibitory	IQSEC3	ENSG00000120645	0,88	0,822636302	0,76	0,84	0,08
Inhibitory	SNAP25	ENSG00000132639	0,916	1,306283357	0,832	0,97	0,21
Inhibitory	PTPRN2	ENSG00000155093	0,92	1,421382435	0,84	0,97	0,21
Inhibitory	CADPS	ENSG00000163618	0,918	1,441645933	0,836	0,98	0,22
Inhibitory	SHANK2	ENSG00000162105	0,874	0,926367262	0,748	0,91	0,15
Inhibitory	ARHGAP44	ENSG00000006740	0,895	1,072561869	0,79	0,93	0,18
Inhibitory	TMEM130	ENSG00000166448	0,877	0,816011651	0,754	0,84	0,08
Inhibitory	PRKAR1B	ENSG00000188191	0,887	0,898521826	0,774	0,91	0,15
Inhibitory	MAST1	ENSG00000105613	0,876	0,801430087	0,752	0,85	0,1
Inhibitory	RUNDC3B	ENSG00000105784	0,869	0,860614013	0,738	0,89	0,14
Inhibitory	FRRS1L	ENSG00000260230	0,885	0,885738038	0,77	0,91	0,16
Inhibitory	ELAVL4	ENSG00000162374	0,876	0,898241692	0,752	0,86	0,11
Inhibitory	ROBO2	ENSG00000185008	0,915	1,947208306	0,83	0,95	0,2
Inhibitory	TENM2	ENSG00000145934	0,909	1,939476844	0,818	0,93	0,18
Inhibitory	NRG1	ENSG00000157168	0,888	1,989118635	0,776	0,88	0,13
Inhibitory	JPH4	ENSG00000092051	0,869	0,765404704	0,738	0,85	0,1
Inhibitory	STXBP5L	ENSG00000145087	0,907	1,415515203	0,814	0,96	0,22
Inhibitory	DNAH14	ENSG00000185842	0,884	1,128068536	0,768	0,89	0,14
Inhibitory	UNC80	ENSG00000144406	0,87	0,960477595	0,74	0,95	0,21
Inhibitory	MIAT	ENSG00000225783	0,864	0,828659603	0,728	0,87	0,12
Inhibitory	EPHA6	ENSG00000080224	0,881	1,615982851	0,762	0,85	0,11
Inhibitory	HECW1	ENSG00000002746	0,863	1,026793938	0,726	0,88	0,14
Inhibitory	WNK2	ENSG00000165238	0,862	0,801954029	0,724	0,9	0,16
Inhibitory	SCN1A	ENSG00000144285	0,876	1,133632597	0,752	0,92	0,18
Inhibitory	PNMA2	ENSG00000240694	0,874	0,909834707	0,748	0,84	0,1
Inhibitory	TUSC3	ENSG00000104723	0,87	0,85947116	0,74	0,86	0,13

Inhibitory	AMPH	ENSG00000078053	0,87	0,950499396	0,74	0,87	0,14
Inhibitory	SYT16	ENSG00000139973	0,87	0,992562711	0,74	0,88	0,15
Inhibitory	CACNA1E	ENSG00000198216	0,866	1,002141388	0,732	0,87	0,14
Inhibitory	NSG2	ENSG00000170091	0,864	0,834742378	0,728	0,86	0,12
Inhibitory	UNC5D	ENSG00000156687	0,878	1,770226423	0,756	0,86	0,12
Inhibitory	GALNT17	ENSG00000185274	0,865	1,068898433	0,73	0,86	0,13
Inhibitory	NHS	ENSG00000188158	0,87	1,037517622	0,74	0,87	0,14
Inhibitory	DCLK1	ENSG00000133083	0,87	1,042346879	0,74	0,96	0,23
Inhibitory	SPTBN4	ENSG00000160460	0,903	1,130729588	0,806	0,96	0,23
Inhibitory	NEXMIF	ENSG00000050030	0,864	0,933752822	0,728	0,86	0,13
Inhibitory	SRRM4	ENSG00000139767	0,86	0,8637414	0,72	0,81	0,08
Inhibitory	OPCML	ENSG00000183715	0,85	1,049931609	0,7	0,93	0,2
Inhibitory	SYBU	ENSG00000147642	0,855	0,812093721	0,71	0,89	0,17
Inhibitory	KCNB2	ENSG00000182674	0,859	1,327553616	0,718	0,8	0,08
Inhibitory	AGBL4	ENSG00000186094	0,901	1,37057013	0,802	0,97	0,25
Inhibitory	FGF14	ENSG00000102466	0,895	1,40444024	0,79	0,99	0,27
Inhibitory	ATCAY	ENSG00000167654	0,857	0,741221493	0,714	0,85	0,12
Inhibitory	SNTG1	ENSG00000147481	0,862	1,428111885	0,724	0,9	0,18
Inhibitory	ELAVL2	ENSG00000107105	0,862	1,019827293	0,724	0,79	0,07
Inhibitory	REEP1	ENSG00000068615	0,859	0,780515137	0,718	0,84	0,12
Inhibitory	GRM7	ENSG00000196277	0,872	1,314210616	0,744	0,93	0,21
Inhibitory	SV2A	ENSG00000159164	0,872	0,924774382	0,744	0,88	0,16
Inhibitory	GRIP1	ENSG00000155974	0,909	1,812895749	0,818	0,94	0,22
Inhibitory	VSNL1	ENSG00000163032	0,86	0,960322804	0,72	0,8	0,09
Inhibitory	BASP1	ENSG00000176788	0,861	0,894255046	0,722	0,91	0,2
Inhibitory	SCN8A	ENSG00000196876	0,877	0,980368003	0,754	0,92	0,2
Inhibitory	ATP2B2	ENSG00000157087	0,852	0,851437559	0,704	0,92	0,21
Inhibitory	TENM3	ENSG00000218336	0,875	1,36597033	0,75	0,9	0,19
Inhibitory	GABRG3	ENSG00000182256	0,862	1,626489973	0,724	0,79	0,08
Inhibitory	ADD2	ENSG00000075340	0,852	0,723632421	0,704	0,81	0,1
Inhibitory	GRM5	ENSG00000168959	0,86	1,259528945	0,72	0,9	0,19
Inhibitory	DOK6	ENSG00000206052	0,861	1,196311109	0,722	0,86	0,15
Inhibitory	CCSER1	ENSG00000184305	0,92	1,593809097	0,84	0,98	0,27
Inhibitory	OSBPL6	ENSG00000079156	0,858	0,922246959	0,716	0,93	0,23
Inhibitory	SNRPN	ENSG00000128739	0,91	1,340384	0,82	0,95	0,25
Inhibitory	SUSD4	ENSG00000143502	0,843	0,727688198	0,686	0,82	0,12
Inhibitory	GRIK2	ENSG00000164418	0,923	1,690183704	0,846	0,98	0,28
Inhibitory	ANK1	ENSG00000029534	0,849	0,90097065	0,698	0,79	0,09
Inhibitory	NOL4	ENSG00000101746	0,839	0,805841303	0,678	0,9	0,2
Inhibitory	FRMPD4	ENSG00000169933	0,852	1,205309007	0,704	0,86	0,16
Inhibitory	GAP43	ENSG00000172020	0,847	0,863428352	0,694	0,8	0,1
Inhibitory	SLC35F1	ENSG00000196376	0,836	0,765124243	0,672	0,91	0,22
Inhibitory	CACNA1A	ENSG00000141837	0,858	0,944166512	0,716	0,96	0,26
Inhibitory	CLSTN3	ENSG00000139182	0,845	0,666068914	0,69	0,79	0,09
Inhibitory	MTUS2	ENSG00000132938	0,848	1,292901538	0,696	0,8	0,11
Inhibitory	ATRNL1	ENSG00000107518	0,828	0,798592829	0,656	0,9	0,2
Inhibitory	KCNC2	ENSG00000166006	0,845	1,185218603	0,69	0,77	0,08
Inhibitory	THY1	ENSG00000154096	0,847	0,841032462	0,694	0,8	0,11
Inhibitory	ZNF385D	ENSG00000151789	0,856	1,494525072	0,712	0,82	0,12
Inhibitory	KCNJ3	ENSG00000162989	0,838	0,906611325	0,676	0,83	0,14
Inhibitory	KCNC1	ENSG00000129159	0,845	0,669656256	0,69	0,78	0,09
Inhibitory	BTBD11	ENSG00000151136	0,839	0,862978323	0,678	0,8	0,11
Inhibitory	RIMBP2	ENSG00000060709	0,848	0,802025713	0,696	0,83	0,14
Inhibitory	PLCB4	ENSG00000101333	0,843	0,930028884	0,686	0,92	0,23
Inhibitory	CACNG2	ENSG00000166862	0,842	0,756705235	0,684	0,79	0,1

Inhibitory	PLPPR4	ENSG00000117600	0,838	0,658868444	0,676	0,8	0,11
Inhibitory	MYH10	ENSG00000133026	0,847	0,770543287	0,694	0,87	0,18
Inhibitory	SLC12A5	ENSG00000124140	0,845	0,689128543	0,69	0,76	0,07
Inhibitory	RPH3A	ENSG00000089169	0,844	0,969802767	0,688	0,77	0,08
Inhibitory	BICDL1	ENSG00000135127	0,842	0,693943328	0,684	0,8	0,12
Inhibitory	RIMS1	ENSG00000079841	0,877	1,096066305	0,754	0,95	0,26
Inhibitory	VAT1L	ENSG00000171724	0,852	0,985925217	0,704	0,83	0,14
Inhibitory	GABRB1	ENSG00000163288	0,859	1,116021983	0,718	0,93	0,25
Inhibitory	GABRB2	ENSG00000145864	0,844	1,191585426	0,688	0,78	0,1
Inhibitory	SGCZ	ENSG00000185053	0,86	1,674728273	0,72	0,86	0,17
Inhibitory	ADAM23	ENSG00000114948	0,846	0,868605947	0,692	0,89	0,2
Inhibitory	NRSN1	ENSG00000152954	0,839	0,675950697	0,678	0,77	0,09
Inhibitory	KIAA1549L	ENSG00000110427	0,833	0,801089812	0,666	0,81	0,13
Inhibitory	STXBP5-AS1	ENSG00000233452	0,847	1,063369731	0,694	0,83	0,15
Inhibitory	SLC41A2	ENSG00000136052	0,836	0,716423378	0,672	0,82	0,14
Inhibitory	CNTNAP5	ENSG00000155052	0,848	1,334142491	0,696	0,86	0,17
Inhibitory	SORBS2	ENSG00000154556	0,84	0,895388351	0,68	0,9	0,22
Inhibitory	KLHL29	ENSG00000119771	0,838	0,838466676	0,676	0,81	0,13
Inhibitory	MAP7D2	ENSG00000184368	0,839	0,645305241	0,678	0,76	0,08
Inhibitory	DPY19L2	ENSG00000177990	0,835	0,708174251	0,67	0,83	0,16
Inhibitory	OLFM3	ENSG00000118733	0,844	1,11639857	0,688	0,8	0,13
Inhibitory	SLC8A3	ENSG00000100678	0,828	0,685829891	0,656	0,81	0,13
Inhibitory	FHOD3	ENSG00000134775	0,839	0,892411753	0,678	0,82	0,14
Inhibitory	GNB5	ENSG00000069966	0,832	0,613790787	0,664	0,81	0,14
Inhibitory	FAM155A	ENSG00000204442	0,92	1,666660882	0,84	1	0,32
Inhibitory	PTPRN	ENSG00000054356	0,837	0,671626395	0,674	0,75	0,07
Inhibitory	CACNB2	ENSG00000165995	0,862	1,116516623	0,724	0,95	0,27
Inhibitory	GUCY1A2	ENSG00000152402	0,841	1,004564084	0,682	0,86	0,19
Inhibitory	KIF5A	ENSG00000155980	0,838	0,648924338	0,676	0,79	0,12
Inhibitory	PLXNA4	ENSG00000221866	0,834	0,908346883	0,668	0,81	0,14
Inhibitory	PRICKLE1	ENSG00000139174	0,831	0,834727785	0,662	0,79	0,11
Inhibitory	ELMOD1	ENSG00000110675	0,827	0,672459681	0,654	0,82	0,14
Inhibitory	PPM1E	ENSG00000175175	0,87	1,038778265	0,74	0,94	0,26
Inhibitory	DSCAM	ENSG00000171587	0,852	0,793775248	0,704	0,97	0,3
Inhibitory	CNTN4	ENSG00000144619	0,848	1,413660015	0,696	0,83	0,16
Inhibitory	KHDRBS2	ENSG00000112232	0,857	1,19826517	0,714	0,9	0,23
Inhibitory	DGKB	ENSG00000136267	0,844	1,170541804	0,688	0,87	0,2
Inhibitory	SYN1	ENSG00000008056	0,834	0,671378849	0,668	0,75	0,08
Inhibitory	SLC24A3	ENSG00000185052	0,828	0,949229612	0,656	0,82	0,15
Inhibitory	TMEM196	ENSG00000173452	0,836	0,757045053	0,672	0,73	0,06
Inhibitory	PTPRR	ENSG00000153233	0,834	0,939827042	0,668	0,75	0,08
Inhibitory	PAM	ENSG00000145730	0,852	1,082241382	0,704	0,93	0,26
Inhibitory	CLVS1	ENSG00000177182	0,826	0,689423136	0,652	0,83	0,17
Inhibitory	CNNM1	ENSG00000119946	0,829	0,592547848	0,658	0,75	0,08
Inhibitory	LRRTM4	ENSG00000176204	0,883	1,560585365	0,766	0,95	0,28
Inhibitory	ABLIM2	ENSG00000163995	0,834	0,73292776	0,668	0,85	0,19
Inhibitory	TENM1	ENSG00000009694	0,84	1,148241861	0,68	0,79	0,13
Inhibitory	SLC38A1	ENSG00000111371	0,819	0,630666083	0,638	0,88	0,22
Inhibitory	SLC8A1	ENSG00000183023	0,814	0,759841661	0,628	0,95	0,28
Inhibitory	CNTN5	ENSG00000149972	0,847	1,800391895	0,694	0,79	0,13
Inhibitory	LHFPL4	ENSG00000156959	0,823	0,585387039	0,646	0,78	0,12
Inhibitory	RYR2	ENSG00000198626	0,886	1,421852643	0,772	0,93	0,27
Inhibitory	RALYL	ENSG00000184672	0,841	1,25587784	0,682	0,9	0,24
Inhibitory	HS6ST3	ENSG00000185352	0,842	1,442066043	0,684	0,84	0,19
Inhibitory	ASIC2	ENSG00000108684	0,837	1,293497585	0,674	0,79	0,13

Inhibitory	RNF175	ENSG00000145428	0,826	0,620386427	0,652	0,74	0,09
Inhibitory	SIDT1	ENSG00000072858	0,823	0,691161446	0,646	0,76	0,1
Inhibitory	C11orf80	ENSG00000173715	0,823	0,643993765	0,646	0,81	0,15
Inhibitory	STXBP1	ENSG00000136854	0,873	0,877591398	0,746	0,94	0,29
Inhibitory	RALGPS2	ENSG00000116191	0,816	0,660407037	0,632	0,84	0,18
Inhibitory	ZNF804A	ENSG00000170396	0,833	1,332745368	0,666	0,79	0,13
Inhibitory	DLGAP1	ENSG00000170579	0,857	1,230465092	0,714	0,93	0,27
Inhibitory	KCNH7	ENSG00000184611	0,831	1,274707872	0,662	0,76	0,1
Inhibitory	SNAP91	ENSG00000065609	0,887	1,067245227	0,774	0,97	0,32
Inhibitory	HSPA4L	ENSG00000164070	0,832	0,727358956	0,664	0,84	0,19
Inhibitory	SYP	ENSG00000102003	0,83	0,68455285	0,66	0,85	0,2
Inhibitory	SLC2A13	ENSG00000151229	0,821	0,867318017	0,642	0,88	0,23
Inhibitory	CNTN1	ENSG00000018236	0,808	0,755257716	0,616	0,98	0,32
Inhibitory	KCND2	ENSG00000184408	0,808	0,770919252	0,616	0,93	0,27
Inhibitory	EPHA5	ENSG00000145242	0,828	1,055605463	0,656	0,75	0,09
Inhibitory	RBFOX3	ENSG00000167281	0,823	0,728881982	0,646	0,73	0,08
Inhibitory	SEZ6L	ENSG00000100095	0,813	0,837740692	0,626	0,81	0,16
Inhibitory	EPB41L4B	ENSG00000095203	0,825	0,726715165	0,65	0,77	0,12
Inhibitory	SLC44A5	ENSG00000137968	0,83	1,150342245	0,66	0,79	0,14
Inhibitory	ANO5	ENSG00000171714	0,812	0,611031978	0,624	0,79	0,14
Inhibitory	CSMD2	ENSG00000121904	0,826	0,844968183	0,652	0,9	0,25
Inhibitory	INA	ENSG00000148798	0,825	0,691027456	0,65	0,71	0,06
Inhibitory	GNAL	ENSG00000141404	0,818	0,703495804	0,636	0,78	0,13
Inhibitory	MDGA2	ENSG00000139915	0,873	1,247088384	0,746	0,98	0,34
Inhibitory	LRRC7	ENSG00000033122	0,858	1,126787265	0,716	0,94	0,3
Inhibitory	NAP1L3	ENSG00000186310	0,826	0,708274419	0,652	0,76	0,12
Inhibitory	SCN7A	ENSG00000136546	0,821	0,738566027	0,642	0,72	0,07
Inhibitory	DENND1B	ENSG00000213047	0,809	0,614360383	0,618	0,81	0,16
Inhibitory	EFNA5	ENSG00000184349	0,819	1,037187884	0,638	0,79	0,14
Inhibitory	ADGRL2	ENSG00000117114	0,823	1,168856954	0,646	0,78	0,13
Inhibitory	TRERF1	ENSG00000124496	0,81	0,64224479	0,62	0,81	0,17
Inhibitory	RNF150	ENSG00000170153	0,799	0,612670477	0,598	0,87	0,23
Inhibitory	PCDH7	ENSG00000169851	0,841	1,223159193	0,682	0,91	0,27
Inhibitory	AC073050.1	ENSG00000228222	0,827	1,094393444	0,654	0,81	0,17
Inhibitory	ASTN1	ENSG00000152092	0,813	0,690379015	0,626	0,91	0,27
Inhibitory	SYT14	ENSG00000143469	0,831	0,745663131	0,662	0,91	0,27
Inhibitory	FP700111.1	ENSG00000224363	0,826	0,764814838	0,652	0,9	0,26
Inhibitory	PRR16	ENSG00000184838	0,818	1,054337686	0,636	0,73	0,09
Inhibitory	AC092683.1	ENSG00000230606	0,888	1,095017179	0,776	0,96	0,32
Inhibitory	CSMD3	ENSG00000164796	0,875	1,301400114	0,75	0,97	0,33
Inhibitory	TMEM59L	ENSG00000105696	0,817	0,681121866	0,634	0,76	0,12
Inhibitory	KIAA1211	ENSG00000109265	0,816	0,760794592	0,632	0,85	0,21
Inhibitory	PODXL2	ENSG00000114631	0,816	0,592125932	0,632	0,82	0,18
Inhibitory	CAP2	ENSG00000112186	0,812	0,62225382	0,624	0,76	0,12
Inhibitory	TSPYL1	ENSG00000189241	0,819	0,665194455	0,638	0,76	0,13
Inhibitory	LINC00599	ENSG00000253230	0,816	0,597439322	0,632	0,72	0,08
Inhibitory	GABRA2	ENSG00000151834	0,814	0,762712277	0,628	0,73	0,1
Inhibitory	CAMK4	ENSG00000152495	0,813	0,758696983	0,626	0,76	0,13
Inhibitory	KCTD16	ENSG00000183775	0,832	1,127332933	0,664	0,84	0,21
Inhibitory	CACNA1D	ENSG00000157388	0,817	0,699645657	0,634	0,91	0,27
Inhibitory	PAK5	ENSG00000101349	0,804	0,590516517	0,608	0,75	0,12
Inhibitory	HCN1	ENSG00000164588	0,817	1,081787809	0,634	0,71	0,08
Inhibitory	SPTAN1	ENSG00000197694	0,838	0,777238692	0,676	0,94	0,31
Inhibitory	PCSK1N	ENSG00000102109	0,836	1,143816	0,672	0,84	0,21
Inhibitory	CIT	ENSG00000122966	0,811	0,606386437	0,622	0,83	0,2

Inhibitory	PWRN1	ENSG00000259905	0,814	0,742698781	0,628	0,88	0,26
Inhibitory	RGS17	ENSG00000091844	0,813	0,699702243	0,626	0,73	0,1
Inhibitory	TSPYL2	ENSG00000184205	0,81	0,621790103	0,62	0,8	0,17
Inhibitory	JAKMIP1	ENSG00000152969	0,808	0,614610455	0,616	0,72	0,1
Inhibitory	NYAP2	ENSG00000144460	0,808	0,626023842	0,616	0,7	0,07
Inhibitory	EPHB1	ENSG00000154928	0,82	0,886315092	0,64	0,8	0,17
Inhibitory	EPB41	ENSG00000159023	0,799	0,590256943	0,598	0,82	0,19
Inhibitory	PCDH15	ENSG00000150275	0,808	1,151708947	0,616	0,81	0,18
Inhibitory	CACNA1C	ENSG00000151067	0,86	0,982182814	0,72	0,96	0,33
Inhibitory	CERS6	ENSG00000172292	0,799	0,654044099	0,598	0,9	0,27
Inhibitory	CNKSR2	ENSG00000149970	0,796	0,678234012	0,592	0,8	0,18
Inhibitory	ANKRD34C-AS1	ENSG00000259234	0,807	0,702402537	0,614	0,69	0,07
Inhibitory	PCLO	ENSG00000186472	0,897	1,195580292	0,794	0,97	0,35
Inhibitory	LONRF2	ENSG00000170500	0,819	0,741615047	0,638	0,86	0,25
Inhibitory	NDRG4	ENSG00000103034	0,803	0,637434458	0,606	0,75	0,13
Inhibitory	SCG2	ENSG00000171951	0,805	0,901597428	0,61	0,7	0,09
Inhibitory	GALNTL6	ENSG00000174473	0,811	1,531383094	0,622	0,74	0,13
Inhibitory	PGM2L1	ENSG00000165434	0,798	0,586661053	0,596	0,72	0,11
Inhibitory	BRINP1	ENSG00000078725	0,792	0,664313409	0,584	0,77	0,16
Inhibitory	NRG3	ENSG00000185737	0,818	0,865418522	0,636	0,98	0,38
Inhibitory	XKR6	ENSG00000171044	0,874	1,080168463	0,748	0,96	0,36
Inhibitory	DAAM1	ENSG00000100592	0,807	0,62545302	0,614	0,91	0,31
Inhibitory	KCNJ6	ENSG00000157542	0,795	0,684701719	0,59	0,7	0,1
Inhibitory	MAP2	ENSG00000078018	0,908	1,262956737	0,816	0,99	0,39
Inhibitory	TMEM132B	ENSG00000139364	0,797	0,806746456	0,594	0,76	0,16
Inhibitory	SEZ6L2	ENSG00000174938	0,808	0,659791481	0,616	0,84	0,24
Inhibitory	SAMD5	ENSG00000203727	0,802	1,081841077	0,604	0,67	0,07
Inhibitory	FBXL2	ENSG00000153558	0,796	0,604574873	0,592	0,85	0,24
Inhibitory	ADCY1	ENSG00000164742	0,792	0,599426349	0,584	0,75	0,14
Inhibitory	GPC6	ENSG00000183098	0,821	1,468298647	0,642	0,8	0,2
Inhibitory	PATJ	ENSG00000132849	0,819	0,788143299	0,638	0,9	0,3
Inhibitory	FRY	ENSG00000073910	0,795	0,663852359	0,59	0,93	0,34
Inhibitory	MPP6	ENSG00000105926	0,793	0,657550084	0,586	0,74	0,15
Inhibitory	NDST3	ENSG00000164100	0,797	0,906800784	0,594	0,68	0,08
Inhibitory	SNCG	ENSG00000173267	0,797	0,730569437	0,594	0,67	0,08
Inhibitory	RAPGEF4	ENSG00000091428	0,805	0,70426135	0,61	0,92	0,33
Inhibitory	AFF2	ENSG00000155966	0,797	0,875558596	0,594	0,67	0,07
Inhibitory	KCNIP4	ENSG00000185774	0,819	1,23998003	0,638	0,87	0,27
Inhibitory	VPS13A	ENSG00000197969	0,793	0,586151107	0,586	0,87	0,28
Inhibitory	PIP5K1B	ENSG00000107242	0,787	0,59102149	0,574	0,74	0,14
Inhibitory	EML6	ENSG00000214595	0,784	0,629050424	0,568	0,82	0,22
Inhibitory	GRM1	ENSG00000152822	0,797	1,010832377	0,594	0,68	0,08
Inhibitory	KIAA0825	ENSG00000185261	0,793	0,653278166	0,586	0,87	0,28
Inhibitory	KCNQ5	ENSG00000185760	0,801	1,625554606	0,602	0,67	0,08
Inhibitory	LINC02389	ENSG00000255693	0,795	0,702492662	0,59	0,67	0,08
Inhibitory	TMEM178B	ENSG00000261115	0,865	1,046041374	0,73	0,96	0,37
Inhibitory	ERC2	ENSG00000187672	0,836	0,967397707	0,672	0,93	0,34
Inhibitory	EEF1A2	ENSG00000101210	0,798	0,661161819	0,596	0,7	0,11
Inhibitory	TMEM108	ENSG00000144868	0,782	0,626305544	0,564	0,85	0,26
Inhibitory	SGSM1	ENSG00000167037	0,796	0,625693084	0,592	0,88	0,29
Inhibitory	UCHL1	ENSG00000154277	0,811	0,772175085	0,622	0,86	0,27
Inhibitory	VSTM2A	ENSG00000170419	0,795	0,640372607	0,59	0,64	0,06
Inhibitory	BEND6	ENSG00000151917	0,789	0,606728012	0,578	0,73	0,14
Inhibitory	SHISA9	ENSG00000237515	0,785	0,854564228	0,57	0,75	0,16

Inhibitory	AL033504.1	ENSG00000227681	0,794	1,068356182	0,588	0,65	0,07
Inhibitory	BAIAP3	ENSG00000007516	0,789	0,703725622	0,578	0,68	0,09
Inhibitory	LINC00632	ENSG00000203930	0,872	0,983036755	0,744	0,95	0,36
Inhibitory	PACRG	ENSG00000112530	0,788	0,693893988	0,576	0,81	0,22
Inhibitory	GABRA1	ENSG00000022355	0,792	0,788009771	0,584	0,65	0,07
Inhibitory	LINC01122	ENSG00000233723	0,783	0,720976516	0,566	0,78	0,2
Inhibitory	DAB1	ENSG00000173406	0,873	1,374225675	0,746	0,95	0,37
Inhibitory	AFF3	ENSG00000144218	0,828	0,848989304	0,656	0,95	0,36
Inhibitory	PLCXD3	ENSG00000182836	0,788	0,823298858	0,576	0,68	0,1
Inhibitory	PCSK2	ENSG00000125851	0,782	0,721793257	0,564	0,69	0,11
Inhibitory	GPR158	ENSG00000151025	0,781	0,655627662	0,562	0,88	0,3
Inhibitory	CCDC85A	ENSG00000055813	0,78	0,704837887	0,56	0,73	0,14
Inhibitory	BRINP3	ENSG00000162670	0,783	0,863121488	0,566	0,78	0,2
Inhibitory	RAB27B	ENSG00000041353	0,787	0,681203621	0,574	0,65	0,07
Inhibitory	FAM189A1	ENSG00000104059	0,783	0,61656823	0,566	0,68	0,1
Inhibitory	CSMD1	ENSG00000183117	0,862	1,208347276	0,724	0,96	0,38
Inhibitory	PRKG1	ENSG00000185532	0,799	1,141678735	0,598	0,82	0,24
Inhibitory	MIR137HG	ENSG00000225206	0,789	0,937050277	0,578	0,67	0,09
Inhibitory	LY6H	ENSG00000176956	0,787	0,67699362	0,574	0,65	0,07
Inhibitory	CSRNP3	ENSG00000178662	0,844	0,855791063	0,688	0,95	0,37
Inhibitory	AC025159.1	ENSG00000257815	0,809	0,892567737	0,618	0,87	0,3
Inhibitory	EPHA7	ENSG00000135333	0,783	0,814235887	0,566	0,66	0,09
Inhibitory	NRXN1	ENSG00000179915	0,826	0,9549001	0,652	0,99	0,42
Inhibitory	SLC35F4	ENSG00000151812	0,786	1,080945425	0,572	0,64	0,07
Inhibitory	RANBP17	ENSG00000204764	0,781	0,649056774	0,562	0,86	0,29
Inhibitory	FAAH2	ENSG00000165591	0,78	0,593010027	0,56	0,72	0,16
Inhibitory	NELL2	ENSG00000184613	0,772	0,662350851	0,544	0,7	0,13
Inhibitory	SCN9A	ENSG00000169432	0,774	0,678715056	0,548	0,71	0,14
Inhibitory	LINC01414	ENSG00000253554	0,782	0,895161395	0,564	0,66	0,09
Inhibitory	FLRT2	ENSG00000185070	0,773	0,757354018	0,546	0,76	0,2
Inhibitory	ZFYVE9	ENSG00000157077	0,79	0,587965924	0,58	0,89	0,33
Inhibitory	FAT3	ENSG00000165323	0,765	0,697816077	0,53	0,77	0,21
Inhibitory	FOCAD	ENSG00000188352	0,836	0,901211492	0,672	0,94	0,38
Inhibitory	SLC25A12	ENSG00000115840	0,814	0,715639321	0,628	0,91	0,35
Inhibitory	KIAA1217	ENSG00000120549	0,782	0,981066822	0,564	0,8	0,24
Inhibitory	LIN7A	ENSG00000111052	0,77	0,585167011	0,54	0,68	0,13
Inhibitory	LINC01250	ENSG00000234423	0,777	0,591919153	0,554	0,63	0,08
Inhibitory	KLHL1	ENSG00000150361	0,773	0,882366615	0,546	0,65	0,1
Inhibitory	PCNX2	ENSG00000135749	0,804	0,639704512	0,608	0,94	0,39
Inhibitory	INPP4B	ENSG00000109452	0,809	1,117520692	0,618	0,83	0,28
Inhibitory	CHRM2	ENSG00000181072	0,775	1,14696824	0,55	0,61	0,06
Inhibitory	RGS7	ENSG00000182901	0,831	1,042741003	0,662	0,96	0,41
Inhibitory	SLC22A17	ENSG00000092096	0,799	0,7092015	0,598	0,88	0,33
Inhibitory	IDS	ENSG00000010404	0,816	0,799009776	0,632	0,89	0,34
Inhibitory	PCDH11X	ENSG00000102290	0,783	1,441847982	0,566	0,65	0,1
Inhibitory	MCF2L2	ENSG00000053524	0,8	0,693422173	0,6	0,91	0,36
Inhibitory	KIFAP3	ENSG00000075945	0,815	0,70150334	0,63	0,92	0,37
Inhibitory	TENM4	ENSG00000149256	0,807	0,875324106	0,614	0,9	0,35
Inhibitory	MAGI3	ENSG00000081026	0,772	0,614709142	0,544	0,85	0,31
Inhibitory	HSPA12A	ENSG00000165868	0,818	0,752969966	0,636	0,92	0,38
Inhibitory	CALM3	ENSG00000160014	0,773	0,612167635	0,546	0,77	0,23
Inhibitory	BEX1	ENSG00000133169	0,77	0,632974569	0,54	0,64	0,1
Inhibitory	MARCH11	ENSG00000183654	0,773	0,612612118	0,546	0,59	0,05
Inhibitory	SORCS3	ENSG00000156395	0,763	0,768088123	0,526	0,68	0,14
Inhibitory	PLEKHA5	ENSG00000052126	0,802	0,698636277	0,604	0,96	0,42

Inhibitory	TMTC1	ENSG00000133687	0,754	0,586473116	0,508	0,77	0,23
Inhibitory	NEFL	ENSG00000277586	0,77	0,614900383	0,54	0,6	0,06
Inhibitory	YWHAG	ENSG00000170027	0,783	0,604144863	0,566	0,89	0,35
Inhibitory	PTPRO	ENSG00000151490	0,765	0,885093642	0,53	0,65	0,11
Inhibitory	KIF26B	ENSG00000162849	0,762	0,776723642	0,524	0,74	0,2
Inhibitory	PEG10	ENSG00000242265	0,765	0,733380884	0,53	0,67	0,14
Inhibitory	DCC	ENSG00000187323	0,778	1,178689617	0,556	0,77	0,24
Inhibitory	FGF13	ENSG00000129682	0,761	0,850179742	0,522	0,61	0,08
Inhibitory	DGKI	ENSG00000157680	0,802	0,78458939	0,604	0,92	0,39
Inhibitory	CLSTN2	ENSG00000158258	0,764	0,871855219	0,528	0,65	0,12
Inhibitory	AC090578.1	ENSG00000253553	0,76	0,632594494	0,52	0,62	0,1
Inhibitory	RUNX1T1	ENSG00000079102	0,752	0,599287068	0,504	0,81	0,28
Inhibitory	ADAM22	ENSG00000008277	0,793	0,663909384	0,586	0,91	0,39
Inhibitory	KCNH5	ENSG00000140015	0,761	0,760245231	0,522	0,6	0,07
Inhibitory	NSF	ENSG00000073969	0,856	0,922774397	0,712	0,96	0,44
Inhibitory	UNC79	ENSG00000133958	0,831	0,817328033	0,662	0,96	0,43
Inhibitory	CTNNA2	ENSG00000066032	0,784	0,750675418	0,568	0,98	0,45
Inhibitory	UNC13C	ENSG00000137766	0,76	0,930225392	0,52	0,6	0,08
Inhibitory	CNTN3	ENSG00000113805	0,749	0,600378802	0,498	0,69	0,17
Inhibitory	MGAT4C	ENSG00000182050	0,757	1,009028254	0,514	0,71	0,19
Inhibitory	KALRN	ENSG00000160145	0,763	0,591984388	0,526	0,93	0,41
Inhibitory	AC120193.1	ENSG00000253535	0,759	1,003448804	0,518	0,63	0,12
Inhibitory	PTCHD4	ENSG00000244694	0,755	0,764093843	0,51	0,59	0,08
Inhibitory	FSTL5	ENSG00000168843	0,772	1,075541621	0,544	0,74	0,22
Inhibitory	VWC2L	ENSG00000174453	0,754	0,701724206	0,508	0,58	0,06
Inhibitory	GRM8	ENSG00000179603	0,757	1,059625104	0,514	0,62	0,11
Inhibitory	SCN1A-AS1	ENSG00000236107	0,753	0,691597659	0,506	0,59	0,08
Inhibitory	UBA6-AS1	ENSG00000248049	0,776	0,727422578	0,552	0,89	0,39
Inhibitory	CACNA2D3	ENSG00000157445	0,748	0,743877261	0,496	0,78	0,28
Inhibitory	PTPRT	ENSG00000196090	0,752	1,165129105	0,504	0,64	0,14
Inhibitory	CDH4	ENSG00000179242	0,757	0,856863091	0,514	0,71	0,22
Inhibitory	TRPC5	ENSG00000072315	0,746	0,702327319	0,492	0,58	0,08
Inhibitory	MCTP1	ENSG00000175471	0,739	0,623524658	0,478	0,66	0,16
Inhibitory	DPP10	ENSG00000175497	0,754	0,732469881	0,508	0,8	0,31
Inhibitory	TAFA2	ENSG00000198673	0,748	0,893919966	0,496	0,7	0,21
Inhibitory	GRIN3A	ENSG00000198785	0,745	0,630432596	0,49	0,55	0,06
Inhibitory	CNTN6	ENSG00000134115	0,745	0,681287378	0,49	0,58	0,08
Inhibitory	NXPH1	ENSG00000122584	0,745	1,249871182	0,49	0,61	0,11
Inhibitory	MYO16	ENSG00000041515	0,75	0,96508435	0,5	0,59	0,11
Inhibitory	RIT2	ENSG00000152214	0,74	0,790470423	0,48	0,59	0,1
Inhibitory	ZNF385B	ENSG00000144331	0,738	0,799711423	0,476	0,59	0,1
Inhibitory	ST6GALNAC5	ENSG00000117069	0,743	1,138927966	0,486	0,54	0,06
Inhibitory	LUZP2	ENSG00000187398	0,728	0,686209141	0,456	0,73	0,24
Inhibitory	ZMAT4	ENSG00000165061	0,739	0,885234803	0,478	0,55	0,07
Inhibitory	GRIN2A	ENSG00000183454	0,737	0,861093227	0,474	0,62	0,14
Inhibitory	FRMD4A	ENSG00000151474	0,832	0,834691255	0,664	0,98	0,5
Inhibitory	HTR2C	ENSG00000147246	0,741	1,324997194	0,482	0,55	0,08
Inhibitory	CDH12	ENSG00000154162	0,757	1,46445356	0,514	0,65	0,17
Inhibitory	ZFPM2	ENSG00000169946	0,747	0,802255189	0,494	0,76	0,28
Inhibitory	PREPL	ENSG00000138078	0,815	0,71226972	0,63	0,94	0,47
Inhibitory	GRIA3	ENSG00000125675	0,743	0,629124702	0,486	0,81	0,34
Inhibitory	CPNE4	ENSG00000196353	0,731	0,708902701	0,462	0,56	0,09
Inhibitory	THSD7A	ENSG00000005108	0,728	0,639084663	0,456	0,74	0,27
Inhibitory	AC233296.1	ENSG00000280870	0,742	0,733442457	0,484	0,81	0,34
Inhibitory	CHRM3	ENSG00000133019	0,735	1,04545439	0,47	0,54	0,07

Inhibitory	SLIT2	ENSG00000145147	0,731	0,789192033	0,462	0,66	0,19
Inhibitory	MPPED2	ENSG00000066382	0,727	0,605157786	0,454	0,65	0,19
Inhibitory	GRID2	ENSG00000152208	0,848	1,294900442	0,696	0,96	0,5
Inhibitory	ZNF804B	ENSG00000182348	0,733	1,201914001	0,466	0,54	0,08
Inhibitory	DANT2	ENSG00000235244	0,79	0,683248501	0,58	0,94	0,48
Inhibitory	RBFOX1	ENSG00000078328	0,795	1,236704788	0,59	0,91	0,45
Inhibitory	HS6ST2	ENSG00000171004	0,727	0,623112734	0,454	0,54	0,08
Inhibitory	DYNC1I1	ENSG00000158560	0,789	0,691993606	0,578	0,96	0,5
Inhibitory	SEMA6D	ENSG00000137872	0,737	0,876412526	0,474	0,73	0,27
Inhibitory	VWC2	ENSG00000188730	0,721	0,588096734	0,442	0,55	0,1
Inhibitory	SLC35F3	ENSG00000183780	0,713	0,605319691	0,426	0,74	0,29
Inhibitory	MACROD2	ENSG00000172264	0,795	0,794784511	0,59	0,98	0,53
Inhibitory	CUX2	ENSG00000111249	0,72	0,676735194	0,44	0,52	0,08
Inhibitory	DENND5B	ENSG00000170456	0,779	0,612499857	0,558	0,95	0,5
Inhibitory	CEP112	ENSG00000154240	0,715	0,59922875	0,43	0,71	0,26
Inhibitory	KCNT2	ENSG00000162687	0,714	0,609211295	0,428	0,57	0,13
Inhibitory	TAFA1	ENSG00000183662	0,715	0,906919816	0,43	0,58	0,14
Inhibitory	GRIK1	ENSG00000171189	0,716	0,938906971	0,432	0,58	0,15
Inhibitory	NELL1	ENSG00000165973	0,718	1,170079019	0,436	0,5	0,07
Inhibitory	NLGN1	ENSG00000169760	0,78	0,779300502	0,56	0,98	0,54
Inhibitory	ANKRD30B	ENSG00000180777	0,716	0,612700257	0,432	0,47	0,04
Inhibitory	LDB2	ENSG00000169744	0,711	0,718556445	0,422	0,6	0,18
Inhibitory	TMEM132D	ENSG00000151952	0,707	0,690964702	0,414	0,56	0,13
Inhibitory	ZFHX3	ENSG00000140836	0,722	0,699366013	0,444	0,84	0,42
Inhibitory	PCDH11Y	ENSG00000099715	0,713	1,121597	0,426	0,51	0,08
Inhibitory	FRAS1	ENSG00000138759	0,707	0,647815308	0,414	0,49	0,07
Inhibitory	CNTNAP2	ENSG00000174469	0,86	1,256891233	0,72	0,99	0,57
Inhibitory	SDK1	ENSG00000146555	0,705	0,70876211	0,41	0,67	0,26
Inhibitory	GULP1	ENSG00000144366	0,706	0,800482515	0,412	0,5	0,09
Inhibitory	LRRC4C	ENSG00000148948	0,811	0,819884656	0,622	0,96	0,54
Inhibitory	PPFIA2	ENSG00000139220	0,795	0,74314529	0,59	0,97	0,56
Inhibitory	SYNE1	ENSG00000131018	0,786	0,585089578	0,572	0,96	0,56
Inhibitory	COL25A1	ENSG00000188517	0,701	0,843559511	0,402	0,49	0,08
Inhibitory	TTTY14	ENSG00000176728	0,745	0,744464688	0,49	0,81	0,41
Inhibitory	GRIA4	ENSG00000152578	0,771	0,742107738	0,542	0,94	0,54
Inhibitory	CDH13	ENSG00000140945	0,704	0,890473727	0,408	0,59	0,2
Inhibitory	HDAC9	ENSG00000048052	0,726	0,613625587	0,452	0,88	0,48
Inhibitory	NBEA	ENSG00000172915	0,87	1,100140504	0,74	0,97	0,58
Inhibitory	AC124312.1	ENSG00000214265	0,89	1,011345238	0,78	0,98	0,6
Inhibitory	ROBO1	ENSG00000169855	0,869	1,518487213	0,738	0,96	0,58
Inhibitory	SMYD3	ENSG00000185420	0,781	0,704915435	0,562	0,96	0,6
Inhibitory	NEGR1	ENSG00000172260	0,817	1,046426234	0,634	0,98	0,62
Inhibitory	GNAS	ENSG00000087460	0,887	1,30332537	0,774	0,98	0,63
Inhibitory	NRXN3	ENSG00000021645	0,896	1,380081004	0,792	0,98	0,63
Inhibitory	KAZN	ENSG00000189337	0,851	1,108212135	0,702	0,98	0,66
Inhibitory	MAP1B	ENSG00000131711	0,81	0,77881359	0,62	0,98	0,67
Inhibitory	NOVA1	ENSG00000139910	0,774	0,670371029	0,548	0,97	0,67
Inhibitory	AHI1	ENSG00000135541	0,851	0,856484916	0,702	0,98	0,68
Inhibitory	PDE4D	ENSG00000113448	0,775	0,820152719	0,55	0,97	0,69
Inhibitory	ANKS1B	ENSG00000185046	0,748	0,608692262	0,496	0,98	0,75
Inhibitory	CAMTA1	ENSG00000171735	0,797	0,611284782	0,594	0,98	0,75
Inhibitory	ADGRB3	ENSG00000135298	0,787	0,72157357	0,574	0,99	0,8
Inhibitory	TNRC6A	ENSG00000090905	0,811	0,632008386	0,622	0,99	0,83
Ependymal	ARMC3	ENSG00000165309	0,988	2,454235417	0,976	0,98	0,06
Ependymal	VWA3A	ENSG00000175267	0,978	2,331218792	0,956	0,96	0,05

Ependymal	SPAG17	ENSG00000155761	0,97	2,649520041	0,94	0,94	0,04
Ependymal	ADGB	ENSG00000118492	0,953	2,436900377	0,906	0,91	0,01
Ependymal	CFAP299	ENSG00000197826	0,969	3,628812551	0,938	0,94	0,04
Ependymal	LMNTD1	ENSG00000152936	0,963	2,26270833	0,926	0,94	0,04
Ependymal	ZBBX	ENSG00000169064	0,959	2,258773969	0,918	0,92	0,03
Ependymal	CFAP157	ENSG00000160401	0,942	2,170514203	0,884	0,88	0,01
Ependymal	LRRIQ1	ENSG00000133640	0,966	2,333707195	0,932	0,94	0,07
Ependymal	DNAH11	ENSG00000105877	0,956	2,66537352	0,912	0,92	0,04
Ependymal	CFAP43	ENSG00000197748	0,979	2,760995413	0,958	0,97	0,09
Ependymal	CFAP47	ENSG00000165164	0,967	2,518603335	0,934	0,94	0,07
Ependymal	DTHD1	ENSG00000197057	0,942	2,230561005	0,884	0,89	0,02
Ependymal	WDR49	ENSG00000174776	0,97	2,12616289	0,94	0,98	0,11
Ependymal	SPATA17	ENSG00000162814	0,949	2,138778585	0,898	0,91	0,04
Ependymal	FRMPD2	ENSG00000170324	0,949	1,814280637	0,898	0,93	0,07
Ependymal	DNAH7	ENSG00000118997	0,981	2,4804796	0,962	0,98	0,12
Ependymal	TOGARAM2	ENSG00000189350	0,964	1,940382989	0,928	0,96	0,11
Ependymal	LRRC9	ENSG00000131951	0,951	2,038646185	0,902	0,91	0,06
Ependymal	CFAP73	ENSG00000186710	0,929	1,73835261	0,858	0,86	0,01
Ependymal	DNAAF1	ENSG00000154099	0,944	1,98066704	0,888	0,9	0,04
Ependymal	CFAP54	ENSG00000188596	0,99	3,074637821	0,98	0,99	0,14
Ependymal	DCDC1	ENSG00000170959	0,964	2,64179765	0,928	0,94	0,09
Ependymal	TEKT1	ENSG00000167858	0,928	1,71393145	0,856	0,86	0,02
Ependymal	TTC6	ENSG00000139865	0,94	2,100981861	0,88	0,9	0,06
Ependymal	TTC29	ENSG00000137473	0,933	2,139794918	0,866	0,87	0,03
Ependymal	KIAA2012	ENSG00000182329	0,935	1,888336335	0,87	0,88	0,04
Ependymal	DNAH5	ENSG00000039139	0,933	2,120426539	0,866	0,88	0,04
Ependymal	SPAG6	ENSG00000077327	0,937	1,934474035	0,874	0,89	0,05
Ependymal	ARMC4	ENSG00000169126	0,924	1,772874942	0,848	0,85	0,02
Ependymal	DNAH6	ENSG00000115423	0,97	2,523769593	0,94	0,95	0,12
Ependymal	C8orf34	ENSG00000165084	0,963	2,418997373	0,926	0,95	0,12
Ependymal	DNAI1	ENSG00000122735	0,927	1,785511969	0,854	0,86	0,03
Ependymal	MAP3K19	ENSG00000176601	0,922	1,818669682	0,844	0,85	0,03
Ependymal	CFAP46	ENSG00000171811	0,945	1,996554482	0,89	0,9	0,08
Ependymal	SERPINI2	ENSG00000114204	0,926	1,604873337	0,852	0,91	0,09
Ependymal	CFAP52	ENSG00000166596	0,921	1,8231822	0,842	0,85	0,03
Ependymal	RSPH1	ENSG00000160188	0,925	1,712179681	0,85	0,86	0,04
Ependymal	VWA3B	ENSG00000168658	0,916	1,616118577	0,832	0,84	0,02
Ependymal	PPP1R42	ENSG00000178125	0,928	1,684137626	0,856	0,88	0,06
Ependymal	NEK5	ENSG00000197168	0,931	1,813790684	0,862	0,88	0,07
Ependymal	C6orf118	ENSG00000112539	0,911	1,48257634	0,822	0,83	0,02
Ependymal	CCDC173	ENSG00000154479	0,912	1,578378327	0,824	0,83	0,03
Ependymal	FANK1	ENSG00000203780	0,942	1,899606156	0,884	0,91	0,1
Ependymal	WDR63	ENSG00000162643	0,905	1,557775845	0,81	0,82	0,02
Ependymal	SLC47A2	ENSG00000180638	0,902	1,639678802	0,804	0,81	0,02
Ependymal	DNAH12	ENSG00000174844	0,938	2,27628678	0,876	0,9	0,11
Ependymal	CFAP61	ENSG00000089101	0,926	1,665951057	0,852	0,88	0,09
Ependymal	CFAP100	ENSG00000163885	0,906	1,575898509	0,812	0,82	0,03
Ependymal	CCDC170	ENSG00000120262	0,907	1,562882606	0,814	0,83	0,05
Ependymal	ROPN1L	ENSG00000145491	0,897	1,522130663	0,794	0,8	0,01
Ependymal	DNAH9	ENSG00000007174	0,967	3,062582906	0,934	0,95	0,17
Ependymal	CFAP221	ENSG00000163075	0,922	1,675093487	0,844	0,87	0,09
Ependymal	LINC01088	ENSG00000249307	0,934	1,864973971	0,868	0,98	0,21
Ependymal	CASC1	ENSG00000118307	0,91	1,710271311	0,82	0,84	0,06
Ependymal	LRGUK	ENSG00000155530	0,905	1,552172179	0,81	0,83	0,06
Ependymal	FAM227A	ENSG00000184949	0,918	1,534906397	0,836	0,87	0,09

Ependymal	FHAD1	ENSG00000142621	0,895	1,622421223	0,79	0,8	0,03
Ependymal	CASC2	ENSG00000177640	0,931	1,806731392	0,862	0,91	0,14
Ependymal	CFAP44	ENSG00000206530	0,97	2,247711058	0,94	0,96	0,19
Ependymal	CCDC40	ENSG00000141519	0,911	1,416005647	0,822	0,87	0,1
Ependymal	DRC3	ENSG00000171962	0,891	1,367044917	0,782	0,8	0,03
Ependymal	DNAH3	ENSG00000158486	0,889	1,66909286	0,778	0,79	0,02
Ependymal	MOK	ENSG00000080823	0,941	1,718603796	0,882	0,92	0,16
Ependymal	RFX2	ENSG00000087903	0,941	1,808324488	0,882	0,93	0,18
Ependymal	CAPS	ENSG00000105519	0,921	2,059121696	0,842	0,88	0,13
Ependymal	PLCH1	ENSG00000114805	0,899	1,499587693	0,798	0,86	0,11
Ependymal	DLEC1	ENSG00000008226	0,882	1,367451258	0,764	0,78	0,03
Ependymal	SPEF2	ENSG00000152582	0,935	1,885036549	0,87	0,9	0,15
Ependymal	DOC2A	ENSG00000149927	0,893	1,563109568	0,786	0,81	0,06
Ependymal	TMEM67	ENSG00000164953	0,914	1,570526022	0,828	0,86	0,11
Ependymal	AL357093.2	ENSG00000258752	0,875	1,490493984	0,75	0,75	0,01
Ependymal	LRRC6	ENSG00000129295	0,915	1,553965198	0,83	0,86	0,12
Ependymal	CFAP69	ENSG00000105792	0,912	1,5683774	0,824	0,86	0,11
Ependymal	RGS22	ENSG00000132554	0,889	1,611392284	0,778	0,81	0,07
Ependymal	WDR78	ENSG00000152763	0,933	1,715816911	0,866	0,91	0,17
Ependymal	C4orf47	ENSG00000205129	0,908	1,507988604	0,816	0,86	0,12
Ependymal	DNAI2	ENSG00000171595	0,871	1,436523874	0,742	0,75	0,01
Ependymal	AL022068.1	ENSG00000228412	0,901	1,800782344	0,802	0,86	0,12
Ependymal	PPIL6	ENSG00000185250	0,891	1,406977731	0,782	0,81	0,08
Ependymal	SPAG8	ENSG00000137098	0,876	1,355107529	0,752	0,77	0,03
Ependymal	PACRG	ENSG00000112530	0,962	2,044212863	0,924	0,97	0,23
Ependymal	ANKFN1	ENSG00000153930	0,905	1,431795043	0,81	0,93	0,19
Ependymal	DNAH10	ENSG00000197653	0,891	1,57662468	0,782	0,8	0,07
Ependymal	LINC02055	ENSG00000254101	0,875	1,980722426	0,75	0,77	0,04
Ependymal	EFHC2	ENSG00000183690	0,873	1,357166171	0,746	0,77	0,04
Ependymal	SOX6	ENSG00000110693	0,887	1,208972419	0,774	0,96	0,23
Ependymal	IQCA1	ENSG00000132321	0,9	1,37229954	0,8	0,9	0,17
Ependymal	EFCAB6	ENSG00000186976	0,919	1,751597302	0,838	0,88	0,15
Ependymal	EYA1	ENSG00000104313	0,875	1,517407545	0,75	0,82	0,1
Ependymal	YAP1	ENSG00000137693	0,871	1,205971198	0,742	0,85	0,12
Ependymal	DRC1	ENSG00000157856	0,871	1,189835292	0,742	0,76	0,03
Ependymal	GLIS3	ENSG00000107249	0,927	1,725164399	0,854	0,98	0,25
Ependymal	TCTEX1D1	ENSG00000152760	0,874	1,322203643	0,748	0,76	0,04
Ependymal	CFAP70	ENSG00000156042	0,939	1,829896505	0,878	0,93	0,21
Ependymal	SLC9C2	ENSG00000162753	0,869	1,319979384	0,738	0,76	0,04
Ependymal	DCDC2	ENSG00000146038	0,87	1,412524163	0,74	0,76	0,04
Ependymal	SHANK2	ENSG00000162105	0,908	1,655712857	0,816	0,89	0,17
Ependymal	AGBL4	ENSG00000186094	0,969	2,276763903	0,938	0,98	0,27
Ependymal	NEK10	ENSG00000163491	0,912	1,740348959	0,824	0,87	0,16
Ependymal	CDHR3	ENSG00000128536	0,896	1,75010446	0,792	0,87	0,15
Ependymal	SPAG1	ENSG00000104450	0,893	1,393255369	0,786	0,84	0,13
Ependymal	COL21A1	ENSG00000124749	0,878	1,468494985	0,756	0,83	0,12
Ependymal	STK33	ENSG00000130413	0,957	1,814424295	0,914	0,97	0,26
Ependymal	DNAH2	ENSG00000183914	0,861	1,288241123	0,722	0,73	0,02
Ependymal	NEK11	ENSG00000114670	0,967	2,093772275	0,934	0,96	0,25
Ependymal	DAW1	ENSG00000123977	0,86	1,248497263	0,72	0,73	0,02
Ependymal	WDR66	ENSG00000158023	0,886	1,462330014	0,772	0,81	0,1
Ependymal	CASC15	ENSG00000272168	0,914	1,775291255	0,828	0,89	0,18
Ependymal	MAATS1	ENSG00000183833	0,881	1,302565411	0,762	0,81	0,11
Ependymal	ADCY2	ENSG00000078295	0,888	1,325373449	0,776	0,95	0,25
Ependymal	CFAP77	ENSG00000188523	0,854	1,195258162	0,708	0,72	0,01

Ependymal	PAMR1	ENSG00000149090	0,85	1,211651764	0,7	0,8	0,1
Ependymal	TTC34	ENSG00000215912	0,854	1,300244938	0,708	0,72	0,02
Ependymal	SPATA6L	ENSG00000106686	0,892	1,384545764	0,784	0,84	0,14
Ependymal	EFCAB1	ENSG00000034239	0,852	1,155345504	0,704	0,71	0,01
Ependymal	TEX9	ENSG00000151575	0,887	1,420646416	0,774	0,84	0,15
Ependymal	C1orf87	ENSG00000162598	0,847	1,37886183	0,694	0,7	0,01
Ependymal	EYA4	ENSG00000112319	0,909	1,836432886	0,818	0,88	0,2
Ependymal	WWC1	ENSG00000113645	0,86	1,280490855	0,72	0,83	0,15
Ependymal	TRDN	ENSG00000186439	0,845	1,570802447	0,69	0,71	0,03
Ependymal	RFX4	ENSG00000111783	0,825	0,885825619	0,65	0,82	0,15
Ependymal	PLTP	ENSG00000100979	0,841	1,14856394	0,682	0,72	0,05
Ependymal	ACOT11	ENSG00000162390	0,864	1,114580896	0,728	0,88	0,2
Ependymal	CEP126	ENSG00000110318	0,941	1,715389292	0,882	0,94	0,27
Ependymal	VWA5B1	ENSG00000158816	0,84	1,18725514	0,68	0,69	0,03
Ependymal	ARMC2	ENSG00000118690	0,913	1,405724083	0,826	0,9	0,24
Ependymal	IQCG	ENSG00000114473	0,868	1,310550311	0,736	0,8	0,13
Ependymal	NRG4	ENSG00000169752	0,852	1,312685997	0,704	0,74	0,07
Ependymal	BMPR1B	ENSG00000138696	0,829	1,073727368	0,658	0,78	0,12
Ependymal	NELL2	ENSG00000184613	0,849	1,241022635	0,698	0,8	0,14
Ependymal	SNTB1	ENSG00000172164	0,836	1,124525927	0,672	0,77	0,11
Ependymal	CCDC60	ENSG00000183273	0,833	1,480096039	0,666	0,67	0,01
Ependymal	CCDC30	ENSG00000186409	0,959	2,070016522	0,918	0,96	0,3
Ependymal	GYG2	ENSG00000056998	0,842	1,179066984	0,684	0,73	0,08
Ependymal	ARHGEF26	ENSG00000114790	0,85	1,123192947	0,7	0,82	0,17
Ependymal	GMPR	ENSG00000137198	0,833	1,153444947	0,666	0,75	0,1
Ependymal	CD36	ENSG00000135218	0,832	1,280499201	0,664	0,68	0,03
Ependymal	IQCH	ENSG00000103599	0,849	1,252289848	0,698	0,75	0,1
Ependymal	CFAP65	ENSG00000181378	0,828	1,044006038	0,656	0,66	0,01
Ependymal	TTLL9	ENSG00000131044	0,869	1,233911488	0,738	0,82	0,17
Ependymal	ADGRA3	ENSG00000152990	0,842	1,112629945	0,684	0,81	0,16
Ependymal	AC013470.2	ENSG00000226690	0,827	1,122063689	0,654	0,66	0,01
Ependymal	IL16	ENSG00000172349	0,829	1,059777987	0,658	0,69	0,04
Ependymal	TMEM232	ENSG00000186952	0,968	2,657294612	0,936	0,97	0,32
Ependymal	RNF213-AS1	ENSG00000263069	0,868	1,362037888	0,736	0,81	0,17
Ependymal	CCDC114	ENSG00000105479	0,823	1,031768051	0,646	0,65	0,01
Ependymal	BAIAP3	ENSG00000007516	0,835	1,130441119	0,67	0,75	0,1
Ependymal	RPGR	ENSG00000156313	0,862	1,141540969	0,724	0,84	0,2
Ependymal	BBOF1	ENSG00000119636	0,852	1,104141155	0,704	0,77	0,13
Ependymal	AK8	ENSG00000165695	0,832	1,182689304	0,664	0,7	0,06
Ependymal	ULK4	ENSG00000168038	0,948	2,281681137	0,896	0,94	0,3
Ependymal	SNCAIP	ENSG00000064692	0,832	1,112367295	0,664	0,73	0,09
Ependymal	DYNLRB2	ENSG00000168589	0,824	1,037597299	0,648	0,66	0,03
Ependymal	IQGAP2	ENSG00000145703	0,819	1,1737774	0,638	0,67	0,04
Ependymal	FBXL13	ENSG00000161040	0,859	1,36415391	0,718	0,79	0,16
Ependymal	MLF1	ENSG00000178053	0,841	1,097757984	0,682	0,74	0,11
Ependymal	EFHC1	ENSG00000096093	0,886	1,329083454	0,772	0,85	0,22
Ependymal	NPHP1	ENSG00000144061	0,851	1,106812861	0,702	0,78	0,15
Ependymal	CFAP53	ENSG00000172361	0,828	1,040011948	0,656	0,69	0,06
Ependymal	GABRG1	ENSG00000163285	0,828	1,117115634	0,656	0,74	0,11
Ependymal	AGBL1	ENSG00000273540	0,849	2,198136071	0,698	0,74	0,11
Ependymal	AP001831.1	ENSG00000254733	0,835	1,20430455	0,67	0,72	0,09
Ependymal	EFCAB12	ENSG00000172771	0,819	0,929371492	0,638	0,65	0,02
Ependymal	KIAA0319	ENSG00000137261	0,835	1,047999666	0,67	0,78	0,15
Ependymal	USP2-AS1	ENSG00000245248	0,821	1,222721476	0,642	0,66	0,03
Ependymal	PLCB4	ENSG00000101333	0,835	1,070906809	0,67	0,87	0,25

Ependymal	MNS1	ENSG00000138587	0,823	1,03852148	0,646	0,68	0,05
Ependymal	EZR	ENSG00000092820	0,813	0,921621389	0,626	0,72	0,09
Ependymal	CRB1	ENSG00000134376	0,911	1,641764319	0,822	0,92	0,3
Ependymal	ARMH1	ENSG00000198520	0,83	1,094163774	0,66	0,74	0,12
Ependymal	ROR2	ENSG00000169071	0,816	1,323982413	0,632	0,66	0,04
Ependymal	CFAP45	ENSG00000213085	0,812	0,94604214	0,624	0,63	0
Ependymal	USP43	ENSG00000154914	0,817	1,096758709	0,634	0,66	0,04
Ependymal	FZD3	ENSG00000104290	0,857	1,234451807	0,714	0,82	0,2
Ependymal	MYLK3	ENSG00000140795	0,812	1,257308618	0,624	0,63	0,01
Ependymal	CLIC6	ENSG00000159212	0,812	1,204604862	0,624	0,63	0,01
Ependymal	CCDC146	ENSG00000135205	0,94	1,775868277	0,88	0,94	0,33
Ependymal	SOX5	ENSG00000134532	0,859	1,179129609	0,718	0,97	0,35
Ependymal	TRMT9B	ENSG00000250305	0,831	1,068429725	0,662	0,76	0,14
Ependymal	GJA1	ENSG00000152661	0,796	0,824219976	0,592	0,76	0,14
Ependymal	C8orf37-AS1	ENSG00000253773	0,822	1,374250045	0,644	0,71	0,1
Ependymal	CCDC81	ENSG00000149201	0,812	1,049029113	0,624	0,65	0,04
Ependymal	NEBL	ENSG00000078114	0,87	1,258221256	0,74	0,98	0,36
Ependymal	C5AR1	ENSG00000197405	0,811	1,01141145	0,622	0,65	0,04
Ependymal	KIAA0825	ENSG00000185261	0,905	1,655306789	0,81	0,9	0,29
Ependymal	C5orf49	ENSG00000215217	0,81	0,987130317	0,62	0,63	0,02
Ependymal	NWD1	ENSG00000188039	0,807	1,118671908	0,614	0,68	0,07
Ependymal	DPP10	ENSG00000175497	0,89	1,89012931	0,78	0,93	0,32
Ependymal	HSPB8	ENSG00000152137	0,813	1,536422278	0,626	0,69	0,08
Ependymal	NSMF	ENSG00000165802	0,824	0,975028771	0,648	0,76	0,15
Ependymal	KIAA1671	ENSG00000197077	0,83	1,021384518	0,66	0,8	0,2
Ependymal	ZBTB7C	ENSG00000184828	0,816	1,067085521	0,632	0,75	0,14
Ependymal	SPATA18	ENSG00000163071	0,805	1,016887799	0,61	0,62	0,01
Ependymal	FMN2	ENSG00000155816	0,86	1,076302125	0,72	0,95	0,34
Ependymal	MARCH10	ENSG00000173838	0,809	1,0756067	0,618	0,64	0,04
Ependymal	CD99	ENSG00000002586	0,801	0,88092445	0,602	0,72	0,12
Ependymal	FAM81B	ENSG00000153347	0,801	0,959816061	0,602	0,61	0,01
Ependymal	WLS	ENSG00000116729	0,805	0,896400044	0,61	0,8	0,2
Ependymal	CFAP97D2	ENSG00000283361	0,801	0,974098542	0,602	0,61	0,01
Ependymal	KIF27	ENSG00000165115	0,865	1,182718719	0,73	0,85	0,25
Ependymal	FOXP2	ENSG00000128573	0,789	0,792212816	0,578	0,77	0,18
Ependymal	KCNN3	ENSG00000143603	0,807	0,737906201	0,614	0,81	0,22
Ependymal	CROCC2	ENSG00000226321	0,799	1,123138377	0,598	0,6	0
Ependymal	CEP112	ENSG00000154240	0,829	0,988159658	0,658	0,87	0,27
Ependymal	WWTR1	ENSG00000018408	0,829	1,147578042	0,658	0,83	0,23
Ependymal	TTC26	ENSG00000105948	0,817	1,011257285	0,634	0,7	0,11
Ependymal	SPAG16	ENSG00000144451	0,932	2,047599244	0,864	0,92	0,33
Ependymal	CNTN3	ENSG00000113805	0,813	1,127145444	0,626	0,77	0,18
Ependymal	NRG3	ENSG00000185737	0,804	0,855570836	0,608	0,98	0,39
Ependymal	AK7	ENSG00000140057	0,801	1,0060597	0,602	0,63	0,04
Ependymal	SDK1	ENSG00000146555	0,849	1,357832247	0,698	0,85	0,26
Ependymal	SLC6A16	ENSG00000063127	0,8	0,928569354	0,6	0,63	0,04
Ependymal	CCDC191	ENSG00000163617	0,827	0,918575121	0,654	0,77	0,19
Ependymal	GRAMD2B	ENSG00000155324	0,862	1,162546894	0,724	0,92	0,34
Ependymal	COL8A1	ENSG00000144810	0,793	1,165453491	0,586	0,62	0,04
Ependymal	CSMD3	ENSG00000164796	0,816	0,895175646	0,632	0,93	0,35
Ependymal	DNAAF4	ENSG00000256061	0,812	0,951449207	0,624	0,71	0,12
Ependymal	AC007906.2	ENSG00000277639	0,791	1,018325377	0,582	0,58	0
Ependymal	CACHD1	ENSG00000158966	0,801	0,880081523	0,602	0,81	0,23
Ependymal	PLCE1	ENSG00000138193	0,794	0,829658111	0,588	0,74	0,16
Ependymal	NME5	ENSG00000112981	0,816	0,993955842	0,632	0,72	0,14

Ependymal	C9orf135	ENSG00000204711	0,789	1,090889269	0,578	0,58	0,01
Ependymal	TTC23L	ENSG00000205838	0,81	1,110603215	0,62	0,68	0,1
Ependymal	SOX9	ENSG00000125398	0,786	0,93103583	0,572	0,67	0,1
Ependymal	ZNF273	ENSG00000198039	0,817	1,018226924	0,634	0,73	0,16
Ependymal	TTC21A	ENSG00000168026	0,8	0,898656453	0,6	0,66	0,09
Ependymal	KNDC1	ENSG00000171798	0,802	0,844034156	0,604	0,72	0,15
Ependymal	DYNC2H1	ENSG00000187240	0,945	1,781094208	0,89	0,96	0,39
Ependymal	LRP2BP	ENSG00000109771	0,821	0,957008021	0,642	0,77	0,2
Ependymal	B3GLCT	ENSG00000187676	0,793	0,920666304	0,586	0,68	0,11
Ependymal	C2orf73	ENSG00000177994	0,788	0,913288249	0,576	0,6	0,04
Ependymal	PARD3	ENSG00000148498	0,873	1,156822995	0,746	0,99	0,42
Ependymal	PPARGC1A	ENSG00000109819	0,8	1,201362692	0,6	0,7	0,13
Ependymal	CNTNAP3B	ENSG00000154529	0,799	0,990036978	0,598	0,75	0,19
Ependymal	GRIN2A	ENSG00000183454	0,795	1,171477865	0,59	0,72	0,15
Ependymal	ZMYND10	ENSG00000004838	0,783	0,948632553	0,566	0,58	0,02
Ependymal	CABCOCO1	ENSG00000183346	0,791	0,969942814	0,582	0,66	0,1
Ependymal	FAM183A	ENSG00000186973	0,78	0,833392645	0,56	0,56	0
Ependymal	TRPC6	ENSG00000137672	0,784	0,947354014	0,568	0,6	0,04
Ependymal	SLC7A11	ENSG00000151012	0,793	0,903816626	0,586	0,79	0,23
Ependymal	PTPRG	ENSG00000144724	0,782	0,622730232	0,564	0,89	0,33
Ependymal	CFAP74	ENSG00000142609	0,782	0,863554608	0,564	0,58	0,02
Ependymal	GRAMD2A	ENSG00000175318	0,782	1,104035599	0,564	0,58	0,02
Ependymal	CDS1	ENSG00000163624	0,796	0,922423001	0,592	0,66	0,1
Ependymal	BBOX1	ENSG00000129151	0,776	0,885035529	0,552	0,62	0,06
Ependymal	EXPH5	ENSG00000110723	0,779	0,983248097	0,558	0,61	0,05
Ependymal	ZFP36L1	ENSG00000185650	0,772	0,770329408	0,544	0,79	0,23
Ependymal	PITPNC1	ENSG00000154217	0,808	0,737383482	0,616	0,94	0,38
Ependymal	SORBS1	ENSG00000095637	0,886	1,367055105	0,772	0,97	0,41
Ependymal	IQUB	ENSG00000164675	0,786	0,868105158	0,572	0,62	0,06
Ependymal	RASSF9	ENSG00000198774	0,777	0,920599678	0,554	0,57	0,01
Ependymal	CCDC175	ENSG00000151838	0,783	0,920112556	0,566	0,61	0,05
Ependymal	PCAT1	ENSG00000253438	0,789	1,424283356	0,578	0,64	0,09
Ependymal	WDR93	ENSG00000140527	0,776	0,884813566	0,552	0,56	0,01
Ependymal	AKAP13	ENSG00000170776	0,837	0,970061832	0,674	0,9	0,36
Ependymal	WDR19	ENSG00000157796	0,814	0,966616118	0,628	0,76	0,22
Ependymal	ENPEP	ENSG00000138792	0,773	0,925245549	0,546	0,56	0,02
Ependymal	ADGRV1	ENSG00000164199	0,791	1,182527578	0,582	0,67	0,13
Ependymal	SSBP4	ENSG00000130511	0,789	0,850708523	0,578	0,68	0,13
Ependymal	AC004949.1	ENSG00000283117	0,774	1,567178066	0,548	0,56	0,02
Ependymal	DZANK1	ENSG00000089091	0,797	0,918195504	0,594	0,69	0,15
Ependymal	PLEKHA5	ENSG00000052126	0,913	1,511321287	0,826	0,97	0,43
Ependymal	TTC8	ENSG00000165533	0,793	0,886674011	0,586	0,69	0,16
Ependymal	DPY19L2	ENSG00000177990	0,787	0,867822284	0,574	0,71	0,17
Ependymal	ANTXR1	ENSG00000169604	0,785	0,850823882	0,57	0,74	0,21
Ependymal	ST8SIA1	ENSG00000111728	0,795	0,955738998	0,59	0,79	0,25
Ependymal	RSPH3	ENSG00000130363	0,786	0,853200815	0,572	0,66	0,12
Ependymal	C7orf57	ENSG00000164746	0,768	0,800724516	0,536	0,54	0
Ependymal	PRKG1	ENSG00000185532	0,767	0,831529738	0,534	0,79	0,26
Ependymal	NELFA	ENSG00000185049	0,825	0,990294643	0,65	0,79	0,26
Ependymal	JHY	ENSG00000109944	0,787	0,861190279	0,574	0,65	0,12
Ependymal	HPSE2	ENSG00000172987	0,759	0,901414064	0,518	0,69	0,16
Ependymal	TRAF3IP1	ENSG00000204104	0,798	0,905769788	0,596	0,72	0,19
Ependymal	RABL2A	ENSG00000144134	0,792	0,93307074	0,584	0,69	0,16
Ependymal	CFAP300	ENSG00000137691	0,767	0,805641109	0,534	0,55	0,03
Ependymal	CAPSL	ENSG00000152611	0,763	0,77972685	0,526	0,53	0

Ependymal	FAM92B	ENSG00000153789	0,763	0,790531355	0,526	0,53	0,01
Ependymal	CC2D2A	ENSG00000048342	0,789	0,889544797	0,578	0,69	0,17
Ependymal	KIF9	ENSG00000088727	0,769	0,792152991	0,538	0,57	0,04
Ependymal	PTPN3	ENSG00000070159	0,762	0,817530978	0,524	0,54	0,02
Ependymal	STRBP	ENSG00000165209	0,871	1,387544565	0,742	0,88	0,36
Ependymal	RAD9A	ENSG00000172613	0,794	0,867267426	0,588	0,76	0,24
Ependymal	EFCAB2	ENSG00000203666	0,893	1,388371832	0,786	0,92	0,4
Ependymal	RIPOR2	ENSG00000111913	0,777	1,030137809	0,554	0,65	0,13
Ependymal	ANKRD45	ENSG00000183831	0,764	0,772485612	0,528	0,55	0,02
Ependymal	GPM6A	ENSG00000150625	0,756	0,740836999	0,512	0,86	0,34
Ependymal	LRRC23	ENSG00000010626	0,779	0,81926431	0,558	0,66	0,14
Ependymal	FLACC1	ENSG00000155749	0,772	0,884365306	0,544	0,6	0,08
Ependymal	AC091078.1	ENSG00000257060	0,767	1,05578499	0,534	0,61	0,09
Ependymal	C11orf88	ENSG00000183644	0,76	0,818285186	0,52	0,52	0
Ependymal	FOS	ENSG00000170345	0,766	1,190732233	0,532	0,59	0,07
Ependymal	PAWR	ENSG00000177425	0,759	0,730566275	0,518	0,62	0,1
Ependymal	JUN	ENSG00000177606	0,777	1,08382925	0,554	0,67	0,15
Ependymal	COLEC12	ENSG00000158270	0,756	0,834003556	0,512	0,63	0,12
Ependymal	CTNNA2	ENSG00000066032	0,832	1,015751618	0,664	0,98	0,46
Ependymal	STON2	ENSG00000140022	0,773	0,77792102	0,546	0,71	0,19
Ependymal	TGFBR3	ENSG00000069702	0,762	0,75928977	0,524	0,65	0,13
Ependymal	ANTXR2	ENSG00000163297	0,761	0,848672746	0,522	0,58	0,06
Ependymal	PPP1R14C	ENSG00000198729	0,77	0,941609747	0,54	0,59	0,08
Ependymal	MED12L	ENSG00000144893	0,782	0,87224637	0,564	0,79	0,28
Ependymal	AC093689.1	ENSG00000250597	0,757	0,792568373	0,514	0,52	0
Ependymal	FAM160A1	ENSG00000164142	0,758	1,042601443	0,516	0,53	0,02
Ependymal	FAM184A	ENSG00000111879	0,798	1,148526244	0,596	0,72	0,21
Ependymal	STIM1	ENSG00000167323	0,79	1,001448619	0,58	0,74	0,23
Ependymal	CCDC180	ENSG00000197816	0,788	0,8938264 11	0,576	0,68	0,17
Ependymal	SYT17	ENSG00000103528	0,758	0,73387949	0,516	0,72	0,2
Ependymal	CD24	ENSG00000272398	0,758	0,958559912	0,516	0,53	0,02
Ependymal	IFT81	ENSG00000122970	0,777	0,798578803	0,554	0,66	0,15
Ependymal	RPGRIP1L	ENSG00000103494	0,776	0,85170169	0,552	0,64	0,13
Ependymal	NFATC2	ENSG00000101096	0,747	0,843589527	0,494	0,63	0,12
Ependymal	PLEKHA7	ENSG00000166689	0,887	1,348984215	0,774	0,92	0,41
Ependymal	TACC2	ENSG00000138162	0,776	0,83884369	0,552	0,67	0,16
Ependymal	ECHDC2	ENSG00000121310	0,772	0,692259219	0,544	0,77	0,26
Ependymal	KIAA1257	ENSG00000114656	0,763	0,806574483	0,526	0,56	0,05
Ependymal	EFHB	ENSG00000163576	0,76	0,817025099	0,52	0,55	0,05
Ependymal	SLC39A12	ENSG00000148482	0,75	0,828448673	0,5	0,57	0,07
Ependymal	ACSS3	ENSG00000111058	0,75	0,670374131	0,5	0,63	0,12
Ependymal	CEP83	ENSG00000173588	0,811	1,06477416	0,622	0,77	0,27
Ependymal	TTC25	ENSG00000204815	0,76	0,73789821	0,52	0,55	0,05
Ependymal	CFAP57	ENSG00000243710	0,754	0,738944581	0,508	0,52	0,01
Ependymal	HYDIN	ENSG00000157423	0,97	2,220043231	0,94	0,97	0,47
Ependymal	DPYSL3	ENSG00000113657	0,765	0,833579225	0,53	0,67	0,16
Ependymal	TMEM47	ENSG00000147027	0,764	0,90804501	0,528	0,62	0,11
Ependymal	TCTN1	ENSG00000204852	0,763	0,761423788	0,526	0,62	0,12
Ependymal	MOB1B	ENSG00000173542	0,787	0,915228596	0,574	0,73	0,23
Ependymal	KIAA1217	ENSG00000120549	0,742	0,649742539	0,484	0,75	0,25
Ependymal	NME9	ENSG00000181322	0,8	1,037394348	0,6	0,75	0,25
Ependymal	AL645937.2	ENSG00000227206	0,751	0,786399229	0,502	0,5	0
Ependymal	LAMA1	ENSG00000101680	0,747	0,757667007	0,494	0,58	0,08
Ependymal	STK32A	ENSG00000169302	0,742	0,670916645	0,484	0,67	0,17
Ependymal	WDR60	ENSG00000126870	0,892	1,296991855	0,784	0,92	0,43

Ependymal	KCNMA1	ENSG00000156113	0,797	0,739794525	0,594	0,95	0,45
Ependymal	ACACB	ENSG00000076555	0,767	0,635691947	0,534	0,8	0,3
Ependymal	FBXO15	ENSG00000141665	0,764	0,869452452	0,528	0,6	0,11
Ependymal	COL6A2	ENSG00000142173	0,746	0,718970707	0,492	0,53	0,03
Ependymal	CCDC88C	ENSG00000015133	0,756	0,793326839	0,512	0,57	0,07
Ependymal	CLHC1	ENSG00000162994	0,77	0,832090657	0,54	0,64	0,15
Ependymal	BCAR3	ENSG00000137936	0,749	0,646287881	0,498	0,71	0,21
Ependymal	SPEF1	ENSG00000101222	0,748	0,724782588	0,496	0,5	0,01
Ependymal	ABCC9	ENSG00000069431	0,744	0,714902451	0,488	0,55	0,06
Ependymal	CSPP1	ENSG00000104218	0,911	1,391476178	0,822	0,94	0,45
Ependymal	INTU	ENSG00000164066	0,826	0,909141851	0,652	0,86	0,37
Ependymal	MAPK15	ENSG00000181085	0,746	0,69580291	0,492	0,49	0
Ependymal	ARHGAP18	ENSG00000146376	0,751	0,755377525	0,502	0,64	0,15
Ependymal	MIPEP	ENSG00000027001	0,784	0,910026463	0,568	0,73	0,24
Ependymal	DNAJB1	ENSG00000132002	0,779	0,883765534	0,558	0,72	0,23
Ependymal	GRIA1	ENSG00000155511	0,735	0,696324603	0,47	0,63	0,14
Ependymal	ANKMY1	ENSG00000144504	0,781	0,845343589	0,562	0,72	0,23
Ependymal	AC234582.1	ENSG00000231064	0,744	0,729399413	0,488	0,52	0,03
Ependymal	RABL2B	ENSG00000079974	0,763	0,747301884	0,526	0,62	0,13
Ependymal	NTRK2	ENSG00000148053	0,87	1,118823473	0,74	0,98	0,49
Ependymal	ZNRF3	ENSG00000183579	0,765	0,744449718	0,53	0,75	0,26
Ependymal	LCA5	ENSG00000135338	0,76	0,793254618	0,52	0,62	0,13
Ependymal	ITGB4	ENSG00000132470	0,734	0,594367268	0,468	0,62	0,13
Ependymal	ODF2L	ENSG00000122417	0,825	1,035040963	0,65	0,83	0,34
Ependymal	NR2F1	ENSG00000175745	0,744	0,659685922	0,488	0,62	0,13
Ependymal	ZNF19	ENSG00000157429	0,745	0,81980082	0,49	0,51	0,03
Ependymal	MAK	ENSG00000111837	0,757	0,748496202	0,514	0,61	0,13
Ependymal	COL6A1	ENSG00000142156	0,748	0,716303751	0,496	0,6	0,12
Ependymal	CCN1	ENSG00000142871	0,743	1,313729223	0,486	0,5	0,02
Ependymal	CFAP58	ENSG00000120051	0,742	0,852299144	0,484	0,49	0,01
Ependymal	CRISPLD1	ENSG00000121005	0,745	0,89853676	0,49	0,55	0,07
Ependymal	TSGA10	ENSG00000135951	0,855	1,349461556	0,71	0,85	0,37
Ependymal	ZNF487	ENSG00000243660	0,753	0,717272295	0,506	0,57	0,09
Ependymal	SYNE2	ENSG00000054654	0,74	0,624420051	0,48	0,63	0,14
Ependymal	BOC	ENSG00000144857	0,733	0,59814224	0,466	0,6	0,12
Ependymal	SDK2	ENSG00000069188	0,753	0,829086491	0,506	0,59	0,11
Ependymal	NR2F1-AS1	ENSG00000237187	0,737	0,673642466	0,474	0,68	0,2
Ependymal	CERKL	ENSG00000188452	0,741	0,75930821	0,482	0,49	0,01
Ependymal	OSBPL6	ENSG00000079156	0,74	0,690168439	0,48	0,72	0,25
Ependymal	TTC12	ENSG00000149292	0,749	0,72172846	0,498	0,6	0,12
Ependymal	MAOB	ENSG00000069535	0,747	0,790593662	0,494	0,62	0,14
Ependymal	LMO2	ENSG00000135363	0,739	0,826018164	0,478	0,56	0,08
Ependymal	C9orf24	ENSG00000164972	0,748	0,79627305	0,496	0,54	0,07
Ependymal	DAAM1	ENSG00000100592	0,776	0,852430519	0,552	0,8	0,32
Ependymal	EML6	ENSG00000214595	0,759	0,822269804	0,518	0,72	0,24
Ependymal	PRR29	ENSG00000224383	0,737	0,794028742	0,474	0,48	0
Ependymal	IQCK	ENSG00000174628	0,802	0,935666464	0,604	0,81	0,34
Ependymal	FOXJ1	ENSG00000129654	0,736	0,760737777	0,472	0,48	0,01
Ependymal	AGBL2	ENSG00000165923	0,736	0,725386982	0,472	0,48	0,01
Ependymal	AGT	ENSG00000135744	0,734	0,729645789	0,468	0,59	0,12
Ependymal	KATNAL2	ENSG00000167216	0,787	0,950760961	0,574	0,77	0,3
Ependymal	SHROOM3	ENSG00000138771	0,738	0,772802507	0,476	0,57	0,1
Ependymal	CCDC57	ENSG00000176155	0,76	0,73614487	0,52	0,68	0,21
Ependymal	FGFR1OP	ENSG00000213066	0,762	0,771196175	0,524	0,67	0,2
Ependymal	COL28A1	ENSG00000215018	0,754	1,167509166	0,508	0,58	0,11

Ependymal	ARMC9	ENSG00000135931	0,773	0,756625475	0,546	0,77	0,3
Ependymal	AK9	ENSG00000155085	0,776	0,835570769	0,552	0,73	0,27
Ependymal	HSPA1B	ENSG00000204388	0,752	0,907624303	0,504	0,67	0,21
Ependymal	PLOD2	ENSG00000152952	0,739	0,659447955	0,478	0,65	0,19
Ependymal	DZIP3	ENSG00000198919	0,795	0,804661616	0,59	0,83	0,37
Ependymal	ANKRD26	ENSG00000107890	0,844	1,035335354	0,688	0,88	0,42
Ependymal	ENKUR	ENSG00000151023	0,734	0,69006597	0,468	0,5	0,04
Ependymal	FBXL2	ENSG00000153558	0,754	0,729641507	0,508	0,72	0,26
Ependymal	AC063979.2	ENSG00000251613	0,733	0,843988121	0,466	0,48	0,02
Ependymal	ID4	ENSG00000172201	0,732	0,711633586	0,464	0,53	0,07
Ependymal	DUSP18	ENSG00000167065	0,751	0,757248271	0,502	0,62	0,16
Ependymal	GNG12	ENSG00000172380	0,731	0,661914644	0,462	0,58	0,12
Ependymal	VIM	ENSG00000026025	0,722	0,692823604	0,444	0,56	0,1
Ependymal	C20orf96	ENSG00000196476	0,735	0,656333732	0,47	0,52	0,06
Ependymal	ANXA1	ENSG00000135046	0,729	0,9829546	0,458	0,48	0,02
Ependymal	FSTL1	ENSG00000163430	0,73	0,642464272	0,46	0,54	0,08
Ependymal	PARD3B	ENSG00000116117	0,922	1,430523538	0,844	0,98	0,52
Ependymal	HSPB1	ENSG00000106211	0,746	0,920917539	0,492	0,66	0,21
Ependymal	DAPK1	ENSG00000196730	0,732	0,648625415	0,464	0,65	0,19
Ependymal	FAM81A	ENSG00000157470	0,744	0,775903465	0,488	0,58	0,12
Ependymal	CROCC	ENSG00000058453	0,781	0,928240375	0,562	0,74	0,29
Ependymal	FAM182B	ENSG00000175170	0,78	0,821406445	0,56	0,8	0,34
Ependymal	DNALI1	ENSG00000163879	0,731	0,629236204	0,462	0,49	0,04
Ependymal	MEIS2	ENSG00000134138	0,794	0,929040642	0,588	0,86	0,41
Ependymal	EFCAB11	ENSG00000140025	0,744	0,826563261	0,488	0,66	0,21
Ependymal	PROS1	ENSG00000184500	0,739	0,881380994	0,478	0,56	0,11
Ependymal	ANKDD1B	ENSG00000189045	0,734	0,839011336	0,468	0,51	0,05
Ependymal	RIBC2	ENSG00000128408	0,727	0,646577224	0,454	0,46	0,01
Ependymal	WNK2	ENSG00000165238	0,725	0,614458114	0,45	0,63	0,18
Ependymal	PRKD1	ENSG00000184304	0,765	0,757728998	0,53	0,85	0,4
Ependymal	LEKR1	ENSG00000197980	0,732	0,84901465	0,464	0,51	0,06
Ependymal	OCA2	ENSG00000104044	0,73	0,882853303	0,46	0,49	0,04
Ependymal	DRC7	ENSG00000159625	0,726	0,67711745	0,452	0,46	0
Ependymal	AEBP1	ENSG00000106624	0,721	0,676058333	0,442	0,51	0,06
Ependymal	KCTD1	ENSG00000134504	0,748	0,766355865	0,496	0,7	0,25
Ependymal	PRICKLE2	ENSG00000163637	0,763	0,94634237	0,526	0,76	0,31
Ependymal	PHF21B	ENSG00000056487	0,725	0,628518054	0,45	0,61	0,16
Ependymal	GALNS	ENSG00000141012	0,734	0,672799735	0,468	0,55	0,1
Ependymal	TUBA4B	ENSG00000243910	0,725	0,725388112	0,45	0,45	0
Ependymal	ECT2L	ENSG00000203734	0,728	0,934484132	0,456	0,48	0,04
Ependymal	BAIAP2	ENSG00000175866	0,737	0,828117624	0,474	0,58	0,14
Ependymal	CATIP	ENSG00000158428	0,723	0,643169254	0,446	0,45	0,01
Ependymal	COL5A1	ENSG00000130635	0,725	0,832430102	0,45	0,48	0,03
Ependymal	ENO4	ENSG00000188316	0,735	0,792163248	0,47	0,56	0,12
Ependymal	BICC1	ENSG00000122870	0,731	0,90190594	0,462	0,55	0,11
Ependymal	PTRH1	ENSG00000187024	0,726	0,630745533	0,452	0,49	0,05
Ependymal	TPPP3	ENSG00000159713	0,739	0,900629982	0,478	0,6	0,16
Ependymal	TUSC3	ENSG00000104723	0,726	0,669091267	0,452	0,59	0,15
Ependymal	DDAH1	ENSG00000153904	0,733	0,719214021	0,466	0,64	0,2
Ependymal	NME7	ENSG00000143156	0,776	0,859995721	0,552	0,78	0,34
Ependymal	STOX1	ENSG00000165730	0,723	0,607669869	0,446	0,53	0,09
Ependymal	PPP1R15A	ENSG00000087074	0,724	0,909492663	0,448	0,49	0,05
Ependymal	AC046134.2	ENSG00000248932	0,762	0,710486058	0,524	0,81	0,37
Ependymal	IFT122	ENSG00000163913	0,738	0,668971619	0,476	0,62	0,18
Ependymal	LINC00880	ENSG00000243629	0,72	0,744290653	0,44	0,46	0,02

Ependymal	DNAH1	ENSG00000114841	0,729	0,624351458	0,458	0,55	0,11
Ependymal	IFT88	ENSG00000032742	0,804	0,881283938	0,608	0,85	0,41
Ependymal	ERICH3	ENSG00000178965	0,73	0,732990162	0,46	0,52	0,09
Ependymal	TCF7L1	ENSG00000152284	0,713	0,633827398	0,426	0,55	0,11
Ependymal	TCF7L2	ENSG00000148737	0,762	0,69571044	0,524	0,86	0,43
Ependymal	FAM167A-AS1	ENSG00000184608	0,719	0,715194244	0,438	0,45	0,02
Ependymal	OSMR-AS1	ENSG00000249740	0,714	0,601600911	0,428	0,52	0,08
Ependymal	TNIK	ENSG00000154310	0,783	0,74783152	0,566	0,94	0,5
Ependymal	HAGHL	ENSG00000103253	0,734	0,703953045	0,468	0,59	0,15
Ependymal	AC110023.1	ENSG00000258631	0,724	1,077486506	0,448	0,52	0,09
Ependymal	REEP1	ENSG00000068615	0,726	0,706403064	0,452	0,58	0,14
Ependymal	HSPH1	ENSG00000120694	0,787	1,148054693	0,574	0,78	0,35
Ependymal	SUN1	ENSG00000164828	0,782	0,757168752	0,564	0,79	0,35
Ependymal	UBXN11	ENSG00000158062	0,721	0,596964785	0,442	0,47	0,04
Ependymal	LINC00271	ENSG00000231028	0,731	0,812189811	0,462	0,58	0,14
Ependymal	MYO5C	ENSG00000128833	0,72	0,776687289	0,44	0,5	0,07
Ependymal	DNAJB13	ENSG00000187726	0,717	0,606422962	0,434	0,44	0,01
Ependymal	DCLK2	ENSG00000170390	0,754	0,744588897	0,508	0,82	0,38
Ependymal	PHTF1	ENSG00000116793	0,731	0,66096666	0,462	0,6	0,17
Ependymal	NADK2	ENSG00000152620	0,734	0,674674001	0,468	0,63	0,2
Ependymal	CLYBL	ENSG00000125246	0,73	0,769321114	0,46	0,6	0,16
Ependymal	TEAD1	ENSG00000187079	0,826	0,970838995	0,652	0,91	0,48
Ependymal	C1orf158	ENSG00000157330	0,715	0,710226984	0,43	0,43	0
Ependymal	ST5	ENSG00000166444	0,728	0,636316799	0,456	0,67	0,24
Ependymal	BMP7	ENSG00000101144	0,721	0,596906301	0,442	0,61	0,18
Ependymal	LMLN	ENSG00000185621	0,732	0,671372974	0,464	0,57	0,14
Ependymal	HIPK1	ENSG00000163349	0,74	0,715885919	0,48	0,65	0,22
Ependymal	FRMD6	ENSG00000139926	0,72	0,698921576	0,44	0,55	0,12
Ependymal	MORN1	ENSG00000116151	0,718	0,616216403	0,436	0,48	0,06
Ependymal	CLU	ENSG00000120885	0,903	1,542070405	0,806	0,97	0,55
Ependymal	TOB1	ENSG00000141232	0,737	0,970789292	0,474	0,59	0,17
Ependymal	CRLF1	ENSG00000006016	0,72	0,724152892	0,44	0,5	0,07
Ependymal	COL4A6	ENSG00000197565	0,712	0,711867116	0,424	0,44	0,01
Ependymal	SYNE1	ENSG00000131018	0,94	1,608089834	0,88	0,99	0,57
Ependymal	IFT140	ENSG00000187535	0,722	0,592561511	0,444	0,55	0,13
Ependymal	LRRC74B	ENSG00000187905	0,712	0,669499902	0,424	0,43	0,01
Ependymal	NSUN7	ENSG00000179299	0,713	0,660243492	0,426	0,45	0,03
Ependymal	LRRC46	ENSG00000141294	0,711	0,60428762	0,422	0,43	0
Ependymal	CCDC113	ENSG00000103021	0,714	0,634987121	0,428	0,46	0,04
Ependymal	CELSR1	ENSG00000075275	0,711	0,630760743	0,422	0,44	0,02
Ependymal	AC016705.2	ENSG00000259495	0,724	0,6932755	0,448	0,58	0,16
Ependymal	IFT43	ENSG00000119650	0,746	0,664232762	0,492	0,71	0,29
Ependymal	GALNT8	ENSG00000130035	0,722	0,699894268	0,444	0,54	0,12
Ependymal	FGFR1	ENSG00000077782	0,728	0,624436044	0,456	0,68	0,27
Ependymal	ASPH	ENSG00000198363	0,77	0,738238746	0,54	0,85	0,43
Ependymal	DSE	ENSG00000111817	0,751	0,763458773	0,502	0,75	0,33
Ependymal	FSIP1	ENSG00000150667	0,717	0,775854236	0,434	0,49	0,07
Ependymal	DENND6B	ENSG00000205593	0,719	0,656430826	0,438	0,51	0,1
Ependymal	FAT1	ENSG00000083857	0,72	0,732760378	0,44	0,57	0,16
Ependymal	LTBP1	ENSG00000049323	0,714	0,685973545	0,428	0,61	0,2
Ependymal	PALLD	ENSG00000129116	0,718	0,679147453	0,436	0,64	0,22
Ependymal	TGFB2	ENSG00000092969	0,705	0,643131914	0,41	0,5	0,09
Ependymal	MUSK	ENSG00000030304	0,707	0,733174412	0,414	0,44	0,03
Ependymal	ROR1	ENSG00000185483	0,705	0,772811759	0,41	0,52	0,11
Ependymal	CDC14A	ENSG00000079335	0,701	0,608458493	0,402	0,57	0,16

Ependymal	STXBP4	ENSG00000166263	0,728	0,683396658	0,456	0,66	0,25
Ependymal	CST3	ENSG00000101439	0,71	0,693113814	0,42	0,76	0,35
Ependymal	PIFO	ENSG00000173947	0,704	0,58585111	0,408	0,41	0,01
Ependymal	METRN	ENSG00000103260	0,744	0,74563816	0,488	0,75	0,34
Ependymal	LINC00907	ENSG00000267586	0,714	1,378390019	0,428	0,5	0,1
Ependymal	RALGPS2	ENSG00000116191	0,706	0,602823429	0,412	0,6	0,2
Ependymal	WDR86	ENSG00000187260	0,703	0,657435804	0,406	0,41	0,01
Ependymal	ANKUB1	ENSG00000206199	0,737	1,09747125	0,474	0,61	0,21
Ependymal	MIR4300HG	ENSG00000245832	0,719	1,224257668	0,438	0,57	0,17
Ependymal	CRNDE	ENSG00000245694	0,711	0,585693865	0,422	0,59	0,19
Ependymal	DGLUCY	ENSG00000133943	0,766	0,77518583	0,532	0,81	0,41
Ependymal	HIPK3	ENSG00000110422	0,78	0,782249061	0,56	0,83	0,43
Ependymal	TUBB4B	ENSG00000188229	0,723	0,890715418	0,446	0,58	0,18
Ependymal	NFIB	ENSG00000147862	0,755	0,659093294	0,51	0,91	0,51
Ependymal	LCLAT1	ENSG00000172954	0,719	0,64097075	0,438	0,62	0,22
Ependymal	BCO2	ENSG00000197580	0,719	0,599727082	0,438	0,6	0,21
Ependymal	SYNGAP1	ENSG00000197283	0,711	0,591158358	0,422	0,52	0,13
Ependymal	HSPD1	ENSG00000144381	0,739	0,814622848	0,478	0,7	0,3
Ependymal	UBE3D	ENSG00000118420	0,751	0,984241137	0,502	0,71	0,32
Ependymal	MAN1C1	ENSG00000117643	0,714	0,659369748	0,428	0,65	0,26
Ependymal	LINC00535	ENSG00000246662	0,701	0,598576535	0,402	0,49	0,1
Ependymal	KIAA0556	ENSG00000047578	0,736	0,674016418	0,472	0,71	0,32
Ependymal	ZFHX2	ENSG00000136367	0,714	0,591010544	0,428	0,59	0,21
Ependymal	C11orf49	ENSG00000149179	0,774	0,786111591	0,548	0,84	0,45
Ependymal	CAPS2	ENSG00000180881	0,743	0,644619797	0,486	0,83	0,44
Ependymal	SUGCT	ENSG00000175600	0,707	0,720597745	0,414	0,57	0,18
Ependymal	CNTRL	ENSG00000119397	0,732	0,648893405	0,464	0,74	0,35
Ependymal	IFT172	ENSG00000138002	0,744	0,675690507	0,488	0,73	0,35
Ependymal	RFX3-AS1	ENSG00000232104	0,722	0,650973064	0,444	0,76	0,38
Ependymal	CDKL3	ENSG00000006837	0,715	0,589283016	0,43	0,66	0,28
Ependymal	CCDC148	ENSG00000153237	0,706	0,678373604	0,412	0,57	0,18
Ependymal	DOCK7	ENSG00000116641	0,72	0,592611227	0,44	0,77	0,39
Ependymal	RHOXF1-AS1	ENSG00000258545	0,701	0,592826815	0,402	0,51	0,13
Ependymal	CCDC138	ENSG00000163006	0,707	0,656786417	0,414	0,61	0,24
Ependymal	TTLL5	ENSG00000119685	0,774	0,722091607	0,548	0,88	0,52
Ependymal	PHACTR1	ENSG00000112137	0,77	0,670021093	0,54	0,92	0,56
Ependymal	CMSS1	ENSG00000184220	0,752	0,898010977	0,504	0,8	0,46
Ependymal	ARNT2	ENSG00000172379	0,748	0,678066861	0,496	0,86	0,52
Ependymal	SRGAP3	ENSG00000196220	0,762	0,666706695	0,524	0,92	0,58
Ependymal	RFX3	ENSG00000080298	0,958	1,550950967	0,916	0,99	0,67
Ependymal	PTGES3	ENSG00000110958	0,759	0,871890276	0,518	0,81	0,49
Ependymal	ITGB8	ENSG00000105855	0,731	0,604959599	0,462	0,87	0,56
Ependymal	DPP6	ENSG00000130226	0,812	0,827587537	0,624	0,98	0,68
Ependymal	MAML2	ENSG00000184384	0,764	0,67282152	0,528	0,96	0,65
Ependymal	MAPK10	ENSG00000109339	0,922	1,231518389	0,844	0,99	0,69
Ependymal	TRPS1	ENSG00000104447	0,823	0,876366553	0,646	0,97	0,67
Ependymal	UBC	ENSG00000150991	0,764	0,856703618	0,528	0,86	0,56
Ependymal	CKB	ENSG00000166165	0,725	0,725297546	0,45	0,86	0,56
Ependymal	TLN2	ENSG00000171914	0,727	0,822715389	0,454	0,82	0,53
Ependymal	LIFR	ENSG00000113594	0,726	0,589247412	0,452	0,9	0,63
Ependymal	LDLRAD4	ENSG00000168675	0,796	0,700832933	0,592	0,96	0,69
Ependymal	EVI5	ENSG00000067208	0,734	0,602330892	0,468	0,86	0,6
Ependymal	MSI2	ENSG00000153944	0,936	1,420196003	0,872	0,99	0,73
Ependymal	PDE4DIP	ENSG00000178104	0,783	0,74275249	0,566	0,96	0,7
Ependymal	ARHGAP5	ENSG00000100852	0,736	0,593741266	0,472	0,89	0,64

Ependymal	MPDZ	ENSG00000107186	0,747	0,641731844	0,494	0,89	0,65
Ependymal	KAZN	ENSG00000189337	0,735	0,830717534	0,47	0,91	0,67
Ependymal	BBS9	ENSG00000122507	0,742	0,628588476	0,484	0,9	0,67
Ependymal	PPP1R12B	ENSG00000077157	0,876	1,076343031	0,752	0,97	0,74
Ependymal	DTNA	ENSG00000134769	0,837	0,799701127	0,674	0,99	0,76
Ependymal	AKAP9	ENSG00000127914	0,759	0,619817434	0,518	0,93	0,71
Ependymal	TMEM161B-AS1	ENSG00000247828	0,711	0,587948878	0,422	0,89	0,67
Ependymal	SSBP2	ENSG00000145687	0,776	0,664457187	0,552	0,96	0,75
Ependymal	NFIA	ENSG00000162599	0,803	0,682544109	0,606	0,98	0,82
Ependymal	MIR99AHG	ENSG00000215386	0,871	1,007117353	0,742	0,98	0,82
Ependymal	HSP90AA1	ENSG00000080824	0,839	1,413441761	0,678	0,96	0,83
Ependymal	WWOX	ENSG00000186153	0,84	0,855489244	0,68	0,99	0,88
CADPS2+ neurons	UNC13C	ENSG00000137766	0,99	2,777175102	0,98	0,99	0,1
CADPS2+ neurons	RBFOX3	ENSG00000167281	0,977	2,47934312	0,954	0,97	0,1
CADPS2+ neurons	ZNF385D	ENSG00000151789	0,985	3,208041293	0,97	0,98	0,15
CADPS2+ neurons	SYT1	ENSG00000067715	0,946	1,951045928	0,892	0,99	0,18
CADPS2+ neurons	CDH18	ENSG00000145526	0,975	2,523615503	0,95	0,99	0,19
CADPS2+ neurons	RELN	ENSG00000189056	0,947	2,31028535	0,894	0,92	0,11
CADPS2+ neurons	CAMK4	ENSG00000152495	0,962	2,487741773	0,924	0,94	0,15
CADPS2+ neurons	GALNT17	ENSG00000185274	0,955	2,076377322	0,91	0,95	0,16
CADPS2+ neurons	ZNF385B	ENSG00000144331	0,931	2,147834852	0,862	0,91	0,12
CADPS2+ neurons	GABRB2	ENSG00000145864	0,936	2,146970592	0,872	0,91	0,12
CADPS2+ neurons	SLIT3	ENSG00000184347	0,918	2,0997395	0,836	0,87	0,09
CADPS2+ neurons	KCNJ3	ENSG00000162989	0,954	2,181757234	0,908	0,94	0,16
CADPS2+ neurons	EPHA6	ENSG00000080224	0,916	1,893206344	0,832	0,91	0,14
CADPS2+ neurons	CA10	ENSG00000154975	0,927	1,863482614	0,854	0,94	0,17
CADPS2+ neurons	CADPS2	ENSG00000081803	0,982	2,605175186	0,964	0,98	0,21
CADPS2+ neurons	MCTP1	ENSG00000175471	0,947	2,105098657	0,894	0,94	0,17
CADPS2+ neurons	SPHKAP	ENSG00000153820	0,893	1,724963498	0,786	0,83	0,07
CADPS2+ neurons	ETV1	ENSG00000006468	0,913	1,984433417	0,826	0,86	0,1
CADPS2+ neurons	SRRM4	ENSG00000139767	0,915	1,889212739	0,83	0,86	0,11
CADPS2+ neurons	CNTN4	ENSG00000144619	0,904	1,542723997	0,808	0,93	0,18
CADPS2+ neurons	STXBP5L	ENSG00000145087	0,979	2,258784124	0,958	0,99	0,24
CADPS2+ neurons	SH3GL2	ENSG00000107295	0,932	2,018139739	0,864	0,92	0,17
CADPS2+ neurons	FSTL5	ENSG00000168843	0,984	2,648378905	0,968	0,98	0,24
CADPS2+ neurons	SNAP25	ENSG00000132639	0,97	2,093971667	0,94	0,98	0,24
CADPS2+ neurons	GRM4	ENSG00000124493	0,893	1,832618989	0,786	0,8	0,06
CADPS2+ neurons	RIMS2	ENSG00000176406	0,896	1,549625106	0,792	0,96	0,22
CADPS2+ neurons	ATP8A2	ENSG00000132932	0,923	1,766792193	0,846	0,93	0,2
CADPS2+ neurons	GRM1	ENSG00000152822	0,893	1,848514542	0,786	0,83	0,11
CADPS2+ neurons	RALYL	ENSG00000184672	0,953	1,993854351	0,906	0,99	0,27
CADPS2+ neurons	TRMT9B	ENSG00000250305	0,91	1,84491925	0,82	0,87	0,15
CADPS2+ neurons	SCN2A	ENSG00000136531	0,929	1,820666991	0,858	0,92	0,21
CADPS2+ neurons	CACNA1A	ENSG00000141837	0,97	2,003253922	0,94	0,99	0,29
CADPS2+ neurons	TRPM3	ENSG00000083067	0,861	1,041799208	0,722	0,97	0,27
CADPS2+ neurons	FGF14	ENSG00000102466	0,975	2,31710241	0,95	0,99	0,29
CADPS2+ neurons	SV2B	ENSG00000185518	0,87	1,829235518	0,74	0,77	0,07
CADPS2+ neurons	OPCML	ENSG00000183715	0,854	1,217549447	0,708	0,93	0,23
CADPS2+ neurons	AC007614.1	ENSG00000279249	0,859	1,770834481	0,718	0,73	0,04
CADPS2+ neurons	KCND2	ENSG00000184408	0,952	2,086957059	0,904	0,98	0,3
CADPS2+ neurons	RIMS1	ENSG00000079841	0,97	2,216184966	0,94	0,98	0,29
CADPS2+ neurons	GRIK2	ENSG00000164418	0,96	2,022130531	0,92	0,99	0,31
CADPS2+ neurons	PLCB4	ENSG00000101333	0,906	1,567689011	0,812	0,93	0,25
CADPS2+ neurons	RIT2	ENSG00000152214	0,875	1,977454083	0,75	0,8	0,12
CADPS2+ neurons	SRRM3	ENSG00000177679	0,865	1,39402854	0,73	0,83	0,15

CADPS2+ neurons	TRHDE	ENSG00000072657	0,858	1,634281126	0,716	0,77	0,09
CADPS2+ neurons	KCNIP4	ENSG00000185774	0,915	1,84229616	0,83	0,97	0,29
CADPS2+ neurons	ZFPM2	ENSG00000169946	0,942	2,020875624	0,884	0,97	0,3
CADPS2+ neurons	RYR2	ENSG00000198626	0,926	1,600233899	0,852	0,97	0,3
CADPS2+ neurons	UBASH3B	ENSG00000154127	0,882	1,777778513	0,764	0,82	0,15
CADPS2+ neurons	MYT1L	ENSG00000186487	0,837	1,200908307	0,674	0,84	0,18
CADPS2+ neurons	SLC35F4	ENSG00000151812	0,849	1,734475227	0,698	0,75	0,09
CADPS2+ neurons	CNKSR2	ENSG00000149970	0,896	1,76927157	0,792	0,86	0,2
CADPS2+ neurons	MTCL1	ENSG00000168502	0,911	1,830723157	0,822	0,87	0,21
CADPS2+ neurons	ARPP21	ENSG00000172995	0,881	1,493840122	0,762	0,9	0,25
CADPS2+ neurons	NMNAT2	ENSG00000157064	0,872	1,509145594	0,744	0,83	0,17
CADPS2+ neurons	TMEM178A	ENSG00000152154	0,871	1,490600331	0,742	0,81	0,17
CADPS2+ neurons	SYN2	ENSG00000157152	0,841	1,315237403	0,682	0,79	0,16
CADPS2+ neurons	ABLIM1	ENSG00000099204	0,913	1,578935198	0,826	0,94	0,31
CADPS2+ neurons	SYNPR	ENSG00000163630	0,826	1,596406008	0,652	0,7	0,07
CADPS2+ neurons	DLGAP1	ENSG00000170579	0,879	1,356443192	0,758	0,93	0,29
CADPS2+ neurons	TENM1	ENSG00000009694	0,853	1,69100763	0,706	0,78	0,15
CADPS2+ neurons	CNTN1	ENSG00000018236	0,876	1,327020006	0,752	0,97	0,35
CADPS2+ neurons	TLL1	ENSG00000038295	0,818	1,62893443	0,636	0,66	0,04
CADPS2+ neurons	CCSER1	ENSG00000184305	0,878	1,565657023	0,756	0,92	0,3
CADPS2+ neurons	EPHB1	ENSG00000154928	0,858	1,480898711	0,716	0,81	0,19
CADPS2+ neurons	PTPRR	ENSG00000153233	0,831	1,513183879	0,662	0,72	0,1
CADPS2+ neurons	MTUS2	ENSG00000132938	0,822	1,30860874	0,644	0,74	0,13
CADPS2+ neurons	MDGA1	ENSG00000112139	0,819	1,245227912	0,638	0,67	0,06
CADPS2+ neurons	ATP2B2	ENSG00000157087	0,854	1,369579412	0,708	0,83	0,23
CADPS2+ neurons	PATJ	ENSG00000132849	0,92	1,688138704	0,84	0,92	0,32
CADPS2+ neurons	PCLO	ENSG00000186472	0,944	1,761554965	0,888	0,97	0,37
CADPS2+ neurons	PDE3B	ENSG00000152270	0,841	1,473390184	0,682	0,8	0,21
CADPS2+ neurons	IL16	ENSG00000172349	0,803	1,379980625	0,606	0,63	0,05
CADPS2+ neurons	SEL1L3	ENSG00000091490	0,804	1,415429278	0,608	0,64	0,06
CADPS2+ neurons	ANK1	ENSG00000029534	0,814	1,385323876	0,628	0,69	0,11
CADPS2+ neurons	KSR2	ENSG00000171435	0,816	1,213782528	0,632	0,77	0,19
CADPS2+ neurons	FGF12	ENSG00000114279	0,788	0,900804714	0,576	0,82	0,24
CADPS2+ neurons	NDRG4	ENSG00000103034	0,83	1,347652309	0,66	0,73	0,15
CADPS2+ neurons	CLVS2	ENSG00000146352	0,812	1,542385605	0,624	0,67	0,1
CADPS2+ neurons	EPB41	ENSG00000159023	0,839	1,370986757	0,678	0,78	0,21
CADPS2+ neurons	UNC80	ENSG00000144406	0,811	1,109186903	0,622	0,8	0,23
CADPS2+ neurons	PLCXD3	ENSG00000182836	0,809	1,451589916	0,618	0,68	0,12
CADPS2+ neurons	PDE1A	ENSG00000115252	0,914	1,621042322	0,828	0,95	0,38
CADPS2+ neurons	MYRIP	ENSG00000170011	0,842	1,131650888	0,684	0,86	0,3
CADPS2+ neurons	FAT2	ENSG00000086570	0,782	1,368735206	0,564	0,57	0,01
CADPS2+ neurons	NRXN1	ENSG00000179915	0,932	1,542046815	0,864	1	0,44
CADPS2+ neurons	LINC01798	ENSG00000232046	0,781	1,447516188	0,562	0,57	0,01
CADPS2+ neurons	RUNX1T1	ENSG00000079102	0,847	1,387376059	0,694	0,85	0,3
CADPS2+ neurons	PAK5	ENSG00000101349	0,812	1,452446843	0,624	0,69	0,14
CADPS2+ neurons	NTRK3	ENSG00000140538	0,803	0,95600179	0,606	0,86	0,31
CADPS2+ neurons	SPTBN4	ENSG00000160460	0,82	1,14172363	0,64	0,8	0,26
CADPS2+ neurons	NRG1	ENSG00000157168	0,78	1,247321151	0,56	0,7	0,16
CADPS2+ neurons	MICAL2	ENSG00000133816	0,815	1,413465944	0,63	0,69	0,15
CADPS2+ neurons	OLFM3	ENSG00000118733	0,79	1,255049656	0,58	0,68	0,15
CADPS2+ neurons	TIAM1	ENSG00000156299	0,993	2,249162453	0,986	1	0,47
CADPS2+ neurons	RGS7	ENSG00000182901	0,907	1,521579769	0,814	0,96	0,43
CADPS2+ neurons	CELF4	ENSG00000101489	0,775	1,132802599	0,55	0,68	0,15
CADPS2+ neurons	RBFOX1	ENSG00000078328	0,939	1,659087428	0,878	1	0,47
CADPS2+ neurons	LINC00599	ENSG00000253230	0,787	1,20496658	0,574	0,63	0,1

CADPS2+ neurons	GRIN2A	ENSG00000183454	0,784	1,260847342	0,568	0,68	0,16
CADPS2+ neurons	CALN1	ENSG00000183166	0,923	1,613049895	0,846	0,97	0,45
CADPS2+ neurons	DGKG	ENSG00000058866	0,777	0,793123841	0,554	0,8	0,28
CADPS2+ neurons	AFF3	ENSG00000144218	0,84	1,133324606	0,68	0,9	0,38
CADPS2+ neurons	CDH22	ENSG00000149654	0,772	1,250915601	0,544	0,58	0,07
CADPS2+ neurons	ZNF521	ENSG00000198795	0,91	1,555541046	0,82	0,93	0,41
CADPS2+ neurons	VWC2	ENSG00000188730	0,775	1,345885903	0,55	0,63	0,11
CADPS2+ neurons	CADPS	ENSG00000163618	0,755	0,716869349	0,51	0,76	0,25
CADPS2+ neurons	XKR6	ENSG00000171044	0,837	1,243804748	0,674	0,88	0,38
CADPS2+ neurons	STMN2	ENSG00000104435	0,769	1,118692197	0,538	0,63	0,12
CADPS2+ neurons	NEBL	ENSG00000078114	0,779	0,818619524	0,558	0,88	0,37
CADPS2+ neurons	CAMK2B	ENSG00000058404	0,78	1,088973388	0,56	0,68	0,18
CADPS2+ neurons	TMEM266	ENSG00000169758	0,77	1,392710289	0,54	0,58	0,08
CADPS2+ neurons	PKIB	ENSG00000135549	0,764	1,239929415	0,528	0,57	0,07
CADPS2+ neurons	ZNF804A	ENSG00000170396	0,772	1,482431553	0,544	0,65	0,15
CADPS2+ neurons	EBF1	ENSG00000164330	0,757	1,043877149	0,514	0,65	0,15
CADPS2+ neurons	MAP2	ENSG00000078018	0,799	0,876222562	0,598	0,9	0,41
CADPS2+ neurons	PPFIA4	ENSG00000143847	0,769	1,217616583	0,538	0,59	0,1
CADPS2+ neurons	ZIC1	ENSG00000152977	0,766	1,081667899	0,532	0,64	0,15
CADPS2+ neurons	ZBTB18	ENSG00000179456	0,772	1,175107218	0,544	0,62	0,13
CADPS2+ neurons	NHSL2	ENSG00000204131	0,763	1,252097596	0,526	0,58	0,11
CADPS2+ neurons	FRY	ENSG00000073910	0,819	1,16009727	0,638	0,83	0,36
CADPS2+ neurons	CACNA1B	ENSG00000148408	0,74	0,829502995	0,48	0,66	0,18
CADPS2+ neurons	AKAP12	ENSG00000131016	0,766	1,04457593	0,532	0,66	0,19
CADPS2+ neurons	SNAP91	ENSG00000065609	0,799	1,045525401	0,598	0,81	0,34
CADPS2+ neurons	AC092957.1	ENSG00000243620	0,742	1,726616911	0,484	0,53	0,06
CADPS2+ neurons	MSRA	ENSG00000175806	0,967	1,924720338	0,934	0,98	0,51
CADPS2+ neurons	LHFPL6	ENSG00000183722	0,774	0,807292673	0,548	0,86	0,39
CADPS2+ neurons	GABBR2	ENSG00000136928	0,752	1,095051228	0,504	0,61	0,14
CADPS2+ neurons	C1orf21	ENSG00000116667	0,771	0,946298144	0,542	0,71	0,24
CADPS2+ neurons	TSPAN9	ENSG00000011105	0,751	1,135777672	0,502	0,58	0,11
CADPS2+ neurons	SCN8A	ENSG00000196876	0,771	1,022719919	0,542	0,69	0,23
CADPS2+ neurons	PCBP3	ENSG00000183570	0,779	1,02077101	0,558	0,71	0,25
CADPS2+ neurons	GRID2	ENSG00000152208	0,844	0,969150871	0,688	0,98	0,52
CADPS2+ neurons	CFAP299	ENSG00000197826	0,734	1,084444667	0,468	0,51	0,05
CADPS2+ neurons	GPR158	ENSG00000151025	0,802	1,26926028	0,604	0,78	0,32
CADPS2+ neurons	ARHGAP44	ENSG00000006740	0,758	1,096229211	0,516	0,66	0,2
CADPS2+ neurons	GRAMD1B	ENSG00000023171	0,774	1,068856908	0,548	0,71	0,26
CADPS2+ neurons	PDE10A	ENSG00000112541	0,773	1,258545359	0,546	0,72	0,27
CADPS2+ neurons	LRCH1	ENSG00000136141	0,767	0,855360081	0,534	0,75	0,3
CADPS2+ neurons	SGCZ	ENSG00000185053	0,731	1,041250763	0,462	0,64	0,2
CADPS2+ neurons	KCNH7	ENSG00000184611	0,735	1,225311505	0,47	0,57	0,13
CADPS2+ neurons	CACNB2	ENSG00000165995	0,736	0,768758949	0,472	0,73	0,29
CADPS2+ neurons	ADD2	ENSG00000075340	0,745	1,007405123	0,49	0,57	0,13
CADPS2+ neurons	IQSEC3	ENSG00000120645	0,738	1,02558318	0,476	0,54	0,11
CADPS2+ neurons	KCNK1	ENSG00000135750	0,781	1,14363409	0,562	0,71	0,27
CADPS2+ neurons	PLD5	ENSG00000180287	0,82	1,165399902	0,64	0,86	0,42
CADPS2+ neurons	KCND3	ENSG00000171385	0,752	1,126814758	0,504	0,64	0,21
CADPS2+ neurons	CDON	ENSG00000064309	0,744	1,188474489	0,488	0,55	0,12
CADPS2+ neurons	LIMA1	ENSG00000050405	0,795	1,347953085	0,59	0,7	0,27
CADPS2+ neurons	CCDC175	ENSG00000151838	0,726	1,131420882	0,452	0,49	0,06
CADPS2+ neurons	WSCD2	ENSG00000075035	0,726	1,025614162	0,452	0,48	0,05
CADPS2+ neurons	TUSC3	ENSG00000104723	0,739	0,975747557	0,478	0,58	0,15
CADPS2+ neurons	CLIP1	ENSG00000130779	0,82	1,138976672	0,64	0,81	0,38
CADPS2+ neurons	EXPH5	ENSG00000110723	0,718	1,044236687	0,436	0,48	0,06

CADPS2+ neurons	ARHGAP29	ENSG00000137962	0,717	0,658605438	0,434	0,57	0,14
CADPS2+ neurons	SEZ6L	ENSG00000100095	0,718	0,899611452	0,436	0,6	0,18
CADPS2+ neurons	ADAM22	ENSG00000008277	0,839	1,277336287	0,678	0,83	0,4
CADPS2+ neurons	KCNC1	ENSG00000129159	0,732	0,918286412	0,464	0,53	0,11
CADPS2+ neurons	ALS2	ENSG00000003393	0,782	1,172662254	0,564	0,69	0,27
CADPS2+ neurons	GPRIN3	ENSG00000185477	0,731	0,973825999	0,462	0,58	0,16
CADPS2+ neurons	ZFYVE28	ENSG00000159733	0,779	1,086869824	0,558	0,72	0,3
CADPS2+ neurons	MMP24	ENSG00000125966	0,736	1,081095847	0,472	0,54	0,13
CADPS2+ neurons	STXBP1	ENSG00000136854	0,777	1,003458479	0,554	0,73	0,31
CADPS2+ neurons	SYNE1	ENSG00000131018	0,942	1,664489256	0,884	0,98	0,57
CADPS2+ neurons	SHROOM3	ENSG00000138771	0,716	0,950792127	0,432	0,52	0,11
CADPS2+ neurons	PLCL2	ENSG00000154822	0,743	0,936467887	0,486	0,64	0,24
CADPS2+ neurons	SNAP25-AS1	ENSG00000227906	0,722	1,035959409	0,444	0,51	0,1
CADPS2+ neurons	DNM1	ENSG00000106976	0,727	0,874696028	0,454	0,59	0,19
CADPS2+ neurons	ADAMTS16	ENSG00000145536	0,706	1,077010064	0,412	0,43	0,02
CADPS2+ neurons	ST7	ENSG00000004866	0,802	1,125357485	0,604	0,79	0,39
CADPS2+ neurons	HCN1	ENSG00000164588	0,712	1,016921978	0,424	0,51	0,1
CADPS2+ neurons	RAPGEF4	ENSG00000091428	0,755	0,921849836	0,51	0,75	0,35
CADPS2+ neurons	SVEP1	ENSG00000165124	0,718	0,856917357	0,436	0,57	0,17
CADPS2+ neurons	CEP112	ENSG00000154240	0,729	0,898009373	0,458	0,68	0,28
CADPS2+ neurons	RASGRP1	ENSG00000172575	0,704	0,967515678	0,408	0,43	0,04
CADPS2+ neurons	MPP7	ENSG00000150054	0,712	1,0606733	0,424	0,48	0,08
CADPS2+ neurons	GALNT13	ENSG00000144278	0,82	1,006310929	0,64	0,91	0,51
CADPS2+ neurons	DAB1	ENSG00000173406	0,749	0,743740085	0,498	0,78	0,39
CADPS2+ neurons	CACNA1C	ENSG00000151067	0,717	0,5936623	0,434	0,75	0,36
CADPS2+ neurons	CDH10	ENSG00000040731	0,706	0,740237817	0,412	0,58	0,19
CADPS2+ neurons	TRIM9	ENSG00000100505	0,829	1,015675256	0,658	0,91	0,52
CADPS2+ neurons	CPE	ENSG00000109472	0,755	0,850678523	0,51	0,76	0,37
CADPS2+ neurons	GRIA4	ENSG00000152578	0,825	0,964462309	0,65	0,94	0,55
CADPS2+ neurons	GAP43	ENSG00000172020	0,714	0,994964158	0,428	0,52	0,13
CADPS2+ neurons	PIP5K1B	ENSG00000107242	0,721	1,121736975	0,442	0,55	0,16
CADPS2+ neurons	LIN7A	ENSG00000111052	0,712	0,837375128	0,424	0,53	0,15
CADPS2+ neurons	POLB	ENSG00000070501	0,719	0,873618733	0,438	0,53	0,15
CADPS2+ neurons	PPP3CA	ENSG00000138814	0,821	1,058364517	0,642	0,93	0,55
CADPS2+ neurons	ADAMTS18	ENSG00000140873	0,711	0,818088167	0,422	0,59	0,22
CADPS2+ neurons	RAP1GAP2	ENSG00000132359	0,714	0,906781899	0,428	0,55	0,18
CADPS2+ neurons	RORA	ENSG00000069667	0,784	0,791220539	0,568	0,95	0,58
CADPS2+ neurons	SPTB	ENSG00000070182	0,703	0,887366873	0,406	0,47	0,09
CADPS2+ neurons	CACNG2	ENSG00000166862	0,706	1,140100424	0,412	0,49	0,12
CADPS2+ neurons	BRINP1	ENSG00000078725	0,707	0,904045364	0,414	0,55	0,18
CADPS2+ neurons	CADM3	ENSG00000162706	0,703	0,853222729	0,406	0,49	0,13
CADPS2+ neurons	BMPER	ENSG00000164619	0,702	1,240819479	0,404	0,48	0,11
CADPS2+ neurons	DPF3	ENSG00000205683	0,757	0,846641078	0,514	0,75	0,39
CADPS2+ neurons	NRXN3	ENSG00000021645	0,871	1,031980454	0,742	1	0,64
CADPS2+ neurons	GLCE	ENSG00000138604	0,752	0,984112971	0,504	0,7	0,34
CADPS2+ neurons	PAG1	ENSG00000076641	0,731	0,734921218	0,462	0,71	0,35
CADPS2+ neurons	ST8SIA5	ENSG00000101638	0,701	0,973396765	0,402	0,49	0,14
CADPS2+ neurons	STK10	ENSG00000072786	0,705	0,883814314	0,41	0,53	0,18
CADPS2+ neurons	CAMK1D	ENSG00000183049	0,702	0,708878357	0,404	0,67	0,32
CADPS2+ neurons	DYNC1I1	ENSG00000158560	0,779	0,898698843	0,558	0,86	0,52
CADPS2+ neurons	SETBP1	ENSG00000152217	0,736	0,850032853	0,472	0,72	0,38
CADPS2+ neurons	UNC79	ENSG00000133958	0,728	0,791577882	0,456	0,79	0,45
CADPS2+ neurons	JAKMIP2	ENSG00000176049	0,842	1,050894358	0,684	0,92	0,6
CADPS2+ neurons	NEGR1	ENSG00000172260	0,842	1,107899666	0,684	0,95	0,63
CADPS2+ neurons	MAML3	ENSG00000196782	0,73	0,832636785	0,46	0,78	0,46

CADPS2+ neurons	NKAIN2	ENSG00000188580	0,74	0,700616497	0,48	0,97	0,66
CADPS2+ neurons	DPP6	ENSG00000130226	0,855	1,099819237	0,71	0,98	0,68
CADPS2+ neurons	KLHL3	ENSG00000146021	0,713	0,648685833	0,426	0,69	0,39
CADPS2+ neurons	PRKCZ	ENSG00000067606	0,722	0,785578973	0,444	0,65	0,35
CADPS2+ neurons	ATP2B1	ENSG00000070961	0,732	0,908466203	0,464	0,67	0,37
CADPS2+ neurons	FAM13A	ENSG00000138640	0,703	0,661217653	0,406	0,66	0,36
CADPS2+ neurons	MEIS1	ENSG00000143995	0,706	0,716552946	0,412	0,7	0,41
CADPS2+ neurons	NBEA	ENSG00000172915	0,811	0,990401087	0,622	0,88	0,6
CADPS2+ neurons	OXR1	ENSG00000164830	0,73	0,887552849	0,46	0,73	0,45
CADPS2+ neurons	CBLB	ENSG00000114423	0,744	0,832855499	0,488	0,73	0,45
CADPS2+ neurons	MICU1	ENSG00000107745	0,741	0,814045893	0,482	0,74	0,46
CADPS2+ neurons	SMYD3	ENSG00000185420	0,78	0,876703342	0,56	0,89	0,62
CADPS2+ neurons	KAZN	ENSG00000189337	0,757	0,66221684	0,514	0,95	0,67
CADPS2+ neurons	SRGAP3	ENSG00000196220	0,804	1,008070216	0,608	0,86	0,59
CADPS2+ neurons	TTC7B	ENSG00000165914	0,74	0,921853061	0,48	0,71	0,44
CADPS2+ neurons	FOXN3	ENSG00000053254	0,761	0,626064643	0,522	0,91	0,64
CADPS2+ neurons	GALNT7	ENSG00000109586	0,709	0,839344542	0,418	0,64	0,38
CADPS2+ neurons	ERC1	ENSG00000082805	0,855	1,007387547	0,71	0,97	0,7
CADPS2+ neurons	FUT9	ENSG00000172461	0,714	0,652529856	0,428	0,82	0,55
CADPS2+ neurons	KIF5C	ENSG00000168280	0,752	0,730467347	0,504	0,84	0,58
CADPS2+ neurons	PRKCE	ENSG00000171132	0,742	0,758957509	0,484	0,79	0,53
CADPS2+ neurons	MAP1B	ENSG00000131711	0,789	0,728825415	0,578	0,93	0,68
CADPS2+ neurons	TSPAN5	ENSG00000168785	0,797	0,889705729	0,594	0,91	0,65
CADPS2+ neurons	SPOCK1	ENSG00000152377	0,744	0,637341688	0,488	0,95	0,7
CADPS2+ neurons	PDE4DIP	ENSG00000178104	0,817	0,816033756	0,634	0,96	0,71
CADPS2+ neurons	RBFOX2	ENSG00000100320	0,737	0,714034663	0,474	0,81	0,56
CADPS2+ neurons	ANKS1B	ENSG00000185046	0,894	1,102245017	0,788	1	0,75
CADPS2+ neurons	CHD7	ENSG00000171316	0,76	0,862719905	0,52	0,83	0,59
CADPS2+ neurons	MAGI1	ENSG00000151276	0,871	1,038017737	0,742	0,98	0,74
CADPS2+ neurons	EPB41L3	ENSG00000082397	0,701	0,719897038	0,402	0,71	0,48
CADPS2+ neurons	AC124312.1	ENSG00000214265	0,73	0,616739448	0,46	0,83	0,61
CADPS2+ neurons	HECTD4	ENSG00000173064	0,739	0,653006008	0,478	0,83	0,62
CADPS2+ neurons	CADM1	ENSG00000182985	0,874	1,018239227	0,748	0,99	0,79
CADPS2+ neurons	CAMK2D	ENSG00000145349	0,719	0,667175024	0,438	0,79	0,6
CADPS2+ neurons	ANKRD36	ENSG00000135976	0,713	0,723485143	0,426	0,72	0,52
CADPS2+ neurons	ADGRB3	ENSG00000135298	0,939	1,261192088	0,878	0,99	0,81
CADPS2+ neurons	CUX1	ENSG00000257923	0,747	0,750673397	0,494	0,86	0,68
CADPS2+ neurons	GLS	ENSG00000115419	0,708	0,757521229	0,416	0,71	0,53
CADPS2+ neurons	MICAL3	ENSG00000243156	0,721	0,67769632	0,442	0,82	0,65
CADPS2+ neurons	BICD1	ENSG00000151746	0,713	0,662328205	0,426	0,77	0,6
CADPS2+ neurons	WAC	ENSG00000095787	0,739	0,657161561	0,478	0,84	0,68
CADPS2+ neurons	RABGAP1L	ENSG00000152061	0,764	0,756795375	0,528	0,91	0,76
CADPS2+ neurons	STXBP5	ENSG00000164506	0,703	0,720059669	0,406	0,74	0,6
CADPS2+ neurons	NFIA	ENSG00000162599	0,789	0,739417036	0,578	0,96	0,82
CADPS2+ neurons	JMJD1C	ENSG00000171988	0,816	0,877343567	0,632	0,94	0,86
CADPS2+ neurons	MED13L	ENSG00000123066	0,719	0,621740245	0,438	0,88	0,81
GABA	SPHKAP	ENSG00000153820	0,989	2,647609868	0,978	0,99	0,06
GABA	SYNPR	ENSG00000163630	0,986	2,686348206	0,972	0,98	0,06
GABA	OTX2-AS1	ENSG00000248550	0,978	2,573779936	0,956	0,96	0,05
GABA	CHRM2	ENSG00000181072	0,979	2,371909041	0,958	0,97	0,06
GABA	ZMAT4	ENSG00000165061	0,986	2,283799187	0,972	0,99	0,08
GABA	GAD2	ENSG00000136750	0,964	1,919867344	0,928	0,95	0,05
GABA	NYAP2	ENSG00000144460	0,982	2,298007962	0,964	0,97	0,09
GABA	UNC13C	ENSG00000137766	0,969	2,172139611	0,938	0,97	0,09
GABA	GALNT14	ENSG00000158089	0,964	2,020474157	0,928	0,94	0,06

GABA	NELL1	ENSG00000165973	0,961	2,360182511	0,922	0,95	0,08
GABA	LINGO2	ENSG00000174482	0,959	2,11564076	0,918	0,98	0,13
GABA	GALNTL6	ENSG00000174473	0,984	2,906185639	0,968	0,99	0,14
GABA	GRIK1	ENSG00000171189	0,998	3,394927869	0,996	1	0,15
GABA	GULP1	ENSG00000144366	0,952	1,850886341	0,904	0,94	0,09
GABA	NR2F2-AS1	ENSG00000247809	0,961	1,977978347	0,922	0,97	0,13
GABA	UNC5D	ENSG00000156687	0,948	1,87900968	0,896	0,98	0,14
GABA	SYN3	ENSG00000185666	0,98	2,293378963	0,96	0,99	0,15
GABA	ZNF385D	ENSG00000151789	0,956	1,732230676	0,912	0,98	0,14
GABA	CELF4	ENSG00000101489	0,944	1,602257529	0,888	0,97	0,14
GABA	BTBD11	ENSG00000151136	0,966	2,015712317	0,932	0,96	0,13
GABA	LINC01414	ENSG00000253554	0,947	1,892171925	0,894	0,94	0,11
GABA	SYT1	ENSG00000067715	0,99	2,753031609	0,98	1	0,17
GABA	SRRM3	ENSG00000177679	0,951	1,562572223	0,902	0,97	0,14
GABA	KIT	ENSG00000157404	0,927	1,50867724	0,854	0,88	0,05
GABA	GRIN1	ENSG00000176884	0,943	1,537260097	0,886	0,96	0,13
GABA	RORB	ENSG00000198963	0,939	1,699842726	0,878	0,94	0,11
GABA	LINC01210	ENSG00000239513	0,915	1,174313518	0,83	0,84	0,01
GABA	PTCHD4	ENSG00000244694	0,927	1,478311548	0,854	0,91	0,08
GABA	SYN2	ENSG00000157152	0,966	2,039598346	0,932	0,97	0,15
GABA	SAMD5	ENSG00000203727	0,92	1,47586386	0,84	0,9	0,08
GABA	CUX2	ENSG00000111249	0,922	1,449598794	0,844	0,9	0,08
GABA	CPNE4	ENSG00000196353	0,93	1,729282361	0,86	0,91	0,1
GABA	FRMPD4	ENSG00000169933	0,966	2,107815977	0,932	0,98	0,17
GABA	CNTN4	ENSG00000144619	0,969	2,244684221	0,938	0,99	0,18
GABA	GAD1	ENSG00000128683	0,925	1,513654713	0,85	0,9	0,08
GABA	GABBR2	ENSG00000136928	0,93	1,444644685	0,86	0,94	0,13
GABA	NRG1	ENSG00000157168	0,932	2,044739082	0,864	0,95	0,15
GABA	DOK6	ENSG00000206052	0,954	1,787237585	0,908	0,97	0,17
GABA	SLC4A10	ENSG00000144290	0,941	1,620011025	0,882	0,95	0,15
GABA	SGCZ	ENSG00000185053	0,943	1,858623351	0,886	0,98	0,19
GABA	MYT1L	ENSG00000186487	0,902	1,298351242	0,804	0,97	0,17
GABA	CNTNAP5	ENSG00000155052	0,968	2,340838035	0,936	0,99	0,19
GABA	KCNJ6	ENSG00000157542	0,921	1,33508856	0,842	0,9	0,11
GABA	GRIN2B	ENSG00000273079	0,933	1,518988977	0,866	0,95	0,15
GABA	VAV3	ENSG00000134215	0,912	1,474312763	0,824	0,88	0,09
GABA	PRICKLE1	ENSG00000139174	0,929	1,586069816	0,858	0,91	0,13
GABA	GRIA1	ENSG00000155511	0,891	1,178327323	0,782	0,92	0,13
GABA	RIMS2	ENSG00000176406	0,938	1,711792365	0,876	0,99	0,21
GABA	TOX	ENSG00000198846	0,942	1,682040428	0,884	0,97	0,19
GABA	GRIP2	ENSG00000144596	0,911	1,315199936	0,822	0,84	0,06
GABA	PAK3	ENSG00000077264	0,906	1,341331338	0,812	0,94	0,15
GABA	KCNJ3	ENSG00000162989	0,926	1,485582623	0,852	0,94	0,16
GABA	ROBO2	ENSG00000185008	0,972	2,491631027	0,944	1	0,22
GABA	CDH13	ENSG00000140945	0,956	1,797938547	0,912	0,98	0,2
GABA	LYPD6B	ENSG00000150556	0,897	1,257055456	0,794	0,82	0,04
GABA	KIAA1549L	ENSG00000110427	0,924	1,404823164	0,848	0,92	0,14
GABA	GRM5	ENSG00000168959	0,955	1,905480605	0,91	0,99	0,21
GABA	OPCML	ENSG00000183715	0,915	1,529749488	0,83	0,99	0,22
GABA	SHANK2	ENSG00000162105	0,933	1,495582205	0,866	0,94	0,17
GABA	CACNA1B	ENSG00000148408	0,888	1,163461345	0,776	0,95	0,18
GABA	RBFOX3	ENSG00000167281	0,898	1,157118278	0,796	0,86	0,09
GABA	MIR124-2HG	ENSG00000254377	0,906	1,249970729	0,812	0,85	0,08
GABA	AFF2	ENSG00000155966	0,897	1,237364955	0,794	0,85	0,08
GABA	IGF1	ENSG00000017427	0,886	1,200808043	0,772	0,79	0,02

GABA	PDZRN3	ENSG00000121440	0,933	1,649977028	0,866	0,95	0,18
GABA	FOXP2	ENSG00000128573	0,904	1,387317363	0,808	0,94	0,18
GABA	ATP8A2	ENSG00000132932	0,91	1,38169639	0,82	0,96	0,2
GABA	FAT3	ENSG00000165323	0,955	1,796782432	0,91	0,99	0,22
GABA	GUCY1A1	ENSG00000164116	0,903	1,309816995	0,806	0,86	0,1
GABA	AL033504.1	ENSG00000227681	0,889	1,339871874	0,778	0,84	0,08
GABA	GABRB3	ENSG00000166206	0,932	1,513750082	0,864	0,95	0,19
GABA	RAB3C	ENSG00000152932	0,909	1,350690844	0,818	0,92	0,16
GABA	KSR2	ENSG00000171435	0,906	1,294100071	0,812	0,94	0,18
GABA	LRFN5	ENSG00000165379	0,898	1,290413426	0,796	0,95	0,19
GABA	CADPS	ENSG00000163618	0,991	2,403798834	0,982	1	0,24
GABA	PAK5	ENSG00000101349	0,907	1,255947147	0,814	0,89	0,13
GABA	CA10	ENSG00000154975	0,887	1,341440112	0,774	0,92	0,16
GABA	LRFN2	ENSG00000156564	0,911	1,426294635	0,822	0,88	0,12
GABA	DLGAP2	ENSG00000198010	0,878	1,113955463	0,756	0,9	0,14
GABA	RELN	ENSG00000189056	0,88	1,122523983	0,76	0,86	0,11
GABA	AMPH	ENSG00000078053	0,901	1,182339531	0,802	0,91	0,16
GABA	PTPRN2	ENSG00000155093	0,914	1,334048527	0,828	0,97	0,23
GABA	RGS6	ENSG00000182732	0,914	1,582186237	0,828	0,94	0,19
GABA	PDE3A	ENSG00000172572	0,886	1,291455315	0,772	0,87	0,12
GABA	CELF5	ENSG00000161082	0,882	1,02414637	0,764	0,87	0,13
GABA	OLFM3	ENSG00000118733	0,893	1,279052469	0,786	0,89	0,14
GABA	XKR4	ENSG00000206579	0,882	1,225444028	0,764	0,93	0,18
GABA	B4GALT6	ENSG00000118276	0,908	1,324166185	0,816	0,86	0,12
GABA	PTPRO	ENSG00000151490	0,892	1,350520964	0,784	0,87	0,13
GABA	LAMB1	ENSG00000091136	0,882	1,057593932	0,764	0,8	0,06
GABA	GREM2	ENSG00000180875	0,881	1,263993869	0,762	0,79	0,05
GABA	GRIN2A	ENSG00000183454	0,909	1,667478628	0,818	0,89	0,15
GABA	NR2F2	ENSG00000185551	0,873	1,060381371	0,746	0,82	0,08
GABA	SNAP25	ENSG00000132639	0,943	1,622563451	0,886	0,97	0,23
GABA	RALYL	ENSG00000184672	0,909	1,426153167	0,818	0,99	0,26
GABA	EPHA4	ENSG00000116106	0,876	1,07758026	0,752	0,85	0,11
GABA	SNTG1	ENSG00000147481	0,848	0,958452766	0,696	0,93	0,19
GABA	STXBP5L	ENSG00000145087	0,893	1,234952586	0,786	0,97	0,24
GABA	PCBP3	ENSG00000183570	0,958	1,858586875	0,916	0,97	0,24
GABA	ELMOD1	ENSG00000110675	0,9	1,221212582	0,8	0,89	0,16
GABA	FAM135B	ENSG00000147724	0,939	1,459690342	0,878	0,96	0,23
GABA	TAFA2	ENSG00000198673	0,905	1,523490288	0,81	0,94	0,22
GABA	EFNA5	ENSG00000184349	0,88	1,351668959	0,76	0,88	0,16
GABA	ATP2B2	ENSG00000157087	0,923	1,448700456	0,846	0,94	0,22
GABA	NHS	ENSG00000188158	0,876	1,092922757	0,752	0,88	0,16
GABA	IGSF3	ENSG00000143061	0,872	1,019742463	0,744	0,77	0,05
GABA	LYPD6	ENSG00000187123	0,863	1,077175376	0,726	0,78	0,06
GABA	KHDRBS2	ENSG00000112232	0,929	1,584325041	0,858	0,96	0,25
GABA	FLRT2	ENSG00000185070	0,878	1,118983491	0,756	0,92	0,21
GABA	KCNIP4	ENSG00000185774	0,991	2,87256816	0,982	1	0,29
GABA	DLGAP1	ENSG00000170579	0,992	2,839151733	0,984	1	0,29
GABA	TRPC5	ENSG00000072315	0,867	1,244012597	0,734	0,8	0,09
GABA	SYT7	ENSG00000011347	0,866	0,898775844	0,732	0,78	0,07
GABA	PTPRT	ENSG00000196090	0,876	1,655021039	0,752	0,86	0,15
GABA	NOL4	ENSG00000101746	0,889	1,174154619	0,778	0,93	0,22
GABA	GRM7	ENSG00000196277	0,851	1,005816243	0,702	0,94	0,23
GABA	ANKRD30BL	ENSG00000163046	0,85	0,992414633	0,7	0,88	0,17
GABA	FGF14	ENSG00000102466	0,935	1,69958546	0,87	0,99	0,29
GABA	SCN2A	ENSG00000136531	0,865	1,010418904	0,73	0,91	0,2

GABA	KCTD16	ENSG00000183775	0,898	1,376447679	0,796	0,93	0,22
GABA	ANKRD34C-AS1	ENSG00000259234	0,864	1,085746487	0,728	0,79	0,08
GABA	HS3ST2	ENSG00000122254	0,858	1,095425728	0,716	0,74	0,04
GABA	KCND2	ENSG00000184408	0,957	2,059504723	0,914	0,99	0,29
GABA	RGS7BP	ENSG00000186479	0,873	1,122198867	0,746	0,81	0,11
GABA	CHD5	ENSG00000116254	0,851	0,816209489	0,702	0,81	0,1
GABA	SLC2A13	ENSG00000151229	0,896	1,201517465	0,792	0,94	0,24
GABA	ANK1	ENSG00000029534	0,853	0,918005087	0,706	0,8	0,1
GABA	PLCB4	ENSG00000101333	0,902	1,302562637	0,804	0,95	0,25
GABA	LRRTM4	ENSG00000176204	0,905	1,458041991	0,81	1	0,3
GABA	GABRB2	ENSG00000145864	0,847	0,99119138	0,694	0,82	0,12
GABA	ZFPM2	ENSG00000169946	0,942	1,714288768	0,884	0,99	0,29
GABA	TMEM108	ENSG00000144868	0,952	1,749097426	0,904	0,97	0,28
GABA	SYNDIG1L	ENSG00000183379	0,853	0,928974568	0,706	0,72	0,02
GABA	SLC8A1	ENSG00000183023	0,934	1,59564252	0,868	1	0,3
GABA	SLC6A11	ENSG00000132164	0,842	0,745199513	0,684	0,82	0,12
GABA	IQSEC3	ENSG00000120645	0,859	0,922125628	0,718	0,8	0,1
GABA	B3GLCT	ENSG00000187676	0,855	0,946947683	0,71	0,81	0,11
GABA	OSBPL6	ENSG00000079156	0,92	1,520107822	0,84	0,94	0,24
GABA	CCSER1	ENSG00000184305	0,92	1,49222058	0,84	0,99	0,29
GABA	CDH12	ENSG00000154162	0,896	1,802703624	0,792	0,88	0,18
GABA	ADGRB1	ENSG00000181790	0,865	0,963464401	0,73	0,82	0,12
GABA	VSNL1	ENSG00000163032	0,847	0,905317336	0,694	0,8	0,11
GABA	ARHGAP44	ENSG00000006740	0,869	1,037249787	0,738	0,89	0,2
GABA	FRMD3	ENSG00000172159	0,865	0,956286613	0,73	0,87	0,18
GABA	PCDH7	ENSG00000169851	0,886	1,26323873	0,772	0,97	0,29
GABA	NPAS2	ENSG00000170485	0,863	0,972014836	0,726	0,92	0,23
GABA	DSCAM	ENSG00000171587	0,921	1,456355375	0,842	1	0,31
GABA	CNKSR2	ENSG00000149970	0,871	1,167768549	0,742	0,88	0,19
GABA	SLC8A3	ENSG00000100678	0,846	0,865627549	0,692	0,83	0,15
GABA	SH3GL2	ENSG00000107295	0,87	1,292463084	0,74	0,85	0,17
GABA	ATRNL1	ENSG00000107518	0,833	0,860479784	0,666	0,9	0,22
GABA	SRRM4	ENSG00000139767	0,847	0,976785024	0,694	0,78	0,1
GABA	MIAT	ENSG00000225783	0,842	0,876893558	0,684	0,82	0,14
GABA	WNK2	ENSG00000165238	0,838	0,83892308	0,676	0,85	0,18
GABA	ARHGEF33	ENSG00000214694	0,846	0,925283923	0,692	0,73	0,05
GABA	SCN3A	ENSG00000153253	0,825	0,809945183	0,65	0,85	0,17
GABA	SEZ6L	ENSG00000100095	0,824	0,808260133	0,648	0,85	0,17
GABA	VSTM2L	ENSG00000132821	0,848	1,017057195	0,696	0,74	0,07
GABA	CACNA1D	ENSG00000157388	0,955	1,94224382	0,91	0,96	0,29
GABA	NSG2	ENSG00000170091	0,853	1,012535087	0,706	0,81	0,14
GABA	SV2C	ENSG00000122012	0,843	1,159715455	0,686	0,73	0,06
GABA	BCL11A	ENSG00000119866	0,838	0,85578602	0,676	0,73	0,06
GABA	PLCH1	ENSG00000114805	0,835	0,902484946	0,67	0,78	0,11
GABA	EPHA3	ENSG00000044524	0,838	1,025617998	0,676	0,77	0,11
GABA	JPH4	ENSG00000092051	0,839	0,841227784	0,678	0,79	0,12
GABA	AGBL4	ENSG00000186094	0,832	0,86935489	0,664	0,93	0,27
GABA	EML6	ENSG00000214595	0,886	1,215620322	0,772	0,91	0,24
GABA	SCN8A	ENSG00000196876	0,867	1,036023212	0,734	0,89	0,22
GABA	CDH10	ENSG00000040731	0,847	1,050027343	0,694	0,85	0,18
GABA	FAM155A	ENSG00000204442	0,959	1,861710595	0,918	1	0,34
GABA	SLC12A5	ENSG00000124140	0,847	0,979615787	0,694	0,75	0,08
GABA	FBN2	ENSG00000138829	0,836	0,968938244	0,672	0,71	0,05
GABA	PLCXD3	ENSG00000182836	0,836	0,957609471	0,672	0,77	0,11

GABA	STXBP5-AS1	ENSG00000233452	0,843	1,057201286	0,686	0,83	0,17
GABA	ADCY8	ENSG00000155897	0,832	0,843447485	0,664	0,87	0,21
GABA	OTX2	ENSG00000165588	0,831	0,837022813	0,662	0,68	0,02
GABA	RYR2	ENSG00000198626	0,906	1,72491355	0,812	0,95	0,29
GABA	LINC00599	ENSG00000253230	0,84	0,853693711	0,68	0,75	0,09
GABA	SORBS2	ENSG00000154556	0,819	0,720597173	0,638	0,9	0,24
GABA	SIPA1L2	ENSG00000116991	0,869	1,062183248	0,738	0,88	0,23
GABA	SPTBN4	ENSG00000160460	0,856	0,97264885	0,712	0,9	0,25
GABA	GALNT18	ENSG00000110328	0,851	0,854746673	0,702	0,9	0,25
GABA	TSPAN18	ENSG00000157570	0,828	0,783538634	0,656	0,7	0,05
GABA	CACNA1E	ENSG00000198216	0,814	0,713433734	0,628	0,81	0,15
GABA	KIRREL1	ENSG00000183853	0,828	0,757996409	0,656	0,71	0,06
GABA	CAMK2B	ENSG00000058404	0,828	0,833711541	0,656	0,83	0,18
GABA	CACHD1	ENSG00000158966	0,845	0,988067465	0,69	0,88	0,23
GABA	NCALD	ENSG00000104490	0,844	1,012550422	0,688	0,83	0,18
GABA	CACNB4	ENSG00000182389	0,835	0,995904634	0,67	0,76	0,11
GABA	LDB2	ENSG00000169744	0,833	1,006503329	0,666	0,83	0,19
GABA	CACNA1A	ENSG00000141837	0,87	1,313194694	0,74	0,93	0,28
GABA	SDK1	ENSG00000146555	0,864	1,476696257	0,728	0,91	0,26
GABA	MDGA2	ENSG00000139915	0,949	1,728672957	0,898	0,99	0,35
GABA	SYT16	ENSG00000139973	0,819	0,792259878	0,638	0,81	0,16
GABA	UNC80	ENSG00000144406	0,797	0,654157993	0,594	0,87	0,23
GABA	ADARB1	ENSG00000197381	0,853	1,001188954	0,706	0,82	0,18
GABA	PLCB1	ENSG00000182621	0,957	1,97142274	0,914	0,99	0,35
GABA	ZEB1	ENSG00000148516	0,922	1,356258245	0,844	0,99	0,35
GABA	GPM6A	ENSG00000150625	0,89	1,240226498	0,78	0,98	0,34
GABA	SIDT1	ENSG00000072858	0,824	0,79454125	0,648	0,76	0,12
GABA	GATA3	ENSG00000107485	0,82	0,69200817	0,64	0,66	0,02
GABA	PHACTR2	ENSG00000112419	0,838	0,888664568	0,676	0,86	0,23
GABA	LIN7A	ENSG00000111052	0,815	0,727567393	0,63	0,77	0,14
GABA	NRSN1	ENSG00000152954	0,825	0,811313907	0,65	0,74	0,1
GABA	ANTXR1	ENSG00000169604	0,824	0,810049999	0,648	0,84	0,21
GABA	SCN1A	ENSG00000144285	0,792	0,669891802	0,584	0,84	0,2
GABA	SNRPN	ENSG00000128739	0,844	0,943297332	0,688	0,9	0,27
GABA	CNTN5	ENSG00000149972	0,816	0,765440942	0,632	0,78	0,15
GABA	CSMD3	ENSG00000164796	0,844	0,93530077	0,688	0,98	0,35
GABA	DNM1	ENSG00000106976	0,827	0,855773332	0,654	0,81	0,18
GABA	GUCY1A2	ENSG00000152402	0,82	0,904866289	0,64	0,83	0,21
GABA	HS6ST3	ENSG00000185352	0,811	0,971360303	0,622	0,83	0,2
GABA	ASIC4	ENSG00000072182	0,814	0,711803981	0,628	0,67	0,04
GABA	CACNA1C	ENSG00000151067	0,901	1,244960428	0,802	0,98	0,35
GABA	PPM1E	ENSG00000175175	0,855	0,997258103	0,71	0,91	0,28
GABA	DLGAP3	ENSG00000116544	0,824	0,749269244	0,648	0,69	0,07
GABA	AKAP12	ENSG00000131016	0,816	0,694857369	0,632	0,81	0,18
GABA	PRSS12	ENSG00000164099	0,815	0,820137223	0,63	0,64	0,02
GABA	KCNIP2	ENSG00000120049	0,818	0,733758117	0,636	0,69	0,06
GABA	CAMK4	ENSG00000152495	0,815	0,837783471	0,63	0,77	0,14
GABA	CASC15	ENSG00000272168	0,823	0,752566565	0,646	0,81	0,18
GABA	NMNAT2	ENSG00000157064	0,796	0,667737757	0,592	0,79	0,17
GABA	CNTN1	ENSG00000018236	0,792	0,695073684	0,584	0,96	0,34
GABA	CASR	ENSG00000036828	0,812	0,952282901	0,624	0,63	0,01
GABA	SEZ6	ENSG00000063015	0,819	0,802161638	0,638	0,69	0,07
GABA	DDAH1	ENSG00000153904	0,819	0,798536439	0,638	0,81	0,19
GABA	GRAMD1B	ENSG00000023171	0,84	0,924342236	0,68	0,87	0,25
GABA	GUCY1B1	ENSG00000061918	0,821	0,788738154	0,642	0,75	0,13

GABA	SLC16A10	ENSG00000112394	0,818	0,840409555	0,636	0,7	0,09
GABA	CACNA1G	ENSG00000006283	0,814	0,721115131	0,628	0,68	0,06
GABA	CLVS2	ENSG00000146352	0,812	0,728424462	0,624	0,71	0,09
GABA	SV2A	ENSG00000159164	0,835	0,981389959	0,67	0,8	0,18
GABA	ADD2	ENSG00000075340	0,81	0,732999698	0,62	0,74	0,12
GABA	SLC38A1	ENSG00000111371	0,819	0,754240776	0,638	0,85	0,23
GABA	TENM3	ENSG00000218336	0,803	0,760257487	0,606	0,83	0,21
GABA	ERC2	ENSG00000187672	0,925	1,415890217	0,85	0,97	0,36
GABA	AC092691.1	ENSG00000239268	0,864	1,101518318	0,728	0,98	0,36
GABA	CLSTN3	ENSG00000139182	0,815	0,774949141	0,63	0,72	0,11
GABA	GSG1L	ENSG00000169181	0,805	0,731114495	0,61	0,73	0,12
GABA	PPP4R4	ENSG00000119698	0,806	0,673374201	0,612	0,76	0,15
GABA	ALK	ENSG00000171094	0,821	0,859444851	0,642	0,84	0,23
GABA	DOK5	ENSG00000101134	0,812	0,802382009	0,624	0,74	0,13
GABA	SYBU	ENSG00000147642	0,794	0,649193671	0,588	0,79	0,19
GABA	NRG3	ENSG00000185737	0,887	1,27568676	0,774	1	0,39
GABA	PGM2L1	ENSG00000165434	0,816	0,834121898	0,632	0,73	0,12
GABA	RIMBP2	ENSG00000060709	0,811	0,737796689	0,622	0,76	0,16
GABA	TRMT9B	ENSG00000250305	0,81	0,79638832	0,62	0,75	0,14
GABA	PPP1R14C	ENSG00000198729	0,808	0,718161903	0,616	0,68	0,07
GABA	GPR158	ENSG00000151025	0,873	1,13629373	0,746	0,92	0,31
GABA	LINC01122	ENSG00000233723	0,819	1,046298261	0,638	0,82	0,21
GABA	SCG2	ENSG00000171951	0,81	0,856580982	0,62	0,71	0,11
GABA	GRM4	ENSG00000124493	0,808	0,655860847	0,616	0,66	0,05
GABA	SMAD9	ENSG00000120693	0,821	0,776709155	0,642	0,81	0,21
GABA	AP001347.1	ENSG00000224905	0,809	0,808088143	0,618	0,78	0,17
GABA	KCNQ2	ENSG00000075043	0,805	0,683611613	0,61	0,72	0,12
GABA	CDH8	ENSG00000150394	0,883	1,232462865	0,766	0,92	0,32
GABA	BASP1	ENSG00000176788	0,796	0,710196535	0,592	0,82	0,22
GABA	HTR2A	ENSG00000102468	0,804	0,721709668	0,608	0,64	0,03
GABA	PLAGL1	ENSG00000118495	0,801	0,667463684	0,602	0,72	0,12
GABA	CSMD1	ENSG00000183117	0,923	1,740636952	0,846	0,99	0,39
GABA	ZEB1-AS1	ENSG00000237036	0,802	0,810352511	0,604	0,69	0,09
GABA	N4BP2	ENSG00000078177	0,808	0,740257969	0,616	0,75	0,15
GABA	TOX2	ENSG00000124191	0,8	0,717376893	0,6	0,73	0,13
GABA	LINC02253	ENSG00000259485	0,8	0,862162275	0,6	0,61	0,01
GABA	EPHA6	ENSG00000080224	0,787	0,65503902	0,574	0,73	0,13
GABA	MAGI3	ENSG00000081026	0,861	1,070791565	0,722	0,92	0,32
GABA	RTN4RL1	ENSG00000185924	0,802	0,701027074	0,604	0,65	0,05
GABA	CEP112	ENSG00000154240	0,863	1,397419275	0,726	0,87	0,27
GABA	CDR2	ENSG00000140743	0,826	0,839853815	0,652	0,86	0,27
GABA	AL390957.1	ENSG00000285280	0,809	1,192740506	0,618	0,67	0,07
GABA	KIFC3	ENSG00000140859	0,825	0,837922821	0,65	0,82	0,23
GABA	PARP8	ENSG00000151883	0,816	0,777596742	0,632	0,86	0,26
GABA	GPC6	ENSG00000183098	0,827	1,322102983	0,654	0,81	0,21
GABA	EPB41	ENSG00000159023	0,792	0,668625179	0,584	0,8	0,21
GABA	PACRG	ENSG00000112530	0,821	0,966986771	0,642	0,83	0,23
GABA	SLC27A6	ENSG00000113396	0,81	1,089674437	0,62	0,7	0,11
GABA	SNAP91	ENSG00000065609	0,836	0,895769717	0,672	0,92	0,33
GABA	KLHL23	ENSG00000213160	0,816	0,734835638	0,632	0,82	0,23
GABA	KCNC1	ENSG00000129159	0,806	0,742173224	0,612	0,7	0,11
GABA	RBMS3	ENSG00000144642	0,791	0,703126089	0,582	0,77	0,18
GABA	CDH18	ENSG00000145526	0,784	0,688645402	0,568	0,77	0,18
GABA	MINAR1	ENSG00000169330	0,798	0,656727239	0,596	0,64	0,05
GABA	FMN2	ENSG00000155816	0,816	0,695077046	0,632	0,93	0,34

GABA	AC016717.2	ENSG00000273301	0,798	0,657741315	0,596	0,61	0,02
GABA	C1orf21	ENSG00000116667	0,794	0,673583839	0,588	0,82	0,23
GABA	PAM	ENSG00000145730	0,783	0,633454247	0,566	0,87	0,28
GABA	FRY	ENSG00000073910	0,85	0,951362935	0,7	0,94	0,35
GABA	ANKRD6	ENSG00000135299	0,792	0,68222377	0,584	0,76	0,17
GABA	CARMIL1	ENSG00000079691	0,783	0,617511229	0,566	0,81	0,23
GABA	HTR1E	ENSG00000168830	0,794	0,791575245	0,588	0,63	0,05
GABA	RNF150	ENSG00000170153	0,788	0,66556317	0,576	0,83	0,25
GABA	RAPGEF4	ENSG00000091428	0,813	0,759317975	0,626	0,93	0,34
GABA	MYH10	ENSG00000133026	0,795	0,697405935	0,59	0,78	0,2
GABA	GABRG2	ENSG00000113327	0,782	0,588302042	0,564	0,69	0,11
GABA	CACNA2D3	ENSG00000157445	0,818	1,011974034	0,636	0,87	0,29
GABA	SYT14	ENSG00000143469	0,812	0,770408634	0,624	0,86	0,28
GABA	EPHB1	ENSG00000154928	0,798	0,827141229	0,596	0,77	0,19
GABA	GRM1	ENSG00000152822	0,784	0,725490518	0,568	0,68	0,1
GABA	TMEM178B	ENSG00000261115	0,916	1,379289481	0,832	0,96	0,38
GABA	REEP1	ENSG00000068615	0,787	0,665879679	0,574	0,72	0,14
GABA	FAM49A	ENSG00000197872	0,796	0,664645806	0,592	0,81	0,23
GABA	ZFYVE28	ENSG00000159733	0,835	0,864759112	0,67	0,87	0,29
GABA	AC004805.1	ENSG00000266076	0,794	0,920716528	0,588	0,65	0,07
GABA	HCN1	ENSG00000164588	0,795	1,116476319	0,59	0,67	0,1
GABA	MCU	ENSG00000156026	0,809	0,747056744	0,618	0,84	0,27
GABA	AFF3	ENSG00000144218	0,87	1,122280181	0,74	0,95	0,38
GABA	SUSD4	ENSG00000143502	0,785	0,673048182	0,57	0,71	0,13
GABA	MRTFB	ENSG00000186260	0,807	0,59483761	0,614	0,9	0,33
GABA	GRK3	ENSG00000100077	0,829	0,826541107	0,658	0,91	0,34
GABA	GRIN3A	ENSG00000198785	0,789	0,816699061	0,578	0,64	0,07
GABA	RALGPS2	ENSG00000116191	0,786	0,704617824	0,572	0,77	0,2
GABA	MEIS2	ENSG00000134138	0,928	1,484955896	0,856	0,98	0,41
GABA	NRG2	ENSG00000158458	0,855	0,991653134	0,71	0,88	0,31
GABA	ME3	ENSG00000151376	0,795	0,699271514	0,59	0,78	0,21
GABA	SEMA3E	ENSG00000170381	0,791	0,939598585	0,582	0,69	0,12
GABA	CPLX1	ENSG00000168993	0,792	0,782714491	0,584	0,65	0,08
GABA	RAVER2	ENSG00000162437	0,795	0,725263429	0,59	0,73	0,16
GABA	SOX4	ENSG00000124766	0,787	0,709991345	0,574	0,62	0,06
GABA	NIPAL2	ENSG00000104361	0,787	0,736973955	0,574	0,67	0,1
GABA	PTPRR	ENSG00000153233	0,782	0,75779732	0,564	0,67	0,1
GABA	MAP2	ENSG00000078018	0,84	0,922163434	0,68	0,97	0,4
GABA	DLGAP4	ENSG00000080845	0,823	0,840903666	0,646	0,83	0,26
GABA	INSYN2B	ENSG00000204767	0,779	0,671829689	0,558	0,74	0,17
GABA	LRRC7	ENSG00000033122	0,803	0,886881654	0,606	0,88	0,31
GABA	KCNH5	ENSG00000140015	0,783	0,792506368	0,566	0,65	0,08
GABA	SLC6A17	ENSG00000197106	0,789	0,682538817	0,578	0,65	0,09
GABA	PRICKLE2	ENSG00000163637	0,788	0,616427883	0,576	0,87	0,31
GABA	SYN1	ENSG00000008056	0,786	0,687499636	0,572	0,67	0,1
GABA	ZNF385B	ENSG00000144331	0,781	0,869549726	0,562	0,68	0,11
GABA	ANO5	ENSG00000171714	0,789	0,752272965	0,578	0,72	0,16
GABA	NEXMIF	ENSG00000050030	0,774	0,65943075	0,548	0,71	0,15
GABA	VASH2	ENSG00000143494	0,785	0,705280842	0,57	0,59	0,02
GABA	RIMS3	ENSG00000117016	0,788	0,666969093	0,576	0,63	0,07
GABA	NRXN1	ENSG00000179915	0,873	1,209069923	0,746	1	0,44
GABA	ZFR2	ENSG00000105278	0,786	0,6626763	0,572	0,68	0,13
GABA	PLXNC1	ENSG00000136040	0,78	0,632778375	0,56	0,72	0,16
GABA	CELF2	ENSG00000048740	0,877	1,088038275	0,754	0,99	0,43
GABA	GABRA2	ENSG00000151834	0,777	0,674706755	0,554	0,67	0,11

GABA	ATCAY	ENSG00000167654	0,775	0,604259047	0,55	0,7	0,14
GABA	CERS6	ENSG00000172292	0,778	0,647469822	0,556	0,85	0,29
GABA	PCLO	ENSG00000186472	0,812	0,747742273	0,624	0,92	0,37
GABA	PMEPA1	ENSG00000124225	0,788	0,665489342	0,576	0,74	0,19
GABA	NREP	ENSG00000134986	0,783	0,738978904	0,566	0,66	0,1
GABA	PPM1L	ENSG00000163590	0,857	1,048012883	0,714	0,92	0,37
GABA	LMO7	ENSG00000136153	0,797	0,704699573	0,594	0,8	0,25
GABA	SCN3B	ENSG00000166257	0,784	0,764381733	0,568	0,63	0,08
GABA	HPCA	ENSG00000121905	0,78	0,721941212	0,56	0,59	0,03
GABA	AC092683.1	ENSG00000230606	0,809	0,781690757	0,618	0,88	0,33
GABA	LRRC49	ENSG00000137821	0,791	0,666776133	0,582	0,8	0,25
GABA	IRAK1BP1	ENSG00000146243	0,803	0,784246805	0,606	0,84	0,29
GABA	DZIP1	ENSG00000134874	0,775	0,595126056	0,55	0,75	0,2
GABA	KIAA0825	ENSG00000185261	0,793	0,772298585	0,586	0,84	0,29
GABA	FNDC5	ENSG00000160097	0,777	0,634297022	0,554	0,59	0,04
GABA	RGS7	ENSG00000182901	0,872	1,1145233	0,744	0,96	0,42
GABA	NUP93	ENSG00000102900	0,801	0,740851274	0,602	0,8	0,26
GABA	PATJ	ENSG00000132849	0,8	0,73300633	0,6	0,86	0,31
GABA	ICA1	ENSG00000003147	0,776	0,676960268	0,552	0,68	0,13
GABA	ADAMTS19	ENSG00000145808	0,78	0,929968394	0,56	0,66	0,12
GABA	NAALAD2	ENSG00000077616	0,786	0,67527952	0,572	0,78	0,24
GABA	SPTAN1	ENSG00000197694	0,786	0,675890073	0,572	0,86	0,32
GABA	AMMECR1	ENSG00000101935	0,778	0,72065931	0,556	0,69	0,15
GABA	STRIP2	ENSG00000128578	0,774	0,592923622	0,548	0,59	0,06
GABA	SLC44A5	ENSG00000137968	0,772	0,915018492	0,544	0,69	0,16
GABA	SESN3	ENSG00000149212	0,807	0,731051081	0,614	0,85	0,31
GABA	CDK14	ENSG00000058091	0,869	1,086900379	0,738	0,94	0,4
GABA	PLEKHA5	ENSG00000052126	0,853	0,906408305	0,706	0,96	0,43
GABA	ARHGEF11	ENSG00000132694	0,828	0,835400091	0,656	0,89	0,35
GABA	CDH22	ENSG00000149654	0,767	0,616690234	0,534	0,6	0,06
GABA	GRIA3	ENSG00000125675	0,828	0,948305313	0,656	0,88	0,35
GABA	KLF12	ENSG00000118922	0,809	0,847579451	0,618	0,89	0,36
GABA	GNAL	ENSG00000141404	0,765	0,643057633	0,53	0,68	0,15
GABA	NPTN	ENSG00000156642	0,841	0,86730376	0,682	0,88	0,35
GABA	SNCB	ENSG00000074317	0,77	0,691822087	0,54	0,6	0,08
GABA	LINC02055	ENSG00000254101	0,771	2,260755515	0,542	0,57	0,04
GABA	HSPA4L	ENSG00000164070	0,763	0,615804554	0,526	0,73	0,21
GABA	AC087280.2	ENSG00000283415	0,768	0,733062079	0,536	0,59	0,07
GABA	MARK1	ENSG00000116141	0,819	0,832869143	0,638	0,88	0,36
GABA	CTNNA2	ENSG00000066032	0,804	0,717072985	0,608	0,99	0,46
GABA	FIGN	ENSG00000182263	0,787	0,746461811	0,574	0,88	0,36
GABA	TSHZ1	ENSG00000179981	0,764	0,596439849	0,528	0,74	0,22
GABA	PTPRN	ENSG00000054356	0,761	0,594748837	0,522	0,61	0,09
GABA	EDA	ENSG00000158813	0,752	0,614236347	0,504	0,7	0,18
GABA	KALRN	ENSG00000160145	0,814	0,819249533	0,628	0,94	0,42
GABA	UPP2	ENSG00000007001	0,754	0,606012261	0,508	0,69	0,18
GABA	LINC00632	ENSG00000203930	0,778	0,629889782	0,556	0,89	0,38
GABA	UNC79	ENSG00000133958	0,889	1,140979466	0,778	0,95	0,45
GABA	NXPH2	ENSG00000144227	0,753	0,865315701	0,506	0,52	0,01
GABA	HIVEP2	ENSG00000010818	0,823	0,851876827	0,646	0,91	0,41
GABA	KIF9-AS1	ENSG00000227398	0,761	0,589648835	0,522	0,83	0,33
GABA	AC006148.1	ENSG00000242593	0,861	1,101134584	0,722	0,95	0,45
GABA	NWD2	ENSG00000174145	0,749	0,656773041	0,498	0,54	0,04
GABA	DGKI	ENSG00000157680	0,801	0,741108195	0,602	0,9	0,4
GABA	MARCH4	ENSG00000144583	0,751	0,603885558	0,502	0,56	0,07

GABA	GTF2IRD1	ENSG00000006704	0,769	0,620678291	0,538	0,86	0,36
GABA	MYO3B	ENSG00000071909	0,749	0,845458574	0,498	0,53	0,04
GABA	VLDLR-AS1	ENSG00000236404	0,749	0,587326805	0,498	0,76	0,27
GABA	PRKCB	ENSG00000166501	0,773	0,635309121	0,546	0,88	0,39
GABA	STRBP	ENSG00000165209	0,772	0,594135823	0,544	0,85	0,36
GABA	LINC02398	ENSG00000256287	0,748	0,708868355	0,496	0,54	0,05
GABA	MAST4	ENSG00000069020	0,812	0,811562295	0,624	0,93	0,44
GABA	FRAS1	ENSG00000138759	0,748	1,151480708	0,496	0,57	0,08
GABA	HDAC9	ENSG00000048052	0,91	1,327607679	0,82	0,97	0,49
GABA	FRMD4A	ENSG00000151474	0,814	0,643620851	0,628	0,99	0,51
GABA	CHRM3	ENSG00000133019	0,73	0,619414193	0,46	0,55	0,08
GABA	ATP2B4	ENSG00000058668	0,776	0,599114926	0,552	0,9	0,43
GABA	GALNT13	ENSG00000144278	0,913	1,352954278	0,826	0,98	0,51
GABA	NOS1AP	ENSG00000198929	0,771	0,663220221	0,542	0,83	0,36
GABA	AL022068.1	ENSG00000228412	0,737	0,733532917	0,474	0,59	0,12
GABA	ADARB2	ENSG00000185736	0,95	1,675549763	0,9	0,99	0,52
GABA	AC024901.1	ENSG00000255910	0,734	0,668766728	0,468	0,55	0,08
GABA	NSF	ENSG00000073969	0,805	0,769549859	0,61	0,91	0,45
GABA	SLC35F4	ENSG00000151812	0,73	0,783070082	0,46	0,55	0,09
GABA	SCAMP5	ENSG00000198794	0,745	0,59755476	0,49	0,72	0,26
GABA	FOCAD	ENSG00000188352	0,768	0,69818207	0,536	0,85	0,39
GABA	PPP2R1A	ENSG00000105568	0,74	0,600481366	0,48	0,74	0,29
GABA	MARCH11	ENSG00000183654	0,729	0,60507198	0,458	0,51	0,06
GABA	OXR1	ENSG00000164830	0,776	0,596282853	0,552	0,89	0,44
GABA	TRIM9	ENSG00000100505	0,835	0,787543828	0,67	0,96	0,51
GABA	FBN1	ENSG00000166147	0,886	1,168816652	0,772	0,95	0,5
GABA	NDST3	ENSG00000164100	0,723	0,691014488	0,446	0,54	0,1
GABA	CALN1	ENSG00000183166	0,746	0,595943137	0,492	0,89	0,44
GABA	DYNC1I1	ENSG00000158560	0,862	1,087665473	0,724	0,96	0,51
GABA	KIFAP3	ENSG00000075945	0,757	0,60180471	0,514	0,83	0,38
GABA	MYO16	ENSG00000041515	0,727	0,749655607	0,454	0,56	0,12
GABA	EVL	ENSG00000196405	0,777	0,597278974	0,554	0,93	0,49
GABA	MSRA	ENSG00000175806	0,789	0,773542648	0,578	0,95	0,51
GABA	NLGN1	ENSG00000169760	0,789	0,690585776	0,578	0,99	0,55
GABA	LRRC4C	ENSG00000148948	0,894	1,260557152	0,788	0,99	0,55
GABA	AL589740.1	ENSG00000271860	0,812	0,960202049	0,624	0,92	0,49
GABA	DENND5B	ENSG00000170456	0,871	0,998259596	0,742	0,95	0,51
GABA	RORA	ENSG00000069667	0,913	1,332318869	0,826	1	0,57
GABA	GRIA4	ENSG00000152578	0,822	0,749704379	0,644	0,97	0,55
GABA	LARGE1	ENSG00000133424	0,832	0,888709994	0,664	0,93	0,51
GABA	PPFIA2	ENSG00000139220	0,88	1,019878084	0,76	0,99	0,57
GABA	KCNQ5	ENSG00000185760	0,708	0,880730547	0,416	0,51	0,1
GABA	FUT9	ENSG00000172461	0,871	1,062985107	0,742	0,96	0,55
GABA	DANT2	ENSG00000235244	0,748	0,589166739	0,496	0,91	0,49
GABA	NPSR1	ENSG00000187258	0,707	1,375458882	0,414	0,43	0,02
GABA	RASAL2	ENSG00000075391	0,802	0,731362537	0,604	0,93	0,52
GABA	SLC6A1	ENSG00000157103	0,786	0,646625841	0,572	0,89	0,49
GABA	PPP3CA	ENSG00000138814	0,81	0,74918684	0,62	0,94	0,54
GABA	ROBO1	ENSG00000169855	0,884	1,038377227	0,768	0,99	0,59
GABA	R3HDM1	ENSG00000048991	0,901	1,163919068	0,802	0,96	0,57
GABA	MLLT3	ENSG00000171843	0,775	0,623026597	0,55	0,93	0,54
GABA	CAMK2D	ENSG00000145349	0,899	1,087626613	0,798	0,98	0,59
GABA	ARHGAP32	ENSG00000134909	0,764	0,595286095	0,528	0,9	0,52
GABA	NBEA	ENSG00000172915	0,802	0,66810167	0,604	0,97	0,59
GABA	RALGAPA2	ENSG00000188559	0,856	0,947087116	0,712	0,94	0,57

GABA	NRXN3	ENSG00000021645	0,964	1,67079416	0,928	1	0,64
GABA	ASTN2	ENSG00000148219	0,803	0,837522633	0,606	0,97	0,61
GABA	KIZ	ENSG00000088970	0,77	0,617478005	0,54	0,91	0,55
GABA	KIAA1958	ENSG00000165185	0,8	0,701811171	0,6	0,94	0,59
GABA	NAV3	ENSG00000067798	0,766	0,72531132	0,532	0,96	0,61
GABA	SEMA3C	ENSG00000075223	0,705	0,831159115	0,41	0,64	0,3
GABA	KAZN	ENSG00000189337	0,83	0,831142378	0,66	0,99	0,67
GABA	RAP1GDS1	ENSG00000138698	0,775	0,623389465	0,55	0,94	0,64
GABA	FBXL17	ENSG00000145743	0,771	0,613100626	0,542	0,95	0,66
GABA	MAGI1	ENSG00000151276	0,815	0,704380838	0,63	0,97	0,74
GABA	LSAMP	ENSG00000185565	0,902	1,165778821	0,804	1	0,79
GABA	CADM1	ENSG00000182985	0,827	0,7228926	0,654	0,99	0,79
GABA	AUTS2	ENSG00000158321	0,898	1,043751165	0,796	0,99	0,86
DaNs	KCNJ6	ENSG00000157542	0,984	2,771104371	0,968	0,99	0,12
DaNs	KLHL1	ENSG00000150361	0,979	2,858055795	0,958	0,99	0,12
DaNs	TTC6	ENSG00000139865	0,935	1,51035325	0,87	0,92	0,07
DaNs	ANK1	ENSG00000029534	0,946	1,566870154	0,892	0,96	0,11
DaNs	GRIA1	ENSG00000155511	0,93	1,558093247	0,86	0,97	0,14
DaNs	STMN2	ENSG00000104435	0,915	1,047288058	0,83	0,95	0,12
DaNs	SLC18A2	ENSG00000165646	0,916	1,665896591	0,832	0,84	0,01
DaNs	ADGRV1	ENSG00000164199	0,95	1,800011928	0,9	0,96	0,14
DaNs	MIAT	ENSG00000225783	0,927	1,211695932	0,854	0,97	0,15
DaNs	CELF4	ENSG00000101489	0,927	1,398864995	0,854	0,97	0,15
DaNs	ELAVL2	ENSG00000107105	0,931	1,710503052	0,862	0,92	0,1
DaNs	MIR137HG	ENSG00000225206	0,927	1,662534138	0,854	0,93	0,11
DaNs	EBF3	ENSG00000108001	0,912	1,224858206	0,824	0,85	0,03
DaNs	GRIN1	ENSG00000176884	0,892	0,912857895	0,784	0,96	0,14
DaNs	GLRA3	ENSG00000145451	0,914	1,172628813	0,828	0,88	0,07
DaNs	SYT1	ENSG00000067715	0,933	2,038381203	0,866	0,99	0,18
DaNs	SV2B	ENSG00000185518	0,913	1,448516286	0,826	0,88	0,07
DaNs	NRG1	ENSG00000157168	0,911	1,791332481	0,822	0,96	0,16
DaNs	SRRM3	ENSG00000177679	0,904	1,090843804	0,808	0,95	0,15
DaNs	CCDC85A	ENSG00000055813	0,909	1,290616122	0,818	0,96	0,16
DaNs	ATP8A2	ENSG00000132932	0,924	1,598246984	0,848	1	0,21
DaNs	SEZ6L	ENSG00000100095	0,918	1,499497304	0,836	0,97	0,18
DaNs	KCNB2	ENSG00000182674	0,903	1,853858188	0,806	0,89	0,1
DaNs	ST8SIA6	ENSG00000148488	0,903	1,598028578	0,806	0,88	0,09
DaNs	CELF5	ENSG00000161082	0,89	0,829964205	0,78	0,92	0,13
DaNs	SLIT1	ENSG00000187122	0,901	1,039244153	0,802	0,87	0,08
DaNs	ZNF385D	ENSG00000151789	0,896	1,1291027	0,792	0,93	0,15
DaNs	TH	ENSG00000180176	0,89	1,360356782	0,78	0,78	0
DaNs	HECW1	ENSG00000002746	0,893	1,232786039	0,786	0,95	0,17
DaNs	CLSTN2	ENSG00000158258	0,917	1,962029507	0,834	0,92	0,14
DaNs	KIAA0319	ENSG00000137261	0,915	1,204056152	0,83	0,93	0,16
DaNs	DNM1	ENSG00000106976	0,885	0,832301033	0,77	0,96	0,18
DaNs	CUX2	ENSG00000111249	0,901	1,67922719	0,802	0,87	0,09
DaNs	NMNAT2	ENSG00000157064	0,904	1,101448859	0,808	0,95	0,17
DaNs	ANKRD30BL	ENSG00000163046	0,911	1,367102117	0,822	0,95	0,18
DaNs	AL445623.2	ENSG00000283982	0,894	1,281911644	0,788	0,84	0,07
DaNs	PCDH15	ENSG00000150275	0,91	1,744737984	0,82	0,97	0,2
DaNs	GRIN2B	ENSG00000273079	0,889	1,240842176	0,778	0,93	0,16
DaNs	RAB3C	ENSG00000152932	0,907	1,51746591	0,814	0,93	0,16
DaNs	MYT1L	ENSG00000186487	0,89	1,357394692	0,78	0,95	0,18
DaNs	DOK6	ENSG00000206052	0,906	1,929995615	0,812	0,95	0,18
DaNs	EPHA5	ENSG00000145242	0,898	1,62794238	0,796	0,88	0,11

DaNs	SCN9A	ENSG00000169432	0,899	1,204124484	0,798	0,92	0,16
DaNs	ADAM23	ENSG00000114948	0,914	1,194575934	0,828	0,99	0,23
DaNs	C11orf80	ENSG00000173715	0,886	0,854754762	0,772	0,93	0,17
DaNs	KCNT2	ENSG00000162687	0,885	1,152450349	0,77	0,91	0,15
DaNs	PAK3	ENSG00000077264	0,892	1,271005043	0,784	0,92	0,16
DaNs	GALNTL6	ENSG00000174473	0,923	3,080935992	0,846	0,91	0,15
DaNs	NYAP2	ENSG00000144460	0,884	1,255026881	0,768	0,85	0,1
DaNs	AMPH	ENSG00000078053	0,877	0,964846588	0,754	0,92	0,16
DaNs	RET	ENSG00000165731	0,882	0,777366532	0,764	0,78	0,03
DaNs	TMEM132B	ENSG00000139364	0,904	1,586101009	0,808	0,93	0,18
DaNs	CADPS	ENSG00000163618	0,953	1,917357794	0,906	1	0,25
DaNs	CACNA1B	ENSG00000148408	0,901	1,667704908	0,802	0,93	0,18
DaNs	MEG8	ENSG00000225746	0,897	1,433918462	0,794	0,92	0,17
DaNs	ROBO2	ENSG00000185008	0,941	2,465836256	0,882	0,97	0,23
DaNs	CAMK2B	ENSG00000058404	0,854	0,678868316	0,708	0,93	0,18
DaNs	AC007091.1	ENSG00000223838	0,875	1,235258506	0,75	0,77	0,02
DaNs	CHSY3	ENSG00000198108	0,91	1,85912369	0,82	0,93	0,19
DaNs	SNAP25	ENSG00000132639	0,902	1,208123276	0,804	0,99	0,24
DaNs	AC120193.1	ENSG00000253535	0,901	1,706458073	0,802	0,88	0,13
DaNs	LINGO2	ENSG00000174482	0,861	1,243643568	0,722	0,88	0,14
DaNs	OLFM3	ENSG00000118733	0,87	1,075263285	0,74	0,89	0,15
DaNs	ELAVL4	ENSG00000162374	0,882	0,975031429	0,764	0,88	0,14
DaNs	RIMS2	ENSG00000176406	0,897	1,475246731	0,794	0,96	0,22
DaNs	FGF12	ENSG00000114279	0,906	1,728378408	0,812	0,97	0,24
DaNs	REEP1	ENSG00000068615	0,87	0,943788377	0,74	0,88	0,14
DaNs	DRD2	ENSG00000149295	0,871	1,05460594	0,742	0,76	0,02
DaNs	TOX2	ENSG00000124191	0,861	0,756591811	0,722	0,87	0,13
DaNs	GABRB1	ENSG00000163288	0,937	1,649110789	0,874	1	0,27
DaNs	SNTG1	ENSG00000147481	0,907	2,001213945	0,814	0,93	0,2
DaNs	RIMBP2	ENSG00000060709	0,889	1,232047727	0,778	0,89	0,16
DaNs	BTBD11	ENSG00000151136	0,876	1,286034884	0,752	0,87	0,14
DaNs	AC073050.1	ENSG00000228222	0,875	1,672393794	0,75	0,92	0,19
DaNs	SCN3A	ENSG00000153253	0,851	0,843510408	0,702	0,91	0,18
DaNs	MAST1	ENSG00000105613	0,86	0,698141517	0,72	0,85	0,12
DaNs	SORBS2	ENSG00000154556	0,858	0,884734462	0,716	0,97	0,25
DaNs	FRMPD4	ENSG00000169933	0,855	1,064189895	0,71	0,91	0,18
DaNs	KCND3	ENSG00000171385	0,872	1,103262367	0,744	0,93	0,21
DaNs	BICDL1	ENSG00000135127	0,868	0,90087443	0,736	0,87	0,14
DaNs	KLHL29	ENSG00000119771	0,881	1,323136934	0,762	0,88	0,16
DaNs	WNK2	ENSG00000165238	0,855	0,786337874	0,71	0,91	0,19
DaNs	RALYL	ENSG00000184672	0,915	1,651309355	0,83	0,99	0,27
DaNs	DCLK1	ENSG00000133083	0,886	1,416713105	0,772	0,97	0,25
DaNs	CRMP1	ENSG00000072832	0,853	0,600897121	0,706	0,85	0,13
DaNs	SPTBN4	ENSG00000160460	0,895	1,171571825	0,79	0,97	0,26
DaNs	PTPRO	ENSG00000151490	0,871	1,68485314	0,742	0,85	0,13
DaNs	IQSEC3	ENSG00000120645	0,863	0,798680362	0,726	0,82	0,11
DaNs	SLC4A10	ENSG00000144290	0,846	0,892481518	0,692	0,88	0,16
DaNs	CACNA1E	ENSG00000198216	0,842	0,698411132	0,684	0,88	0,16
DaNs	GRIP1	ENSG00000155974	0,903	1,544158913	0,806	0,96	0,24
DaNs	PRICKLE1	ENSG00000139174	0,854	0,970103074	0,708	0,85	0,14
DaNs	UNC13C	ENSG00000137766	0,856	2,012335496	0,712	0,81	0,1
DaNs	EPHA6	ENSG00000080224	0,87	1,686949984	0,74	0,85	0,14
DaNs	UNC80	ENSG00000144406	0,853	0,869394575	0,706	0,95	0,23
DaNs	B4GALT6	ENSG00000118276	0,853	0,730467837	0,706	0,84	0,13
DaNs	GABRG2	ENSG00000113327	0,848	0,702032848	0,696	0,82	0,11

DaNs	PRKG1	ENSG00000185532	0,879	1,385967314	0,758	0,97	0,26
DaNs	PGM2L1	ENSG00000165434	0,853	0,703575569	0,706	0,84	0,13
DaNs	SLC35F1	ENSG00000196376	0,867	1,068150055	0,734	0,95	0,24
DaNs	INPP4B	ENSG00000109452	0,907	1,920887302	0,814	1	0,3
DaNs	SLC44A5	ENSG00000137968	0,875	1,620813001	0,75	0,87	0,16
DaNs	MIR2052HG	ENSG00000254349	0,869	1,20760234	0,738	0,88	0,18
DaNs	XKR4	ENSG00000206579	0,851	1,005912065	0,702	0,89	0,19
DaNs	ARHGEF28	ENSG00000214944	0,848	0,720262513	0,696	0,84	0,14
DaNs	EML6	ENSG00000214595	0,868	1,010085564	0,736	0,95	0,25
DaNs	OSBPL10	ENSG00000144645	0,863	1,046949046	0,726	0,8	0,1
DaNs	SCN2A	ENSG00000136531	0,849	0,942927833	0,698	0,91	0,21
DaNs	LMX1B	ENSG00000136944	0,85	0,742152179	0,7	0,72	0,02
DaNs	PRR16	ENSG00000184838	0,867	1,658253999	0,734	0,81	0,11
DaNs	GABBR2	ENSG00000136928	0,844	0,956204686	0,688	0,84	0,14
DaNs	PTPRN2	ENSG00000155093	0,895	1,425941436	0,79	0,93	0,24
DaNs	GAP43	ENSG00000172020	0,852	0,892588927	0,704	0,82	0,13
DaNs	SYT14	ENSG00000143469	0,861	0,845373375	0,722	0,99	0,29
DaNs	HSPA4L	ENSG00000164070	0,852	0,812136132	0,704	0,91	0,21
DaNs	MTUS2	ENSG00000132938	0,845	1,152007129	0,69	0,82	0,13
DaNs	JAKMIP1	ENSG00000152969	0,856	1,065759831	0,712	0,81	0,12
DaNs	GABRB3	ENSG00000166206	0,85	1,067647018	0,7	0,89	0,2
DaNs	RNF150	ENSG00000170153	0,858	1,13174591	0,716	0,95	0,25
DaNs	KCNIP4	ENSG00000185774	0,893	1,484625756	0,786	0,99	0,29
DaNs	STXBP5-AS1	ENSG00000233452	0,85	1,013409342	0,7	0,87	0,17
DaNs	VWC2L	ENSG00000174453	0,845	1,010153699	0,69	0,77	0,08
DaNs	GPC6	ENSG00000183098	0,895	2,151896855	0,79	0,91	0,22
DaNs	GPRIN3	ENSG00000185477	0,827	0,672297519	0,654	0,85	0,16
DaNs	CACNA1A	ENSG00000141837	0,868	1,222818632	0,736	0,97	0,29
DaNs	SCG2	ENSG00000171951	0,858	1,123992558	0,716	0,8	0,11
DaNs	ST6GALNAC5	ENSG00000117069	0,847	1,531780677	0,694	0,76	0,07
DaNs	MEG3	ENSG00000214548	0,848	0,721916938	0,696	0,78	0,1
DaNs	SHANK2	ENSG00000162105	0,849	1,162604021	0,698	0,87	0,18
DaNs	SLC2A13	ENSG00000151229	0,874	1,550862993	0,748	0,93	0,25
DaNs	KCNQ3	ENSG00000184156	0,88	1,218153204	0,76	0,97	0,29
DaNs	LRRC7	ENSG00000033122	0,825	0,760011767	0,65	1	0,32
DaNs	SLC8A1	ENSG00000183023	0,85	1,128561898	0,7	0,99	0,31
DaNs	KSR2	ENSG00000171435	0,852	1,102830872	0,704	0,87	0,19
DaNs	LRFN5	ENSG00000165379	0,825	0,916875232	0,65	0,88	0,2
DaNs	SRRM4	ENSG00000139767	0,828	0,651324741	0,656	0,78	0,11
DaNs	NSG2	ENSG00000170091	0,827	0,742520899	0,654	0,82	0,15
DaNs	CCSER1	ENSG00000184305	0,914	1,629477831	0,828	0,97	0,3
DaNs	SCN7A	ENSG00000136546	0,83	0,61310342	0,66	0,77	0,1
DaNs	ARHGAP44	ENSG00000006740	0,859	0,993344928	0,718	0,88	0,2
DaNs	TENM3	ENSG00000218336	0,829	0,79758148	0,658	0,89	0,22
DaNs	FRRS1L	ENSG00000260230	0,837	0,715652319	0,674	0,87	0,19
DaNs	SEMA6D	ENSG00000137872	0,938	1,883607961	0,876	0,96	0,29
DaNs	PPM1E	ENSG00000175175	0,891	1,353958387	0,782	0,96	0,29
DaNs	ADD2	ENSG00000075340	0,824	0,683472328	0,648	0,8	0,13
DaNs	DLGAP2	ENSG00000198010	0,834	1,07649953	0,668	0,82	0,15
DaNs	GNAL	ENSG00000141404	0,822	0,706076027	0,644	0,82	0,15
DaNs	KIAA1211	ENSG00000109265	0,823	0,732494248	0,646	0,91	0,24
DaNs	SLITRK5	ENSG00000165300	0,83	0,641415881	0,66	0,82	0,15
DaNs	SHISA9	ENSG00000237515	0,81	0,713551764	0,62	0,85	0,18
DaNs	BASP1	ENSG00000176788	0,817	0,640713258	0,634	0,89	0,22
DaNs	ABLIM2	ENSG00000163995	0,851	0,866429879	0,702	0,88	0,21

DaNs	SYT16	ENSG00000139973	0,828	0,788884101	0,656	0,84	0,17
DaNs	PCDH7	ENSG00000169851	0,869	1,29847983	0,738	0,96	0,29
DaNs	UCHL1	ENSG00000154277	0,871	0,888589733	0,742	0,96	0,29
DaNs	SCN8A	ENSG00000196876	0,851	0,959322918	0,702	0,89	0,23
DaNs	DLGAP1	ENSG00000170579	0,833	0,797915923	0,666	0,96	0,3
DaNs	MYRIP	ENSG00000170011	0,907	1,443324607	0,814	0,96	0,3
DaNs	RAP1GAP2	ENSG00000132359	0,832	0,871659909	0,664	0,84	0,18
DaNs	EPB41	ENSG00000159023	0,808	0,588163749	0,616	0,88	0,22
DaNs	LINC02389	ENSG00000255693	0,828	0,789464665	0,656	0,76	0,1
DaNs	ATP2B2	ENSG00000157087	0,806	0,607009546	0,612	0,89	0,23
DaNs	SYBU	ENSG00000147642	0,818	0,682740789	0,636	0,85	0,19
DaNs	NDRG4	ENSG00000103034	0,814	0,588448657	0,628	0,81	0,15
DaNs	RUNDC3B	ENSG00000105784	0,82	0,698308801	0,64	0,82	0,17
DaNs	RERG	ENSG00000134533	0,824	0,946497074	0,648	0,76	0,1
DaNs	FAM155A	ENSG00000204442	0,925	1,616422039	0,85	1	0,34
DaNs	RIMS1	ENSG00000079841	0,878	1,400431217	0,756	0,95	0,29
DaNs	PID1	ENSG00000153823	0,854	1,358558733	0,708	0,89	0,24
DaNs	KIF26B	ENSG00000162849	0,832	0,980266303	0,664	0,88	0,22
DaNs	CALY	ENSG00000130643	0,818	0,6673734	0,636	0,78	0,13
DaNs	DNAH14	ENSG00000185842	0,831	0,847290114	0,662	0,82	0,17
DaNs	SLC8A3	ENSG00000100678	0,816	0,643909329	0,632	0,81	0,16
DaNs	FOXP2	ENSG00000128573	0,839	1,267497713	0,678	0,84	0,19
DaNs	PEG10	ENSG00000242265	0,847	1,150751595	0,694	0,81	0,16
DaNs	DSCAM	ENSG00000171587	0,852	0,972294583	0,704	0,97	0,32
DaNs	MCC	ENSG00000171444	0,825	1,088258699	0,65	0,88	0,23
DaNs	KHDRBS2	ENSG00000112232	0,806	0,650369836	0,612	0,91	0,25
DaNs	CADPS2	ENSG00000081803	0,882	2,009136908	0,764	0,87	0,22
DaNs	PIP5K1B	ENSG00000107242	0,829	0,891753269	0,658	0,81	0,16
DaNs	PLXNA4	ENSG00000221866	0,826	0,901814505	0,652	0,81	0,16
DaNs	CNNM1	ENSG00000119946	0,822	0,611453039	0,644	0,76	0,11
DaNs	SDC2	ENSG00000169439	0,827	0,925071963	0,654	0,76	0,11
DaNs	PAM	ENSG00000145730	0,847	1,12936238	0,694	0,93	0,29
DaNs	AGBL4	ENSG00000186094	0,838	1,038281538	0,676	0,92	0,27
DaNs	FAM189A1	ENSG00000104059	0,819	0,704198799	0,638	0,77	0,12
DaNs	CSMD2	ENSG00000121904	0,854	1,250258683	0,708	0,92	0,27
DaNs	EFNA5	ENSG00000184349	0,835	1,282367134	0,67	0,81	0,17
DaNs	KIAA1549L	ENSG00000110427	0,814	0,742904454	0,628	0,8	0,15
DaNs	LMTK3	ENSG00000142235	0,819	0,645609255	0,638	0,87	0,22
DaNs	PLA2R1	ENSG00000153246	0,823	0,827750448	0,646	0,74	0,1
DaNs	GRIN3A	ENSG00000198785	0,824	0,860284607	0,648	0,72	0,08
DaNs	SVOP	ENSG00000166111	0,821	0,622714711	0,642	0,73	0,09
DaNs	AMMECR1	ENSG00000101935	0,846	1,145124449	0,692	0,8	0,16
DaNs	LMX1A	ENSG00000162761	0,819	0,976499459	0,638	0,65	0,01
DaNs	PLCB4	ENSG00000101333	0,812	0,803340858	0,624	0,89	0,25
DaNs	GRIK2	ENSG00000164418	0,804	0,678332838	0,608	0,95	0,31
DaNs	DGKH	ENSG00000102780	0,81	0,716554387	0,62	0,84	0,2
DaNs	RAB27B	ENSG00000041353	0,817	0,743104703	0,634	0,73	0,1
DaNs	CPLX2	ENSG00000145920	0,815	0,594112422	0,63	0,72	0,08
DaNs	UBASH3B	ENSG00000154127	0,812	0,624185151	0,624	0,78	0,15
DaNs	SNRPN	ENSG00000128739	0,855	1,293582977	0,71	0,91	0,27
DaNs	STXBP5L	ENSG00000145087	0,828	1,005364762	0,656	0,88	0,25
DaNs	ADAMTS2	ENSG00000087116	0,814	0,714754162	0,628	0,69	0,06
DaNs	TENM2	ENSG00000145934	0,827	1,565636885	0,654	0,84	0,21
DaNs	SLC41A2	ENSG00000136052	0,806	0,605275396	0,612	0,8	0,17
DaNs	DGKB	ENSG00000136267	0,795	0,711481884	0,59	0,85	0,22

DaNs	KIF5A	ENSG00000155980	0,815	0,610862767	0,63	0,77	0,14
DaNs	MGAT4C	ENSG00000182050	0,814	0,929893928	0,628	0,84	0,21
DaNs	LINC01414	ENSG00000253554	0,809	0,742829482	0,618	0,74	0,11
DaNs	DCX	ENSG00000077279	0,814	0,598048916	0,628	0,72	0,09
DaNs	LRRTM4	ENSG00000176204	0,821	0,950410994	0,642	0,93	0,31
DaNs	CNTN1	ENSG00000018236	0,861	1,260486471	0,722	0,97	0,35
DaNs	CNKSR2	ENSG00000149970	0,804	0,740771685	0,608	0,82	0,2
DaNs	CHL1	ENSG00000134121	0,797	0,669147685	0,594	0,89	0,27
DaNs	KIF9-AS1	ENSG00000227398	0,83	0,696732618	0,66	0,96	0,34
DaNs	STXBP1	ENSG00000136854	0,822	0,714320998	0,644	0,93	0,31
DaNs	RPH3A	ENSG00000089169	0,805	0,790145174	0,61	0,73	0,11
DaNs	WDR17	ENSG00000150627	0,833	0,745025434	0,666	0,91	0,29
DaNs	AC092683.1	ENSG00000230606	0,832	0,756749929	0,664	0,96	0,34
DaNs	FGF13	ENSG00000129682	0,803	0,59485551	0,606	0,72	0,1
DaNs	MYH10	ENSG00000133026	0,795	0,645017266	0,59	0,82	0,21
DaNs	AC025159.1	ENSG00000257815	0,851	0,93202621	0,702	0,93	0,32
DaNs	SHISA6	ENSG00000188803	0,821	1,385350857	0,642	0,76	0,15
DaNs	CERS6	ENSG00000172292	0,821	0,833744555	0,642	0,91	0,29
DaNs	CACNA1D	ENSG00000157388	0,827	0,83202211	0,654	0,91	0,3
DaNs	RGS6	ENSG00000182732	0,828	1,530262441	0,656	0,81	0,2
DaNs	RBMS1	ENSG00000153250	0,803	0,691712212	0,606	0,91	0,3
DaNs	ERC2	ENSG00000187672	0,879	1,385498872	0,758	0,97	0,37
DaNs	FAM135B	ENSG00000147724	0,788	0,752514064	0,576	0,85	0,24
DaNs	GABRA4	ENSG00000109158	0,803	0,599580537	0,606	0,66	0,06
DaNs	PKNOX2	ENSG00000165495	0,798	0,626069649	0,596	0,77	0,16
DaNs	SLIT2	ENSG00000145147	0,824	1,139033346	0,648	0,81	0,21
DaNs	CAP2	ENSG00000112186	0,803	0,678237146	0,606	0,74	0,14
DaNs	TMEM255A	ENSG00000125355	0,802	0,715829669	0,604	0,68	0,07
DaNs	TRPC6	ENSG00000137672	0,806	1,139566268	0,612	0,65	0,05
DaNs	PRKAR2B	ENSG00000005249	0,805	0,633905783	0,61	0,74	0,14
DaNs	SPTAN1	ENSG00000197694	0,801	0,785461872	0,602	0,93	0,33
DaNs	VSNL1	ENSG00000163032	0,788	0,681907218	0,576	0,72	0,11
DaNs	ANKRD29	ENSG00000154065	0,801	0,665658288	0,602	0,69	0,09
DaNs	FBXO16	ENSG00000214050	0,798	0,613261658	0,596	0,73	0,13
DaNs	ADGRL2	ENSG00000117114	0,812	1,299549671	0,624	0,76	0,16
DaNs	FP700111.1	ENSG00000224363	0,79	0,615787832	0,58	0,88	0,28
DaNs	CSMD1	ENSG00000183117	0,923	1,779680559	0,846	1	0,4
DaNs	TMEM178B	ENSG00000261115	0,887	1,213787511	0,774	0,99	0,39
DaNs	CNTNAP3B	ENSG00000154529	0,795	0,668362454	0,59	0,8	0,2
DaNs	CNTN4	ENSG00000144619	0,791	0,897558323	0,582	0,78	0,19
DaNs	DAB1	ENSG00000173406	0,892	1,642859848	0,784	0,99	0,39
DaNs	CEP126	ENSG00000110318	0,801	0,601850533	0,602	0,88	0,28
DaNs	SYN2	ENSG00000157152	0,779	0,59040119	0,558	0,76	0,16
DaNs	SDK1	ENSG00000146555	0,808	1,006711809	0,616	0,87	0,27
DaNs	CACNG2	ENSG00000166862	0,793	0,616214279	0,586	0,72	0,12
DaNs	PRICKLE2	ENSG00000163637	0,825	0,882908199	0,65	0,91	0,31
DaNs	SLC6A3	ENSG00000142319	0,796	1,262554146	0,592	0,6	0
DaNs	CSMD3	ENSG00000164796	0,816	0,951944498	0,632	0,95	0,36
DaNs	PCLO	ENSG00000186472	0,87	1,10661562	0,74	0,96	0,37
DaNs	LINC01876	ENSG00000226383	0,796	1,225363121	0,592	0,62	0,04
DaNs	ANKRD34C-AS1	ENSG00000259234	0,787	0,625168342	0,574	0,68	0,09
DaNs	SV2C	ENSG00000122012	0,804	1,617055077	0,608	0,65	0,06
DaNs	PPP2R2C	ENSG00000074211	0,799	0,63738079	0,598	0,96	0,37
DaNs	GRIN2A	ENSG00000183454	0,806	1,331535571	0,612	0,74	0,16

DaNs	FNBP1L	ENSG00000137942	0,776	0,60049794	0,552	0,82	0,24
DaNs	LINC01250	ENSG00000234423	0,79	0,651523801	0,58	0,68	0,1
DaNs	EML5	ENSG00000165521	0,789	0,662516574	0,578	0,8	0,22
DaNs	GRIA3	ENSG00000125675	0,862	1,043525073	0,724	0,93	0,35
DaNs	CLVS1	ENSG00000177182	0,783	0,601981978	0,566	0,77	0,19
DaNs	PLCB1	ENSG00000182621	0,809	0,993094325	0,618	0,93	0,35
DaNs	GFRA1	ENSG00000151892	0,797	1,411927978	0,594	0,65	0,07
DaNs	FHOD3	ENSG00000134775	0,774	0,603659678	0,548	0,74	0,16
DaNs	PCSK2	ENSG00000125851	0,786	0,723189831	0,572	0,7	0,13
DaNs	LINC00632	ENSG00000203930	0,839	0,780204268	0,678	0,96	0,38
DaNs	SGSM1	ENSG00000167037	0,813	0,704595154	0,626	0,89	0,32
DaNs	DAAM1	ENSG00000100592	0,796	0,593579826	0,592	0,91	0,33
DaNs	GRM8	ENSG00000179603	0,789	1,121700753	0,578	0,7	0,13
DaNs	HSPA12A	ENSG00000165868	0,844	0,778157028	0,688	0,97	0,4
DaNs	TENM1	ENSG00000009694	0,79	0,894527276	0,58	0,73	0,15
DaNs	TUSC3	ENSG00000104723	0,782	0,590387624	0,564	0,73	0,15
DaNs	AC092691.1	ENSG00000239268	0,809	0,96578097	0,618	0,95	0,37
DaNs	FBXL2	ENSG00000153558	0,797	0,671326784	0,594	0,84	0,26
DaNs	FGF14	ENSG00000102466	0,81	1,139988751	0,62	0,87	0,29
DaNs	RSPO2	ENSG00000147655	0,788	1,15088128	0,576	0,61	0,04
DaNs	ARHGAP6	ENSG00000047648	0,775	0,647723939	0,55	0,74	0,17
DaNs	RAPGEF4	ENSG00000091428	0,773	0,733689381	0,546	0,92	0,35
DaNs	ME1	ENSG00000065833	0,797	0,638328157	0,594	0,88	0,31
DaNs	CNTNAP5	ENSG00000155052	0,766	0,713998699	0,532	0,77	0,2
DaNs	BNC2	ENSG00000173068	0,778	0,891698968	0,556	0,73	0,16
DaNs	FLRT2	ENSG00000185070	0,771	0,634463374	0,542	0,78	0,22
DaNs	UBA6-AS1	ENSG00000248049	0,852	1,108161759	0,704	0,97	0,41
DaNs	CDH4	ENSG00000179242	0,804	1,061303198	0,608	0,8	0,23
DaNs	PLEKHA5	ENSG00000052126	0,867	1,185637213	0,734	1	0,44
DaNs	SPAG16	ENSG00000144451	0,774	0,623193672	0,548	0,91	0,34
DaNs	MAP2	ENSG00000078018	0,897	1,289059443	0,794	0,97	0,41
DaNs	KCNH7	ENSG00000184611	0,786	1,077519189	0,572	0,69	0,13
DaNs	NPNT	ENSG00000168743	0,782	0,898523508	0,564	0,62	0,06
DaNs	AC024901.1	ENSG00000255910	0,781	0,812051321	0,562	0,65	0,09
DaNs	AFF3	ENSG00000144218	0,856	1,241022613	0,712	0,95	0,38
DaNs	HS6ST3	ENSG00000185352	0,775	1,016353674	0,55	0,77	0,21
DaNs	FRY	ENSG00000073910	0,765	0,745253497	0,53	0,92	0,36
DaNs	NOL4	ENSG00000101746	0,779	0,903241687	0,558	0,78	0,22
DaNs	PLCXD3	ENSG00000182836	0,781	0,922197864	0,562	0,68	0,12
DaNs	LARP1B	ENSG00000138709	0,769	0,621661892	0,538	0,92	0,36
DaNs	AC008591.1	ENSG00000251680	0,783	1,164105598	0,566	0,61	0,05
DaNs	ASXL3	ENSG00000141431	0,768	0,613829474	0,536	0,81	0,26
DaNs	TMEM108	ENSG00000144868	0,756	0,600298054	0,512	0,84	0,28
DaNs	PPIP5K2	ENSG00000145725	0,811	0,663111521	0,622	0,92	0,37
DaNs	SNAP91	ENSG00000065609	0,791	0,706960103	0,582	0,89	0,34
DaNs	TRPC5	ENSG00000072315	0,785	1,154301705	0,57	0,65	0,1
DaNs	CACNG3	ENSG00000006116	0,779	0,688203954	0,558	0,6	0,04
DaNs	AC096711.2	ENSG00000251555	0,82	0,705614137	0,64	0,92	0,37
DaNs	CSRNP3	ENSG00000178662	0,791	0,793898853	0,582	0,95	0,4
DaNs	MAGI3	ENSG00000081026	0,777	0,724590628	0,554	0,88	0,33
DaNs	NEXMIF	ENSG00000050030	0,769	0,687361534	0,538	0,7	0,15
DaNs	EPB41L4B	ENSG00000095203	0,775	0,605956499	0,55	0,69	0,14
DaNs	MTCL1	ENSG00000168502	0,772	0,769889209	0,544	0,76	0,21
DaNs	NRXN1	ENSG00000179915	0,82	1,010984375	0,64	0,99	0,44
DaNs	FSTL4	ENSG00000053108	0,781	1,253062732	0,562	0,64	0,1

DaNs	NTN1	ENSG00000065320	0,768	0,826013722	0,536	0,65	0,11
DaNs	MPPED2	ENSG00000066382	0,757	0,630847775	0,514	0,74	0,2
DaNs	TBC1D19	ENSG00000109680	0,802	0,76635956	0,604	0,96	0,42
DaNs	NELL2	ENSG00000184613	0,765	0,724634353	0,53	0,69	0,15
DaNs	CACNA1C	ENSG00000151067	0,793	0,758218625	0,586	0,89	0,36
DaNs	MIR4500HG	ENSG00000228824	0,769	0,835369001	0,538	0,58	0,05
DaNs	SLC35F4	ENSG00000151812	0,765	0,942761115	0,53	0,62	0,09
DaNs	HCN1	ENSG00000164588	0,759	0,631511268	0,518	0,64	0,1
DaNs	GPR158	ENSG00000151025	0,755	0,681937303	0,51	0,85	0,32
DaNs	AJAP1	ENSG00000196581	0,766	0,620368918	0,532	0,74	0,21
DaNs	ZFHX3	ENSG00000140836	0,815	1,181505683	0,63	0,96	0,43
DaNs	CDH18	ENSG00000145526	0,768	1,163151253	0,536	0,72	0,19
DaNs	RIT2	ENSG00000152214	0,766	0,838298261	0,532	0,65	0,12
DaNs	MCTP1	ENSG00000175471	0,758	0,632368088	0,516	0,7	0,18
DaNs	CDH10	ENSG00000040731	0,754	0,629404768	0,508	0,72	0,19
DaNs	FOCAD	ENSG00000188352	0,812	0,793063968	0,624	0,92	0,4
DaNs	CDK14	ENSG00000058091	0,805	0,935113215	0,61	0,93	0,41
DaNs	ZNF804A	ENSG00000170396	0,745	0,672002643	0,49	0,68	0,15
DaNs	GSG1L	ENSG00000169181	0,758	0,638938351	0,516	0,65	0,13
DaNs	TMEM232	ENSG00000186952	0,756	0,632851406	0,512	0,85	0,33
DaNs	MARCH4	ENSG00000144583	0,762	0,606069977	0,524	0,6	0,07
DaNs	AC090578.1	ENSG00000253553	0,756	0,607791043	0,512	0,64	0,11
DaNs	KCNH5	ENSG00000140015	0,758	0,725573892	0,516	0,61	0,09
DaNs	NSF	ENSG00000073969	0,8	0,740208914	0,6	0,97	0,46
DaNs	CTNNA2	ENSG00000066032	0,763	0,625049744	0,526	0,99	0,47
DaNs	ANAPC10	ENSG00000164162	0,737	0,593153015	0,474	0,88	0,36
DaNs	CDH8	ENSG00000150394	0,753	0,887677497	0,506	0,84	0,32
DaNs	GRM5	ENSG00000168959	0,733	0,742365981	0,466	0,73	0,22
DaNs	EBF1	ENSG00000164330	0,751	0,797821781	0,502	0,66	0,15
DaNs	LUZP2	ENSG00000187398	0,738	0,742092532	0,476	0,77	0,26
DaNs	GPC5	ENSG00000179399	0,762	1,097840493	0,524	0,8	0,29
DaNs	MIPOL1	ENSG00000151338	0,76	0,659368541	0,52	0,82	0,32
DaNs	DCC	ENSG00000187323	0,79	1,775809387	0,58	0,76	0,26
DaNs	CACNB4	ENSG00000182389	0,75	0,728600388	0,5	0,62	0,12
DaNs	APBA1	ENSG00000107282	0,806	0,814823635	0,612	0,92	0,42
DaNs	CACNA2D3	ENSG00000157445	0,758	0,690366413	0,516	0,8	0,3
DaNs	IQCJ-SCHIP1	ENSG00000283154	0,94	2,108105232	0,88	1	0,5
DaNs	XKR6	ENSG00000171044	0,809	0,975997368	0,618	0,88	0,38
DaNs	CDH12	ENSG00000154162	0,746	1,054422692	0,492	0,69	0,19
DaNs	MCF2L2	ENSG00000053524	0,774	0,636180447	0,548	0,88	0,38
DaNs	HS6ST2	ENSG00000171004	0,751	0,814583329	0,502	0,6	0,1
DaNs	RGS7	ENSG00000182901	0,778	0,7800691	0,556	0,92	0,43
DaNs	PWRN1	ENSG00000259905	0,743	0,681748771	0,486	0,77	0,28
DaNs	NEDD4L	ENSG00000049759	0,723	0,599164296	0,446	0,91	0,42
DaNs	FRMD4A	ENSG00000151474	0,882	1,322370089	0,764	1	0,52
DaNs	SGCD	ENSG00000170624	0,902	2,000750288	0,804	0,96	0,48
DaNs	CNTN6	ENSG00000134115	0,734	0,71543005	0,468	0,58	0,1
DaNs	LINC00535	ENSG00000246662	0,738	0,631922882	0,476	0,58	0,1
DaNs	LINC01322	ENSG00000244128	0,736	0,617903283	0,472	0,65	0,17
DaNs	DYNC1I1	ENSG00000158560	0,83	1,023774422	0,66	0,99	0,52
DaNs	ZNF385B	ENSG00000144331	0,721	0,593009581	0,442	0,58	0,12
DaNs	UNC5D	ENSG00000156687	0,727	0,893914827	0,454	0,61	0,15
DaNs	MACROD2	ENSG00000172264	0,819	1,008889209	0,638	1	0,54
DaNs	UNC79	ENSG00000133958	0,76	0,630301902	0,52	0,91	0,45
DaNs	DENND5B	ENSG00000170456	0,817	0,73606362	0,634	0,96	0,52

DaNs	GDAP1	ENSG00000104381	0,803	0,812026449	0,606	0,95	0,51
DaNs	NLGN1	ENSG00000169760	0,785	0,753292243	0,57	0,99	0,56
DaNs	KCNAB1	ENSG00000169282	0,711	0,587018497	0,422	0,65	0,23
DaNs	AC110023.1	ENSG00000258631	0,714	0,85164163	0,428	0,51	0,09
DaNs	PACS1	ENSG00000175115	0,732	0,641774828	0,464	0,85	0,43
DaNs	AEBP2	ENSG00000139154	0,736	0,616646584	0,472	0,89	0,48
DaNs	CNTNAP2	ENSG00000174469	0,888	1,407147392	0,776	1	0,59
DaNs	PPFIA2	ENSG00000139220	0,818	1,188265231	0,636	0,99	0,57
DaNs	KCNC2	ENSG00000166006	0,702	0,634367481	0,404	0,51	0,1
DaNs	GABRG3	ENSG00000182256	0,701	0,777904688	0,402	0,51	0,1
DaNs	SORCS3	ENSG00000156395	0,702	0,720069837	0,404	0,57	0,16
DaNs	TOX3	ENSG00000103460	0,713	0,644170737	0,426	0,65	0,24
DaNs	PAPPA	ENSG00000182752	0,706	0,624749272	0,412	0,45	0,04
DaNs	SAMD3	ENSG00000164483	0,708	0,861698327	0,416	0,46	0,05
DaNs	FUT9	ENSG00000172461	0,773	0,735281675	0,546	0,96	0,55
DaNs	PPP3CA	ENSG00000138814	0,78	0,706015091	0,56	0,95	0,55
DaNs	CPEB3	ENSG00000107864	0,748	0,620375132	0,496	0,96	0,58
DaNs	ADARB2	ENSG00000185736	0,841	1,354470447	0,682	0,91	0,53
DaNs	NBEA	ENSG00000172915	0,802	0,997220246	0,604	0,97	0,6
DaNs	PBX1	ENSG00000185630	0,944	1,741966297	0,888	0,99	0,62
DaNs	PBX3	ENSG00000167081	0,745	0,710847109	0,49	0,87	0,5
DaNs	AC124312.1	ENSG00000214265	0,787	0,720682119	0,574	0,97	0,61
DaNs	SMYD3	ENSG00000185420	0,764	0,716942337	0,528	0,97	0,62
DaNs	NEGR1	ENSG00000172260	0,81	1,168034816	0,62	0,99	0,63
DaNs	GRID2	ENSG00000152208	0,708	0,797802324	0,416	0,87	0,52
DaNs	RASGEF1B	ENSG00000138670	0,73	0,703904302	0,46	0,95	0,61
DaNs	NRXN3	ENSG00000021645	0,842	1,443983858	0,684	0,97	0,64
DaNs	BICD1	ENSG00000151746	0,738	0,64064816	0,476	0,93	0,6
DaNs	KAZN	ENSG00000189337	0,864	1,057962532	0,728	1	0,68
DaNs	MAP1B	ENSG00000131711	0,829	0,795301905	0,658	1	0,68
DaNs	PDE4D	ENSG00000113448	0,874	1,73363943	0,748	0,99	0,7
DaNs	FBXL17	ENSG00000145743	0,707	0,674476807	0,414	0,95	0,66
DaNs	ANKS1B	ENSG00000185046	0,707	0,641848242	0,414	1	0,75
DaNs	DOCK3	ENSG00000088538	0,719	0,616625413	0,438	0,96	0,76
DaNs	ADGRL3	ENSG00000150471	0,752	0,774304415	0,504	0,99	0,79
DaNs	LSAMP	ENSG00000185565	0,785	0,887660475	0,57	0,99	0,8
DaNs	LRP1B	ENSG00000168702	0,704	0,738664677	0,408	0,99	0,8
DaNs	CADM2	ENSG00000175161	0,751	0,714638904	0,502	1	0,83
DaNs	ERBB4	ENSG00000178568	0,705	0,952400165	0,41	0,88	0,72
DaNs	TNRC6A	ENSG00000090905	0,784	0,61695903	0,568	0,99	0,83
DaNs	ANK2	ENSG00000145362	0,773	0,774117771	0,546	0,99	0,84
DaNs	FTX	ENSG00000230590	0,74	0,625379613	0,48	1	0,93

myAUC Area under the curve
avg_diff Mean log2 expression difference
pct.1 Percentage of expressing cells of the query cell type
pct.2 Percentage of expressing cells of the all but the query cell type

Supplementary Table 4 PD-associated variant enrichment in genes with cell type-specific expression patterns

Control + IPD					
Cell type	**Ngenes**	**Beta**	**Beta SD**	**SE**	**P**
Astrocytes	288	0.1017	0.012776	0.057773	0.039178
CADPS2	135	0.036384	0.0031427	0.085945	0.33603
DaNs	3558	0.031252	0.012457	0.01794	0.040758
Ependymal	789	0.021755	0.0044587	0.034048	0.26143
Excitatory	3326	0.038489	0.014951	0.018401	0.018243
GABA	1944	0.0038755	0.0012041	0.022954	0.43296
Inhibitory	3653	0.032494	0.01308	0.017858	0.034424
Microglia	312	0.12692	0.016583	0.05239	0.00771
ODC	545	0.024234	0.0041571	0.040358	0.2741
OPC	346	0.093397	0.012838	0.055126	0.04512
Pericytes	763	0.04785	0.0096511	0.034697	0.083947
endothelial	425	-0.025419	-0.0038638	0.046468	0.70781
IPD					
Cell type	**Ngenes**	**Beta**	**Beta SD**	**SE**	**P**
Astrocytes	272	0.08916	0.010889	0.060035	0.068766
CADPS2	61	0.043147	0.0025103	0.12181	0.36159
DaNs	3298	0.0051904	0.0020097	0.018263	0.38813
Endothelial	418	-0.0079903	-0.0012047	0.047089	0.56737
Ependymal	811	0.057624	0.011966	0.033824	0.044233
Excitatory	3196	0.035544	0.013595	0.018639	0.028275
GABA	1217	0.022821	0.0057358	0.028402	0.21085
Inhibitory	3716	0.041095	0.016648	0.017732	0.010245
Microglia	335	0.12451	0.016846	0.050777	0.0071079
OPC	355	0.059049	0.0082196	0.054881	0.14098
ODC	610	0.018569	0.0033636	0.038035	0.31271
Pericytes	418	0.067611	0.010194	0.046413	0.072609
Controls					
Cell type	**Ngenes**	**Beta**	**Beta SD**	**SE**	**P**
Astrocytes	292	0.086154	0.010896	0.056941	0.065146
DaNs	177	0.023938	0.0023648	0.071795	0.36941
Endothelial	441	-0.028609	-0.0044278	0.045705	0.73432
Ependymal	635	0.05483	0.010126	0.037248	0.070521
Excitatory	2846	0.025134	0.0091787	0.019482	0.09851
GABA	2451	0.0060464	0.0020757	0.020663	0.38491
Inhibitory	3547	0.026985	0.010743	0.01801	0.067032
Microglia	254	0.065616	0.007748	0.058365	0.13047
OPC	347	0.10118	0.013928	0.054997	0.032914
ODC	481	0.019398	0.0031317	0.042521	0.32413
Pericytes	442	0.089193	0.013819	0.045315	0.024526

Ngenes: the number of genes
Beta: the regression coefficient of the variable
Beta SD: the semi-standardized regression coefficient, corresponding to the predicted change in Z-value given a change of one standard deviation in the predictor gene set
SE: the standard error of the regression coefficient
P: p-value for the variable

Supplementary table 5 Per-gene information for every significant cell type within the MAGMA enrichment analysis. See separate Excel file

Supplementary Table 6 T-test results for the cell type composition differences between IPD and control samples.

Cell type	mean cell/sample (control)	mean cell/sample (IPD)	Statistic	Parameter	P.value
Astrocytes	0.1003201348	0.1350897162	-2.750440529	5.671063782	0.03527224809
CADPS2+ neurons	0.0006756662773	0.00716654498	-4.143674419	3.08556866	0.02416713591
DaNs	0.002254081783	0.002534306896	-0.1628600317	4.926478174	0.8770978439
Endothelial cells	0.03712579331	0.03379641715	0.2551487087	6.405729353	0.8066043354
Ependymal	0.008691805579	0.01714801578	-1.763472461	6.174108097	0.1268821922
Excitatory	0.07705083796	0.06105230529	0.8389981942	8.563349355	0.4242711062
GABA	0.01057109988	0.01355919251	-0.6523500725	8.899491317	0.5306619457
Inhibitory	0.03591306145	0.03436051229	0.1246382728	8.849982953	0.9035949956
Microglia	0.05494681848	0.1293926796	-2.967776818	4.335692391	0.03727960072
OPCs	0.0717005494	0.06304498374	1.108974963	5.978794357	0.3100451593
Oligodendrocytes	0.5772245274	0.4762349461	2.004862556	6.698913849	0.08684078533
Pericytes	0.0247274284	0.02906674112	-0.5552624256	6.296609446	0.5978755141

Cell type: Midbrain cell type.
mean %cell/sample (control): Mean fraction of cells per sample for controls
mean %cell/sample (IPD): Mean fraction of cells per sample for IPD
Statistic: the value of the t-statistic.
Parameter: the degrees of freedom for the t-statistic.
P.value: the p-value of the test.

Supplementary Table 7 T-test results of imaging results

DaNs									
Region	**.y.**	**group1**	**group2**	**p-val**	**p.adj**	**p.format**	**p.signif**	**method**	**# samples**
SN	Area	Control	IPD	0.01164196	0.035	0.012	*	T-test	Control n=6; IPD n=5.
Neuromelanin									
Region	**.y.**	**group1**	**group2**	**p**	**p.adj**	**p.format**	**p.signif**	**method**	**# samples**
SN	Area	Control	IPD	0.006934968	0.0069	0.0069	**	T-test	Control n=6; IPD n=5.
Microglia									
Region	**.y.**	**group1**	**group2**	**p**	**p.adj**	**p.format**	**p.signif**	**method**	**# samples**
CC	Area	Control	IPD	0.60947311	1	0.609	ns	T-test	Control n=6; IPD n=5.
Midbrain	Area	Control	IPD	0.29191107	0.88	0.292	ns	T-test	
NR	Area	Control	IPD	0.61652105	1	0.617	ns	T-test	
SN	Area	Control	IPD	0.02375746	0.12	0.024	*	T-test	
TT	Area	Control	IPD	0.04090638	0.16	0.041	*	T-test	
Microglia ramification									
Region	**.y.**	**group1**	**group2**	**p**	**p.adj**	**p.format**	**p.signif**	**method**	**# samples**
SN	BranchPerc	IPD	Control	1,57E-32	6.30E-38	< 2e-16	****	T-test	Control n=5685; IPD n=6894.
Astrocytes									
Region	**.y.**	**group1**	**group2**	**p**	**p.adj**	**p.format**	**p.signif**	**method**	**# samples**
CC	Area	Control	IPD	0.6390098	1	0.64	ns	T-test	Control n=6; IPD n=5.
Midbrain	Area	Control	IPD	0.1077312	0.54	0.11	ns	T-test	
NR	Area	Control	IPD	0.5876515	1	0.59	ns	T-test	
SN	Area	Control	IPD	0.1085478	0.54	0.11	ns	T-test	
TT	Area	Control	IPD	0.2826889	0.85	0.28	ns	T-test	
Oligodendrocytes									
Region	**.y.**	**group1**	**group2**	**p**	**p.adj**	**p.format**	**p.signif**	**method**	**# samples**
CC	Area	Control	IPD	0.565291	1	0.565	ns	T-test	Control n=6l; IPD n=5.
Midbrain	Area	Control	IPD	0.1221451	0.49	0.122	ns	T-test	
NR	Area	Control	IPD	0.5709309	1	0.571	ns	T-test	
SN	Area	Control	IPD	0.0477596	0.24	0.048	*	T-test	
TT	Area	Control	IPD	0.8594471	1	0.859	ns	T-test	

CC: Crus cerebri
NR: Nucleus ruber
SN: Substantia nigra
TT: Tectum and tegmentum of the midbrain

Supplementary Table 8 Differentially activated genes along glial activation in IPD midbrain and differentially expressed genes in each cell type

The Supplementary Table 8 is stored at
https://github.com/SpielmannLab/pd_human_midbrain_snrnaseq/blob/main/scrnaseq/data/Supplementary%20Table%208.xlsx.zip

3.1.4 Additional data to Manuscript I

To additionally validate our results concerning CADPS2^{high} neurons in an independent disease model, we used iPSC from five IPD patients and three matched controls. We first generated smNPCs (Reinhardt *et al.*, 2013), and then further differentiated them into 60-day old midbrain neurons (three independent differentiations). From these cultures, we extracted RNA for cDNA synthesis. We then measured *CADPS2* gene expression relative to the housekeeping *ACTB* gene, equally revealing an upregulation of *CADPS2* in the PD patient neurons (Fig. 3.1.A).

Inspired by these results, we further wanted to characterise our CADPS2^{high} cluster from IPD midbrain tissues. With cell cycle scoring, excitatory, inhibitory, GABAergic, and DaNs neurons were found in a resting state (G0/G1) (Fig. 3.1.B). Contrarily, a large portion of CADPS2^{high} neurons was classified as cycling (G2/M/S) (Fig. 3.1.B). We then utilised a published snRNAseq dataset of human embryonic midbrain (La Manno *et al.*, 2016). After co-embedding of our DaN and CADPS2^{high} populations with the developing neuronal cell types of the midbrain (6-11 weeks-old) (Fig. 3.1.C), the DaNs from our study were transcriptionaly more similar to differentiated embryonal DaNs (hDA0/1/2) (Fig. 3.1.C,D). However, our CADPS2^{high} neurons were clustered closely to embryonal neuroblasts (hNbM, hNbML1/5, hNProg) (Fig. 3.1.C,D). These results might suggest a possible cell cycle re-entry attempting to re-activate the developmental machinery in CADPS2^{high} neurons.

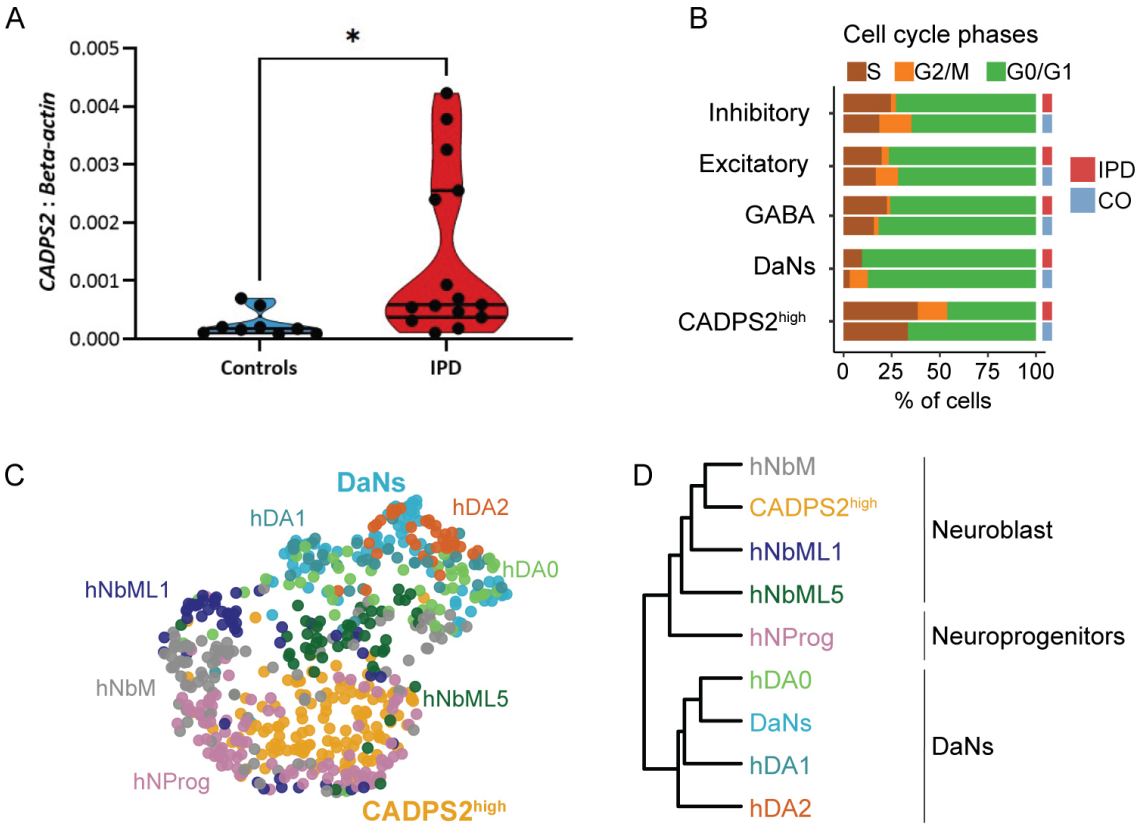

Figure 3.1: CADPS2 validation in iPSC-derived neurons and human embryo midbrain. (A) *CADPS2* gene expression in iPSC-derived midbrain dopaminergic neurons. *CADPS2* expression was measured by real-time PCR in 2D neuronal cultures from 5 IPD patients and 3 matched controls. *Beta-Actin* served as a housekeeping gene. The *CADPS2:Beta-actin* ratio revealed an upregulation of *CADPS2* in IPD neurons compared to control neurons. *$p < 0.05$. (B) Cell cycle phase scoring reveals that ~50% of IPD CADPS2^{high} neurons are cycling cells. (C) UMAP co-embedding of snRNAseq profiles of DaNs and CADPS2^{high} neurons with snRNAseq profiles of neuronal subpopulations in human embryo midbrain (La Manno *et al.*, 2016). (D) The mature DaNs from adult IPD and control midbrain tissue cluster closely with the embryonic DaNs (hDA0/1/2). The CADPS2^{high} neurons cluster closely with the embryonic neuroblasts (hNbM, hNbML1/5) and neural progenitors (hNProg).

3.2 Manuscript II

Neuromelanin alleviates *GPNMB* expression in reactive microglia in idiopathic Parkinson's disease

Semra Smajić[1], Sylvie Delcambre[1], Katja Badanjak[1], Jenny Ghelfi[1], Christopher M. Morris[2], Jens C. Schwamborn[1,3], Malte Spielmann[4], Paul M. Antony[1,5], Anne Grünewald[1,6]

Author affiliations:

[1] Luxembourg Centre for Systems Biomedicine, University of Luxembourg, Esch-sur-Alzette, Luxembourg

[2] Newcastle Brain Tissue Resource, Translational and Clinical Research Institute, Faculty of Medical Sciences, Newcastle University, Newcastle upon Tyne, United Kingdom

[3] OrganoTherapeutics SARL-S, Esch-sur-Alzette, Luxembourg

[4] Institute of Human Genetics, University of Lübeck, Lübeck, Germany

[5] Disease Modeling and Screening Platform (DMSP), Luxembourg Institute of Systems Biomedicine, University of Luxembourg and Luxembourg Institute of Health, Luxembourg, Luxembourg

[6] Institute of Neurogenetics, University of Lübeck, Lübeck, Germany

Corresponding author:

Anne Grünewald, Ph.D., Luxembourg Centre for Systems Biomedicine, University of Luxembourg, 6 avenue du Swing, L-4367 Belvaux, Luxembourg, phone: (+352) 46 66 44 9793, e-mail: anne.gruenewald@uni.lu

This article is in preparation to be submitted to *Movement Disorders*.

3.2.1 Preface

Microglia and inflammatory processes have, in recent time, gained the reputation of a major contributor to PD progression (Obeso *et al.*, 2017). With ageing, or upon a chronic exposure to stress agents, microglia can multiply, migrate and change their profile from protective to detrimental (Imamura *et al.*, 2003; Ouchi *et al.*, 2009; Liddelow *et al.*, 2017). One such stressor, already present after the death of the first DaN, is NM. NM is a 'brain pigment' which progressively accumulates with age, and consists of waste products, misfolded proteins, toxins, lipids or oxidised DA. Once DaNs deteriorate, the toxic NM content is exposed to the surroundings, where it can be sensed by microglia.

In our previous work, we reported microgliosis in the SN with *GPNMB* upregulation in IPD patients as a major disease characteristic. Here, we aimed to investigate the association of NM and microglia by (i) examining the NM distribution in the IPD and control samples, (II) assessing the microglia abundancy, (III) determining the NM-driven microglia accumulation and (iv) investigating NM-driven *GPNMB* expression in microglia.

In IPD tissues, we observed a loss of neuronal NM (nNM) and an increase in NM particles (pNM). We also show that NM leads to amoeboid morphological changes in IPD microglia indicative of their activation. Additionally, we show that such microglia upregulate *GPNMB* expression.

In this article, I contributed to the development of the method for automated image acquisition of a manually precisely-defined region of interest on a large tissue surface. I also participated in the experimental design and the conduction of experimental procedures (immunohistochemical staining, imaging, LCM and RNA extraction, cDNA synthesis). I further performed data analysis, figure and table creation, wrote the first draft and later edited the manuscript.

3.2.2 Manuscript

Research article

Neuromelanin alleviates *GPNMB* expression in reactive microglia in idiopathic Parkinson's disease

Semra Smajic[1], Sylvie Delcambre[1], Katja Badanjak[1], Jenny Ghelfi[1], Christopher M. Morris[2], Jens C. Schwamborn[1,3], Malte Spielmann[5], Paul M. Antony[1,4], Anne Grünewald[1,6]

1 Luxembourg Centre for Systems Biomedicine, University of Luxembourg, Esch-sur-Alzette, Luxembourg

2 Newcastle Brain Tissue Resource, Translational and Clinical Research Institute, Faculty of Medical Sciences, Newcastle University, Newcastle upon Tyne, United Kingdom

3 OrganoTherapeutics SARL-S, Esch-sur-Alzette, Luxembourg

4 Disease Modeling and Screening Platform (DMSP), Luxembourg Institute of Systems Biomedicine, University of Luxembourg and Luxembourg Institute of Health, Luxembourg, Luxembourg

5 Institute of Human Genetics, University of Lübeck, Lübeck, Germany

6 Institute of Neurogenetics, University of Lübeck, Lübeck, Germany

Corresponding author:

Anne Grünewald, Ph.D., Luxembourg Centre for Systems Biomedicine, University of Luxembourg, 6 avenue du Swing, L-4367 Belvaux, Luxembourg, phone: (+352) 46 66 44 9793, e-mail: anne.gruenewald@uni.lu

Word count: Text: 4790, abstract: 241, title: 11, figures: 5, supplementary tables: 2.

References:

Relevant conflicts of interest/financial disclosures: The authors declare no conflict of interest

Funding sources: SS received funding from the Luxembourg National Research Fund (FNR) within the PARK-QC DTU (PRIDE17/12244779/PARK-QC). SD, JG and AG received the FNR INTER grant 'ProtectMove' (INTER/DFG/19/14429377). KB was supported by the Luxembourg National Research Fund (FNR) through the PRIDE15/10907093/CriTiCS grant. JG and AG are also supported by the FNR within the framework of the ATTRACT (Model-idiopathic Parkinson's disease, FNR9631103) career development program. Moreover, AG received the FNR funding as part of the National Centre of Excellence in Research on Parkinson's disease (NCER-Parkinson's disease, FNR11264123) and the FNR CORE grant 'MiRisk-Parkinson's disease' (C17/BM/11676395).

Abstract

Background. Large reactive microglia subtype characterized by *GPNMB* upregulation was found in idiopathic Parkinson's disease post-mortem midbrain. Similarly, in Alzheimer's disease brain, the $GPNMB^{+}$ microglia accumulated around amyloid-beta plaques to clear it. In Parkinson's disease, the increase in microglial abundance was found specific to substantia nigra. Moreover, these microglia exhibit amoeboid morphology, which all together suggests a nigra-centric inflammation specific to Parkinson's disease.

Objectives. We aimed to investigate the contribution of neuromelanin to nigra-specific inflammatory GPNMB-state of microglia.

Methods.We utilized human post-mortem midbrain tissue from Parkinson's disease patients and age- and sex-matched controls. Immunohistochemical staining was employed to assess the distribution of dopaminergic neurons, neuromelanin and microglia. Laser-microdissection and transcriptomics were employed to investigate the relationship between microglia and neuromelanin.

Results. With this approach, we confirmed the loss of dopaminergic neurons and neuromelanin, and increase in microglia in idiopathic Parkinson's disease patients. However, we also found a larger proportion of undegraded neuromelanin particles in patient tissues. Moreover, we showed that the patient's microglia tend to accumulate around neuromelanin deposits. The neuromelanin-laden microglia in patients exhibited extremely amoeboid morphology, indicative of a toxic character of neuromelanin in Parkinson's disease substantia nigra. Additionally, the

patient's microglia around neuromelanin exhibited alleviated *GPNMB* expression suggesting a similar mechanism of clearance as in Alzheimer's disease plaques.

Conclusions. These results implicate neuromelanin as a major contributor to inflammation in Parkinson's disease patients, and open a new door to a potential treatment of neuroinflammation with neuromelanin modulation.

Introduction

Parkinson's disease (PD) is a chronic, progressive and complex neurodegenerative disorder affecting over 1% of the world population above 60 years[1]. This number is expected to double by the year 2040[2]. The key pathological feature of PD is the loss of neuromelanin (NM)-containing dopaminergic neurons (DaNs) from the substantia nigra (SN), which leads to a deficiency in dopamine levels in the brain. The disease is characterized by various symptoms, ranging from motor and non-motor to vegetative changes[1]. Despite being described for the first time more than 200 years ago, the exact cause of PD remains unknown. Age, gender, environmental and genetic factors are considered as contributing elements to the etiology of PD. However, the vast majority of PD cases do not have a known genetic origin, and are therefore classified as idiopathic patients (IPD)[3].

Previously, the main focus of PD research was on DaN function. In recent years, however, the pathological changes in cells other than neurons are being increasingly recognised. Microglia and inflammatory processes have emerged as an important factor in the progression of PD[4]. On the one hand, they act protective by clearing out waste material and pathogens from the brain. On the other hand, with aging and extended exposure to stress, microglia can acquire damaging morphological and functional characteristics[4,5], and exhibit detrimental properties to which nigral neurons react particularly sensitively[4–7]. One solid candidate that can be culpable for microgliosis is NM, an often overlooked factor in PD.

NM becomes visible at the age of three, and continues to increase in size and density as it binds the excess dopamine[8]. Besides dopamine, NM is a powerful quencher of metal ions, toxins or undegraded cellular parts and proteins[8–12]. By binding of noxious molecules inside neurons, NM

prevents their harmful reactions in the brain and is thus considered neuroprotective. However, in PD, the lifetime-accumulated, insoluble and toxic NM content is released extracellularly as a result of DaN demise[13,14]. Once the NM cargo leaked into the tissue parenchyma, it is reasonable to suspect an activation of the surrounding microglia to produce proinflammatory agents that contribute further to neuronal death and consequent NM release. Indeed, *in vivo* and *in vitro* studies in mice demonstrated strong proinflammatory phenotypes and chemotaxis of microglia as a response to NM[15–18]. In contrast to humans, rodents do not accumulate neuromelanin. Therefore, the animal models are based on artificial injection of NM preparations, viral transfection or toxin treatments[16,19]. In addition, rodents lack the complexity and the nature of the human brain. Thus, although these studies provide valuable information on the microglia-NM interplay, they have not yet been validated in human endogenous models.

In the current study, we applied immunohistochemistry, high-throughput confocal imaging and laser microdissection-based transcriptomics to postmortem midbrain tissue from IPD patients and controls to elucidate the relationship between NM and microglia at single-cell resolution. Using this approach, we identified darker NM in IPD patients as an important driver of morphological and transcriptional changes in microglial activation.

Materials and Methods

Human midbrain tissue. Formalin-fixed paraffin-embedded (FFPE) midbrain tissue sections were provided from the Parkinson's UK Brain Bank. According to the pathological reports, the brain was divided by the midline to separate the two hemispheres together with the hemi-midbrains. With a transverse section, the right hemi-midbrain was removed and then formalin-fixed, embedded into paraffin and sectioned transversely at ~5µm thickness. The sections were then stored at 4°C. The brain banks collected written informed consent from the patients and controls, which, together with the ethics review panel of the University of Luxembourg, approved the study.

Genotyping of Parkinson's disease samples using NeuroChip. DNA samples from PD cases were genotyped at the Institute of Human Genetics at the Helmholtz Zentrum München with the Illumina (San Diego, CA) NeuroChip[20]. SNP imputation was performed on NeuroChip data using the Michigan Imputation Server[21] to produce a final list of common (minor allele frequency ≥ 1%) variants. Imputed SNP positions were based on Genome Reference Consortium Human 37/human genome version 19 (GRCh37/hg19). All PD cases were screened for disease-associated genetic variants in known major Parkinson's disease genes (*SNCA*, *LRRK2*, *DJ-1*, *PRKN*, *GBA*, *PINK1*, *ATP13A2*, *VPS35*, *MAPT*, *DCTN1*, *DNAJC6*, *SYNJ1*, *VPS13C,* and *MAPT*) covered by the NeuroChip.

Immunohistochemistry of midbrain sections. Stainings were performed as described previously[22,23]. Briefly, FFPE midbrain sections were first deparaffinized by incubating at 60°C for 30 minutes. Secondly, the tissues were cleared with serial washes in Histoclear (2 x 5 minutes), ethanol (99%, 99%, 95%, 70% v/v, each 5 minutes) and distilled water (1 x 10

minutes). Then, the sections were treated with 1mM EDTA for 40 minutes in a pressure cooker for antigen retrieval, followed by washing for 5 minutes in distilled water, and 5 minutes in 1% TBST. Blocking was done for 1 hour at room temperature in 10% natural goat serum (NGS) in 1% TBST. Finally, the staining was performed by an overnight incubation in primary antibody solution (anti-tyrosine hydroxylase (TH) MAB318, 1:100, Millipore; anti-IBA1 019-19741, 1:500, FUJIFILM Wako) diluted in 1% NGS in 0,1% TBST. The next day, the sections were washed 3 x 5 min in 1% TBST, and incubated at room temperature for 1 hour in secondary antibody solution (goat anti-mouse IgG1 Alexa Fluor 647, 1:100, A21240; goat anti-rabbit IgG Alexa Fluor 488, 1:100, A27034, Life Technologies) diluted in 1% NGS in 0.1% TBST. Lastly, the sections were washed 3 x 5 minutes in 1% TBST, incubated in 0.3% Sudan black for 2 minutes and then rewashed 3 x 5 minutes in 1% TBST. Dried sections were mounted in Prolong Gold mounting medium with DAPI.

Image acquisition. Images of the SN were acquired with a Yokogawa Cellvoyager CV8000. First, the desired region for acquisition was encircled on the slide with a marker pen. Next, a Matlab script was employed to screen the entire tissue slide in one plane using the 4x objective. This approach allowed for later identification of the drawn region. With a second script, the Yokogawa was programmed to reacquire the images inside the identified region with a 20x objective and in 3D resolution (five planes with 1µm increment).

Automated image analysis. The analysis was performed with Matlab R2020a. All acquired planes of an image were first fused into a maximum projection, and then stitched into one large image for each channel used in the downstream analysis. Due to heterogeneity in NM intensity between the tissues, the intensity threshold for NM identification was manually selected for each tissue and imported as a .txt file into the in-house-developed Matlab algorithm for automated

segmentation of NM objects. The algorithm selects a brightfield channel and segments individual NM objects with the intensity below the selected threshold. These objects are then filtered by area size and only those between 27 and 5000 are retained with the *'bwareafilt'* function. Then the algorithm calculates the roundness of each object by dividing the area and perimeter, and keeps objects with a roundness > 1. Due to the complexity of human brain tissue, even with the strict set of filters that was applied, the analysis resulted in false-positive objects. Therefore, each output image mask was additionally inspected by eye, and false-positive objects were marked manually with using the *'ObjectSelector'* GUI script. The analysis was reinitiated, and the marked objects were excluded from the downstream analysis.

In addition, we designed automated image analysis algorithms, which select the fluorescent channels and segment TH-positive (DaNs) and IBA1-positive (microglia) objects extracting different features such as area, intensity, perimeter or proximity and overlap with NM. In brief, the segmentation of microglia was determined by convolving the raw IBA1 channel with a *Gaussian* filter (*hsize = 5; sigma = 1*). Only objects with intensity > 700, and an area size between 9 and 2000 were retained. Another set of analyzed features concerned microglial ramification. The respective algorithm performed a morphological assessment of the image using the *'imopen'* function which utilizes a 'disk-shaped' structuring element with a radius of 6 pixels to identify the microglia soma. Then, with the *'bwmorph'* function and *'skel'* operation, the image skeleton was extracted.

The proximity of microglia objects to NM accumulations was performed by dilating the NM object mask with structuring element *'disk'* of a size 60. Then, the IBA1-positive area was quantified inside each of the dilated NM masks.

The segmentation of dopaminergic neurons was computed by filtering for noise of the raw TH channel with the *'medfilt2'* function. Then, only areas with an intensity >610 were retained. Next, we applied the 'difference of *Gaussians'* filter for additional noise removal. To only keep the soma, the algorithm removes objects smaller than 1000 pixels with *'bwareaopen'*. Since the intensity of the TH staining varied between healthy and PD samples, this analysis also resulted in false-positives. Therefore, we applied the same '*ObjectSelector*' GUi script that was previously applied to NM objects. Here, we confirmed the true positives by manual selection. Then, when the final analysis was reinitiated, only selected objects were further analyzed. Due to the inadequate TH staining, we excluded 2 IPD and 2 healthy control cases from the analysis that involves TH area readouts.

Laser-capture microdissection of frozen tissue. Frozen human postmortem midbrain tissue sections from 5 IPD and 5 control cases were obtained from Newcastle Brain Tissue Resource. According to the sampling procedure in neuropathological reports, the left hemi-midbrain block was snap-frozen at -120°C. Next, the tissue was sectioned at 20 µm thickness onto PEN slides, which were stored at -80°C. Frozen sections were submerged in ice-cold 75% ethanol for 3 minute, and then in 99% ethanol for 1 minute[24]. After short air-drying, tissue was cut with PALM Microbeam (Zeiss), and captured in 20 µL nuclease-free water with 0.2 U/µL RNase inhibitor (Roche).

RNA extraction and cDNA synthesis. RNA was extracted with NucleoSpin RNA XS purification kit (Macherey-Nagel) in accordance with the manufacturer's instructions. The cDNA was synthesized with SuperScript III Reverse Transcriptase (ThermoFisher).

dPCR analysis. Gene expression was quantified by means of digital PCR (dPCR) using the QuantStudio™ 3D Digital PCR System (Applied Biosystems). Samples were prepared following the manufacturer's instructions using QuantStudio™ 3D digital Master Mix v2 (A26359, Life Technologies). The following primers/probes were purchased from ThermoFisher Scientific: AIF1-VIC-MGB (4448489_Hs00610419_g1), Actin-VIC-MGB (4448489_Hs01060665_g1) and TH-FAM-MGB (4331182_Hs00165941_m1). The sequences for GPNMB are: forward 3'-CCCACGGAGGTCTGTACCAT-5', reverse 3'-GCAGACTGTGTTCTGGGTGATC-5' and probe FAM-TTCTGACCCCACCTGC-MGB. The sequences for MAP2 are: forward 3'-CCATCTTGGTGCCGAGTGA-5', reverse 3'-GGAGTCGCAGGAGATTTTGG-5'and probe FAM-AGGTCGCCATCATAC-MGB.. Samples were loaded on a QuantStudio™ 3D digital PCR Chip v2 using the QuantStudio™ 3D Digital PCR Chip loader. The PCR was then performed on the ProFlex™ 2X Flat PCR System using the following parameters: 95 °C for 5 min, 45 cycles of 95 °C for 10 s, and 60 °C for 10 s, 72°C for 10 s. The chips were read using the QuantStudio™ 3D Digital PCR Instrument and the data were analysed using the QuantStudio™ 3D AnalysisSuite, version 3.1.6-PRC-build18

Statistical analysis. All statistical analyses and graphical representation of the results was performed with R (v. 4.1.2). An independent t-test was used to determine statistical significance ($p < 0.05$). A standardized mean difference, or Cohen's *d*, was used to determine the effect size (insignificant $d < 0.2$, small $d > 0.2$, moderate $d > 0.5$, large $d > 0.8$, very large $d > 1.2$)[25]. To determine the modality of the data, we used Hartigan's dip test[26] in a '*diptest*' R package (v. 0.76-0). The bimodality was assessed with '*LaplacesDemon*' (v. 16.1.6) and the bimodality coefficient[27] was calculated with '*mousetrap*' (v. 3.2.1) (bimodal BC > 0.555). Further, package

'*cutoff*" (v. 0.1.0) was used to determine the bimodality cutoff in the data. The snRNAseq data was analyzed with '*Seurat*' (v. 4.1.0) as described by Smajić et al[23].

Results

We obtained human midbrain tissue sections from seven iPD cases with severe neuronal loss in the SN (Table S1). We isolated the DNA and performed SNP-Chip profiling[20] of 179,467 known variants associated with neurological diseases, including PD, and confirmed the idiopathic status of all PD samples. Additionally, we included seven matched control cases without reported neurological diseases (Table S1). The average age of the patients was ~78 (SEM 2.6 years), and of matched controls ~82 years (SEM 3.6 years) (Table S1). Both groups had similar postmortem intervals (PD: 24 hours, SEM 1.5 hours; controls: 18 hours, SEM 4 hours) (Table S1).

To elucidate the relationship between inflammation and NM in PD in more detail, we applied a two-step approach (Fig. 1A). First, by means of immunofluorescent labeling and automated imaging analysis, we assessed the abundance and spatial distribution of DaNs, microglia and NM. Second, with laser-capture microdissection (LCM), we assessed the expression of selected inflammatory and dopaminergic markers in relation to NM (Fig. 1A).

To re-evaluate our previous findings concerning the loss of NM and DaNs in the SN of IPD patients[23], we immunostained the midbrain tissues with the dopaminergic marker TH (Fig. 1B). The SN tissue from the IPD cases showed a significant decrease in the abundance of DaNs compared to control cases with a large effect size (d = 1.43) (Fig 1C). After a closer examination of the tissues, we observed that IPD DaNs often lack NM. Therefore, we segregated our DaN population according to NM load to TH^+/NM^+ and TH^+/NM^-. An independent t-test reported a significant increase in the amount of TH^+/NM^+ compared to TH^+/NM^- DaNs for both groups, with a large effect (control d = 1.38, IPD d = 1.02) (Fig. 1D). However, the average amount of

NM^+ DaNs in control samples was about 6-fold higher, whereas, in IPD, NM^+ DaNs were only ~3 times more abundant than NM- DaNs.

When comparing the abundance of TH^+/NM^+ and TH^+/NM^- DaNs between the conditions, we observed that IPD cases were characterized by significantly less TH^+/NM^+ DaNs than controls and this difference was found to have a large effect size (d = 1.55) (Fig. 1E). By contrast, no difference between the conditions was observed with respect to the abundance of TH^+/NM^- DaNs (Fig. 1E). Together, these results indicate a higher loss of NM^+ DaNs in comparison to NM^- DaNs in IPD patients.

Next, we analyzed the NM content inside the TH^+ neurons and found a decrease in IPD samples compared to controls which, however, did not reach significance threshold (p = 0.055), but had a very large effect size (d = 1.23) (Fig. 1F).

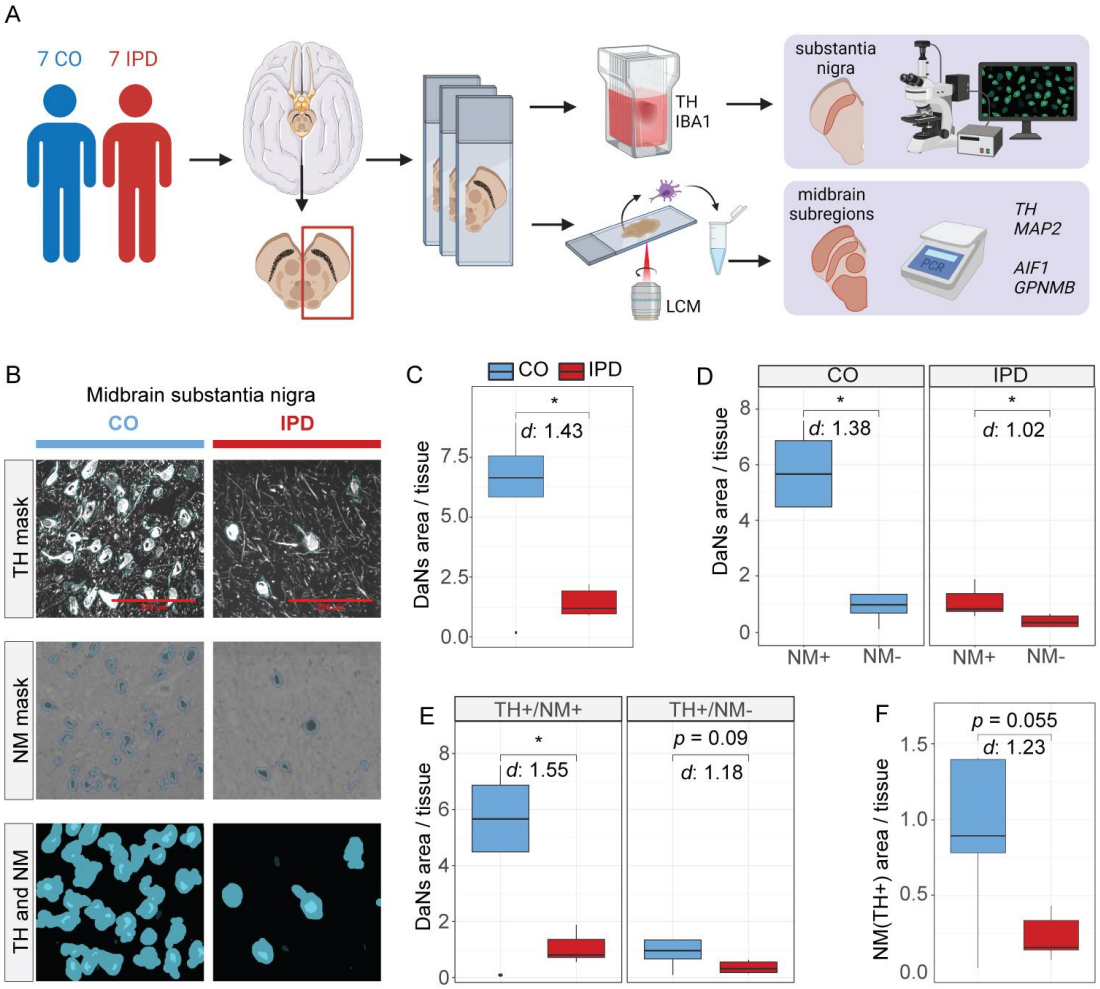

Fig. 1 The IPD SN is characterized by the previously described loss of TH^+ neurons and a lack of NM deposits. (**A**) Experimental overview to characterize the neurodegenerative and neuroinflammatory phenotype of SN. The tissue sections were immuno-stained and laser-microdissected for imaging and quantitative PCR. (**B**) Representative TH immunofluorescence and brightfield NM images of IPD and control SN sections. (**C**) TH^+ areas in the SN of 10 individuals. IPD midbrain SN is associated with less TH^+ areas ($p = 0.04$). (**D**) TH^+ areas divided by NM content. IPD and control SN contained more NM-laden than NM-empty DaNs ($p = 0.03$ and $p = 0.04$, respectively). (**E**) IPD midbrain SN tissue is characterized by loss of NM-laden DaNs areas ($p = 0.04$). The amount of NM-empty TH^+ areas at similar levels as in controls. (**F**) IPD SN tissue showed a trend towards depletion of

dopaminergic NM+ areas. PD, red bar; control, blue bar; scale bar = 500µm; p-value range (* $p < 0.05$, ** $p < 0.01$, *** $p < 0.001$, **** $p < 0.0001$); Cohen's d range (insignificant $d < 0.2$, small $d > 0.2$, moderate $d > 0.5$, large $d > 0.8$, very large $d > 1.2$).

Previously, we reported that, apart from being inside the TH^+ DaNs, NM particles could be observed in the extracellular space in the tissue, or found within MAP2+/TH- nigral neurons[23,28]. Therefore, we expanded our cohort to 7 IPD and 7 control cases, and focused on quantifying the overall NM load, regardless of TH abundance. With automated image analysis, we identified NM deposits based on a specific intensity threshold in the brightfield channel (Fig. 2A). We ordered the NM objects according to their area size in a distribution plot and revealed two distinct populations. The bimodality coefficient (BC) = 0.69 confirmed the bimodality of the data, separated by a dip at 899.092 pixels (Fig. 2B). Moreover, an analysis of the size distribution of NM deposits within TH-positive neurons in IPD and control SN tissue revealed that neuronal NM deposits are typically >1000 pixels in area (Fig. 2C). Based on these findings, we defined two NM populations applying this cut-off: (i) *'neuronal NM'* (nNM) with a pixel size > 899.092 and (ii) *'NM particles'* (pNM) with a pixel size < 899.092. We then quantified the proportions of the nNM and pNM fractions within each sample. We detected a smaller percentage of nNM deposits in IPD compared to control tissue (Fig. 2C). By contrast, the abundance of pNM was significantly increased in IPD samples in comparison to controls ($d = 1.56$) (Fig. 2D). These results are reflected in a shift of the nNM to pNM in the IPD cases, which may suggest enhanced NM degradation or release in IPD (control $d = 0.77$, IPD $d = 2.08$) (Fig. 2E).

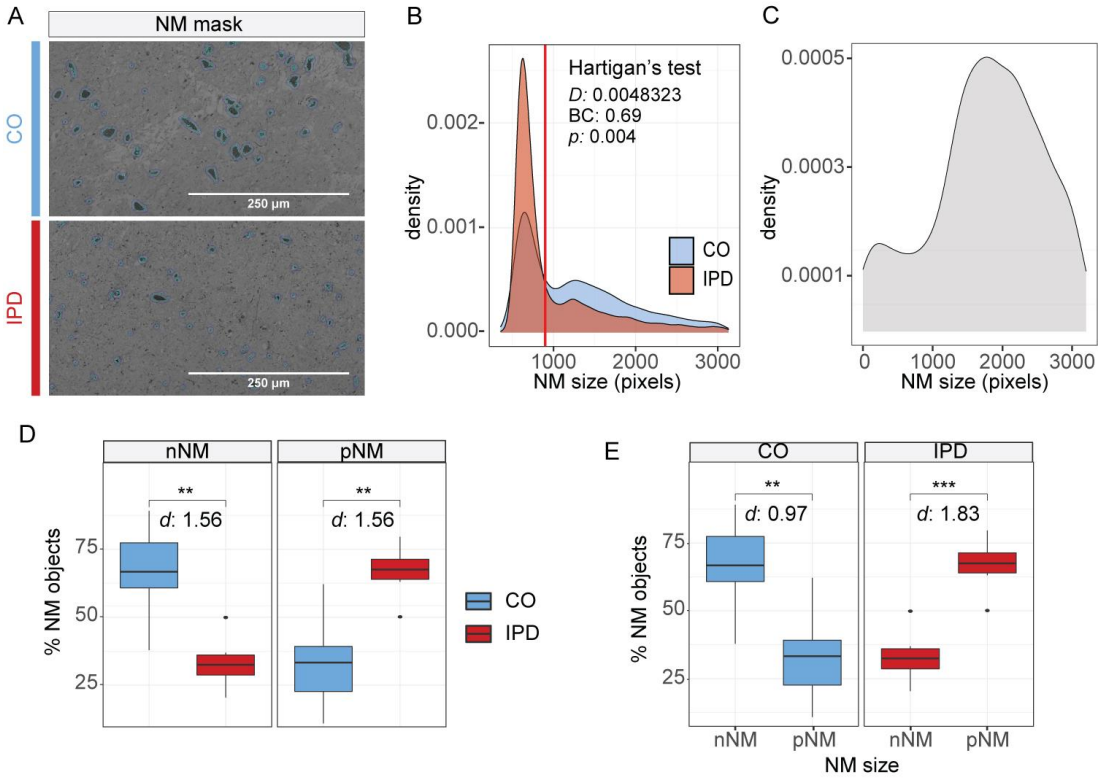

Fig. 2 Quantification of NM deposits in SN tissues. (**A**) Brigtfield image of NM deposits in control and IPD midbrain SN. (**B**) Distribution of NM deposits over size from 14 individuals. Two subpopulations can be identified by a dip of the NM size at 899.092 pixels. (**C**) Size distribution of NM deposits within TH-positive neurons in IPD and control SN tissue. The histogram indicates that neuronal NM deposits are typically >1000 pixels in area, implicating that the first peaks for IPD patients and controls in (**B**) are of neuronal origin. (**D**) Percentage of 'large' and 'small' subpopulations of NM deposits between the control and IPD cases (p = 0.0014). (**E**) Percentage of 'large' and 'small' subpopulations within a condition group (control, p = 0.004; IPD p = 0.00058). PD, red bar; control, blue bar; scale bar = 250 µm; p-value range (* p < 0.05, ** p < 0.01, *** p < 0.001, **** p < 0.0001); Cohen's d range (insignificant d < 0.2, small d > 0.2, moderate d > 0.5, large d > 0.8, very large d > 1.2); D, Hartigan's dip statistics; BC, bimodality coefficient.

Next, we aimed to investigate the association of NM and microglia between the conditions. First, we labeled the tissue from the seven IPD patients and healthy control individuals with the microglial marker IBA1 (Fig. 3A), and compared the IBA1-positive areas between the control and IPD condition (Fig. 3A, B). In line with previous reports[23,28], we observed an increased fraction of microglia in IPD SN tissue compared to the controls ($p = 0.04$) (Fig. 3B). Next, we overlaid the microglia masks with the NM masks from the brightfield channel to assess the overlap between the two features (Fig. 3A, bottom panel). Thus, we explored the presence of NM^+ and NM^- microglia with this analysis. Independent of the presence of NM, IPD samples showed an increase in both microglial populations compared to control samples, which was statistically significant for the NM^- microglia population ($p = 0.04$) (Fig. 3C). Further image analysis of microglial morphological features in the SN of age- and sex-matched IPD and control cases (Fig. 3A, mid panel) identified an IPD-related decrease in microglial ramification, suggesting cellular activation ($p < 0.00001$) (Fig. 3D). Further segregation of microglia according to NM content revealed that NM-laden IPD microglia exhibited the least ramified morphology when compared to NM^- IPD and control microglia ($p < 0.00001$) (Fig. 3E). Together, these results confirm an IPD-specific increase in microgliosis and suggest that NM can lead to microglial activation in the human brain.

In PD, microglia are exposed to chronic stimuli which can lead to their overactivation[4]. Therefore, we next examined the relationship between nNM and microglia by quantifying the IBA1 area in the proximity of nNM. With an adjusted script, we defined an exact border (green ring) around each nNM (Fig. 3F). Then, we quantified the amount of $IBA1^+$ areas in the surroundings of nNM and identified an accumulation of microglia in the vicinity of nigral IPD

nNM, compared to that of controls ($p < 0.00001$) (Fig. 3G). At present, these findings classify IPD microglia as activated and sensitized by NM.

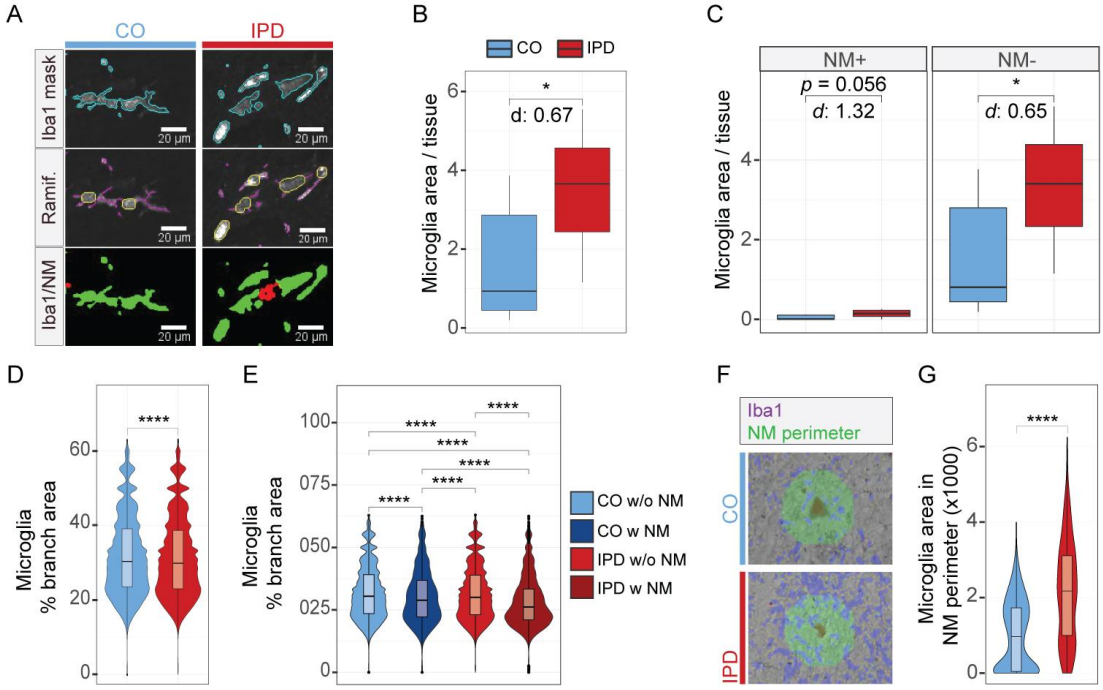

Fig. 3 Microgliosis is an IPD phenotype trait and is associated with NM. (**A**) IBA1 immunolabeled tissues with morphology analysis. Upper panel shows the microglia area, the mid panel shows the skeletonization mask of microglia, and the bottom panel shows microglia mask in green and NM mask in red. (**B**) IBA1$^+$ areas in SN of 14 individuals. IPD midbrain is characterized with more microglia areas than controls ($p = 0.04$). (**C**) IBA1$^+$ areas divided by the NM content. IPD midbrain SN shows a trend towards an increase in NM$^+$ microglia ($p = 0.056$) together with an increase in NM- microglia ($p = 0.04$). (**D**) Morphological analysis of IBA1$^+$ areas reveals overall more amoeboid microglia in the SN of IPD cases ($p < 0.00001$). (**E**) The amoeboid morphology of microglia is more pronounced in IPD especially in NM$^+$ microglia ($p < 0.00001$). (**F**) IBA1 immunolabeled areas in proximity to NM deposits. (**G**) IPD NM deposits are more surrounded with microglia than control NM ($p < 0.00001$). IPD, red bar; control, blue bar; w, with; w/o, without; scale bar = 20 µm; p-value range (* $p < 0.05$, ** $p < 0.01$, *** $p < 0.001$,

**** $p < 0.0001$); Cohen's d range (insignificant $d < 0.2$, small $d > 0.2$, moderate $d > 0.5$, large $d > 0.8$, very large $d > 1.2$).

In our previous work [23], we reported an IPD-specific microgliosis with several activated microglia subpopulations increased in IPD samples. The largest subpopulation was characterized by alleviated *GPNMB* expression (Fig. 4A). To explore this phenotype in another form of PD, we merged our two published datasets of IPD and control samples (GSE157783)[23] with *PRKN*-mutant sample (GSE166790)[29]. *PRKN*-mutant midbrain exhibited an even larger upshift in the microglial cell cluster when compared to IPD and controls [29]. In this population of 45.608 nuclei, among the marker genes of activated subclusters [23], *GPNMB* and *IL1B* were found exclusively in microglia (Fig. 4B). Next, we compared the expression of either of the genes between the samples (Fig. 4C). We observed that the *GPNMB* upregulation is solely specific to IPD microglia, while the upregulation of *IL1B* is a characteristic of *PRKN*-mutant microglia (Fig. 4C). Our results suggest that the IPD midbrains are characterized by a unique inflammatory response labeled with *GPNMB* upregulation. Glycoprotein nonmetastatic melanoma protein B (GPNMB) was reported as a phagocytic protein which controls cellular debris trafficking for degradation[30,31]. Considering remaining large amounts of NM particles in IPD samples, we hypothesized that *GPNMB* upregulation in microglia could be NM-dependent.

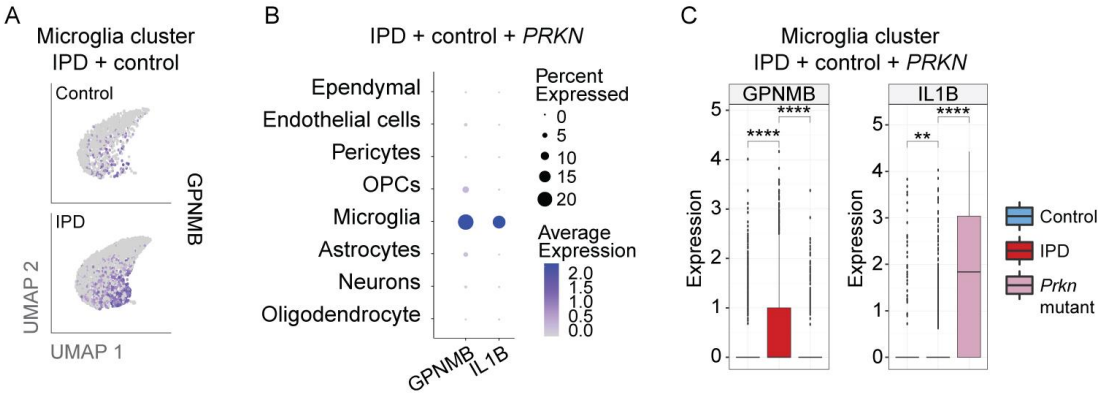

Fig. 4. *GPNMB* expression is alleviated in IPD microglia. (**A**) Feature plot of microglial cluster shows a larger GPNMB^{+} microglia subpopulation (purple) in IPD compared to control samples. (**B**) The extended single-nuclei population consisting of IPD, control and Parkin midbrain shows the expression of the two highly abundant microglia-specific genes *GPNMB* and *IL1B*. (**C**) *GPNMB* expression is specific to IPD microglia, while *IL1B* expression is specific to Parkin microglia. OPCs, oligodendrocyte precursor cells; IPD, red bar; control, blue bar; *PRKN*-mutant, pink bar; p-value range (* $p < 0.05$, ** $p < 0.01$, *** $p < 0.001$, **** $p < 0.0001$).

Taken together, our current and previous results in IPD brain tissue show: (i) a microgliosis in the SN[23], (ii) a *GPNMB*-specific activation, (iii) an increase in pNM over nNM, (iv) more amoeboid NM-laden microglia in the SN and (v) an increase in microglia accumulation around NM. We, therefore, sought to assess the spatial distribution of *GPNMB* expression in the midbrain and to investigate whether NM can be a trigger of *GPNMB* dysregulation. We utilized frozen midbrain sections of 5 IPD and 5 control cases and microdissected (LCM) six different areas of the midbrain: 100 dark NM (D-NM) areas, 100 light NM (L-NM) areas and 100 NM-empty (No-NM) areas in the SN per individual, as well as size-matched areas of *crus cerebri* (CC), *nucleus ruber* (NR) and *tectum/tegmentum* (T/T) (Fig. 5A). To gain an impression of cellular enrichment in each of the regions, we examined the immunofluorescent images of the entire midbrain (Fig. 5B). The CC region mainly consists of neural tracts[32] and therefore lacks

cell nuclei (DAPI staining) (Fig. 5B). Accordingly, microglia appeared well-distributed throughout the entire midbrain, except for the CC (Fig. 5B). Lastly, in line with established neuropathological knowledge, high TH signal was detected in the SN (Fig. 5B).

Due to the lack of adequate antibodies for immunohistochemical labeling, we then proceeded to quantify *GPNMB* abundance in the midbrain by means of dPCR. For this purpose, we employed an independent group of frozen midbrain samples from 5 IPD and 5 control cases (Table S2). First, to verify the identity of the dissected midbrain subregion, we examined the *TH* abundance. This analysis validated the SN as the region with the highest *TH* expression (Fig. 5C). Second, we measured *GPNMB* expression in all the midbrain subregions. *GPNMB* was also detected at the highest levels in the SN, and somewhat lower in the T/T region (Fig. 5D). These results implicate a spatially distinct distribution of *GPNMB* in the midbrain, directing our further analyses towards the SN.

To validate the quality of our nigral LCM preparations, we assessed the expression of *TH* in NM-containing areas and NM-empty areas. We found a significantly higher *TH* abundance in areas with NM than in areas without NM, confirming the accuracy of our approach in sampling DaNs and the remnant SN tissue (Fig. 5E). We then aimed to assess the microglial abundance throughout the SN. Thus, we stratified the NM group into D-NM and L-NM and compared the two cell populations with the No-NM group. dPCR analysis revealed a major upregulation of the microglial marker (*AIF1*) in the D-NM group suggestive of microglial infiltration (Fig. 5E). On the contrary, No-NM areas isolated from the SN showed reduced *AIF1* expression, indicative of reduced microglia abundance (Fig. 5F). Thus, we focused our further analysis on NM-laden areas. When comparing the *GPNMB* expression between controls and IPD cases, we revealed a tendency of an IPD-specific *GPNMB* upregulation (FC ~5) in microglia around D-NM (Fig. 5G).

This effect was less pronounced in the L-NM group (FC ~2) (Fig. 5G). While our results did not reach statistical significance, possibly due to the small number of samples included in the study, the effect size (d = 2.79) of the D-NM-mediated phenotype in the IPD samples was very large (Fig. 5G).

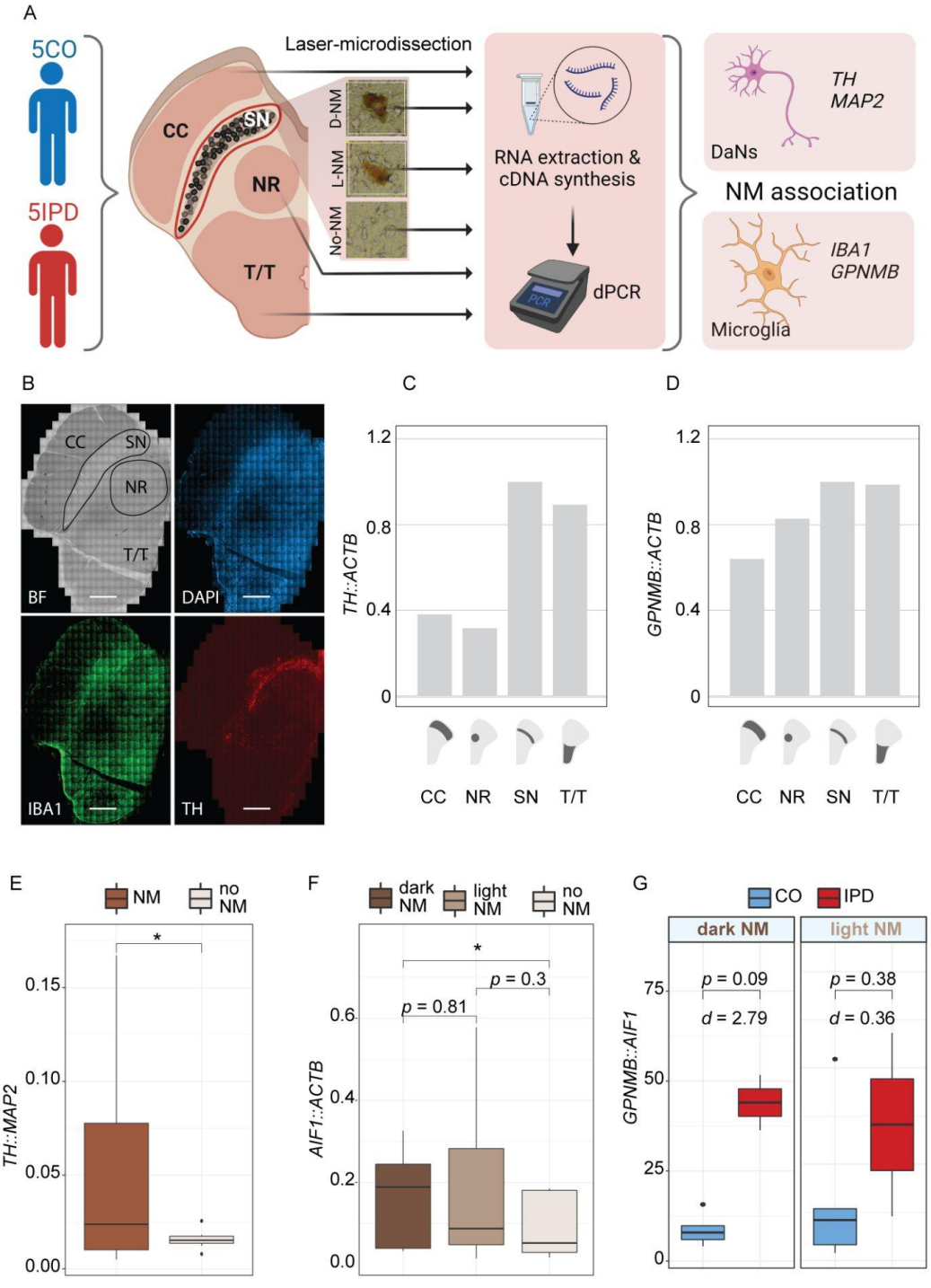
A
5CO
5IPD
Laser-microdissection
CC
SN
NR
T/T
D-NM
L-NM
No-NM
RNA extraction &
cDNA synthesis
dPCR
TH
MAP2
DaNs
NM association
IBA1
GPNMB
Microglia
B
BF
DAPI
IBA1
TH
C
TH::ACTB
CC NR SN T/T
D
GPNMB::ACTB
CC NR SN T/T
E
NM
no NM
TH::MAP2
F
dark NM
light NM
no NM
p = 0.81
p = 0.3
AIF1::ACTB
G
CO
IPD
dark NM
light NM
p = 0.09
d = 2.79
p = 0.38
d = 0.36
GPNMB::AIF1

Fig. 5. *GPNMB* expression is alleviated in microglia surrounding D-NM. (**A**) Experimental approach to laser microdissection of frozen midbrain tissues for digital PCR. (**B**) Microscopy image of immunohistochemical staining of midbrain tissue showing brightfield (BF), nuclei (DAPI), microglia (IBA1) and DaNs (TH). (**C**) Midbrain: dPCR quantification of *TH* expression normalized to housekeeping gene *ACTB* revealed the highest expression in SN, followed by T/T. (**D**) Midbrain: dPCR detection of *GPNMB* expression normalized to housekeeping gene *ACTB* showed the highest abundance in SN, followed by T/T. (**E**) SN: expression of *TH* normalized to *MAP2* was found significantly higher in NM-containing areas of SN compared to NM-empty areas of SN ($p = 0.017$). (**F**) SN: the segregation to D-NM, L-NM and No-NM revealed the highest *AIF1* expression (microglia) normalized to housekeeping gene *ACTB* around D-NM ($p = 0.016$). (**G**) SN: *GPNMB/AIF1* ratio served as an indicator of *GPNMB* upregulation in microglia, which showed higher *GPNMB* expression around IPD NM. IPD, red bar; control, blue bar; CC, crus cerebri; SN, substantia nigra; NR, nucleus ruber; T/T, tectum/tegmentum; scale bar = 3 mm; p-value range (* $p < 0.05$, ** $p < 0.01$, *** $p < 0.001$, **** $p < 0.0001$); Cohen's d range (insignificant $d < 0.2$, small $d > 0.2$, moderate $d > 0.5$, large $d > 0.8$, very large $d > 1.2$).

Discussion

Over the past years, neuroinflammation gained a considerable interest in PD pathology focusing on the destructive roles of microglia. In our recent work[23], we reported an IPD-specific GPNMB$^+$ subset of activated microglia. Another study in Alzheimer's disease (AD) reported *GPNMB* overexpressing microglia accumulating around amyloid plaques in the brain[33]. Thus, through a multilevel approach, we examined this novel inflammatory state of microglia and a potential link to NM in PD. By using postmortem human midbrain tissues, we assessed the spatial context of DaNs, NM and microglia in IPD. In addition, we explored the relationship of *GPNMB* expression in microglia with NM deposits in DaNs.

When assessing DaNs and NM abundance, our results confirmed a significant depletion of both features in IPD samples compared to controls. These neuropathological results align with the advanced Braak stages described in the neuropathological reports of the individuals (Table S1). A more detailed inspection of the remaining DaNs revealed a significant reduction in NM$^+$ DaNs in IPD when compared to the controls. On the contrary, the levels of NM$^-$ DaNs, despite being generally lower, were not different. Together, these findings indicate a higher vulnerability of NM-laden DaNs in PD[34,35]. Of note, NM accumulation and PD progression, both correlate with aging. Likewise, these two processes are only specific to humans[36]. In post-mortem midbrain tissue of PD patients and incidental Lewy body disease (ILBD) cases, intraneuronal NM was found to be denser than in healthy age-matched control individuals, and thus considered to accumulate faster to a pathogenic level[19]. Moreover, common molecular processes in PD pathology, such as inflammation, formation of inclusion bodies, mitochondrial damage, increased ROS levels or proteasome dysfunction, were found to occur as a consequence of

pathogenic levels of NM in rodent models[19,35]. Such processes likely cause neuronal demise and consequent NM release, inducing a proinflammatory state in microglia [37].

Supporting this hypothesis, we found a larger fraction of pNM in IPD compared to control tissue. Due to accelerated neuronal death and consequent release of NM in IPD, these pigmented particles may, in fact, represent the remains of released undegraded NM. Accordingly, we observed a PD-specific increase in microglia - the mediators of the innate immune system of the brain. In addition, we reported a trend towards a higher abundance of microglia containing NM particles in IPD compared to control midbrains. NM can activate microglia, lead to their migration and to the adoption of immunoreactive properties such as cytokine secretion, proliferation and morphological changes[15,18,38,39]. Previously, the treatment with human NM was reported non-toxic to neuronal cultures, and the neurotoxic effect was achieved only in presence of microglia [40]. This was an indication that NM-induced reactive microglia were detrimental to the surrounding neurons.

Indicative of NM-activated microglia, we detected a larger proportion of microglia accumulating around NM deposits in nigral IPD compared to control tissue. In addition, IPD microglia acquired a more amoeboid shape, suggestive of a reactive state. Furthermore, we found this morphology change the most pronounced in NM^+ IPD microglia. Together, these results implicate NM as a potential trigger of neuroinflammation in IPD. While the movement disorder is typically diagnosed at a stage when ~50% of DaNs are already degenerated[41], the release of neuronal NM likely starts with the death of the first DaNs. Thus, it is reasonable to consider that NM-mediated neuroinflammation is a key pathological process throughout the development of PD. Therefore, modulating NM clearance could be considered as a potential strategy to slow down, or even prevent disease progression and to halt inflammation in the PD brain.

Earlier, we reported a *GPNMB*-related inflammatory trajectory in IPD microglia[23]. GPNMB$^+$ microglia comprised the largest fraction of the activated microglia cluster in the patients. Remarkably, *GPNMB* upregulation in microglia is specific to IPD. Microglia in *PRKN*-mutant midbrain tissue, the most frequent recessively inherited form of PD, do not express *GPNMB*. This suggests that the microglial response in PD depends on the genotype and that different molecular processes can lead to an induction of a distinctive proinflammatory cascade in the patients.

Only recently, GPNMB gained attention in the field of neurodegenerative diseases. It was first found to be expressed in amoeboid microglia surrounding amyloid beta plaques in AD brains[33,42]. A study on ectopically overexpression of *GPNMB* in the hippocampus of an AD mouse model reported enhanced autophagy and amyloid beta clearance, which ultimately improved AD-like behaviours[43]. Thus, we sought to investigate whether the GPNMB+ microglia can also be found in the vicinity of NM-containing DaNs.

Using a combination of quantitative immunofluorescence and dPCR analyses, we found an increase in amoeboid IBA1$^+$ cells as well as an upregulation of *AIF1* and *GPNMB* expression around NM-laden DaNs. Implicating an SN-specific effect, we detected the highest levels of microglial *GPNMB* in this region. Enhanced nigral expression of *GPNMB* has already previously been linked to PD[44]. In addition, we found higher *AIF1* expression in NM-laden SN areas suggestive of NM-driven microgliosis. Finally, we reveal that *GPNMB* is overabundant in NM-laden areas in IPD, with highest levels in microglia surrounding D-NM-containing DaNs. NM accumulates and darkens with age. According to the literature, D-NM accumulates faster, and thus ‘ages’ faster to the point where it becomes detrimental[19,34,45]. Additionally, D-NM

appears earlier in PD patients[39] and therefore, is considered to reach this pathological threshold at an earlier stage[19].

Taken together, based on our findings, we hypothesize that high levels of D-NM in IPD DaNs are detrimental and interfere with the functioning of the cells, ultimately leading to their demise. This event is sensed by the surrounding microglia, which in turn upregulate *GPNMB* to mitigate phagocytosis[31]. By contrast, once a critical NM load is reached, NM particles may be released from the dying neurons together with other cellular content, which can act as a chronic stimulus for microglia. In turn, activated microglia become detrimental to neurons and overall brain homeostasis in IPD[15]. Accordingly, GPNMB might serve as a progression marker already during the early stages of IPD. Moreover, if we could modulate NM levels in individuals with high GPNMB abundance to counteract neuroinflammation decades before a potential onset of PD, neuronal demise may be halted. However, more research into the interplay of NM and GPNMB in the context of neurodegeneration and -inflammation is warranted to enable such an innovative treatment strategy.

Abbreviations

PD	Parkinson's disease
AD	Alzheimer's disease
NM	Neuromelanin
DaNs	Dopaminergic neurons
SN	Substantia nigra
IPD	Idiopathic Parkinson's disease
FFPE	Formalin-fixed paraffin-embedded
NGS	Natural goat serum
TBST	Tris-buffered saline with 0.1% Tween20
BC	bimodality coefficient
d	Cohen's d coefficient
D	Hartigan's dip statistics
GPNMB	Glycoprotein nonmetastatic melanoma protein B

Acknowledgements

We thank the patients and their families for their generous participation.

Authors' roles

SS contributed to study design, conducted experiments, generated computer scripts, analyzed that data, prepared the figures, wrote the original draft and reviewed and edited the manuscript. SD, KB, JG conducted experiments, reviewed and edited the manuscript. SD analyzed data and contributed to figure creation. CMM collected the tissue, reviewed and edited the manuscript. JCS reviewed and edited the manuscript. PA developed the scripts for imaging, reviewed and edited the manuscript. AG supervised the project, conceived and designed the study, obtained funding for the project, as well as reviewed and edited the manuscript.

Availability of data and materials

Raw data for the midbrain tissue samples are available publicly in GEO (PRKN mutation carrier GSE166790, IPD and control GSE157783). Other data in this article are available upon request.

Citations

1. Saikia, A., Hussain, M., Barua, A. R. & Paul, S. Chapter 9 - An insight into Parkinson's disease: researches and its complexities. in *Smart Healthcare for Disease Diagnosis and Prevention* (eds. Paul, S. & Bhatia, D.) 59–80 (Academic Press, 2020).
2. Day, J. O. & Mullin, S. The Genetics of Parkinson's Disease and Implications for Clinical Practice. *Genes* **12**, (2021).
3. Inamdar, N. N., Arulmozhi, D. K., Tandon, A. & Bodhankar, S. L. Parkinson's disease: genetics and beyond. *Curr. Neuropharmacol.* **5**, 99–113 (2007).
4. Badanjak, K., Fixemer, S., Smajić, S., Skupin, A. & Grünewald, A. The Contribution of Microglia to Neuroinflammation in Parkinson's Disease. *Int. J. Mol. Sci.* **22**, (2021).
5. Lecours, C. *et al.* Microglial Implication in Parkinson's Disease: Loss of Beneficial Physiological Roles or Gain of Inflammatory Functions? *Front. Cell. Neurosci.* **12**, 282 (2018).
6. Gao, H.-M. *et al.* Microglial activation-mediated delayed and progressive degeneration of rat nigral dopaminergic neurons: relevance to Parkinson's disease. *J. Neurochem.* **81**, 1285–1297 (2002).
7. Marinova-Mutafchieva, L. *et al.* Relationship between microglial activation and dopaminergic neuronal loss in the substantia nigra: a time course study in a 6-hydroxydopamine model of Parkinson's disease. *J. Neurochem.* **110**, 966–975 (2009).
8. Fedorow, H. *et al.* Evidence for specific phases in the development of human neuromelanin. *Neurobiol. Aging* **27**, 506–512 (2006).
9. Zucca, F. A. *et al.* Neuromelanin organelles are specialized autolysosomes that accumulate undegraded proteins and lipids in aging human brain and are likely involved in Parkinson's disease. *NPJ Parkinsons Dis* **4**, 17 (2018).
10. Zecca, L. *et al.* New melanic pigments in the human brain that accumulate in aging and block environmental toxic metals. *Proc. Natl. Acad. Sci. U. S. A.* **105**, 17567–17572 (2008).

11. Moreno-García, A., Kun, A., Calero, M. & Calero, O. The Neuromelanin Paradox and Its Dual Role in Oxidative Stress and Neurodegeneration. *Antioxidants (Basel)* **10**, (2021).
12. Plum, S. *et al.* Proteomic characterization of neuromelanin granules isolated from human substantia nigra by laser-microdissection. *Sci. Rep.* **6**, 37139 (2016).
13. Zecca, L. *et al.* Iron and other metals in neuromelanin, substantia nigra, and putamen of human brain. *J. Neurochem.* **62**, 1097–1101 (1994).
14. Zecca, L. *et al.* The absolute concentration of nigral neuromelanin, assayed by a new sensitive method, increases throughout the life and is dramatically decreased in Parkinson's disease. *FEBS Lett.* **510**, 216–220 (2002).
15. Zhang, W. *et al.* Neuromelanin activates microglia and induces degeneration of dopaminergic neurons: implications for progression of Parkinson's disease. *Neurotox. Res.* **19**, 63–72 (2011).
16. Zecca, L. *et al.* Human neuromelanin induces neuroinflammation and neurodegeneration in the rat substantia nigra: implications for Parkinson's disease. *Acta Neuropathol.* **116**, 47–55 (2008).
17. Viceconte, N. *et al.* Neuromelanin activates proinflammatory microglia through a caspase-8-dependent mechanism. *J. Neuroinflammation* **12**, 5 (2015).
18. Wilms, H. *et al.* Activation of microglia by human neuromelanin is NF-kappaB dependent and involves p38 mitogen-activated protein kinase: implications for Parkinson's disease. *FASEB J.* **17**, 500–502 (2003).
19. Carballo-Carbajal, I. *et al.* Brain tyrosinase overexpression implicates age-dependent neuromelanin production in Parkinson's disease pathogenesis. *Nat. Commun.* **10**, 973 (2019).
20. Blauwendraat, C. *et al.* NeuroChip, an updated version of the NeuroX genotyping platform to rapidly screen for variants associated with neurological diseases. *Neurobiol. Aging* **57**, 247.e9–247.e13 (2017).
21. Das, S. *et al.* Next-generation genotype imputation service and methods. *Nat. Genet.* **48**, 1284–1287 (2016).
22. Grünewald, A. *et al.* Quantitative quadruple-label immunofluorescence of mitochondrial and

cytoplasmic proteins in single neurons from human midbrain tissue. *J. Neurosci. Methods* **232**, 143–149 (2014).

23. Smajić, S. *et al.* Single-cell sequencing of human midbrain reveals glial activation and a Parkinson-specific neuronal state. *Brain* (2021) doi:10.1093/brain/awab446.
24. Clément-Ziza, M., Munnich, A., Lyonnet, S., Jaubert, F. & Besmond, C. Stabilization of RNA during laser capture microdissection by performing experiments under argon atmosphere or using ethanol as a solvent in staining solutions. *RNA* **14**, 2698–2704 (2008).
25. Cohen & Jacob. *Statistical power analysis for the behavioral sciences*. (L. Erlbaum Associates, 1988).
26. Hartigan, J. A. & Hartigan, P. M. The Dip Test of Unimodality. *aos* **13**, 70–84 (1985).
27. Pfister, R., Schwarz, K. A., Janczyk, M., Dale, R. & Freeman, J. B. Good things peak in pairs: a note on the bimodality coefficient. *Front. Psychol.* **4**, 700 (2013).
28. Smajić, S., Prada-Medina, C. A., Landoulsi, Z., Dietrich, C. & Spielmann, M. Single-cell sequencing of the human midbrain reveals glial activation and a neuronal state specific to Parkinson's disease. (2020) doi:10.1101/2020.09.28.20202812.
29. Wasner, K. *et al.* Parkin Deficiency Impairs Mitochondrial DNA Dynamics and Propagates Inflammation. *Mov. Disord.* **37**, 1405–1415 (2022).
30. Budge, K. M., Neal, M. L., Richardson, J. R. & Safadi, F. F. Glycoprotein NMB: an Emerging Role in Neurodegenerative Disease. *Mol. Neurobiol.* **55**, 5167–5176 (2018).
31. Li, B. *et al.* The melanoma-associated transmembrane glycoprotein Gpnmb controls trafficking of cellular debris for degradation and is essential for tissue repair. *FASEB J.* **24**, 4767–4781 (2010).
32. Hirsch, W. L. *et al.* Anatomy of the brainstem: correlation of in vitro MR images with histologic sections. *AJNR Am. J. Neuroradiol.* **10**, 923–928 (1989).
33. Hüttenrauch, M. *et al.* Glycoprotein NMB: a novel Alzheimer's disease associated marker expressed in a subset of activated microglia. *Acta Neuropathol Commun* **6**, 108 (2018).
34. Hirsch, E. C., Graybiel, A. M. & Agid, Y. Selective vulnerability of pigmented dopaminergic

neurons in Parkinson's disease. *Acta Neurol. Scand. Suppl.* **126**, 19–22 (1989).

35. Vila, M. Neuromelanin, aging, and neuronal vulnerability in Parkinson's disease. *Mov. Disord.* **34**, 1440–1451 (2019).
36. Marsden, C. D. Pigmentation in the nucleus substantiae nigrae of mammals. *J. Anat.* **95**, 256–261 (1961).
37. Pajares, M., I Rojo, A., Manda, G., Boscá, L. & Cuadrado, A. Inflammation in Parkinson's Disease: Mechanisms and Therapeutic Implications. *Cells* **9**, (2020).
38. Beach, T. G. *et al.* Marked microglial reaction in normal aging human substantia nigra: correlation with extraneuronal neuromelanin pigment deposits. *Acta Neuropathol.* **114**, 419–424 (2007).
39. Braak, H. *et al.* Staging of brain pathology related to sporadic Parkinson's disease. *Neurobiol. Aging* **24**, 197–211 (2003).
40. Zhang, W. *et al.* Human neuromelanin: an endogenous microglial activator for dopaminergic neuron death. *Front. Biosci.* **5**, 1–11 (2013).
41. Kalia, L. V. & Lang, A. E. Parkinson's disease. *Lancet* **386**, 896–912 (2015).
42. Satoh, J.-I., Kino, Y., Yanaizu, M., Ishida, T. & Saito, Y. Microglia express GPNMB in the brains of Alzheimer's disease and Nasu-Hakola disease. *Intractable Rare Dis Res* **8**, 120–128 (2019).
43. Zhu, Z. *et al.* GPNMB mitigates Alzheimer's disease and enhances autophagy via suppressing the mTOR signal. *Neurosci. Lett.* **767**, 136300 (2022).
44. Neal, M. L., Boyle, A. M., Budge, K. M., Safadi, F. F. & Richardson, J. R. The glycoprotein GPNMB attenuates astrocyte inflammatory responses through the CD44 receptor. *J. Neuroinflammation* **15**, 73 (2018).
45. Hirsch, E., Graybiel, A. M. & Agid, Y. A. Melanized dopaminergic neurons are differentially susceptible to degeneration in Parkinson's disease. *Nature* **334**, 345–348 (1988).

Supplementary materials

Table S1 Information of patients from which the FFPE midbrain tissue was obtained.

Case	Sex	Age at onset	Age at death	Disease duration	PMI (h)	Non-motor features	SN neuron loss
PD1	M	-	82	-	23	dementia	severe
PD2	M	65	84	20	22	diabetes, dementia	severe
PD3	F	65	86	21	17	ovarian cancer	severe
PD4	F	68	75	7	29	recurrent thyroid cancer.	severe
PD5	M	-	79	-	25	blindness, memory impairment	severe
PD6	M	61	73	13	26	diabetes II	severe
PD7	M	57	66	10	24	hallucinations, paranoia	severe
mean		**63.2**	**77.8**	**14.2**	**23.7**		
SEM		**1.9**	**2.6**	**2.7**	**1.4**		
C1	F	-	69	-	33	-	none
C2	M	-	90	-	12	-	none
C3	M	-	84	-	5	-	none
C4	M	-	77	-	22	-	none
C5	M	-	66	-	16	-	none
C6	M	-	88	-	8	-	none
C7	M	-	87	-	31	-	none
mean			**80.1**		**18.1**		
SEM			**3.634678**		**4.137106**		

IPD: idiopathic Parkinson's disease

C: control

PMI: post-mortem interval

SN: substantia nigra

Table S2 Information of patients from which the frozen midbrain tissue was obtained.

Case	Sex	Age at onset	Age at death	Disease duration	PMI (h)	Non-motor features	SN neuron loss
IPD8	M	69	81	12	13	Cognitive impairment, hallucinations, depression	severe
IPD9	M	56	61	5	90	hypophonia	severe
IPD10	M	70	80	10	34	Impaired memory, hallucinations	severe
IPD11	M	67	72	5	41	No cognitive impairments	severe
IPD12	F	66	81	15	35	dementia, impaired consciousness, auditory and visual hallucinations	severe
C8	F	-	93	-	29	-	mild
C9	M	-	81	-	34	Cognitive decline	none
C10	M	-	90	-	80	-	none
C11	M	-	96	-	16	-	none
C12	M	-	92	-	9		none

IPD: idiopathic Parkinson's disease

C: control

PMI: post-mortem interval

SN: substantia nigra

3.2.3 Supplementary data to Manuscript II

Supplementary materials

Table S1 Information of patients from which the FFPE midbrain tissue was obtained.

Case	Sex	Age at onset	Age at death	Disease duration	PMI (h)	Non-motor features	SN neuron loss
PD1	M	-	82	-	23	dementia	severe
PD2	M	65	84	20	22	diabetes, dementia	severe
PD3	F	65	86	21	17	ovarian cancer	severe
PD4	F	68	75	7	29	recurrent thyroid cancer.	severe
PD5	M	-	79	-	25	blindness, memory impairment	severe
PD6	M	61	73	13	26	diabetes II	severe
PD7	M	57	66	10	24	hallucinations, paranoia	severe
mean		**63.2**	**77.8**	**14.2**	**23.7**		
SEM		**1.9**	**2.6**	**2.7**	**1.4**		
C1	F	-	69	-	33	-	none
C2	M	-	90	-	12	-	none
C3	M	-	84	-	5	-	none
C4	M	-	77	-	22	-	none
C5	M	-	66	-	16	-	none
C6	M	-	88	-	8	-	none
C7	M	-	87	-	31	-	none
mean			**80.1**		**18.1**		
SEM			**3.634678**		**4.137106**		

IPD: idiopathic Parkinson's disease

C: control

PMI: post-mortem interval

SN: substantia nigra

Table S2 Information of patients from which the frozen midbrain tissue was obtained.

Case	Sex	Age at onset	Age at death	Disease duration	PMI (h)	Non-motor features	SN neuron loss
IPD8	M	69	81	12	13	Cognitive impairment, hallucinations, depression	severe
IPD9	M	56	61	5	90	hypophonia	severe
IPD10	M	70	80	10	34	Impaired memory, hallucinations	severe
IPD11	M	67	72	5	41	No cognitive impairments	severe
IPD12	F	66	81	15	35	dementia, impaired consciousness, auditory and visual hallucinations	severe
C8	F	-	93	-	29	-	mild
C9	M	-	81	-	34	Cognitive decline	none
C10	M	-	90	-	80	-	none
C11	M	-	96	-	16	-	none
C12	M	-	92	-	9		none

IPD: idiopathic Parkinson's disease

C: control

PMI: post-mortem interval

SN: substantia nigra

Chapter 4

Discussion

Since the discovery of PD, research efforts have neither been able to elucidate the cause nor the progression mechanisms of PD. The majority of studies have focused on several key characteristics of the disease. Moreover, many of these studies were performed in monocellular cultures like iPSC-derived neurons alone. Recent advancement in iPSC technology enabled the development of brain organoids, which are considered a more physiologically and morphologically relevant multicellular model, but they still lack some adult brain cell types. Even the more complex animal models neither provide the classic LB pathology nor the clear formation of NM. All these efforts, although providing valuable insight into certain disease mechanisms, also emphasise the lack of the multifactorial nature of PD models. Additionally, the importance of cells other than neurons has been recently highlighted.

In this thesis, I aimed to extend the sparse knowledge of PD-specific changes in cellular distribution and expression in PD pathology. Additionally, I wanted to investigate the association of NM, neuroinflammation and neurodegeneration. This work resulted in the first single-cell transcriptome dataset of the human midbrain in IPD. We reported that PD leads to important changes in cell type-specific representation as well as in gene expression (Manuscript I). We further uncovered an IPD-specific population of DaNs which was characterised by high *CADPS2* expression. Amongst various perturbations, we also identified microgliosis as one of the most prominent processes occurring in the IPD SN, defined by high *GPNMB* expression. Lastly, microglia were found to accumulate around D-NM deposits and upregulate *GPNMB* (Manuscript II).

4.1 Study advantages and limitations

Prior to our work, the existing RNA expression studies were based on bulk RNAseq technologies. Bulk RNAseq provides the expression of a single gene as an average value of the entire sample, thus masking the contribution of individual cell types to disease pathology. Due to the complex nature of PD and the incomplete knowledge of cell type-specific mechanisms underlying PD, we decided to employ snRNAseq - a recently developed single-cell transcriptomics method.

Nuclei isolation protocol from frozen tissue sections. The nuclei isolation for RNAseq, from limited amounts of frozen ~15 m brain tissue sections, was rather challenging. The existing protocols were designed for tissue blocks and involve an extensive sample clean-up process to remove cellular debris and myelin, which otherwise interfere with later sequencing quality. However, these protocols were not suited for the type of samples we obtained due to (i) a lengthy procedure (nuclei quality is compromised with extensive manipulation), (ii) repeated and rough washing steps (each washing step also removes part of the nuclei population) and (iii) a small sample amount. Therefore, we established a short protocol which included a FACS sorting step. Using our approach, we successfully obtained intact and clean nuclei suitable for sequencing. This protocol was later found favourable in nuclei isolation from various frozen tissues, including mouse organs and iPSC-derived midbrain organoids.

Single-cell atlas of PD midbrain. While providing valuable information regarding PD-related phenotypes at a single-cell level, this work also has limitations. Considering the lack and rarity of postmortem brain tissues, we based our study on samples from 11 individuals. Therefore, our findings need to be validated in a larger cohort. Additionally, scRNAseq and snRNAseq studies do not provide anatomical or spatial information, which requires further validation experiments. Our and other subsequent RNAseq studies of the midbrain or the SN failed to adequately recover DaNs possibly due to: (i) the large volume of DaN nuclei, which may have been preferentially cut during tissue

sectioning and (ii) a higher sensitivity of DaN nuclei to nuclei extraction procedures (Kamath *et al.*, 2022; Wang *et al.*, 2022). To overcome the sampling challenges of DaN nuclei, additional protocols are needed in order to specifically enrich the DaN population (Kamath *et al.*, 2022). However, despite the small population size, DaNs in our study faithfully presented an enrichment of PD-related risk variant genes, such as *SNCA* and *TMEM175*, when combined with the latest genome-wide association study (GWAS). In addition, we obtained a large glial population, which enabled us, for the first time, to describe transcriptional changes and further strengthen the importance of glial cells in PD.

Postmortem tissue as a study model. The primary understanding of any human disease is based on examination of the affected tissue. Tissues provide a legitimate representation of the disease status, encompassing almost every underlying alteration. Studies in tissue can also uncover disease-specific cellular subpopulations that would, otherwise, be inexistent in other models. Moreover, the generation of truthful *in vivo* and *in vitro* disease models depends on the knowledge obtained in studies investigating human-derived samples. In case of complex diseases such as PD, no other model recapitulates the full complexity of the brain tissue. However, postmortem brain samples represent the last stage of disease pathology at the time of death, and thus are deficient in providing any developmental aspect of the disease.

There is also a dilemma whether the remaining cellular population at the time of death is accurately presenting the fundamental disease-carrying cells. In other words, certain DaNs in PD are more susceptible to death and are lost at the beginning of the disease. Therefore, we miss the information about the differences between those primarily-vulnerable DaNs, and the remaining DaNs which, for what we know, may exhibit a distinct disease-related phenotype.

Also, the elapsed time (usually in hours, or days) between an individual's death and brain sample collection impacts the sample quality. Therefore, the changes we detect with subsequent analyses will not only be disease-related, but also influenced

with biochemical perturbations occurring at the time of death (Donaldson and Lamont, 2013).

However, despite all these limitations, human postmortem brain tissue is a precious material that provides a basis for the understanding of any neurodegenerative disease.

4.2 Patient-specific cellular landscape of the midbrain

To gain an insight into the cell type composition of the IPD midbrain, we applied snRNAseq to postmortem tissue from patients and age- and sex-matched healthy controls, thus obtaining a population of 41.435 single midbrain nuclei. This population consisted of 12 major cell types.

4.2.1 Neurons

The neuronal population represented ~12% of the isolated midbrain nuclei. We identified five neuronal subtypes, including GABAergic, inhibitory, excitatory, DaNs and CADPS2^{high} neurons. Consequent pathway analysis of these PD risk gene sets that were also found to be DaNs-specific marker genes revealed an important dysregulation in processes concerning 'protein phosphorylation', 'mitochondria' or 'kinase activity', all previously associated with PD pathology. The following immunohistochemistry exploration of the abundance of the DaN marker tyrosine hydroxylase in two separate studies (Manuscript I and Manuscript II), consistently confirmed the PD-related loss of DaNs and NM in the SN of patients.

Previous studies of the PD transcriptome utilised bulk RNAseq techniques, which failed to identify cell type specificity. Therefore, having generated the first single-nucleus IPD midbrain transcriptome dataset, we were able to identify a distinct state of midbrain neurons, which was specific to IPD samples. These neurons are characterised by *CADPS2* overexpression, and low *TH* expression (Manuscript I). Therefore,

we named this cluster CADPS2^{high}. Apart from CADPS2^{high}, we found that DaNs were the only other cell type that also expressed *CADPS2*. The calcium-dependent activator of secretion (CADPS2) is involved in the regulation of exocytosis of synaptic and dense-core vesicles in neurons and neuroendocrine cells (Berwin, Floor and Martin, 1998; Tandon *et al.*, 1998; Renden *et al.*, 2001). CADPS2 promotes the uptake and storage of monoamines, such as dopamine (Brunk *et al.*, 2009; Paget-Blanc *et al.*, 2022). A recent study on the dopaminergic synapse proteome in mouse striatum reported CADPS2 as a new and highly abundant synaptic protein with an important role in the nigro-striatal pathway (Paget-Blanc *et al.*, 2022). In addition, *TIAM1* was also highly expressed in the CADPS2^{high} cluster. TIAM1 is known to regulate DaN differentiation via the Wnt/Dv1/Rac1 signalling pathway (Čajánek *et al.*, 2013). Besides *CADPS2* expression, the PD-specific cluster was defined by genes such as *UNC13C, RELN,* or *SLIT*, which are involved in the regulation of dopaminergic synapses and neuronal development (Dugan *et al.*, 2011; Arioka *et al.*, 2018, 2020; Banerjee *et al.*, 2020). In line with these findings, cell cycle scoring revealed that a great part of CADPS2^{high} neurons were found in the cycling phase (G2/M/S phase), and were more similar to embryonic midbrain neuroblasts than to embryonic midbrain DaNs (Additional data to Manuscript I). Moreover, a study in human postmortem midbrain tissue showed a PD-specific upregulation of mitotic genes in adult DaNs (Höglinger *et al.*, 2007). This phenomenon resulted in an incomplete cell cycle re-entry and failure to restart developmental processes, leading to DaN death (Höglinger *et al.*, 2007).

Considering these findings, and due to the lack of evidence of adult neurogenesis of DaNs, we hypothesised that the CADPS2^{high} population might represent degenerating DaNs because: (i) CADPS2^{high} neurons are exclusive to the PD phenotype, (ii) when comparing with other neuronal subtypes, DaNs show the most similar expression, (iii) CADPS2^{high} neurons are characterised by a high expression of genes involved in synaptic vesicle trafficking and dopaminergic differentiation and (iv) show a mitosis-associated cell cycle profile.

To evaluate this hypothesis, we analysed the *CADPS2* gene expression from 150 NM-

containing DaNs, extracted by means of LCM from midbrain SN tissue. Here, we used an independent cohort of 5 IPD and 5 age- and sex-matched control tissue samples. We observed that IPD DaNs overexpress *CADPS2* when compared to controls, confirming that the CADPS2^{high} neuronal cluster is of dopaminergic origin. To validate our hypothesis even further, we analysed the *CADPS2* gene expression in iPSC-derived neurons from IPD and healthy control individuals (see additional data to Manuscript I for details). Again, we observed a significantly higher expression in IPD-derived neurons than in control neurons. In line with our findings, a consecutive snRNAseq study described a specific cluster of degenerating DaNs in PD, which also showed high *CADPS2* expression (Wang *et al.*, 2022).

While *CADPS2* was not (yet) reported amongst the established PD-causing genes, a mutation in *CADPS2* was recently shown to cause PD-like symptoms and neurodegenerative phenotype in parrots (Lorenzo-Betancor *et al.*, 2022).

In summary, this unprecedented discovery may have identified a novel putative marker of neuronal malfunction in PD. However, it is yet to be elucidated whether *CADPS2* might potentially be used as an indicator of neuronal loss during the early stages of PD. Additional investigation is needed to understand the functioning of CAPDS2 in DaNs, which might provide important insight into the pathophysiology in PD neurons and possible treatment options.

4.2.2 Glial cells

Glial cells made up to ~80% of the entire midbrain, where oligodendrocytes were the most numerous (~50%), followed by astrocytes, microglia and oligodendrocyte precursor cells (OPCs) (~12%, ~10% and ~6% respectively).

Microglia in PD. With the snRNAseq approach, we detected that every PD patient analysed experienced a microglial population increase compared to the controls, indicative of upregulated immune activity in the brain. Active microglia can further affect sur-

rounding glial cells, such as astrocytes or oligodendrocytes, causing neurotoxic effects (Liddelow *et al.*, 2017). We detected massive perturbations in IPD microglia, which are discussed in detail in a separate section (see section 4.3.) of this thesis.

Oligodendrocytes in PD. For decades, it has been widely accepted that myelination of neuronal axons is virtually the principal role of oligodendrocytes (Simons and Nave, 2015). Interestingly, with image analysis, we showed that this highly abundant cell type is almost equally distributed throughout the midbrain, including the SN. However, nigral DaN axons are not (or are very poorly) myelinated (Braak and Del Tredici, 2004). Therefore, the finding of a large oligodendrocytic population in the SN region suggests that their role in the midbrain goes beyond axonal insulation. Others have shown that the survival of cultured SN neurons was enhanced in the presence of oligodendrocyte lineage cells, since they provide trophic support to surrounding neurons (Takeshima, Johnston and Commissiong, 1994; Sortwell *et al.*, 2000; Du and Dreyfus, 2002). A closer look into our snRNA dataset showed an IPD-related decrease in oligodendrocyte numbers in the midbrain. To give this observation a spatial context, we performed immunohistochemistry and image analysis of the same tissue. We detected that oligodendrocyte depletion is specific to the SN of IPD patients, further suggesting an association with PD pathology. Nigral depletion of oligodendrocytes might lead to reduced trophic support of neurons, and thus interfere with neuronal functioning.

This hypothesis is supported by recent literature implicating oligodendrocytes in PD. One study showed a high association of PD-risk genes to oligodendrocytes in healthy postmortem human SN tissue (Agarwal *et al.*, 2020). In addition, a transcriptomic study in mice proposed that alterations in oligodendrocytes are associated with PD (Bryois *et al.*, 2020). Here, we provided evidence of IPD-related 'stressed' oligodendrocytes characterised by the expression of *S100B*. The upregulation of *S100B* in the brain of an AD rat model, in response to cytokine stimuli, resulted in the formation of dystrophic neurites (Sheng *et al.*, 1996). Thus, it is reasonable to suggest that these 'stressed' oligodendrocytes in IPD might emerge as a result of a higher inflammatory response detected in microglia and astrocytes (Liddelow *et al.*, 2017). Nevertheless, more research is needed

to further elucidate the role of oligodendrocytes in PD.

Astrocytes in PD. The second largest glial population in the midbrain was astrocytes. In a healthy brain, astrocytes perform versatile roles to ensure proper neuronal homeostasis (Kim, Park and Choi, 2019). On the contrary, in diseases such as PD and AD, they can acquire toxic properties that can lead to worsening of the disease (Bouvier *et al.*, 2022). In our study, we found an increased astrocytic population in PD. The inferred activation trajectory revealed that this increase is driven by $CD44^{+}$ astrocytes. *CD44* was previously reported as a marker for reactive astrogliosis in the human brain (Bradford, Wijaya and Mabbott, 2019). Pathway analysis in these PD-specific activated astrocytes revealed a perturbation in ion homeostasis pathways and the unfolded protein response (UPR) previously shown to be a characteristic of reactive astrocytes (Smith *et al.*, 2020). The reactive astrocytes underwent secretome changes, and these perturbations in neurotrophic secretion were found to be toxic to neurons (Smith *et al.*, 2020).

4.3 Neuroinflammation in Parkinson's disease

Neuroinflammation emerged as a key pathological process in PD in recent years (Badanjak *et al.*, 2021). This process in the brain is mediated mainly by microglia. When stimulated, microglia undergo microgliosis, a process where they alter their secretome and morphology in an attempt to protect their surroundings from damaging agents (Joers *et al.*, 2017; Liddelow *et al.*, 2017). However, upon constant stimulation, they can become reactive and detrimental to the tissue. We detected the most significant alteration related to cell type distribution in PD in microglia.

4.3.1 Microglia

To validate and spatially characterise our observation of PD-related microgliosis, we sought to reveal the regional specificity of microglial abundance with immunohisto-

chemical labelling. In PD, we found that microglia numbers are specifically alleviated in the SN, which is suggestive of a nigra-specific dysregulation. Moreover, we found that SN microglia are more amoeboid in PD than in controls, which confirmed their activated state (Lecours *et al.*, 2018; Badanjak *et al.*, 2021). In addition, we found a large subpopulation of reactive microglia in PD characterised by *GPNMB* expression. In agreement with our risk-association study, others have recently also reported that microglia share the strongest association with common PD-risk genetic variants, highlighting PD microglia as a central disease risk determinant (Langston *et al.*, 2022). Thus, microglia-mediated inflammation might be considered as a central mechanism in PD pathology.

In our follow-up study (Manuscript II), we confirmed the microgliosis phenotype in a larger cohort and, in addition, showed that IPD NM is a notable driver of microglial morphology changes and activation.

4.3.2 Neuromelanin

As it progressively accumulates with age, NM in the adult human brain consists largely of undegraded proteins, lipids, chemical toxicants and pigmentosus components, which together can occupy the majority of the cytoplasm. Such 'appropriation' of intracellular space by toxic NM content can compromise the integrity and functionality of DaNs, which can precede neuronal death (Vila, 2019). In parallel to neuronal death, microglia are recruited towards released NM in the parenchyma (Beach *et al.*, 2007; Depboylu *et al.*, 2011; Carballo-Carbajal *et al.*, 2019). However, NM is a substance that is difficult to degrade in a tube (Sulzer *et al.*, 2008; Engelen *et al.*, 2012). Further, NM pigment consists of a soluble and an insoluble fraction (Engelen *et al.*, 2012), which supports the notion that there is no evidence, to date, of a complete NM degradation in the human brain.

On the one hand, we found a larger population of small NM particles in the SN of PD tissues when compared to matching controls (Manuscript II). These NM residues were

possibly the products of ineffective degradation by microglia. The incomplete degradation might be a result of one, or the combination of the following issues: (i) aged microglia are less effective, (ii) PD-microglia are dysfunctional and (iii) a large number of PD DaNs deteriorate, resulting in a large NM release, which is toxic to cells. While remaining in the tissue for a long time, NM could act as a chronic microglial stimulus and lead to a persistent immune activation. Therefore, modulation of NM accumulation could prove a valid therapeutic approach from multiple disease aspects. For instance, faster accumulation of NM was found in PD and is related to neuronal vulnerability (Carballo-Carbajal *et al.*, 2019; Vila, 2019). By controlling the rate of NM production, one could prevent premature DaN loss. This would further reduce the amounts of extraneuronal NM, and therefore limit reactive microgliosis, potentially delaying the occurrence of PD.

On the other hand, we also reported PD-specific microgliosis around NM and a predominantly amoeboid phenotype in NM^+ PD microglia. Considering these results, we hypothesised that NM from PD midbrain is more toxic than the NM in control tissues. Therefore, we investigated whether the previously reported reactive $GPNMB^+$ microglial population (Manuscript I) is overabundant in the SN and, furthermore, specific to NM-rich areas in PD (Manuscript II) (discussed in the next chapter).

4.3.3 $GPNMB^+$ microglia and neuromelanin

Together, our results provide evidence of a specific reactive microglial state characterised by *GPNMB* expression predominantly found around NM in the PD SN. GPNMB was reported as a phagocytic protein important for degradation of lysosomal content (Li *et al.*, 2010). Thus, *GPNMB* in microglia might be upregulated as a result of the NM degradation process. However, as previously discussed, the degradation is most likely incomplete due to the insoluble nature of NM, or due to the toxic effect it might have on the cell. Further corroborating our hypothesis of incomplete NM clearance by microglia, the remaining undegraded NM particles might burden the cell and affect the

lysosomal functioning. Accordingly, induction of lysosomal stress was shown to further elevate *GPNMB* expression (Moloney *et al.*, 2018), which is reported as a part of the inflammatory response of activated microglia in different neurodegenerative diseases (Keren-Shaul *et al.*, 2017; Krasemann *et al.*, 2017; Hüttenrauch *et al.*, 2018; van der Poel *et al.*, 2019). However, whether *GPNMB* mediates anti- or pro-inflammatory responses is still under debate.

On the one hand, suggestive of a pro-inflammatory role, GPNMB inhibition resulted in a reduction of pro-inflammatory cytokines in microglia (Shi *et al.*, 2014). In addition, the treatment with anti-inflammatory cytokines alleviated GPNMB expression (Yu *et al.*, 2016).

On the other hand, suggestive of an anti-inflammatory role, studies in amyotrophic lateral sclerosis (ALS) reported increased neuronal death upon GPNMB inhibition (Tanaka *et al.*, 2012). Moreover, the treatment with recombinant GPNMB resulted in diminished cell death, suggestive of a neuroprotective function (Tanaka *et al.*, 2012; Ono *et al.*, 2016). Corroborating further the anti-inflammatory role, administration of recombinant GPNMB protein to astrocyte cultures decreased their pro-inflammatory response through the interaction with astrocytic CD44 receptors (Neal *et al.*, 2018), which were reported as a marker of reactive astrogliosis (Zamanian *et al.*, 2012; Bradford, Wijaya and Mabbott, 2019). The extracellular domain of GPNMB can be cleaved by ADAM10 (Rose *et al.*, 2010), and this soluble fragment can then bind CD44 receptors (Sondag *et al.*, 2016). Interestingly, in IPD midbrain samples, we described large populations of $GPNMB^+$ microglia and $CD44^+$ astrocytes. Thus, it could be speculated that the upregulation of GPNMB in microglia regulates the neuroinflammatory phenotype of astrocytes, and possibly other cell types. Therefore, GPNMB might be considered a valid therapeutic target for detecting and reducing the neuroinflammatory status in PD, which warrants further investigation.

Chapter 5

Conclusions and perspectives

During my doctoral study, I have optimised a protocol for single-nuclei isolation from 20µm thick frozen brain sections for RNAseq, which led to the generation of the first snRNAseq dataset of human midbrain of PD patients and healthy individuals. This dataset uncovered, besides the loss of DaNs, a specific PD-related neuronal state characterised by *CADPS2* uregulation. Further, we revealed the different distribution of brain cell types in PD: an increase in microglia and astrocytes, and a decrease in oligodendrocytes. The altered expression profile of these cell types was indicative of pan-glial activation as a fundamental process in IPD pathology. Our study further showed that PD-risk genes association depends on the disease context. Thus, we found that IPD-microglia share the strongest association with PD-risk genes, whereas control microglia do not. Therefore, we further focused our study on the microglia population and characterised NM-induced GPNMB-expressing microglia.

Future validation experiments. To expand and strenghten our novel findings, we plan to explore the effect of NM treatment in human iPSC-derived microglia cultures. Exposing IPD and control microglia to NM would enable the evaluation of microglial phagocytic properties, their morphology and *GPNMB* expression. Furthermore, taking into account the activation-dependent shedding of GPNMB extracellularly, we aim to apply ELISA to the cultured medium. As a future perspective, we suggest performing RNAseq on NM-treated microglia cultures to identify a set of differentially expressed genes and dysregulated pathways. By employing such a dataset, we could further build gene-gene interaction networks to understand the functional relationship of *GPNMB* and its targets.

PD and control NM characterisation. From a different perspective, it would be of great interest to characterise IPD and control NM. So far, proteomic and lipidomic studies have been done on NM from control subjects. However, considering that NM from PD patients differs in amount, intensity and size from NM in control subjects, it can be expected that their compositions are different. Given that NM acts as a "sponge" that entraps excess and detrimental material (such as proteins) in a neuron during a lifetime, it can be considered as a "time capsule" that holds the information of early stages of neuronal dysfunction in PD. Although such a study could be vital in understanding the development of PD, it would be very challenging due to the limitations in the availability of human brain tissue, and even further, the small amounts of NM in PD.

Disease model improvement for NM studies. Lastly, to study the effects of NM in a developing brain, one could further improve existing models. Animal models, such as mice, were successfully generated to develop NM-producing DaNs. Moreover, mice are living organisms with an entire range of mature brain cells. However, it is unattainable to model an idiopathic form of PD in mice. In addition, the physiological and pathological responses of mouse cells are different from the response of human cells.

Thus, the IPD-derived iPSC models are a persuasive solution. With recent development of microglia-containing midbrain organoids, it could be possible to identify the pathological NM threshold and to understand the effect it has on neurons, microglia or other surrounding cells. Furthermore, the iPSC-derived models are also beneficial for therapeutic testing and monitoring of the effects of modulation of the target mechanisms. However, the NM formation is a years-long spontaneous process, and the induction of NM in cellular models usually depends on external chemical stimuli that affect many more than just a mere NM-formation process.

In summary, a human-derived model with immune cells, which is durable and robust with fast and intrinsic NM formation would be ideal for the exploration of NM-mediated effects on brain homeostasis.

Bibliography

Agarwal, D. et al. (2020) 'A single-cell atlas of the human substantia nigra reveals cell-specific pathways associated with neurological disorders', Nature communications, 11(1), p. 4183.

de Araújo, F.M. et al. (2021) 'Role of Microgliosis and NLRP3 Inflammasome in Parkinson's Disease Pathogenesis and Therapy', Cellular and molecular neurobiology [Preprint]. doi:10.1007/s10571-020-01027-6.

Arioka, Y. et al. (2018) 'Single-cell trajectory analysis of human homogenous neurons carrying a rare RELN variant', Translational psychiatry, 8(1), p. 129.

Arioka, Y. et al. (2020) 'Cell body shape and directional movement stability in human-induced pluripotent stem cell-derived dopaminergic neurons', Scientific reports, 10(1), p. 5820.

Askew, K. et al. (2017) 'Coupled Proliferation and Apoptosis Maintain the Rapid Turnover of Microglia in the Adult Brain', Cell reports, 18(2), pp. 391–405.

Badanjak, K. et al. (2021) 'The Contribution of Microglia to Neuroinflammation in Parkinson's Disease', International journal of molecular sciences, 22(9). doi:10.3390/ijms22094676.

Ballard, P.A., Tetrud, J.W. and Langston, J.W. (1985) 'Permanent human parkinsonism due to 1-methyl-4-phenyl-1,2,3,6-tetrahydropyridine (MPTP): seven cases', Neurology, 35(7), pp. 949–956.

Banerjee, A. et al. (2020) 'Molecular and functional architecture of striatal dopamine release sites', bioRxiv. doi:10.1101/2020.11.25.398255.

Beach, T.G. et al. (2007) 'Marked microglial reaction in normal aging human substantia nigra: correlation with extraneuronal neuromelanin pigment deposits', Acta neu-

ropathologica, 114(4), pp. 419–424.

Berwin, B., Floor, E. and Martin, T.F. (1998) 'CAPS (mammalian UNC-31) protein localizes to membranes involved in dense-core vesicle exocytosis', Neuron, 21(1), pp. 137–145.

Biber, K. et al. (2007) 'Neuronal "On" and "Off" signals control microglia', Trends in neurosciences, 30(11), pp. 596–602.

Blesa, J. and Przedborski, S. (2014) 'Parkinson's disease: animal models and dopaminergic cell vulnerability', Frontiers in neuroanatomy, 8, p. 155.

Bouvier, D.S. et al. (2022) 'The Multifaceted Neurotoxicity of Astrocytes in Ageing and Age-Related Neurodegenerative Diseases: A Translational Perspective', Frontiers in physiology, 13, p. 814889.

Bové, J. et al. (2005) 'Toxin-induced models of Parkinson's disease', NeuroRx: the journal of the American Society for Experimental NeuroTherapeutics, 2(3), pp. 484–494.

Braak, H. et al. (2003) 'Staging of brain pathology related to sporadic Parkinson's disease', Neurobiology of aging, 24(2), pp. 197–211.

Braak, H. and Del Tredici, K. (2004) 'Poor and protracted myelination as a contributory factor to neurodegenerative disorders', Neurobiology of aging, pp. 19–23.

Braak, H. and Del Tredici, K. (2011) 'The pathological process underlying Alzheimer's disease in individuals under thirty', Acta neuropathologica, 121(2), pp. 171–181.

Bradford, B.M., Wijaya, C.A.W. and Mabbott, N.A. (2019) 'Discrimination of Prion Strain Targeting in the Central Nervous System via Reactive Astrocyte Heterogeneity in CD44 Expression', Frontiers in cellular neuroscience, 13, p. 411.

Brunk, I. et al. (2009) 'Ca2+-dependent activator proteins of secretion promote vesicular monoamine uptake', The Journal of biological chemistry, 284(2), pp. 1050–1056.

Bruttger, J. et al. (2015) 'Genetic Cell Ablation Reveals Clusters of Local Self-Renewing

Microglia in the Mammalian Central Nervous System', Immunity, 43(1), pp. 92–106.

Bryois, J. et al. (2020) 'Genetic identification of cell types underlying brain complex traits yields insights into the etiology of Parkinson's disease', Nature genetics, 52(5), pp. 482–493.

Buchman, A.S. et al. (2012) 'Nigral pathology and parkinsonian signs in elders without Parkinson disease', Annals of neurology, 71(2), pp. 258–266.

Čajánek, L. et al. (2013) 'Tiam1 regulates the Wnt/Dvl/Rac1 signaling pathway and the differentiation of midbrain dopaminergic neurons', Molecular and cellular biology, 33(1), pp. 59–70.

Carballo-Carbajal, I. et al. (2019) 'Brain tyrosinase overexpression implicates age-dependent neuromelanin production in Parkinson's disease pathogenesis', Nature communications, 10(1), p. 973.

Carstam, R. et al. (1991) 'The neuromelanin of the human substantia nigra', Biochimica et biophysica acta, 1097(2), pp. 152–160.

Checchin, D. et al. (2006) 'Potential role of microglia in retinal blood vessel formation', Investigative ophthalmology visual science, 47(8), pp. 3595–3602.

Cheng, J. et al. (2020) 'Microglial autophagy defect causes parkinson disease-like symptoms by accelerating inflammasome activation in mice', Autophagy, 16(12), pp. 2193–2205.

Clarke, C.E. (2007) 'Parkinson's disease', BMJ , 335(7617), pp. 441–445.

Cunningham, C.L., Martínez-Cerdeño, V. and Noctor, S.C. (2013) 'Microglia regulate the number of neural precursor cells in the developing cerebral cortex', The Journal of neuroscience: the official journal of the Society for Neuroscience, 33(10), pp. 4216–4233.

Day, J.O. and Mullin, S. (2021) 'The Genetics of Parkinson's Disease and Implications for Clinical Practice', Genes, 12(7). doi:10.3390/genes12071006.

Depboylu, C. et al. (2011) 'Possible involvement of complement factor C1q in the clearance of extracellular neuromelanin from the substantia nigra in Parkinson disease', Journal of neuropathology and experimental neurology, 70(2), pp. 125–132.

Donaldson, A.E. and Lamont, I.L. (2013) 'Biochemistry changes that occur after death: potential markers for determining post-mortem interval', PloS one, 8(11), p. e82011.

Dugan, J.P. et al. (2011) 'Midbrain dopaminergic axons are guided longitudinally through the diencephalon by Slit/Robo signals', Molecular and cellular neurosciences, 46(1), pp. 347–356.

Du, Y. and Dreyfus, C.F. (2002) 'Oligodendrocytes as providers of growth factors', Journal of neuroscience research, 68(6), pp. 647–654.

El-Gamal, M. et al. (2021) 'Neurotoxin-Induced Rodent Models of Parkinson's Disease: Benefits and Drawbacks', Neurotoxicity research, 39(3), pp. 897–923.

Emamzadeh, F.N. and Surguchov, A. (2018) 'Parkinson's Disease: Biomarkers, Treatment, and Risk Factors', Frontiers in neuroscience, 12, p. 612.

Engelen, M. et al. (2012) 'Neuromelanins of human brain have soluble and insoluble components with dolichols attached to the melanic structure', PloS one, 7(11), p. e48490.

Fantin, A. et al. (2010) 'Tissue macrophages act as cellular chaperones for vascular anastomosis downstream of VEGF-mediated endothelial tip cell induction', Blood, 116(5), pp. 829–840.

Fasano, M. et al. (2003) 'Residual substantia nigra neuromelanin in Parkinson's disease is cross-linked to alpha-synuclein', Neurochemistry international, 42(7), pp. 603–606.

Fedorow, H. et al. (2006) 'Evidence for specific phases in the development of human neuromelanin', Neurobiology of aging, 27(3), pp. 506–512.

Fenichel, G.M. and Bazelon, M. (1968) 'Studies on neuromelanin. II. Melanin in the brainstems of infants and children', Neurology, 18(8), pp. 817–820.

Foix et al. (1925) Anatomie c??r??brale; les noyaux gris centraux et la r??gion m??senc??phalo-sous-optique, suivi d'un appendice sur l'anatomie pathologique de la maladie de Parkinson,. Paris: Masson et cie.

GBD 2016 Parkinson's Disease Collaborators (2018) 'Global, regional, and national burden of Parkinson's disease, 1990-2016: a systematic analysis for the Global Burden of Disease Study 2016', Lancet neurology, 17(11), pp. 939–953.

Gorell, J.M. et al. (1998) 'The risk of Parkinson's disease with exposure to pesticides, farming, well water, and rural living', Neurology, 50(5), pp. 1346–1350.

Gorell, J.M. et al. (1999) 'Occupational exposure to manganese, copper, lead, iron, mercury and zinc and the risk of Parkinson's disease', Neurotoxicology, 20(2-3), pp. 239–247.

Green, D.R., Oguin, T.H. and Martinez, J. (2016) 'The clearance of dying cells: table for two', Cell death and differentiation, 23(6), pp. 915–926.

Halliday, G.M. et al. (2005) 'Alpha-synuclein redistributes to neuromelanin lipid in the substantia nigra early in Parkinson's disease', Brain: a journal of neurology, 128(Pt 11), pp. 2654–2664.

Hassler, R. (1938) '1238 Zur Pathologic der Paralysis Agitans und des Post-Enzephalitischen Parkinsonismus', J. Psychol. Neurol, 18, p. 387.

Herrero, M.T. et al. (1993) 'Neuromelanin accumulation with age in catecholaminergic neurons from Macaca fascicularis brainstem', Developmental neuroscience, 15(1), pp. 37–48.

Höglinger, G.U. et al. (2007) 'The pRb/E2F cell-cycle pathway mediates cell death in Parkinson's disease', Proceedings of the National Academy of Sciences of the United States of America, 104(9), pp. 3585–3590.

Hüttenrauch, M. et al. (2018) 'Glycoprotein NMB: a novel Alzheimer's disease associated marker expressed in a subset of activated microglia', Acta neuropathologica

communications, 6(1), p. 108.

Imamura, K. et al. (2003) 'Distribution of major histocompatibility complex class II-positive microglia and cytokine profile of Parkinson's disease brains', Acta neuropathologica, 106(6), pp. 518–526.

Jafari, S. et al. (2013) 'Head injury and risk of Parkinson disease: a systematic review and meta-analysis', Movement disorders: official journal of the Movement Disorder Society, 28(9), pp. 1222–1229.

Jagmag, S.A. et al. (2015) 'Evaluation of Models of Parkinson's Disease', Frontiers in neuroscience, 9, p. 503.

Joers, V. et al. (2017) 'Microglial phenotypes in Parkinson's disease and animal models of the disease', Progress in neurobiology, 155, pp. 57–75.

Kalia, L.V. and Lang, A.E. (2015) 'Parkinson's disease', The Lancet, 386(9996), pp. 896–912.

Kamath, T. et al. (2022) 'Single-cell genomic profiling of human dopamine neurons identifies a population that selectively degenerates in Parkinson's disease', Nature neuroscience, 25(5), pp. 588–595.

Kastner, A. et al. (1992) 'Is the vulnerability of neurons in the substantia nigra of patients with Parkinson's disease related to their neuromelanin content?', Journal of neurochemistry, 59(3), pp. 1080–1089.

Kemali, M. and Gioffré, D. (1985) 'Anatomical localisation of neuromelanin in the brains of the frog and tadpole. Ultrastructural comparison of neuromelanin with other melanins', Journal of anatomy, 142, pp. 73–83.

Keren-Shaul, H. et al. (2017) 'A Unique Microglia Type Associated with Restricting Development of Alzheimer's Disease', Cell, 169(7), pp. 1276–1290.e17.

Kierdorf, K. and Prinz, M. (2017) 'Microglia in steady state', The Journal of clinical

investigation, 127(9), pp. 3201–3209.

Kim, Y., Park, J. and Choi, Y.K. (2019) 'The Role of Astrocytes in the Central Nervous System Focused on BK Channel and Heme Oxygenase Metabolites: A Review', Antioxidants (Basel, Switzerland), 8(5). doi:10.3390/antiox8050121.

Klein, C. and Westenberger, A. (2012) 'Genetics of Parkinson's disease', Cold Spring Harbor perspectives in medicine, 2(1), p. a008888.

Krasemann, S. et al. (2017) 'The TREM2-APOE Pathway Drives the Transcriptional Phenotype of Dysfunctional Microglia in Neurodegenerative Diseases', Immunity, 47(3), pp. 566–581.e9.

Kubota, Y. et al. (2009) 'M-CSF inhibition selectively targets pathological angiogenesis and lymphangiogenesis', The Journal of experimental medicine, 206(5), pp. 1089–1102.

La Manno, G. et al. (2016) 'Molecular Diversity of Midbrain Development in Mouse, Human, and Stem Cells', Cell, 167(2), pp. 566–580.e19.

Lang, A.E. and Lozano, A.M. (1998) 'Parkinson's disease. First of two parts', The New England journal of medicine, 339(15), pp. 1044–1053.

Langston, R.G. et al. (2022) 'Association of a common genetic variant with Parkinson's disease is mediated by microglia', Science translational medicine, 14(655), p. eabp8869.

Lecours, C. et al. (2018) 'Microglial Implication in Parkinson's Disease: Loss of Beneficial Physiological Roles or Gain of Inflammatory Functions?', Frontiers in cellular neuroscience, 12, p. 282.

Li, B. et al. (2010) 'The melanoma-associated transmembrane glycoprotein Gpnmb controls trafficking of cellular debris for degradation and is essential for tissue repair', FASEB journal: official publication of the Federation of American Societies for Experimental Biology, 24(12), pp. 4767–4781.

Liddelow, S.A. et al. (2017) 'Neurotoxic reactive astrocytes are induced by activated

microglia', Nature, 541(7638), pp. 481–487.

Lorenzo-Betancor, O. et al. (2022) 'Homozygous CADPS2 mutations cause neurodegenerative disease with Lewy bodies in parrots', bioRxiv. doi:10.1101/2022.03.30.483987.

Lu, Y. et al. (2018) 'Toll-like Receptors and Inflammatory Bowel Disease', Frontiers in immunology, 9, p. 72.

McGeer, P.L. et al. (1988) 'Reactive microglia are positive for HLA-DR in the substantia nigra of Parkinson's and Alzheimer's disease brains', Neurology, 38(8), pp. 1285–1291.

Moloney, E.B. et al. (2018) 'The glycoprotein GPNMB is selectively elevated in the substantia nigra of Parkinson's disease patients and increases after lysosomal stress', Neurobiology of disease, 120, pp. 1–11.

Murros, K.E. et al. (2021) 'Desulfovibrio Bacteria Are Associated With Parkinson's Disease', Frontiers in cellular and infection microbiology, 11, p. 652617.

Nagatsu, T., Levitt, M. and Udenfriend, S. (1964) 'TYROSINE HYDROXYLASE. THE INITIAL STEP IN NOREPINEPHRINE BIOSYNTHESIS', The Journal of biological chemistry, 239, pp. 2910–2917.

Neal, M.L. et al. (2018) 'The glycoprotein GPNMB attenuates astrocyte inflammatory responses through the CD44 receptor', Journal of neuroinflammation, 15(1), p. 73.

Niehaus, I. and Lange, J.H. (2003) 'Endotoxin: is it an environmental factor in the cause of Parkinson's disease?', Occupational and environmental medicine, 60(5), p. 378.

Nimmerjahn, A., Kirchhoff, F. and Helmchen, F. (2005) 'Resting microglial cells are highly dynamic surveillants of brain parenchyma in vivo', Science, 308(5726), pp. 1314–1318.

Obeso, J.A. et al. (2017) 'Past, present, and future of Parkinson's disease: A special essay on the 200th Anniversary of the Shaking Palsy', Movement disorders: official journal of the Movement Disorder Society, 32(9), pp. 1264–1310.

Ono, Y. et al. (2016) 'Glycoprotein nonmetastatic melanoma protein B extracellu-

lar fragment shows neuroprotective effects and activates the PI3K/Akt and MEK/ERK pathways via the Na+/K+-ATPase', Scientific reports, 6, p. 23241.

Ouchi, Y. et al. (2009) 'Neuroinflammation in the living brain of Parkinson's disease', Parkinsonism related disorders, 15 Suppl 3, pp. S200–4.

Paget-Blanc, V. et al. (2022) 'A synaptomic analysis reveals dopamine hub synapses in the mouse striatum', Nature communications, 13(1), p. 3102.

Paolini, M., Sapone, A. and Gonzalez, F.J. (2004) 'Parkinson's disease, pesticides and individual vulnerability', Trends in pharmacological sciences, 25(3), pp. 124–129.

Parkhurst, C.N. et al. (2013) 'Microglia promote learning-dependent synapse formation through brain-derived neurotrophic factor', Cell, 155(7), pp. 1596–1609.

Plum, S. et al. (2016) 'Proteomic characterization of neuromelanin granules isolated from human substantia nigra by laser-microdissection', Scientific reports, 6, p. 37139.

van der Poel, M. et al. (2019) 'Transcriptional profiling of human microglia reveals grey-white matter heterogeneity and multiple sclerosis-associated changes', Nature communications, 10(1), p. 1139.

Reeve, A., Simcox, E. and Turnbull, D. (2014) 'Ageing and Parkinson's disease: why is advancing age the biggest risk factor?', Ageing research reviews, 14, pp. 19–30.

Reinhardt, P. et al. (2013) 'Derivation and expansion using only small molecules of human neural progenitors for neurodegenerative disease modeling', PloS one, 8(3), p. e59252.

Renden, R. et al. (2001) 'Drosophila CAPS is an essential gene that regulates dense-core vesicle release and synaptic vesicle fusion', Neuron, 31(3), pp. 421–437.

Rizek, P., Kumar, N. and Jog, M.S. (2016) 'An update on the diagnosis and treatment of Parkinson disease', CMAJ: Canadian Medical Association journal = journal de l'Association medicale canadienne, 188(16), pp. 1157–1165.

Rose, A.A.N. et al. (2010) 'ADAM10 releases a soluble form of the GPNMB/Osteoactivin extracellular domain with angiogenic properties', PloS one, 5(8), p. e12093.

Rosengren, E., Linder-Eliasson, E. and Carlsson, A. (1985) 'Detection of 5-S-cysteinyldopamine in human brain', Journal of neural transmission , 63(3-4), pp. 247–253.

Rymo, S.F. et al. (2011) 'A two-way communication between microglial cells and angiogenic sprouts regulates angiogenesis in aortic ring cultures', PloS one, 6(1), p. e15846.

Sacchini, S. et al. (2018) 'Locus coeruleus complex of the family Delphinidae', Scientific reports, 8(1), p. 5486.

Saikia, A. et al. (2020) 'Chapter 9 - An insight into Parkinson's disease: researches and its complexities', in Paul, S. and Bhatia, D. (eds) Smart Healthcare for Disease Diagnosis and Prevention. Academic Press, pp. 59–80.

Semchuk, K.M., Love, E.J. and Lee, R.G. (1992) 'Parkinson's disease and exposure to agricultural work and pesticide chemicals', Neurology, 42(7), pp. 1328–1335.

Sheng, J.G. et al. (1996) 'In vivo and in vitro evidence supporting a role for the inflammatory cytokine interleukin-1 as a driving force in Alzheimer pathogenesis', Neurobiology of aging, 17(5), pp. 761–766.

Shi, F. et al. (2014) 'Induction of matrix metalloproteinase-3 (MMP-3) expression in the microglia by lipopolysaccharide (LPS) via upregulation of glycoprotein nonmetastatic melanoma B (GPNMB) expression', Journal of molecular neuroscience: MN, 54(2), pp. 234–242.

Simons, M. and Nave, K.-A. (2015) 'Oligodendrocytes: Myelination and Axonal Support', Cold Spring Harbor perspectives in biology, 8(1), p. a020479.

Smith, H.L. et al. (2020) 'Astrocyte Unfolded Protein Response Induces a Specific Reactivity State that Causes Non-Cell-Autonomous Neuronal Degeneration', Neuron, 105(5), pp. 855–866.e5.

Sondag, G.R. et al. (2016) 'Osteoactivin inhibition of osteoclastogenesis is mediated through CD44-ERK signaling', Experimental molecular medicine, 48(9), p. e257.

Sortwell, C.E. et al. (2000) 'Oligodendrocyte-type 2 astrocyte-derived trophic factors increase survival of developing dopamine neurons through the inhibition of apoptotic cell death', The Journal of comparative neurology, 426(1), pp. 143–153.

Sulzer, D. et al. (2008) 'Neuronal pigmented autophagic vacuoles: lipofuscin, neuromelanin, and ceroid as macroautophagic responses during aging and disease', Journal of neurochemistry, 106(1), pp. 24–36.

Takeshima, T., Johnston, J.M. and Commissiong, J.W. (1994) 'Oligodendrocyte-type-2 astrocyte (O-2A) progenitors increase the survival of rat mesencephalic, dopaminergic neurons from death induced by serum deprivation', Neuroscience letters, 166(2), pp. 178–182.

Tanaka, H. et al. (2012) 'The potential of GPNMB as novel neuroprotective factor in amyotrophic lateral sclerosis', Scientific reports, 2, p. 573.

Tandon, A. et al. (1998) 'Differential regulation of exocytosis by calcium and CAPS in semi-intact synaptosomes', Neuron, 21(1), pp. 147–154.

Tay, T.L. et al. (2017) 'A new fate mapping system reveals context-dependent random or clonal expansion of microglia', Nature neuroscience, 20(6), pp. 793–803.

Tribl, F. et al. (2005) '"Subcellular proteomics" of neuromelanin granules isolated from the human brain', Molecular cellular proteomics: MCP, 4(7), pp. 945–957.

Tronnes, A.A. et al. (2016) 'Effects of Lipopolysaccharide and Progesterone Exposures on Embryonic Cerebral Cortex Development in Mice', Reproductive sciences , 23(6), pp. 771–778.

Ueno, M. et al. (2013) 'Layer V cortical neurons require microglial support for survival during postnatal development', Nature neuroscience, 16(5), pp. 543–551.

Viceconte, N. et al. (2015) 'Neuromelanin activates proinflammatory microglia through a caspase-8-dependent mechanism', Journal of neuroinflammation, 12, p. 5.

Vila, M. (2019) 'Neuromelanin, aging, and neuronal vulnerability in Parkinson's disease', Movement disorders: official journal of the Movement Disorder Society, 34(10), pp. 1440–1451.

Wang, Q. et al. (2022) 'Single-cell transcriptomic atlas of the human substantia nigra in Parkinson's disease', bioRxiv. doi:10.1101/2022.03.25.485846.

Wang, Y. et al. (2014) 'Interleukin-1 induces blood-brain barrier disruption by down-regulating Sonic hedgehog in astrocytes', PloS one, 9(10), p. e110024.

Witting, A. et al. (2000) 'Phagocytic clearance of apoptotic neurons by Microglia/Brain macrophages in vitro: involvement of lectin-, integrin-, and phosphatidylserine-mediated recognition', Journal of neurochemistry, 75(3), pp. 1060–1070.

Wolf, S.A., Boddeke, H.W.G.M. and Kettenmann, H. (2017) 'Microglia in Physiology and Disease', Annual review of physiology, 79, pp. 619–643.

Wood-Kaczmar, A., Gandhi, S. and Wood, N.W. (2006) 'Understanding the molecular causes of Parkinson's disease', Trends in molecular medicine, 12(11), pp. 521–528.

Wooten, G.F. et al. (2004) 'Are men at greater risk for Parkinson's disease than women?', Journal of neurology, neurosurgery, and psychiatry, 75(4), pp. 637–639.

Ye, R. et al. (2016) 'The Relationship between Parkinson Disease and Brain Tumor: A Meta-Analysis', PloS one, 11(10), p. e0164388.

Yu, B. et al. (2016) 'Macrophage-Associated Osteoactivin/GPNMB Mediates Mesenchymal Stem Cell Survival, Proliferation, and Migration Via a CD44-Dependent Mechanism', Journal of cellular biochemistry, 117(7), pp. 1511–1521.

Zamanian, J.L. et al. (2012) 'Genomic analysis of reactive astrogliosis', The Journal of neuroscience: the official journal of the Society for Neuroscience, 32(18), pp. 6391–6410.

Zecca, L. et al. (1992) 'The chemical characterization of melanin contained in substantia nigra of human brain', Biochimica et biophysica acta, 1138(1), pp. 6–10.

Zecca, L. et al. (2001) 'Substantia nigra neuromelanin: structure, synthesis, and molecular behaviour', Molecular pathology: MP, 54(6), pp. 414–418.

Zecca, L. et al. (2003) 'Neuromelanin of the substantia nigra: a neuronal black hole with protective and toxic characteristics', Trends in neurosciences, 26(11), pp. 578–580.

Zecca, L. et al. (2008) 'New melanic pigments in the human brain that accumulate in aging and block environmental toxic metals', Proceedings of the National Academy of Sciences of the United States of America, 105(45), pp. 17567–17572.

Zhang, W. et al. (2011) 'Neuromelanin activates microglia and induces degeneration of dopaminergic neurons: implications for progression of Parkinson's disease', Neurotoxicity research, 19(1), pp. 63–72.

Zhang, W. et al. (2013) 'Human neuromelanin: an endogenous microglial activator for dopaminergic neuron death', Frontiers in bioscience , 5(1), pp. 1–11.

Zucca, F.A. et al. (2004) 'The neuromelanin of human substantia nigra: physiological and pathogenic aspects', Pigment cell research / sponsored by the European Society for Pigment Cell Research and the International Pigment Cell Society, 17(6), pp. 610–617.

Zucca, F.A. et al. (2017) 'Interactions of iron, dopamine and neuromelanin pathways in brain aging and Parkinson's disease', Progress in neurobiology, 155, pp. 96–119.

Zucca, F.A. et al. (2018) 'Neuromelanin organelles are specialized autolysosomes that accumulate undegraded proteins and lipids in aging human brain and are likely involved in Parkinson's disease', NPJ Parkinson's disease, 4, p. 17.

Appendices

Manuscript III

RESEARCH ARTICLE

Parkin Deficiency Impairs Mitochondrial DNA Dynamics and Propagates Inflammation

Kobi Wasner, PhD,[1] Semra Smajic, MSc,[1] Jenny Ghelfi, BSc,[1] Sylvie Delcambre, PhD,[1] Cesar A. Prada-Medina, PhD,[2] Evelyn Knappe, MSc,[3] Giuseppe Arena, PhD,[1] Patrycja Mulica, MSc,[1] Gideon Agyeah, MSc,[1] Aleksandar Rakovic, PhD,[3] Ibrahim Boussaad, PhD,[1,4] Katja Badanjak, MSc,[1] Jochen Ohnmacht, PhD,[1,5] Jean-Jacques Gérardy, BSc,[6] Masashi Takanashi, MD,[7] Joanne Trinh, PhD,[3] Michel Mittelbronn, MD,[1,6,8,9] Nobutaka Hattori, MD, PhD,[7] Christine Klein, MD,[3] Paul Antony, PhD,[1,4] Philip Seibler, PhD,[3] Malte Spielmann, MD,[2,10] Sandro L. Pereira, PhD,[1,7] and Anne Grünewald, PhD[1,3*]

[1]*Luxembourg Centre for Systems Biomedicine, University of Luxembourg, Esch-sur-Alzette*
[2]*Max Planck Institute for Molecular Genetics, Berlin, Germany*
[3]*Institute of Neurogenetics, University of Lübeck, Lübeck, Germany*
[4]*Disease Modeling and Screening Platform, Luxembourg Centre of Systems Biomedicine, University of Luxembourg & Luxembourg Institute of Health, Luxembourg*
[5]*Department of Life Science and Medicine, University of Luxembourg, Esch-sur-Alzette, Luxembourg*
[6]*National Center of Pathology, Laboratoire National de Santé, Dudelange, Luxembourg*
[7]*Department of Neurology, Juntendo University, Tokyo, Japan*
[8]*Luxembourg Center of Neuropathology, Dudelange, Luxembourg*
[9]*Department of Cancer Research, Luxembourg Institute of Health, Luxembourg, Luxembourg*
[10]*Institute of Human Genetics, University of Lübeck, Lübeck, Germany*

ABSTRACT: Background: Mutations in the E3 ubiquitin ligase parkin cause autosomal recessive Parkinson's disease (PD). Together with PTEN-induced kinase 1 (*PINK1*), parkin regulates the clearance of dysfunctional mitochondria. New mitochondria are generated through an interplay of nuclear- and mitochondrial-encoded proteins, and recent studies suggest that parkin influences this process at both levels. In addition, parkin was shown to prevent mitochondrial membrane permeability, impeding mitochondrial DNA (mtDNA) escape and subsequent neuroinflammation. However, parkin's regulatory roles independent of mitophagy are not well described in patient-derived neurons.

Objectives: We sought to investigate parkin's role in preventing neuronal mtDNA dyshomeostasis, release, and glial activation at the endogenous level.

Methods: We generated induced pluripotent stem cell (iPSC)–derived midbrain neurons from PD patients with parkin (*PRKN*) mutations and healthy controls. Live-cell imaging, proteomic, mtDNA integrity, and gene expression analyses were employed to investigate mitochondrial biogenesis and genome maintenance. To assess neuroinflammation, we performed single-nuclei RNA sequencing in postmortem tissue and quantified interleukin expression in mtDNA/lipopolysaccharides (LPS)-treated iPSC-derived neuron–microglia co-cultures.

Results: Neurons from patients with *PRKN* mutations revealed deficits in the mitochondrial biogenesis pathway, resulting in mtDNA dyshomeostasis. Moreover, the energy sensor sirtuin 1, which controls mitochondrial biogenesis and clearance, was downregulated in parkin-deficient cells. Linking mtDNA disintegration to neuroinflammation, in postmortem midbrain with *PRKN* mutations, we confirmed mtDNA dyshomeostasis and detected an upregulation of microglia overexpressing proinflammatory cytokines. Finally, parkin-deficient neuron–microglia co-cultures elicited an enhanced immune response when exposed to mtDNA/LPS.

Conclusions: Our findings suggest that parkin coregulates mitophagy, mitochondrial biogenesis, and mtDNA maintenance pathways, thereby protecting midbrain neurons from neuroinflammation and degeneration.

Key Words: Parkinson's disease; mitochondrial DNA; induced pluripotent stem cells; parkin; neuroinflammation

***Correspondence to:** Dr. Anne Grünewald, Luxembourg Centre for Systems Biomedicine, University of Luxembourg, 6 Avenue du Swing, L-4367 Belvaux. E-mail: anne.gruenewald@uni.lu

Semra Smajic and Jenny Ghelfi contributed equally.

Relevant conflicts of interest/financial disclosures: The authors report no conflicts of interest.

Received: 22 December 2021; **Revised:** 7 March 2022; **Accepted:** 27 March 2022

Published online 23 April 2022 in Wiley Online Library (wileyonlinelibrary.com). DOI: 10.1002/mds.29025

Introduction

Dopaminergic neurons (DANs) of the substantia nigra pars compacta (SNpc) in the midbrain are critically involved in the regulation of movement.[1] Loss of DANs results in clinical motor disturbances of patients with Parkinson's disease (PD)—the second most common neurodegenerative disorder.[2] Although the underlying biological mechanisms causing neuronal loss are still under investigation, mitochondrial dysfunction has been well implicated in PD pathology.[3]

The majority of patients with PD are sporadic, with individuals manifesting the disease at ≥65 years of age. The remainder are caused by genetic mutations, of which many are linked to mitochondrial dysfunction. Roughly 50% of patients with early-onset PD harbor mutations in parkin (*PRKN*).[2,4]

PRKN encodes the E3 ubiquitin ligase parkin—an established regulator of mitochondrial clearance.[5] However, parkin's substrates are involved in several fundamental cellular processes. For instance, parkin targets parkin-interacting substrate (PARIS)—an inhibitor of the mitochondrial biogenesis regulator peroxisome gamma coactivator 1-alpha (PGC1-α).[6] Moreover, *PRKN* overexpression in cell models revealed an association with the mitochondrial genome and a direct interaction with mitochondral transcription factor A (TFAM)—the main transcription factor of mitochondrial DNA (mtDNA).

mtDNA has gained recent interest as a determinant of aging and age-associated diseases, including PD.[7] Improper mtDNA maintenance has been shown to allow its escape from the mitochondrial compartment, triggering an immune response.[8,9] This phenomenon was furthermore demonstrated in parkin-knockout (KO) "mutator" mice, which harbor an error-prone version of DNA polymerase γ (POLG). These animals show elevated extracellular mtDNA levels and cyclic GMP-AMP synthase (cGAS)-stimulator of interferon genes (STING) signaling under stress conditions.[10] However, parkin's involvement in these cellular processes has yet to be investigated in patient-derived neurons.

To explore the role of parkin in mtDNA maintenance endogenously, we generated induced pluripotent stem cell (iPSC)–derived midbrain neurons from patients with PD with biallelic *PRKN* mutations. We found that parkin-deficient neurons exhibit impaired mitochondrial biogenesis, mtDNA dynamics, and increased cytosolic mtDNA levels. Parkin knockdown during mutagenic stress mirrored these phenotypes and evidenced upregulations of the cGAS protein and extracellular mtDNA. Moreover, treatment with lipopolysaccharides (LPS) and mtDNA elicited a stronger inflammatory response in *PRKN*-mutant compared with control neuron–microglia co-cultures. Finally, single-nuclei RNA sequencing (snRNAseq) of postmortem midbrain sections from a patient with *PRKN*-PD revealed microgliosis and proinflammatory signaling. Our findings elucidate novel parkin-regulated mitophagy-independent mechanisms contributing toward mitochondrial quality control. We show that parkin coordinates mitochondrial biogenesis and mtDNA maintenance and is essential to prevent neuroinflammation and neurodegeneration.

Materials and Methods

Generation of iPSCs was performed as described,[11] and DANs and microglia were derived using established protocols.[12-14] To isolate tyrosine hydroxylase (TH)–positive cells, iPSC-derived neurons were subjected to fluorescence-activated cell sorting (FACS) using an adapted protocol.[15] Production of lentiviral vectors expressing short hairpin RNA (shRNA) against human *PRKN* or a control plasmid was performed as described.[16] SH-SY5Y neuroblastoma cells were treated with 200 μM cobalt chloride ($CoCl_2$).[17] Nicotinamide adenine dinucleotide:nicotinamide adenine dinucleotide hydrogen (NAD^+:NADH) ratios were determined using a kit (Sigma, St. Louis, MO). Respiratory chain complex I (CI) and citrate synthase activities were assessed in mitochondrial fractions by means of spectrophotometry.[18,19] Isolated extracellular mtDNA was quantified using a Digital PCR System (Applied Biosystems, Waltham, MA) and TaqMan probes specific for mitochondrially encoded NADH:ubiquinone oxidoreductase core subunit 1 (*MT-ND1*) and beta-2-microglobulin (*B2M*).[20,21] Polar metabolites from 30 day-old neurons were extracted and then derivatized and measured as published.[22] All experiments using iPSC-derived neurons and SH-SY5Y cells were performed with at least three biological replicates. Unpaired two-tailed Student's *t* tests or one-way analysis of variance followed by post hoc Tukey tests were used to determine statistical significance ($P < 0.05$).

Midbrain sections were immunostained, and TH-positive neurons were isolated through laser capture microdissection (LCM) using the PALM MicroBeam (Zeiss, Oberkochen, Germany).[20] Nuclei isolation, snRNAseq, and data analysis of the *PRKN*-mutant midbrain was carried out as described.[23]

A detailed description of the materials and methods can be found in the supplement.

Results

Parkin Deficiency Impairs Mitochondrial Biogenesis in the Neurons of Patients with PD

We generated iPSC-derived midbrain neurons from healthy controls and *PRKN* mutation carriers (Fig. S1A, B), which lack the parkin protein (Fig. S1C). Furthermore, we employed SH-SY5Y wild-type (WT) and

isogenic parkin-KO cells, which were generated using clustered regularly interspaced short palindromic repeats and CRISPR-associated protein 9 (CRISPR/Cas9) technology (Fig. S1D).

Parkin targets a plethora of proteins,[24] with mounting evidence supporting regulatory roles in diverse cellular mechanisms beyond mitophagy. Given that mitophagy and mitochondrial biogenesis are tightly linked to preserve bioenergetic homeostasis,[25] we sought to investigate possible alterations in mitochondrial biogenesis in our models. Previous research demonstrated that parkin overexpression enhances mitochondrial biogenesis through PGC1-α, either directly or via PARIS, its transcriptional repressor.[6,26,27] We found significantly lower levels of PGC1-α protein in parkin-deficient neurons and SH-SY5Y cells compared with controls (Fig. 1A,B). Interestingly, neither cell model showed differences in the PARIS protein under basal conditions (Fig. 1A,C).

Conversely, parkin deficiency substantially reduced sirtuin 1 (SIRT1) levels (Fig. 1A,D), an NAD^+-dependent energy sensor acting on mitochondrial biogenesis through regulation of PGC1-α gene expression and protein deacetylation.[28,29] Moreover, in parkin-deficient neurons, we detected higher lactate:pyruvate ratios (Fig. 1E), which suggests a lack of free NAD^+ based on the chemical equilibrium principle.[30]

PGC1-α regulates the transcription of nuclear respiratory factors (NRFs), which in turn mediates gene expressions of mtDNA transcription factors and replication activators TFAM and mitochondrial transcription factor B2 (TFB2M).[31] In agreement with reduced PGC1-α abundance, we found that parkin deficiency resulted in decreased NRF1 protein levels (Fig. 1A,F) and reduced *TFAM* and *TFB2M* expression (Fig. 1G, H). In addition, we detected significantly downregulated mRNA levels of twinkle mtDNA helicase (*TWNK*), a factor mainly involved in mtDNA replication (Fig. 1I).

Parkin Influences mtDNA Dynamics and Respiratory Chain Function

Mitochondrial biogenesis may be defined as the division and growth of preexisting mitochondria and is accomplished by the import of nuclear-encoded proteins and transcription and replication of the mitochondrial genome, which contains genes encoding subunits

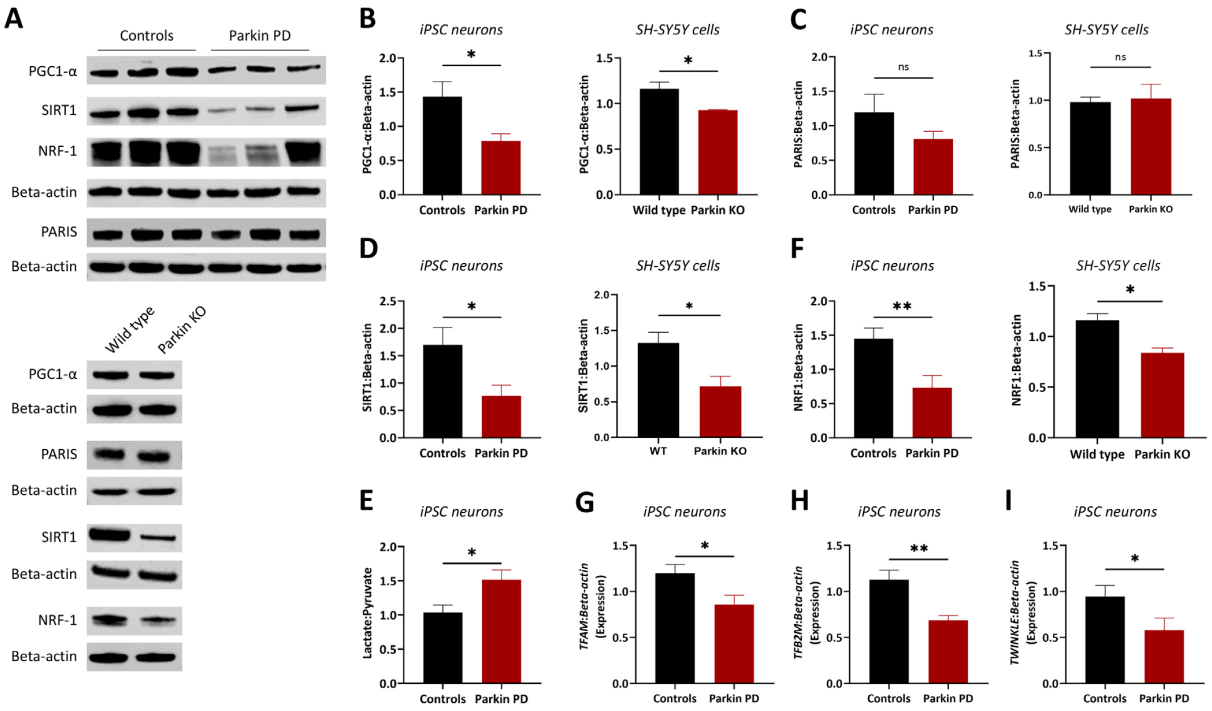

FIG. 1. Mitochondrial biogenesis is impaired in parkin-deficient cells. (**A**) Representative cropped Western blot images of total cell lysates from induced pluripotent stem cell (iPSC)–derived neurons from controls and patients with parkin-associated Parkinson's disease (Parkin PD) as well as wild-type and parkin-knockout (KO) SH-SY5Y neuroblastoma cells. (**B**-**E**) Quantifications from (**A**) peroxisome gamma coactivator 1-alpha (PGC1-α) (**B**), parkin-interacting substrate (PARIS) (**C**), sirtuin 1 (SIRT1) (**D**) and nuclear respiratory factor 1 (NRF1) (**F**) protein levels normalized to beta-actin. (**E**) Lactate-to-pyruvate ratios served as a proxy measure for free nicotinamide adenine dinucleotide:nicotinamide adenine dinucleotide hydrogen (NAD^+/NADH) ratios. (**G**-**I**) Quantitative polymerase chain reaction (qPCR) was used to quantify gene expression of mitochondrial transcription factor A (*TFAM*) (**G**), mitochondrial transcription factor B2 (*TFB2M*) (**H**) and twinkle mtDNA helicase (*TWNK*) (**I**) in iPSC-derived neurons from controls and patients with parkin-associated PD normalized to beta-actin. Data are presented as the mean ± SEM. SEM = standard error of the mean, $^*P < 0.05$, $^{**}P < 0.01$; ns = not significant as determined by Student's *t* test.

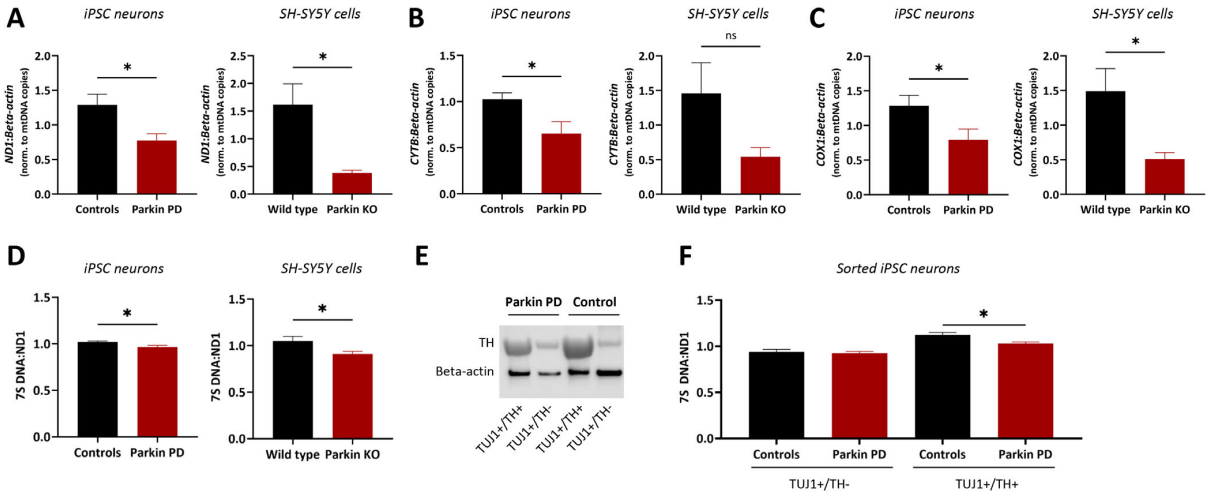

FIG. 2. Parkin influences mitochondrial DNA (mtDNA) dynamics. (**A**-**C**) Quantitative polymerase chain reaction (qPCR) was used to measure expression of mtDNA-encoded genes NADH:ubiquinone oxidoreductase core subunit 1 (*ND1*) (**A**), cytochrome B (*CYTB*) (**B**), and (**C**) cytochrome C oxidase I *(COX1)* in induced pluripotent stem cell (iPSC)–derived neurons from controls and Parkinson's disease patients with mutations in parkin (Parkin PD) and wild-type and parkin-knockout (KO) SH-SY5Y neuroblastoma cells. Gene expression was normalized to beta-actin and mtDNA copy number. (**D**) A multiplex real-time polymerase chain reaction (RT-PCR) assay was used to quantify transcription-associated 7S DNA per mtDNA molecule (with probes targeting *ND1*) in iPSC-derived neurons and SH-SY5Y cells. (**E, F**) Neuronal cultures from three controls and three *PRKN* mutation carriers were sorted using the pan-neuronal marker β-Tubulin 3 (TUJ1) and the dopaminergic neuron (DAN) marker tyrosine hydroxylase (TH) and subjected to Western blotting and RT-PCR analyses. (**E**) Representative cropped Western blotting images of TH and TUJ1 protein abundances in sorted control and patient neurons. (**F**) TUJ1/TH double-positive iPSC-derived neurons were separated from TUJ1-positive/TH-negative neurons derived from controls and patients with *PRKN* mutations. The resulting cell populations underwent multiplex RT-PCR to quantify the abundance of 7S DNA per mtDNA molecule (with a probe targeting *ND1*). RT-PCR results are from two technical replicates. n = 3 biological replicates; data are presented as the mean ± SEM; SEM = standard error of the mean, $^*P < 0.05$, ns = not significant as determined by Student's *t* test.

of the electron transport chain (ETC).[32] Our experiments suggest decreases in nuclear-encoded factors controlling mitochondrial biogenesis. We next sought to assess mtDNA dynamics by measuring the expression of mtDNA-encoded genes. The expression of mitochondrially encoded NADH:ubiquinone oxidoreductase core subunit 1 (*MT-ND1*), mitochondrially encoded cythochrome B (*MT-CYTB*), and mitochondrially encoded cytochrome C oxidase I (*MT-COX1*) (encoding subunits of complexes I, III, and IV, respectively) per mtDNA molecule was significantly downregulated in our parkin-deficient models (Fig. 2A–C). In line with this, both parkin-deficient iPSC-derived neurons and SH-SY5Y cells showed diminished 7S DNA: *MT-ND1* ratios, suggestive of fewer transcription initiation events (Fig. 2D).[20] Moreover, we used FACS to isolate TH-positive neurons and found that the 7S DNA phenotype is specific to DANs (Fig. 2E,F).

Because parkin overexpression was reported to enhance the selective removal of mitochondria harboring deleterious mtDNA mutations,[33] we explored the abundance of somatic major arc deletions. By contrast, we did not find differences between groups (data not shown). We further evaluated the mtDNA copy number and detected significantly higher mtDNA levels in parkin-deficient cells using both real-time polymerase chain reaction (RT-PCR) (Fig. 3A) and immunocytochemistry (Fig. 3B). Finally, we assessed respiratory chain function in SH-SY5Y cells and found that parkin-KO cells exhibited significantly reduced CI activity compared with WT cells (Fig. 3C). These results suggest that although parkin deficiency leads to an accumulation of mtDNA molecules, it also hinders the mtDNA transcription process, which likely contributes to ETC dysfunction.

Parkin Mitigates Cytosolic mtDNA Infiltration

Consistent with its evolutionary bacterial origin, mtDNA has been identified as a damage-associated molecular pattern (DAMP). Cytosolic mtDNA molecules can activate the innate immune system via the cGAS-STING pathway.[8] Implicating mtDNA release in the pathogenesis of *PRKN*-PD, our previous research showed increased levels of circulating cell-free mtDNA (ccf-mtDNA) and inflammatory cytokines in serum from *PRKN* mutation carriers.[34] Several mechanisms have been proposed to facilitate mtDNA release into the cytosol, including TFAM depletion.[8] We next confirmed that reduced *TFAM* gene expression detected in parkin-deficient neurons resulted in diminished TFAM (protein):mtDNA ratios (Fig. 3D, Fig. S2A). TFAM also acts as a packaging factor compacting the mtDNA molecule to form the mitochondrial nucleoid, and disruption of this process is associated with mtDNA extrusion from mitochondria. To investigate if impaired TFAM:mtDNA ratios coupled to disrupted mtDNA

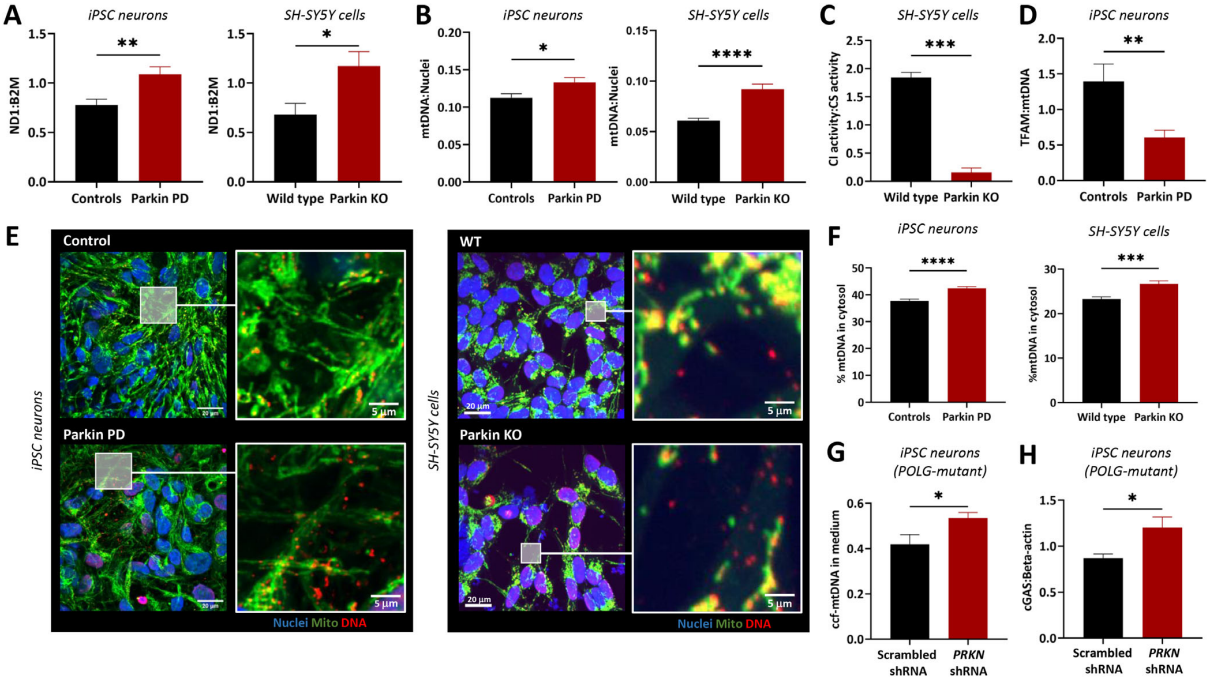

FIG. 3. Parkin attenuates cytosolic mitochondrial DNA (mtDNA) infiltration at baseline and extracellular mtDNA release during mutagenic stress. (**A**) A real-time polymerase chain reaction (RT-PCR) assay was used to quantify mtDNA copy number (with a probe targeting NADH:ubiquinone oxidoreductase core subunit 1 [*ND1*]) relative to the nuclear single copy gene beta-1-microglobulin (*B2M*) in induced pluripotent stem cell (iPSC)–derived neurons and SH-SY5Y neuroblastoma cells in healthy controls and patients with parkin-associated Parkinson's disease (Parkin PD) as well as wild-type (WT) and parkin-knockout (KO) SH-SY5Y cells. (**B**) Immunocytochemistry analysis of mtDNA copy number in iPSC-derived neurons and SH-SY5Y cells. Copy number was determined by mtDNA volume:nuclei volume. (**C**) Quantification of mitochondrial complex I activity normalized to citrate synthase activity in SH-SY5Y cells. (**D**) Quantification of mitochondrial transcription factor A (TFAM) protein abundance normalized to mtDNA copy number in iPSC-derived neurons. (**E**) Representative cropped immunocytochemistry images used to assess mtDNA subcellular location by targeting mtDNA, nuclei (Hoechst 33342), the mitochondrial marker translocase of outer mitochondrial membrane 20 (TOM20) and cytosol (high content screening CellMask Orange Stain [ThermoFisher Scientific, Waltham, MA]). (**F**) Analysis of mtDNA localization in iPSC-derived neurons and SH-SY5Y cells from (**E**). Percentage of mtDNA in cytosol was calculated by dividing the mtDNA volume outside mitochondria by total mtDNA volume. (**G**) Extracellular circulating cell-free mtDNA (ccf-mtDNA) in medium from polymerase γ (POLG)–mutant iPSC-derived neurons transduced with scrambled or *PRKN* short hairpin RNA (shRNA). Quantification by means of multiplex digital PCR (dPCR) targeting the mtDNA fragment *ND1* and the nuclear single-copy gene *B2M*. ccf-mtDNA was calculated as the ratio of extracellular *ND1* normalized to extracellular *B2M* copies to the sum of intra- and extracellular *ND1* normalized by their respective intra- and extracellular *B2M* copies. (**H**) cyclic GMP-AMP synthase (cGAS)-stimulator of interferon genes (STING) signaling in *POLG*-mutant iPSC-derived neurons transduced with scrambled or *PRKN* shRNA. Quantification of cGAS protein levels relative to beta-actin from Figure S2E. n = 3 or 5 biological replicates; data are presented as the mean ± SEM; SEM = standard error of the mean, $^{*}P < 0.05$, $^{**}P < 0.01$, $^{***}P < 0.001$, $^{****}P < 0.0001$ as determined by Student's *t* test.

dynamics could result in elevated mtDNA release, we assessed the subcellular localization of mtDNA molecules with an imaging approach. Indeed, patient neurons and parkin-KO SH-SY5Y cells harbored significantly more mtDNA molecules in the cytosol compared with controls (Fig. 3E,F). This mtDNA shift from mitochondria to the cytosol was independently validated by applying an RT-PCR approach to cellular fractions from control and parkin-KO SH-SY5Y cells (Fig. S2B).

Hypoxic Conditions Mirror mtDNA Phenotypes Observed in Parkin-Deficient Cells

To test our hypothesis of metabolic remodeling as the underlying cause of mtDNA dyshomeostasis in *PRKN*-PD, we exposed WT SH-SY5Y cells to the hypoxia-inducing agent $CoCl_2$.[17] $CoCl_2$ treatment triggered an upregulation of the hypoxia-inducible factor 1-α (Fig. 4A) and a shift from oxidative phosphorylation to glycolysis as indicated by increased NAD^+:NADH ratios (Fig. 4B). In line with the cellular function of SIRT1, the protein was less abundant under hypoxic conditions (Fig. 4A,C). We then investigated the SIRT1 target PGC1-α, which was also downregulated in $CoCl_2$-treated cells (Fig. 4A,D). To explore the impact of PGC1-α depletion on mtDNA maintenance, we next determined the protein levels of NRF1 and TFAM, which were both downregulated in response to $CoCl_2$ exposure (Fig. 4A,E,F). In addition, the treatment reduced the 7S DNA:*MT-ND1* ratio (Fig. 4G) and *MT-ND1* mRNA levels (Fig. 4H).

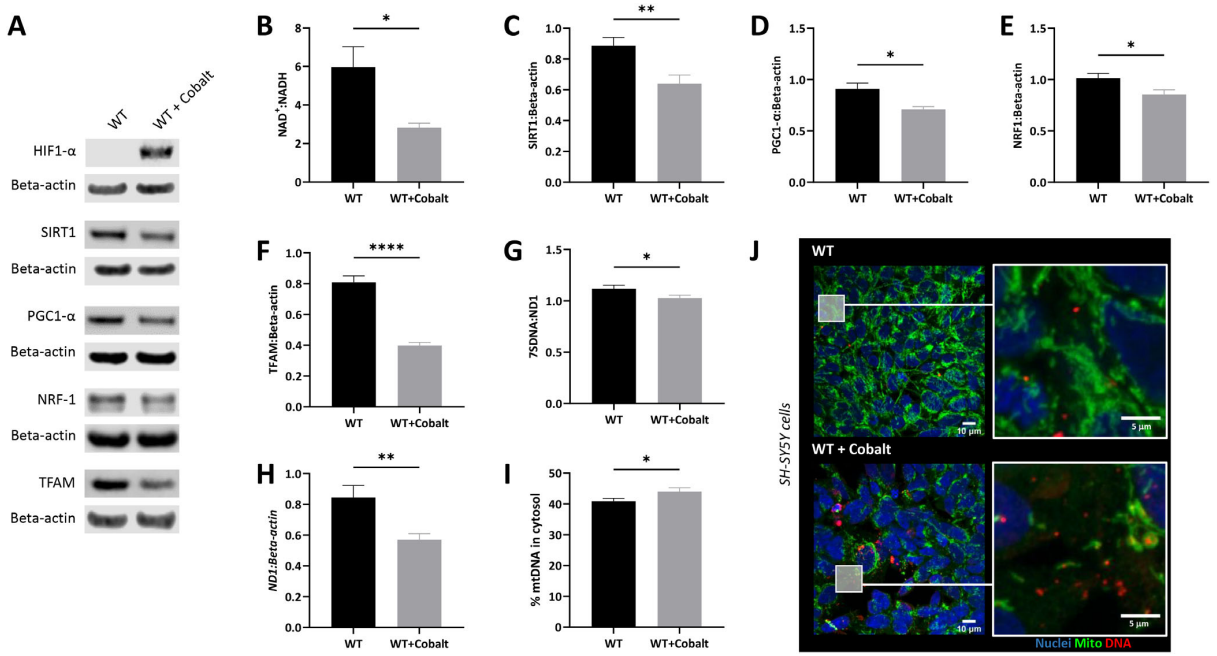

FIG. 4. Hypoxia-mediated metabolic alterations induce mitochondrial DNA (mtDNA) dyshomeostasis. (**A**) Representative cropped Western blot images of total cell lysates from untreated and cobalt chloride ($CoCl_2$)-treated wild-type (WT) SH-SY5Y neuroblastoma cells. (**B**) Nicotinamide adenine dinucleotide:nicotinamide adenine dinucleotide hydrogen (NAD^+/NADH) ratios measured in cellular extracts from untreated and $CoCl_2$-treated WT SH-SY5Y cells. Quantifications from (**A**) sirtuin 1 (SIRT1) (**C**), peroxisome gamma coactivator 1-alpha (PGC1-α) (**D**), nuclear respiratory factor 1 (NRF1) (**E**), mitochondrial transcription factor A (TFAM) (**F**) protein levels normalized to Beta-actin. (**G**) Real-time polymerase chain reaction quantification of transcription-associated 7S DNA per mtDNA molecule. (**H**) qPCR was used to quantify gene expression of the mtDNA gene NADH:ubiquinone oxidoreductase core subunit 1(*ND1*). (**I**) Analysis of mtDNA localization in untreated and $CoCl_2$-treated WT SH-SY5Y cells (**J**). Percentage of mtDNA in cytosol was calculated by dividing the mtDNA volume outside mitochondria by total mtDNA volume. (**J**) Representative cropped immunocytochemistry images used to assess mtDNA subcellular location by targeting mtDNA, nuclei (Hoechst 33342), the mitochondrial marker translocase of outer mitochondrial membrane 20 (TOM20), and cytosol (high content screening CellMask Orange Stain [ThermoFisher Scientific, Waltham, MA]). n ≤ 3 biological replicates; data are presented as the mean ± SEM; SEM = standard error of the mean, $^*P < 0.05$, $^{**}P < 0.01$, $^{****}P < 0.0001$ as determined by Student's *t* test.

Finally, we tested whether the $CoCl_2$-induced metabolic shift was sufficient to trigger mtDNA release. Indeed, high-throughput imaging revealed elevated cytosolic mtDNA levels in treated SH-SY5Y cells (Fig. 4I,J). These data indicate that metabolic impairments can interfere with mtDNA dynamics.

Mutagenic Stress Exacerbates Parkin-Mediated Mitochondrial Biogenesis and mtDNA Transcription Deficits

Next, we further explored the downstream effects of parkin deficiency–induced mtDNA dyshomeostasis. Although we observed an increase of cytosolic mtDNA in parkin-mutant neurons, this mtDNA release from the mitochondria was not accompanied by an upregulation of extracellular mtDNA or immune-related factors (Fig. S2C,D), which may be explained by the inability of iPSC-derived cultures to model age-associated phenotypes such as inflammation.[35] To overcome the rejuvenation-associated limitations of iPSC-derived neurons, we adapted a mitochondrial aging strategy from mice. Recently, an innovative mouse strain was generated that, contrary to most established rodent PD models, recapitulates motor phenotypes during the short lifetime of the animals.[10] To simulate mitochondrial aging, parkin-KO mice were crossed with animals harboring an error-prone version of POLG, which causes mtDNA mutagenic stress. The resulting parkin-KO "mutator" mice showed increased serum levels of ccf-mtDNA and inflammatory cytokines mediated by cGAS-STING signaling.[9] Inspired by this work, we differentiated iPSCs from a patient with compound-heterozygous mutations in *POLG* and subjected the resulting neurons to shRNA to reduce parkin expression (Fig. S3A).

Compared with *POLG*-mutant cells transduced with scrambled shRNA, parkin shRNA reduced 7S DNA:*MT-ND1* ratios (Fig. S3B) and showed significantly lower levels of mitochondrial biogenesis factors PGC1-α and NRF1 (Fig. S3A,C,D), strengthening our findings in *PRKN*-mutant neurons. Next, we quantified ccf-mtDNA in the extracellular medium and found a

significant upregulation, suggesting that parkin reduction in the presence of mtDNA stress elevated the release of mtDNA from mitochondria into the extracellular space (Fig. 3G). Furthermore, we found an increase in protein abundance of the cytosolic DNA sensor cGAS (Fig. 3H). Finally, we assessed the expression of key cytokines that were previously shown to be upregulated in serum from parkin-KO "mutator" mice and patients with *PRKN* mutations in response to cGas/STING signaling.[9] By contrast, RT-PCR analyses still revealed very low levels of interleukin 6 (*IL6*) and interleukin-1-beta (*IL1B*) in any of the investigated neurons (Fig. S3E), likely attributed to the absence of microglia in the cultures.

mtDNA Maintenance Impairments Propagate Neuroinflammation in *PRKN*-PD Tissue

Although iPSC-derived neurons allow the study of parkin-related mitochondrial functions, the cultures do not reflect the cellular diversity of the midbrain. Recent publications implicate glia-mediated inflammation in the pathogenesis of *PRKN*-associated PD.[9,34] In light of these findings, we next used postmortem tissue from a patient with PD with compound-heterozygous *PRKN* mutations and two healthy controls to assess the extent and possible consequences of mtDNA disintegration in a more comprehensive environment (Fig. 5A).

We first sought to validate our findings concerning mtDNA maintenance in human brain tissue. We

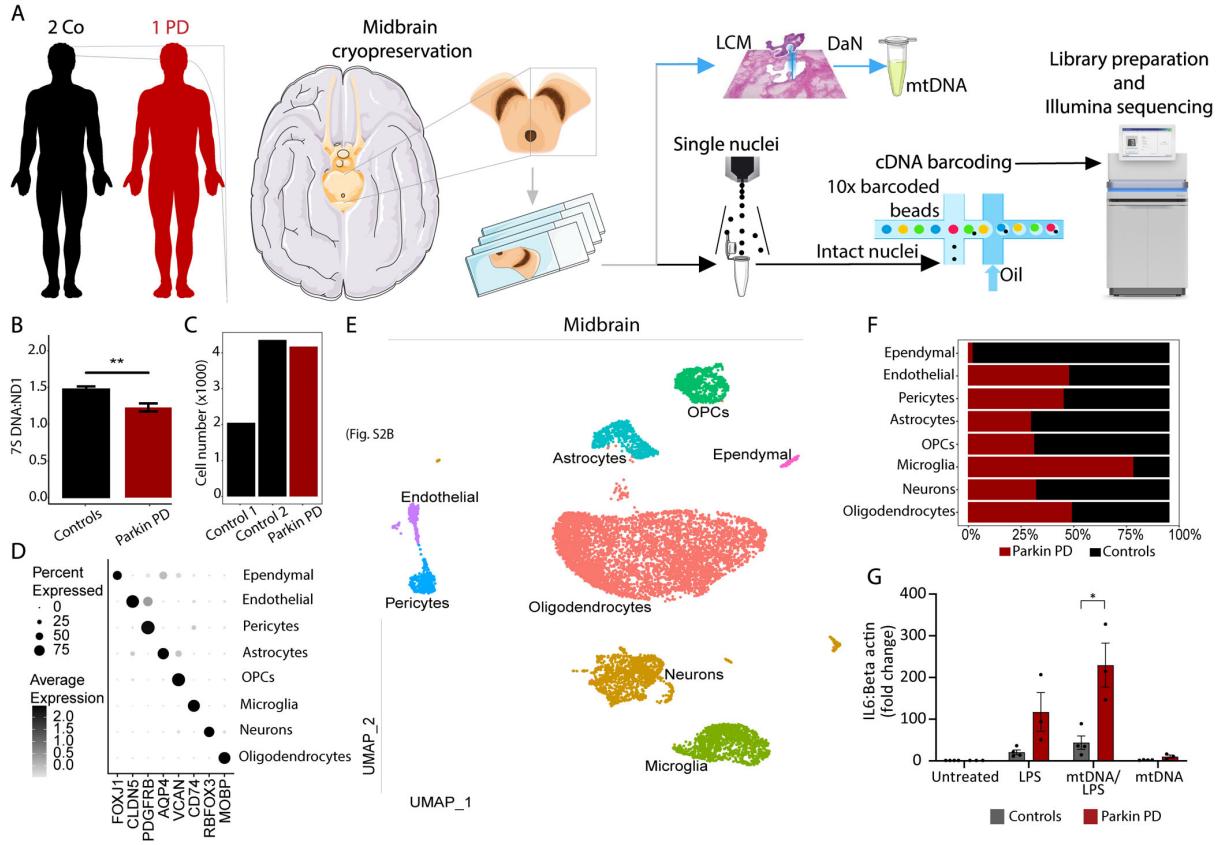

FIG. 5. Cell-type differences in human *PRKN*-mutant and control midbrains. (**A**) Handling of the midbrain tissue for single-cell studies. Midbrain sections were used for (1) laser capture microdissection (LCM) of dopaminergic neurons (DAN) and (2) nuclei isolation, 10X Genomics platform processing, and Illumina sequencing. (**B**) 7S DNA:mitochondrially encoded NADH:ubiquinone oxidoreductase core subunit 1 (7SDNA:*MT-ND1*) ratios quantified via multiplex real-time polymerase chain reaction from single postmortem DANs of the substantia nigra pars compacta. (**C**) Number of nuclei per sample. The analyzed population is composed of 4173 *PRKN*-mutant nuclei and 6405 control nuclei, making a population of 10,578 nuclei. (**D**) Representative cell-type specific marker genes. (**E**) The population of 10,578 nuclei projected onto a uniform manifold approximation and projection (UMAP) space. (**F**) Percentage of *PRKN*-mutant and control cell-type specific nuclei. (**G**) Fold change of interleukin 6 (*IL6*) expression at baseline (NT = nontreated) or after treatment with mitochondrial DNA (mtDNA), lipopolysaccharides (LPS), or both. n = 3 patients and n = 4 controls; data are presented as the mean ± SEM; SEM = standard error of the mean, *P < 0.05, **P < 0.01, ns = not significant as determined by two-way analysis of variance and Sidak's multiple comparisons test. Co = healty control subjects, PD/Parkin PD = Parkinson's disease patient with mutations in parkin, OPCs = oligodendrocyte precursor cells, *FOXj1* = forkhead box J1, *CLDN5* = claudin 5, *PDGFRB* = platelet derived growth factor receptor beta, *AQP4* = aquaporin 4, *VCAN* = versican, *RBFOX3* = RNA binding fox-1 homolog 3, *MOBP* = myelin associated oligodendrocyte basic protein.

applied LCM to midbrain tissue to isolate single neuromelanin- and TH-positive neurons (n = 10 per sample) from the SNpc, which were then subjected to RT-PCR. In line with our previous results, we found significantly reduced 7S DNA:*MT-ND1* ratios in postmortem patient DANs (Fig. 5B). However, we did not detect any differences in mtDNA deletion levels or in mtDNA copy number (data not shown).

Next, to determine whether *PRKN* mutation carriers suffer from neuroinflammation, we performed snRNAseq from postmortem ventral midbrain sections (Fig. 5A). A total of 10,578 high-quality nuclei (patient = 4173, controls = 2047 and 4358) were projected into two dimensions with the uniform manifold approximation and projection (UMAP) algorithm (Fig. 5C,E). We found eight major cell types including neurons and glial cells (Fig. 5D,E). Each cell cluster was annotated based on the expression of marker genes (Fig. 5D, Table S1). The most abundant cell type making ≈52.5% of the midbrain population are oligodendrocytes, followed by neurons (≈14.6%), microglia (≈11.6%), oligodendrocyte precursor cells (≈7.3%), and astrocytes (≈6.6%). Residual abundances were detected for other cell types. To assess neuroinflammation, we first compared cell density distributions in UMAP and observed a large increase in the microglial population and a decreased fraction of neurons and astrocytes (Fig. 5F) in the *PRKN*-mutant midbrain. Our results confirm the alteration in glial cell populations in the *PRKN* mutation carriers reported previously.[36] This shift infers an incorrect immune response, which likely leads to neuroinflammation. The resulting decrease of the *PRKN* midbrain neuronal population (Fig. 5F) compared with controls may be a trigger or downstream effect of the aforementioned immune response. Furthermore, the proinflammatory cytokines *IL1B* and tumor necrosis factor (*TNF)* were differentially expressed and upregulated in *PRKN*-mutant microglia compared with controls (Table S2). Accordingly, the immune response pathways, primarily the interleukin signaling pathways, were most perturbed in microglia from the *PRKN* mutation carrier (Tables S3 and S4).

Finally, to assess the causal link between mtDNA dyshomeostasis and neuroinflammation in *PRKN*-associated PD, we generated iPSC-derived neuron–microglia co-cultures from controls and patients with *PRKN* mutations and exposed them to LPS, mtDNA isolated from patients with *PRKN*-PD, or both. The composition of the co-cultures with regard to DANs and microglia was not affected by the different treatments (Fig. S4A,B). Moreover, stimulation by mtDNA or LPS alone did not reveal any differences in the expression of cytokines in cells lacking parkin. However, when mtDNA was added as a secondary trigger after LPS priming, we observed that patient-derived co-cultures showed a greater response in the expression of *IL6* (Fig. 5G). Although *IL1B* was equally upregulated after LPS/mtDNA treatment, the difference between *PRKN*-PD and control co-cultures was not significant (Fig. S4C).

Discussion

Using a multimodal approach, we explored novel mechanisms of mitochondrial quality control exerted by parkin. Although most parkin studies focused on its role in mitochondrial clearance, the wide range of parkin substrates suggests that the protein functions in cellular processes beyond mitophagy.[24] Thus, we decided to investigate the mitochondrial biogenesis and mtDNA maintenance pathways in parkin-deficient cells.

Mitochondrial biogenesis is synchronized in the nucleus, with PGC1-α acting as the master regulator.[27] Studies found a direct interaction between parkin and PGC1-α,[27] whereas others have shown an interaction with PARIS—a PGC1-α transcriptional repressor.[6] In the current study, parkin-depleted cells showed reduced PGC1-α protein levels while the abundance of PARIS remained unchanged, insinuating an alternative mechanism of PGC1-α reduction. We looked upstream and found that the SIRT1 protein was reduced in parkin-deficient cells. *PGC1-α* gene expression and protein deacetylation is regulated by the NAD^+-dependent energy sensor SIRT1.[28,29] Moreover, our and a published metabolic study in parkin-deficient neurons revealed increased lactate:pyruvate ratios, suggesting lower levels of freely accessible NAD^+ as a result of metabolic remodeling from oxidative phosphorylation to glycolysis.[30,37]

PGC1-α can activate the NRFs, which control the expression of the mitochondrial transcription factors *TFAM* and *TFB2M*.[31] Our gene expression and protein analyses confirmed disruptions of this pathway at each level in cells lacking parkin. The sole semiautonomous organelle of human cells, mitochondria, encompass their own system to coordinate mtDNA transcription, replication, translation, and repair. Because of its dynamic nature and proximity to the ETC, mtDNA maintenance is exceptionally important for ensuring homogeneity and preventing the expansion of aberrant mtDNA molecules. Studies in mitotically active parkin-overexpressing cells have shown a direct interaction of parkin with TFAM and an association with the mitochondrial genome.[26,38]

Focusing on mtDNA integrity, we found significantly less 7S DNA per mtDNA molecule in iPSC-derived neurons, SH-SY5Y cells, and postmortem DANs lacking parkin. This is in agreement with previous findings in postmortem DANs isolated from patients with idiopathic PD (IPD).[20] The D-loop region of the

mitochondrial genome serves as the initiation site for its replication and transcription. The synthesis of 7S DNA in the D-loop is stimulated by TFAM, consistent with evidence showing that elevated TFAM matrix levels increase the rate of 7S DNA synthesis.[39] Indeed, calculating TFAM:mtDNA ratios, parkin-deficient neurons exhibited a significant reduction. Moreover, we observed decreased mtDNA gene expression that coincided with diminished ETC CI activity in parkin-KO SH-SY5Y cells. Of note, we previously reported ETC CI impairments in iPSC-derived neurons from our *PRKN*-mutant samples.[40] Interestingly, experiments in purified TH-positive neurons from patients with *PRKN* mutations highlighted that the 7S DNA phenotype is more pronounced in DANs, suggesting a link between mtDNA homeostasis and dopamine signaling. Because of their high energy requirements and the autoxidation properties of the neurotransmitter, DANs are particularly vulnerable to metabolic changes.[41,42] Interestingly, hypoxic conditions mimicked the mtDNA phenotypes observed in parkin-deficient cells. These findings further strengthened our hypothesis that a shift from oxidative phosphorylation to glycolysis triggers mtDNA dyshomeostasis in the absence of parkin.

Beyond alterations in the mitochondrial biogenesis pathway, we detected elevated mtDNA copy numbers but diminished TFAM abundance per mitochondrial genome in parkin-deficient neurons. TFAM reduction has previously been shown to allow mtDNA to escape from mitochondria into the cytosol, where it is recognized by the cytosolic DNA sensor cGAS, provoking activation of an innate immune response.[8] Indeed, we observed that neurons from patients with PD and parkin-KO SH-SY5Y cells incur higher levels of mtDNA in the cytosolic compartment compared with controls. We also quantified mtDNA molecules in the extracellular medium of our cellular samples, yet we did not detect any differences compared with controls or increases in inflammatory cytokines.

However, keeping in mind that reprogramming of postnatal cells can cause artificial rejuvenation,[35] we burdened parkin-deficient cells with mitochondrial mutagenic stress—a normal aging phenomenon[43]—to investigate mtDNA release and inflammation. To create a neuronal aging model of *PRKN*-PD, we adopted an approach by Pickrell and colleagues who crossed parkin-KO with *POLG*-mutant mice.[10] These animals exhibited levodopa-reversible motor deficits, a selective loss of nigral DANs, impaired mtDNA dynamics, and cGas/STING-mediated inflammation.[9,10] Accordingly, we generated iPSC-derived midbrain neurons from a patient with Alper's disease with compound-heterozygous *POLG* mutations and subjected the cultures to either scramble or parkin shRNA. Parkin knockdown in *POLG*-mutant neurons replicated the 7S DNA phenotype as well as disruptions of the mitochondrial biogenesis pathway. In addition, we detected elevated ccf-mtDNA levels in the cellular medium and an increase in cGAS protein abundance. In agreement with previous results in parkin-KO "mutator" mice, this suggests that parkin depletion combined with mitochondrial mutagenic stress triggers the release of mtDNA into the cytosol and extracellular space in patient neurons.

Microglia are considered the resident innate immune cells in the brain, which can be activated by various DAMPs. The lack of microglial cells in our neuronal cultures may explain the inability to detect inflammation in our samples. We therefore decided to use postmortem tissue from a patient with compound-heterozygous *PRKN*-PD and controls to investigate a potential link between parkin dysfunction and neuroinflammation using snRNAseq. Our results showed a strong infiltration of microglia in the *PRKN*-mutant midbrain and an upregulation of the proinflammatory cytokines *IL1B* and *TNF*. This dysregulation resulted in the perturbation of immune and oxidative stress response pathways.

To additionally evaluate the extent of the microglia phenotype in *PRKN*-PD, we made use of our recently published single-cell data set of five patients with IPD and six controls.[23] Comparing the cell-type distribution across the three groups (Fig. S5A-D), the *PRKN*-mutant midbrain showed an even larger percentage of microglia than the IPD tissue samples (Fig. S5D). Moreover, the expression of microglia activation markers heat shock protein 90 alpha family class A member 1 (*HSP90AA1*) and *IL1B* was the highest in the *PRKN*-mutant cell population (Fig. S5E). Thus, despite the limitation of examining brain tissue from a single mutant case, this cross-comparison further supports a role for microglia in the pathogenesis of *PRKN*-PD.

With regard to the distribution of other glial cells, we detected a reduction in astrocytes in *PRKN*-PD (Fig. S4D), which is in line with previous observations in the *PRKN*-mutant midbrain.[36] The resulting lack of astroglial neuron support likely perpetuates the inflammatory phenotypes in *PRKN*-PD as indicated by elevated expression of the astrocyte activation marker cluster of differentiation 44 (*CD44*) (Fig. S5F). Interestingly, despite lower overall astrocyte numbers, *CD44* levels in *PRKN*-PD astrocytes were even higher than in IPD astrocytes (Fig. S5F). Although additional rare *PRKN*-mutant midbrain samples need to be studied in the future, our snRNAseq analysis, which also considered our published results from IPD cases, provides valuable insights into the cell-type composition and transcriptomic landscape of the *PRKN*-PD midbrain.

Finally, to assess whether mtDNA dyshomeostasis and inflammation are causally linked in *PRKN*-PD, we generated iPSC-derived neuron–microglia co-cultures from controls and patients with *PRKN* mutations, which were treated with mtDNA isolated from *PRKN*-mutant cells. Our results showed that, when added as a secondary stimulus to LPS priming, mtDNA caused *IL6* overexpression

in cells lacking parkin, suggesting that parkin deficiency renders cells more responsive to proinflammatory stimuli.

Taken together, our study highlights parkin's involvement in mtDNA maintenance and supports a link between mtDNA dyshomeostasis and inflammation in human cellular models of PD. In iPSC-derived cultures from patients with *PRKN* mutations, we observed that mtDNA transcription-associated 7S DNA is preferentially depleted in DANs. This TFAM deficiency-mediated phenotype is likely the consequence of SIRT1 depletion and inactivation in response to a lack of free NAD^+ in the absence of parkin. However, the origin of the mitochondrial energy deficit in *PRKN*-mutant neurons currently remains elusive. Interestingly, recent studies suggest that parkin deficiency can be a driver of altered mitochondrial metabolism. Either via its function in mitochondrial clearance or through translational control of nuclear-encoded ETC mRNAs,[5,26] the mutant protein could trigger the respiratory complex impairments detected in patient neurons. With SIRT1 acting as a connector between cell metabolism, mitophagy, and biogenesis pathways, further research will be needed to determine the exact sequence of events triggering mitochondrial dysfunction in parkin-deficient DANs.[44] Moreover, additional analyses in iPSC-derived co-culture systems should aim at the identification of the immune signaling pathways activated in microglia in response to neuronal release of mitochondrial DAMPs, including mtDNA. Such investigations will pave the way for innovative anti-inflammatory treatment approaches in PD.

Acknowledgments: We express our gratitude to the tissue donors and their families for their generous participation. Postmortem tissue for this study was provided by the Newcastle Brain Tissue Resource and Juntendo University. Moreover, Prof. Dr. Doug Turnbull (Wellcome Trust Centre for Mitochondrial Research, Newcastle University) kindly provided fibroblasts for the study from a patient with Alper's disease. We are grateful to Thea Maria Van Wüllen (Luxembourg Centre for Systems Biomedicine) and Carola Dietrich (Max-Planck-Institute for Human Molecular Genetics, Berlin) for their assistance in postmortem sample preparation for single-cell RNA sequencing. We thank Nassima Ouzren and Ursula Heins-Marroquin for optimizing protocols for experiments used in the study. In addition, the authors thank Dr. Christian Jäger and Xiangyi Dong from the Luxembourg Centre for Systems Biomedicine Metabolomics Platform for the generation of metabolomics data. Finally, this project was supported by the Imaging Facility and the Disease Modelling and Screening Platform, Luxembourg Centre for Systems Biomedicine, University of Luxembourg, and Luxembourg Institute of Health, Luxembourg. Open access funding enabled and organized by Projekt DEAL.

Data Availability Statement

Raw data for the midbrain tissue sample from the *PRKN* mutation carrier is available in the GEO with accession number GSE166790. Raw data for the two control samples were previously sequenced used in this study are available in the GEO with the accession number GSE157783 (data sets: C2-GSM4774937, C3-GSM4774938). Other data are available upon request.

References

1. Panigrahi B, Martin KA, Li Y, et al. Dopamine Is Required for the Neural Representation and Control of Movement Vigor. Cell 2015; 162(6):1418–1430. https://doi.org/10.1016/j.cell.2015.08.014
2. Lücking CB, Dürr A, Bonifati V, et al. Association between early-onset Parkinson's disease and mutations in the parkin gene. N Engl J Med 2000;342(21):1560–1567. https://doi.org/10.1056/NEJM200005253422103
3. Grünewald A, Kumar KR, Sue CM. New insights into the complex role of mitochondria in Parkinson's disease. Prog Neurobiol 2019; 177:73–93. https://doi.org/10.1016/j.pneurobio.2018.09.003
4. Kitada T, Asakawa S, Hattori N, et al. Mutations in the parkin gene cause autosomal recessive juvenile parkinsonism. Nature 1998; 392(6676):605–608. https://doi.org/10.1038/33416
5. Narendra D, Tanaka A, Suen DF, Youle RJ. Parkin is recruited selectively to impaired mitochondria and promotes their autophagy. J Cell Biol 2008;183(5):795–803. https://doi.org/10.1083/jcb.200809125
6. Shin JH, Ko HS, Kang H, et al. PARIS (ZNF746) repression of PGC-1α contributes to neurodegeneration in Parkinson's disease. Cell 2011;144(5):689–702. https://doi.org/10.1016/j.cell.2011.02.010
7. Chocron ES, Munkácsy E, Pickering AM. Cause or casualty: The role of mitochondrial DNA in aging and age-associated disease. Biochim Biophys Acta Mol Basis Dis 2019;1865(2):285–297. https://doi.org/10.1016/j.bbadis.2018.09.035
8. West AP, Khoury-Hanold W, Staron M, et al. Mitochondrial DNA stress primes the antiviral innate immune response. Nature 2015; 520(7548):553–557. https://doi.org/10.1038/nature14156
9. Sliter DA, Martinez J, Hao L, et al. Parkin and PINK1 mitigate STING-induced inflammation. Nature 2018;561(7722):258–262. https://doi.org/10.1038/s41586-018-0448-9
10. Pickrell AM, Huang CH, Kennedy SR, et al. Endogenous Parkin Preserves Dopaminergic Substantia Nigral Neurons following Mitochondrial DNA Mutagenic Stress. Neuron 2015;87(2):371–381. https://doi.org/10.1016/j.neuron.2015.06.034
11. Seibler P, Graziotto J, Jeong H, Simunovic F, Klein C, Krainc D. Mitochondrial Parkin recruitment is impaired in neurons derived from mutant PINK1 induced pluripotent stem cells. J Neurosci Off J Soc Neurosci. 2011;31(16):5970–5976. https://doi.org/10.1523/JNEUROSCI.4441-10.2011
12. Kriks S, Shim JW, Piao J, et al. Dopamine neurons derived from human ES cells efficiently engraft in animal models of Parkinson's disease. Nature 2011;480(7378):547–551. https://doi.org/10.1038/nature10648
13. Haenseler W, Sansom SN, Buchrieser J, et al. A Highly Efficient Human Pluripotent Stem Cell Microglia Model Displays a Neuronal-Co-culture-Specific Expression Profile and Inflammatory Response. Stem Cell Rep 2017;8(6):1727–1742. https://doi.org/10.1016/j.stemcr.2017.05.017
14. Reinhardt P, Glatza M, Hemmer K, et al. Derivation and expansion using only small molecules of human neural progenitors for neurodegenerative disease modeling. PloS One 2013;8(3):e59252. https://doi.org/10.1371/journal.pone.0059252
15. Sandor C, Robertson P, Lang C, et al. Transcriptomic profiling of purified patient-derived dopamine neurons identifies convergent perturbations and therapeutics for Parkinson's disease. Hum Mol Genet 2017;26(3):552–566. https://doi.org/10.1093/hmg/ddw412
16. Arena G, Cissé MY, Pyrdziak S, et al. Mitochondrial MDM2 Regulates Respiratory Complex I Activity Independently of p53. Mol Cell 2018;69(4):594–609.e8. https://doi.org/10.1016/j.molcel.2018.01.023
17. Vengellur A, LaPres JJ. The role of hypoxia inducible factor 1alpha in cobalt chloride induced cell death in mouse embryonic fibroblasts. Toxicol Sci Off J Soc Toxicol 2004;82(2):638–646. https://doi.org/10.1093/toxsci/kfh278
18. McCormack JG. Mitochondria. A practical approach; Edited by V M Darley-Usmar, D Rickwood and M T Wilson. pp 340. IRL Press, Oxford. 1987. £29 or £18 (pbk) ISBN 1-85221-034-6 or 033-8 (pbk). Biochem Educ 1988;16(2):118. https://doi.org/10.1016/0307-4412(88)90107-0

19. Delcambre S, Ghelfi J, Ouzren N, et al. Mitochondrial Mechanisms of LRRK2 G2019S Penetrance. Front Neurol 2020;11:881. https://doi.org/10.3389/fneur.2020.00881
20. Grünewald A, Rygiel KA, Hepplewhite PD, Morris CM, Picard M, Turnbull DM. Mitochondrial DNA Depletion in Respiratory Chain-Deficient Parkinson Disease Neurons. Ann Neurol 2016;79(3):366–378. https://doi.org/10.1002/ana.24571
21. Rygiel KA, Grady JP, Taylor RW, Tuppen HAL, Turnbull DM. Triplex real-time PCR--an improved method to detect a wide spectrum of mitochondrial DNA deletions in single cells. Sci Rep 2015;5:9906. https://doi.org/10.1038/srep09906
22. Meiser J, Delcambre S, Wegner A, et al. Loss of DJ-1 impairs antioxidant response by altered glutamine and serine metabolism. Neurobiol Dis 2016;89:112–125. https://doi.org/10.1016/j.nbd.2016.01.019
23. Smajić S, Prada-Medina CA, Landoulsi Z, et al. Single-cell sequencing of human midbrain reveals glial activation and a Parkinson-specific neuronal state. Brain J Neurol. Published online December 17 2021;awab446. https://doi.org/10.1093/brain/awab446
24. Sarraf SA, Raman M, Guarani-Pereira V, et al. Landscape of the PARKIN-dependent ubiquitylome in response to mitochondrial depolarization. Nature 2013;496(7445):372–376. https://doi.org/10.1038/nature12043
25. Palikaras K, Lionaki E, Tavernarakis N. Balancing mitochondrial biogenesis and mitophagy to maintain energy metabolism homeostasis. Cell Death Differ 2015;22(9):1399–1401. https://doi.org/10.1038/cdd.2015.86
26. Kuroda Y, Mitsui T, Kunishige M, et al. Parkin enhances mitochondrial biogenesis in proliferating cells. Hum Mol Genet 2006;15(6):883–895. https://doi.org/10.1093/hmg/ddl006
27. Zheng L, Bernard-Marissal N, Moullan N, et al. Parkin functionally interacts with PGC-1α to preserve mitochondria and protect dopaminergic neurons. Hum Mol Genet 2017;26(3):582–598. https://doi.org/10.1093/hmg/ddw418
28. Cantó C, Auwerx J. PGC-1alpha, SIRT1 and AMPK, an energy sensing network that controls energy expenditure. Curr Opin Lipidol 2009;20(2):98–105. https://doi.org/10.1097/MOL.0b013e328328d0a4
29. Amat R, Planavila A, Chen SL, Iglesias R, Giralt M, Villarroya F. SIRT1 controls the transcription of the peroxisome proliferator-activated receptor-gamma Co-activator-1alpha (PGC-1alpha) gene in skeletal muscle through the PGC-1alpha autoregulatory loop and interaction with MyoD. J Biol Chem 2009;284(33):21872–21880. https://doi.org/10.1074/jbc.M109.022749
30. Williamson DH, Lund P, Krebs HA. The redox state of free nicotinamide-adenine dinucleotide in the cytoplasm and mitochondria of rat liver. Biochem J 1967;103(2):514–527. https://doi.org/10.1042/bj1030514
31. Gleyzer N, Vercauteren K, Scarpulla RC. Control of mitochondrial transcription specificity factors (TFB1M and TFB2M) by nuclear respiratory factors (NRF-1 and NRF-2) and PGC-1 family coactivators. Mol Cell Biol 2005;25(4):1354–1366. https://doi.org/10.1128/MCB.25.4.1354-1366.2005
32. Jornayvaz FR, Shulman GI. Regulation of mitochondrial biogenesis. Essays Biochem 2010;47:69–84. https://doi.org/10.1042/bse0470069
33. Suen DF, Narendra DP, Tanaka A, Manfredi G, Youle RJ. Parkin overexpression selects against a deleterious mtDNA mutation in heteroplasmic cybrid cells. Proc Natl Acad Sci U S A 2010;107(26):11835–11840. https://doi.org/10.1073/pnas.0914569107
34. Borsche M, König IR, Delcambre S, et al. Mitochondrial damage-associated inflammation highlights biomarkers in PRKN/PINK1 parkinsonism. Brain J Neurol 2020;143(10):3041–3051. https://doi.org/10.1093/brain/awaa246
35. Mertens J, Paquola ACM, Ku M, et al. Directly Reprogrammed Human Neurons Retain Aging-Associated Transcriptomic Signatures and Reveal Age-Related Nucleocytoplasmic Defects. Cell Stem Cell 2015;17(6):705–718. https://doi.org/10.1016/j.stem.2015.09.001
36. Kano M, Takanashi M, Oyama G, et al. Reduced astrocytic reactivity in human brains and midbrain organoids with PRKN mutations. NPJ Park Dis 2020;6(1):33. https://doi.org/10.1038/s41531-020-00137-8
37. Okarmus J, Havelund JF, Ryding M, et al. Identification of bioactive metabolites in human iPSC-derived dopaminergic neurons with PARK2 mutation: Altered mitochondrial and energy metabolism. Stem Cell Rep. 2021;16(6):1510–1526. https://doi.org/10.1016/j.stemcr.2021.04.022
38. Rothfuss O, Fischer H, Hasegawa T, et al. Parkin protects mitochondrial genome integrity and supports mitochondrial DNA repair. Hum Mol Genet 2009;18(20):3832–3850. https://doi.org/10.1093/hmg/ddp327
39. Gensler S, Weber K, Schmitt WE, et al. Mechanism of mammalian mitochondrial DNA replication: import of mitochondrial transcription factor A into isolated mitochondria stimulates 7S DNA synthesis. Nucleic Acids Res 2001;29(17):3657–3663. https://doi.org/10.1093/nar/29.17.3657
40. Zanon A, Kalvakuri S, Rakovic A, et al. SLP-2 interacts with Parkin in mitochondria and prevents mitochondrial dysfunction in Parkin-deficient human iPSC-derived neurons and Drosophila. Hum Mol Genet 2017;26(13):2412–2425. https://doi.org/10.1093/hmg/ddx132
41. LaVoie MJ, Hastings TG. Dopamine quinone formation and protein modification associated with the striatal neurotoxicity of methamphetamine: evidence against a role for extracellular dopamine. J Neurosci Off J Soc Neurosci 1999;19(4):1484–1491.
42. Graves SM, Xie Z, Stout KA, et al. Dopamine metabolism by a monoamine oxidase mitochondrial shuttle activates the electron transport chain. Nat Neurosci 2020;23(1):15–20. https://doi.org/10.1038/s41593-019-0556-3
43. Reeve A, Simcox E, Turnbull D. Ageing and Parkinson's disease: why is advancing age the biggest risk factor? Ageing Res Rev 2014;14:19–30. https://doi.org/10.1016/j.arr.2014.01.004
44. Agarwal E, Goldman AR, Tang HY, et al. A cancer ubiquitome landscape identifies metabolic reprogramming as target of Parkin tumor suppression. Sci Adv 2021;7(35):eabg7287. https://doi.org/10.1126/sciadv.abg7287

Supporting Data

Additional Supporting Information may be found in the online version of this article at the publisher's web-site.

Parkin deficiency impairs mitochondrial DNA dynamics and propagates inflammation

Kobi Wasner, PhD[1], Semra Smajic, MSc[1]*, Jenny Ghelfi, BSc[1]*, Sylvie Delcambre, PhD[1], Cesar A. Prada-Medina, PhD[2], Evelyn Knappe, MSc[3], Giuseppe Arena, PhD[1], Patrycja Mulica, MSc[1], Gideon Agyeah, MSc[1], Aleksandar Rakovic, PhD[3], Ibrahim Boussaad, PhD[1,9], Katja Badanjak, MSc[1], Jochen Ohnmacht, PhD[1,8], Jean-Jacques Gérardy, BSc[5], Masashi Takanashi, MD[4], Joanne Trinh, PhD[3], Michel Mittelbronn, MD,[1,5-8], Nobutaka Hattori, MD, PhD[4], Christine Klein, MD[3], Paul Antony, PhD[1,9], Philip Seibler, PhD[3], Malte Spielmann, MD[2,10], Sandro L. Pereira, PhD[1,7], and Anne Grünewald, PhD[1,3]

*These authors contributed equally.

1 Luxembourg Centre for Systems Biomedicine, University of Luxembourg, Esch-sur-Alzette, Luxembourg

2 Max Planck Institute for Molecular Genetics, Berlin, Germany

3 Institute of Neurogenetics, University of Lübeck, Lübeck, Germany

4 Department of Neurology, Juntendo University, Tokyo, Japan

5 National Center of Pathology, Laboratoire National de Santé, Dudelange, Luxembourg

6 Luxembourg Center of Neuropathology, Dudelange, Luxembourg

7 Department of Oncology, Luxembourg Institute of Health, Luxembourg, Luxembourg

8 Department of Life Science and Medicine, University of Luxembourg, Esch-sur-Alzette, Luxembourg

9 Disease Modelling and Screening Platform, Luxembourg Centre of Systems Biomedicine, University of Luxembourg & Luxembourg Institute of Health, Luxembourg

10 Institute of Human Genetics, University of Lübeck, Lübeck, Germany

Corresponding author:

Anne Grünewald, Ph.D., Luxembourg Centre for Systems Biomedicine, University of Luxembourg, 6 avenue du Swing, L-4367 Belvaux, Luxembourg, phone: (+352) 46 66 44 9793, e-mail: anne.gruenewald@uni.lu

List of content

1. Supplementary methods

1.1. Cell culture

1.1.1. Generation of small molecule neural precursor cells (smNPCs)

smNPCs were cultured and expanded in N2B27 medium - Neurobasal (Gibco)/DMEM-F12 (Gibco) 50:50 with 1% B27 lacking vitamin A (ThermoFisher), 0.5% N2 (Life Technologies), 1% penicillin-streptomycin (ThermoFisher) and 1% 200 mM glutamine (Westburg) - supplemented with 3 µM CHIR 99021 (Sigma), 150 µM ascorbic acid (AA) (Sigma) and 0.5 µM purmorphamine (Sigma). The medium was changed every second day.

1.1.2. Generation of midbrain neurons

To initiate neuronal differentiation, smNPCs were counted using the Countess II FL Automated Cell Counter (ThermoFisher) and seeded onto Matrigel-coated (Corning) 6-well plates in N2/B27 medium supplemented with 1 µM purmorphamine, 200 µM ascorbic acid (AA) and 100 ng FGF8 (PeproTech) for 8 days. For the next 2 days, cells were cultured in N2/B27 medium with 0.5 µM purmorphamine and 200 µM AA. For the remainder of the differentiation (22 days), cells were maintained in Maturation medium: N2/B27 supplemented with 200 µM AA, 500 µM dibutyryl-cAMP (Applichem), 1 ng/mL TGF-β3 (Peprotech), 10 ng/mL GDNF (Peprotech) and 20 ng/mL BDNF (PeproTech). The medium was changed every second day.

1.1.3. Generation of induced pluripotent stem cells (iPSCs)

Skin fibroblasts obtained from an Alper's disease patient with *POLG* mutations (Fig. S1A) were reprogrammed into iPSCs using the Epi5^{TM} Episomal iPSC Reprogramming Kit (ThermoFisher) according to the manufacturer's instructions. Briefly, fibroblasts were maintained in DMEM supplemented with 10% FBS and 1% Penicillin-Streptomycin. Once 75-90% confluent, fibroblasts were washed with PBS (Gibco) and detached by adding 0.05% Trypsin/EDTA (ThermoFisher) for 5 min at 37°C. Cells were then collected and counted using the Countess II FL Automated Cell Counter. Next, 1 x 10^7 cells were removed, centrifuged at 200 x g for 5 min and transduced with Epi5™ Reprogramming Vectors and Epi5™ p53 & EBNA Vectors using the Amaxa Nucleofector I (Lonza) with 3 pulses at 1650 V for 10 ms. After transfection, cells were seeded onto irritated mouse embryonic fibroblasts and cultured

in mTeSR™ 1 complete medium (STEMCELL Technologies). The medium was changed every day. After ~1 month, iPSC colonies were picked based on their stem-cell-like morphology and expanded on Matrigel-coated plates. The generation of smNPCs and midbrain neurons was performed identically as described for iPSCs from Parkin mutation carriers.

1.1.4. Generation of isogenic Parkin-knockout neuroblastoma cells

Parkin knockout neuroblastoma (SH-SY5Y) cells were generated using an RNA-guided CRISPR/Cas9 endonuclease. For this, SH-SY5Y cells were transiently cotransfected with plasmids expressing either a human codon-optimized Cas9 (hCas9 was a gift from George Church [Addgene plasmid # 41815]) and a guide RNA (gRNA_Cloning Vector was a gift from George Church [Addgene plasmid # 41824]) containing a 19-base long sequence that matches the human *PRKN* target sequence 5'- GTGGTTGCTAAGCGACAGG -3'. Upon transfection, cells were re-suspended in growth medium, counted and plated onto Petri dishes at a density of 1 cell/cm2. Cells were grown until they formed distinct, monoclonal colonies. The colonies were scraped off, transferred into different wells of a 6-well plate, and propagated to obtain enough material for the DNA extraction for Sanger sequencing. We identified one clonal cell line carrying a homozygous mutation c.100_101insC (p.Q34PfsX5) in the *PRKN* gene resulting in a premature stop codon, further leading to nonsense-mediated decay. To induce hypoxia, SH-SY5Y cells were plated onto a 6-well plate at a density of 1.1 million cells/well and, the following day, treated for 24h with 200 µM $CoCl_2$ (Merck, C8661) in MOPS (ROTH, 6979.2) buffer.

1.2. Parkin silencing

For Parkin knockdown, the lentiviral pLKO.1 vector (Addgene) was used to express short hairpin RNA (shRNA) against human Parkin (Sense: ccggCCAGTAGCTTTGCACCTGATTctcgagAATCAGGTGCAAAGCTACTGGtttttg).[1] The MISSION pLKO.1-puro Non-Mammalian shRNA control Plasmid DNA (Sigma), targeting no known mammalian genes, was used as negative control for lentiviral transduction (Sense: CCGGCAACAAGATGAAGAGCACCAACTC-GAGTTGGTGCTCTTCATCTTGTTGTTTTT). Lentiviral constructs, as well as 2nd generation packaging plasmids (psPAX2, pMD2G), were transfected in HEK293T cells by calcium phosphate precipitation in the presence of 25 µM

chloroquine. HEK293T cell culture medium, containing the respective lentiviral particles, were harvested 48 hrs post-transfection, passed through 0.45 µM filters and used to transduce target cells overnight, in presence of 8 µg/mL Polybrene.

1.3. Generation and treatment of iPSC-derived neuron-microglia co-cultures

DANs and microglia cells were generated according to previously described protocols.[2-4] At day 92 of neuronal differentiation, $4x10^5$ microglia precursor cells were plated onto corresponding cell lines of neurons leading to their maturation. Equal amounts of both cell types were co-cultured for 35 days before treatment with LPS (100 ng/mL) for 3 hours and mtDNA (300 ng) for 1 hour. A mixture of mtDNA extracted from all *PRKN*-mutant patients was used.

1.4. Immunocytochemistry

SH-SY5Y cells, iPSC-derived smNPCs and midbrains neurons were fixed in 4% paraformaldehyde for 15 min at room temperature and then washed three times in PBS (Gibco). Cells were then permeabilized in the blocking buffer (1% bovine serum albumin [Sigma], 0.25% Triton-X 100 [Sigma] in PBS) for 1 hr at room temperature. Cells were then stained overnight at 4°C with primary antibodies in blocking buffer. For smNPCs, cells received antibodies against Nestin (R&D Systems, MAB1259), Pax6 (BioLegend, 901301) and Musashi (Abcam, ab21628). For neurons, cells were subjected to several combinations of antibodies (depending upon the experiment) against TUBB3 (BioLegend, 801202), tyrosine hydroxylase (Sigma T8700), DNA (Progen AC-30-10), TOM20 (Santa Cruz SC-17764). The next day, cells were washed three times in PBS and then stained with fluorescent secondary antibodies in blocking buffer for 1h at room temperature. Cells were then washed three times in PBS, and incubated with Hoechst 33342 (ThermoFisher) for 10 min. For the assessment of mtDNA release into the cytosol, cells were incubated for 30 minutes at room temperature with HCS CellMask™ Orange stain (ThermoFisher) prior to the nuclear staining and following the manufacturer's indications. Images were taken using a 20X objective (for smNPCs) or 40X objective (for neurons) using the Zeiss Axio Imager 2 microscope, or 60X objective for neurons and SH-SY5Y cells on the Cell Voyager CV8000 high-content screening confocal microscope (Yokogawa Electric Corporation).

1.5. Western blotting

Antibodies used in the study: Parkin (Santa Cruz sc-32282), SIRT1 (Abcam ab32441), PGC1-α (Novus Biologicals NBP1-04676), NRF1 (Abcam ab175932), NRF2 (Cell Signaling abe1047), VDAC (Abcam ab14734), LC3A/B (Cell Signaling, 4108), TFAM (Abcam ab47517), TUBB3 (Tuj1) (BioLegend 801202), tyrosine hydroxylase (Sigma T8700), cGAS (Santa Cruz sc-515777) and beta-actin (Sigma A1978).

1.6. Metabolite extraction and metabolomics analysis

Metabolites from 35d-old neurons were extracted using a Methanol/Water-Chloroform mix. Neurons were seeded in 12-well plates at day 25 of differentiation and then maintained for 5 days. Cells were washed once with 0.9% NaCl (Sigma). Metabolism was quenched with 200 µL ice-cold methanol (Roth). 80 µL of 4°C water was added and the plate was placed on an orbital shaker for 10 min at 4°C. The mixture was transferred to a tube containing 100 µL of ice-cold chloroform (Roth) and then shaken on a thermomixer at 4°C for 5 min. An additional 100 µL of ice-cold chloroform and 4°C water were added. The samples were then vortexed and centrifuged for 5 min at 21000 x g, 4°C. 125 µL of the upper phase were transferred to a glass vial and dried in a vacuum centrifuge. Samples were capped and kept at -80°C until measurement.

Polar metabolites were derivatized and measured by GC-MS using an Agilent 7890B GC coupled to an Agilent 5977A Mass Selective Detector (Agilent Technologies) following an established method. The MetaboliteDetector software package (Version 3.220180913) was used for mass spectrometry (MS) data post processing and quantification. NAD^+:NADH ratios were determined using the colorimetric NAD/NADH Quantification Kit from Sigma following the manufacturer's instructions.

1.7. Mitochondrial extraction

SH-SY5Y cells were resuspended and washed in homogenization buffer (HB) (10 mM Tris, pH 7.4, 1 mM EDTA, 250 mM Sucrose) with protease and phosphatase inhibitors (Halt Protease & Phosphatase inhibitor cocktail). After washing the pellet at 4000 x g for 5 min at 4°C, fresh HB was added and the pellet was homogenized for 1 min on ice

using a pellet pestle (Sigma). Homogenates were then centrifuged at 1500 x g for 10 min at 4°C and the supernatant was removed. After two washing steps in HB, mitochondria were pelleted by centrifugation at 8000 x g for 10 min.

1.8. NADH-COQ1 reductase assay

To measure complex I activity, mitochondrial homogenates were subjected to three freeze/thaw cycles in HB buffer and then placed in buffer containing 20 mM K^+Phosphate buffer (sodium phosphate (VWR), magnesium chloride (Sigma), 150 µM NADH (Sigma), 1 mM potassium cyanide (Sigma), and bovine serum albumin (BSA) (Sigma)) followed by an additional three freeze/thaw cycles. Samples were then placed into a 96-well plate (Greiner Bio-One) and kinetic measurement was evaluated at 340 nm using the Biotek Cytation 5 plate reader (Biotek). We first measured baseline activity for 3 min, then added 50 µM ubiquinone (Sigma) and measured kinetics for 10 min, and finally added 10 µM rotenone (Abcam) and measured for 10 min.

1.9. Citrate synthase assay

The citrate synthase assay was performed on the same mitochondrial extracts as in the NADH-COQ1 assay. Here, we followed a modified protocol based on Coore *et al.*[5] First, we subjected mitochondria to three freeze/thaw cycles in HB buffer and then added a buffer containing 100 mM Tris (Sigma), 100 µM acetyl CoA (Sigma), 100 µM DTNB (Sigma) and 0.1% Triton X (Sigma), followed by three more freeze/thaw cycles. The samples were then added to a 96-well plate (Greiner Bio-One) and kinetic measurement was performed at 412 nm in the BioTek Cytation 5 plate reader (BioTek) at baseline for 3.5 min. We then added 100 µM oxaloacetic acid (Sigma) and measured for an additional 10 min.

1.10. Quantitative PCR analyses

1.10.1. MtDNA integrity and copy number analyses

DNA was extracted using the QIAmp DNA Mini Kit (Qiagen) following the manufacturer's instructions. Transcription and copy number were measured using a real-time polymerase chain reaction (RT-PCR) method on the LightCycler

480 (Roche) with TaqMan probes for *D-loop, MT-ND1*, *MT-ND4,* and the nuclear single copy gene *B2M* as described.[6,7]

1.10.2. Digital PCR

DNA was quantified using a digital PCR (dPCR) assay with TaqMan probes specific for *MT-ND1* and *B2M*. dPCR was executed using the QuantStudio 3D Digital PCR System (Applied Biosystems) as published.[6, 7]

1.10.3. RNA extraction and quantitative PCR

RNA was prepared by using the RNeasy Mini Kit (Qiagen). RNA was then reverse-transcribed into cDNA using SuperScript III Reverse Transcriptase (ThermoFisher) and measured via RT-PCR using iQ SYBR Green Supermix (Biorad) on the LightCycler 480. Primer sequences are summarized in Table S5.

1.11. Laser capture microdissection

Frozen sections were fixed with 4% paraformaldehyde for 10 min and then washed in distilled water for 10 min. After three 5 min washes in TBST buffer, a TH primary antibody (Merck) was applied for 1 hr at room temperature. After three more washes, a secondary antibody (Santa Cruz) was applied for 30 min at room temperature. Following more washing, sections were incubated with DAB (Millipore) and 3% H2O2 for 4 min at room temperature and then washed in distilled water for 5 min. Single TH-positive neurons were isolated through laser capture microdissection (LCM) using the PALM MicroBeam (Zeiss) and captured in 15 µL of lysis buffer (50 mM Tris-HCl, pH 8.5, 1 mM EDTA, 0.5% Tween-20, 200 ng/mL proteinase K), centrifuged for 10 min at 20,000 x g at 4°C and then incubated for 3 hr at 55°C and 10 min at 95°C.

1.12. Single-nuclei RNA sequencing (snRNAseq) and data analysis

1.12.1. Tissue processing

Eight sections of the *PRKN*-mutant brain were pooled together for nuclei isolation. Tissue was collected in cold lysis buffer (10 mM Tris-HCl, 10 mM NaCl, 3 mM MgCl2, 0.1% NonidetTM P40). The resulting tissue suspension was

filtered and pelleted by centrifugation. Pellets were washed with 'nuclei wash and resuspension buffer' (1xPBS, 1% BSA, 0.2 U/µL RNase inhibitor) and then filtered and re-pelleted. Next, pelleted nuclei were incubated in DAPI solution (1.5 µM DAPI in 1x PBS) for 5 min prior to FACS-sorting. After dissociation, the nuclei suspension was subjected to FACS-sorting with FACSDiva Cell Sorter (BD Biosciences). Single DAPI-positive nuclei were sorted. To sequence harvested nuclei and prepare cDNA libraries, the Chromium Next GEM Single Cell 3'Kit v3.1 was used. The quality of resulting cDNA was assessed with the Agilent 2100 Bioanalyzer System.

1.12.2. Sequencing and data analysis

Sequencing was performed via Illumina NovaSeq 600-S2. Resulting data was processed identically to controls.[8] Briefly, after sequencing, the quantification of transcripts and filtering FASTQ files were produced from raw base call outputs with the Cell Ranger (10X Genomics) *mkfastq* pipeline v.3.0. Further, with the Cell Ranger (10X Genomics) count pipeline v.3.0 with default parameters, we obtained a gene-barcode UMI count matrix per sample. Considering that nuclei rather than cells were sequenced, we utilized the Cell Ranger recommended variation of the human reference transcriptome (hg38), which also annotates introns as exons. Only barcodes with more than 1500 UMIs and 1000 genes were included. Moreover, only those with less than 10% of mitochondrial-encoded and 10% ribosomal encoded genes were kept. Only genes detected in more than three barcodes were retained and ribosomal and mitochondrial-encoded genes were removed. With Scrubblet57, possible multiplet barcodes were identified, and such were kept with an estimated duplet score smaller than 0.15.

To determine the cell types comprising human midbrain tissue samples, we pooled the samples in a single embedding following the Seurat v3 integration workflow.[9] The top 4000 most variable genes were identified with *SelectIntegrationFeatures*, and used to determine the between-sample cell-anchors with *FindIntegrationAnchors*. The *IntegrateData* function was used to build a centered expression matrix, which was further used for principal component analysis. After, the Shared Nearest Neighbor (SNN) cell graph was built with the top 25 principal components and then clustered using the Louvain algorithm (resolution = 1.5) with the *FindClusters* function. With the FindAllMarkers function we detected the marker genes (expressed in minimally 25% of the cluster) for each cluster by using the default 'wilcox' test. With such top marker genes, each cell cluster was cell-type annotated. To

identify the differentially expressed genes in microglia, *FindMarkers* function with *logfc.threshold=0.25* and *min.pct=0.05* was used to compare microglia clusters between control and Parkin conditions. This list of differentially expressed genes was further utilized in pathway enrichment analysis with MetaCore software.

2. Supplementary figures

A

Disease Status	Sample	Sex	Age of Sampling	AAO	Gene	Mutation
Healthy	Control 1	M	39	N/A	N/A	N/A
Healthy	Control 2	F	37	N/A	N/A	N/A
Healthy	Control 3	M	40	N/A	N/A	N/A
Parkinson's disease	Parkin-PD 1	M	58	43	*PRKN*	c.1072Tdel (hom)
Parkinson's disease	Parkin-PD 2	M	57	15	*PRKN*	delEx4; + c.924C>T
Parkinson's disease	Parkin-PD 3	F	41	37	*PRKN*	del Ex1;c.924C>T
Alpers' disease	POLG	M	1 month	Birth	*POLG*	c.1399G>A; c.2740A>C

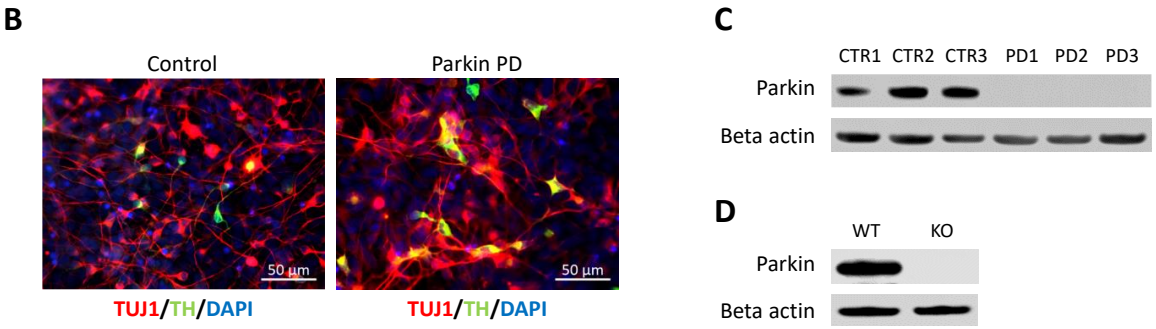

Figure S1 Derivation and characterization of iPSC-derived midbrain neurons and SH-SY5Y cells. (A) Overview of patients and controls included in the *in vitro* part of the study. **(B)** iPSC-derived neurons were stained for the neuronal marker TUJ1 and the catecholamine rate limiting enzyme tyrosine hydroxylase (TH). Images were taken using a 40x objective. **(C)** Parkin protein abundance in iPSC-derived patient and control neurons. Protein was extracted and subjected to Western blotting analysis using anti-Parkin and anti-beta-actin antibodies. Representative cropped images are shown. **(D)** Parkin protein abundance in control and isogenic Parkin-knockout SH-SY5Y cells. Representative cropped images are shown.

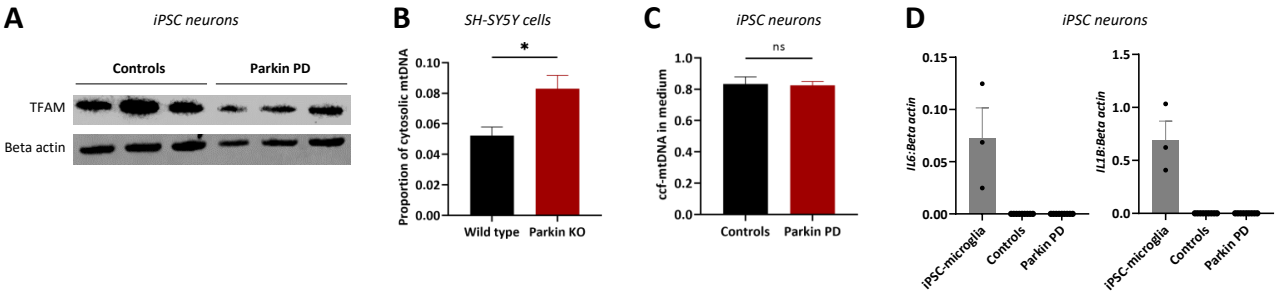

Figure S2 MtDNA dynamics and inflammation in PRKN-mutant and control iPSC-derived neurons. (A) Representative cropped Western blot images of TFAM and beta-actin. **(B)** Quantification of mtDNA in cytosolic and mitochondrial fractions from Parkin-PD and control iPSC-derived neurons. mtDNA levels were quantified by means of real-time PCR targeting the mtDNA fragment *ND1* and the nuclear single copy gene *B2M*. The proportion of cytosolic mtDNA normalized to cytosolic *B2M* copies was calculated relative to the total amount of cellular mtDNA copies. **(C)** Extracellular ccf-mtDNA in medium from Parkin-PD and control iPSC-derived neurons. Quantification by means of multiplex dPCR with probes against *ND1* and *B2M.* The proportion of extracellular *ND1* normalized to extracellular *B2M* copies was calculated relative to the total amount of mtDNA copies present in the medium and cells. **(D)** *IL6* and *IL1B* gene expression. *IL6* and *IL1B* levels were measured relative to the house-keeping gene *Beta-actin*. *IL6* and *IL1B* expression in iPSC-derived control microglia served as a positive control. n = 3 or 5 biological replicates, data are presented as the mean ± SEM; **P* < 0.05, ***P* < 0.01, ns = not significant as determined by student's t-test.

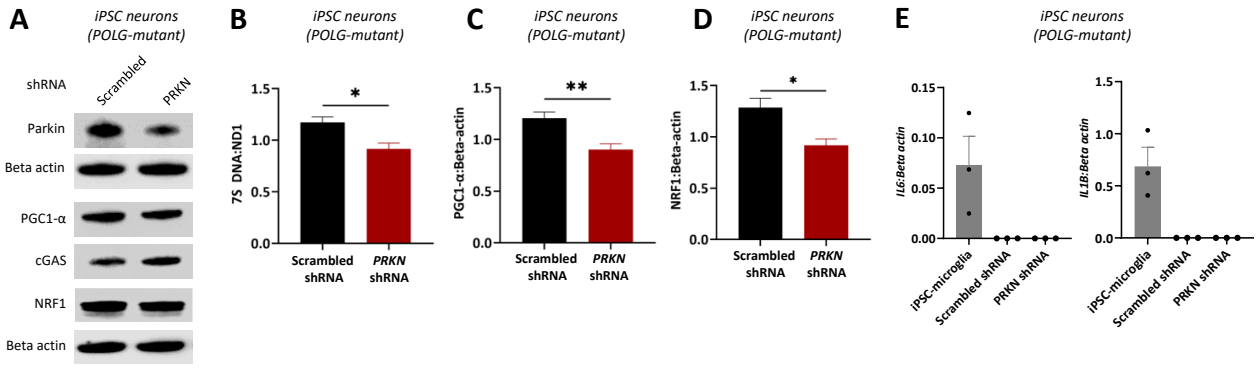

Figure S3 MtDNA dynamics and inflammation in iPSC-derived neurons from a compound-heterozygous POLG mutation carrier transduced with scrambled or PRKN shRNA. (A) Representative cropped images of Western blot membranes of whole cell lysates. Cells were harvested 5 days post transduction and subjected to Western blot analysis. **(B)** Quantification of 7S-associated transcription via multiplex RT-PCR. mtDNA transcription initiation events were determined by calculating the 7S DNA:ND1 ratios. **(C)** Quantification of PGC1-α protein levels relative to Beta-actin from (A). **(D)** Quantification of NRF1 protein levels relative to Beta-actin from (A). **(E)** *IL6* and *IL1B* gene expression in *POLG*-mutant iPSC-derived neurons transduced with scrambled or *RRKN* shRNA. *IL6* and *IL1B* levels were measured relative to *Beta-actin*. *IL6* and *IL1B* expression in iPSC-derived control microglia served as a positive control. n = 3 or 5 biological replicates, data are presented as the mean ± SEM; **P* < 0.05, ***P* < 0.01, as determined by student's t-test.

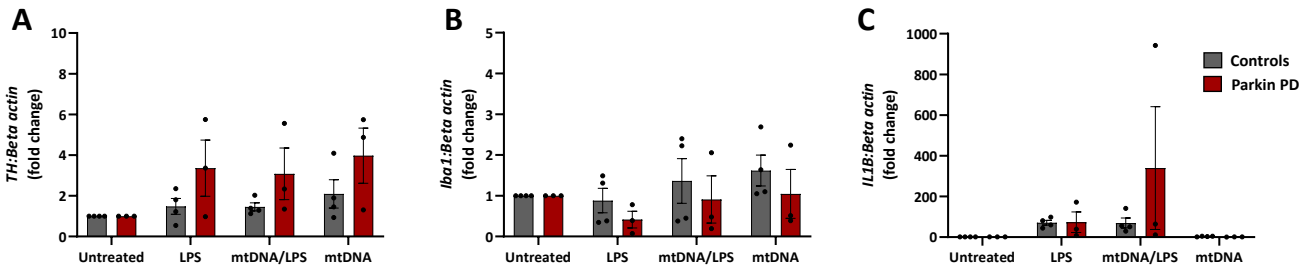

Figure S4 Expression of neuronal, microglial and inflammatory marker genes in PRKN-PD and control neuron-microglia co-cultures. (A) Dopaminergic neuron abundances in co-cultures. Expression of *TH* was measured relative to *Beta-actin* by means of qPCR. This assessment did not reveal significant differences between lines and treatments. **(B)** Microglia abundance in co-cultures. Quantifying the expression of the microglial marker gene *Iba1* relative to the house-keeping gene *Beta-actin* by qPCR did not show differences between investigated lines and treatments. **(C)** Pro-inflammatory cytokine analysis. Quantitative gene expression analysis of *IL1B* relative to *Beta-actin* revealed a non-significant upregulation in *PRKN*-PD co-cultures after co-treatment with LPS and mtDNA.

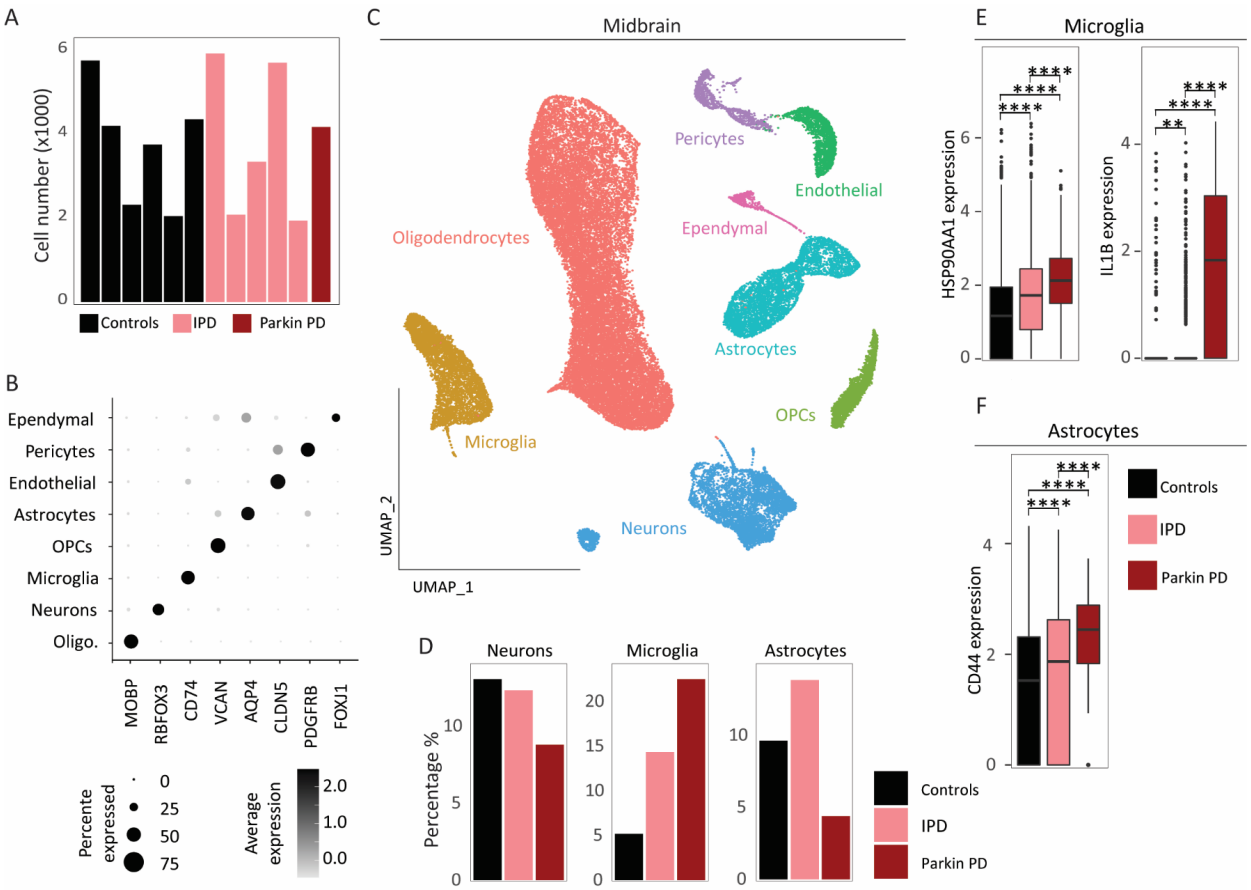

Figure S5 PRKN-mutant midbrain single-nuclei transcriptome comparison with six healthy controls and five idiopathic Parkinson's disease (IPD) cases. (A) Number of nuclei per sample. **(B)** Cell-type specific marker genes. **(C)** UMAP representation of 45.608 nuclei from *PRKN*-mutant, control and IPD midbrain samples. **(D)** Percentage of *PRKN*-mutant, control and IPD neuronal, astrocytic and microglia nuclei. **(E)** *CD44* gene expression in astrocytes in *PRKN*-mutant, control and IPD samples. **(F)** *HSP90AA1* and *IL1B* gene expression in microglia in *PRKN*-mutant, control and IPD samples.

3. Supplementary tables

Table S1 Marker genes for cell clusters

Table S2 Differentially expressed genes in *PRKN*-mutant midbrain microglia

Table S3 *PRKN*-mutant midbrain microglia; upregulated pathways

Table S4 *PRKN*-mutant midbrain microglia; downregulated pathways

(Tables S2-4 were submitted as csv files)

Table S5 Sequences of primers used in the study

Gene	Forward	Reverse
Beta-actin	5' - CGAGGACTTTGATTGCACATTGTT	5' - TGGGGTGGCTTTTAGGATGG
MT-ND1	5'- ATACCCACACCCACCCAAGAAC	5'- GGTTTGAGGGGGAATGCTGGA
MT-CYTB	5'- CTGATCCTCCAAATCACCACAG	5'- GCGCCATTGGCGTGAAGGTA
MT-COX1	5'-GGAGCAGGAACAGGTTGAACAG	5'-GTTGTGATGAAATTGATGGC
TFAM	5'-AAGATTCCAAGAAGCTAAGGGTGA	5'-CAGAGTCAGACAGATTTTTCCAGT
TFB2M	5'-TCTGGCAATTAGCTTGTGAG	5'-CTTACGCTTTGGGTTTTCCA
Twinkle	5'-ATTGTAGAAGGACGTGGACG	5'-TGCAGAGCTCACTCTAGGTG

4. References

1. Arena G, Cissé MY, Pyrdziak S, et al. Mitochondrial MDM2 Regulates Respiratory Complex I Activity Independently of p53. *Mol Cell*. 2018;69(4):594-609.e8. doi:10.1016/j.molcel.2018.01.023

1. Kriks S, Shim JW, Piao J, et al. Dopamine neurons derived from human ES cells efficiently engraft in animal models of Parkinson's disease. *Nature*. 2011;480(7378):547-551. doi:10.1038/nature10648

2. Haenseler W, Sansom SN, Buchrieser J, et al. A Highly Efficient Human Pluripotent Stem Cell Microglia Model Displays a Neuronal-Co-culture-Specific Expression Profile and Inflammatory Response. *Stem Cell Rep*. 2017;8(6):1727-1742. doi:10.1016/j.stemcr.2017.05.017

3. Reinhardt P, Glatza M, Hemmer K, et al. Derivation and expansion using only small molecules of human neural progenitors for neurodegenerative disease modeling. *PloS One*. 2013;8(3):e59252. doi:10.1371/journal.pone.0059252

4. Coore HG, Denton RM, Martin BR, Randle PJ. Regulation of adipose-tissue pyruvate dehydrogenase by insulin and other hormones. *Biochem J*. 1971;125(1):115-127

5. Grünewald A, Rygiel KA, Hepplewhite PD, Morris CM, Picard M, Turnbull DM. Mitochondrial DNA Depletion in Respiratory Chain-Deficient Parkinson Disease Neurons. *Ann Neurol*. 2016;79(3):366-378. doi:10.1002/ana.24571

6. Rygiel KA, Grady JP, Taylor RW, Tuppen HAL, Turnbull DM. Triplex real-time PCR--an improved method to detect a wide spectrum of mitochondrial DNA deletions in single cells. *Sci Rep*. 2015;5:9906. doi:10.1038/srep09906

7. Smajić S, Prada-Medina CA, Landoulsi Z, et al. Single-cell sequencing of human midbrain reveals glial activation and a Parkinson-specific neuronal state. *Brain*. Published online December 17, 2021:awab446. doi:10.1093/brain/awab446

8. Stuart T, Butler A, Hoffman P, et al. Comprehensive Integration of Single-Cell Data. *Cell*. 2019;177(7):1888-1902.e21. doi:10.1016/j.cell.2019.05.031

Manuscript IV

ARTICLE

Midbrain organoids mimic early embryonic neurodevelopment and recapitulate LRRK2-p.Gly2019Ser-associated gene expression

Graphical Abstract

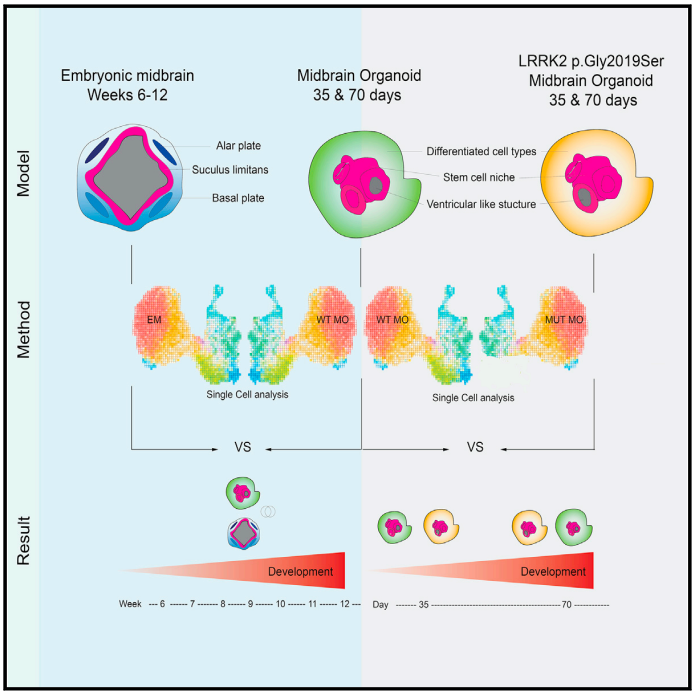

Authors

Alise Zagare, Kyriaki Barmpa, Semra Smajic, ..., Alexander Skupin, Sarah L. Nickels, Jens C. Schwamborn

Correspondence

sarah.nickels@uni.lu **(S.L.N.)**,
jens.schwamborn@uni.lu **(J.C.S.)**

Zagare et al., 2022, The American Journal of Human Genetics *109*, 311–327
February 3, 2022 © **2021 The Author(s).**
https://doi.org/10.1016/j.ajhg.2021.12.009

ARTICLE

Midbrain organoids mimic early embryonic neurodevelopment and recapitulate LRRK2-p.Gly2019Ser-associated gene expression

Alise Zagare,[1,2] Kyriaki Barmpa,[1,2] Semra Smajic,[1] Lisa M. Smits,[1] Kamil Grzyb,[1] Anne Grünewald,[1] Alexander Skupin,[1] Sarah L. Nickels,[1,*] and Jens C. Schwamborn[1,*]

Summary

Human brain organoid models that recapitulate the physiology and complexity of the human brain have a great potential for *in vitro* disease modeling, in particular for neurodegenerative diseases, such as Parkinson disease. In the present study, we compare single-cell RNA-sequencing data of human midbrain organoids to the developing human embryonic midbrain. We demonstrate that the *in vitro* model is comparable to its *in vivo* equivalents in terms of developmental path and cellular composition. Moreover, we investigate the potential of midbrain organoids for modeling early developmental changes in Parkinson disease. Therefore, we compare the single-cell RNA-sequencing data of healthy-individual-derived midbrain organoids to their isogenic LRRK2-p.Gly2019Ser-mutant counterparts. We show that the LRRK2 p.Gly2019Ser variant alters neurodevelopment, resulting in an untimely and incomplete differentiation with reduced cellular variability. Finally, we present four candidate genes, *APP*, *DNAJC6*, *GATA3*, and *PTN*, that might contribute to the LRRK2-p.Gly2019Ser-associated transcriptome changes that occur during early neurodevelopment.

Introduction

Parkinson disease (PD) is a multifactorial neurodegenerative disorder with varying motor and non-motor symptoms, characterized by the loss of dopaminergic neurons (DNs) in the substantia nigra pars compacta (SNpc) of the midbrain.[1] The most common mutation associated with PD is c.6055G>A (p.Gly2019Ser) in leucine-rich repeat kinase 2 (*LRRK2*) (GenBank: NM_198578.4).[2–4] LRRK2 is a multidomain protein involved in many cellular functions, including cell proliferation, survival regulation of neural stem cells (NSCs), and neurogenesis.[5,6] Altered neurogenesis and neurodevelopment have been suggested to have major implications in the development of neurodegenerative diseases, including PD.[7] Accordingly, various studies show an accelerated neuronal differentiation in *LRRK2*-mutant human cellular models, with a simultaneous impairment specifically of DN development.[8–10] In particular, the interaction of LRRK2 with the canonical Wnt/b-catenin signaling pathway has been linked to the development of DNs through the regulation of axonal guidance, dendritic morphogenesis, and synapse formation.[11–14]

Taking into consideration the complexity of the etiology of PD related to age, genetics, and environmental causes and the possibility of a neurodevelopmental component in PD, it is essential to have an adequate model, which can represent the human brain development and the manifestation of the disease. Studies on human postmortem brain tissue provided precious understanding of PD-associated alterations.[15] However, postmortem tissues are generally available at the end stage of the disease and display a late stage in the disease progression. In order to overcome the limitation of understanding the disease development throughout life, we rely on various experimental models. Our understanding of pathological mechanisms underlying the disease largely depends on models that do not fully portray the complexity of the disease pathology or the cellular composition of the human brain. Genetic and toxin-based animal models often are not able to adequately capture the critical aspects of human PD, resulting in incomplete disease phenotypes.[16] The discovery of induced pluripotent stem cells (iPSCs) and CRISPR-Cas9 technology surpassed this obstacle and enabled the access to human-derived cells for isogenic disease modeling.[17–19] Although such 2D cultures capture the specific effect of mutation-induced PD and its molecular mechanisms, they still lack the cellular diversity of the human brain. To overcome these limitations, the recent developments in self-organizing 3D human-derived midbrain organoids represent a promising advancement in modeling neurodegenerative diseases.[9,20–24]

In order to study the role of human LRRK2 p.Gly2019Ser in a physiological context of early human development, we used previously published single-cell RNA-sequencing (scRNA-seq) datasets of human embryonic midbrain between developmental week 6 and week 11[25] as well as healthy-individual-derived isogenic wild-type (WT) and LRRK2 p.Gly2019Ser midbrain organoids of 35 and 70 days of differentiation.[26] We have previously demonstrated that the respective midbrain organoids comprise different neuronal types, including dopaminergic, GABAergic,

[1]University of Luxembourg, Luxembourg Centre for Systems Biomedicine, 6, Avenue du Swing, L-4367 Belvaux, Luxembourg
[2]These authors contributed equally
*Correspondence: sarah.nickels@uni.lu (S.L.N.), jens.schwamborn@uni.lu (J.C.S.)
https://doi.org/10.1016/j.ajhg.2021.12.009.

glutamatergic, and serotonergic neurons as well as glia cells.[26] First, we sought to use the single-cell transcriptomes of healthy midbrain organoids and the human embryonic midbrain to analyze the shared cellular identities and correlation between the *in vitro* and *in vivo* systems. Further, we exploit the transcriptome of the healthy and isogenic (in which LRRK2 p.Gly2019Ser has been inserted) midbrain organoids to investigate the LRRK2-p.Gly2019Ser-dependent changes in gene expression. We report that the midbrain organoids share proportionately similar transcriptomic profile and cell-type diversity with the developing human midbrain. Additionally, our analysis shows that midbrain organoids accurately adopt human midbrain development and are able to capture a LRRK2-p.Gly2019Ser-associated gene expression profile that might underlie *LRRK2*-mutation-related phenotypes.

Material and methods

Midbrain organoid generation from midbrain floorplate neural progenitor cells

Neural progenitor cells (NPCs) were derived from iPSCs of a healthy individual and isogenic LRRK2-p.Gly2019Ser-inserted cell line. Gene-editing of the iPSCs was done with CRISP-Cas9 and piggyBac systems, and it has been described in Qing et al., 2017.[27] The derivation of NPCs from iPSCs and further organoid generation have been described in detail previously[9,26] (Table S1). In brief, NPCs were cultured in N2B27 base medium supplemented with 2.5 μM SB-431542 (SB, Ascent Scientific), 100 nM LDN-193189 (LDN, Sigma), 3 μM CHIR99021 (CHIR, Axon Medchem), 200 μM ascorbic acid (AA, Sigma), and 0.5 μM SAG (Merck). For the derivation of midbrain, 3,000 NPCs were seeded per well in an ultra-low-attachment 96-well plate. For 7 days, cells were kept under maintenance conditions, following 3 days of pre-pattering where LDN and SB were withdrawn, and CHIR concentration was reduced to 0.7 μM. On day 9 of organoid culture, the differentiation was induced by changing the medium to N2B27 with 10 ng/mL brain-derived neurotrophic factor (BDNF, Peprotech), 10 ng/mL glial-cell-derived neurotrophic factor (GDNF, Peprotech), 200 μM AA, 500 μM dibutyryl cAMP (Sigma), 1 ng/mL TGF-β3 (Peprotech), 10 μM dual antiplatelet therapy (DAPT) (Cayman), and 2.5 ng/mL ActivinA (Peprotech). The organoids were cultured under static conditions with media changes every third day for 35 or 70 days. 30 midbrain organoids of each condition (WT35, WT70, MUT35, and MUT70) were pulled for Drop-seq analysis as described in Smits et al., 2020.[26]

Immunofluorescence staining

Midbrain organoids were fixed with 4% paraformaldehyde (PFA) overnight at 4°C followed by three washes with PBS for 15 min. The washed organoids were embedded in 3%–4% low-melting point agarose in PBS. Embedded organoids were sectioned into 50 μm sections with vibratome (Leica VT1000s). Organoid sections were blocked with 0.5% Triton X-100, 0.1% sodium azide, 0.1% sodium citrate, 2% BSA, and 5% normal donkey serum in PBS for 90 min at room temperature (RT) on a shaker. We diluted the primary antibodies in the same solution but with 0.1% Triton X-100 instead. The sections were incubated with the primary antibodies for 48 h at 4°C. Next, they were washed three times with PBS and subsequently blocked for 30 min at RT on a shaker. Next, sections were incubated with the secondary antibodies diluted in 0.05% Tween-20 in PBS for 2 h at RT and subsequently washed twice with 0.05% Tween-20 in PBS and once with Milli-Q water before mounting them in Fluoromount-G mounting medium (Southern Biotech). The primary antibodies used were TH rabbit Abcam ab112, FOXA2 mouse Santa Cruz sc-101060, and EN1 goat Santa Cruz sc- 46101. The secondary antibodies used were Hoechst 33342 solution (20 mM) Invitrogen 62249, anti-rabbit secondary 488 Thermo Fisher a21206, anti-mouse secondary 568 Invitrogen A10037, and anti-goat secondary 647 Invitrogen A21447.

Data pre-processing

In this study, we used already published scRNA-seq datasets. The midbrain organoids dataset was published from our lab,[26] while the other three datasets (embryonic midbrain, embryonic prefrontal cortex, and cortical organoids) are external[25,28,29] (Figure S1). scRNA-seq data from 30 pooled midbrain organoids per cell line and time point were generated following the Drop-seq pipeline.[30] Reads were mapped to human reference genome hg38 (GRCh38.87). From midbrain organoids datasets, cells having unique feature counts over 2,500 were removed as probable doublets or multiplets. Similarly, low-quality cells or empty droplets were further filtered out with unique feature counts below 100 (for day 35 data) and 200 (for day 70 data) and mitochondrial transcripts above 30% (Figure S2). Embryonic midbrain scRNA-seq data did not include any mitochondrial (MT) genes, thus to make midbrain organoid data more comparable to the embryonic midbrain data, we removed all MT genes from midbrain organoid datasets after quality control (QC). After QC, WT35 midbrain organoids included 2,864 cells, WT70 included 2,005 cells, MUT35 included 2,946 cells, and MUT70 included 2,660 cells.

The external datasets of embryonic midbrain, prefrontal cortex, and cortex organoid did not show any outliers in terms of doublets or empty droplets. Therefore, no additional QC was applied to these datasets.

Embryonic midbrain data of developmental week 6 to 11 included in total 1,977 cells, embryonic prefrontal cortex data at developmental stages between gestational weeks 8 and 26 included 2,309 cells, and cortex organoid data from 1 month old organoid comprised 4,832 cells.

Data integration and normalization

To better transmit the biological information between *in vivo* and *in vitro* ventral midbrain datasets, midbrain organoid data (WT35, WT70, MUT35, and MUT70) and embryonic midbrain data were integrated with the Seurat integration analysis workflow.[31] Integration was performed on the basis of the top 20 dimensions. RNA assay data of integrated object were log normalized and scaled to 10,000 transcripts per cell.

Cell type identification

After the integration of embryonic midbrain and midbrain organoid datasets, integrated object was scaled and principal-component analysis (PCA) was applied. Cell clustering was performed on the basis of the top 20 principal components via Louvain algorithm modularity optimization with a resolution of 0.5. Uniform manifold approximation and projection (UMAP) was used for cell cluster visualization.[32] Nine distinct cell clusters were identified in the UMAP plot. Clusters 0 and 7 were present only in

midbrain organoids and located in a close proximity to each other in the UMAP plot, indicating their high similarity and *in vitro* specificity. Because of this overclustering both clusters were pulled, resulting in eight distinct cellular identities labeled 1–8. For cell type identification, a binarized gene list across cell types from La Manno et al., 2016[25] was used. This list of genes comprises information about the marker genes in a binarized manner, where 1 means that gene is marking a specific cell population and 0 means that it cannot be considered as a marker gene. For more details on how this list is generated, please refer to La Manno et al., 2016.[25] Expression of each cluster-defining gene was overlapped with the marker gene (1) in the marker matrix from La Manno et al., 2016.[25] The total number of marker genes of a particular cell type of La Manno et al., 2016[25] that was present in each cluster of embryonic-midbrain- and midbrain-organoid-integrated dataset is visualized in Figure S4A. Cellular subtypes described by La Manno et al., 2016[25] were grouped in five major neuronal identity clusters—neurons subdivided in dopaminergic neurons (DNs) and non-dopaminergic neurons (non-DNs), then neuroblasts (NBs), progenitors (PROGs), and radial glia cells (RGLs). In addition, we identified non-neuronal identity cell populations—pericytes and endothelial cells. Cell types were assigned on the basis of the highest number of major cluster marker genes being expressed in the respective clusters of integrated embryonic midbrain and midbrain organoid dataset.

Differential gene expression analysis

Differentially expressed genes (DEGs) were detected with the FindMarkers function of the Seurat pipeline with the default thresholds. In all comparisons, we used the MUT midbrain organoids as ident.1 and the WT midbrain organoids as ident.2.

Pathway analysis

Pathway enrichment analysis was performed with MetaCore version 21.1 build 70400 on the basis of DEGs detected with the FindMarkers function from Seurat. DEGs were filtered for fold change (FC) > 0.25 and p adj. value < 0.05. From the analysis, we obtained the most significant enriched pathways, GO processes, network processes, and related diseases lists. The most significantly enriched pathways were illustrated in GraphPad Prism 9.

Cytoscape

Cell-cluster-specific genes were identified with the FindAllMarkers function from Seurat. The top 100 marker genes of each cell cluster were visualized in the network created with the Cytoscape software version 3.8.0.

Pseudotime analysis

Pseudotime analysis was performed with the Monocle package version 3. Merged Seurat object was uploaded in the Monocle workflow. Cell clustering was performed on the basis of 150 principal components with default settings. UMAP was used for visualization. Because Monocle does not allow a full metadata integration from Seurat object, we assigned cell identities manually to correspond to the ones previously defined. For the comparison between developmental stages of embryonic midbrain and midbrain organoid, we used the align_cds function to remove the batch effect between *in vivo* and *in vitro* midbrain systems. As a starting point for cell ordering along the pseudotime trajectory, the NB *in vitro* cluster of WT35 was chosen. For the comparison between developmental stages of WT midbrain organoids and MUT midbrain organoids, the same starting point of the NB *in vitro* cluster of WT35 was chosen. Genes that vary the most over the pseudotime were computed with the fit_models function. Midbrain-organoid- and embryonic-midbrain-integrated Seurat object was subset by pseudotime genes for the visualization of their expression in midbrain organoids.

Statistical analysis

If not stated otherwise, statistical analysis of scRNA-seq data was performed with RStudio R version 3.6.2 with the ggplot2 package. For all comparison, non-parametric Kruskal-Wallis test was performed. Statistical significance between comparisons are represented with asterisks: $p < 0.05$*, $p < 0.01$**, $p < 0.001$***, $p < 0.00001$****.

In vitro and *in vivo* midbrain data comparison to the cortex

WT midbrain organoids and embryonic midbrain were merged with embryonic prefrontal cortex and integrated on the basis of the top 20 dimensions. SCTransform normalization was applied to reduce the technical variation in the data and stabilize gene abundance levels, which can be highly variable between *in vitro* and *in vivo* tissues, especially between different tissue types—midbrain and cortex.[33] We determined mutual genes between midbrain organoids, embryonic midbrain, and embryonic prefrontal cortex by intersecting row names of respective datasets. Integrated object was subset by mutual genes. The top 2,000 variable genes in this subset of complete integrated dataset were detected with the FindVariableFeature function.

For the comparison of embryonic midbrain to cortical organoid, datasets were merged, SCTranformed, and subset by the mutual genes for the correlation analysis.

Ethical approval

The responsible national ethical commission has approved the study under the CNER report no. 201901/01. Written informed consent was obtained from all individuals who donated samples to this study (Smits et al., 2020).[26] The cell lines used in this study are summarized in Table S1.

Results

Midbrain organoids show a gene expression signature comparable to the human embryonic midbrain

To assess the similarity between the *in vitro* and *in vivo* midbrain systems, we compared scRNA-seq data of midbrain organoids cultured for 35 days (WT35) and 70 days (WT70)[26] to the human embryonic midbrain of developmental weeks 6–11.[25] In addition, to investigate possible transcriptome similarities between midbrain organoids and other brain regions during early development, we compared the scRNA-seq data of midbrain organoids to scRNA-seq data of the human embryonic prefrontal cortex.[28]

The transcriptome datasets of midbrain organoids, embryonic midbrain, and embryonic prefrontal cortex were embedded into a single Seurat object (Figure S3A). The average expression of the top 500 variable mutual genes

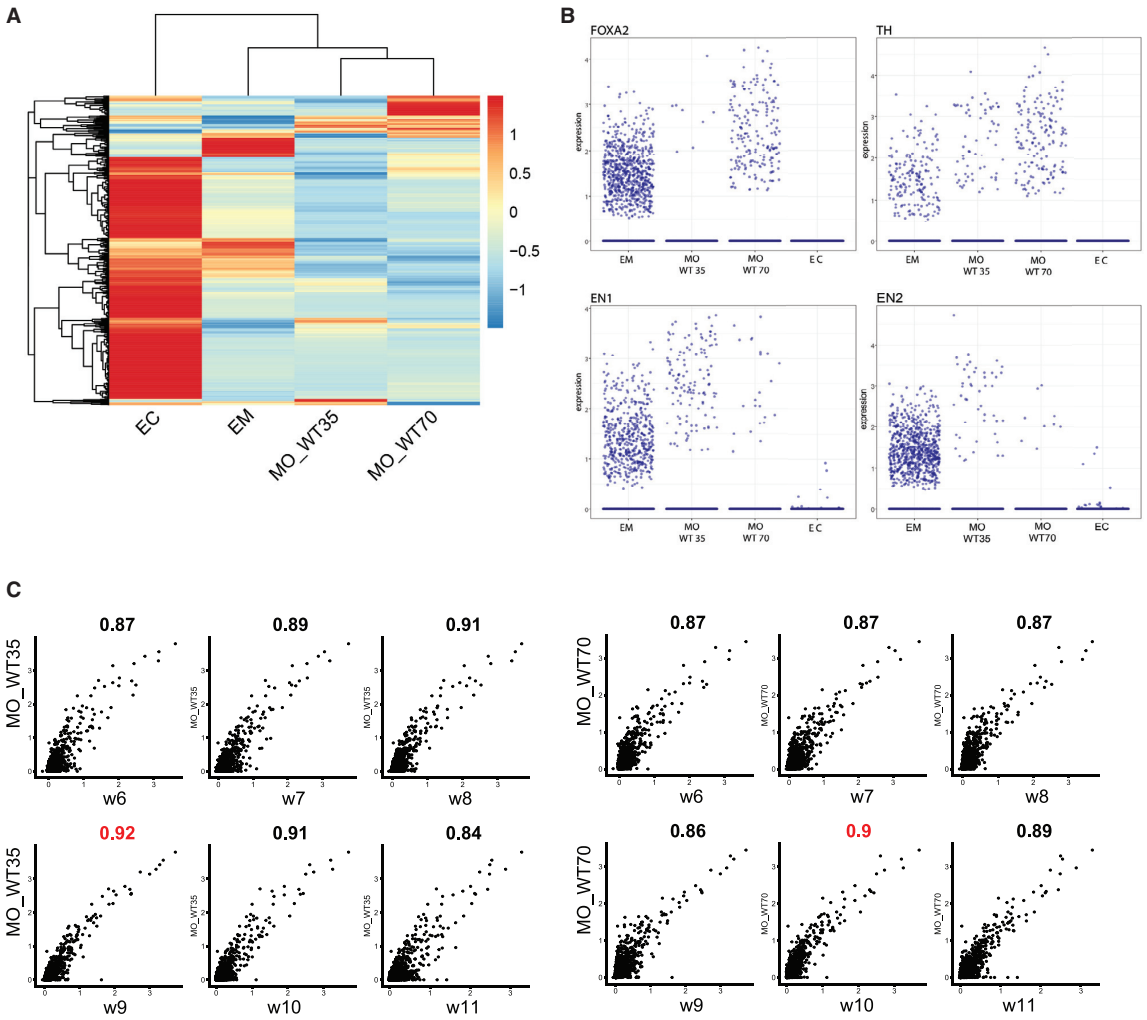

Figure 1. Midbrain organoids show a genetic signature comparable to the embryonic midbrain

(A) The top 1,000 most variable genes of Seurat integrated object of merged scRNA-seq datasets of embryonic cortex (EC), embryonic midbrain (EM), midbrain organoids 35 days of differentiation (MO_WT35), and midbrain organoids 70 days of differentiation (MO_WT70). The average gene expression visualized after *Z* score normalization.

(B) Expression of midbrain markers *FOXA2*, *TH*, *EN1*, and *EN2* in Seurat integrated object of merged scRNA-seq datasets of embryonic cortex (EC), embryonic midbrain (EM), midbrain organoids 35 days of differentiation (MO_WT35), and midbrain organoids 70 days of differentiation (MO_WT70). Each dot represents a single cell.

(C) The average common gene expression correlation between midbrain organoids 35 days of differentiation (MO_WT35) and midbrain organoids 70 days of differentiation (MO_WT70) and embryonic midbrain (EM) developmental weeks (w6–w11). The Pearson correlation coefficient is displayed above each comparison. The highest correlation between midbrain organoids and embryonic developmental time point is highlighted in red. Each dot represents a single cell.

showed a clear separation of the embryonic prefrontal cortex from midbrain organoids and the embryonic midbrain (Figure 1A). This separation indicates the expected greater similarity between midbrain organoids and the embryonic midbrain than the embryonic prefrontal cortex. The following correlation analysis of the average expression of all common genes confirmed that the transcriptome of midbrain organoids is more similar to the embryonic midbrain ($\rho > 0.7$) than to the embryonic prefrontal cortex ($\rho < 0.7$) (Figure S3B). Moreover, the embryonic midbrain and midbrain organoids express typical midbrain markers, such as *TH*, *FOXA2*, *EN1*, and *EN2*, which were absent or expressed at low levels in the embryonic prefrontal cortex (Figure 1B). The expression of TH, FOXA2, and EN1 in midbrain organoids was also validated by immunofluorescence staining (Figure S3C). In addition, we aimed to associate midbrain organoids to different time points in embryonic midbrain development by comparing the expression of the common genes between both datasets. The WT35 midbrain organoids highly correlated with embryonic

week 9 (R = 0.92), while the midbrain organoids WT70 highly correlated with the week 10 (R = 0.90) (Figure 1C). These findings not only suggest that *in-vitro*-derived midbrain organoids show high gene expression similarities with the human embryonic midbrain but also manifest a developmental pattern comparable to their *in vivo* counterpart. In order to further validate the brain regional specificity of the organoids, we compared the scRNA-seq data of the embryonic midbrain to a cortex organoid[29] in the same manner (Figure S3D). The Pearson correlation coefficient of 0.05 showed insignificant correlation between the embryonic midbrain and the cortex organoid, providing evidence that organoids derived from different brain regions exhibit no close transcriptome similarities with the developing embryonic midbrain *in vivo*.

Midbrain organoids inherit physiological-relevant cellular populations that are shared with the developing embryonic midbrain

After confirming that midbrain organoids present a gene expression signature comparable to embryonic midbrain *in vivo*, we used the integration workflow from Seurat[31] to identify shared cellular populations across the *in vivo* and *in vitro* midbrain systems. We integrated the scRNA-seq data of the embryonic midbrain with healthy control and LRRK2-p.Gly2019Ser-mutant midbrain organoids of both differentiation time points 35 and 70 days (WT35, WT70, MUT35, and MUT70, respectively). We identified eight different cell types and visualized them by using UMAP (Figure 2A). To define cellular identities, we used the cell type marker gene list proposed by La Manno and colleagues[25] and compared it to the marker gene list per cluster of the integrated object (Figure S4). We verified each marker expression in every cell cluster identified in the integrated Seurat object. The number of marker genes that were present in the cell populations (corresponding to the cell types defined in La Manno et al., 2016[25]) are shown in Figure S5A. La Manno and colleagues[25] reported the presence of 25 cellular identities in the embryonic midbrain, including several sub-clusters of radial glia, progenitors, and dopaminergic neurons. To simplify cell identification, we grouped all 25 cell identities in more generic cell type clusters, such as neurons (NEURs), neuroblasts (NBs), progenitors, glia, pericytes, and endothelial cells. Neurons were further separated in non-dopaminergic neurons (non-DNs) and dopaminergic neurons (DNs). Cell identities were assigned to cell populations within the integrated Seurat object on the basis of the highest number of marker genes defining each generic cell type (Figure S5A). Once these clusters were broadly defined, using the embryonic midbrain data,[25] we verified and refined the assigned cell identities on the basis of additional cell type and maturity-specific marker expression (Figure 2B, Figure S5B). We confirmed the particularly high expression of neuronal maturity markers[34] and dopaminergic markers[9] in DNs. Therefore, we defined DNs as mature DNs (mDNs). The neuronal cluster presenting lower expression of maturity and neuronal-type-specific marker expression, we defined as young neurons (yNEURs) (Figure S5B). The vast majority of cells in the yNEUR cluster showed a stable expression of young neuronal markers such as *NCAM1*, *STMN1*, and *DCX* (Figure 2B). The mature neuronal marker *MAP2* as well as synaptic genes such as *SYP* and *SYT1* were expressed in the mDN and non-DN clusters. Lastly, expression of the DN markers *TH*, *KCNJ6*, and *NR4A2* as well as of the DN-specific synaptic markers *ROBO1* and *DCC* were confirmed in yNEURs and mDNs. Importantly, midbrain identity markers *FOXA2* and *LMX1A* were expressed in most of the cell types (glia, progenitors, yNEURs, and mDNs). The radial glia marker *SLC1A3* and neural progenitor markers *SOX2* and *MSI1* showed high expression in the glia and progenitor clusters, suggesting that glia cells are rather immature at this stage of embryonic midbrain development and, thus, display a genetic signature of early development in midbrain organoids. However, also more specific glial markers such as *GFAP* and *S100B* were already detectable in some of the cells. Endothelial cell identity was confirmed by the positive expression of the *CDH5*, while pericyte cells showed robust expression of the blood vessel development regulator *CSPG4*. Cells belonging to the NB cluster were positive for neural stem cell marker (*SOX2*) as well as immature (*DCX*) and mature neural *(SYT1*) and DN markers (*TH* and *KCNJ6*). However, none of these markers showed a constantly high expression among all cells in the NB cluster. This suggests that the identity of NBs is rather yet undefined and might be a specific feature of *in vitro* cultures, with the potential to develop into more mature neural cell types over time.

Further, we visualized UMAP embeddings of cell types and split them by datasets to reveal common and distinct cell types across embryonic midbrain and midbrain organoids (Figure 2C). Clusters of progenitors, yNEURs, mDNs, non-DNs, and glia were present in the embryonic midbrain as well as midbrain organoids, demonstrating that most cell types are common between the *in vitro* and *in vivo* midbrain systems. We observed that the NB cluster was present mainly in midbrain organoids and not in the embryonic midbrain and therefore was called NBs *in vitro*. Pericytes were found in midbrain organoids and the embryonic midbrain, however more mature endothelial cells were only present in the embryonic midbrain.

Next, we investigated the most variable gene expression pattern between the defined cell types (Figure 2D). The top 100 most variable genes led to a clustering of yNEURS, mDNs, non-DNs, and NBs together, confirming the common neuronal expression profile of these cell types. Pericytes and endothelial cells showed rather distinct genetic signature, consistent with the fact that these cells have non-neuronal identity. Glia and progenitors formed another separate cluster with a similar transcriptomic profile, implying again an early developmental stage of the glial cells.

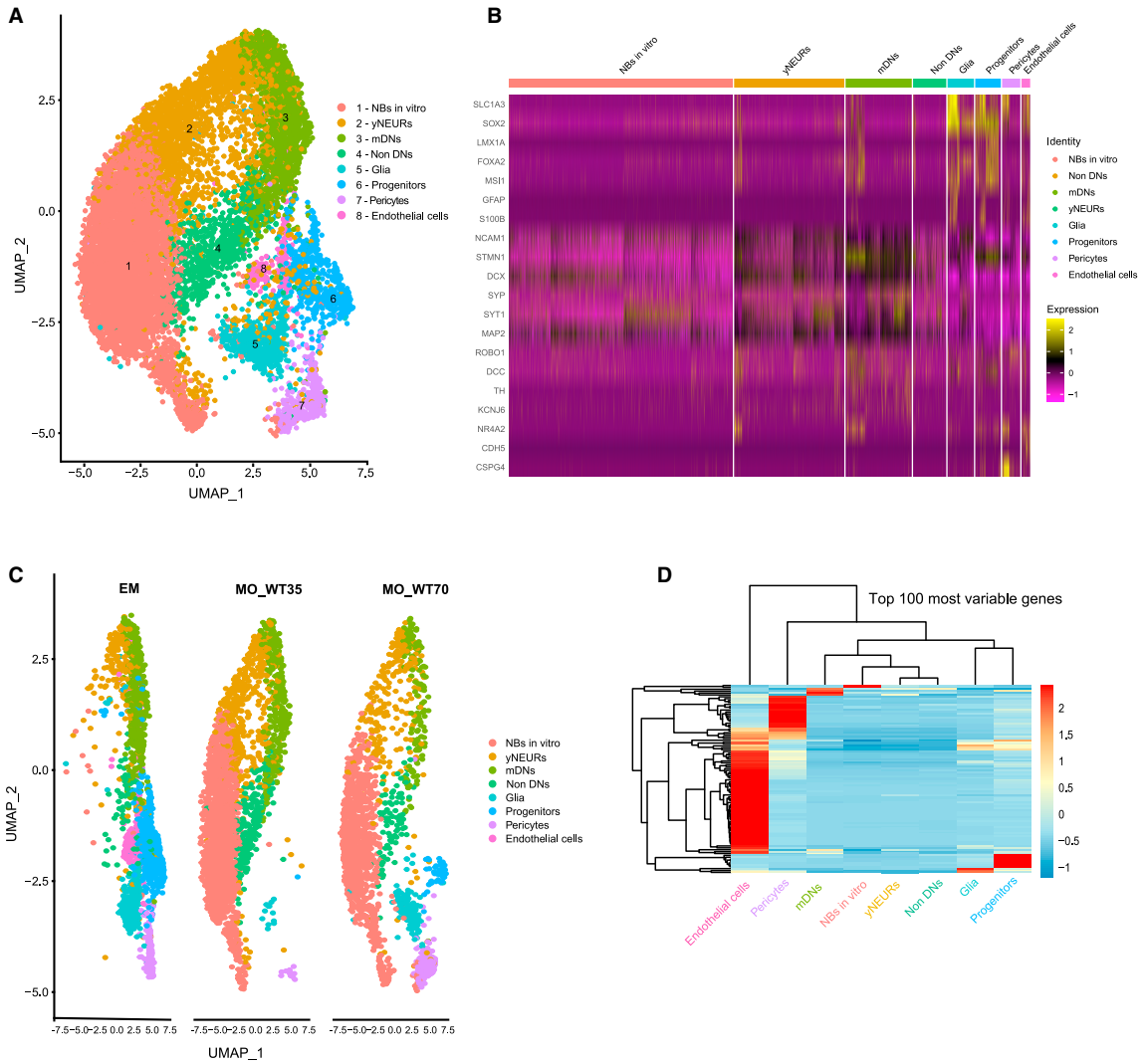

Figure 2. Midbrain organoids inherit physiological-relevant cellular populations that are shared with the developing embryonic midbrain

(A) UMAP of integrated Seurat object of merged scRNA-seq datasets of embryonic midbrain, and WT and MUT midbrain organoids 35 and 70 days of differentiation, showing cell clusters 1–8, after manual correction of oversampling. Each dot represents a single cell and is colored according to the cell identity.

(B) Identity heatmap showing cell-type-specific marker expression in identified cell clusters.

(C) UMAP of cell clusters in embryonic midbrain (EM), WT midbrain organoids of 35 days of differentiation (MO_WT35), and 70 days of differentiation (MO_WT70). Each dot represents a single cell and is colored according to the cell identity.

(D) Unsupervised hierarchical clustering of cell types, using the average expression of the top 100 most variable genes, visualized after *Z* score normalization.

Differential gene expression analysis reveals a *LRRK2*-related PD phenotype in the mutant midbrain organoids

Further, we assessed the potential of midbrain organoids in disease modeling by comparing the transcriptomic signature of the midbrain organoids derived from the healthy control where the LRRK2 p.Gly2019Ser variant was inserted with the isogenic WT counterpart.[27] As with the WT midbrain scRNA-seq data, we analyzed MUT midbrain organoid scRNA-seq data from organoids sampled at day 35 and day 70 of differentiation. We verified *LRRK2* expression in midbrain organoids and observed that it is expressed in a larger proportion of cells at later time points in both WT and MUT midbrain organoids (Figure S6A). In order to identify the key differences in the transcriptomic signature between MUT midbrain organoids and WT midbrain organoids, we computed the DEGs across both time points and all cell types with subsequent pathway enrichment analysis. The combined enrichment analysis of DEGs of both time

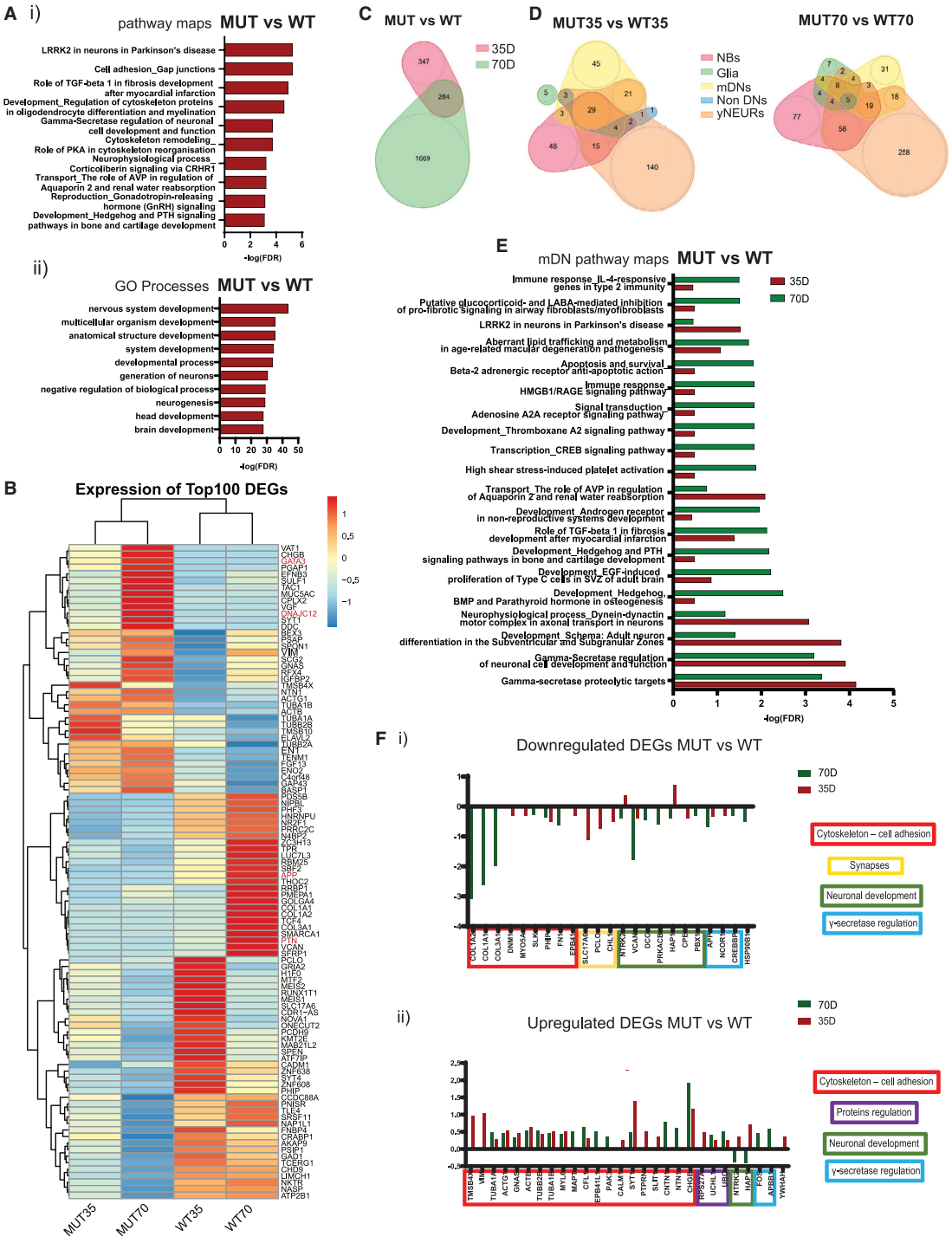

Figure 3. LRRK2-p.Gly2019Ser-mutant midbrain organoids recapitulate PD-associated pathways

(A) Pathway maps (i) and GO processes (ii) of the enrichment analysis of 294 DEG (p adj. value < 0.05) between MUT and WT midbrain organoids.

(B) Heatmap of to 100 DEG (p adj. value < 0.05) between MUT and WT midbrain organoids. Genes highlighted in red are the potential LRRK2 p.Gly2019Ser target genes involved in the neurodevelopment (see also Figure 6)

(legend continued on next page)

points showed the most significant enrichment in the pathway of LRRK2 role in neurons in PD (Figure 3Ai). Moreover, other pathways associated with *LRRK2*, such as cytoskeleton regulation and cell adhesion, were also enriched in the MUT midbrain organoids. In addition, we found a significant DEG enrichment in protein kinase cAMP-dependent signaling and the γ-secretase regulation pathway. We identified that the most significant Gene Ontology (GO) and network processes were related to the neuronal development and axonal guidance (Figure 3Aii, Figure S6Bi). Furthermore, the most enriched diseases were linked to the brain and nervous system, confirming a diseased state of MUT midbrain organoids (Figure S6Bii). Last, the top 100 DEGs (adj. p value < 0.05) clustered MUT midbrain organoids separately from the WT midbrain organoids for both time points, confirming that LRRK2 p.Gly2019Ser induced changes in gene expression (Figure 3B). Interestingly, in the WT midbrain organoids, the expression levels of the DEGs differ between the two time points of differentiation, while in the MUT35 and MUT70 midbrain organoids, DEGs showed very similar expression patterns, indicating a potential developmental impairment of MUT organoids. Similarly, the top 100 DEGs separated the majority of different cell types of the MUT midbrain organoids from the WT midbrain organoids for both time points (Figure S5C), indicating that the presence of the *LRRK2* variant is responsible for gene expression changes in all cell types in at least one of the time points. However, the pathway enrichment analysis combined for all cell types showed a higher significance in the enrichment of cytoskeleton remodeling, γ-secretase regulation, and LRRK2-related pathways for day 70, suggesting a stronger manifestation of the LRRK2-p.Gly2019Ser-associated changes overtime (Figure S6D). In support of that, we identified in total 347 DEGs (adj. p value < 0.05) at day 35 and 1,669 DEGs (adj. p value < 0.05) at day 70 between the MUT and WT midbrain organoids. 264 DEGs were common between both time points (Figure 3C). Next, we overlapped all DEGs (adj. p value < 0.05) between cell types and saw that the highest number of DEGs at both time points were present in NBs *in vitro*, yNEURs, and mDNs (Figure 3D, Figure S7A). Pathway enrichment analysis identified that the cytoskeleton-regulation-related pathways were significant in the MUT35 and MUT70 midbrain organoids in all three respective cell types, while LRRK2-PD-related pathway occurred to be highly significant in NBs *in vitro*. (Figure 3E, Figure S7Bi). In mDNs and yNEURs, the γ-secretase and neurodevelopmental regulation pathways were identified as the most enriched for both time points (Figure 3E, Figure S6Bii), additionally indicating a possible link between LRRK2 p.Gly2019Ser and γ-secretase function.

In order to investigate the gene expression profiles between the MUT and WT midbrain organoids in more detail, we visualized the fold changes of the genes involved in the most significantly enriched pathways (Figures 3Fi and 3Fii). Genes related to cytoskeleton dysregulations, such as *COL1A2*, *COL1A1*, *COL3A1*, *DNM1*, *MYO5A*, *PHIP*, *SLK*, *FN1*, and *EPB41*, were found to be downregulated with a log2FC between −0.26 and −3, while others, such as *TMSB4X*, *VIM*, *TUBA1A*, *ACTG1*, *GNAS*, *TUBB2B*, *TUBA1B*, *MYL6*, *MAPT*, *CFL1*, *EPB41L1*, *PAK3*, *CALM1*, *SYT1*, *PTPRN*, *SLIT1*, *CNTN1*, *NTN1*, and *CHGB*, were found upregulated (log2FC between 0.26 and 1.93) in MUT midbrain organoids at the majority of both time points. Synapses-related genes, such as *SLC17A6*, *PCLO*, and *CHL1*, were particularly downregulated (log2FC between −0.5 and −1.12) in MUT35 midbrain organoids, but they were not differentially expressed in MUT70 midbrain organoids. Genes that are associated with neuronal development, such as *NTRK2*, *VCAN*, *DCC*, *PRKACB*, *HAP1*, *CPE*, and *PBX1*, were also dysregulated in MUT midbrain organoids. The majority of them were downregulated (log2FC between −0.38 and −1.77) in MUT70 midbrain organoids, while *NTRK2* and *HAP1* were upregulated (log2FC 0.36 and 0.72, respectively) in MUT35 midbrain organoids. Protein regulation-associated genes, such as *RPS27A*, *UCHL1*, and *UBC*, were upregulated (log2FC between 0.25 and 0.52) at both time points. Additionally, genes that are related to the γ-secretase regulation pathway, such as *APP*, *NCOR1*, and *CREBBP*, were downregulated (log2FC between −0.31 and −0.68) in MUT35 and MUT70 midbrain organoids, but *FOS* and *APBB1* were upregulated (log2FC 0.47 and 0.59, respectively), particularly in MUT70 midbrain organoids. We also observed a dysregulation of *HSP90B1*, which was downregulated (log2FC −0.51) at MUT70 midbrain organoids and *YWHAH* showing upregulation (log2FC 0.36) in MUT35 midbrain organoids. These genes encode HSP90B1 and 14-3-3 family proteins, respectively, known as direct interacting partners with LRRK2.

Mutant midbrain organoids have a distinct cellular composition and correlate differently with the stages of embryonic development

We observed that MUT midbrain organoids differ from WT midbrain organoids in their cellular composition. In the UMAP embedding plot split by models and colored by cell types (Figure S8A), we saw that progenitors and pericytes, which are shared cellular populations between WT midbrain organoids and embryonic midbrain, are not present in MUT

(C) Venn diagram, showing the number of DEGs between MUT and WT midbrain organoids found at 35 days and 70 days of differentiation (p adj. value < 0.05).
(D) Venn diagrams, showing the number of DEGs found in each cell type between MUT and WT midbrain organoids fat 35 days and 70 days (p adj. value < 0.05).
(E) Mature DN pathway processes enrichment based on the DEGs identified in mDNs between MUT and WT midbrain organoids (p adj. value < 0.05).
(F) Fold changes of genes selected from the top enriched pathways dysregulated in mDNs.

midbrain organoids at any time point. On the contrary, we observed that the glia population is more enriched in MUT35 than in WT35 midbrain organoids. To confirm our observations, we subset the integrated Seurat object by the respective cell clusters and plotted them separately in the embryonic midbrain and in the WT as well as in the MUT midbrain organoids for both time points (Figure 4A). We saw that pericytes positive for the endothelial lineage marker *MCAM* and for the major regulator of angiogenic events, *SPARC*, are highly represented in WT70 midbrain organoids and in the embryonic midbrain but not in MUT midbrain organoids. Similarly, progenitors positive for the G2-proliferation-associated *CENPF* marker were only detected in the embryonic midbrain and WT70 midbrain organoids. A higher number of glia cells expressing *VIM* were already detected in MUT35 midbrain organoids compared to WT35 midbrain organoids. However, an increase of glia over time is more evident in WT than in MUT midbrain organoids.

Next, we calculated the proportion of each cell type present in WT and MUT midbrain organoids at both time points (Figure 4B). We saw a reduction of NBs *in vitro* (62%→51%) and yNEURs (17%→12%) from WT35 to the WT70. This reduction of less mature cells in WT35 midbrain organoids resulted in an increased variety of cell types present in WT70 midbrain organoids. Moreover, the cellular profile of WT70 midbrain organoids was quite similar to the cellular diversity observed in embryonic midbrain (Figure S8B). The major difference here was a high percentage of progenitors in the embryonic midbrain that seemed to be replaced by the presence of NBs *in vitro* in WT70 midbrain organoids.

Contrary to the WT midbrain organoids, in the MUT midbrain organoids, there was no evident difference in cell-type evolution over time. The same cell types were present in the MUT35 and MUT70 midbrain organoids, besides the fact that NBs *in vitro* almost doubled over time. Furthermore, the average gene expression correlation between MUT midbrain organoids and embryonic midbrain developmental time points showed that MUT35 midbrain organoids correlated better with embryonic development for all time points, compared to WT35 midbrain organoids (Figure 1C, Figure 4C). On the other hand, MUT70 midbrain organoids had a weaker correlation with the embryonic midbrain than the WT70 midbrain organoids, especially for week 11, which is also the latest and therefore most mature time point (R WT = 0.89 versus R MUT = 0.83). All together, these finding suggest that MUT midbrain organoids have a different developmental path compared to WT midbrain organoids and embryonic midbrain.

To further investigate the developmental differences between the MUT and WT midbrain organoids, we computed pseudotime trajectories to explore pseudotemporal ordering of midbrain organoid cell populations compared to the embryonic midbrain developmental time points. As the root, we chose WT35 NBs *in vitro* and we visualized the trajectories in UMAP plots colored by cell types and developmental time points of midbrain organoids and embryonic midbrain (Figures 4Di and 4Dii). We observed that mDNs of WT35 midbrain organoids are placed closer to embryonic developmental week 9 (branch point 2 and red circle 1 in Figure 4Dii), while mDNs of WT70 midbrain organoids were closer to embryonic developmental week 10 (branch point 2 and red circle 2 in Figure 4Dii), which is consistent with the gene average expression correlation analysis between WT midbrain organoids and embryonic midbrain. In clear contrast to this, we observed that mDNs of MUT35 and MUT70 midbrain organoids are placed closely to each other and formed a separate branch (branch point 3 to the endpoint 3 in Figure 4Di), which did not align with the embryonic midbrain trajectory. Further, we observed that glia cells of MUT70 and WT70 midbrain organoids (endpoint 2 and endpoint 8 in Figure 4Di) were arranged in close proximity to embryonic week 11 (endpoint 2 in Figure 4Dii), presenting appropriate developmental pattern, where gliogenesis follows neurogenesis. The similar distribution of MUT and WT glia within the pseudotemporal space indicates that the previously observed stagnation in glial development is linked to its number and not its quality. In general, the cells of MUT70 midbrain organoids were placed further from the embryonic developmental trajectory in the UMAP plot than the cells of WT70 midbrain organoids. This indicates that MUT midbrain organoids manifest a developmental deviation, while the development of WT midbrain organoids is more similar to embryonic midbrain *in vivo*. Moreover, MUT70 midbrain organoids demonstrated a more cyclic trajectory, confirming a limited cellular developmental path that is resulting in less variable cellular identities.

Mutant midbrain organoids compared to wild-type midbrain organoids show impaired pseudotemporal development that manifests in an untimely and incomplete differentiation

In order to further explore the developmental deviation of the MUT midbrain organoids from WT midbrain organoids, we computed a developmental pseudotime trajectory only across midbrain organoids (WT35, WT70, MUT35, and MUT70), excluding the embryonic midbrain. The cell distribution along the trajectory starting from NBs *in vitro* of WT35, demonstrated accelerated differentiation of MUT35 midbrain organoids with subsequent developmental withhold (Figure 5A). We observed that mDNs might be the most affected cellular population. We saw that mDNs of WT midbrain organoids follow a differentiation path along the pseudotime trajectory from WT35 to the edge of WT70 midbrain organoids (endpoint 4 to 9). Contrary, mDNs of MUT35 midbrain organoids were located in close proximity to mDNs of MUT70 midbrain organoids (between endpoints 1 and 6), implying the impaired mDN maturation. In addition, glia cells of MUT35 midbrain organoids were located close to the WT70 midbrain organoids on the pseudotime trajectory (between branch points 7 and 8), confirming forwarded glia differentiation of MUT35 midbrain organoids.

Next, we computed genes with a clear expression switch across the developmental trajectory between WT35 and

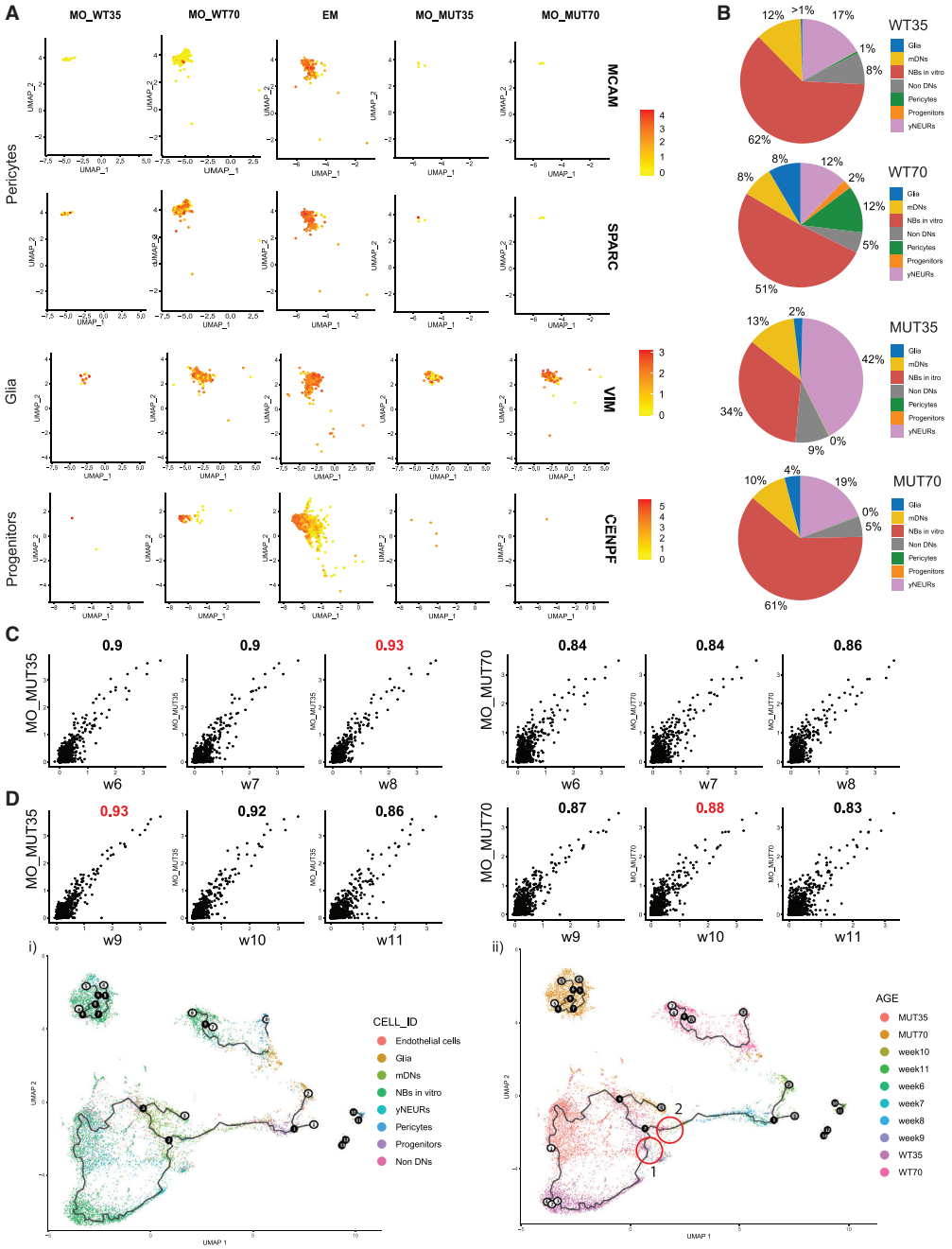

Figure 4. LRRK2-p.Gly2019Ser-mutant midbrain organoids have a different cellular composition and correlate differently with the stages of embryonic midbrain development

(A) Cell cluster identities defined by typical marker expression between WT and MUT midbrain organoids for pericytes, glia, and progenitor cells. Each dot represents a single cell and is colored according to the expression level.

(B) Percentage of cell identities in WT35, WT70, MUT35, and MUT70 midbrain organoids.

(C) The average gene expression correlation between MUT midbrain organoids 35 days of differentiation (MO_MUT35) and 70 days of differentiation (MO_MUT70) compared to the embryonic midbrain (EM) developmental weeks (w6–w11). The Pearson correlation coefficient is displayed above each comparison. Each dot represents a single cell.

(D) Batch-corrected pseudotime analysis based on the 150 dimensions. Each dot represents a single cell. The starting point is WT35 NBs *in vitro*. Cell distribution along the trajectory colored by cell identities (i) and by datasets (ii). Black nodes define branchpoints of the trajectory, white nodes define trajectory graph nodes, and gray nodes define endpoints of the certain trajectory leaf. Red circles indicate the position of mDNs of WT35 and WT70 midbrain organoids.

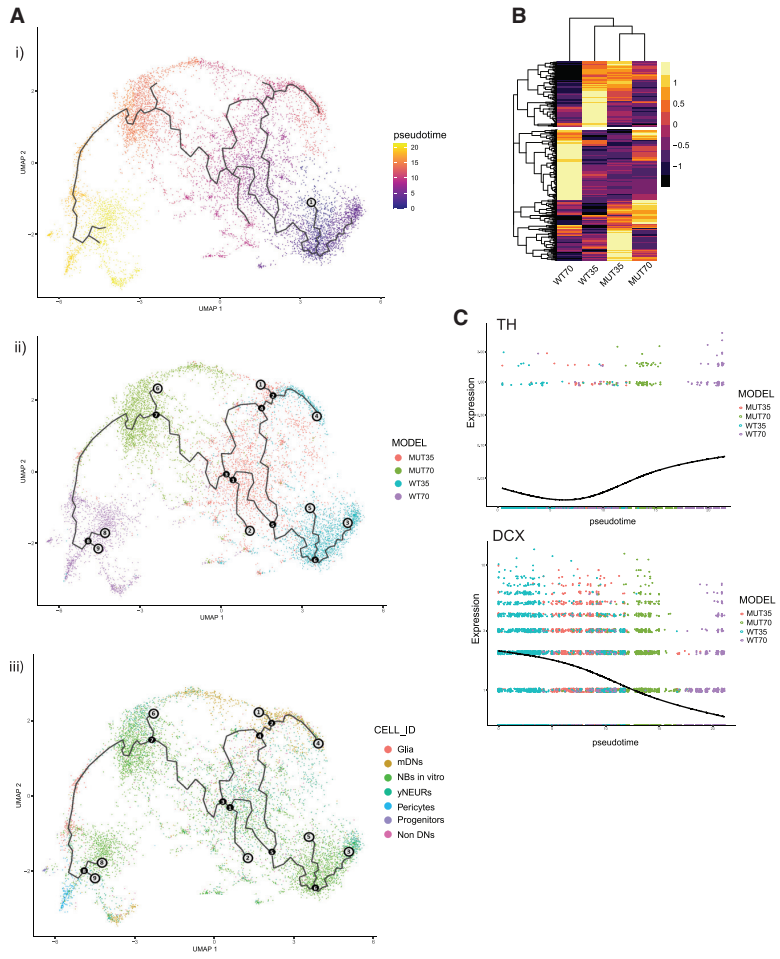

Figure 5. Transcriptome signatures over time reveal impaired development of LRRK2-p.Gly2019Ser-mutant midbrain organoids

(A) Pseudotime analysis of midbrain organoids with the root node WT35 NBs *in vitro* (i). Pseudotime trajectory, cells colored by the model: WT35, WT70, MUT35, and MUT70 (ii). Pseudotime trajectory, cells colored by cell identity (iii). Black nodes define branchpoints of the trajectory and gray nodes define endpoints/outcomes of the certain trajectory leaf.

(B) Genes with fitted expression pattern along the trajectory between WT35 and WT70 midbrain organoids, visualized in heatmap after *Z* score normalization in WT and MUT organoids.

(C) Pseudotemporal expression of *TH* and *DCX* across the cells in WT and MUT midbrain organoids. Each dot represents a single cell.

WT70 midbrain organoids (Figure 5B, Figure S8C). We investigated whether the same genes that have a temporal dynamic expression pattern in WT midbrain organoids show similar expression tendency in MUT midbrain organoids (Figure 5B). We observed that MUT midbrain organoids presented a completely different expression of the same genes, suggesting that MUT midbrain organoids do not follow the same developmental process as WT midbrain organoids. Furthermore, we highlighted the temporal expression of the rate-limiting enzyme of dopamine synthesis, tyrosine hydroxylase (*TH*), and the developing neuronal marker doublecortin (*DCX*). *TH* expression showed an increase over time in WT midbrain organoids but was impaired in the MUT midbrain organoids at both time points. *DCX* showed a clear decrease in the expression between WT35 and WT70 midbrain organoids. While in MUT35 midbrain organoids its expression was already further declined, it was still expressed at MUT70 midbrain organoids, further supporting an accelerated differentiation in MUT midbrain organoids at early time points of development accompanied by an incomplete differentiation at later developmental stages.

These results imply that mutant midbrain organoids reach a deadlock at some point during development.

Identification of potential LRRK2 p.Gly2019Ser target genes that could underlie impaired neurodevelopment and contribute to explain the PD-associated genetic signature

On the basis of the DEG analysis and after pseudotime trajectory examination, we distinguished four potentially promising candidate genes that have already been associated with PD[35–40]—*DNAJC12*, *GATA3*, *PTN*, and *APP* (Figure 3B). These genes showed a temporal dynamic expression in the developing embryo and were significantly differentially expressed in MUT midbrain organoids compared to WT midbrain organoids. Their considerable change in expression during embryonic development indicates an active role in neurodevelopment (Figure 6A). Moreover, differential expression between MUT and WT midbrain organoids further supports altered MUT midbrain organoid neurodevelopment. *DNAJC12* and *GATA3* showed a significant upregulation in every neuronal cell type and glia in MUT midbrain organoids compared to WT midbrain organoids in both time points (Figures 6B and 6C). In addition, in MUT organoids, *DNAJC12* and *GATA3* expression increased over time in contrast to the embryonic midbrain where the expression decreased after peaking at week 9. In the neuronal clusters of WT midbrain organoids, the expression pattern of these two genes was comparable to embryonic development, showing highest expression levels at 35 days (corresponding to week 9). In contrast, *PTN* and *APP* were found to be significantly downregulated

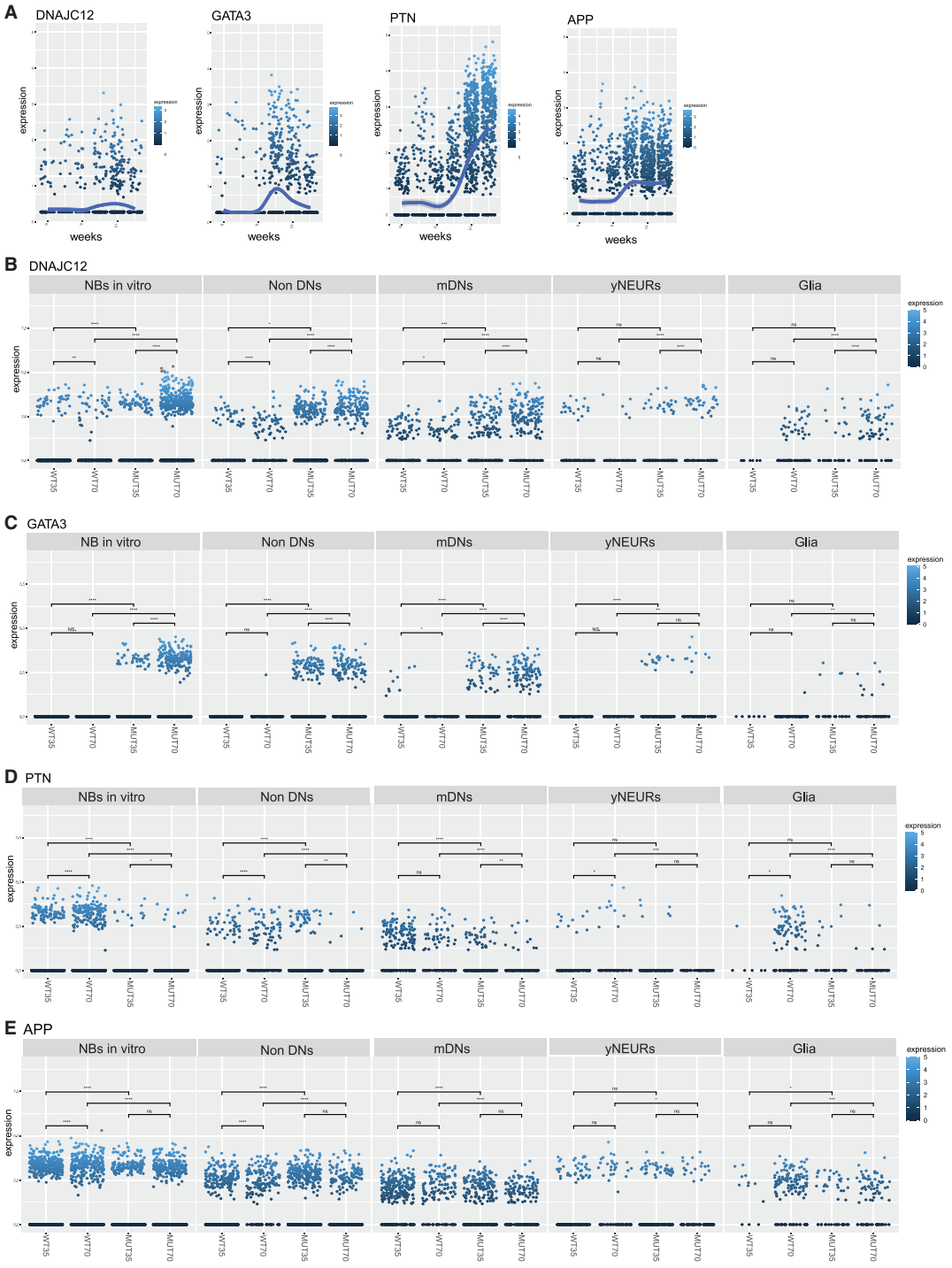

Figure 6. Discovery of potential LRRK2 p.Gly2019Ser target genes that might be involved in impaired neurodevelopment of mutant midbrain organoids

(A) *DNAJC12*, *GATA3*, *PTN*, and *APP* expression profile over the embryonic development time points (w6–w11). Each dot represents a single cell of embryonic midbrain and is colored according to the expression level.

(legend continued on next page)

in MUT midbrain organoid neuronal cell types and glia compared to WT midbrain organoids (Figures 6D and 6E). We observed that both *PTN* and *APP* expression tended to increase over time in embryonic midbrain development. A similar expression pattern was observed in NBs *in vitro*, yNEURs, and glia of WT midbrain organoid but not in MUT midbrain organoids. These results highlight a dysregulation of genes with essential roles in neuronal development and neuroprotection that might be directly associated with the LRRK2 p.Gly2019Ser variant, linking *LRRK2* to the regulation of nigrostriatal system development.

Discussion

Our analysis of scRNA-seq data of human midbrain organoids and embryonic midbrain highlights the physiological relevance of midbrain organoids and their potential in disease modeling. Over the recent years, midbrain organoids have become a widely used model in PD studies, as the midbrain is the most affected region in the brain of PD patients.[9,20,23,41,42] In the present study, we were able to show the developmental correlation of healthy control-derived midbrain organoids from 35 and 70 days of culture[9] with human embryonic midbrain.[25] Importantly, midbrain organoids showed a higher degree of correlation with embryonic midbrain development than with the embryonic prefrontal cortex, validating the midbrain identity of the organoids. In support of this, we did not find a significant correlation between the cortex organoids[29] and embryonic midbrain, which further validates the specificity of the brain regional organoids. In addition, our analysis implicates developmental maturation of midbrain organoids after long time culture (e.g., 70 days), which showed a better correlation with the later stages of embryonic midbrain development.

Previous studies have demonstrated the cellular heterogeneity of human brain organoids and their similarities with their fetal counterparts.[43,44] Similarly, our analysis showed that midbrain organoids exhibit a shared cellular composition with the developing embryonic midbrain. One interesting finding is the identification of pericytes in midbrain organoids. It has been reported that pericytes can originate from the neuroectoderm and contribute to the formation of vasculature in the CNS.[45–47] The presence of mesenchymal cells was also originally reported by Smits et al., 2020.[26] Moreover, recent studies showed that a mesenchymal-like cell population appears in the early development of the cortex, even before the beginning of neurogenesis.[48] Nevertheless, because the cells in midbrain organoids are guided toward midbrain identity by the expansion of the neuroepithelium, the presence of more mature endothelial cells is not expected. Accordingly, the endothelial cell cluster was found only in the embryonic midbrain and not in midbrain organoids. In contrast, the NB *in vitro* cluster was almost uniquely present in the midbrain organoids. Although these cells did not show a significant variable gene expression profile and clustered with neuronal cell types, there was no expression of reliable marker genes. Due to their unclear gene expression profile, NBs *in vitro* seemed to be less comparable to the physiological cell types shared between midbrain organoids and embryonic midbrain. We speculate that this NB cluster represents mfNPCs, which is the starting cell population for midbrain organoid generation. Although these cells are artificially patterned toward midbrain identity[49] and show unspecific genetic identity,[50] they can give rise to multiple physiologically relevant neuronal cell types and glia, similar to their *in vivo* neural progenitor counterpart.

When comparing MUT to WT midbrain organoids, clear differences become visible regarding their cellular composition, revealing PD-associated phenotypic differences. The MUT midbrain organoids reveal a faster differentiation profile that limits the development of a more variable and mature cellular composition. The accelerated differentiation phenotype at 35 days that we observed with pseudotime analysis has been described before in *LRRK2*-related PD.[8–10] In addition, the MUT midbrain organoids have no evident differences in the cell type populations at both time points and pseudotime analysis revealed that besides the untimely differentiation, the MUT70 midbrain organoids face a premature arrest or slowdown of the differentiation capacity. Importantly, the mDNs were the most affected population of cells. They showed no indication of maturation along the trajectory in the MUT70 compared to the MUT35 midbrain organoids and had a reduced expression of TH in MUT midbrain organoids. The doubling of the number of NBs *in vitro* in MUT70 midbrain organoids might be a compensation strategy linked to the incapacity of terminal differentiation or an increase in mature cell death. Moreover, we observed that the MUT midbrain organoids contain a higher number of glial cells than WT midbrain organoids at early time points. A situation that is inverted in longer cultures (MUT70 and WT70). The pseudotime trajectory confirmed that glial cells of MUT35 midbrain organoids were located closer to the WT70 midbrain organoids, indicating a faster gliogenesis. Finally, and most importantly, in contrast to MUT midbrain organoids, WT midbrain organoids from longer cultures are capable of capturing the cellular diversity found in human embryonic midbrain development *in vivo*.

Regarding the developmental pattern of organoids and embryonal tissue, MUT midbrain organoids showed a different developmental path compared to WT midbrain

(B–E) *DNAJC12*, *GATA3*, *PTN*, and *APP* expression across major cell types in WT and MUT midbrain organoids at 35 days and 70 days of differentiation. Each dot represents a single cell of midbrain organoid and is colored according to the expression level. Kruskal-Wallis test $p < 0.05$*, $p < 0.01$**, $p < 0.001$***, $p < 0.00001$***.

organoids. From the correlation analysis, we saw that the MUT70 midbrain organoids have lower correlation than MUT35 midbrain organoids with the different time points of embryonic midbrain development. Furthermore, cells of MUT70 midbrain organoids were positioned further away from the embryonic pseudotemporal developmental trajectory in the UMAP plot, while cells of WT70 midbrain organoids have a development trail closer to embryonic development.

On the basis of the here-presented data, we propose that LRRK2 p.Gly2019Ser could be responsible for the observed developmental defects and the impaired cellular composition. Our *LRRK2* midbrain organoid model was able to capture the dysregulation of gene expression linked to *LRRK2*-induced PD. The analysis of DEGs between MUT and WT midbrain organoids showed the significance of LRRK2-related pathway in PD and highlighted GO processes related to nervous system development. In addition to individual gene dysregulation of LRRK2-associated pathways, the overall DEG analysis showed a clear separation of the MUT and WT midbrain organoid clusters, confirming the presence of disease-associated phenotypes.

The major dysregulated pathways were cytoskeleton remodeling and cell adhesion. It is well known that LRRK2 plays an important role in actin and microtubule dynamics. LRRK2 p.Gly2019Ser has been reported to disturb the cytoskeleton processes through increased kinase activity.[51,52] The dysregulation of actin and microtubule genes, which are key components of cytoskeleton dynamics, may lead to failure of the proper cellular differentiation process.[26] Cytoskeleton-related proteins, such as MYO5A, DNM1, EPB41, ACTB, MAPT, and VIM, are direct interacting partners of LRRK2.[53] We found that the corresponding genes have a dysregulated expression in the MUT midbrain organoids, indicating that altered LRRK2 function is able to impair the gene expression profile of its interactome. Altered LRRK2 function has also been described to have a role in impaired synaptogenesis.[51,54,55] Here, we identified significant downregulation of the synapse-related genes *SLC17A6*, *PCLO*, and *CHL1* specifically in MUT35 but not in MUT70 midbrain organoids. This observation suggests an impaired synaptogenesis occurring in early neurodevelopment of MUT midbrain organoids.

Further, direct LRRK2-interacting partners such as HSP90B1 and YWHAH have also been altered upon presence of the LRRK2 p.Gly2019Ser. HSP90B1 along with the other heat-shock proteins is involved in protein folding and has been linked to PD.[56] HSP90B1 is a chaperone protein from the HSP90 family that interacts with LRRK2. This interaction is important for the proteasomal degradation of LRRK2.[57] Thus, the downregulation of *HSP90B1* in MUT70 midbrain organoids could be linked to the toxic aggregation of mutant LRRK2. *YWHAH* encodes the 14-3-3 eta, known to regulate the activity of kinases, including LRRK2.[58]

Additionally, we identified dysregulation of genes related to the γ-secretase pathway. APP belongs to this pathway and shows a severe dysregulation in MUT midbrain organoid. *APP* encodes the β-amyloid precursor protein that has an important role in the development of neurodegenerative pathologies such as Alzheimer disease because of the accumulation of its derivative amyloid-beta (Aβ) peptide, which is induced by cleavage from secretases including the γ-secretase.[59,60] A link between Aβ accumulation and LRRK2 p.Gly2019Ser PD cases has also been made. LRRK2 phosphorylates the intracellular domain (AICD) of APP, which regulates the transcription of cytoskeleton-related genes and has a role in the loss of dopaminergic neurons in the midbrain of PD cases by induced neurotoxicity.[61] APP has also an important role in neurogenesis, gliogenesis, and neuroprotection in the developing brain.[35,60,62] Therefore, dysregulation of *APP* can be associated not only with the neurodegeneration but also with the aberrations of neuronal development. Indeed, during embryonic midbrain development, we observed a strong increase of *APP* expression over time, whereas in MUT midbrain organoids, we observed a significant reduction compared to WT midbrain organoids, especially in mDNs and glia cells.

Further evidence of altered cellular development of MUT midbrain organoids comes also from the changed expression of three PD-associated DEG candidates, *DNAJC12*, *GATA3*, and *PTN*. The expression pattern of these genes in the embryonic midbrain suggests their important role in development and differentiation of the cells, although these findings would benefit from further experimental validation. DNAJC12 is described to have a role in protein folding and export. Bi-allelic mutations of *DNAJC12* have been associated with hyperphenylalaninemia and neurodevelopmental delay in children. However, recent findings link mutation in *DNAJC12* to early-onset PD because of its interaction with aromatic amino-acid hydroxylases, including TH.[37,63] GATA3 has been described as an important regulator of CNS development and neuronal fate.[36] An association with PD has been reported via GATA family transcriptional regulation of *TRPM2* and *SNCA*.[38,64] Until now, there is no reported interaction of GATA3 and DNAJC12 with LRRK2. However, the notable upregulation of *GATA3* and *DNAJC12* in MUT midbrain organoids suggests their possible dysregulation due to LRRK2 p.Gly2019Ser and might explain the accelerated differentiation phenotype, subsequent maturation decline, and decreased expression of *TH*. In contrast, we observed that *PTN* is expressed significantly higher in WT midbrain organoids. PTN is a neurotrophic factor, highly expressed during development of nigrostriatal dopamine system, and later plays a role in cellular recovery and repair.[39,40] It has been shown to restore neuronal survival and functionality in a 6-OHDA mouse model.[39] The high expression of *PTN* in NBs *in vitro* of WT midbrain organoids may explain their better developmental trail compared to MUT midbrain organoids.

In summary, we demonstrated a high degree of transcriptome similarity between human midbrain organoids and embryonic midbrain, supporting the potential of midbrain

organoids to recapitulate human brain physiology. Moreover, our study showed the ability of midbrain organoids to capture LRRK2-p.Gly2019Ser-dependent alterations in gene expression, which highlights cellular processes related to cytoskeleton regulation, cell adhesion, and γ-secretase regulation during neuronal development. Finally, we observed developmental aberrations in MUT midbrain organoids and altered gene expression patterns along pseudotemporal trajectories, supporting a neurodevelopmental component in LRRK2-p.Gly2019Ser-associated PD.

Data and code availability

WT midbrain organoid scRNA-seq datasets are available at the following doi: https://doi.org/10.17881/lcsb.20190326.01. LRRK2-G2019S MUT midbrain organoid scRNA-seq datasets are available at the following doi: https://doi.org/10.17881/rc4f-nk07. The accession number for the raw data for WT and MUT midbrain organoids is GEO: GSE133894. The accession number for the raw data for the human embryo ventral midbrain between 6 and 11 weeks is GEO: GSE76381. The accession number for the raw data for scRNA-seq data of prefrontal cortex at developmental stages between gestational weeks 8 and 26 is GEO: GSE104276. The accession number for the raw data for scRNA-seq data of human cortical organoids is GEO: GSE130238. We used data only of 1-month-old cortical organoid, which better corresponds to the developmental stage of midbrain organoids. Data were analyzed with R version 3.6.2 with single-cell analysis toolkit Seurat version 3.2.0[31,65,66] and Monocle 3.[67] All scripts used for the analysis are available via GitHub: https://github.com/LCSB-DVB.

Supplemental information

Supplemental information can be found online at https://doi.org/10.1016/j.ajhg.2021.12.009.

Acknowledgments

This work was supported by the National Centre of Excellence in Research on Parkinson Disease (NCER-PD), which is funded by the Luxembourg National Research Fund (FNR/NCER13/BM/11264123). S.S. is supported by the FNR-funded doctoral training program PARK-QC (PRIDE17/12244779/PARK-QC). L.M.S. was supported by a fellowship from the FNR (AFR, Aides à la Formation-Recherche). A.G. received funding from the FNR within the framework of the ATTRACT (FNR9631103) and INTER (INTER/DFG/19/14429377) programs. Additionally, we would like to acknowledge support by an LCSB flagship project.

Declaration of interests

J.C.S. is co-inventor on a patent covering the generation of the here-described midbrain organoids (WO2017060884A1). Furthermore, J.C.S. is co-founder and shareholder of the company OrganoTherapeutics, which makes use of the midbrain organoid technology. The other authors declare no competing interests.

Received: June 14, 2021
Accepted: December 13, 2021
Published: January 24, 2022

Web resources

Metacore, https://portal.genego.com/
nVenn, http://degradome.uniovi.es/cgi-bin/nVenn/nvenn.cgi

References

1. Inamdar, N.N., Arulmozhi, D.K., Tandon, A., and Bodhankar, S.L. (2007). Parkinson's disease: genetics and beyond. Curr. Neuropharmacol. *5*, 99–113.
2. Paisán-Ruíz, C., Jain, S., Evans, E.W., Gilks, W.P., Simón, J., van der Brug, M., López de Munain, A., Aparicio, S., Gil, A.M., Khan, N., et al. (2004). Cloning of the gene containing mutations that cause PARK8-linked Parkinson's disease. Neuron *44*, 595–600.
3. Zimprich, A., Biskup, S., Leitner, P., Lichtner, P., Farrer, M., Lincoln, S., Kachergus, J., Hulihan, M., Uitti, R.J., Calne, D.B., et al. (2004). Mutations in LRRK2 cause autosomal-dominant parkinsonism with pleomorphic pathology. Neuron *44*, 601–607.
4. Ren, C., Ding, Y., Wei, S., Guan, L., Zhang, C., Ji, Y., Wang, F., Yin, S., and Yin, P. (2019). G2019S Variation in LRRK2: An Ideal Model for the Study of Parkinson's Disease? Front. Hum. Neurosci. *13*, 306.
5. Nickels, S.L., Walter, J., Bolognin, S., Gérard, D., Jaeger, C., Qing, X., Tisserand, J., Jarazo, J., Hemmer, K., Harms, A., et al. (2019). Impaired serine metabolism complements LRRK2-G2019S pathogenicity in PD patients. Parkinsonism Relat. Disord. *67*, 48–55.
6. Liu, G.H., Qu, J., Suzuki, K., Nivet, E., Li, M., Montserrat, N., Yi, F., Xu, X., Ruiz, S., Zhang, W., et al. (2012). Progressive degeneration of human neural stem cells caused by pathogenic LRRK2. Nature *491*, 603–607.
7. Winner, B., Kohl, Z., and Gage, F.H. (2011). Neurodegenerative disease and adult neurogenesis. Eur. J. Neurosci. *33*, 1139–1151.
8. Milosevic, J., Schwarz, S.C., Ogunlade, V., Meyer, A.K., Storch, A., and Schwarz, J. (2009). Emerging role of LRRK2 in human neural progenitor cell cycle progression, survival and differentiation. Mol. Neurodegener. *4*, 25.
9. Smits, L.M., Reinhardt, L., Reinhardt, P., Glatza, M., Monzel, A.S., Stanslowsky, N., Rosato-Siri, M.D., Zanon, A., Antony, P.M., Bellmann, J., et al. (2019). Modeling Parkinson's disease in midbrain-like organoids. NPJ Parkinsons Dis. *5*, 5.
10. Schulz, C., Paus, M., Frey, K., Schmid, R., Kohl, Z., Mennerich, D., Winkler, J., and Gillardon, F. (2011). Leucine-rich repeat kinase 2 modulates retinoic acid-induced neuronal differentiation of murine embryonic stem cells. PLoS ONE *6*, e20820.
11. Le Grand, J.N., Gonzalez-Cano, L., Pavlou, M.A., and Schwamborn, J.C. (2015). Neural stem cells in Parkinson's disease: a role for neurogenesis defects in onset and progression. Cell. Mol. Life Sci. *72*, 773–797.
12. Sancho, R.M., Law, B.M.H., and Harvey, K. (2009). Mutations in the LRRK2 Roc-COR tandem domain link Parkinson's disease to Wnt signalling pathways. Hum. Mol. Genet. *18*, 3955–3968.
13. Winner, B., Melrose, H.L., Zhao, C., Hinkle, K.M., Yue, M., Kent, C., Braithwaite, A.T., Ogholikhan, S., Aigner, R., Winkler, J., et al. (2011). Adult neurogenesis and neurite outgrowth are impaired in LRRK2 G2019S mice. Neurobiol. Dis. *41*, 706–716.
14. Berwick, D.C., and Harvey, K. (2012). LRRK2 functions as a Wnt signaling scaffold, bridging cytosolic proteins and membrane-localized LRP6. Hum. Mol. Genet. *21*, 4966–4979.

15. Hartmann, A. (2004). Postmortem studies in Parkinson's disease. Dialogues Clin. Neurosci. *6*, 281–293.
16. Blesa, J., and Przedborski, S. (2014). Parkinson's disease: animal models and dopaminergic cell vulnerability. Front. Neuroanat. *8*, 155.
17. Takahashi, K., and Yamanaka, S. (2006). Induction of pluripotent stem cells from mouse embryonic and adult fibroblast cultures by defined factors. Cell *126*, 663–676.
18. Arias-Fuenzalida, J., Jarazo, J., Qing, X., Walter, J., Gomez-Giro, G., Nickels, S.L., Zaehres, H., Schöler, H.R., and Schwamborn, J.C. (2017). FACS-Assisted CRISPR-Cas9 Genome Editing Facilitates Parkinson's Disease Modeling. Stem Cell Reports *9*, 1423–1431.
19. Vermilyea, S.C., Babinski, A., Tran, N., To, S., Guthrie, S., Kluss, J.H., Schmidt, J.K., Wiepz, G.J., Meyer, M.G., Murphy, M.E., et al. (2020). In Vitro CRISPR/Cas9-Directed Gene Editing to Model LRRK2 G2019S Parkinson's Disease in Common Marmosets. Sci. Rep. *10*, 3447.
20. Monzel, A.S., Smits, L.M., Hemmer, K., Hachi, S., Moreno, E.L., van Wuellen, T., Jarazo, J., Walter, J., Brüggemann, I., Boussaad, I., et al. (2017). Derivation of Human Midbrain-Specific Organoids from Neuroepithelial Stem Cells. Stem Cell Reports *8*, 1144–1154.
21. Schwamborn, J.C. (2018). Is Parkinson's disease a neurodevelopmental disorder and will brain organoids help us to understand it? Stem Cells Dev. *27*, 968–975.
22. Chlebanowska, P., Tejchman, A., Sułkowski, M., Skrzypek, K., and Majka, M. (2020). Use of 3D organoids as a model to study idiopathic form of parkinson's disease. Int. J. Mol. Sci. *21*, 694.
23. Kim, H., Park, H.J., Choi, H., Chang, Y., Park, H., Shin, J., Kim, J., Lengner, C.J., Lee, Y.K., and Kim, J. (2019). Modeling G2019S-LRRK2 Sporadic Parkinson's Disease in 3D Midbrain Organoids. Stem Cell Reports *12*, 518–531.
24. Kwak, T.H., Kang, J.H., Hali, S., Kim, J., Kim, K.P., Park, C., Lee, J.H., Ryu, H.K., Na, J.E., Jo, J., et al. (2020). Generation of homogeneous midbrain organoids with in vivo-like cellular composition facilitates neurotoxin-based Parkinson's disease modeling. Stem Cells *38*, 727–740.
25. La Manno, G., Gyllborg, D., Codeluppi, S., Nishimura, K., Salto, C., Zeisel, A., Borm, L.E., Stott, S.R.W., Toledo, E.M., Villaescusa, J.C., et al. (2016). Molecular Diversity of Midbrain Development in Mouse, Human, and Stem Cells. Cell *167*, 566–580.e19.
26. Smits, L.M., Magni, S., Kinugawa, K., Grzyb, K., Luginbühl, J., Sabate-Soler, S., Bolognin, S., Shin, J.W., Mori, E., Skupin, A., and Schwamborn, J.C. (2020). Single-cell transcriptomics reveals multiple neuronal cell types in human midbrain-specific organoids. Cell Tissue Res. *382*, 463–476.
27. Qing, X., Walter, J., Jarazo, J., Arias-Fuenzalida, J., Hillje, A.L., and Schwamborn, J.C. (2017). CRISPR/Cas9 and piggyBac-mediated footprint-free LRRK2-G2019S knock-in reveals neuronal complexity phenotypes and α-Synuclein modulation in dopaminergic neurons. Stem Cell Res. (Amst.) *24*, 44–50.
28. Zhong, S., Zhang, S., Fan, X., Wu, Q., Yan, L., Dong, J., Zhang, H., Li, L., Sun, L., Pan, N., et al. (2018). A single-cell RNA-seq survey of the developmental landscape of the human prefrontal cortex. Nature *555*, 524–528.
29. Trujillo, C.A., Gao, R., Negraes, P.D., Gu, J., Buchanan, J., Preissl, S., Wang, A., Wu, W., Haddad, G.G., Chaim, I.A., et al. (2019). Complex Oscillatory Waves Emerging from Cortical Organoids Model Early Human Brain Network Development. Cell Stem Cell *25*, 558–569.e7.
30. Macosko, E.Z., Basu, A., Satija, R., Nemesh, J., Shekhar, K., Goldman, M., Tirosh, I., Bialas, A.R., Kamitaki, N., Martersteck, E.M., et al. (2015). Highly parallel genome-wide expression profiling of individual cells using nanoliter droplets. Cell *161*, 1202–1214.
31. Stuart, T., Butler, A., Hoffman, P., Hafemeister, C., Papalexi, E., Mauck, W.M., 3rd, Hao, Y., Stoeckius, M., Smibert, P., and Satija, R. (2019). Comprehensive Integration of Single-Cell Data. Cell *177*, 1888–1902.e21.
32. Becht, E., McInnes, L., Healy, J., Dutertre, C.A., Kwok, I.W.H., Ng, L.G., Ginhoux, F., and Newell, E.W. (2018). Dimensionality reduction for visualizing single-cell data using UMAP. Nat. Biotechnol. *37*, 38–47.
33. Hafemeister, C., and Satija, R. (2019). Normalization and variance stabilization of single-cell RNA-seq data using regularized negative binomial regression. Genome Biol. *20*, 296.
34. Chen, X., Zhang, K., Zhou, L., Gao, X., Wang, J., Yao, Y., He, F., Luo, Y., Yu, Y., Li, S., et al. (2016). Coupled electrophysiological recording and single cell transcriptome analyses revealed molecular mechanisms underlying neuronal maturation. Protein Cell *7*, 175–186.
35. Zhou, Z.D., Chan, C.H.S., Ma, Q.H., Xu, X.H., Xiao, Z.C., and Tan, E.K. (2011). The roles of amyloid precursor protein (APP) in neurogenesis, implications to pathogenesis and therapy of alzheimer Disease (AD). Cell Adh. Migr. *5*, 280–292.
36. Tsarovina, K., Reiff, T., Stubbusch, J., Kurek, D., Grosveld, F.G., Parlato, R., Schütz, G., and Rohrer, H. (2010). The Gata3 transcription factor is required for the survival of embryonic and adult sympathetic neurons. J. Neurosci. *30*, 10833–10843.
37. Cortès-Saladelafont, E., Lipstein, N., and García-Cazorla, À. (2018). Presynaptic disorders: a clinical and pathophysiological approach focused on the synaptic vesicle. J. Inherit. Metab. Dis. *41*, 1131–1145.
38. Scherzer, C.R., Grass, J.A., Liao, Z., Pepivani, I., Zheng, B., Eklund, A.C., Ney, P.A., Ng, J., McGoldrick, M., Mollenhauer, B., et al. (2008). GATA transcription factors directly regulate the Parkinson's disease-linked gene α-synuclein. Proc. Natl. Acad. Sci. USA *105*, 10907–10912.
39. Gombash, S.E., Lipton, J.W., Collier, T.J., Madhavan, L., Steece-Collier, K., Cole-Strauss, A., Terpstra, B.T., Spieles-Engemann, A.L., Daley, B.F., Wohlgenant, S.L., et al. (2012). Striatal pleiotrophin overexpression provides functional and morphological neuroprotection in the 6-hydroxydopamine model. Mol. Ther. *20*, 544–554.
40. Marchionini, D.M., Lehrmann, E., Chu, Y., He, B., Sortwell, C.E., Becker, K.G., Freed, W.J., Kordower, J.H., and Collier, T.J. (2007). Role of heparin binding growth factors in nigrostriatal dopamine system development and Parkinson's disease. Brain Res. *1147*, 77–88.
41. Galet, B., Cheval, H., and Ravassard, P. (2020). Patient-Derived Midbrain Organoids to Explore the Molecular Basis of Parkinson's Disease. Front. Neurol. *11*, 1005.
42. Nickels, S.L., Modamio, J., Mendes-Pinheiro, B., Monzel, A.S., Betsou, F., and Schwamborn, J.C. (2020). Reproducible generation of human midbrain organoids for in vitro modeling of Parkinson's disease. Stem Cell Res. (Amst.) *46*, 101870.
43. Quadrato, G., Nguyen, T., Macosko, E.Z., Sherwood, J.L., Min Yang, S., Berger, D.R., Maria, N., Scholvin, J., Goldman, M., Kinney, J.P., et al. (2017). Cell diversity and network dynamics in photosensitive human brain organoids. Nature *545*, 48–53.
44. Camp, J.G., Badsha, F., Florio, M., Kanton, S., Gerber, T., Wilsch-Bräuninger, M., Lewitus, E., Sykes, A., Hevers, W.,

Lancaster, M., et al. (2015). Human cerebral organoids recapitulate gene expression programs of fetal neocortex development. Proc. Natl. Acad. Sci. USA *112*, 15672–15677.

45. Payne, L.B., Hoque, M., Houk, C., Darden, J., and Chappell, J.C. (2020). Pericytes in Vascular Development. Curr. Tissue Microenviron. Rep. *1*, 143–154.
46. Korn, J., Christ, B., and Kurz, H. (2002). Neuroectodermal origin of brain pericytes and vascular smooth muscle cells. J. Comp. Neurol. *442*, 78–88.
47. Yamazaki, T., and Mukouyama, Y.S. (2018). Tissue Specific Origin, Development, and Pathological Perspectives of Pericytes. Front. Cardiovasc. Med. *5*, 78.
48. Eze, U., Bhaduri, A., Haeussler, M., Nowakowski, T., and Kriegstein, A. (2020). Single-Cell Atlas of Early Human Brain Development Highlights Heterogeneity of Human Neuroepithelial Cells and Early Radial Glia. Nat. Neurosci. *1*, 143–154.
49. Reinhardt, P., Glatza, M., Hemmer, K., Tsytsyura, Y., Thiel, C.S., Höing, S., Moritz, S., Parga, J.A., Wagner, L., Bruder, J.M., et al. (2013). Derivation and expansion using only small molecules of human neural progenitors for neurodegenerative disease modeling. PLoS ONE *8*, e59252.
50. van den Hurk, M., and Bardy, C. (2019). Single-cell multimodal transcriptomics to study neuronal diversity in human stem cell-derived brain tissue and organoid models. J. Neurosci. Methods *325*, 108350.
51. Jeong, G.R., and Lee, B.D. (2020). Pathological Functions of LRRK2 in Parkinson's Disease. Cells *9*, 1–19.
52. Häbig, K., Gellhaar, S., Heim, B., Djuric, V., Giesert, F., Wurst, W., Walter, C., Hentrich, T., Riess, O., and Bonin, M. (2013). LRRK2 guides the actin cytoskeleton at growth cones together with ARHGEF7 and Tropomyosin 4. Biochim. Biophys. Acta *1832*, 2352–2367.
53. Manzoni, C., Denny, P., Lovering, R.C., and Lewis, P.A. (2015). Computational analysis of the LRRK2 interactome. PeerJ *3*, e778.
54. Matikainen-Ankney, B.A., Kezunovic, N., Mesias, R.E., Tian, Y., Williams, F.M., Huntley, G.W., and Benson, D.L. (2016). Altered development of synapse structure and function in striatum caused by Parkinson's disease-linked LRRK2-G2019S mutation. J. Neurosci. *36*, 7128–7141.
55. Lamonaca, G., and Volta, M. (2020). Alpha-Synuclein and LRRK2 in Synaptic Autophagy: Linking Early Dysfunction to Late-Stage Pathology in Parkinson's Disease. Cells *9*, 1115.
56. Vergara, D., Gaballo, A., Signorile, A., Ferretta, A., Tanzarella, P., Pacelli, C., Di Paola, M., Cocco, T., and Maffia, M. (2017). Resveratrol Modulation of Protein Expression in *parkin*-Mutant Human Skin Fibroblasts: A Proteomic Approach. Oxid. Med. Cell. Longev. *2017*, 2198243.
57. Ko, H.S., Bailey, R., Smith, W.W., Liu, Z., Shin, J.H., Lee, Y.I., Zhang, Y.J., Jiang, H., Ross, C.A., Moore, D.J., et al. (2009). CHIP regulates leucine-rich repeat kinase-2 ubiquitination, degradation, and toxicity. Proc. Natl. Acad. Sci. USA *106*, 2897–2902.
58. Obsilova, V., and Obsil, T. (2020). The 14-3-3 proteins as important allosteric regulators of protein kinases. Int. J. Mol. Sci. *21*, 1–16.
59. Zhang, X., Li, Y., Xu, H., and Zhang, Y.W. (2014). The γ-secretase complex: from structure to function. Front. Cell. Neurosci. *8*, 427.
60. O'Brien, R.J., and Wong, P.C. (2011). Amyloid precursor protein processing and Alzheimer's disease. Annu. Rev. Neurosci. *34*, 185–204.
61. Chen, Z.C., Zhang, W., Chua, L.L., Chai, C., Li, R., Lin, L., Cao, Z., Angeles, D.C., Stanton, L.W., Peng, J.H., et al. (2017). Phosphorylation of amyloid precursor protein by mutant LRRK2 promotes AICD activity and neurotoxicity in Parkinson's disease. Sci. Signal. *10*, 1–12.
62. Bergström, P., Agholme, L., Nazir, F.H., Satir, T.M., Toombs, J., Wellington, H., Strandberg, J., Bontell, T.O., Kvartsberg, H., Holmström, M., et al. (2016). Amyloid precursor protein expression and processing are differentially regulated during cortical neuron differentiation. Sci. Rep. *6*, 29200.
63. Straniero, L., Guella, I., Cilia, R., Parkkinen, L., Rimoldi, V., Young, A., Asselta, R., Soldà, G., Sossi, V., Stoessl, A.J., et al. (2017). DNAJC12 and dopa-responsive nonprogressive parkinsonism. Ann. Neurol. *82*, 640–646.
64. Zhou, Y., and Han, D. (2017). GATA3 modulates neuronal survival through regulating TRPM2 in Parkinson's disease. Int. J. Clin. Exp. Med. *10*, 15178–15186.
65. Hao, Y., Hao, S., Andersen-nissen, E., Iii, W.M.M., Zheng, S., Lee, M.J., Wilk, A.J., Darby, C., Zagar, M., Hoffman, P., et al. (2020). Integrated analysis of multimodal single-cell data. bioRxiv. https://doi.org/10.1101/2020.10.12.335331.
66. Butler, A., Hoffman, P., Smibert, P., Papalexi, E., and Satija, R. (2018). Integrating single-cell transcriptomic data across different conditions, technologies, and species. Nat. Biotechnol. *36*, 411–420.
67. Cao, J., Spielmann, M., Qiu, X., Huang, X., Ibrahim, D.M., Hill, A.J., Zhang, F., Mundlos, S., Christiansen, L., Steemers, F.J., et al. (2019). The single-cell transcriptional landscape of mammalian organogenesis. Nature *566*, 496–502.

The American Journal of Human Genetics, Volume *109*

Supplemental information

Midbrain organoids mimic early embryonic neurodevelopment and recapitulate LRRK2-p.Gly2019Ser-associated gene expression

Alise Zagare, Kyriaki Barmpa, Semra Smajic, Lisa M. Smits, Kamil Grzyb, Anne Grünewald, Alexander Skupin, Sarah L. Nickels, and Jens C. Schwamborn

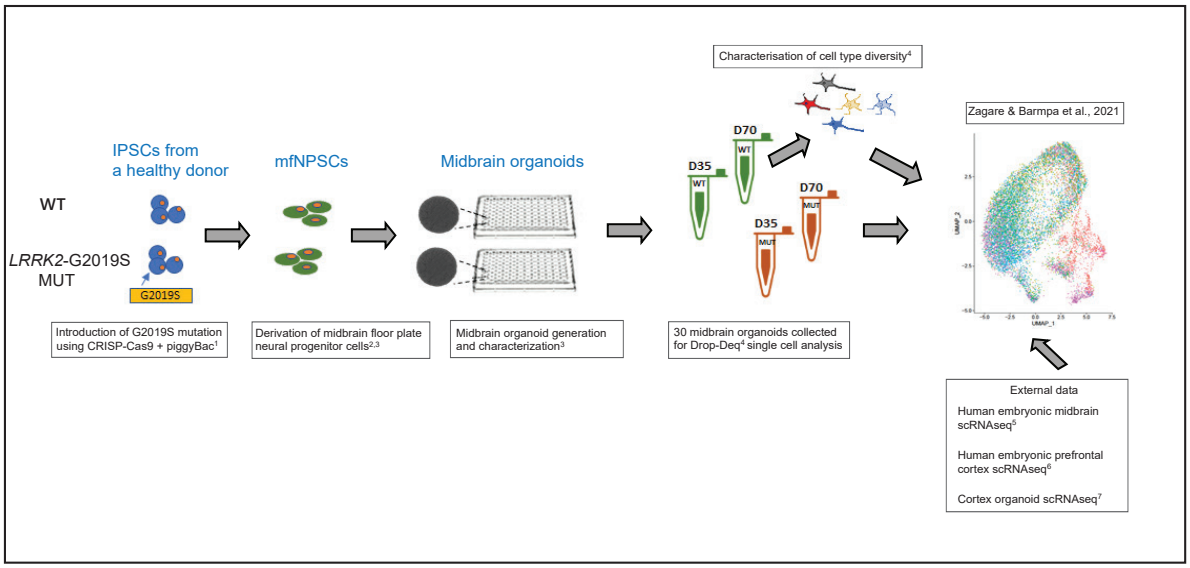

Figure S1. Graphical representation showing the origin of the data used in this study. WT and LRRK2 MUT midbrain organoids were generated in paralel in our lab. WT midbrain organoids were characterized in previous studies of Smits et al. [3,4] The present study comprises analysis of internal scRNAseq data from the respective midbrain organoids and comparison to external datasets [5,6,7].

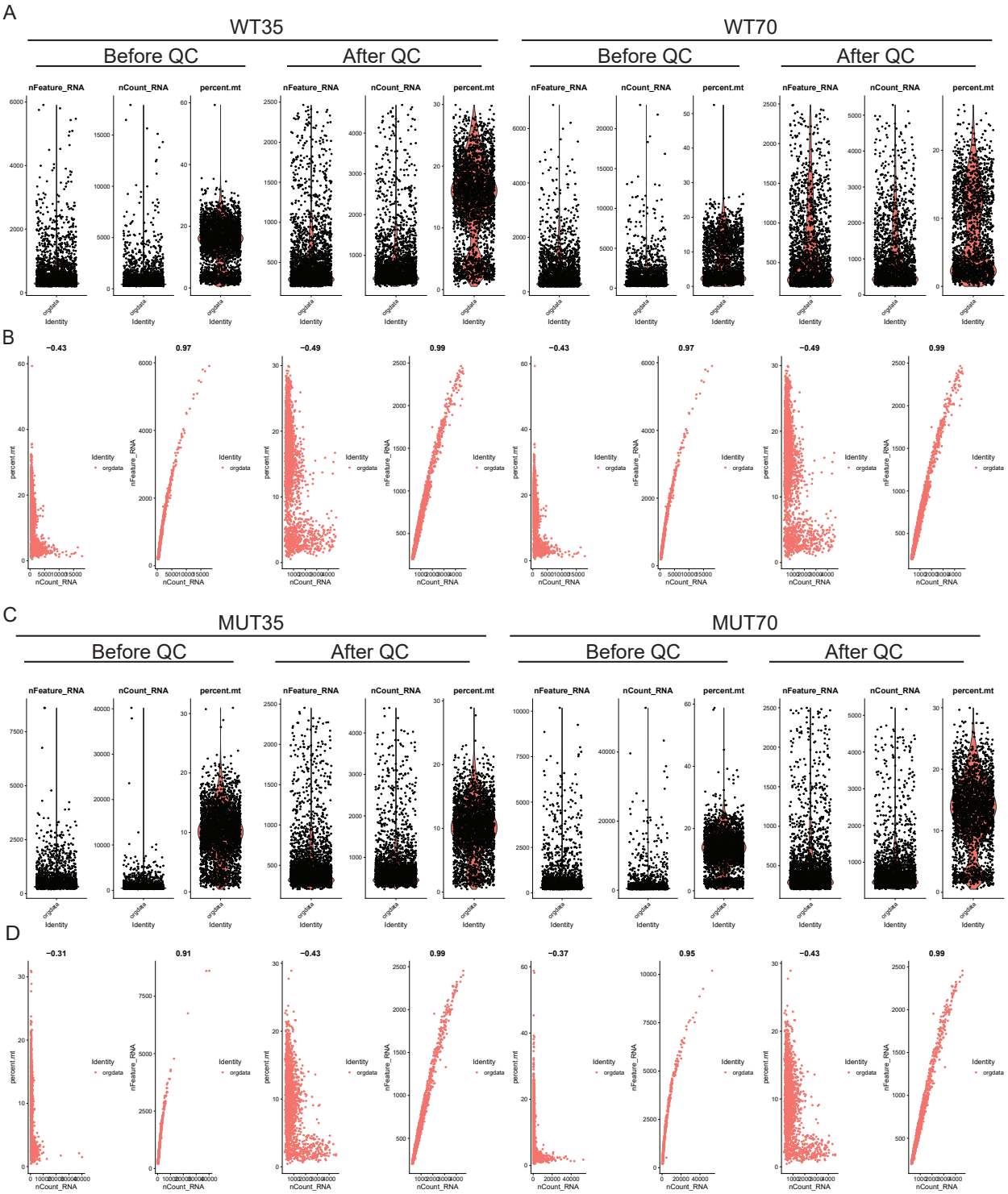

Figure S2. Quality control of midbrain organoid scRNAseq datasets. **A)** Number of genes (nFeature_RNA), total number of molecules (nCount), percent of mitochondrial genes, detected in each cell for WT35 and WT70 midbrain organoids, before and after quality control. **B)** Correlations between percentage of mitochondrial genes, the number of genes and the total number of molecules for WT35 and WT70 midbrain organoids, before and after quality control. **C)** Same as (A), for MUT35 and MUT70 midbrain organoids. **D)** Same as (B), for MUT35 and MUT70 midbrain organoids.

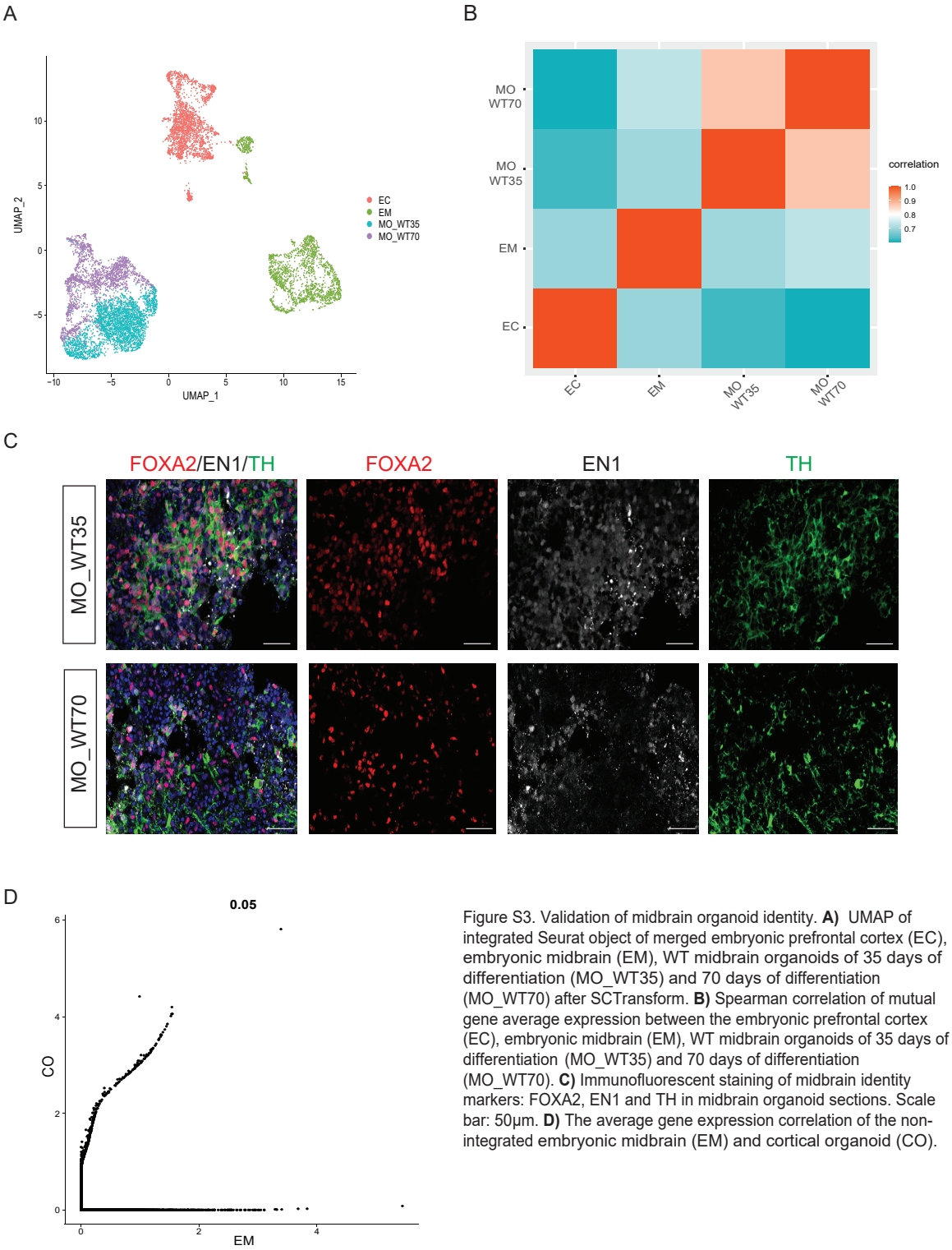

Figure S3. Validation of midbrain organoid identity. **A)** UMAP of integrated Seurat object of merged embryonic prefrontal cortex (EC), embryonic midbrain (EM), WT midbrain organoids of 35 days of differentiation (MO_WT35) and 70 days of differentiation (MO_WT70) after SCTransform. **B)** Spearman correlation of mutual gene average expression between the embryonic prefrontal cortex (EC), embryonic midbrain (EM), WT midbrain organoids of 35 days of differentiation (MO_WT35) and 70 days of differentiation (MO_WT70). **C)** Immunofluorescent staining of midbrain identity markers: FOXA2, EN1 and TH in midbrain organoid sections. Scale bar: 50µm. **D)** The average gene expression correlation of the non-integrated embryonic midbrain (EM) and cortical organoid (CO).

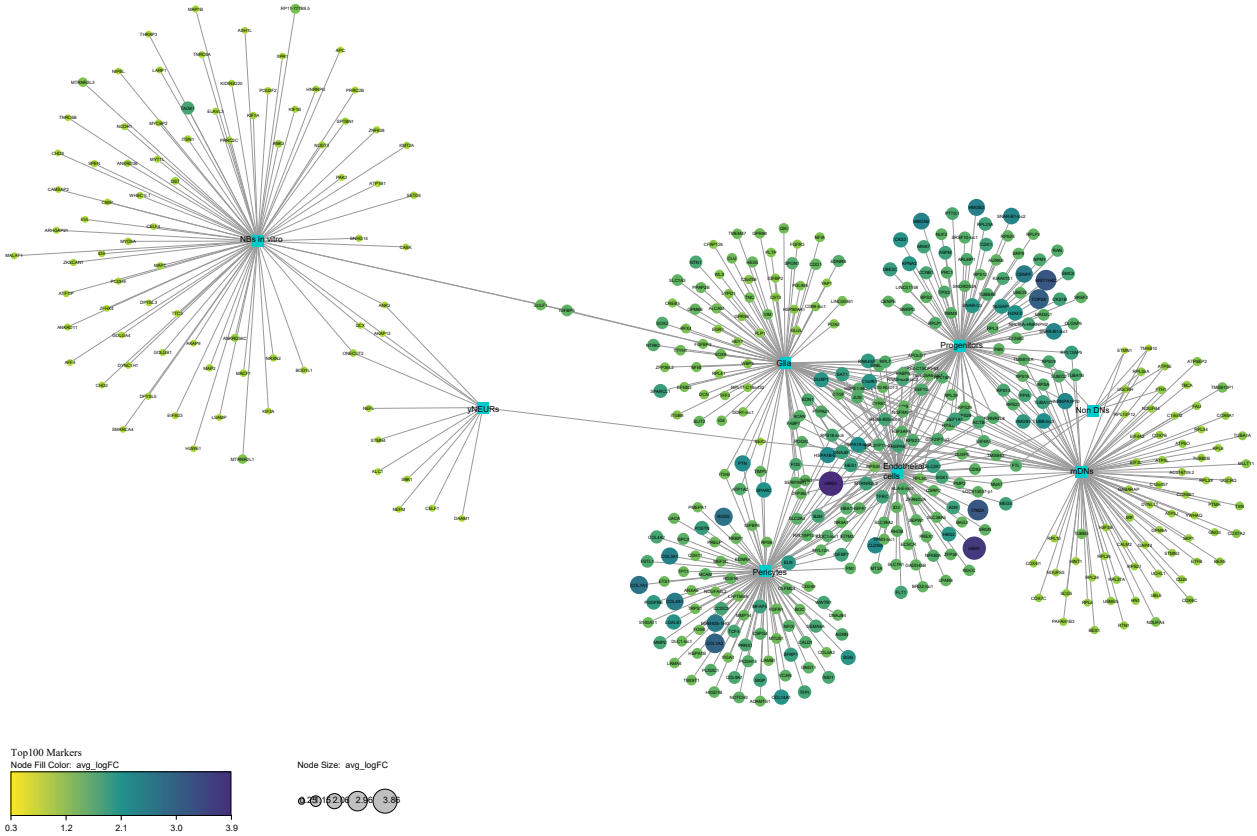

Figure S4. Network representing top marker genes for each cell cluster.
The top 100 cell type markers identified by the FindAllMarkers function. The size and color of nodes represent logarithmic fold change (avg_logFC) of each marker expression in the particular cell type compared to its expression in other cell clusters.

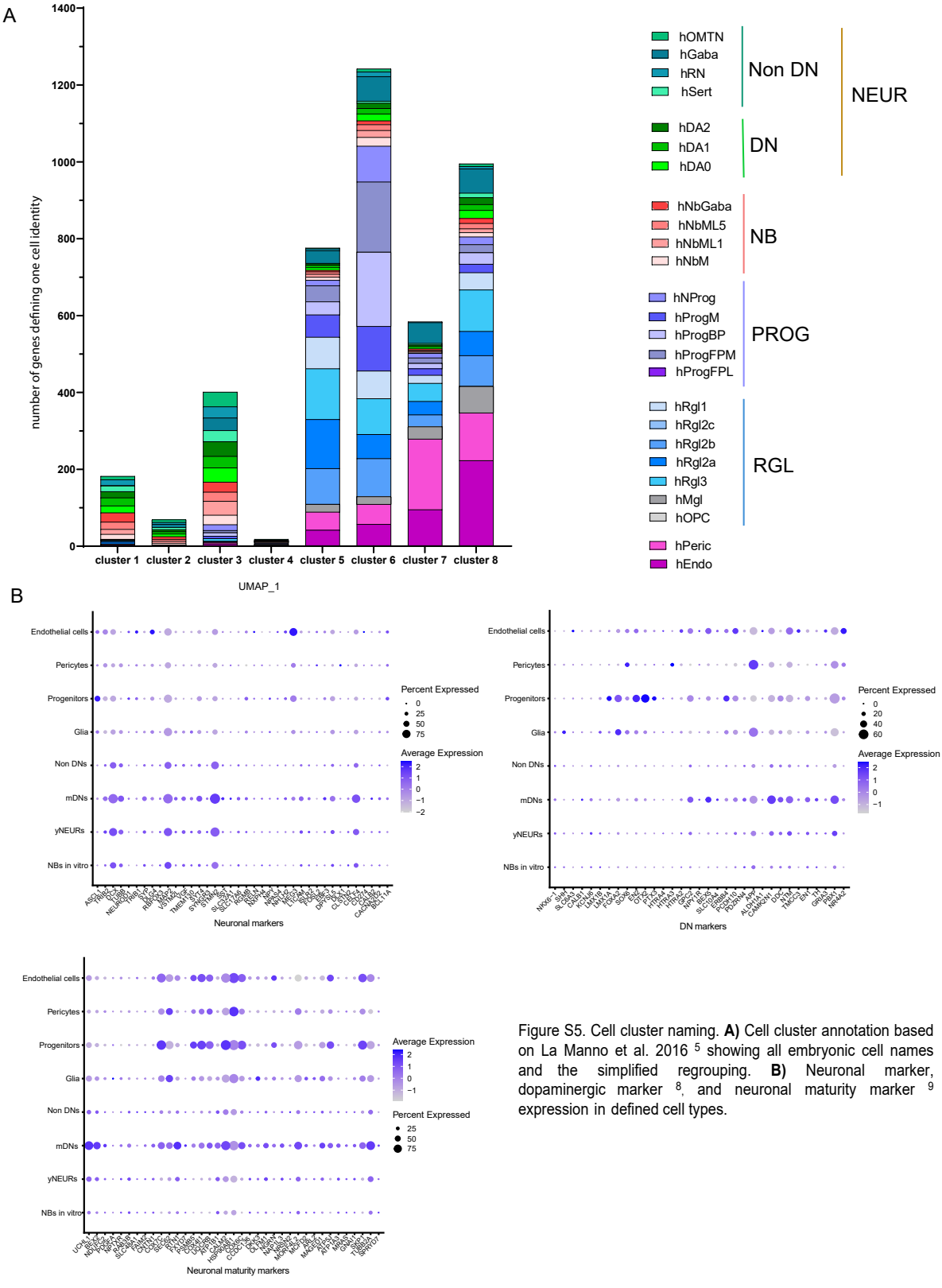

Figure S5. Cell cluster naming. **A)** Cell cluster annotation based on La Manno et al. 2016 [5] showing all embryonic cell names and the simplified regrouping. **B)** Neuronal marker, dopaminergic marker [8], and neuronal maturity marker [9] expression in defined cell types.

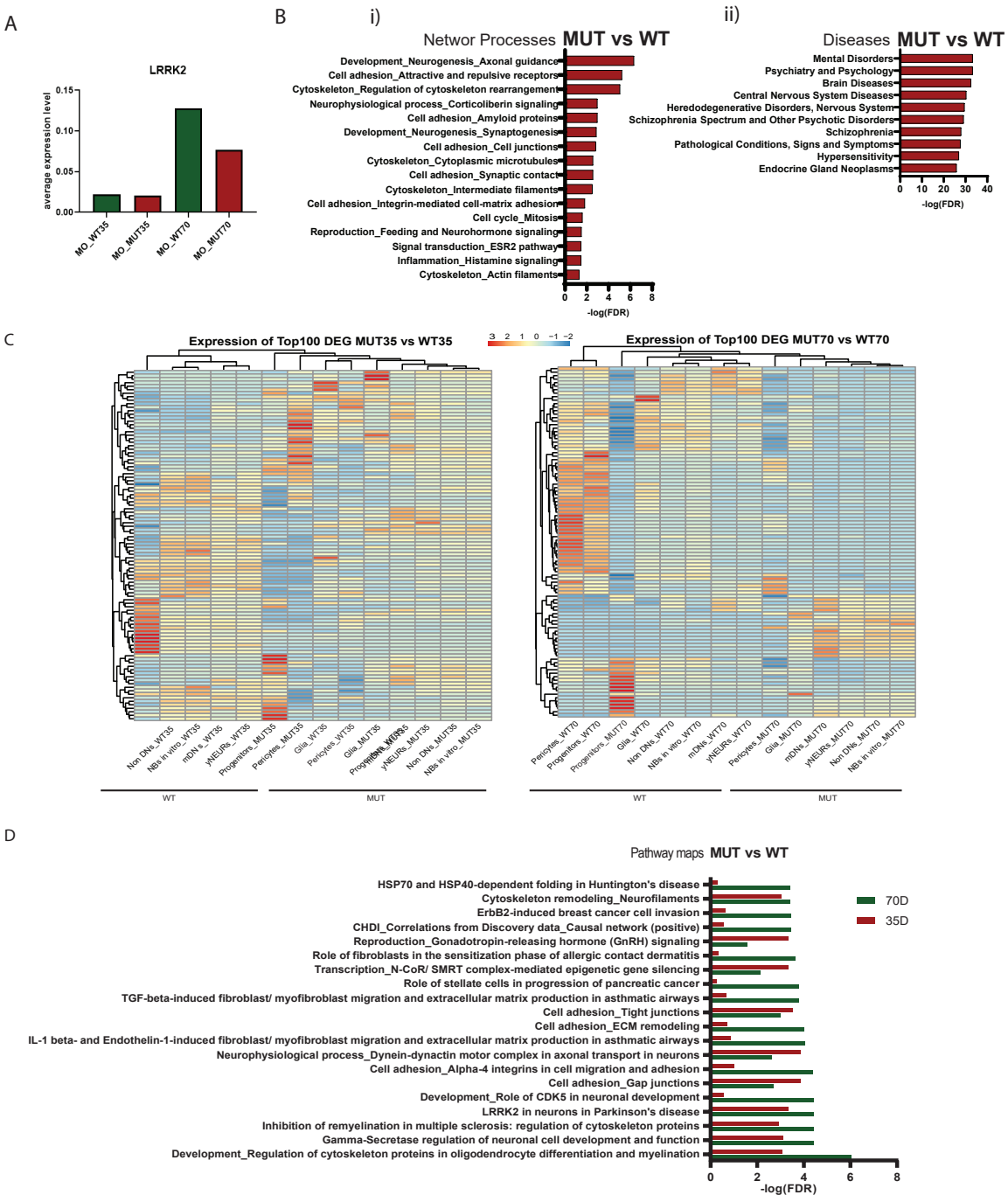

Figure S6. Differentially expressed gene analysis I. **A)** The bulk average *LRRK2* expression in midbrain organoids. **B)** i) Network processes and ii) diseases from the enrichment analysis of 294 DEGs (adjusted p-value < 0.05) between MUT and WT midbrain organoids. **C)** Heatmaps of top 100 DEGs (adjusted p-value < 0.05) at day 35 and day 70 respectively, showing the cell type unsupervised clustering between MUT and WT organoids. **D)** Pathway processes based on MUT vs WT midbrain organoid DEGs (adjusted p-value < 0.05).

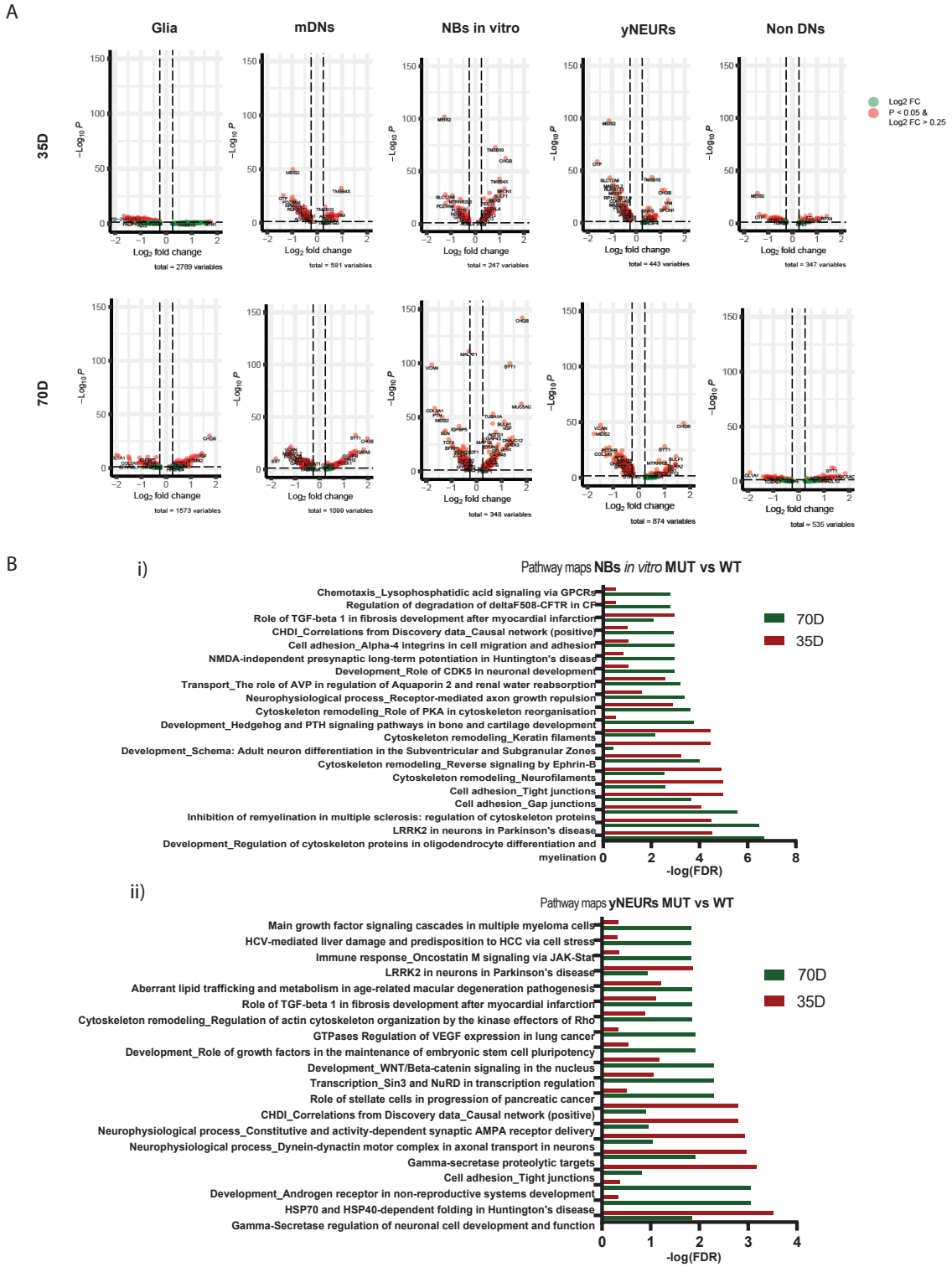

Figure S7. Differentially expressed gene analysis II. **A)** Volcano plots showing DEG fold changes in cell clusters between MUT and WT midbrain organoids. **B)** Pathway enrichment analysis in i) yNEURs and ii) NBs in vitro based on the DEGs in the respective cell clusters (adjusted p-value < 0.05).

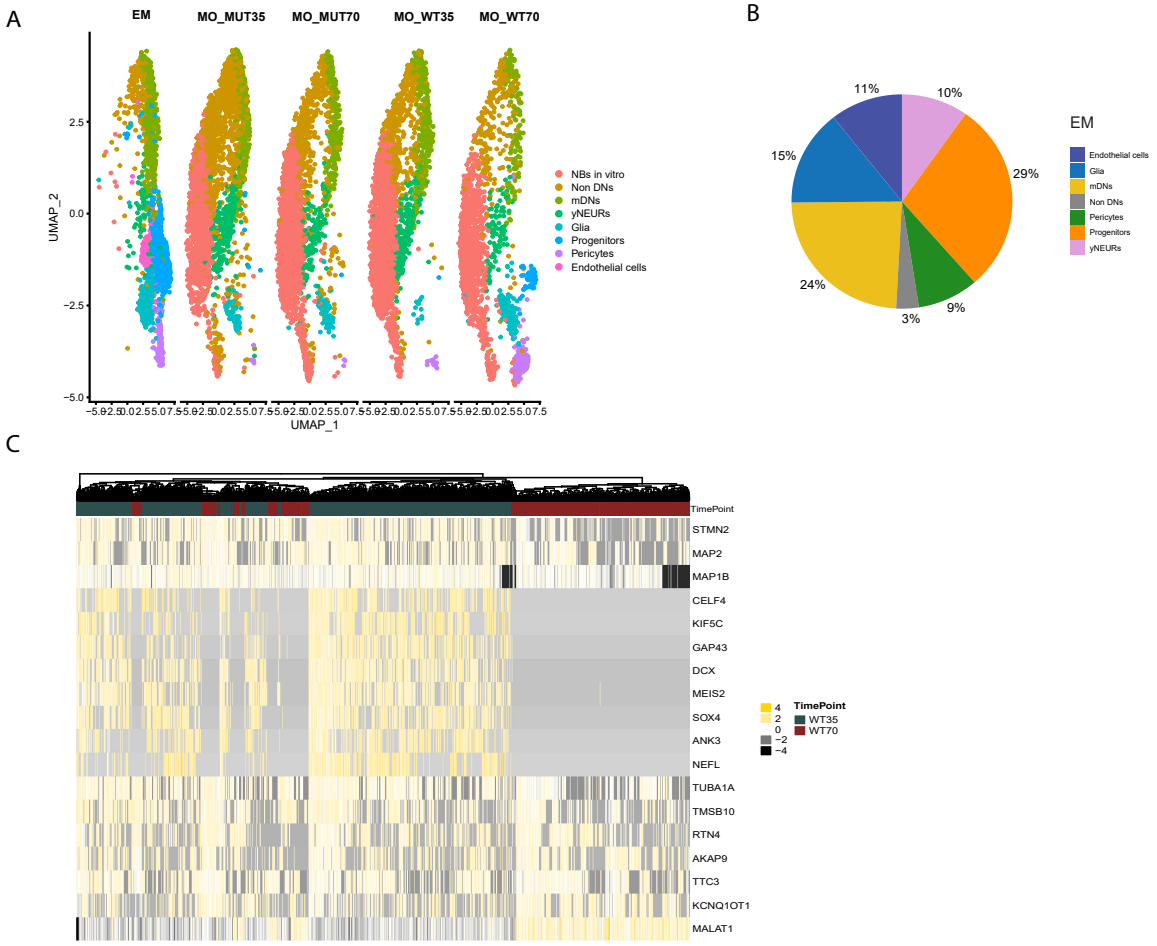

Figure S8. *LRRK2*-G2019S mutant midbrain organoids have a different cellular composition and altered developmental path. **A)** UMAP of integrated Seurat object of merged scRNAseq datasets of embryonic midbrain, and WT and MUT midbrain organoids 35 and 70 days of differentiation, colored by cell clusters and split by the dataset. **B)** Percentage of cell identities present in the embryonic midbrain (EM). **C)** Heatmap of genes with changed expression pattern in at least 50% of cells between WT35 and WT70 midbrain organoids.

Source of iPSCs	Mutation	Age at sampling	Sex	Corresponding midbrain organoid culture
The Wellcome Trust Sanger Institute, Cambridge, UK	-	55	Male	MO_WT35 MO_WT70
The Wellcome Trust Sanger Institute, Cambridge, UK	Introduced LRRK2 G2019S[1]	55	Male	MO_MUT35 MO_MUT70

Table S1. Cell lines used to generate midbrain floor plate neural progenitor cells and further the midbrain organoids for scRNAseq.

References of Supplemental Data

1. Qing, X., Walter, J., Jarazo, J., Arias-Fuenzalida, J., Hillje, A.L., and Schwamborn, J.C. (2017). CRISPR/Cas9 and piggyBac-mediated footprint-free LRRK2-G2019S knock-in reveals neuronal complexity phenotypes and α-Synuclein modulation in dopaminergic neurons. Stem Cell Res. *24*, 44–50.

2. Smits, L.M., Reinhardt, L., Reinhardt, P., Glatza, M., Monzel, A.S., Stanslowsky, N., Rosato-Siri, M.D., Zanon, A., Antony, P.M., Bellmann, J., et al. (2019). Modeling Parkinson's disease in midbrain-like organoids. Npj Park. Dis. *5*,.

3. Reinhardt, P., Glatza, M., Hemmer, K., Tsytsyura, Y., Thiel, C.S., Höing, S., Moritz, S., Parga, J.A., Wagner, L., Bruder, J.M., et al. (2013). Derivation and Expansion Using Only Small Molecules of Human Neural Progenitors for Neurodegenerative Disease Modeling. PLoS One *8*,.

4. Smits, L.M., Magni, S., Kinugawa, K., Grzyb, K., Luginbühl, J., Sabate-Soler, S., Bolognin, S., Shin, J.W., Mori, E., Skupin, A., et al. (2020). Single-cell transcriptomics reveals multiple neuronal cell types in human midbrain-specific organoids. Cell Tissue Res. *382*, 463–476.

5. La Manno, G., Gyllborg, D., Codeluppi, S., Nishimura, K., Salto, C., Zeisel, A., Borm, L.E., Stott, S.R.W., Toledo, E.M., Villaescusa, J.C., et al. (2016). Molecular Diversity of Midbrain Development in Mouse, Human, and Stem Cells. Cell 167, 566-580.e19.

6. Zhong, S., Zhang, S., Fan, X., Wu, Q., Yan, L., Dong, J., Zhang, H., Li, L., Sun, L., Pan, N., et al. (2018). A single-cell RNA-seq survey of the developmental landscape of the human prefrontal cortex. Nature 555, 524–528.

7. Trujillo, C.A., Gao, R., Negraes, P.D., Gu, J., Buchanan, J., Preissl, S., Wang, A., Wu, W., Haddad, G.G., Chaim, I.A., et al. (2019). Complex Oscillatory Waves Emerging from Cortical Organoids Model Early Human Brain Network Development. Cell Stem Cell 25, 558-569.e7.

8. Paisán-Ruíz, C., Jain, S., Evans, E.W., Gilks, W.P., Simón, J., Van Der Brug, M., De Munain, A.L., Aparicio, S., Gil, A.M., Khan, N., et al. (2004). Cloning of the gene containing mutations that cause PARK8-linked Parkinson's disease. Neuron 44, 595–600.

9. Ren, C., Ding, Y., Wei, S., Guan, L., Zhang, C., Ji, Y., Wang, F., Yin, S., and Yin, P.(2019). G2019S Variation in LRRK2: An Ideal Model for the Study of Parkinson's Disease? Front. Hum. Neurosci. 13, 1–6.

Manuscript V

DE GRUYTER medizinische genetik 2022; aop

Joanne Trinh, Emma L. Schymanski, Semra Smajic, Meike Kasten, Esther Sammler, and Anne Grünewald*

Molecular mechanisms defining penetrance of *LRRK2*-associated Parkinson's disease

https://doi.org/10.1515/medgen-2022-2127

Abstract: Mutations in *Leucine-rich repeat kinase 2* (*LRRK2*) are the most frequent cause of dominantly inherited Parkinson's disease (PD). *LRRK2* mutations, among which p.G2019S is the most frequent, are inherited with reduced penetrance. Interestingly, the disease risk associated with *LRRK2* G2019S can vary dramatically depending on the ethnic background of the carrier. While this would suggest a genetic component in the definition of *LRRK2*-PD penetrance, only few variants have been shown to modify the age at onset of patients harbouring *LRRK2* mutations, and the exact cellular pathways controlling the transition from a healthy to a diseased state currently remain elusive. In light of this knowledge gap, recent studies also explored environmental and lifestyle factors as potential modifiers of *LRRK2*-PD. In this article, we (i) describe the clinical characteristics of *LRRK2* mutation carriers, (ii) review known genes linked to *LRRK2*-PD onset and (iii) summarize the cellular functions of *LRRK2* with particular emphasis on potential penetrance-related molecular mechanisms. This section covers *LRRK2*'s involvement in Rab GTPase and immune signalling as well as in the regulation of mitochondrial homeostasis and dynamics. Additionally, we explored the literature with regard to (iv) lifestyle and (v) environmental factors that may influence the penetrance of *LRRK2* mutations, with a view towards further exposomics studies. Finally, based on this comprehensive overview, we propose potential future *in vivo*, *in vitro* and *in silico* studies that could provide a better understanding of the processes triggering PD in individuals with *LRRK2* mutations.

Keywords: Parkinson's disease, *LRRK2*, penetrance, genetic modifiers, Rab signalling, mitochondria, environment, toxin exposure

***Corresponding author: Anne Grünewald,** Luxembourg Centre for Systems Biomedicine, University of Luxembourg, Esch-sur-Alzette, Luxembourg; and Institute of Neurogenetics, University of Lübeck, Lübeck, Germany, e-mail: anne.gruenewald@uni.lu

Joanne Trinh, Institute of Neurogenetics, University of Lübeck, Lübeck, Germany

Emma L. Schymanski, Semra Smajic, Luxembourg Centre for Systems Biomedicine, University of Luxembourg, Esch-sur-Alzette, Luxembourg

Meike Kasten, Institute of Neurogenetics, University of Lübeck, Lübeck, Germany; and Department of Psychiatry and Psychotherapy, University of Lübeck, Lübeck, Germany

Esther Sammler, Medical Research Council (MRC) Protein Phosphorylation and Ubiquitylation Unit, School of Life Sciences, University of Dundee, Dundee, UK; and Department of Neurology, School of Medicine, Dundee, Ninewells Hospital, Dundee, UK

Clinical characteristics of *LRRK2*-associated Parkinson's disease

Mutations in the *Leucine-rich repeat kinase 2* (*LRRK2*) gene are the most common monogenic cause of Parkinson's disease (PD) [1]. They account for 1–2 % of PD cases and considerably more cases in certain populations such as North African Arab Berbers [2]. While idiopathic PD (IPD) is more common in men, this may not be the case for monogenic PD. In particular, *LRRK2*-PD seems to be more common in females. A recent meta-analysis of 64 studies and 32,452 patients reported a higher prevalence in women with a pooled relative risk of 1.22 (95 % confidence interval [CI] 1.14–1.30), and analyses of subgroups by mutation type suggested that this effect was restricted to G2019S mutations [3]. The cumulative incidence in Tunisian Arab Berber women with *LRRK2* G2019S is higher compared to that in males [4].

Systematic data on the clinical picture and course of *LRRK2*-PD are still scarce [3], rendering findings on clinical characteristics somewhat uncertain and to be interpreted with care.

LRRK2-PD resembles IPD in age at onset (AAO) and clinical signs, symptoms and progression [5, 6] with potential exceptions. Furthermore, there are different mutations known in *LRRK2*. A systematic review including comparisons of these mutations did not show clinical differences [7]. On the other hand, case numbers vary widely between mutations with p.G2019S being the most well known and common. Looking at clinical subtypes, i. e. tremor dominant, postural instability gait disorders and intermediate, the most frequent clinical subtype in *LRRK2*-PD is the postural instability gait disorder subtype [8]. Two

studies found first a similar [8] and second a slower disease progression [9]. Interestingly there are several differences with regard to non-motor signs. *LRRK2*-PD patients have less impairment in cognition, smell and sleep [4, 10–14]. According to MDSGene, the most common cardinal feature was bradykinesia for p.G2019S mutation carriers (97 %, 152 out of 156), dyskinesia was reported in 66 % (69 cases of 105), dystonia in 39 % (24 of 61 cases) and motor fluctuations in 64 % (44 of 69 cases) of the included patients. However, these findings need to be interpreted with some caution as there are currently only two studies where longitudinal patient information was available [8, 9]. Cognitive decline occurred in 35 % (45 of 130 cases) and psychotic symptoms in 40 % (28 of 69 cases) of cases [7, 14]. In a meta-analysis focusing on cognitive and psychiatric features, dementia was relatively rare in *LRRK2*-PD compared to other monogenic forms of PD with the exception of Parkin [15] (58.8 % PINK1, 53.9 % SNCA, 50 % DJ1, 29.2 % VPS35, 15.7 % *LRRK2* and 7.4 % Parkin). However, cases with dementia have been reported [16]. Similar rates of depression between IPD and *LRRK2*-PD have been observed [17]. With a reported prevalence of 42 %, depression is, however, common in *LRRK2*-PD [15]. An examination of healthy *LRRK2* carriers and non-carriers detected increased UPDRS motor scores, more common urinary problems and fewer hours of sleep in carriers [18]. This may indicate either early signs or a *forme fruste* pointing towards incomplete penetrance and variable expression.

Genetics and penetrance

Multiple pathogenic variants in *LRRK2* have been described: p.N1437H, p.R1441G/H, p.Y1699C, p.G2019S and p.I2020T [7]. These pathogenic variants are present at variable frequencies across the globe. Specifically, *LRRK2* p.R1441G is present at higher frequencies in familial PD in the Spanish Basque region (~4–16.4 %), and the frequency of *LRRK2* p.R1441C is ~4 % in Belgium [19, 20]. The most common *LRRK2* mutation is p.G2019S, with an estimated prevalence of ~1 % in European familial PD populations and higher in North African Arab Berber or Ashkenazi Jewish populations (~15–40 %). Importantly, the penetrance estimates are variable, initial estimates ranging from 28 % at age 59 years, 51 % at 69 years and 74 % at 79 years [6]. Since then, more estimates have been provided by different statistical means (Table 1). Of note, population-specific differences were seen between Tunisian Arab Berbers and Norwegian *LRRK2* p.G2019S carriers using a comparison of cumulative incidence [21]. Though not significantly different, a kin-cohort analysis showed that the risk of PD in non-Ashkenazi Jewish relatives who carry an *LRRK2* p.G2019S mutation was 42.5 % compared to 26 % in Ashkenazi Jews [22] (Table 1). The estimates vary but unequivocally show that there is reduced penetrance for *LRRK2* p.G2019S.

Genetic modifiers have been proposed to influence *LRRK2* penetrance or AAO. A variant located in the intronic region of *CORO1C* on chromosome 12 (rs77395454) was found to be associated with *LRRK2* penetrance and a suggestive association on chromosome 3 was found to be associated in an AAO model in a large cohort [23]. Previously, in a smaller homogeneous Tunisian Arab Berber population, *LRRK2* AAO was associated with a signal on chromosome 1, within *DNM3* [24]. Other linkage regions on chromosomes 1, 3, 4, 17 and 21 have been found to be linked to penetrance in G2019S families [24, 25]. *SNCA* and *MAPT* polymorphisms that were already significantly associated in PD GWAS have also been nominated as candidates [26, 27]. Besides the nuclear genome, mitochondrial DNA (mtDNA) and function has been shown to modify the affection status of *LRRK2* carriers [28]. The effect sizes from genetic studies thus far have been small. Still, only common SNP associations have been reported and thorough investigation of genetic modifiers using large-scale genome sequencing to elucidate the influence of structural variants, repeats, coding variants and regulatory regions is warranted.

Cellular function of *LRRK2*

The *LRRK2* protein and its functions

LRRK2 is a large (2,527 amino acids), multifunctional protein with a catalytic core harbouring a Ras-like GTPase (Ras-of-complex [ROC] in tandem with a C-terminal ROC [COR] domain [ROC-COR GTPase domain]) and a second enzymatically active serine/threonine kinase domain. In addition, its N-terminal end comprises repetitive protein interaction motifs (armadillo, ankyrin and leucine-rich repeats [LRRs]) that are followed by its catalytic core and a tryptophan–aspartic acid repeat WD40 domain at the C-terminal end (Figure 1). There are only four proteins, including *LRRK2*, its shorter homologue *LRRK1*, death-associated protein kinase (DAPK) and a scaffolding protein (MASL1), that contain a ROC-COR GTPase domain [29]. The latter has been shown to be an active GTPase domain, albeit with low micromolar affinity so that *LRRK2* is found

Table 1: Estimates of *LRRK2* p.Gly2019Ser age-associated cumulative incidence and penetrance.

Ethnicity	Sample	Statistical analysis	Age range (cumulative incidence or penetrance)	Reference
Norway, United States, Ireland and Poland	13 *LRRK2* families 22 familial affected carriers	Proportion of affected/total carriers	50–70 (17–85 %)	[30]
French and North African families	2 *LRRK2* families 6 familial affected carriers	Not reported	55–76 (33–100 %)	[31]
Ashkenazi Jews	2,975 familial relatives of 459 probands	Kin cohort [32] *No relatives were genotyped for mutation: probability of carrying mutation was estimated	60–80 (12–24 %)	[33]
Ashkenazi Jews	22 affected carriers	Penetrance calculated from odds ratio	Lifetime risk = 35 %	[34]
Italian (UK Parkinson's Disease Brain Bank)	36 familial affected carriers	Kaplan–Meier [35]	60–80 (15–32 %)	[36]*
Worldwide (mostly European)	133 *LRRK2* families 327 affected members	Kaplan–Meier [35]	59–79 (28–74 %)	[6]*
International multisite	22 familial affected carriers	Product limit survival estimate [35]	60–80 (30–55 %)	[37]*
Arab-Berber	72 affected carriers	Kaplan Meier [35]	60–80 (50–100 %)	[38]
European countries, mainly Italy	154 first-degree relatives and 190 second-degree relatives of 10 p.G2019S carrier probands	Kin cohort [32] *No relatives were genotyped for mutation: probability of carrying mutation was estimated	1st degree 60–80 (12–33 %) 2nd degree 60–80 (10–30 %)	[39]*
Northern Spain (Cantabria)	32 carriers	Kaplan–Meier [35]	60–80 (12–47 %)	[40]
Tunisian Arab Berber	266 *LRRK2* carriers from Tunisia	Kaplan–Meier and kin cohort [32, 35]	80 % by 70 years	[4]
Tunisian Arab Berber and Norwegian	220 affected *LRRK2* p.G2019S carriers, 6 unaffected from Tunisia. 27 affected *LRRK2* p.G2019S carriers and 57 unaffected carriers from Norway	Kaplan–Meier [35]	In Tunisia: 30 %, 61 % and 86 % of *LRRK2* p.G2019S carriers had developed parkinsonism by 50, 60 and 70 years of age. In Norway: 3 %, 20 % and 43 % had developed parkinsonism by 50, 60 and 70 years of age	[21]
Tunisian, Norwegian, Israeli Ashkenazi Jewish	220 affected *LRRK2* p.G2019S carriers and 6 unaffected from Tunisia. 27 affected *LRRK2* p.G2019S carriers and 57 unaffected carriers from Norway	Kaplan–Meier [35]	In Tunisia: 30 %, 61 % and 86 % of *LRRK2* p.G2019S carriers had developed parkinsonism by 50, 60 and 70 years of age. In Israeli Ashkenazi Jews: 30 %, 61 % and 86 % of *LRRK2* p.G2019S carriers had developed parkinsonism by 50, 60 and 70 years of age. In Norway: 3 %, 20 % and 43 % had developed parkinsonism by 50, 60 and 70 years of age	[41]
Ashkenazi Jewish	2,270 relatives of 474 Ashkenazi Jewish Parkinson's disease probands	Kin-cohort [32]	Risk of PD in relatives predicted to carry an *LRRK2* G2019S mutation was 0.26 (95 % CI 0.18–0.36) to age 80 years	[22]
Non-Ashkenazi Jewish	474 first-degree relatives of 69 non-Ashkenazi Jewish *LRRK2* p.G2019S carrier probands	Kin cohort [32]	Risk of PD in non-Ashkenazi Jewish relatives who carry an *LRRK2* p.G2019S mutation was 42.5 % (95 % CI 26.3–65.8 %) to age 80	[42]

Carriers refers to unrelated patients with *LRRK2* p.G2019S (unless otherwise specified). *Meta-analysis of previous reports. All studies are cross-sectional.

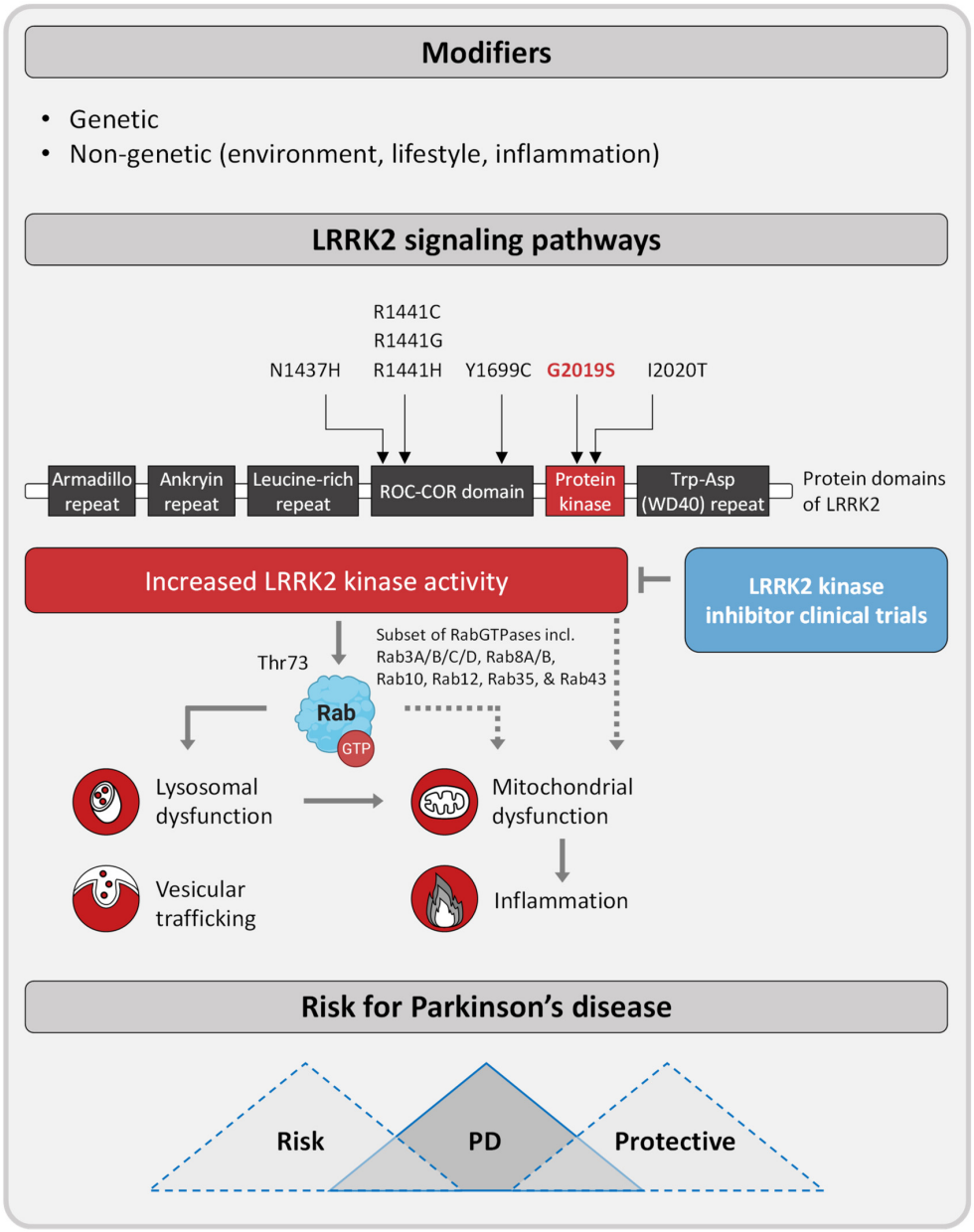

Figure 1: Scheme summarizing the levels of impact of genetic and non-genetic modifiers on the penetrance of mutations in Leucine-rich repeat kinase 2 (*LRRK2*). The most frequent mutation in *LRRK2*, G2019S, is situated in the kinase domain of the protein. Enhanced kinase activity due to G2019S increases the phosphorylation of a subgroup of Rab GTPases that were identified as substrates of *LRRK2*. Via Rabs, *LRRK2* acts on cellular functions such as lysosomal degradation and vesicular trafficking, which in turn may interfere with mitochondrial homeostasis and dynamics as well as immune signalling. How these molecular mechanisms control the transition of an *LRRK2* G2019S mutation carrier from healthy to diseased currently remains elusive. Nonetheless, significant efforts are being made to develop and advance *LRRK2* small molecule inhibitors into clinical trials as kinase inhibition is thought to slow the advancement of the movement disorder. Scheme adapted from Alessi and Sammler (2018) [43]. The figure was created using BioRender.com.

predominantly in the GTP-bound state [44]. GTP binding in turn is essential for *LRRK2* kinase function as point mutations introduced in the ROC domain such as Thr1348Asn that disrupt GTP binding abolish *LRRK2* kinase activity [45]. The kinase activity of *LRRK2* is of particular interest as all clearly disease-associated variants in *LRRK2* result in a gain of kinase function and kinase hyperactivation is a common mechanism in many diseases, including cancer, which has propelled the protein kinase family to become one the most important drug targets in the twenty-first century [46]. In fact, there are currently 62 FDA-approved small molecule kinase inhibitors targeting over 20 different kinases and much effort has gone into developing [47] and advancing *LRRK2* small molecule inhibitors in clinical trials (www.denalitherapeutics.com) (Figure 1).

Pathogenic variants in the ROC GTPase (p.N1437H, the p.R1441 hotspot) and COR (p.Y1699C) domains suppress GTPase activity and promote GTP binding [48] and subsequently cause a 3–4-fold increase in *LRRK2* kinase activity [49, 50]. The common pathogenic p.G2019S and p.I2020T variants are located in the kinase domain and enhance *LRRK2* kinase activity moderately by about 2-fold by domain disruption [29].

Of interest is a cluster of constitutively phosphorylated serine residues (Ser910, Ser935, Ser955 and Ser973) located between the ANK and LRR domains that play a role in regulating 14-3-3 binding (Ser910/935) and cytosolic localization [51, 52]. These residues have received a lot of attention as potential biomarker sites as they are dephosphorylated in response to *LRRK2* inhibition [53], which has been widely used as *in vivo* pharmacokinetic markers, especially Ser935, for small molecule *LRRK2* kinase inhibitor compounds [54–56]. It is also clear that phosphorylation of these residues does not correlate with intrinsic *LRRK2* kinase activity [29], and emerging structural [57] and *LRRK2* kinase inhibitor profiling [58] studies suggest that these biomarker sites report on *LRRK2* conformation in an either inactive 'open' or active 'closed' conformation. Furthermore, various pathogenic variants such as p.R1441G, p.Y1699C and p.I2020T suppress the phosphorylation of Ser910 and Ser935 [57, 59] likely via mutation-induced conformational changes of *LRRK2*. In this context, microtubule association of *LRRK2* is also important as structural data have shown that pathogenic *LRRK2* variants that induce the closed active conformation become capable of microtubule binding in an ordered, oligomeric periodic manner, while the association of wild-type *LRRK2* or even the pathogenic p.G2019S variant with microtubules is significantly less efficient [57, 60]. Lastly, the serine residue 1292 of *LRRK2* deserves mentioning as it is a true *LRRK2* autophosphorylation site that correlates with intrinsic *LRRK2* kinase activity, but its low stoichiometry hinders the exploitation of Ser1292 as an *in vivo* biomarker site for *LRRK2* kinase activation [61].

Rab GTPases and *LRRK2*

The reversible phosphorylation of proteins by kinases is a key regulatory mechanism that controls nearly every aspect of cellular life [62]. It was therefore a major step forward when a subgroup of Rab GTPases was unambiguously identified as endogenous substrates of *LRRK2* in 2016 – 12 years after the discovery that pathogenic variants in *LRRK2* cause PD [50]. In humans, there are over 60 Rab GTPases that are localized to distinct intracellular compartments and regulate membrane trafficking [63]. They exist in GDP-bound 'inactive' and GTP-bound 'active' states, with only the active state allowing the recruitment of cytosolic effector proteins via an α-helical Switch-II motif and subsequent formation of dynamic functional membrane domains for membrane trafficking, vesicle formation, movement along actin and tubular tracks and membrane fusion [29, 63, 64]. The *LRRK2* kinase phosphorylates Rab GTPases at a conserved Thr/Ser motif that lies at the centre of the Switch-II effector-binding domain [50]. As a result, the conformation-dependent interaction between Rab GTPases and their effector proteins including GDP dissociation inhibitors is perturbed with Rab GTPases becoming trapped at the membrane and generally inactive [63, 64].

LRRK2 is predominantly localized in the cytosol and excluded from the nucleus, but about 10 % of *LRRK2* is membrane-bound, where it phosphorylates Rab GTPases [66]. Ten Rab GTPases have been shown to be endogenously phosphorylated by the *LRRK2* kinase including Rab3A/B/C/D, Rab8A/B, Rab10, Rab12, Rab35 and Rab43 [50] (Figure 1). Interestingly, some Rab GTPase effectors including Rab interacting lysosomal-like protein 1 (RILPL1) and RILPL2 preferentially bind Rab8 and Rab10 upon *LRRK2* phosphorylation, thereby interfering with ciliogenesis [50, 67, 68]. In the mouse brain, it has been shown that knock-in of the *LRRK2* kinase activating R1441G mutation impacts ciliary signalling in cholinergic interneurons in the dorsal striatum in terms of an attenuated neuroprotective response to a Sonic hedgehog signal received from dopaminergic neurons [67]. Another exciting discovery is PPM1H as the specific phosphatase that counteracts *LRRK2* signalling by dephosphorylating Rab GTPases [69]. Similar to pathogenic gain-of-kinase-function *LRRK2*

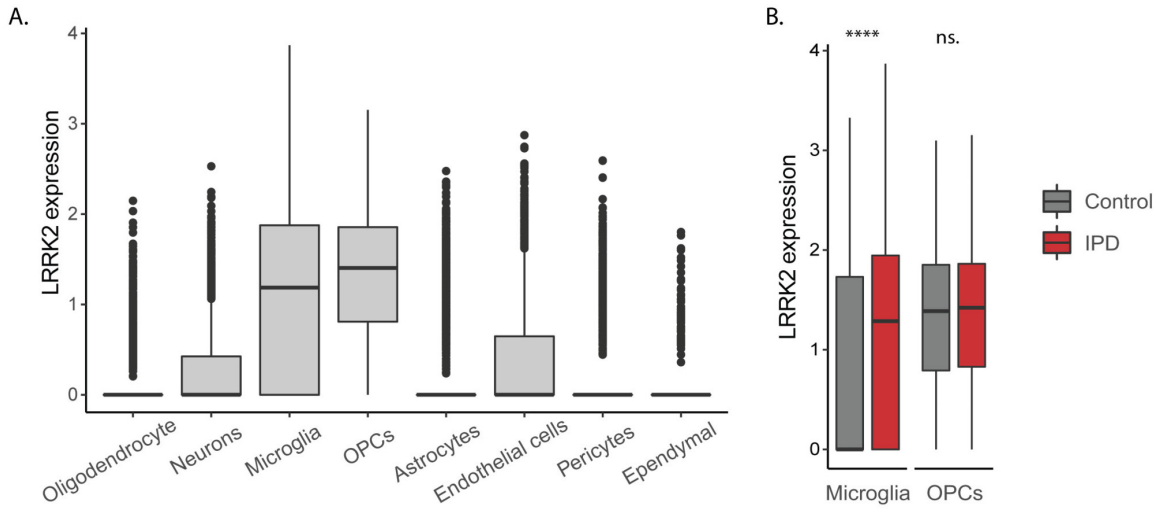

Figure 2: *LRRK2* gene expression in single cells from postmortem midbrain of idiopathic Parkinson's disease (PD) patients and aged controls. We extracted *LRRK2* expression data from our previously generated single-nuclei RNA sequencing atlas of the human midbrain that is available on GEO under the accession number GSE157783 [65]. This analysis revealed highest levels of *LRRK2* in microglia and oligodendrocyte progenitor cells (OPCs). Comparison of the *LRRK2* mRNA abundance in these two cell types derived from IPD patients and controls revealed a disease-specific upregulation only in microglia.

mutations, knock-down of PPM1H suppresses primary ciliogenesis [69]. While future research will need to elucidate the role, effectors and downstream biology of the many other *LRRK2*-phosphorylated Rab GTPases as well as the link to PD, the development of tools and technologies such as phospho-specific monoclonal antibodies and sensitive proteomics mass spectrometry assays has aided in interrogating *LRRK2* kinase pathway activity *in vivo*, including in human peripheral blood [70–73]. In fact, human peripheral blood neutrophils and monocytes lend themselves for interrogating *LRRK2* kinase pathway activity as they are relatively easy to obtain and both represent homogenous blood cell types with relatively high expression of both *LRRK2* and Rab GTPases. So far, peripheral blood neutrophils and monocytes have been used to demonstrate that PD patients carrying a pathogenic heterozygous VPS35 D620N mutation as well as carriers of the *LRRK2* R1441G variant have significantly increased *LRRK2*-dependent Rab10 phosphorylation levels [74, 75]. Such an enhancement has not been observed with the pathogenic *LRRK2* G2019S variant and this has likely to do with the sensitivity of the assay using Rab10 phosphorylation as a readout – as the *LRRK2* G2019S mutation activates *LRRK2* kinase activity only about 2-fold while the *LRRK2* R1441G and VPS35 D620N mutations result in a 3–4- and 4–6-fold increase, respectively [43]. In the future, it will be interesting to utilize alternative assays and readouts including other *LRRK2*-phosphorylated Rab GTPases for measuring *LRRK2* pathway activity.

LRRK2 in immune signalling

There is compelling evidence for a role of *LRRK2* in immune signalling (Figure 1). The protein is expressed in various immune cells including microglia [76], the resident macrophages of the brain [77]. When analysing an in-house single-nuclei RNA sequencing data set from postmortem IPD and control midbrain tissue, the highest levels of *LRRK2* transcripts were detected in oligodendrocyte precursor cells and microglia. However, only in the latter cell type, a disease-specific upregulation was observed (Figure 2). In line with these findings, *LRRK2* protein expression was detected in microglia derived from human induced pluripotent stem cells (iPSCs). The levels of *LRRK2* increased further after treatment with the immune stimulator interferon-gamma [78]. In this cellular system, *LRRK2* was shown to be involved in the recruitment of Rab8a and Rab10 to phagosomes, suggesting that the kinase functions at the intersection between phagosome maturation and recycling pathways [78]. Moreover, single-cell RNA sequencing of control iPSC-derived microglia revealed a strong induction of the mitochondrial antioxidant SOD2 upon treatment with α-synuclein pre-formed fibrils. This response was drastically reduced in microglia lacking

LRRK2, strongly implicating the kinase in neuroinflammatory processes in the PD brain [77].

Yet, *LRRK2*'s immune action is not limited to the CNS. GWAS identified a variant in *LRRK2* that conferred an increased risk for Crohn's disease [79] – an inflammatory bowel disease. Moreover, in Norwegian *LRRK2* families a high incidence of rheumatoid arthritis was reported [80]. Consistent with elevated *LRRK2* levels in B cells, T cells [81], macrophages [82], monocytes and neutrophils [71], the kinase is thought to regulate the immune response to pathogens [83]. *LRRK2* KO mice are more susceptible to intestinal *Listeria monocytogenes* infection than wild-type animals [84]. Similarly, *LRRK2*-deficient mice show increased bacterial colonization and reduced survival after infection with *Salmonella typhimurium* [85]. A mechanistic study in murine macrophages revealed that *LRRK2* kinase activity is crucial for the activation of the NLRC4 inflammasome during the host defence response [85].

Based on the current literature, scientists speculate that an overactivated *LRRK2* kinase may be beneficial during early life, protecting mutation carriers against infections [43, 83]. By contrast, with advancing age, chronic pro-inflammatory signalling may increase the permeability of the blood–brain barrier and facilitate microglial priming [43, 83], which in turn could aggravate neuronal degeneration. Thus, in accordance with the 'second hit hypothesis' in PD, the number and severity of infections that an *LRRK2* mutation carrier has to endure may define the penetrance of the movement disorder in this individual.

The ability of *LRRK2* to induce an immune reaction after infections may at least in part also explain the mitochondrial phenotypes observed in cellular models of *LRRK2*-PD. As an ancestor of a eubacterial endosymbiont [86], mitochondria harbour their own circular genome, which is characterized by low-level methylation [87]. In this way, mtDNA is distinct from nuclear DNA, and when released into the cytosol or extracellular space, it may be mistaken as foreign, triggering an autoimmune response against the patient's own mitochondria. The research into the contribution of mitochondria to the pathogenesis in *LRRK2*-PD is manifold and will be briefly summarized in the next section.

LRRK2 and mitochondria

When investigating the subcellular localization of *LRRK2*, the protein was found to be associated with membranes, including the outer mitochondrial membrane [88]. A combination of co-immunoprecipitation, super-resolution microscopy and 3D virtual reality-assisted image analysis further uncovered that *LRRK2* interacts with subunits of the translocase of outer mitochondrial membrane (TOM) complex [89].

Inspired by its localization, researchers investigated mitochondrial morphology in cellular models of *LRRK2*-PD with diverging results. While early work showed elongated mitochondria in G2019S mutant fibroblasts [90], later phenotyping studies suggested a fragmentation of the mitochondrial network in patient cells [91, 92]. The latter observation is supported by functional experiments revealing a direct interaction between *LRRK2* and the mitochondrial fission protein DLP1 [88]. By modulating the abundance of DRP1 at the mitochondria, *LRRK2* kinase activity can regulate mitochondrial dynamics. Overexpression of wild-type *LRRK2* led to increased mitochondrial fission – a phenomenon that was further enhanced in the presence of PD mutations [93].

While the above-described network analyses in fixed patient cells only provided a static idea of the impairments caused by mutant *LRRK2*, mitochondrial motility assessments in *LRRK2* G2019S mutants were used to acquire further mechanistic insight. According to these analyses, *LRRK2* is involved in the removal of Miro1, which, together with Milton, anchors mitochondria to motors and microtubules for organellar transport [94]. In the presence of mutations in *LRRK2*, this link is stabilized by Miro1, thereby preventing the arrest and subsequent lysosomal degradation of dysfunctional organelles [94] (Figure 1).

Thus, there is evidence that *LRRK2* does not only interfere with mitochondrial clearance in this indirect fashion [88] (Figure 1). In fibroblasts from PD patients harbouring the G2019S mutation in *LRRK2*, increased mitochondrial–lysosomal co-localization was observed [91]. Moreover, analyses in patient fibroblasts harbouring the G2019S mutation and in HeLa cells overexpressing *LRRK2* G2019S revealed elevated protein levels of the autophagy markers p62 and LC3II [92, 95]. This result could either be suggestive of reduced lysosomal turnover or indicate accelerated mitophagy in *LRRK2* mutant cells. Interestingly, data to support both of these scenarios have been published. While Su and colleagues reported that overexpressed *LRRK2* G2019S phosphorylates Bcl-2 at Thr56, which exacerbates mitophagy in HeLa cells and primary rat neurons [95], Bonello et al. showed that Parkin-induced mitophagy is impaired in fibroblasts from patients carrying the G2019S mutation in *LRRK2* [96].

In line with an accumulation of damaged mitochondria, a multitude of studies described increased ROS generation and enhanced susceptibility to free radicals in cellular models of *LRRK2*-PD [97]. However, the oxidative

stress phenotype may also be explained through *LRRK2*'s interaction with the mitochondrial antioxidant PRDX3. The peroxidase is phosphorylated by mutant *LRRK2*, which causes mitochondrial dysfunction and oxidative damage [97]. In addition, *LRRK2* G2019S was shown to increase the abundance of UCP2, which mediates mitochondrial uncoupling and proton leakage [92, 98]. This impact on respiratory chain function is further evidenced by reduced complex I activity [99] and oxygen consumption rates [100] in patient cells with the G2019S mutation.

Possibly as a result of increased oxidative stress, the mitochondrial impairments in *LRRK2*-PD extend to the mtDNA. Lesions in the mitochondrial genome were observed in neuronal cells derived from patients with the G2019S mutation [101]. Moreover, overexpression experiments in primary rat neurons showed that the mtDNA phenotype caused by *LRRK2* G2019S is midbrain-specific. Interestingly, treatment of these cells with an *LRRK2* kinase inhibitor sufficed to rescue the detected damage, suggesting that mtDNA disintegration in *LRRK2*-PD is kinase-dependent [102].

While the wide spectrum of mitochondrial alterations strongly implicate mitochondria in the pathology of the movement disorder, few functional studies focussed on the contribution of the organelles to the penetrance of *LRRK2*-PD. Our own research revealed that mtDNA major arc deletions are more abundant in manifesting compared to non-manifesting G2019S mutation carriers [28]. In addition, mtDNA replication was shown to be impaired in affected but not unaffected individuals harbouring *LRRK2* G2019S [103]. These disease-specific changes in mtDNA integrity and homeostasis appear to interfere with respiratory chain function as manifesting G2019S mutation carriers show lower complex I activity than their non-manifesting counterparts [99]. Increased mtDNA copy number and mitochondrial mass in patients with *LRRK2* G2019S may implicate impaired mitochondrial clearance as a penetrance-defining mechanism in these individuals [99]. Interestingly, in carriers of the G2019S mutation, also a PD-specific overexpression of *Nrf2* was detected. The transcription factor is part of the NF-E2-related factor 2–antioxidant responsive element (Nrf2–ARE) pathway, which is induced by ROS. Further strengthening this finding, Bakshi and colleagues performed a biomarker study in a large cohort of *LRRK2* mutation carriers and detected increased levels of the Nrf2 activator urate in affected compared to unaffected individuals [104]. Experiments in neurons from G2019S isogenic pairs highlight the contribution of the genetic background to the pathology of *LRRK2*-PD. In this study, in three iPSC lines, CRISPR/Cas9 gene editing was used to insert the G2019S mutation in *LRRK2* into a genetic control background. In another three lines, the G2019S mutation was corrected in a patient background. Various parameters of neuronal and mitochondrial morphology were then used in a cluster analysis, which resulted in a grouping by genotype. Moreover, an assessment of tyrosine hydroxylase abundance in the 3D cultures revealed that the generation of G2019S in the control background induced DA neuron demise. By contrast, *LRRK2* mutation correction in the patient background did not lead to a rescue of the DA neuron phenotype [105]. While these results could be explained by the genetic signature of a patient alone, they may also be reflective of the impact of environmental factors. Toxin exposure may exacerbate the molecular effects of increased *LRRK2* kinase activity in a patient in an irreversible manner (e. g. at the level of the epigenome and/or the mtDNA), thereby triggering the onset of PD in an individual.

LRRK2 and clinical lifestyle data

A combination of genetic and/or environmental factors influences PD susceptibility. For example, a meta-analysis has shown that smoking had a robust negative association with PD risk [106]. Furthermore, smoking is correlated with a later onset of motor and non-motor symptoms [107]. The causal protective relationship of smoking initiation has been supported by a recent Mendelian randomization study [108]. Although a direct causal relationship between PD onset and other lifestyle factors has yet to be established, coffee drinking is equally correlated with a reduced risk of PD [106]. Slower progression of motor and non-motor signs and symptoms has been shown for coffee consumers in a longitudinal study [109]. By contrast, with regard to environmental factors affecting PD, pesticide exposure is associated with an increased risk [106, 110]. The effects of environmental and lifestyle factors on AAO of *LRRK2* p.Gly2019Ser have yet to be thoroughly investigated. Reports have shown an association of smoking in *LRRK2* p.Gly2019Ser mutation carriers [111]: tobacco use is associated with later AAO in patients carrying the *LRRK2* p.G2019S mutation and the intensity and duration of smoking is correlated with AAO in these individuals. An effect of tobacco use was observed exclusively on non-motor symptoms but not on motor symptoms after adjustment for disease duration. Additional exploratory analyses on other lifestyle and environmental exposures revealed an interesting joint but

independent effect for smoking and black tea drinking, indicating that a more complex interaction exists. Non-steroidal anti-inflammatory drugs (NSAIDs) have also recently been shown to correlate with *LRRK2* penetrance [112, 113]. The odds ratio for use of any NSAID was 0.34 (95 % CI 0.21–0.57); for ibuprofen it was 0.19 (0.07–0.50); and for aspirin it was 0.51 (0.28–0.91). A similar benefit was observed when NSAID treatment was five years before AAO [113].

Given the effects of lifestyle and environment on *LRRK2* [111] and the protective effects of smoking, caffeine and anti-inflammatory drugs on IPD [106, 109], there is ongoing interest in AAO, penetrance and other lifestyle factors in *LRRK2* parkinsonism (Figure 1).

Environmental toxins as modifier of *LRRK2*-PD penetrance

Toxins are a subset of environmental factors that may influence PD susceptibility, yet the sheer number of potential toxins humans are exposed to in their daily environment renders this both an analytical and biomedical challenge. Estimates of chemicals in household use and/or on the market in significant amounts (i. e. tonnes of chemical) range between ~70,000 to 350,000 [114, 115]; the largest open chemical databases now contain well over 100 million chemicals [116]. While many of the lifestyle factors mentioned above can be directly associated with particular chemicals (smoking and nicotine; coffee/tea and caffeine), nicotine and caffeine are only two of hundreds of other chemicals known to be present in cigarettes and tea/coffee, respectively (see references within [117]). Similarly, NSAIDs are also a large group of chemicals, with 159 NSAIDs mentioned in the Chemicals of Biological Interest (ChEBI) NSAID page (CHEBI:35475) alone (https://www.ebi.ac.uk/chebi) [118]. Pesticides are even more challenging, with over 3,000 agrochemicals (approximately synonymous with pesticides) listed in PubChem (3,101 dated 31 July, 2021) [116]. To date, epidemiology and exposomics studies have generally focussed on only a narrow range of dozens of known chemicals (toxins, often the so-called priority pollutants) or biomarkers in a targeted manner, which is unable to handle this sheer number of chemicals [119].

The rise of non-targeted high-resolution mass spectrometry (NT-HRMS) in environmental chemistry, metabolomics and thus also exposomics is opening the window to investigate further chemicals [119]. One of the biggest challenges in the exposome, which aims to not only measure the environmental exposure but also the biological perturbations that result, is the range of concentrations expected in samples. For example, biological signals in blood are at concentrations many orders of magnitude higher than the concentrations at which pesticides and other chemicals toxic in very low amounts could be expected to have an effect [120]. Some pharmaceuticals and other chemicals, such as caffeine and NSAIDs, can be closer to endogenous metabolites in concentration [120]. While information such as medical records and/or current blood samples could reveal present or past medication regimes of a patient, previous toxin exposure – potentially decades before disease onset in the case of PD – is much more difficult to capture. For instance, patients have been known to respond 'no' to questions regarding pesticide use, yet answer positively to 'have you used Round-Up in your garden' (the active ingredient, glyphosate, is a well-known pesticide) [117].

The definition of chemicals relevant for exposomics studies is an area of active research, since browsing the chemical space of tens of millions is not feasible. In one study, a set of 1,243 literature-mind neurotoxins (with more than five references) connected to distinct disease endpoints including PD was included in online databases and as an interactive Excel macro [117]. 'CECScreen' contains ~70,000 structures and was an outcome of the Human Biomonitoring for EU (HBM4EU) project [121]; the Blood Exposome database contains ~65,000 chemicals [122], while PubChemLite for Exposomics, a highly annotated subset of PubChem most relevant for exposomics studies, contains approximately 380,000 chemicals [123], including pharmaceuticals, pesticides, biomolecular pathways and all chemicals with associated disorders and diseases. Narrowing this down to a specific disease and gene reduces the window much further. The Comparative Toxicogenomics Database (CTD) [124] lists 78 chemicals interacting with *LRRK2* (http://ctdbase.org/detail.go?type=gene&acc=120892), with the most interactions belonging to several chemicals, including three pesticides often associated with PD: paraquat, maneb and rotenone (none of which, however, are approved for use in Europe), MPP+ (commonly associated with PD), as well as manganese and magnesium, benzo(a)pyrene and some biological molecules (lipopolysaccharides, adenosine triphosphate) and a steroid (corticosterone). These few chemicals alone would require several different analytical methods for detection [117]. Thus, the gap between literature associations [124], what can be detected in humans [120] and what is permitted and detected in environmental observations is still a challenge. However, the necessary tools to tackle these challenges are now available. A convergence

of genetic-based disease interpretation and the influence of the environment via the concept of the exposome is likely to become a reality in the next few years as the fields slowly become aware of the mutual aims and challenges involved in merging the large amount of information available and forming concrete interpretations.

Outlook

An unexpected outcome of recent major sequencing and gene identification efforts was the finding of a surprisingly large number of carriers of a putatively pathogenic mutation who remained free of the disease in question. This phenomenon of 'reduced penetrance' appears to have been substantially underestimated and the concept of protection against disease or delay of its AAO has been largely neglected within the genomic research community. The identification of such factors could have important implications for treatment and genetic counselling of patients. In the context of *LRRK2* parkinsonism, genetic and lifestyle penetrance modifiers can help in patient counselling and set the premise for future studies of endogenous protection.

The advent of iPSC technologies now permits the generation of patient-derived neuron and glia models, which allow studying the effects of drugs and pollutants at the endogenous level also in neurodegenerative disorders such as genetic PD. By contrast, investigating the effects of toxins in a systemic fashion will remain a challenge. While novel protocols for 2D or 3D co-culture systems and organoids are being developed, we are still far away from modelling the complexity of the brain in a dish. Still, large data sets that are being generated by applying especially 'omics' analysis methods to patient-derived cultures can inform *in silico* models of cellular function in response to stressors in PD. With regard to the human metabolome, a virtual database has already been generated ([125]; www.vmh.life) and efforts are being made to extend this work to specific cell types in PD [126]. However, currently, these models do not consider disruptions due to environmental insults, which may at least partially stem from the fact that the landscape of chemicals relevant in the pathogenesis of PD is not well defined.

Large data aggregators or knowledge bases such as PubChem can play a role in delineating the role of toxins in PD and even in the case of specific genes such as *LRRK2*. By integrating data from many resources, a single gene page provides an overview of several connections between the gene and chemicals, including from resources such as CTD [116, 127]. The data overview indicates quickly that literature observations conflict for the top chemicals mentioned in CTD such as benzo(a)pyrene and valproic acid. The top gene–chemical co-occurrences in literature listed on the *LRRK2* page in PubChem reveals several chemicals related to PD, some of those mentioned in CTD, and other chemicals of potential interest, which could be investigated proactively in patient samples via a suspect screening approach using NT-HRMS. Knowing the chemicals of interest in advance can assist in scoping and designing the appropriate analytical measurements. However, one disrupting factor in exposomics-based PD studies is the general disruption of the gut in PD patients compared with controls, which tends to lead to many perturbations related to gut dysfunction in blood/serum samples that may overwhelm the significance of any toxin signals [128–130] and thus interfere with the data interpretation. In this regard, other samples to capture patient exposure, such as dust samples [131] or surface and wastewater as a wider environmental proxy at the population level [132], are potentially of interest in the future to complement cohort studies and to advance research in patient-based cellular models as described above.

Research funding: JT, MK and AG obtained funding from the German Research Foundation ('ProtectMove'; FOR 2488). JT is the recipient of funding from the Canadian Institutes of Health Research (CIHR) (FRN152440), the Peter and Traudl Engelhorn Foundation and the Joachim Herz Stiftung (850022). ELS acknowledges funding support from the Luxembourg National Research Fund (FNR) for project A18/BM/12341006. SS received funding from the FNR within the PARK-QC DTU (PRIDE17/12244779/PARK-QC). MK was supported within the framework of the Lübeck International Parkinson Disease (LIPAD) study funded by Centogene Rostock. ES was supported by grants from the Michael J. Fox Foundation (MJFF-019271) and Tenovus Scotland as well as a Senior Clinical Academic Fellowship from CSO NHS Research Scotland. AG was funded by the FNR within the ATTRACT ('Model-IPD', FNR9631103) and INTER programs ('ProtectMove', INTER/DFG/19/14429377). The funding organization(s) played no role in the study design; in the collection, analysis, and Interpretation of data; in the writing of the report; or in the decision to submit the report for publication.

Competing interests: Authors state no conflict of interest.

Informed consent: Not applicable.

Ethical approval: Not applicable.

References

[1] Paisan-Ruiz C et al. Cloning of the gene containing mutations that cause PARK8-linked Parkinson's disease. Neuron. 2004;44(4):595–600.
[2] Paisan-Ruiz C, Lewis PA, Singleton AB. *LRRK2*: cause, risk, and mechanism. J Parkinsons Dis. 2013;3(2):85–103.
[3] Chen W et al. Gender differences in prevalence of *LRRK2*-associated Parkinson disease: A meta-analysis of observational studies. Neurosci Lett. 2020;715:134609.
[4] Trinh J et al. Comparative study of Parkinson's disease and leucine-rich repeat kinase 2 p.G2019S parkinsonism. Neurobiol Aging. 2014;35(5):1125–31.
[5] Aasly JO et al. Clinical features of *LRRK2*-associated Parkinson's disease in central Norway. Ann Neurol. 2005;57(5):762–5.
[6] Healy DG et al. Phenotype, genotype, and worldwide genetic penetrance of *LRRK2*-associated Parkinson's disease: a case-control study. Lancet Neurol. 2008;7(7):583–90.
[7] Trinh J et al. Genotype-phenotype relations for the Parkinson's disease genes SNCA, *LRRK2*, VPS35: MDSGene systematic review. Mov Disord. 2018;33(12):1857–70.
[8] Nabli F et al. Motor phenotype of *LRRK2*-associated Parkinson's disease: a Tunisian longitudinal study. Mov Disord. 2015;30(2):253–8.
[9] Saunders-Pullman R et al. Progression in the *LRRK2*-Associated Parkinson Disease Population. JAMA Neurol. 2018;75(3):312–9.
[10] Marras C et al. Phenotype in parkinsonian and nonparkinsonian *LRRK2* G2019S mutation carriers. Neurology. 2011;77(4):325–33.
[11] Marras C et al. Motor and nonmotor heterogeneity of *LRRK2*-related and idiopathic Parkinson's disease. Mov Disord. 2016;31(8):1192–202.
[12] Ben Sassi S et al. Cognitive dysfunction in Tunisian *LRRK2* associated Parkinson's disease. Parkinsonism Relat Disord. 2012;18(3):243–6.
[13] Saunders-Pullman R et al. Olfactory identification in *LRRK2* G2019S mutation carriers: a relevant marker? Ann Clin Transl Neurol. 2014;1(9):670–8.
[14] Saunders-Pullman R et al. REM sleep behavior disorder, as assessed by questionnaire, in G2019S *LRRK2* mutation PD and carriers. Mov Disord. 2015;30(13):1834–9.
[15] Piredda R et al. Cognitive and psychiatric symptoms in genetically determined Parkinson's disease: a systematic review. Eur J Neurol. 2020;27(2):229–34.
[16] O'Grady SM, Cooper KE, Rae JL. Cyclic GMP regulation of a voltage-activated K channel in dissociated enterocytes. J Membr Biol. 1991;124(2):159–67.
[17] Lohmann E et al. A clinical, neuropsychological and olfactory evaluation of a large family with *LRRK2* mutations. Parkinsonism Relat Disord. 2009;15(4):273–6.
[18] Johansen KK et al. Subclinical signs in *LRRK2* mutation carriers. Parkinsonism Relat Disord. 2011;17(7):528–32.
[19] Nuytemans K et al. Founder mutation p.R1441C in the leucine-rich repeat kinase 2 gene in Belgian Parkinson's disease patients. Eur J Hum Genet. 2008;16(4):471–9.
[20] Biskup S, West AB. Zeroing in on *LRRK2*-linked pathogenic mechanisms in Parkinson's disease. Biochim Biophys Acta. 2009;1792(7):625–33.
[21] Hentati F et al. *LRRK2* parkinsonism in Tunisia and Norway: a comparative analysis of disease penetrance. Neurology. 2014;83(6):568–9.
[22] Marder K et al. Age-specific penetrance of *LRRK2* G2019S in the Michael J. Fox Ashkenazi Jewish *LRRK2* Consortium. Neurology. 2015;85(1):89–95.
[23] Lai D et al. Genomewide Association Studies of *LRRK2* Modifiers of Parkinson's Disease. Ann Neurol. 2021;90(1):76–88.
[24] Trinh J et al. DNM3 and genetic modifiers of age of onset in *LRRK2* Gly2019Ser parkinsonism: a genome-wide linkage and association study. Lancet Neurol. 2016;15(12):1248–56.
[25] Latourelle JC et al. Genomewide association study for onset age in Parkinson disease. BMC Med Genet. 2009;10:98.
[26] Gan-Or Z et al. The age at motor symptoms onset in *LRRK2*-associated Parkinson's disease is affected by a variation in the MAPT locus: a possible interaction. J Mol Neurosci. 2012;46(3):541–4.
[27] Fernandez-Santiago R et al. alpha-synuclein (SNCA) but not dynamin 3 (DNM3) influences age at onset of leucine-rich repeat kinase 2 (*LRRK2*) Parkinson's disease in Spain. Mov Disord. 2018;33(4):637–41.
[28] Ouzren N et al. Mitochondrial DNA Deletions Discriminate Affected from Unaffected *LRRK2* Mutation Carriers. Ann Neurol. 2019;86(2):324–6.
[29] Taylor M, Alessi DR. Advances in elucidating the function of leucine-rich repeat protein kinase-2 in normal cells and Parkinson's disease. Curr Opin Cell Biol. 2020;63:102–13.
[30] Kachergus J et al. Identification of a novel *LRRK2* mutation linked to autosomal dominant parkinsonism: evidence of a common founder across European populations. Am J Hum Genet. 2005;76(4):672–80.
[31] Lesage S et al. G2019S *LRRK2* mutation in French and North African families with Parkinson's disease. Ann Neurol. 2005;58(5):784–7.
[32] Wacholder S et al. The kin-cohort study for estimating penetrance. Am J Epidemiol. 1998;148(7):623–30.
[33] Clark LN et al. Frequency of *LRRK2* mutations in early- and late-onset Parkinson disease. Neurology. 2006;67(10):1786–91.
[34] Ozelius LJ et al. *LRRK2* G2019S as a cause of Parkinson's disease in Ashkenazi Jews. N Engl J Med. 2006;354(4):424–5.
[35] Kaplan EL, Meier P. Nonparametric-Estimation from Incomplete Observations. J Am Stat Assoc. 1958;53(282):457–81.
[36] Goldwurm S et al. Evaluation of *LRRK2* G2019S penetrance: relevance for genetic counseling in Parkinson disease. Neurology. 2007;68(14):1141–3.
[37] Latourelle JC et al. The Gly2019Ser mutation in *LRRK2* is not fully penetrant in familial Parkinson's disease: the GenePD study. BMC Med. 2008;6:32.
[38] Hulihan MM et al. *LRRK2* Gly2019Ser penetrance in Arab-Berber patients from Tunisia: a case-control genetic study. Lancet Neurol. 2008;7(7):591–4.
[39] Goldwurm S et al. Kin-cohort analysis of *LRRK2*-G2019S penetrance in Parkinson's disease. Mov Disord. 2011;26(11):2144–5.
[40] Sierra M et al. High frequency and reduced penetrance of *LRRK2* G2019S mutation among Parkinson's disease patients in Cantabria (Spain). Mov Disord. 2011;26(13):2343–6.

[41] Trinh J, Guella I, Farrer MJ. Disease penetrance of late-onset parkinsonism: a meta-analysis. JAMA Neurol. 2014;71(12):1535–9.
[42] Lee AJ et al. Penetrance estimate of *LRRK2* p.G2019S mutation in individuals of non-Ashkenazi Jewish ancestry. Mov Disord. 2017;32(10):1432–8.
[43] Alessi DR, Sammler E. *LRRK2* kinase in Parkinson's disease. Science. 2018;360(6384):36–7.
[44] Ito G et al. GTP binding is essential to the protein kinase activity of *LRRK2*, a causative gene product for familial Parkinson's disease. Biochemistry. 2007;46(5):1380–8.
[45] Purlyte E et al. Rab29 activation of the Parkinson's disease-associated *LRRK2* kinase. EMBO J. 2018;37(1):1–18.
[46] Roskoski R Jr. Properties of FDA-approved small molecule protein kinase inhibitors: A 2021 update. Pharmacol Res. 2021;165:105463.
[47] Galatsis P. Leucine-rich repeat kinase 2 inhibitors: a patent review (2014–2016). Expert Opin Ther Pat. 2017;27(6):667–76.
[48] Nguyen AP, Moore DJ. Understanding the GTPase Activity of *LRRK2*: Regulation, Function, and Neurotoxicity. Adv Neurobiol. 2017;14:71–88.
[49] Greggio E et al. Kinase activity is required for the toxic effects of mutant *LRRK2/dardarin*. Neurobiol Dis. 2006;23(2):329–41.
[50] Steger M et al. Phosphoproteomics reveals that Parkinson's disease kinase *LRRK2* regulates a subset of Rab GTPases. Elife. 2016;5:e12813.
[51] Nichols RJ et al. 14-3-3 binding to *LRRK2* is disrupted by multiple Parkinson's disease-associated mutations and regulates cytoplasmic localization. Biochem J. 2010;430(3):393–404.
[52] Doggett EA et al. Phosphorylation of *LRRK2* serines 955 and 973 is disrupted by Parkinson's disease mutations and *LRRK2* pharmacological inhibition. J Neurochem. 2012;120(1):37–45.
[53] Dzamko N et al. Inhibition of *LRRK2* kinase activity leads to dephosphorylation of Ser(910)/Ser(935), disruption of 14-3-3 binding and altered cytoplasmic localization. Biochem J. 2010;430(3):405–13.
[54] Deng X et al. Characterization of a selective inhibitor of the Parkinson's disease kinase *LRRK2*. Nat Chem Biol. 2011;7(4):203–5.
[55] Reith AD et al. GSK2578215A; a potent and highly selective 2-arylmethyloxy-5-substitutent-N-arylbenzamide *LRRK2* kinase inhibitor. Bioorg Med Chem Lett. 2012;22(17):5625–9.
[56] Fell MJ et al. MLi-2, a Potent, Selective, and Centrally Active Compound for Exploring the Therapeutic Potential and Safety of *LRRK2* Kinase Inhibition. J Pharmacol Exp Ther. 2015;355(3):397–409.
[57] Deniston CK et al. Structure of *LRRK2* in Parkinson's disease and model for microtubule interaction. Nature. 2020;588(7837):344–9.
[58] Tasegian A et al. Impact of Type II *LRRK2* inhibitors on signalling and mitophagy. bioRxiv, 2021.
[59] Lowenstein H. Characterization and chemical modification of isolated allergens from horse hair and dandruff. Int Arch Allergy Appl Immunol. 1978;57(4):349–57.
[60] Watanabe R et al. The In Situ Structure of Parkinson's Disease-Linked *LRRK2*. Cell. 2020;182(6):1508–18.e16.
[61] Sheng Z et al. Ser1292 autophosphorylation is an indicator of *LRRK2* kinase activity and contributes to the cellular effects of PD mutations. Sci Transl Med. 2012;4(164):164ra161.
[62] Cohen P. The origins of protein phosphorylation. Nat Cell Biol. 2002;4(5):E127–30.
[63] Stenmark H. Rab GTPases as coordinators of vesicle traffic. Nat Rev Mol Cell Biol. 2009;10(8):513–25.
[64] Pfeffer SR. *LRRK2* and Rab GTPases. Biochem Soc Trans. 2018;46(6):1707–12.
[65] Smajić S et al. Single-cell sequencing of human midbrain reveals glial activation and a Parkinson-specific neuronal state. Brain. 2022;145(3):964–78.
[66] Gomez RC et al. Membrane association but not identity is required for *LRRK2* activation and phosphorylation of Rab GTPases. J Cell Biol. 2019;218(12):4157–70.
[67] Dhekne HS et al. A pathway for Parkinson's Disease *LRRK2* kinase to block primary cilia and Sonic hedgehog signaling in the brain. Elife. 2018;7:e40202.
[68] Lara Ordonez AJ et al. RAB8, RAB10 and RILPL1 contribute to both *LRRK2* kinase-mediated centrosomal cohesion and ciliogenesis deficits. Hum Mol Genet. 2019;28(21):3552–68.
[69] Berndsen K et al. PPM1H phosphatase counteracts *LRRK2* signaling by selectively dephosphorylating Rab proteins. Elife. 2019;8:e50416.
[70] Lis P et al. Development of phospho-specific Rab protein antibodies to monitor in vivo activity of the *LRRK2* Parkinson's disease kinase. Biochem J. 2018;475(1):1–22.
[71] Fan Y et al. Interrogating Parkinson's disease *LRRK2* kinase pathway activity by assessing Rab10 phosphorylation in human neutrophils. Biochem J. 2018;475(1):23–44.
[72] Karayel O et al. Accurate MS-based Rab10 Phosphorylation Stoichiometry Determination as Readout for *LRRK2* Activity in Parkinson's Disease. Mol Cell Proteomics. 2020;19(9):1546–60.
[73] Nirujogi RS et al. Development of a multiplexed targeted mass spectrometry assay for *LRRK2*-phosphorylated Rabs and Ser910/Ser935 biomarker sites. Biochem J. 2021;478(2):299–326.
[74] Fan Y et al. R1441G but not G2019S mutation enhances *LRRK2* mediated Rab10 phosphorylation in human peripheral blood neutrophils. Acta Neuropathol. 2021;142(3):475–94.
[75] Mir R et al. The Parkinson's disease VPS35[D620N] mutation enhances *LRRK2*-mediated Rab protein phosphorylation in mouse and human. Biochem J. 2018;475(11):1861–83.
[76] Miklossy J et al. *LRRK2* expression in normal and pathologic human brain and in human cell lines. J Neuropathol Exp Neurol. 2006;65(10):953–63.
[77] Russo I et al. Transcriptome analysis of *LRRK2* knock-out microglia cells reveals alterations of inflammatory- and oxidative stress-related pathways upon treatment with alpha-synuclein fibrils. Neurobiol Dis. 2019;129:67–78.
[78] Lee H et al. *LRRK2* Is Recruited to Phagosomes and Co-recruits RAB8 and RAB10 in Human Pluripotent Stem Cell-Derived Macrophages. Stem Cell Rep. 2020;14(5):940–55.
[79] Hui KY et al. Functional variants in the *LRRK2* gene confer shared effects on risk for Crohn's disease and Parkinson's disease. Sci Transl Med. 2018;10(423):e50416.
[80] Aasly JO. Inflammatory Diseases Among Norwegian *LRRK2* Mutation Carriers. A 15-Years Follow-Up of a Cohort. Front Neurosci. 2021;15:634666.
[81] Cook DA et al. *LRRK2* levels in immune cells are increased in

Parkinson's disease. NPJ Parkinsons Dis. 2017;3:11.
[82] Hartlova A et al. *LRRK2* is a negative regulator of Mycobacterium tuberculosis phagosome maturation in macrophages. EMBO J. 2018;37(12):e98694.
[83] Wallings RL, Herrick MK, Tansey MG. *LRRK2* at the Interface Between Peripheral and Central Immune Function in Parkinson's. Front Neurosci. 2020;14:443.
[84] Zhang Q et al. Commensal bacteria direct selective cargo sorting to promote symbiosis. Nat Immunol. 2015;16(9):918–26.
[85] Liu W et al. *LRRK2* promotes the activation of NLRC4 inflammasome during Salmonella Typhimurium infection. J Exp Med. 2017;214(10):3051–66.
[86] Gray MW, Burger G, Lang BF. Mitochondrial evolution. Science. 1999;283(5407):1476–81.
[87] Mechta M et al. Evidence Suggesting Absence of Mitochondrial DNA Methylation. Front Genet. 2017;8:166.
[88] Singh A, Zhi L, Zhang H. *LRRK2* and mitochondria: Recent advances and current views. Brain Res. 2019;1702:96–104.
[89] Neethling A et al. Wild-type and mutant (G2019S) leucine-rich repeat kinase 2 (*LRRK2*) associate with subunits of the translocase of outer mitochondrial membrane (TOM) complex. Exp Cell Res. 2019;375(2):72–9.
[90] Mortiboys H et al. Mitochondrial impairment in patients with Parkinson disease with the G2019S mutation in *LRRK2*. Neurology. 2010;75(22):2017–20.
[91] Smith GA et al. Fibroblast Biomarkers of Sporadic Parkinson's Disease and *LRRK2* Kinase Inhibition. Mol Neurobiol. 2016;53(8):5161–77.
[92] Grunewald A et al. Does uncoupling protein 2 expression qualify as marker of disease status in *LRRK2*-associated Parkinson's disease? Antioxid Redox Signal. 2014;20(13):1955–60.
[93] Wang X et al. *LRRK2* regulates mitochondrial dynamics and function through direct interaction with DLP1. Hum Mol Genet. 2012;21(9):1931–44.
[94] Hsieh CH et al. Functional Impairment in Miro Degradation and Mitophagy Is a Shared Feature in Familial and Sporadic Parkinson's Disease. Cell Stem Cell. 2016;19(6):709–24.
[95] Su YC, Guo X, Qi X. Threonine 56 phosphorylation of Bcl-2 is required for *LRRK2* G2019S-induced mitochondrial depolarization and autophagy. Biochim Biophys Acta. 2015;1852(1):12–21.
[96] Bonello F et al. *LRRK2* impairs PINK1/Parkin-dependent mitophagy via its kinase activity: pathologic insights into Parkinson's disease. Hum Mol Genet. 2019;28(10):1645–60.
[97] Dias V, Junn E, Mouradian MM. The role of oxidative stress in Parkinson's disease. J Parkinsons Dis. 2013;3(4):461–91.
[98] Papkovskaia TD et al. G2019S leucine-rich repeat kinase 2 causes uncoupling protein-mediated mitochondrial depolarization. Hum Mol Genet. 2012;21(19):4201–13.
[99] Delcambre S et al. Mitochondrial Mechanisms of *LRRK2* G2019S Penetrance. Front Neurol. 2020;11:881.
[100] Cooper O et al. Pharmacological rescue of mitochondrial deficits in iPSC-derived neural cells from patients with familial Parkinson's disease. Sci Transl Med. 2012;4(141):141ra90.
[101] Sanders LH et al. *LRRK2* mutations cause mitochondrial DNA damage in iPSC-derived neural cells from Parkinson's disease patients: reversal by gene correction. Neurobiol Dis. 2014;62:381–6.
[102] Howlett EH et al. *LRRK2* G2019S-induced mitochondrial DNA damage is *LRRK2* kinase dependent and inhibition restores mtDNA integrity in Parkinson's disease. Hum Mol Genet. 2017;26(22):4340–51.
[103] Podlesniy P et al. Accumulation of mitochondrial 7S DNA in idiopathic and *LRRK2* associated Parkinson's disease. eBioMedicine. 2019;48:554–67.
[104] Bakshi R et al. Higher urate in *LRRK2* mutation carriers resistant to Parkinson disease. Ann Neurol. 2019;85(4):593–9.
[105] Bolognin S et al. 3D Cultures of Parkinson's Disease-Specific Dopaminergic Neurons for High Content Phenotyping and Drug Testing. Adv Sci (Weinh). 2019;6(1):1800927.
[106] Noyce AJ et al. Meta-analysis of early nonmotor features and risk factors for Parkinson disease. Ann Neurol. 2012;72(6):893–901.
[107] Gigante AF et al. Smoking and age-at-onset of both motor and non-motor symptoms in Parkinson's disease. Parkinsonism Relat Disord. 2017;45:94–6.
[108] Grover S et al. Risky behaviors and Parkinson disease: A mendelian randomization study. Neurology. 2019;93(15):e1412–24.
[109] Paul KC et al. The association between lifestyle factors and Parkinson's disease progression and mortality. Mov Disord. 2019;34(1):58–66.
[110] Ascherio A et al. Pesticide exposure and risk for Parkinson's disease. Ann Neurol. 2006;60(2):197–203.
[111] Luth T et al. Age at Onset of *LRRK2* p.Gly2019Ser Is Related to Environmental and Lifestyle Factors. Mov Disord. 2020;35(10):1854–8.
[112] Fyfe I. Aspirin and ibuprofen could lower risk of *LRRK2* Parkinson disease. Nat Rev Neurol. 2020;16(9):460.
[113] San Luciano M et al. Nonsteroidal Anti-inflammatory Use and *LRRK2* Parkinson's Disease Penetrance. Mov Disord. 2020;35(10):1755–64.
[114] Schwarzenbach RP et al. The challenge of micropollutants in aquatic systems. Science. 2006;313(5790):1072–7.
[115] Wang Z et al. Toward a Global Understanding of Chemical Pollution: A First Comprehensive Analysis of National and Regional Chemical Inventories. Environ Sci Technol. 2020;54(5):2575–84.
[116] Kim S et al. PubChem in 2021: new data content and improved web interfaces. Nucleic Acids Res. 2021;49(D1):D1388–95.
[117] Schymanski EL et al. Connecting environmental exposure and neurodegeneration using cheminformatics and high resolution mass spectrometry: potential and challenges. Environ Sci Process Impacts. 2019;21(9):1426–45.
[118] Hastings J et al. ChEBI in 2016: Improved services and an expanding collection of metabolites. Nucleic Acids Res. 2016;44(D1):D1214–9.
[119] Vermeulen R et al. The exposome and health: Where chemistry meets biology. Science. 2020;367(6476):392–6.
[120] Rappaport SM et al. The blood exposome and its role in discovering causes of disease. Environ Health Perspect. 2014;122(8):769–74.
[121] Meijer J et al. An annotation database for chemicals of emerging concern in exposome research. Environ Int. 2021;152:106511.
[122] Barupal DK, Fiehn O. Generating the Blood Exposome

Database Using a Comprehensive Text Mining and Database Fusion Approach. Environ Health Perspect. 2019;127(9):97008.
[123] Schymanski EL et al. Empowering large chemical knowledge bases for exposomics: PubChemLite meets MetFrag. J Cheminformatics. 2021;13(1):19.
[124] Davis AP et al. Comparative Toxicogenomics Database (CTD): update 2021. Nucleic Acids Res. 2021;49(D1):D1138–43.
[125] Brunk E et al. Recon3D enables a three-dimensional view of gene variation in human metabolism. Nat Biotechnol. 2018;36(3):272–81.
[126] Mao L et al. A constraint-based modelling approach to metabolic dysfunction in Parkinson's disease. Comput Struct Biotechnol J. 2015;13:484–91.
[127] Zaslavsky L et al. Discovering and Summarizing Relationships Between Chemicals, Genes, Proteins, and Diseases in PubChem. Front Res Metr Anal. 2021;6:689059.
[128] Elfil M et al. Implications of the Gut Microbiome in Parkinson's Disease. Mov Disord. 2020;35(6):921–33.
[129] Cirstea MS et al. Microbiota Composition and Metabolism Are Associated With Gut Function in Parkinson's Disease. Mov Disord. 2020;35(7):1208–17.
[130] Boertien JM et al. Increasing Comparability and Utility of Gut Microbiome Studies in Parkinson's Disease: A Systematic Review. J Parkinsons Dis. 2019;9(s2):S297–312.
[131] Rostkowski P et al. The strength in numbers: comprehensive characterization of house dust using complementary mass spectrometric techniques. Anal Bioanal Chem. 2019;411(10):1957–77.
[132] Escher BI, Stapleton HM, Schymanski EL. Tracking complex mixtures of chemicals in our changing environment. Science. 2020;367(6476):388–92.

Joanne Trinh
Institute of Neurogenetics, University of Lübeck, Lübeck, Germany

Emma L. Schymanski
Luxembourg Centre for Systems Biomedicine, University of Luxembourg, Esch-sur-Alzette, Luxembourg

Semra Smajic
Luxembourg Centre for Systems Biomedicine, University of Luxembourg, Esch-sur-Alzette, Luxembourg

Meike Kasten
Institute of Neurogenetics, University of Lübeck, Lübeck, Germany
Department of Psychiatry and Psychotherapy, University of Lübeck, Lübeck, Germany

Esther Sammler
Medical Research Council (MRC) Protein Phosphorylation and Ubiquitylation Unit, School of Life Sciences, University of Dundee, Dundee, UK
Department of Neurology, School of Medicine, Dundee, Ninewells Hospital, Dundee, UK

Anne Grünewald, PhD
Luxembourg Centre for Systems Biomedicine, University of Luxembourg, Esch-sur-Alzette, Luxembourg
Institute of Neurogenetics, University of Lübeck, Lübeck, Germany
anne.gruenewald@uni.lu

Manuscript VI

frontiers in Cell and Developmental Biology

ORIGINAL RESEARCH
published: 05 November 2021
doi: 10.3389/fcell.2021.740758

iPSC-Derived Microglia as a Model to Study Inflammation in Idiopathic Parkinson's Disease

*Katja Badanjak[1], Patrycja Mulica[1], Semra Smajic[1], Sylvie Delcambre[1], Leon-Charles Tranchevent[1], Nico Diederich[2], Thomas Rauen[3], Jens C. Schwamborn[1], Enrico Glaab[1], Sally A. Cowley[4], Paul M. A. Antony[1,5], Sandro L. Pereira[1], Carmen Venegas[1] and Anne Grünewald[1,6]**

[1] Luxembourg Centre for Systems Biomedicine, University of Luxembourg, Luxembourg, Luxembourg, [2] Centre Hospitalier de Luxembourg (CHL), Luxembourg, Luxembourg, [3] Department of Cell and Developmental Biology, Max Planck Institute for Molecular Biomedicine, Münster, Germany, [4] James Martin Stem Cell Facility, Sir William Dunn School of Pathology, University of Oxford, Oxford, United Kingdom, [5] Disease Modeling and Screening Platform (DMSP), Luxembourg Institute of Systems Biomedicine, University of Luxembourg and Luxembourg Institute of Health, Luxembourg, Luxembourg, [6] Institute of Neurogenetics, University of Lübeck, Lübeck, Germany

OPEN ACCESS

Edited by:
Andreas Hermann, University Hospital Rostock, Germany

Reviewed by:
Qian Chen, Warren Alpert Medical School of Brown University, United States
Björn Spittau, Bielefeld University, Germany

***Correspondence:**
Anne Grünewald
anne.gruenewald@uni.lu

Specialty section:
This article was submitted to Stem Cell Research, a section of the journal Frontiers in Cell and Developmental Biology

Received: *13 July 2021*
Accepted: *08 October 2021*
Published: *05 November 2021*

Citation:
Badanjak K, Mulica P, Smajic S, Delcambre S, Tranchevent L-C, Diederich N, Rauen T, Schwamborn JC, Glaab E, Cowley SA, Antony PMA, Pereira SL, Venegas C and Grünewald A (2021) iPSC-Derived Microglia as a Model to Study Inflammation in Idiopathic Parkinson's Disease. Front. Cell Dev. Biol. 9:740758. doi: 10.3389/fcell.2021.740758

Parkinson's disease (PD) is a neurodegenerative disease with unknown cause in the majority of patients, who are therefore considered "idiopathic" (IPD). PD predominantly affects dopaminergic neurons in the substantia nigra pars compacta (SNpc), yet the pathology is not limited to this cell type. Advancing age is considered the main risk factor for the development of IPD and greatly influences the function of microglia, the immune cells of the brain. With increasing age, microglia become dysfunctional and release pro-inflammatory factors into the extracellular space, which promote neuronal cell death. Accordingly, neuroinflammation has also been described as a feature of PD. So far, studies exploring inflammatory pathways in IPD patient samples have primarily focused on blood-derived immune cells or brain sections, but rarely investigated patient microglia *in vitro*. Accordingly, we decided to explore the contribution of microglia to IPD in a comparative manner using, both, iPSC-derived cultures and postmortem tissue. Our meta-analysis of published RNAseq datasets indicated an upregulation of *IL10* and *IL1B* in nigral tissue from IPD patients. We observed increased expression levels of these cytokines in microglia compared to neurons using our single-cell midbrain atlas. Moreover, *IL10* and *IL1B* were upregulated in IPD compared to control microglia. Next, to validate these findings *in vitro*, we generated IPD patient microglia from iPSCs using an established differentiation protocol. IPD microglia were more readily primed as indicated by elevated *IL1B* and *IL10* gene expression and higher mRNA and protein levels of NLRP3 after LPS treatment. In addition, IPD microglia had higher phagocytic capacity under basal conditions—a phenotype that was further exacerbated upon stimulation with LPS, suggesting an aberrant microglial function. Our results demonstrate the significance of microglia as the key player in the neuroinflammation process in IPD. While our study highlights the importance of microglia-mediated inflammatory signaling in IPD, further investigations will be needed to explore particular disease mechanisms in these cells.

Keywords: microglia, iPSC, neuroinflammation, idiopathic Parkinson's disease, disease modeling

INTRODUCTION

Parkinson's disease (PD) is an age-related, multifactorial disorder, resulting in the demise of dopaminergic neurons in the substantia nigra pars compacta (SNpc) of the midbrain, which subsequently leads to motor difficulties, tremor, and postural instability in affected individuals (Pang et al., 2019). While there is a genetic component to the disease, with 10% of all cases carrying a mutation in one of the causal PD genes, 90% of patients are deemed idiopathic.

The majority of studies published to date describe molecular mechanisms centered around α-synuclein aggregation, mitochondrial dysfunction, dysregulated autophagy flux, and neuroinflammation as the underlying causes of PD (Wang et al., 2015; Maiti et al., 2017). Interestingly, all of these processes are also affected by aging, which leads to functional decline, both at the physiological and molecular level. Thus, it is not surprising that aging is considered a major risk factor for the development of PD (Jin et al., 2020).

Additionally, "inflammaging" is a novel term coined to define basal, low-level inflammation during adult life that, with time, turns into a destructive, pathological process. On the one hand, lower levels of inflammation are considered to have a positive outcome on the overall cellular state. On the other hand, during prolonged inflammation, beneficial mechanisms of defense start to wear off while damaging insults increase. This phenomenon might explain why seemingly low-grade inflammatory occurrences can have a significant negative impact on health in older individuals (Calabrese et al., 2018).

Inflammation is one of the hallmarks of PD and it is propagated mostly through microglia cells, which are responsible for the innate immune defense of the brain. Early brain tissue studies showed an upregulation of microglial cells in the SNpc and higher expression of human major histocompatibility complex class II (MHC-II) molecules, while in human serum and cerebrospinal fluid (CSF), increased concentrations of cytokines such as IL-1β, IL-6, TNF-α, IL-2, IL-18, and, IL-10 were detected (Nagatsu and Sawada, 2005; Brodacki et al., 2008; Long-Smith et al., 2009; Collins et al., 2012; Wang et al., 2015; Badanjak et al., 2021). In line with these results, our own immunohistochemistry and single-nuclei transcriptomic analyses in postmortem midbrain tissue revealed an increase in abundance and a decrease in the complexity of microglia in IPD tissue, suggestive of an activated state. Moreover, patient microglia presented a disease-specific gene expression signature, indicating a significant role of these cells in the pathogenesis of the movement disorder (Smajić et al., 2020). Also, most recently, genes of the IFN-γ signaling pathway were found to be dysregulated in IPD patients (Magalhaes et al., 2021).

One of the most commonly implicated inflammatory pathways in PD is the inflammasome pathway (Chao et al., 2014; Sebastian-Valverde and Pasinetti, 2020; Yan et al., 2020). The NOD-, LRR-, and pyrin domain-containing protein 3 (NLRP3) is by far the most studied inflammasome, the main function of which is the clearance of pathogens. NLRP3 is a cytosolic sensor of intracellular and extracellular stimuli such as damage-associated and pathogen-associated molecular patterns (DAMPs and PAMPs, respectively). Two signals are necessary to fully activate this pathway, a priming signal and an activation signal. The priming signal is characterized by the upregulation of *IL1B* and *NLRP3* expression, while the secondary signal is characterized by the release of mature cytokines (Swanson et al., 2019). Underlining the relevance of the NLRP3 inflammasome, IL-1β has been associated with disease pathogenesis in multiple PD biomarker studies (Koprich et al., 2008; Su et al., 2008; Nakahira et al., 2011; Gillardon et al., 2012; Pike et al., 2021).

In our current study, we investigated inflammation markers in different models of IPD. First, we explored available RNAseq transcriptomic datasets from postmortem midbrain tissues to assess the expression of key cytokines in IPD. Next, we differentiated microglia from iPSC from IPD and control donors to test whether these cells can mirror the phenotypes observed in the brain. We detected elevated levels of *IL1B* and *IL10* in whole tissue or single cell RNAseq datasets from IPD nigral or midbrain sections. Indicative of the fidelity of iPSC-derived cellular PD models, both *IL1B* and *IL10* were also upregulated in patient microglia upon lipopolysaccharide (LPS) treatment. This coincided with increased protein abundance of NLRP3 in these cells, further implicating the inflammasome in the pathogenesis of PD.

MATERIALS AND METHODS

Bulk RNA Cytokine Expression Analysis

To profile the expression of cytokines in human SN tissue, we used a differential expression meta-analysis of publicly available case-control transcriptomics datasets, including only SN samples, as previously described (Glaab and Schneider, 2015). This provided meta-analysis Z-scores and FDR significance scores for candidate genes of interest (see **Supplementary Table 1**).

Postmortem Single-Nuclei RNA Sequencing of Human Midbrain

To analyze cytokine expression in a single-cell landscape, in this study, we used our previously published snRNAseq dataset from five IPD and six control postmortem midbrain tissues (GSE157783). The normalization, sample integration and cell clustering were performed using *Seurat* (version 3.1.5) in R 4.0.0., as described in Smajić et al. (2020).

The gene expression analysis was performed in neuronal and microglial clusters derived from our snRNAseq dataset (Smajić et al., 2020). For each of the two clusters, pseudobulk populations were created by merging all cells in the cluster from every individual in order to present the overall expression of cytokines. Then, the expression was presented as a sum of expressions of each individual cell and displayed in a bar plot using *"ggplot2"* and *"gg.gap"* packages. The cytokine expression in microglia was shown in both conditions using the *"DotPlot"* function.

Differentiation of Human iPSCs Into Microglia

An IPD patient as well as an age- and gender-matched control (both female, age: 68; IPD patient AAO: 60), who donated skin biopsies for the study, gave written and informed consent. Skin fibroblasts were reprogrammed into iPSCs as previously described (Arias-Fuenzalida et al., 2017). The study was approved by the Comité National d'Ethique de Recherche Luxembourg (CNER, vote 201411/05 V1.3). iPSCs were maintained in mTeSR^{TM}1 complete medium (StemCell Technologies). Microglia were differentiated from iPSCs following an established protocol (van Wilgenburg et al., 2013; Haenseler et al., 2017). In brief, embryoid bodies (EBs) were generated from iPSCs in mTeSR Plus (STEMCELL Technologies) supplemented with 50 ng/ml BMP-4 (Invitrogen), 50 ng/ml VEGF (Invitrogen) and 20 ng/ml SCF (Miltenyi). On day 4, EBs were transferred to a low attachment 6-well plate and were replenished with fresh EB media. On day 7, the medium was changed to X-VIVO 15 (Lonza) supplemented with 25 ng/ml IL-3 (Invitrogen), 100 ng/ml M-CSF (Invitrogen), 2 mM Glutamax (Gibco), 1% P/S (Gibco) and 0.055 mM β-mercaptoethanol (Gibco) and the EBs were transferred to T75 flasks (factories). These conditions promoted the generation of macrophage precursors. The factories were kept in culture for up to 6–8 months and macrophage precursors were harvested regularly. Terminal differentiation was achieved by culturing macrophage precursors in advanced DMEM/F12 supplemented with N2, Glutamax, P/S, β-mercaptoethanol, 100 ng/ml IL-34 (Peprotech) and 10 ng/ml GM-CSF (Peprotech). During all steps of the differentiation, cells were incubated at 37°C, 5% CO_2.

Microglia Treatments

Microglia were seeded into 6-well plates at a density of 1 × 10^6 cells/well. Upon treatment with 100 ng/ml LPS (Thermo Fisher Scientific 00-4976-93) for 3 h, cells were subjected to protein and RNA extractions. For functional analyses, microglia were seeded into 96-well glass-bottom plates at a density of 25,000 cells/well. Cells were treated with 50,000 Zymosan bioparticles (Thermo Fisher Scientific) per well for 45 min. After, cells were subjected to fixation (described in more detail below).

RNA Isolation and Quantitative PCR

RNA was isolated from microglia using the RNeasy RNA isolation kit (Qiagen, 74106) following the manufacturer's instructions for direct RNA extraction from the plate. cDNA was synthesized from 200 ng of RNA using the SuperScript^{TM} III Reverse Transcriptase (Invitrogen, 18080044). Quantitative PCR (qPCR) was performed using iQ SYBR Green (Biorad, 170-8885). The PCR reaction was run on a LightCycler 480 (Roche). The samples were denatured for 5 min at 95°C. Amplification ran over 45 cycles with a denaturation step of 10 s at 95°C, primer annealing of 10 s at 60°C, and elongation of 10 s at 75°C. The expression of *IL1B*, *IL10, LRRK2*, and *NLRP3* was normalized to the expression of the housekeeping gene *ACTB*.

Western Blotting

Total protein from microglia cultures were extracted directly from the plate, using ice cold RIPA buffer (Pierce) supplemented with 1X Protease/phosphatase Inhibitor Cocktail (Thermo Fisher Scientific). The whole well was washed multiple times, on ice, and the lysate suspension was transferred to an Eppendorf tube and vortexed for 20 s followed by incubation on ice for 20 min. The samples were centrifuged at 21,130 g for 20 min at 4°C. The protein concentration of the cell lysates was measured using a bicinchoninic acid assay using Pierce^{TM} BCA protein kit (Thermo Fisher Scientific) following the manufacturer's instructions.

Cell lysates were denatured in a loading buffer at 95°C for 5 min prior to loading on the gels. Proteins were then separated on NuPAGE 4–12% Bis-Tris gels (Invitrogen) in NuPAGE MES Running Buffer (NP0002) and transferred on a 0.2 μm nitrocellulose membrane. Membranes were blocked with 5% milk in TBS supplemented with Tween-20 (TBST, 10 mM Tris-HCl, 150 mM NaCl, 0.1% Tween-20, pH 8.0) for 1 h at RT. Thereafter, membranes were incubated overnight at 4°C with the following primary antibodies: 1:1,000 anti-NLRP3 (D4D8T, Cell Signaling), 1:500 anti-LRRK2 (75–188, UC Davis), 1:10,000 anti-β-actin (A1978, Sigma). On the next day, membranes were washed three times in TBST and incubated with the respective secondary antibodies for 1 h at RT. Immunoreactivity was detected by enhanced chemiluminescence reaction (ECL select Western blotting detection reagent, GE Healthcare) or near-infrared detection (Odyssey, Li-COR).

Immunocytochemistry and Image Analysis

IPSCs and microglia were fixed in 4% PFA (Thermo Fisher Scientific, Alfa Aesar J61899) for 15 min and washed twice with PBS (Westburg, LO BE17-513F). The cells were permeabilized and blocked in PBS containing 0.25% Triton X-100 and 1% BSA for 1 h at RT followed by overnight incubation with primary antibodies: anti-Nanog (3580S, Bioke), anti-Sox2 (sc-365823, Santa Cruz), anti-Oct4 (ab19857, Abcam), anti-Iba1 (ab5076, Abcam), anti-P2RY12 (APR-020-F, Alomone labs). On the next day, cells were washed and incubated with the corresponding secondary antibodies. Thereafter, another three washing steps with PBS were completed and Hoechst was used as a counterstain at 0.1 mg/ml for 15 min in PBS. To mount the cover slips onto slides, Prolong Antifade mounting media (Thermo Fisher Scientific) was used. Acquisition of microglia images was performed using a Zeiss LSM 710 and Yokogawa CV8000 microscope, and images of iPSC were acquired with a Zeiss Axio Imager M2. All acquired images were normalized for secondary-only antibody control, to confirm specificity of the signal observed.

For quantitative image analysis, custom code was implemented using MATLAB 2020a, and computations were performed using the High-Performance Computing (HPC) infrastructure of the University of Luxembourg (Varrette et al., 2014). Briefly, the "ZymosanAreaByIba1Area" is the ratio between Zymosan positive pixels and Iba1 positive pixels per

field of view. Furthermore, the mean abundance of Iba1 has been quantified as ratio of Iba1 area per nuclei count. The underlying MATLAB code is available upon request.

Statistics

All experiments carried out using iPSC-derived microglia were performed with 3–4 biological replicates. The data was normalized by the average of values per replicate. For statistical analyses, GraphPad Prism software (version 9) was used. To evaluate the presence of outliers, we used the ROUT test. Two-way ANOVA was used for grouped values. Differences were considered significant (*) when *p*-values were below 0.05.

RESULTS

Idiopathic Postmortem Midbrain Tissue Is Exhibiting Increased Cytokine Gene Expression

Studies implicating inflammatory cytokines in PD have been mostly conducted on neurotoxin and genetic animal models, or by analyzing peripheral blood samples and CSF from PD patients (Badanjak et al., 2021). To further confirm if these findings are indeed occurring in the brain of IPD patients, we analyzed available transcriptomic datasets. The transcriptomics data of human IPD and control SN revealed a significant increase in *IL1B* and *IL10* expression in the patient tissue (*FDR* = 0.023; *FDR* = 0.0067, respectively) (**Figure 1A** and **Supplementary Table 1**). A recent study showed that inflammation is not only mediated by microglia but can also be observed in neurons from an IPD mouse model (Panicker et al., 2020). In order to understand whether the detected immune signatures in the human SN are also cell-type specific, we examined our midbrain snRNAseq dataset to obtain an insight into transcriptional changes with single-cell resolution. We confirmed that the expression of cytokines is specific to microglia (**Figure 1B**). Further analysis of the microglia population revealed higher expression and a larger percentage of expressing cells in IPD compared to control tissue (**Figure 1C** and **Supplementary Table 2**).

Characterization of iPSC-Derived Microglia Model

IPD patient and control microglia were generated using an established protocol (van Wilgenburg et al., 2013; Haenseler et al., 2017; **Figure 2A**). The available iPSC lines were characterized by immunostaining with the stem cell markers Nanog, Sox2 and Oct4 (**Figure 2B**). Differentiation of iPSCs into microglia was achieved with the addition of multiple factors throughout the differentiation process (**Figure 2A**) to mimic microglia development in the human embryo. The microglial identity of cells was confirmed by positive expression of Iba1 and purinergic receptor (P2RY12) (**Figure 2C**). Comparable Iba1 areas per nuclei suggest that the disease status of the investigated lines did not have an impact on the differentiation procedure (**Figure 2D**). Additionally, we wanted to functionally characterize microglia cells by treating them with Zymosan bioparticles and assessing their phagocytic ability. While both control and IPD microglia were able to phagocyte the bioparticles, IPD microglia had a higher capacity (mean: 0.02493, *SD* = 0.02472) compared to control microglia (mean: 0.01606, *SD* = 0.01304; ANOVA: $^{***}p = 0.0004$). Furthermore, although the mean phagocytic capacity after LPS treatment was not significantly different between untreated and treated cells, IPD microglia had a significantly higher uptake of Zymosan particles compared to control cells upon addition of LPS (CTR/LPS mean: 0.01897, *SD* = 0.01695; IPD/LPS mean: 0.02683, *SD* = 0.02835; ANOVA: $^{**}p = 0.0070$) (**Figure 3**).

Upregulation of NOD-, LRR- and Pyrin Domain-Containing Protein 3 Inflammasome Components in Idiopathic Microglia

To test the transferability of our findings from postmortem single-nuclei transcriptomics to live cells, we investigated the gene expression of *IL1B* and *IL10* in iPSC-derived IPD microglia. Moreover, we quantified the mRNA and protein levels of the NLRP3 inflammasome, the inflammatory pathway most associated with chronic inflammation in PD. The priming step in inflammasome assembly is frequently mimicked by LPS

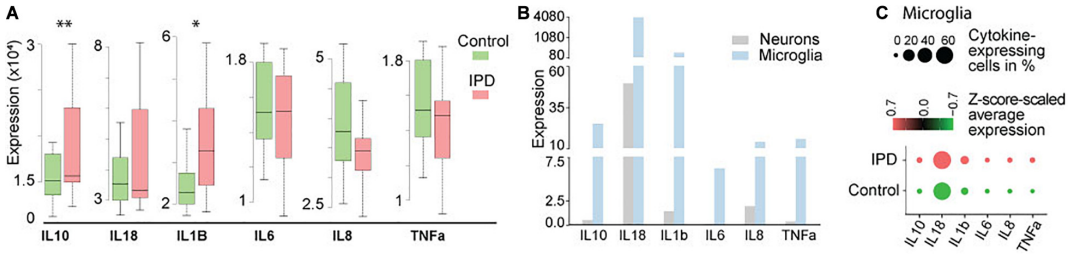

FIGURE 1 | Cytokine expression in bulk RNA-seq and single-nuclei RNA-seq datasets. **(A)** Bulk analysis of SN tissue displays higher expression of *IL1B* and *IL10* in IPD (*FDR* = 0.023; *FDR* = 0.0067). **(B)** Single-nuclei analysis of the human midbrain shows that the overall expression of cytokines is higher in microglia (3903 cells) than in neurons (5314 cells). **(C)** Cytokines are expressed in a large number of IPD and control microglia. Z-score-scaled average expression per cluster shows higher levels in IPD compared to control microglia. "*DotPlot*" function (Seurat package) was used to visualize expression and percentage of cytokine-expressing cells. $^{*}p < 0.05$; $^{**}p < 0.01$; IPD, idiopathic PD.

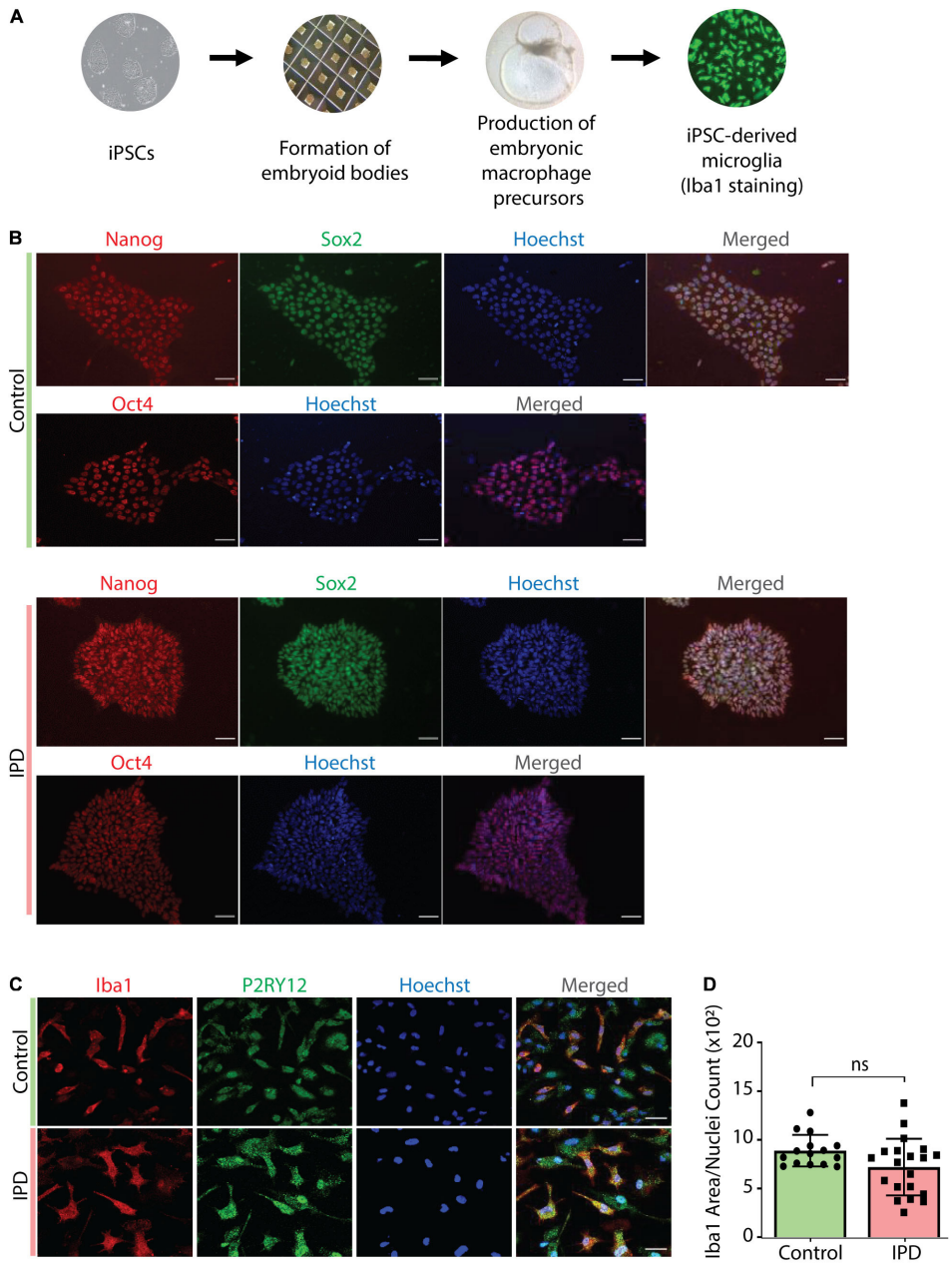

FIGURE 2 | Characterization of cellular models used in the study. **(A)** Overview of the protocol used to derive microglia from iPSCs. **(B)** Immunostaining with Nanog, Sox-2 and Oct-4, coupled with nuclear staining with Hoechst, confirmed the iPSC identity of our cells. Scale bar, 50 μm. **(C)** Terminally differentiated microglia were confirmed to express the microglia-specific markers Iba1 and P2RY12. Scale bar, 30 μm. **(D)** Quantification of data from **(C)**; no difference in Iba1 protein levels (Iba1 area was normalized for nuclei count); IPD, idiopathic PD; CTR, healthy control.

treatment (McKee and Coll, 2020). At baseline, IPD and control microglia did not show significant differences (data not shown). However, upon LPS treatment, the expression levels of *IL1B* and *IL10* increased significantly in both conditions compared to the respective untreated cells (*IL1B* CTR/LPS fold mean: 1.558, $SD = 0.117$; ANOVA: $^{**}p = 0.0098$; IPD/LPS fold mean: 3.880, $SD = 0.323$; ANOVA: $^{****}p < 0.0001$; *IL10* CTR/LPS fold mean: 3.409, $SD = 0.342$, ANOVA: $^{****}p < 0.0001$; IPD/LPS

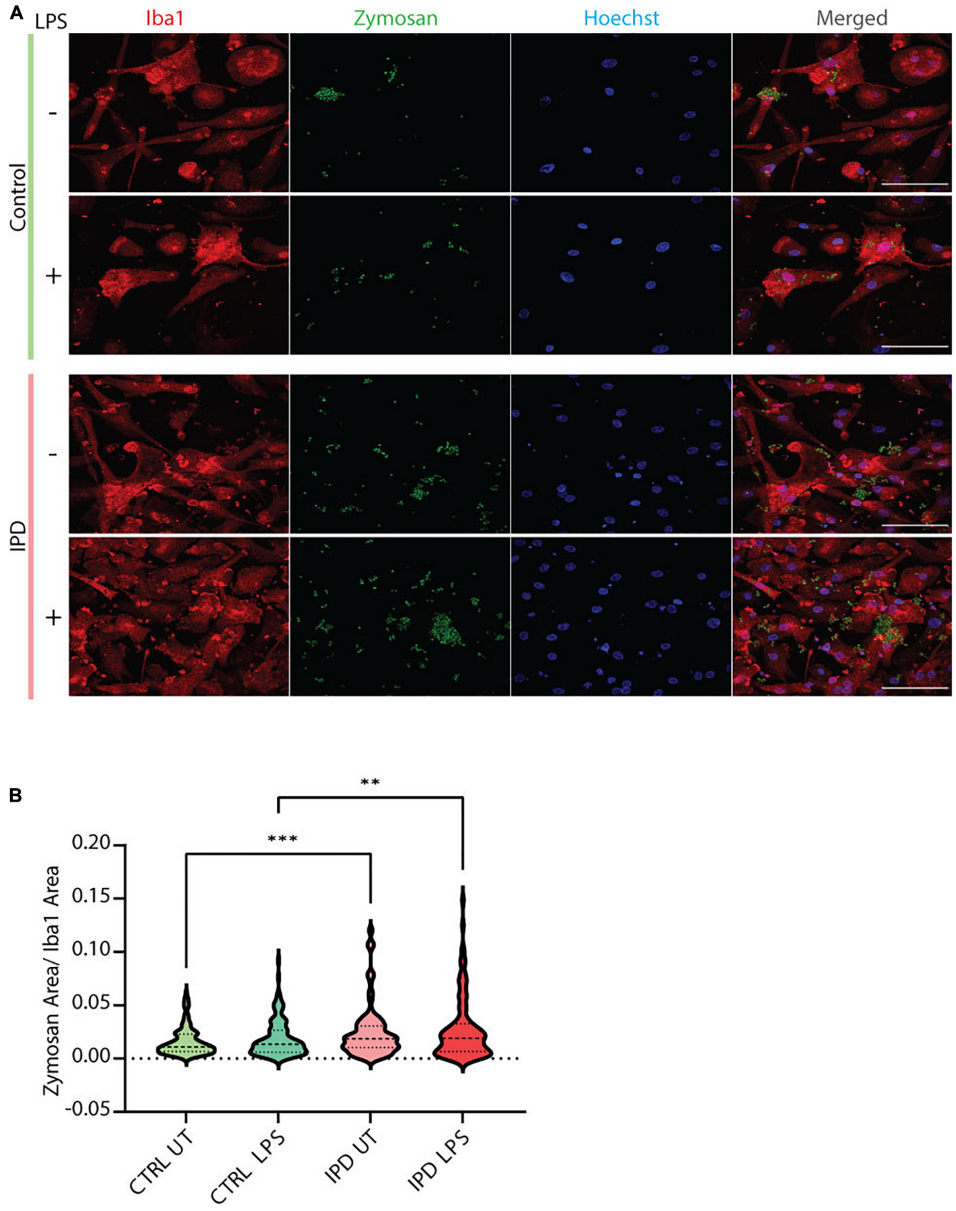

FIGURE 3 | Functional assessment of iPSC-derived microglia. **(A)** Representative immunostaining showing the functional ability of cultured control and IPD microglia treated with Zymosan bioparticles. Scale bar, 50 μm. **(B)** Quantification of data from **(A)**; IPD microglia have higher phagocytic capacity (Zymosan area was normalized for Iba1 area) compared to control cells. $^{**}p < 0.01$; $^{***}p < 0.001$; IPD, idiopathic PD; CTRL, healthy control.

fold mean: 7.717, $SD = 0.530$, ANOVA: $^{****}p < 0.0001$). When comparing the treatment response between both conditions, IPD microglia showed significantly higher *IL1B* and *IL10* expressions fold changes compared to control cells (*IL1B* LPS mean: 2.719, $SD = 1.642$; ANOVA: $^{****}p < 0.0001$; *IL10* LPS mean: 5.563, $SD = 3.047$, ANOVA: $^{****}p < 0.0001$). Additionally, when investigating *NLRP3* expression, only IPD microglia showed a significant upregulation upon LPS treatment, compared to both untreated IPD cells (*NLRP3* IPD/LPS fold mean: 3.984, $SD = 0.250$; ANOVA: $^{****}p < 0.0001$) and to LPS-treated healthy microglia (*NLRP3* LPS mean: 2.627, $SD = 1.918$; ANOVA: $^{****}p < 0.0001$) (**Figure 4A**).

Furthermore, NLRP3 protein levels corroborated the gene expression results. Again, both control and IPD microglia had significantly higher NLRP3 protein levels upon LPS addition compared to their respective basal levels (CTR/LPS fold mean:

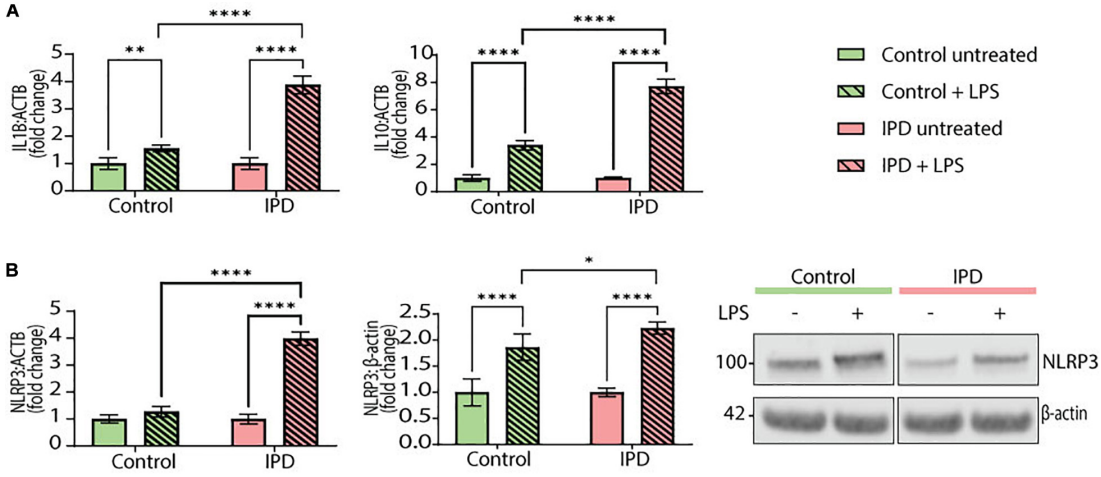

FIGURE 4 | Inflammatory phenotype and LRRK2 levels in iPSC-derived microglia. **(A)** *IL1B* and *IL10* gene expression (normalized to *ACTB*) in control and IPD microglia; a quantitative PCR showed higher gene expressions of *IL1B* and *IL10* in IPD compared to control cells upon priming with LPS (100 ng/ml). Values are represented as fold changes of untreated cells. **(B)** NLRP3 mRNA and protein levels (normalized to *ACTB* and β-actin, respectively) are increased in IPD microglia compared to control cells upon priming with LPS (100 ng/ml). Values are represented as fold change of untreated cells. $^{*}p < 0.05$; $^{**}p < 0.01$; $^{****}p < 0.0001$; IPD, idiopathic PD, NLRP3, NOD-, LRR-, and pyrin domain-containing protein 3.

1.866, $SD = 0.254$; IPD/LPS fold mean: 2.231, SD = 0.115; ANOVA: $^{****}p < 0.0001$). However, when comparing across conditions, IPD microglia showed a significant upregulation compared to treated control glia (LPS mean: 2.048, $SD = 0.2585$; ANOVA: $^{*}p = 0.0416$) (**Figure 4B**).

Downregulation of Leucine-Rich Repeat Kinase 2 Upon Lipopolysaccharide Treatment in Idiopathic Microglia

Leucine-rich repeat kinase 2 (LRRK2) is a protein implicated in both the idiopathic and genetic forms of PD. It is highly expressed in cells of the immune system and associated with immune disorders (Van Limbergen et al., 2009; Umeno et al., 2011) as well as infectious diseases (Zhang et al., 2009; Weindel et al., 2020). Its pathogenic effects have been extensively studied in the context of LRRK2-PD and in some instances in IPD. Basal levels of *LRRK2* expression were significantly downregulated in IPD microglia (CTR mean: 1.355, $SD = 0.136$; IPD mean: 0.929, $SD = 0.244$; ANOVA: $^{*}p = 0.0226$), while control cells had significantly lower expression upon LPS treatment (CTR mean: 1.355, $SD = 0.136$; CTR/LPS mean: 0.915, $SD = 0.178$; ANOVA: $^{*}p = 0.0186$) (**Figure 5A**). Furthermore, we investigated LRRK2 protein levels in our iPSC-derived microglia and saw a non-significant downregulation in untreated IPD microglia compared to controls (CTR mean: 1.332, $SD = 0.257$; IPD mean: 0.615, $SD = 0.425$; ANOVA: $p = 0.0593$). Moreover, after stimulating the cells with LPS, IPD microglia had significantly less LRRK2 protein compared to LPS-treated control glia (CTR/LPS mean: 1.649, $SD = 0.391$; IPD/LPS mean: 0.402, $SD = 0.215$; ANOVA: $^{**}p = 0.0036$) (**Figure 5B**).

DISCUSSION

Although the majority of PD cases suffer from the idiopathic form of the movement disorder, the cause of neurodegeneration in these individuals has not been extensively investigated. Genome wide association studies (GWAS) identified over 40 PD risk loci, the majority of which overlaps with known autosomal dominant PD genes, most notably *SNCA* and *LRRK2*, while other studies revealed the presence of heterozygous variants in autosomal recessively inherited PD genes (Simón-Sánchez et al., 2009; Nalls et al., 2014; Zeng et al., 2018; Germer et al., 2019; Lai et al., 2020). The main difficulty scientists are facing when studying IPD is the heterogeneous nature of the disease, which is further exacerbated by a plethora of environmental and epigenetic influences.

Inflammation has been considered a hallmark of PD since the late 1980's, when an upregulation of reactive microglia was first seen in patient brain tissue samples (McGeer et al., 1988). Positron emission tomography (PET) imaging dyes, which allow visualizing activated microglia *in vivo* over time, have been tested as biomarkers for disease progression (Gerhard et al., 2006; Terada et al., 2016; Roussakis and Piccini, 2018). Unfortunately, however, the findings from PET studies have not been successfully transferred to the clinic and the exact molecular mechanisms triggering neuroinflammation in PD currently remain elusive.

Thus, in this study, we investigated patient-derived microglia to explore the inflammatory component of IPD. First, we made use of publicly available transcriptomic data from nigral postmortem tissue to assess the expression of different cytokines in IPD patients compared to age-matched controls. Previous reports established certain secreted cytokines as reliable biomarkers in serum and plasma of PD patients, among them

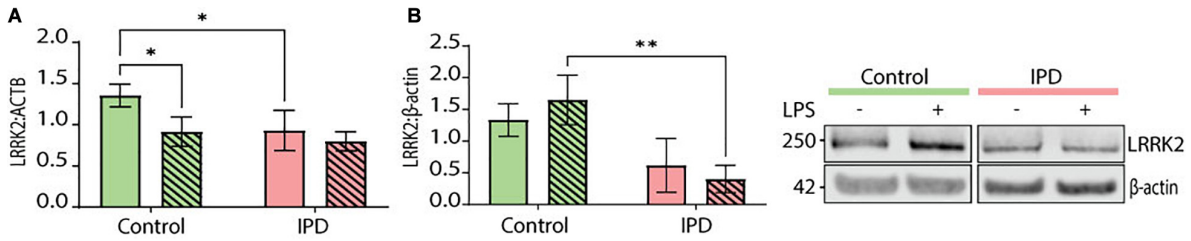

FIGURE 5 | LRRK2 levels in iPSC-derived microglia. **(A)** IPD microglia have a significant decrease of *LRRK2* expression at basal level (normalized to *ACTB*). **(B)** IPD microglia show a significant downregulation of total LRRK2 protein levels (normalized to β-actin) compared to control cells upon LPS treatment only. $*p < 0.05$; $**p < 0.01$; IPD, idiopathic PD; LRRK2, Leucine-rich repeat kinase 2.

IL-1β, IL-18, IL-6, IL-10, IL-8, TNF-α (Nagatsu et al., 2000; Brodacki et al., 2008; Qin et al., 2016). In line with these studies, our meta-analysis of published brain SNpc case-control transcriptomics datasets indicated elevated levels of *IL10* and *IL1B* in IPD patients.

To explore the cellular origin of this upregulation in IPD, we made use of our previously generated snRNAseq dataset from midbrain IPD and control tissue. Multiple cytokines, including *IL10* and *IL1B*, were predominantly expressed in microglia. This is in accordance with microglia acting as the main player of the immune system in the CNS. Moreover, in the same published dataset, we observed an increase in the microglia number as well as morphological alterations, indicative of an activated state, in IPD patients (Smajić et al., 2020). Next, to corroborate our findings from homogenized SN tissue, we investigated whether any of the aforementioned cytokines show an IPD-specific expression pattern in microglia. While we observed an increase in the expression of all investigated candidates in the patient compared to control cells, the levels of *IL10*, *IL18*, and *IL1B* were the most abundant.

Albeit informative, these postmortem results may be confounded by the fact that they only represent the molecular situation during the latest stage of the disease. Thus, to study inflammatory phenotypes and pathways in an *in vitro* IPD model, we differentiated microglia from control and patient-derived iPSCs using a published protocol (van Wilgenburg et al., 2013; Haenseler et al., 2017). While cultured IPD microglia did not show altered morphology (data not shown), we observed elevated phagocytosis in these cells indicative of overactive immune function. Phagocytosis is an integral part of microglial homeostatic function, and is not only involved in the recognition of self and non-self threats, but also in the engulfment of synaptic elements and the pruning process. Furthermore, enhanced and uncontrolled clearance is contributing to synaptic degeneration. Indeed, multiple PD studies showed loss of presynaptic terminals and synaptic changes in PD patient compared to control brains (Delva et al., 2020; Matuskey et al., 2020). It is also worth noting that disrupting the phagocytic ability of mouse glia was sufficient to rescue the neuronal degeneration phenotype observed in these animals after LPS injection (Bodea et al., 2014). Since we observed the differences in phagocytosis already at basal level, one may speculate that the genetic background in IPD glia contributes to the development of the disease. However, it is still unclear whether overactive, defective or perturbed uptake triggers PD pathogenesis (Janda et al., 2018).

To further validate our findings from postmortem tissue, we analyzed different inflammasome components in the iPSC-derived microglia cultures. IPD microglia were more reactive after priming with LPS, as indicated by enhanced expressions of *IL1B* and *IL10*, and higher mRNA and protein levels of NLRP3 compared to treated control cells. Higher levels of *IL1B* and NLRP3 in IPD microglia indicate a stronger priming step, which is necessary for downstream inflammasome activation and immune response. While we are the first to show NLRP3 dysregulation in iPSC-derived IPD microglia, our results are in agreement with findings from genetic PD models. Specifically, α-synuclein fibrils were shown to induce NLRP3 activation, and loss of the PD-associated protein Parkin triggered the release of mitoDAMPs into the cytosol, which in turn activated the NLRP3 inflammasome in mice (Zhong et al., 2016; Gordon et al., 2018; Ji et al., 2020; Pike et al., 2021). Moreover, NLRP3 was shown to regulate *IL10* levels in mice macrophages, with *IL10* production being decreased in NLRP3$^{-/-}$ mice (Gurung et al., 2015; Kobayashi et al., 2016). This is consistent with our observation of *IL10* and *NLRP3* co-regulation. In line with a biomarker study in serum, IPD patients had higher levels of IL-10 compared to healthy individuals (Rentzos et al., 2009). Furthermore, while the relationship of IL-1β and IL-10 has not been extensively studied in the context of PD, there are reports showing that, under inflammatory conditions, IL-10 selectively inhibits the release of IL-1β (Sun et al., 2019). Patient-derived microglia will be a useful model to explore the molecular mechanisms linking IL-10 and IL-1β in PD in more detail.

Further of interest with regard to inflammation in genetic but also IPD is the kinase LRRK2. Affected individuals harboring mutations in LRRK2 closely mirror the clinical picture of IPD patients (Tolosa et al., 2020) with kinase activity dysregulation being a shared feature of both forms of the disease. Due to its high abundance in immune cells, researchers have speculated that LRRK2 may be crucially involved in the regulation of neuroinflammatory processes (Gardet et al., 2010; Di Maio et al., 2018; Fyfe, 2018). Studies investigating *LRRK2* expression in IPD brain tissue showed a significant downregulation in dopaminergic neurons, which may contribute to the pathology

of the movement disorder (Simunovic et al., 2009; Sharma et al., 2011; Yılmazer et al., 2021). In agreement with these reports, we detected significantly reduced *LRRK2* expression and a trend toward lower LRRK2 protein abundance in IPD patient microglia at baseline. Inflammatory insults exacerbated this phenotype, leading to a further reduction in LRRK2 protein levels in the IPD patient-derived cells. However, the exact pathways connecting LRRK2 downregulation to microglia dysfunction in IPD warrant further investigation.

Taken together, inspired by published biomarker studies, we investigated inflammatory phenotypes in different models of IPD. In both, nigral and midbrain RNAseq datasets, we observed a disease-specific upregulation of *IL10* and *IL1B*. Furthermore, from our postmortem single-cell results, we derived that this overexpression predominantly stems from microglia. Next, to test whether we could reproduce this phenotype in a dish, we generated iPSC-derived IPD microglia. Further implicating *IL10* and *IL1B*, in IPD, the expression of these cytokines was also enhanced in patient microglia upon LPS treatment. Finally, we identified an upregulation of NLRP3 on RNA and protein level, corroborating our findings concerning *IL10* and *IL1B*. However, in light of the variability of sporadic PD, our results from a small sample may only be representative for a subset of IPD cases, warranting validation studies in larger cohorts. Moreover, while our study highlights the relevance of microglia in IPD, further experiments will be needed to decipher the exact pathways triggering neuroinflammation in sporadic PD patients.

DATA AVAILABILITY STATEMENT

The datasets presented in this study can be found in online repositories. The names of the repository/repositories and accession number(s) can be found below: https://www.ncbi.nlm.nih.gov/geo/, GSE157783; https://www.ncbi.nlm.nih.gov/geo/, GSE8397.

ETHICS STATEMENT

Patients gave written and informed consent. The study was approved by the Comité National d'Ethique de Recherche Luxembourg (CNER, vote 201411/05 V1.3).

AUTHOR CONTRIBUTIONS

SAC provided training in iPSC-derived microglia. KB, PM, SD, and SLP collected the data. KB, PM, SS, L-CT, PMAA, and EG performed the analysis. KB, PM, SS, PMAA, CV, and AG wrote the manuscript, which was reviewed by all authors. CV and AG conceived the study. ND, TR, and JCS contributed to the establishment of fibroblast cultures and iPSC generation from patient and control cells. AG acquired funding for the study and was in charge of direction and planning of the study.

FUNDING

KB was supported by the Luxembourg National Research Fund (FNR) through the PRIDE15/10907093/CriTiCS grant. SS and PM received funding from the FNR within the framework of the PARK-QC DTU (PRIDE17/12244779/PARK-QC). TR was supported by the EU Joint Programme—Neurodegenerative Disease Research (JPND) project 3DPD. CV was supported by the FNR through the C20/BM/14548100 CORE Junior grant. AG was awarded an FNR ATTRACT career development grant (Model IPD, FNR9631103). Moreover, AG and JCS were supported by the FNR as part of the National Centre of Excellence in Research on Parkinson's disease (NCER-PD, FNR/NCER13/BM/11264123).

ACKNOWLEDGMENTS

We would like to thank Jane Vowles and Cathy Browne from the University of Oxford for sharing their expertise and giving us valuable in-person training on iPSC-derived microglia protocol. In addition, we would like to express our gratitude to Anna-Lena Hallmann and Hans R. Schöler from the Max Planck Institute for Molecular Biomedicine for reprogramming fibroblasts into iPSCs.

SUPPLEMENTARY MATERIAL

The Supplementary Material for this article can be found online at: https://www.frontiersin.org/articles/10.3389/fcell.2021.740758/full#supplementary-material

REFERENCES

Arias-Fuenzalida, J., Jarazo, J., Qing, X., Walter, J., Gomez-Giro, G., Nickels, S. L., et al. (2017). FACS-Assisted CRISPR-Cas9 Genome Editing Facilitates Parkinson's Disease Modeling. *Stem Cell Rep.* 9, 1423–1431. doi: 10.1016/j.stemcr.2017.08.026

Badanjak, K., Fixemer, S., Smajić, S., Skupin, A., and Grünewald, A. (2021). The Contribution of Microglia to Neuroinflammation in Parkinson's Disease. *Int. J. Mol. Sci.* 22:ijms22094676. doi: 10.3390/ijms22094676

Bodea, L.-G., Wang, Y., Linnartz-Gerlach, B., Kopatz, J., Sinkkonen, L., Musgrove, R., et al. (2014). Neurodegeneration by activation of the microglial complement-phagosome pathway. *J. Neurosci.* 34, 8546–8556. doi: 10.1523/JNEUROSCI.5002-13.2014

Brodacki, B., Staszewski, J., Toczyłowska, B., Kozłowska, E., Drela, N., Chalimoniuk, M., et al. (2008). Serum interleukin (IL-2, IL-10, IL-6, IL-4), TNFalpha, and INFgamma concentrations are elevated in patients with atypical and idiopathic parkinsonism. *Neurosci. Lett.* 441, 158–162. doi: 10.1016/j.neulet.2008.06.040

Calabrese, V., Santoro, A., Monti, D., Crupi, R., Di Paola, R., Latteri, S., et al. (2018). Aging and Parkinson's Disease: Inflammaging, neuroinflammation and biological remodeling as key factors in pathogenesis. *Free Radic. Biol. Med.* 115, 80–91. doi: 10.1016/j.freeradbiomed.2017.10.379

Chao, Y., Wong, S. C., and Tan, E. K. (2014). Evidence of inflammatory system involvement in Parkinson's disease. *Biomed Res. Int.* 2014:308654.

Collins, L. M., Toulouse, A., Connor, T. J., and Nolan, Y. M. (2012). Contributions of central and systemic inflammation to the pathophysiology of Parkinson's

disease. *Neuropharmacology* 62, 2154–2168. doi: 10.1016/j.neuropharm.2012.01.028

Delva, A., Van Weehaeghe, D., Koole, M., Van Laere, K., and Vandenberghe, W. (2020). Loss of Presynaptic Terminal Integrity in the Substantia Nigra in Early Parkinson's Disease. *Mov. Disord.* 35, 1977–1986.

Di Maio, R., Hoffman, E. K., Rocha, E. M., Keeney, M. T., Sanders, L. H., De Miranda, B. R., et al. (2018). LRRK2 activation in idiopathic Parkinson's disease. *Sci. Transl. Med.* 10:aar5429. doi: 10.1126/scitranslmed.aar5429

Fyfe, I. (2018). Familial PD gene involved in idiopathic disease. *Nat. Rev. Neurol.* 14:508.

Gardet, A., Benita, Y., Li, C., Sands, B. E., Ballester, I., Stevens, C., et al. (2010). LRRK2 is involved in the IFN-gamma response and host response to pathogens. *J. Immunol.* 185, 5577–5585. doi: 10.4049/jimmunol.1000548

Gerhard, A., Pavese, N., Hotton, G., Turkheimer, F., Es, M., Hammers, A., et al. (2006). In vivo imaging of microglial activation with [11C](R)-PK11195 PET in idiopathic Parkinson's disease. *Neurobiol. Dis.* 21, 404–412. doi: 10.1016/j.nbd.2005.08.002

Germer, E. L., Imhoff, S., Vilariño-Güell, C., Kasten, M., Seibler, P., Brüggemann, N., et al. (2019). The Role of Rare Coding Variants in Parkinson's Disease GWAS Loci. *Front. Neurol.* 10:1284. doi: 10.3389/fneur.2019.01284

Gillardon, F., Schmid, R., and Draheim, H. (2012). Parkinson's disease-linked leucine-rich repeat kinase 2(R1441G) mutation increases proinflammatory cytokine release from activated primary microglial cells and resultant neurotoxicity. *Neuroscience* 208, 41–48. doi: 10.1016/j.neuroscience.2012.02.001

Glaab, E., and Schneider, R. (2015). Comparative pathway and network analysis of brain transcriptome changes during adult aging and in Parkinson's disease. *Neurobiol. Dis.* 74, 1–13. doi: 10.1016/j.nbd.2014.11.002

Gordon, R., Albornoz, E. A., Christie, D. C., Langley, M. R., Kumar, V., Mantovani, S., et al. (2018). Inflammasome inhibition prevents α-synuclein pathology and dopaminergic neurodegeneration in mice. *Sci. Transl. Med.* 10:aah4066. doi: 10.1126/scitranslmed.aah4066

Gurung, P., Li, B., Subbarao Malireddi, R. K., Lamkanfi, M., Geiger, T. L., and Kanneganti, T.-D. (2015). Chronic TLR Stimulation Controls NLRP3 Inflammasome Activation through IL-10 Mediated Regulation of NLRP3 Expression and Caspase-8 Activation. *Sci. Rep.* 5:14488. doi: 10.1038/srep14488

Haenseler, W., Sansom, S. N., Buchrieser, J., Newey, S. E., Moore, C. S., Nicholls, F. J., et al. (2017). A Highly Efficient Human Pluripotent Stem Cell Microglia Model Displays a Neuronal-Co-culture-Specific Expression Profile and Inflammatory Response. *Stem Cell Rep.* 8, 1727–1742. doi: 10.1016/j.stemcr.2017.05.017

Janda, E., Boi, L., and Carta, A. R. (2018). Microglial Phagocytosis and Its Regulation: A Therapeutic Target in Parkinson's Disease? *Front. Mol. Neurosci.* 11:144. doi: 10.3389/fnmol.2018.00144

Ji, Y.-J., Wang, H.-L., Yin, B.-L., and Ren, X.-Y. (2020). Down-regulation of DJ-1 Augments Neuroinflammation via Nrf2/Trx1/NLRP3 Axis in MPTP-induced Parkinson's Disease Mouse Model. *Neuroscience* 442, 253–263. doi: 10.1016/j.neuroscience.2020.06.001

Jin, H., Gu, H.-Y., Mao, C.-J., Chen, J., and Liu, C.-F. (2020). Association of inflammatory factors and aging in Parkinson's disease. *Neurosci. Lett.* 736:135259. doi: 10.1016/j.neulet.2020.135259

Kobayashi, M., Usui, F., Karasawa, T., Kawashima, A., Kimura, H., Mizushina, Y., et al. (2016). NLRP3 Deficiency Reduces Macrophage Interleukin-10 Production and Enhances the Susceptibility to Doxorubicin-induced Cardiotoxicity. *Sci. Rep.* 6:26489. doi: 10.1038/srep26489

Koprich, J. B., Reske-Nielsen, C., Mithal, P., and Isacson, O. (2008). Neuroinflammation mediated by IL-1beta increases susceptibility of dopamine neurons to degeneration in an animal model of Parkinson's disease. *J. Neuroinflamm.* 5:8. doi: 10.1186/1742-2094-5-8

Lai, D., PhD, Alipanahi, B., PhD, Fontanillas, P., PhD, et al. (2020). Genome-wide association studies of LRRK2 modifiers of Parkinson's disease. *Ann. Neurol.* 90, 76–88. doi: 10.1101/2020.12.14.20224378

Long-Smith, C. M., Sullivan, A. M., and Nolan, Y. M. (2009). The influence of microglia on the pathogenesis of Parkinson's disease. *Prog. Neurobiol.* 89, 277–287. doi: 10.1016/j.pneurobio.2009.08.001

Magalhaes, J., Tresse, E., Ejlerskov, P., Hu, E., Liu, Y., Marin, A., et al. (2021). PIAS2-mediated blockade of IFN-β signaling: a basis for sporadic Parkinson disease dementia. *Mol. Psychiatry* 2021:01207–w. doi: 10.1038/s41380-021-01207-w

Maiti, P., Manna, J., and Dunbar, G. L. (2017). Current understanding of the molecular mechanisms in Parkinson's disease: Targets for potential treatments. *Transl. Neurodegener.* 6:28.

Matuskey, D., Tinaz, S., Wilcox, K. C., Naganawa, M., Toyonaga, T., Dias, M., et al. (2020). Synaptic Changes in Parkinson Disease Assessed with in vivo Imaging. *Ann. Neurol.* 87, 329–338. doi: 10.1002/ana.25682

McGeer, P. L., Itagaki, S., Boyes, B. E., and McGeer, E. G. (1988). Reactive microglia are positive for HLA-DR in the substantia nigra of Parkinson's and Alzheimer's disease brains. *Neurology* 38, 1285–1291. doi: 10.1212/wnl.38.8.1285

McKee, C. M., and Coll, R. C. (2020). NLRP3 inflammasome priming: A riddle wrapped in a mystery inside an enigma. *J. Leukoc. Biol.* 108, 937–952. doi: 10.1002/JLB.3MR0720-513R

Nagatsu, T., and Sawada, M. (2005). Inflammatory process in Parkinson's disease: role for cytokines. *Curr. Pharm. Des.* 11, 999–1016. doi: 10.2174/1381612053381620

Nagatsu, T., Mogi, M., Ichinose, H., and Togari, A. (2000). Cytokines in Parkinson's disease. *J. Neural Transm. Suppl.* 2000, 143–151.

Nakahira, K., Haspel, J. A., Rathinam, V. A. K., Lee, S.-J., Dolinay, T., Lam, H. C., et al. (2011). Autophagy proteins regulate innate immune responses by inhibiting the release of mitochondrial DNA mediated by the NALP3 inflammasome. *Nat. Immunol.* 12, 222–230. doi: 10.1038/ni.1980

Nalls, M. A., Pankratz, N., Lill, C. M., Do, C. B., Hernandez, D. G., Saad, M., et al. (2014). Large-scale meta-analysis of genome-wide association data identifies six new risk loci for Parkinson's disease. *Nat. Genet.* 46, 989–993.

Pang, S. Y.-Y., Ho, P. W.-L., Liu, H.-F., Leung, C.-T., Li, L., Chang, E. E. S., et al. (2019). The interplay of aging, genetics and environmental factors in the pathogenesis of Parkinson's disease. *Transl. Neurodegener.* 8:23.

Panicker, N., Kam, T.-I., Neifert, S., Hinkle, J., Mao, X., Karuppagounder, S., et al. (2020). NLRP3 inflammasome activation in dopamine neurons contributes to neurodegeneration in Parkinson's Disease. *FASEB J.* 34, 1–1.

Pike, A. F., Varanita, T., Herrebout, M. A. C., Plug, B. C., Kole, J., Musters, R. J. P., et al. (2021). α-Synuclein evokes NLRP3 inflammasome-mediated IL-1β secretion from primary human microglia. *Glia* 69, 1413–1428. doi: 10.1002/glia.23970

Qin, X.-Y., Zhang, S.-P., Cao, C., Loh, Y. P., and Cheng, Y. (2016). Aberrations in Peripheral Inflammatory Cytokine Levels in Parkinson Disease: A Systematic Review and Meta-analysis. *JAMA Neurol.* 73, 1316–1324. doi: 10.1001/jamaneurol.2016.2742

Rentzos, M., Nikolaou, C., Andreadou, E., Paraskevas, G. P., Rombos, A., Zoga, M., et al. (2009). Circulating interleukin-10 and interleukin-12 in Parkinson's disease. *Acta Neurol. Scand.* 119, 332–337. doi: 10.1111/j.1600-0404.2008.01103.x

Roussakis, A.-A., and Piccini, P. (2018). Molecular Imaging of Neuroinflammation in Idiopathic Parkinson's Disease. *Int. Rev. Neurobiol.* 141, 347–363. doi: 10.1016/bs.irn.2018.08.009

Sebastian-Valverde, M., and Pasinetti, G. M. (2020). The NLRP3 Inflammasome as a Critical Actor in the Inflammaging Process. *Cells* 9:cells9061552. doi: 10.3390/cells9061552

Sharma, S., Bandopadhyay, R., Lashley, T., Renton, A. E. M., Kingsbury, A. E., Kumaran, R., et al. (2011). LRRK2 expression in idiopathic and G2019S positive Parkinson's disease subjects: a morphological and quantitative study. *Neuropathol. Appl. Neurobiol.* 37, 777–790. doi: 10.1111/j.1365-2990.2011.01187.x

Simón-Sánchez, J., Schulte, C., Bras, J. M., Sharma, M., Gibbs, J. R., Berg, D., et al. (2009). Genome-wide association study reveals genetic risk underlying Parkinson's disease. *Nat. Genet.* 41, 1308–1312.

Simunovic, F., Yi, M., Wang, Y., Macey, L., Brown, L. T., Krichevsky, A. M., et al. (2009). Gene expression profiling of substantia nigra dopamine neurons: further insights into Parkinson's disease pathology. *Brain* 132, 1795–1809. doi: 10.1093/brain/awn323

Smajić, S., Prada-Medina, C. A., Landoulsi, Z., Dietrich, C., Jarazo, J., Henck, J., et al. (2020). Single-cell sequencing of the human midbrain reveals glial activation and a neuronal state specific to Parkinson's disease. *bioRxiv* [Preprint]. doi: 10.1101/2020.09.28.20202812

Su, X., Maguire-Zeiss, K. A., Giuliano, R., Prifti, L., Venkatesh, K., and Federoff, H. J. (2008). Synuclein activates microglia in a model of Parkinson's

disease. *Neurobiol. Aging* 29, 1690–1701. doi: 10.1016/j.neurobiolaging.2007.04.006

Sun, Y., Ma, J., Li, D., Li, P., Zhou, X., Li, Y., et al. (2019). Interleukin-10 inhibits interleukin-1β production and inflammasome activation of microglia in epileptic seizures. *J. Neuroinflamm.* 16:66. doi: 10.1186/s12974-019-1452-1

Swanson, K. V., Deng, M., and Ting, J. P.-Y. (2019). The NLRP3 inflammasome: molecular activation and regulation to therapeutics. *Nat. Rev. Immunol.* 19, 477–489. doi: 10.1038/s41577-019-0165-0

Terada, T., Yokokura, M., Yoshikawa, E., Futatsubashi, M., Kono, S., Konishi, T., et al. (2016). Extrastriatal spreading of microglial activation in Parkinson's disease: a positron emission tomography study. *Ann. Nucl. Med.* 30, 579–587. doi: 10.1007/s12149-016-1099-2

Tolosa, E., Vila, M., Klein, C., and Rascol, O. (2020). LRRK2 in Parkinson disease: challenges of clinical trials. *Nat. Rev. Neurol.* 16, 97–107.

Umeno, J., Asano, K., Matsushita, T., Matsumoto, T., Kiyohara, Y., Iida, M., et al. (2011). Meta-analysis of published studies identified eight additional common susceptibility loci for Crohn's disease and ulcerative colitis. *Inflamm. Bowel Dis.* 17, 2407–2415. doi: 10.1002/ibd.21651

Van Limbergen, J., Wilson, D. C., and Satsangi, J. (2009). The genetics of Crohn's disease. *Annu. Rev. Genomics Hum. Genet.* 10, 89–116.

van Wilgenburg, B., Browne, C., Vowles, J., and Cowley, S. A. (2013). Efficient, long term production of monocyte-derived macrophages from human pluripotent stem cells under partly-defined and fully-defined conditions. *PLoS One* 8:e71098. doi: 10.1371/journal.pone.0071098

Varrette, S., Bouvry, P., Cartiaux, H., and Georgatos, F. (2014). "Management of an academic HPC cluster: The UL experience," in *2014 International Conference on High Performance Computing Simulation (HPCS)*, (Bologna: HPCS), 959–967.

Wang, Q., Liu, Y., and Zhou, J. (2015). Neuroinflammation in Parkinson's disease and its potential as therapeutic target. *Transl. Neurodegener.* 4:19.

Weindel, C. G., Bell, S. L., Vail, K. J., West, K. O., Patrick, K. L., and Watson, R. O. (2020). LRRK2 maintains mitochondrial homeostasis and regulates innate immune responses to Mycobacterium tuberculosis. *Elife* 9:51071. doi: 10.7554/eLife.51071

Yan, Y.-Q., Fang, Y., Zheng, R., Pu, J.-L., and Zhang, B.-R. (2020). NLRP3 Inflammasomes in Parkinson's disease and their Regulation by Parkin. *Neuroscience* 446, 323–334. doi: 10.1016/j.neuroscience.2020.08.004

Yılmazer, S., Candaş, E., Genç, G., Alaylıoğlu, M., Şengül, B., Gündüz, A., et al. (2021). Low Levels of LRRK2 Gene Expression are Associated with LRRK2 SNPs and Contribute to Parkinson's Disease Progression. *Neuromol. Med.* 23, 292–304. doi: 10.1007/s12017-020-08619-x

Zeng, X.-S., Geng, W.-S., Jia, J.-J., Chen, L., and Zhang, P.-P. (2018). Cellular and Molecular Basis of Neurodegeneration in Parkinson Disease. *Front. Aging Neurosci.* 10:109. doi: 10.3389/fnagi.2018.00109

Zhang, F.-R., Huang, W., Chen, S.-M., Sun, L.-D., Liu, H., Li, Y., et al. (2009). Genomewide association study of leprosy. *N. Engl. J. Med.* 361, 2609–2618.

Zhong, Z., Umemura, A., Sanchez-Lopez, E., Liang, S., Shalapour, S., Wong, J., et al. (2016). NF-κB Restricts Inflammasome Activation via Elimination of Damaged Mitochondria. *Cell* 164, 896–910. doi: 10.1016/j.cell.2015.12.057

Conflict of Interest: The authors declare that the research was conducted in the absence of any commercial or financial relationships that could be construed as a potential conflict of interest.

Publisher's Note: All claims expressed in this article are solely those of the authors and do not necessarily represent those of their affiliated organizations, or those of the publisher, the editors and the reviewers. Any product that may be evaluated in this article, or claim that may be made by its manufacturer, is not guaranteed or endorsed by the publisher.

Supplementary Table 1. Gene expression analysis of human IPD and control SN transcriptome.

Gene symbol	Z-score	FDR
IL1B	2.273739646	0.022981645
IL6	-0.293008563	0.769515607
IL10	2.710259928	0.00672305
IL18	1.512416069	0.13042805
IL8	1.290107048	0.197013493
TNF	-0.37382918	0.708531408

Supplementary Table 2. Gene expression analysis in IPD and control microglia of the human midbrain single-cell transcriptome.

Gene symbol	Average expression	Percent expressed	cluster_id
IL1B	0.325002368	5.55967383	Microglia_IPD
IL6	0.003882633	0.11119348	Microglia_IPD
IL18	3.170897328	63.45441067	Microglia_IPD
TNF	0.011861339	0.48183840	Microglia_IPD
IL10	0.015103408	0.70422535	Microglia_IPD
IL8	0.014423550	0.29651594	Microglia_IPD
IL1B	0.306312685	2.98755187	Microglia_Control
IL6	0.002964900	0.08298755	Microglia_Control
IL18	3.089786862	59.33609959	Microglia_Control
TNF	0.000000000	0.00000000	Microglia_Control
IL10	0.007378525	0.24896266	Microglia_Control
IL8	0.002578054	0.08298755	Microglia_Control

Manuscript VII

International Journal of
Molecular Sciences

MDPI

Review

The Contribution of Microglia to Neuroinflammation in Parkinson's Disease

Katja Badanjak [1], Sonja Fixemer [1,2], Semra Smajić [1], Alexander Skupin [1,3] and Anne Grünewald [1,4,*]

[1] Luxembourg Centre for Systems Biomedicine, University of Luxembourg, L-4367 Esch-sur-Alzette, Luxembourg; katja.badanjak@uni.lu (K.B.); sonja.fixemer@uni.lu (S.F.); semra.smajic@uni.lu (S.S.); alexander.skupin@uni.lu (A.S.)
[2] Luxembourg Centre for Neuropathology (LCNP), L-3555 Dudelange, Luxembourg
[3] Department of Neuroscience, University California San Diego, La Jolla, CA 92093, USA
[4] Institute of Neurogenetics, University of Lübeck, 23562 Lübeck, Germany
* Correspondence: anne.gruenewald@uni.lu

Abstract: With the world's population ageing, the incidence of Parkinson's disease (PD) is on the rise. In recent years, inflammatory processes have emerged as prominent contributors to the pathology of PD. There is great evidence that microglia have a significant neuroprotective role, and that impaired and over activated microglial phenotypes are present in brains of PD patients. Thereby, PD progression is potentially driven by a vicious cycle between dying neurons and microglia through the instigation of oxidative stress, mitophagy and autophagy dysfunctions, a-synuclein accumulation, and pro-inflammatory cytokine release. Hence, investigating the involvement of microglia is of great importance for future research and treatment of PD. The purpose of this review is to highlight recent findings concerning the microglia-neuronal interplay in PD with a focus on human postmortem immunohistochemistry and single-cell studies, their relation to animal and iPSC-derived models, newly emerging technologies, and the resulting potential of new anti-inflammatory therapies for PD.

Keywords: neuroinflammation; microglia; brain; neurodegeneration; animal models; iPSC; Parkinson's disease

Citation: Badanjak, K.; Fixemer, S.; Smajić, S.; Skupin, A.; Grünewald, A. The Contribution of Microglia to Neuroinflammation in Parkinson's Disease. *Int. J. Mol. Sci.* **2021**, *22*, 4676. https://doi.org/10.3390/ijms22094676

Academic Editor: Antonella Scorziello

Received: 31 March 2021
Accepted: 24 April 2021
Published: 28 April 2021

1. Introduction

1.1. Parkinson's Disease

Parkinson's disease (PD) is one of the most common neurodegenerative disorders with prevalence of around 1% in people aged above 65 years [1]. It is caused by a chronic and progressive loss of dopaminergic neurons in the substantia nigra (SN) pars compacta (pc) [2]. Despite great advances in research, it is still an elusive field of medical science, with around 10% of all cases being of genetic and others of idiopathic origin [3]. Genetic forms of PD include mutations in 23 loci, some of which have been studied intensely in the past two decades: *LRRK2* (*PARK8*), *SNCA* (*PARK1*), *PRKN* (*PARK2*), *PINK-1* (*PARK6*), and *DJ-1* (*PARK7*) [4,5]. Age is considered a major risk factor for the development of PD [6,7]. However, in addition, the genetic predisposition and exposure to environmental factors contribute to pathogenesis, making PD an age-related multifactorial disease. Environmental factors such as herbicides or pesticides can induce oxidative stress, DNA damage, and neuronal cell death [8]. The demise of dopaminergic neurons leads to lower levels of dopamine that is released into the striatum and thus, with progression of the disease, patients endure characteristic motor symptoms (tremor, rigidity, bradykinesia), cognitive decline (dementia) and even psychiatric signs (depression, apathy, anxiety) coupled with constipation and sleep disturbances [1,9,10].

A first clue to what might be the underlying mechanism of parkinsonism symptoms came unexpectedly in 1982 from a group of drug addicts who, after injection of a synthetic heroin, began experiencing symptoms commonly seen in PD patients. The drug was found

to be 1-methyl-4-phenyl-1,2,3,6-tetrahydropyridine (MPTP). MPTP, when transformed into its ion 1-methyl-4-phenylpyridinium (MPP+), acts as a highly potent initiator of neuronal cell death through inhibition of complex 1 of the respiratory chain machinery in mitochondria [11,12]. Besides the demise of dopaminergic neurons and mitochondrial dysfunction, other molecular pathologies have been linked to PD since the late 20th century. They include aggregation of α-synuclein, formation of α-synuclein-containing Lewy bodies and neurites, somatic mtDNA alterations, autophagy dysfunction, and activation of microglia cells [13–17].

As of today, most common therapies are purely symptomatic, and they usually include substitution of dopamine by administering the drug Levodopa. Current treatments also have their drawbacks: 1. they only relieve some of the symptoms; 2. they do not slow the progression of the disease; 3. they have limited long-term efficacy. Therefore, PD researchers have turned their focus on how to diagnose the disease during its early phases. Motor symptoms occur at a rather late stage of the disease—only after 50% of dopaminergic neurons have been lost, patients experience impaired movement [18]. Thus, there is hope that with the discovery of early-stage biomarkers, we will be able to target molecular impairments and inflammatory phenotypes during the prodromal phase of the disease, thereby preventing the worst motor symptoms [19]. Among others, promising biomarkers would be indicators of inflammation, cytokines and chemokines, released by microglia into the extracellular space.

1.2. Microglia

Microglia are immune cells of the brain, representing the neural tissue's defense system [20]. Microglia cells were first discovered more than 100 years ago by Pío Del Río Hortega, using a silver carbonate staining method which allowed identifying them in brain tissue samples. He called microglia "the true third element" in addition to neurons and astrocytes [21]. He described microglia as a heterogeneous cell type with various morphologies ranging from highly ramified to ameboid shaped cells providing a first indication for the existence of microglia sub-populations [22].

During fetal development, microglia migrate from the yolk sac as primitive macrophages to the central nervous system's (CNS) neuroepithelium. In the CNS, they constitute up to 12% of all cells, and their density changes depending on the brain region [23]. Early studies in mice showed that bone-marrow-derived hematopoietic cells move to the CNS, where they differentiate into microglia-like cells. Accordingly, microglia cannot be replenished from the internal CNS pool but peripheral cells need to be recruited to maintain a sufficient number of microglia [24]. By contrast, these studies employed whole-body irradiation techniques, which led to impaired blood-brain barrier (BBB) integrity, giving rise to peripheral cell entry. With innovative conditional cell depletion techniques, it was recently shown that microglia have the ability to self-renew, and that interleukin-1 (IL-1) signaling is enabling this process [25]. Just like the abundance of microglia is region-specific, microglial morphology varies from brain area to brain area. In a resting state, microglia survey the brain microenvironment and show ramified morphology. Surveillance encompasses multiple functions: clearance of accumulated or deteriorated neuronal and tissue elements, dynamic interaction with neurons whilst regulating the synaptic pruning process, and maintaining overall brain homeostasis [26,27]. Once activated upon brain damage and certain host or non-host stimuli, microglia are quickly undergoing a morphology change into an ameboid-like form, coupled with the release of inflammatory molecules, cytokines and chemokines. With regard to their activation, microglia are commonly divided into two classes: M1 (pro-inflammatory) or M2 (anti-inflammatory). Even though, by now, it is known that the states of activation are much more heterogeneous and diverse.

New approaches are being developed to determine sub-populations of microglia, mostly through single-cell gene expression studies and by determining fine morphological differences using computational methods [28–30]. With age, microglia tend to express more IL-1β and they become more phagocytic in nature compared to microglia from younger

brains [31–33]. These phenotypic changes over time can influence their ability to function normally and attain the neuronal homeostasis and support. Eventually, an accumulation of non-functional, senescent microglia could contribute to irreversible and progressive neurodegeneration in PD.

2. Human Post-Mortem Tissue Studies

The first neuropathological evidence suggesting an involvement of microglia in PD was published in 1988 [14]. Compared to age-matched non-neurologic cases, the authors observed an enrichment of reactive microglia in post-mortem SN samples from PD patients characterized by the activation of human major histocompatibility class II (MHC2) proteins which function in antigen presentation and inflammatory signalling. While these MHC2-positive cells covered the whole range of microglia morphologies, the reactive ameboid shape was strongly enriched indicating the association with a neuropathological activity.

A more recent study confirmed these observations in post-mortem SN tissue of PD patients and additionally described MHC2-positive microglia in the putamen, transentorhinal cortex, cingulate cortex and the temporal cortex of these individuals [34]. Further analysis in PD post-mortem brain tissue also revealed a correlation between ameboid shaped microglia appearance and α-synuclein pathology in the SN and the hippocampus (HPC), as well as a SN-specific Toll-like receptor 2 upregulation in these MHC2-positive microglia. Altogether, this work implicated a region-dependent and possibly disease stage-dependent microglia heterogeneity in PD [34].

To complement these morphology-based analyses of microglia heterogeneity on the transcriptional level, single-cell laser capture microscopy was applied to microglia in post-mortem PD brains [35]. This approach allowed exclusively collecting microglia, thereby creating an advantage over common bulk RNA analyses of brain homogenates, which are either contaminated by other cell types or exhibit sorting-induced skewed RNA profiles. The single-cell study revealed that the transcriptional profiles of microglia differ between brain regions (SN, HPC) in both control subjects and PD patients. PD samples exhibited unique active pathways compared to controls, including inflammation-related aldosterone and reactive oxygen species metabolism. A comparison of isolated microglia from the HPC or the SN in PD samples showed that biological pathways linked to behavior, regulation of transport and synaptic transmission were among the most differentially regulated ones. Thus, this study was the first to demonstrate microglia transcriptional heterogeneity when comparing different brain regions from control subjects and PD patients.

During the last decade, high-throughput techniques for single-cell RNA sequencing (scRNAseq) have been developed, which have revolutionized our capability to decipher cellular heterogeneity at the transcriptional level. Most of these high-throughput methods rely on the dissociation of the sample into individual cells and can therefore mainly be applied to cultured cells, frozen tissue from young animals or fresh tissue.

A comprehensive cross-species single-cell microglia transcriptomic analysis in brain tissue confirmed the existence of different microglia transcriptional subpopulations in animals and humans. In addition, the study revealed that human microglia heterogeneity is more complex in humans than any of the tested animal species. Especially microglia pathways suspected to be implicated in neurodegenerative diseases such as the complement system and phagocytosis, as well as PD risk factors are more profoundly expressed in humans compared to rodents as the typical animal model [36].

To circumvent dissociation issues with more mature and solid samples, the RNA sequencing methodology was adapted to single-nuclei (sn). snRNAseq does not rely on intact cells but intact individual cell nuclei. This approach is applicable to frozen human post-mortem brain tissue, the most accessible sample type provided by biobanks (in light of the general unavailability of fresh brain tissue samples from living patients).

One of the first snRNAseq studies of human cortical and nigral tissue was performed by Agarwal and colleagues [37]. They created a single-cell atlas based on healthy control tissue. Their analysis indicated an enrichment in PD risks variants in neurons. By contrast,

they reported no such association in microglia. On the one hand, the lack of PD risk association in microglia may be due to reduced sensitivity of snRNAseq compared to scRNAseq [38] that suggests that snRNAseq might not be ideal to recover microglial states in human tissue. On the other hand, it is possible that exclusively employing control brain samples may mask PD associations in certain cell types. This hypothesis is supported by our own results. Applying snRNAseq analysis to frozen post-mortem midbrain tissue from idiopathic PD patients and controls, we identified a disease-specific upregulation of microglia [39]. In PD patients, activated microglia split into two activation branches; one with GPNMB-high microglia and the other with IL-1β-high microglia. Moreover, employing immunofluorescence and quantitative imaging analyses, we showed that the increase in microglia abundance is restricted to the PD nigra. Additional morphological analyses confirmed that PD patient microglia are more amoeboid supporting cell activation in the SN [39]. Contrary to the findings by Agarwal et al., we observed a significant PD risk variant enrichment in microglia and neurons when focusing on patient midbrain sections. For example, variants in *LRRK2* were highly associated with PD in microglia, which is in accordance with previous research [40].

Overall, very few sc- or snRNAseq datasets from post-mortem brain tissue from PD patients have been published so far, certainly due to the only very recent availability of advanced RNAseq techniques (Table 1). This low number of studies, which typically include only few samples, also does not yet allow for a definitive conclusion about the exact relevance of microglia transcriptional heterogeneity but strongly suggest a functional role of microglia in PD.

Based on the above-mentioned studies, human microglia are considerably more heterogeneous in terms of morphology and transcriptomics when comparing different brain regions than rodents and possibly show disease-specific signatures. These findings highlight the need for further in-depth studies in human tissue to characterize the role of microglia heterogeneity in PD. Beyond human postmortem brain tissue, also the application of single-cell technologies to iPSC-derived patient models may be useful to further elucidate microglia functions and mechanisms in PD (see Section 4.2 for information on this topic).

Int. J. Mol. Sci. **2021**, *22*, 4676

Table 1. Overview of human single cell and single nuclei studies.

Reference	Condition	Samples	Brain Region	Gender	Age (Years)	Tissue State	Method	Analyzed Microglia	Major Outcomes
Mastroeni et al. 2018 [35]	Age-matched control subjects (absence of PD pathology), PD patients	Controls: $n = 6$, PD patients: $n = 6$	SN, HPC (CA1)	All M	controls: 73.6 ± 6 PD patients: 74.6 ± 15.6	Post-mortem frozen unfixed	RT-PCR of immunolabeled (LN3) laser-captured microdissected microglia	Control SN $n = 3600$ microglia cells, control CA1 $n = 3600$ microglia cells, PD SN $n = 3600$ microglia cells, PD CA1 $n = 3600$ microglia cells	Regional heterogeneity (inter- and intra-condition), PD-specific active pathways including inflammation-related aldosterone and reactive oxygen species metabolism
Geirsdottir et al. 2019 [36]	Control subjects (absence of neuropathology)	controls: $n = 6$	Various	3 F, 3 M	9–55	Fresh (surgically removed excess tissue surrounding epileptic focal)	scRNAseq (MARS-seq2.0)	$n = 1069$ microglia cells	Complex human microglia heterogeneity, Neurodegeneration-linked pathways and PD risk factors most profoundly expressed in human microglia
Agarwal et al. 2020 [37]	Age-matched control subjects (no neurological disease)	Controls: $n = 5$	Cortex (middle frontal gyrus), SN (central portion at the level of the third nerve encompassing both ventral and dorsal tiers)	Cortex: 1 F, 3 M; SN: 2 F, 4M	55–70	Post-mortem frozen unfixed	snRNAseq (10X Genomics Chromium Single Cell Kit [v2 chemistry])	Cortex $n = 500$ microglia nuclei, SN $n = 325$ microglia nuclei	PD risk variants in neurons but not in microglia
Smajic et al. 2021 [39]	Age-matched control subjects, idiopathic PD patients	Controls: $n = 6$, PD patients: $n = 5$	Midbrain	Control: 1 F, 5 M; PD: 1 F, 4 M	Controls: 65–95; PD patients: 65–85	Post-mortem frozen unfixed	snRNAseq (10X Genomics Chromium Next GEM Single Cell 3′ Kit v3.1)	$n = 3903$ microglia nuclei	Disease-specific upregulation of microglia, into two branches: GPNMB-high resp. IL-1β-high microglia PD risk variants enrichment in neurons and microglia

3. (Neuro) Inflammation in PD

With a high degree of neuroplasticity and with low capacity to self-regenerate, the brain is especially sensitive to outer stimuli and injury. In addition, being protected by a blood-brain and blood-cerebrospinal fluid barrier, the brain was considered an "immune-privileged" organ. By contrast, in the last decade, this perception has been challenged and studies have changed our understanding of the immune response in the brain.

Inflammatory processes are considered to be a "double-edged sword": on the one hand, they help to clear out toxins and unwanted pathogens, while on the other hand, they promote cytotoxicity and neurodegeneration. Several studies suggested mechanisms of immune response and how they can influence neuronal cell death in PD. Already by the end of the 20th century, cytokines and complement proteins, which are components of the innate immune system, were found to be upregulated in brain, cerebrospinal fluid (CSF) and sera of PD patients [41]. Specifically, TNFα, Il-1β and IL6 were discussed as possible PD biomarkers [42–45]. In addition, Mount and colleagues showed a rise of IFN-γ plasma levels in PD patients compared to healthy controls [46]. Interestingly, the concentration of these markers in peripheral tissues might depend on PD severity and progression. Higher levels of TNFα in serum were characteristic of PD patients with more severe clinical features of impaired cognition, depression, sleep disturbances and fatigue [47,48]. As those studies identified that some of the prodromal symptoms are coupled with an underlying inflammatory response, the question arises whether inflammation really is only a consequence, rather than an active contributor to neurodegeneration.

The adaptive immune response has also been associated with neuropathological features of PD and, initially, the importance of microglial Fcγ receptor was studied. Immunoglobulins from PD patients activated Fcγ receptor positive (Fcγ R+/+) microglia cells in mice, which further promoted dopaminergic neuron cell death, while Fcγ R-/- microglia are not activated and no neuronal loss is detected [49]. There are a number of candidates in PD pathology capable of eliciting immune response and in vitro studies are focusing on components released by dying neurons. Significantly increased levels of autoantibodies were found against neuronal cells, brain lysate, and dsDNA accompanied with significantly higher titers of all three in sera of PD patients compared to healthy individuals [50]. Corroborating this, some studies focused on investigating the amount of mitochondrial DNA (mtDNA) in serum of PD patients. MtDNA, like some other mitochondrial compounds, is considered a damage-associated molecular pattern (DAMP), triggering pro-inflammatory signalling [51,52]. Our own biomarker study revealed higher serum levels of circulating cell-free mtDNA in patients with mutations in *PRKN* or *PINK1* compared to patients with idiopathic PD (IPD) [45]. On another note, studies also showed PD patients having higher autoantibody levels against α-synuclein in blood serum. Those differences highly correlate with inheritance mode of the disease but not with other disease-associated factors, while IPD cases were not significantly different from healthy controls [53]. A different study also showed increased levels of antibodies towards monomeric α-synuclein in serum of PD patients compared to controls, but ELISA responses reduced as PD progressed [54]. Neuromelanin is another neuronal component implicated in the disease. PD patients had elevated levels of autoantibodies against melanin in sera samples. Interestingly, ELISA absorbance response was significantly and negatively correlated with disease duration [55].

With regard to the adaptive immune system, studies investigating postmortem brain samples found reactive CD4+ and CD8+ T cells in postmortem brain samples from PD patients [56,57], suggesting a "porous" BBB and an impact of additional inflammatory mechanisms on the CNS. Furthermore, in the periphery, PD patients have elevated numbers of Th17 cells, which primarily produce IL-17. Interestingly, IL-17 was also found to have a detrimental effect on dopaminergic neuron iPSC-derived autologous cultures [57]. Another study, which explored peripheral immunity in PD, found a reduction in CD4+ T cells in patients. In addition, these cells were observed to preferentially differentiate towards a Th1-reactive state [58]. Recent PD research also showed differentially expressed genes in peripheral blood mononuclear cells (PBMCs), with patients presenting an elevated

abundance of CD49d+ Treg cells, which are known to suppress inflammatory processes [59]. When investigating the interaction of microglia and peripheral immune cells in PD, a recent study in rats found an important role of infiltrating T cells. These cells induce a microglial pro-inflammatory response to α-synuclein through upregulation of microglial MHC-II. In turn, this cell-cell communication causes neuronal cell death [60]. Considering the previously mentioned phenomenon of a "leaky" BBB in PD, the above-described phenotypes might be a mere consequence of dysfunctional pathways in brain cells, which release DAMPs into the periphery, causing an ongoing inflammatory loop. It is yet to be investigated how peripheral and CNS immune regulation is achieved in PD. These studies provide insights into the early immune response in PD and highlight novel targets for immunotherapies, which are further discussed in Section 5.

4. Disease Modeling: Animal Models, Patient-Derived iPSC Models, and Cell-Based 3D Models and Platforms

Since the discovery of microglia cells more than 100 years ago, multiple models have been designed to study inflammation in PD. Some of the most widely used models are summarized in Figure 1. In next sections, we will summarize key studies performed in animal and human patient-derived microglial model systems.

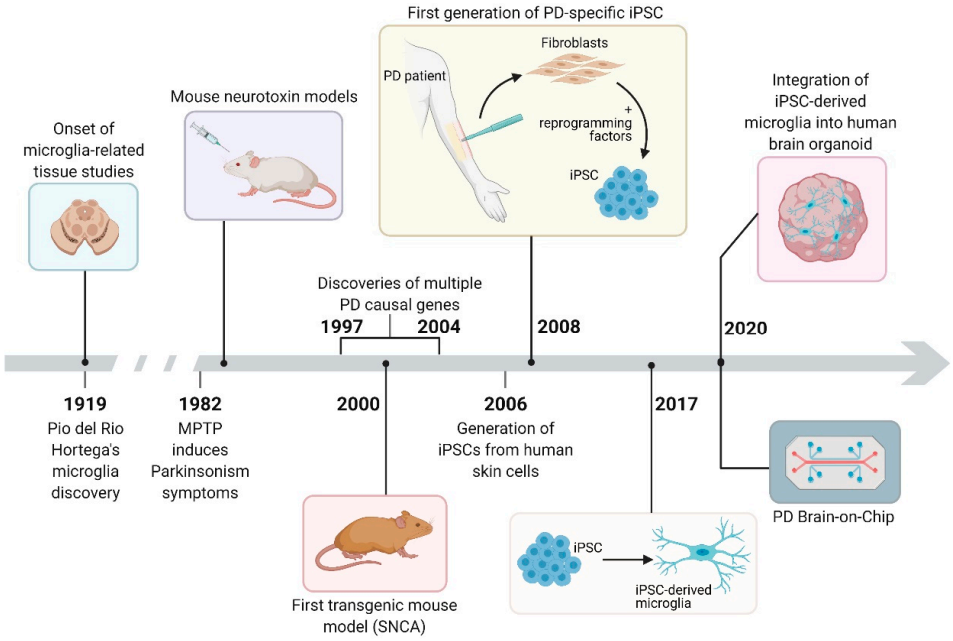

Figure 1. Historical overview of the different model systems used in PD microglia research. Figure created using BioRender.com.

4.1. Animal Models

PD animal studies may be either of genetic or neurotoxin nature. In vivo animal models are an essential part of pre-clinical trials in drug development. They are highly valuable when investigating the relevance of mutations, tissue pathology, motor symptoms and behavioral patterns in many diseases [61]. In addition, although these models cannot exhibit full neuropathological mechanisms, the progressive nature of PD and sometimes even robust neurodegeneration, they have proven to be invaluable resources of knowledge for researchers. Furthermore, in vitro models include primary microglia isolated from mice or rats, and immortalized murine microglia cell lines like BV-2, which can be greatly expanded and ultimately lead to reduction of animals used in studies. In the next section,

we will briefly summarize the inflammatory phenotypes observed in in vivo and in vitro models of PD.

4.1.1. Neurotoxin Model

Not long after the discovery that mitochondrial respiratory chain inhibition can induce parkinsonism symptoms in healthy individuals, scientists around the world studied the neurotoxic effects of such agents in invertebrate, vertebrate and non-human primates model systems and immortalized cell lines. Among the most commonly used neurotoxins is MPTP, while other studies have also investigated the impact of rotenone or paraquat.

One of the first studies performed in mice with MPTP-induced PD found a significant increase in microglia numbers and altered/activated microglia morphology in the SN early upon treatment, while dopaminergic neurons were depleted days after microglial activation [62]. Furthermore, blocking microglia activation with minocycline (a tetracycline compound with anti-inflammatory properties) after MPTP exposure not only prevented IL-1β formation but also diminished the demise of dopaminergic neurons. Minocycline treatment also reduced MPTP-induced iNOS activity, NADPH-oxidase (both enzymes known for microglia-mediated neurotoxicity), and TNF-α production [63,64]. TNF-α mRNA expression was upregulated in MPTP-treated mice compared to saline-treated animals. This increase preceded the loss of dopaminergic markers such as TH and dopamine, suggesting the involvement of inflammatory pathways prior to neurodegeneration. In addition, upon MPTP treatment, transgenic mice lacking TNF receptors did not exhibit dopamine or dopaminergic neuron loss [65]. Of note, MPTP-treated macaques had increased serum levels of IFN-γ and TNF-α compared to controls, even 5 years after neurotoxin exposure. Monkeys with severe parkinsonism (displaying symptoms of rigidity and a curved posture) showed significant dopaminergic neuronal loss, and activation of microglia and astrocytes [66].

Using knockout (KO) mouse models, molecular mechanisms of IFN-γ and TNF-α were further investigated. Upon MPTP treatment, IFN-γ KO mice had a completely rescued phenotype, while TNF-α KO mice had a minor activation of microglia, thus implying a synergistic effect of TNF-α and IFN-γ signaling pathways [66]. IFN-γ was shown to have a significant role in promoting neuronal cell loss after rotenone treatment, but only in the presence of microglia. Treatment of dopaminergic neuron-microglia co-cultures with rotenone revealed that cultures with wildtype but not IFN-γ receptor-deficient microglia had a significant loss of dopaminergic neurons [46]. In rats, rotenone together with lipopolysaccharide (LPS) is initiating neurodegeneration through microglia-mediated NADPH oxidase activation and release of ROS [67]. This NADPH activation was further found to be a direct consequence of HMGB1 (high-mobility group box 1) release from microglia and dying neurons upon ongoing LPS treatment, thereby propagating the detrimental inflammatory loop [68]. Although there have been reports that rotenone cannot directly activate microglia cells [69], additional work confirmed that the activation process is indeed mediated by p38-MAPK signaling [70].

4.1.2. SNCA

The aggregation of α-synuclein and formation of a-synuclein-containing Lewy bodies and neurites have been established as hallmarks of PD pathology since the first immunohistochemistry analysis of SNpc tissue [13]. Duplication, triplication and point mutations (A30P, A53T, E46K, H50Q, and G51D) in the *SNCA* gene cause an autosomal dominant form of PD [71–76]. SNCA mouse models include α-synuclein treatments, overexpression (OE) of human α-synuclein, and transgenic models with inserted human α-synuclein point mutations. Aggregation and neurotoxicity of a-synuclein are subsequent events of oxidative stress, genetic alterations and post-translational modifications like phosphorylation, nitration, ubiquitination and others [77]. Nitrated α-synuclein can activate not only microglia, but also peripheral leukocytes, thus accelerating neurodegeneration [78,79]. Furthermore, when released, a-synuclein can trigger microglia activation and an inflammatory

Int. J. Mol. Sci. 2021, 22, 4676

response (Figure 2). In rat midbrain neuron-microglia co-cultures, extracellular α-synuclein had a strong neurotoxic effect, which was mediated by an increase in ROS. Interestingly, neurotoxicity was abolished when microglia were depleted [80]. When priming microglia with α-synuclein injected into the SNpc, mice were more susceptible to environmental insults [81]. This finding suggests a more intricate relationship between the CNS and the peripheral immune response. In addition, both, treatment of primary mouse microglia with α-synuclein and α-synuclein OE in mice, are known to give rise to microglial ROS, TNF-α, IL-1β, COX2, iNOS [82,83]. Furthermore, α-synuclein exposure enhances the gene expression of toll-like receptors (TLRs) as well as of adapters and transcription factors such as MyD88 and NF-κB [84,85]. These results implicate α-synuclein as a damage-associated molecular pattern (DAMP). In agreement with this hypothesis, the activation of TLRs was found to be temporally and regionally induced after α-synuclein treatment, with an early response specifically in the nigrostriatal pathway [83]. Fibrils of α-synuclein but not monomers, can activate the NLR family pyrin domain containing 3 (NLRP3) inflammasome, induce the production and release of IL-1β and cleaved caspase-1, and mediate the release of ASC specks into the extracellular space. Pre-treatment of mice microglia with the small-molecule NLRP3 inhibitor MCC950, ameliorated α-synuclein-mediated inflammation [86,87]. With regard to point mutations in α-synuclein, some studies have shown their greater potential to activate microglia compared to wildtype α-synuclein [88–90]. Treatments with mutated α-synuclein triggered diverse phenotypes of microglia activation (based on cellular morphology and pro-inflammatory cytokine expression). While A53T-mutant α-synuclein has shown the strongest effect, wt and E46K had little to no effect on microglia activation. In addition, A53T-mutant α-synuclein is implicated in the NF-κB/AP-1/Nrf2 pathway, which can lead to higher cytokine expression and elevated ROS levels (Figure 2) [88]. Together, these studies suggest a molecular link between α-synuclein aggregation and neuroinflammation in PD.

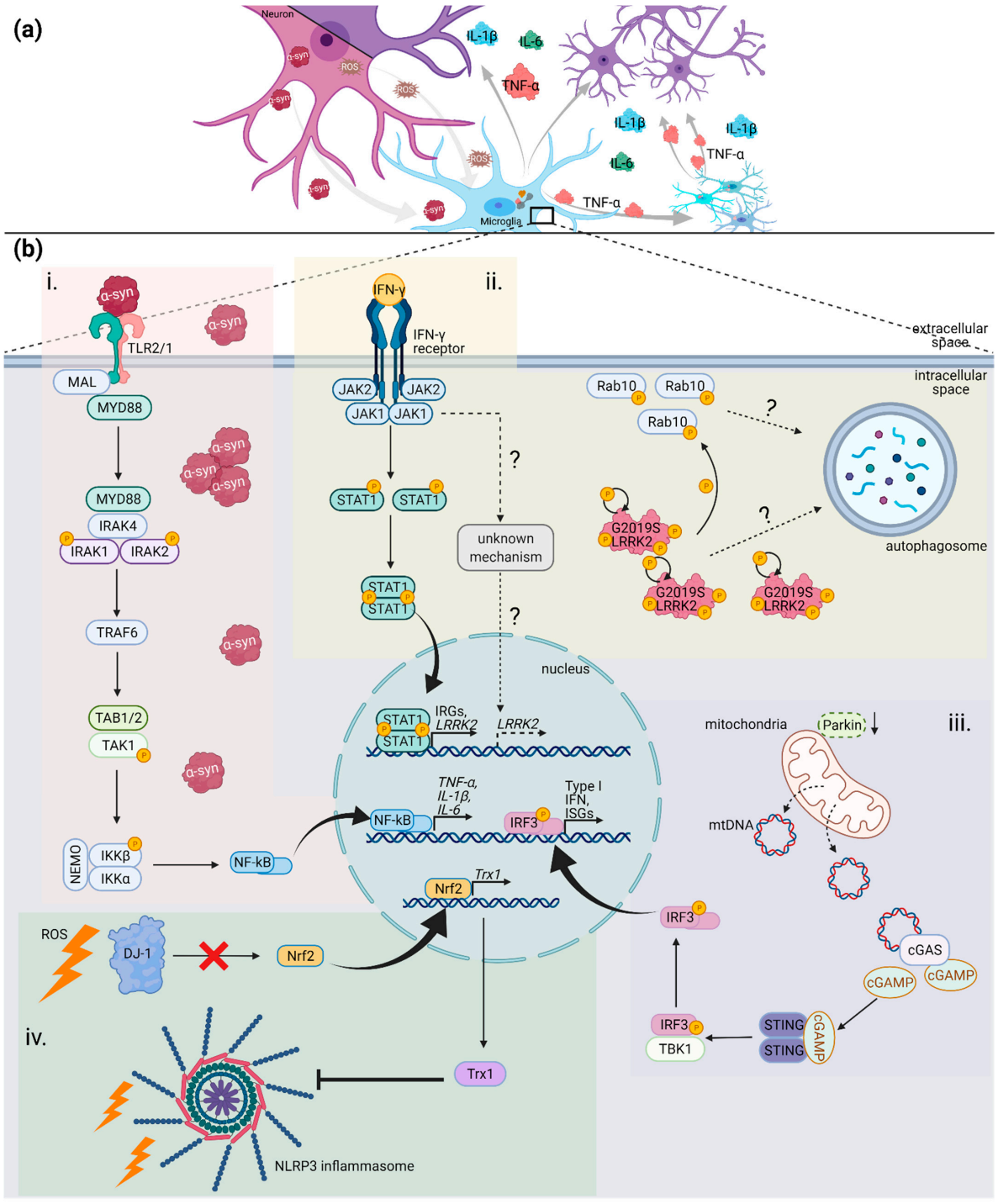

Figure 2. Neuron-microglia cross talk and selected inflammatory pathways involved in PD. (**a**) Inflammatory loop initiated by neuronal demise and propagated by microglial dysfunction. (**b**) Inflammatory pathways associated with α-synuclein (i), LRRK2 (ii), parkin (iii) or DJ-1 (iv) in the context of PD pathology. This figure was created with BioRender.com.

4.1.3. LRRK2

Mutations in the *leucine rich repeat kinase 2* (*LRRK2*) gene are the most common cause of PD, having been associated with up to 3% of idiopathic and 5–15% of all familial PD cases [91]. Pathogenic variants include R1441C and N1437H in the Ras-of-complex (ROC) domain, Y1699C in the C-terminal of ROC (COR) domain, and G2019S and I2020T in the kinase domain. Mutations in *LRRK2* are autosomal dominantly inherited. The complex structure of the protein with several active domains may be one reason why the function of LRRK2 is still not fully understood. LRRK2 is predominantly expressed in immune cells (macrophages and monocytes) of the CNS, certain peripheral tissues, and blood, which led to the hypothesis that LRRK2 has its main function in innate immunity [92–94]. In this context, it is also important to note that single nucleotide polymorphisms (SNPs) in *LRRK2* have been associated with higher susceptibility to bacterial infections and chronic inflammatory diseases such as Crohn's disease and leprosy [95–98]. Unlike other alterations in LRRK2, the most common mutation, G2019S, is not completely penetrant, meaning that not all individuals harboring the single nucleotide change will develop PD [99]. Thus, a "multiple-hit" model was suggested, where a "second-hit" is required for the onset of PD in a G2019S mutation carrier. This model is further corroborated by studies in transgenic LRRK2-mutant mice, which show little to no neurodegeneration [100,101]. Upon stimulation of LRRK2 R1441G transgenic mice with LPS, LRRK2 levels significantly increased [94]. Interestingly, although in primary microglia LRRK2 protein levels were consistently elevated upon LPS stimulation, some studies showed no upregulation at mRNA level, implicating complex post-translational modifications [102]. In addition, LPS-treated transgenic microglia released higher levels of pro-inflammatory TNF-α, IL-1β and IL-6, and lower levels of anti-inflammatory IL-10. The same results were obtained when studying the gene expression of these cytokines, indicating an upstream role of LRRK2 in cytokine modulation. When assessing the neurotoxic effect of microglia-derived molecules, conditioned medium from LPS-stimulated transgenic microglia caused more severe neurodegeneration than medium from LPS-stimulated wildtype microglia [94]. Furthermore, the knockdown of LRRK2 (LRRK2-KD) almost completely abrogated microglial pro-inflammatory phenotypes (with *TNF-α*, *IL-1β* and *IL-6* being significantly reduced) in LPS-treated microglia [103]. These findings in LRRK2-KD microglia were consistent with results obtained after exposure of wildtype microglia to a small-molecule kinase inhibitor, implicating both *LRRK2* expression and kinase activity in the induction of pro-inflammatory mechanisms (Figure 2) [102]. The activation of LRRK2 can be induced through TLR pathways in a MyD88-dependent manner [104]. This finding further illustrates the connection between the innate immune response and LRRK2 function in PD.

4.1.4. PRKN

Somatic mutations in the *PRKN* gene cause early-onset familial PD, and they are inherited in an autosomal recessive manner [105]. *PRKN* codes for parkin, an E3 ubiquitin ligase, and it is involved in the removal of damaged mitochondria, a process also known as mitophagy [106]. Parkin mutations are rare, but have a strong "mitochondrial phenotype" [107]. The frequency of *PRKN* mutation can reach up to 10–25% in early-onset PD patients, suggesting a strong genetic role in the pathology of PD [108]. Although inflammatory phenotypes in *PRKN*-associated PD have only recently became a research focus, mitochondria have the potential to enable immune responses through several of its components such as ROS, N-formyl peptides, cytochrome c, cardiolipin, and mtDNA, mutually referred to as mito-DAMPs [109]. Deficiencies in both mitophagy and autophagy pathways can lead to the release of these components into the cytosol and the activation of the NLRP3 inflammasome [110,111]. In wt mice, the treatment with rotenone upon an insult with LPS and ATP enabled mtDNA translocation into the cytosol, which, in turn, contributed to the secretion of the pro-inflammatory cytokines IL-1β and IL-18 [111]. First studies in parkin-/- mice could not conclude any differences in neurodegeneration between wt and mutants, prior or even upon acute treatment with LPS. Only upon chronic LPS administration, parkin-/- mice had SNpc dopaminergic neuron degeneration and fine-motor

function deficits [112]. The protective role of parkin in immune cells has been reported in multiple studies. Parkin-deficient macrophages had enhanced mtDNA release, mtROS levels, and IL-1β extracellular release upon NLRP3 agonist (LPS and ATP) treatment. Parkin can prevent the accumulation of damaged mitochondria. In Parkin-silenced cells, a buildup of damaged mitochondria was observed upon LPS and ATP insult. The study implicated NF-κB-p62 anti-inflammatory signaling, since parkin recruitment to mitochondria is crucial for p62 tagging within the mitophagy/autophagy process [113]. In addition, parkin is suspected to regulate the transcription of A20, an inhibitor of NF-κB-mediated cytokine expression [114]. Surprisingly, another study found that LPS-treated microglia and macrophages have reduced mRNA levels of *PRKN* and this was prevented by blocking NF-κB signaling [115]. Thus, chronic neuroinflammation can phenocopy parkin depletion, where anti-inflammatory pathways may not be enough to rescue the exacerbated inflammatory phenotype. Furthermore, mtDNA can be detected by the cyclic GMP-AMP synthase (cGAS)—stimulator of interferon genes (STING) pathway. A brief report showed higher mtDNA release in Parkin-/- mice under exhaustive exercise. Moreover, Parkin-/- mice that were crossed with mutator mice (that harbor a defective mtDNA proofreading polymerase) had higher mtDNA release and production of pro-inflammatory cytokines. This increased cytokine expression was abrogated upon STING deletion, implicating mtDNA release and cGAS-STING signalling in the observed phenotypes (Figure 2) [44]. Finally, parkin has the ability to prevent the presentation of mitochondrial antigens on the surface of immune cells by inhibiting mitochondria-derived vesicles (MDVs), linking also autoimmune mechanisms to PD [116].

4.1.5. DJ-1

Although *DJ-1* was first described as an oncogene, mutations in this gene are associated with an early-onset PD. The inheritance of *DJ-1* is autosomal recessive and mutations are rare [107]. DJ-1 is expressed in cells with high-energy demand, and it can successfully "buffer" oxidative stress through stabilization of nuclear factor erythroid-derived 2-like 2 (Nrf2) protein [117]. Its role in microglia and inflammatory pathways has not been extensively studied since the focus has primarily been on its expression in dopaminergic neurons, which are particularly energy-demanding cells. Nevertheless, together with its antioxidant activity, some studies concluded DJ-1 has a major anti-inflammatory role in the brain. DJ-1 KO mice had elevated basal levels of IFN-γ in SNpc compared to control mice and this was aggravated after LPS administration [118]. In mouse microglia, DJ-1 can prevent prolonged phosphorylation of signal-transducers and activators of transcription (STAT1) proteins upon IFN-γ treatment by enabling the interaction between Src-homology 2 domain-containing 101 protein tyrosine phosphatase-1 (SHP-1) and STAT1. DJ-1 KO microglia had elevated levels of nuclear p-STAT1, higher expression of *COX-2*, *iNOS*, and *TNF-α* [119]. In addition, DJ-1-deficient microglia had increased mitochondrial activity, which resulted in elevated ROS levels compared to control microglia and those were further exacerbated upon LPS exposure. LPS-treated DJ-1-deficient microglia had higher levels of nitric oxide (NO) and secreted cytokines but lower levels of anti-inflammatory triggering receptor expressed on myeloid cells 2 (TREM2) protein [120]. Although the same group of authors reported higher phagocytosis ability based on zymosan particle uptake, another study showed reduced uptake of soluble α-synuclein in DJ-1 KD microglial cells [121]. α-synuclein could significantly increase the secretion of IL-1β, IL-6, and NO. Also, DJ-1 KD microglia had impaired degradation of p62 and LC3-II upon activation of autophagy. Furthermore, control cells accumulated more α-synuclein upon inhibition of autophagy, while this effect was observed to a lesser extent in DJ-1 KD microglia [121]. Additionally, an extensive study found shared pathways between DJ-1 and NLRP3, which to some extent explains the upregulation of pro-inflammatory cytokines (Figure 2). After MPTP treatment, DJ-1 can suppress NLRP3 activity through upregulation of the antioxidant pathway Nrf2/Trx1, while DJ-1-deficient cells could only be partially rescued by overexpression of

Nrf2 [122]. More studies will be needed to further explore the link between DJ-1 regulation of oxidative stress and neuroinflammation.

4.2. Human Induced Pluripotent Stem Cell (iPSC) Studies

Advancements in stem cell techniques had a significant impact on the quality of research, especially in neuroscience, since patient material is hard to obtain and animal models in the majority of cases do not fully mirror PD-associated neurodegeneration. Two major classes of iPSC models can be distinguished: gene-modified (in which PD causing mutations are either inserted or corrected) and patient-derived cells. The biggest advantage of iPSC models, which also constitutes their biggest disadvantage, is the genetic background. The original genetic signature of a patient can, on the one hand, help to decipher the potentially multifaceted molecular mechanisms underlying PD in this particular case, while on the other hand, it may cause (functional) heterogeneity between different patient lines. Further information on this topic can be found in a detailed review by Volpato and colleagues [123]. Although, currently, PD studies employing iPSCs are mainly focusing on neuronal differentiation protocols, in the next few paragraphs, we will briefly summarize the available literature exploring iPSC-derived microglia and macrophages in the context of PD.

4.2.1. SNCA

To our knowledge, only one study investigating *SNCA*-mutant iPSC-derived microglia and/or macrophages has been published to date. Differences between control, A53T and *SNCA* triplication macrophages were assessed. *SNCA* triplication cells had higher intracellular levels and an increased release rate of α-synuclein compared to, both, A53T and control cells. The CXCL1, IL-18, and IL-22 cytokine levels in the supernatant of *SNCA* triplication macrophage cultures were significantly upregulated compared to all other investigated cultures. By contrast, there was no difference with regard to the levels of released CCL17, IL-4, IL-6, IL-8, IL-10, and TNF-α between healthy and *SNCA*-mutant macrophages. In addition, in *SNCA* triplication cells, the phagocytic ability was significantly reduced. Further strengthening this result, treating control cells with monomeric α-synuclein had the same impact. Accordingly, high levels of exogenous and endogenous α-synuclein severely disrupt the functionality of iPSC-derived macrophages. The authors found differences with regard to the uptake mechanisms of fibrillar and monomeric α-synuclein [124]. Finally, a very recent study investigated the effect of an α-synuclein antibody on iPSC-derived microglia. Surprisingly, misfolded α-synuclein bound to the antibody triggered inflammatory signalling through the upregulation of the NLRP3 inflammasome [125]. This finding calls into question ongoing clinical trials with antibodies against α-synuclein (see Section 5 for details).

4.2.2. LRRK2

As described in the previous sections, LRRK2 is highly abundant in immune cells. Thus, iPSC-derived microglia and macrophages are used to explore the impact of LRRK2 mutations on immune signalling in PD. First research revealed that LRRK2 is involved in the later stages of phagosome maturation. Furthermore, the localization of LRRK2 is essential for the recruitment of Rab8 and Rab10 to phagosomes, which is mediated by LRRK2 kinase activity. Moreover, it was confirmed that IFN-γ directly upregulates *LRRK2* gene expression [126]. In another study, LRRK2 G2019S microglia showed increased motility compared to healthy control and LRRK2 KO microglia. This motility reached control levels upon IFN-γ treatment. An assessment of the phagocytic ability showed that G2019S microglia have an increased capacity to engulf fluorescent beads. In addition, LRRK2 G2019S microglia had reduced levels of nuclear NF-kB, upon treatment with both LPS and IFN-γ, suggesting impaired inflammatory signaling mediated by this transcription factor. Moreover, when the supernatant from LPS-treated G2019S microglia was added to control or G2019S iPSC-derived neurons a shortening of the neurite length was ob-

served [127]. Conversely, a study investigating the motility of iPSC-derived monocytes found that G2019S knock-in cells were less motile than wild type cells [128]. In light of opposing findings in microglia, this suggests a cell-type specific impact of the G2019S mutation in LRRK2.

4.3. Human Cell-Based 3D Models and Platforms

On the one hand, the complex tissue organization in the brain makes cell-cell communication and interactions difficult to study in in vivo models. On the other hand, in vitro models do not cover the full scope of signalling between all types of brain cells. However, thanks to the development of iPSC-derived co-culture systems, it is now possible to investigate the role of non-neuronal cells in neurodegeneration at least to some degree. Excitingly, 3D cultures, such as brain organoids and brain spheres, have recently emerged as highly valuable tools to model multiple cellular interactions and the pathophysiology of numerous concurrent processes in vivo. Brain organoids have been particularly useful in the research of developmental and neurodegenerative diseases as well as brain cancers [129–136]. By contrast, only a few studies have focused on PD pathogenesis so far [137,138]. Since brain organoids consist of cells from the neuroectodermal region, microglial cells, which originate from the yolk sac, need to be "artificially" added to the 3D culture. While multiple groups have successfully integrated microglia into cortical organoids and brain sphere cultures [139–141], some researchers observed spontaneous microglia formation in cortical organoids under differentiation conditions, which do not inhibit non-neuronal lineages [142]. First results suggest that the incorporated microglia support neuronal development and maturation in cortical organoids. Moreover, the microglia appear to become more ramified and matured as the organoid grows [141]. Several research teams, including our close collaborators, are investigating microglial inflammatory signalling in midbrain-specific organoids from PD patients. Though, this work is not without its hurdles. A major challenge of microglia-midbrain organoid cultures is to obtain (and maintain) physiological ratios and distributions of different brain cell types. Significant scientific efforts are currently ongoing to configure cell culture media compositions that will facilitate the simultaneous growth of all cell types, thereby achieving a more physiological microenvironment that prevents the activation of microglia (which is, for instance, commonly observed in the dead core of organoids). Furthermore, cell-based microfluidics systems (also known as Brain-on-Chip technology) have been developed to investigate microglia interactions with astrocytes and neurons under the impact of a continuous fluid flow [143–145]. To mimic the BBB composition, some systems are designed to contain a layer of microvascular endothelial cells and pericytes. Exposing a human Brain-Chip (which mirrored the microenvironment of the substantia nigra) to α-synuclein fibrils initiated dopaminergic neuron death, mitochondrial dysfunction and neuroinflammation, while BBB was significantly compromised [145]. Due to their capacity to model the BBB, both organoids and microfluidic systems have emerged as highly promising resources for therapeutic testing in brain diseases [146,147].

5. Immunotherapies in Parkinson's Disease

5.1. Anti-Inflammatory Treatments in PD

In a number of animal PD models, the use of nonsteroidal anti-inflammatory drugs (NSAIDs) showed promising results [148]. Exemplary, in an MPTP mouse model, treatment with acetylsalicylic acid, which inhibits the cyclooxygenase isoenzymes COX-1 and COX-2, prevents neuronal loss in the substantia nigra [149]. By contrast, clinical trials exploring the neuroprotective effect of NSAIDs were less conclusive. While several studies reported that NSAIDs may be able to delay or even prevent the onset of PD [148,150], there have also been reports of no impact of NSAID intake on PD risk [148]. A recent meta-analysis that comprised 15 studies on the use of NSAIDs and PD risk found no association. Moreover, a dose-response analysis revealed that the amount and duration of NSAIDs administration did not influence the outcome [151].

In light of these results, alternative approaches that specifically target the transition of microglia from a proinflammatory (M1) to an anti-inflammatory (M2) state have been suggested [148]. Suppression of the M1 state may be achieved by acting at the level of the proinflammatory cytokines TNF-α, IL-1β and IFN-γ [148]. Supporting this hypothesis, the overexpression of dominant negative TNF (DN-TNF) in the nigra of 6-OHDA-treated rats reduced the loss of dopaminergic neurons [152]. An alternative approach may be to modify the endocannabinoid system with the aim to reduce pro-inflammatory microglial toxicity [148]. The expression of the cannabinoid receptor CB2 was found to be increased in glial cells in various conditions affecting the CNS, including AD and PD [153]. Interestingly, while the abundance of CB2 is enhanced in activated PD microglia, an immunolabeling study in human postmortem nigral tissue revealed that CB2 levels are decreased in dopaminergic neurons from PD patients. This observation coincided with diminished numbers of tyrosine hydroxylase-containing neurons in the PD tissue [153]. In line with these findings, administering the CB2 agonist β-caryophyllene to rotenone-challenged rats reduced the release of proinflammatory cytokines which, in turn, prevented dopaminergic neuron demise and the activation of glial cells [154].

Also strategies that actively promote a shift of microglia from M1 to M2 have been considered [148]. For instance, the cerebral infusion of a recombinant adeno-associated viral vector expressing human *interleukin-10* (*IL-10*) was tested in an MPTP mouse model. Enhancing the abundance of the anti-inflammatory cytokine led to an increase in striatal TH protein levels [155]. Further of interest in this regard, the multiple sclerosis drug Glatiramer acetate was shown to decrease microglial activation by promoting an M2 state [156]. As in the case of *IL-10* overexpression, treatment of MPTP mice with Glatiramer acetate rescued tyrosine hydroxylase (TH) protein levels in the striatum. Moreover, exposure to the immuno-modulatory agent reversed motor phenotypes in these animals [157]. However, none of the proposed treatments facilitating a shift from M1 to M2 has been tested in humans (for a more detailed review of immuno-modulatory treatment approaches in PD—including a study comparison in tabular form—see Subramaniam and Federoff [148]). Thus, further research in PD patient-derived cellular models will be required to understand the molecular consequences of microglial activation regulators, which will be a prerequisite to eventually use such agents in clinical trials.

5.2. Anti-α-Synuclein Immunotherapies

One of the best studied hallmarks of PD are α-synuclein aggregates. As mentioned above, the protein can act as DAMP triggering inflammatory processes. Thus, one research focus in PD is the development of immunotherapeutic approaches that reduce intra- and extracellular α-synuclein levels in the brain. Specifically, antibodies hold the promise of alleviating α-synuclein toxicity and promoting the protein's degradation [158]. Various epitopes have been tested in preclinical studies with α-synuclein transgenic mice. In two independent studies, administration of antibodies that target the C-terminus (Ab274, 1H7 or 5C1) reduced microgliosis and improved neuronal survival [159,160]. In animals that received ab274, there is even evidence that microglia block the cell-to-cell transfer of α-synuclein by enhancing the clearance of neuron-derived aggregates [160]. With regard to antibodies that are directed against the N-terminus, no improvement of microgliosis phenotypes was observed [158]. Finally, when focusing on antibodies that recognize oligomeric or fibrilar forms of α-synuclein, Syn-O1, Syn-O4 and Syn-F1 effectively reduced protein aggregation and neurodegeneration in transgenic mice [161]. Only animals treated with Syn-O4 displayed decreased microglia levels and showed reduced ramification of these cells in the hippocampus [161].

In light of the overall promising results from immunotherapeutic analyses in mice, several antibodies are being tested in phase I clinical trials, which focus primarily on the safety of treatments [162]. By contrast, only two antibodies have so far been moved forward into phase II clinical trials [162], which aim to establish the clinical efficiency of the immunotherapeutics. In the PASADENA study (ClinicalTrials.gov Identifier: NCT03100149),

Prasinezumab (PRX002) is currently being tested in patients with early PD. Initial results indicate that the primary outcome of the study was not achieved. At week 52, the MDS-UPDRS total score was not significantly different between the treatment and the placebo group. Nevertheless, some parameters suggest that the antibody delays the progression of motor symptoms in PD patients. However, whether Prasinezumab has a positive impact on microglial phenotypes in these individuals currently remains elusive. In addition, the SPARK study (ClinicalTrials.gov Identifier: NCT03318523), which aims to evaluate the clinical benefits of the α-synuclein antibody BIIB054, is currently ongoing.

6. Outlook

The complex and diverse aetiology of PD represents a major obstacle for effective therapeutic interventions. The here described recent findings highlight the importance of neuroinflammatory processes and put microglia as the immanent immune cells of the brain in the focus of novel therapeutic approaches. In particular, this immunological entry point could not only support the identification of common mechanisms underlying the different genetic and idiopathic disease developments but also allow to target disease progression not on the cellular but on the (immune) system level of the brain. While the evidence for the contribution of microglia to disease progression clearly demonstrates the large potential for alternative treatments, further detailed investigations are required to reveal underlying mechanisms and to dissect cellular heterogeneity of microglia in the disease context. Thus, scRNAseq has shown that microglia diversity goes beyond the traditional M1/M2 description and that PD-associated signatures are species- and human-specific but the impact of the microenvironment is still elusive. The recent developments in spatial transcriptomics [163,164] and the application to human iPSC model systems such as organoids [141] and the brain [165] will allow for further insights into the regulation of the complex ecosystem within the brain and how intercellular interactions contribute to PD progression. A major challenge for these studies is the lack of physiologically realistic model systems due to the general limitations of animal models and the not yet resolved issue in human organoid systems, which do not reflect the brain composition of the affected brain regions as described above. Hence, addressing these current limitations is essential to deepen our understanding of the multicellular dimension of PD development and particularly the impact of microglia and their role in neuroimmunology that will not only support the development of new therapeutic strategies in PD but may also provide a more unifying perspective on neurodegeneration given the recent indications for the involvement of microglia in Alzheimer's disease and multiple sclerosis [165,166].

Author Contributions: All authors contributed to the conception, literature review and writing of the manuscript, and reviewed the final document. All authors have read and agreed to the published version of the manuscript.

Funding: KB was supported by the Luxembourg National Research Fund (FNR) through the PRIDE15/10907093/CriTiCS grant. SF and SS received funding from the Luxembourg National Research Fund (FNR) within the PARK-QC DTU (PRIDE17/12244779/PARK-QC). AG received funding from the FNR within the framework of the ATTRACT (FNR9631103) and INTER (INTER/DFG/19/14429377) programmes. In addition, AG and AS are supported by the FNR as members of the Luxembourgish National Centre of Excellence in Research on Parkinson's Disease (NCER-PD). In addition, AG was supported by the German Research Foundation (DFG, GR 3731/5-2, FOR 2488/2).

Institutional Review Board Statement: Not applicable.

Informed Consent Statement: Not applicable.

Data Availability Statement: No new data were created or analyzed in this study. Data sharing is not applicable to this article.

Conflicts of Interest: The authors declare no conflict of interest.

References

1. Toulouse, A.; Sullivan, A.M. Progress in Parkinson's Disease-Where Do We Stand? *Prog. Neurobiol.* **2008**, *85*, 376–392. [CrossRef]
2. Forno, L.S. Neuropathology of Parkinson's Disease. *J. Neuropathol. Exp. Neurol.* **1996**, *55*, 259–272. [CrossRef]
3. Deng, H.; Dodson, M.W.; Huang, H.; Guo, M. The Parkinson's Disease Genes pink1 and Parkin Promote Mitochondrial Fission And/or Inhibit Fusion in Drosophila. *Proc. Natl. Acad. Sci. USA* **2008**, *105*, 14503–14508. [CrossRef]
4. Klein, C.; Westenberger, A. Genetics of Parkinson's Disease. *Cold Spring Harb. Perspect. Med.* **2012**, *2*, a008888. [CrossRef]
5. Del Rey, N.L.-G.; Quiroga-Varela, A.; Garbayo, E.; Carballo-Carbajal, I.; Fernández-Santiago, R.; Monje, M.H.G.; Trigo-Damas, I.; Blanco-Prieto, M.J.; Blesa, J. Advances in Parkinson's Disease: 200 Years Later. *Front. Neuroanat.* **2018**, *12*, 113. [CrossRef]
6. Hindle, J.V. Ageing, Neurodegeneration and Parkinson's Disease. *Age Ageing* **2010**, *39*, 156–161. [CrossRef]
7. Collier, T.J.; Kanaan, N.M.; Kordower, J.H. Ageing as a Primary Risk Factor for Parkinson's Disease: Evidence from Studies of Non-Human Primates. *Nat. Rev. Neurosci.* **2011**, *12*, 359–366. [CrossRef] [PubMed]
8. Chade, A.R.; Kasten, M.; Tanner, C.M. Nongenetic Causes of Parkinson's Disease. In *Parkinson's Disease and Related Disorders*; Springer: Vienna, Austria, 2006; pp. 147–151.
9. Braak, H.; Rüb, U.; Del Tredici, K. Cognitive Decline Correlates with Neuropathological Stage in Parkinson's Disease. *J. Neurol. Sci.* **2006**, *248*, 255–258. [CrossRef] [PubMed]
10. Schapira, A.H.V.; Chaudhuri, K.R.; Jenner, P. Non-Motor Features of Parkinson Disease. *Nat. Rev. Neurosci.* **2017**, *18*, 435–450. [CrossRef] [PubMed]
11. Langston, J.W.; Forno, L.S.; Tetrud, J.; Reeves, A.G.; Kaplan, J.A.; Karluk, D. Evidence of Active Nerve Cell Degeneration in the Substantia Nigra of Humans Years after 1-Methyl-4-Phenyl-1,2,3,6-Tetrahydropyridine Exposure. *Ann. Neurol.* **1999**, *46*, 598–605. [CrossRef]
12. Langston, J.W.; Ballard, P.; Tetrud, J.W.; Irwin, I. Chronic Parkinsonism in Humans due to a Product of Meperidine-Analog Synthesis. *Science* **1983**, *219*, 979–980. [CrossRef]
13. Spillantini, M.G.; Schmidt, M.L.; Lee, V.M.; Trojanowski, J.Q.; Jakes, R.; Goedert, M. Alpha-Synuclein in Lewy Bodies. *Nature* **1997**, *388*, 839–840. [CrossRef]
14. McGeer, P.L.; Itagaki, S.; Boyes, B.E.; McGeer, E.G. Reactive Microglia Are Positive for HLA-DR in the Substantia Nigra of Parkinson's and Alzheimer's Disease Brains. *Neurology* **1988**, *38*, 1285–1291. [CrossRef]
15. Grünewald, A.; Kumar, K.R.; Sue, C.M. New Insights into the Complex Role of Mitochondria in Parkinson's Disease. *Prog. Neurobiol.* **2019**, *177*, 73–93. [CrossRef]
16. Hauser, D.N.; Hastings, T.G. Mitochondrial Dysfunction and Oxidative Stress in Parkinson's Disease and Monogenic Parkinsonism. *Neurobiol. Dis.* **2013**, *51*, 35–42. [CrossRef] [PubMed]
17. Park, J.-S.; Davis, R.L.; Sue, C.M. Mitochondrial Dysfunction in Parkinson's Disease: New Mechanistic Insights and Therapeutic Perspectives. *Curr. Neurol. Neurosci. Rep.* **2018**, *18*, 21. [CrossRef]
18. Lang, A.E.; Lozano, A.M. Parkinson's Disease. First of Two Parts. *N. Engl. J. Med.* **1998**, *339*, 1044–1053. [CrossRef]
19. Gao, H.-M.; Hong, J.-S. Why Neurodegenerative Diseases Are Progressive: Uncontrolled Inflammation Drives Disease Progression. *Trends Immunol.* **2008**, *29*, 357–365. [CrossRef] [PubMed]
20. Verkhratsky, A.; Ho, M.S.; Zorec, R.; Parpura, V. (Eds.) *Neuroglia in Neurodegenerative Diseases*; Springer: Singapore, 2019.
21. Pérez-Cerdá, F.; Sánchez-Gómez, M.V.; Matute, C. Pío Del Río Hortega and the Discovery of the Oligodendrocytes. *Front. Neuroanat.* **2015**, *9*, 92. [CrossRef]
22. Sierra, A.; de Castro, F.; Del Río-Hortega, J.; Rafael Iglesias-Rozas, J.; Garrosa, M.; Kettenmann, H. The "Big-Bang" for Modern Glial Biology: Translation and Comments on Pío Del Río-Hortega 1919 Series of Papers on Microglia. *Glia* **2016**, *64*, 1801–1840. [CrossRef]
23. Hickman, S.; Izzy, S.; Sen, P.; Morsett, L.; El Khoury, J. Microglia in Neurodegeneration. *Nat. Neurosci.* **2018**, *21*, 1359–1369. [CrossRef]
24. Priller, J.; Flügel, A.; Wehner, T.; Boentert, M.; Haas, C.A.; Prinz, M.; Fernández-Klett, F.; Prass, K.; Bechmann, I.; de Boer, B.A.; et al. Targeting Gene-Modified Hematopoietic Cells to the Central Nervous System: Use of Green Fluorescent Protein Uncovers Microglial Engraftment. *Nat. Med.* **2001**, *7*, 1356–1361. [CrossRef] [PubMed]
25. Bruttger, J.; Karram, K.; Wörtge, S.; Regen, T.; Marini, F.; Hoppmann, N.; Klein, M.; Blank, T.; Yona, S.; Wolf, Y.; et al. Genetic Cell Ablation Reveals Clusters of Local Self-Renewing Microglia in the Mammalian Central Nervous System. *Immunity* **2015**, *43*, 92–106. [CrossRef]
26. Ueno, M.; Fujita, Y.; Tanaka, T.; Nakamura, Y.; Kikuta, J.; Ishii, M.; Yamashita, T. Layer V Cortical Neurons Require Microglial Support for Survival during Postnatal Development. *Nat. Neurosci.* **2013**, *16*, 543–551. [CrossRef] [PubMed]
27. Nimmerjahn, A.; Kirchhoff, F.; Helmchen, F. Resting Microglial Cells Are Highly Dynamic Surveillants of Brain Parenchyma in Vivo. *Science* **2005**, *308*, 1314–1318. [CrossRef]
28. Bennett, M.L.; Bennett, F.C.; Liddelow, S.A.; Ajami, B.; Zamanian, J.L.; Fernhoff, N.B.; Mulinyawe, S.B.; Bohlen, C.J.; Adil, A.; Tucker, A.; et al. New Tools for Studying Microglia in the Mouse and Human CNS. *Proc. Natl. Acad. Sci. USA* **2016**, *113*, E1738–E1746. [CrossRef]
29. Friedman, B.A.; Srinivasan, K.; Ayalon, G.; Meilandt, W.J.; Lin, H.; Huntley, M.A.; Cao, Y.; Lee, S.-H.; Haddick, P.C.G.; Ngu, H.; et al. Diverse Brain Myeloid Expression Profiles Reveal Distinct Microglial Activation States and Aspects of Alzheimer's Disease Not Evident in Mouse Models. *Cell Rep.* **2018**, *22*, 832–847. [CrossRef] [PubMed]

30. Walker, D.G.; Tang, T.M.; Mendsaikhan, A.; Tooyama, I.; Serrano, G.E.; Sue, L.I.; Beach, T.G.; Lue, L.-F. Patterns of Expression of Purinergic Receptor P2RY12, a Putative Marker for Non-Activated Microglia, in Aged and Alzheimer's Disease Brains. *Int. J. Mol. Sci.* **2020**, *21*, 678. [CrossRef]
31. Sheng, J.G.; Mrak, R.E.; Griffin, W.S. Enlarged and Phagocytic, but Not Primed, Interleukin-1 Alpha-Immunoreactive Microglia Increase with Age in Normal Human Brain. *Acta Neuropathol.* **1998**, *95*, 229–234. [CrossRef]
32. Conde, J.R.; Streit, W.J. Microglia in the Aging Brain. *J. Neuropathol. Exp. Neurol.* **2006**, *65*, 199–203. [CrossRef]
33. Gao, X.; Wang, X.; Xiong, W.; Chen, J. In Vivo Reprogramming Reactive Glia into iPSCs to Produce New Neurons in the Cortex Following Traumatic Brain Injury. *Sci. Rep.* **2016**, *6*, 22490. [CrossRef]
34. Imamura, K.; Hishikawa, N.; Sawada, M.; Nagatsu, T.; Yoshida, M.; Hashizume, Y. Distribution of Major Histocompatibility Complex Class II-Positive Microglia and Cytokine Profile of Parkinson's Disease Brains. *Acta Neuropathol.* **2003**, *106*, 518–526. [CrossRef]
35. Mastroeni, D.; Nolz, J.; Sekar, S.; Delvaux, E.; Serrano, G.; Cuyugan, L.; Liang, W.S.; Beach, T.G.; Rogers, J.; Coleman, P.D. Laser-Captured Microglia in the Alzheimer's and Parkinson's Brain Reveal Unique Regional Expression Profiles and Suggest a Potential Role for Hepatitis B in the Alzheimer's Brain. *Neurobiol. Aging* **2018**, *63*, 12–21. [CrossRef]
36. Geirsdottir, L.; David, E.; Keren-Shaul, H.; Weiner, A.; Bohlen, S.C.; Neuber, J.; Balic, A.; Giladi, A.; Sheban, F.; Dutertre, C.-A.; et al. Cross-Species Single-Cell Analysis Reveals Divergence of the Primate Microglia Program. *Cell* **2019**, *179*, 1609–1622.e16. [CrossRef]
37. Agarwal, D.; Sandor, C.; Volpato, V.; Caffrey, T.M.; Monzón-Sandoval, J.; Bowden, R.; Alegre-Abarrategui, J.; Wade-Martins, R.; Webber, C. A Single-Cell Atlas of the Human Substantia Nigra Reveals Cell-Specific Pathways Associated with Neurological Disorders. *Nat. Commun.* **2020**, *11*, 4183. [CrossRef] [PubMed]
38. Thrupp, N.; Sala Frigerio, C.; Wolfs, L.; Skene, N.G.; Poovathingal, S.; Fourne, Y.; Matthews, P.M.; Theys, T.; Mancuso, R.; de Strooper, B.; et al. Single Nucleus Sequencing Fails to Detect Microglial Activation in Human Tissue. *bioRxiv* **2020**. [CrossRef]
39. Smajić, S.; Prada-Medina, C.A.; Landoulsi, Z.; Dietrich, C.; Spielmann, M. Single-Cell Sequencing of the Human Midbrain Reveals Glial Activation and a Neuronal State Specific to Parkinson's Disease. *medRxiv* **2020**. [CrossRef]
40. Alessi, D.R.; Sammler, E. LRRK2 Kinase in Parkinson's Disease. *Science* **2018**, *360*, 36–37. [CrossRef] [PubMed]
41. Liu, B.; Gao, H.-M.; Hong, J.-S. Parkinson's Disease and Exposure to Infectious Agents and Pesticides and the Occurrence of Brain Injuries: Role of Neuroinflammation. *Environ. Health Perspect.* **2003**, *111*, 1065–1073. [CrossRef]
42. Dobbs, R.J.; Charlett, A.; Purkiss, A.G.; Dobbs, S.M.; Weller, C.; Peterson, D.W. Association of Circulating TNF-Alpha and IL-6 with Ageing and Parkinsonism. *Acta Neurol. Scand.* **1999**, *100*, 34–41. [CrossRef]
43. Scalzo, P.; Kümmer, A.; Cardoso, F.; Teixeira, A.L. Increased Serum Levels of Soluble Tumor Necrosis Factor-Alpha Receptor-1 in Patients with Parkinson's Disease. *J. Neuroimmunol.* **2009**, *216*, 122–125. [CrossRef]
44. Sliter, D.A.; Martinez, J.; Hao, L.; Chen, X.; Sun, N.; Fischer, T.D.; Burman, J.L.; Li, Y.; Zhang, Z.; Narendra, D.P.; et al. Parkin and PINK1 Mitigate STING-Induced Inflammation. *Nature* **2018**, *561*, 258–262. [CrossRef] [PubMed]
45. Borsche, M.; König, I.R.; Delcambre, S.; Petrucci, S.; Balck, A.; Brüggemann, N.; Zimprich, A.; Wasner, K.; Pereira, S.L.; Avenali, M.; et al. Mitochondrial Damage-Associated Inflammation Highlights Biomarkers in PRKN/PINK1 Parkinsonism. *Brain* **2020**, *143*, 3041–3051. [CrossRef]
46. Mount, M.P.; Lira, A.; Grimes, D.; Smith, P.D.; Faucher, S.; Slack, R.; Anisman, H.; Hayley, S.; Park, D.S. Involvement of Interferon-Gamma in Microglial-Mediated Loss of Dopaminergic Neurons. *J. Neurosci.* **2007**, *27*, 3328–3337. [CrossRef] [PubMed]
47. Menza, M.; Dobkin, R.D.; Marin, H.; Mark, M.H.; Gara, M.; Bienfait, K.; Dicke, A.; Kusnekov, A. The Role of Inflammatory Cytokines in Cognition and Other Non-Motor Symptoms of Parkinson's Disease. *Psychosomatics* **2010**, *51*, 474–479. [CrossRef] [PubMed]
48. Lindqvist, D.; Kaufman, E.; Brundin, L.; Hall, S.; Surova, Y.; Hansson, O. Non-Motor Symptoms in Patients with Parkinson's Disease—Correlations with Inflammatory Cytokines in Serum. *PLoS ONE* **2012**, *7*, e47387. [CrossRef]
49. He, Y.; Le, W.-D.; Appel, S.H. Role of Fcgamma Receptors in Nigral Cell Injury Induced by Parkinson Disease Immunoglobulin Injection into Mouse Substantia Nigra. *Exp. Neurol.* **2002**, *176*, 322–327. [CrossRef]
50. Benkler, M.; Agmon-Levin, N.; Hassin-Baer, S.; Cohen, O.S.; Ortega-Hernandez, O.-D.; Levy, A.; Moscavitch, S.-D.; Szyper-Kravitz, M.; Damianovich, M.; Blank, M.; et al. Immunology, Autoimmunity, and Autoantibodies in Parkinson's Disease. *Clin. Rev. Allergy Immunol.* **2012**, *42*, 164–171. [CrossRef]
51. Zhang, Q.; Raoof, M.; Chen, Y.; Sumi, Y.; Sursal, T.; Junger, W.; Brohi, K.; Itagaki, K.; Hauser, C.J. Circulating Mitochondrial DAMPs Cause Inflammatory Responses to Injury. *Nature* **2010**, *464*, 104–107. [CrossRef]
52. Grazioli, S.; Pugin, J. Mitochondrial Damage-Associated Molecular Patterns: From Inflammatory Signaling to Human Diseases. *Front. Immunol.* **2018**, *9*, 832. [CrossRef]
53. Papachroni, K.K.; Ninkina, N.; Papapanagiotou, A.; Hadjigeorgiou, G.M.; Xiromerisiou, G.; Papadimitriou, A.; Kalofoutis, A.; Buchman, V.L. Autoantibodies to Alpha-Synuclein in Inherited Parkinson's Disease. *J. Neurochem.* **2007**, *101*, 749–756. [CrossRef]
54. Yanamandra, K.; Gruden, M.A.; Casaite, V.; Meskys, R.; Forsgren, L.; Morozova-Roche, L.A. α-Synuclein Reactive Antibodies as Diagnostic Biomarkers in Blood Sera of Parkinson's Disease Patients. *PLoS ONE* **2011**, *6*, e18513. [CrossRef]
55. Double, K.L.; Rowe, D.B.; Carew-Jones, F.M.; Hayes, M.; Chan, D.K.Y.; Blackie, J.; Corbett, A.; Joffe, R.; Fung, V.S.; Morris, J.; et al. Anti-Melanin Antibodies Are Increased in Sera in Parkinson's Disease. *Exp. Neurol.* **2009**, *217*, 297–301. [CrossRef]

56. Brochard, V.; Combadière, B.; Prigent, A.; Laouar, Y.; Perrin, A.; Beray-Berthat, V.; Bonduelle, O.; Alvarez-Fischer, D.; Callebert, J.; Launay, J.-M.; et al. Infiltration of CD4+ Lymphocytes into the Brain Contributes to Neurodegeneration in a Mouse Model of Parkinson Disease. *J. Clin. Investig.* **2009**, *119*, 182–192. [CrossRef]
57. Sommer, A.; Marxreiter, F.; Krach, F.; Fadler, T.; Grosch, J.; Maroni, M.; Graef, D.; Eberhardt, E.; Riemenschneider, M.J.; Yeo, G.W.; et al. Th17 Lymphocytes Induce Neuronal Cell Death in a Human iPSC-Based Model of Parkinson's Disease. *Cell Stem Cell* **2018**, *23*, 123–131.e6. [CrossRef] [PubMed]
58. Kustrimovic, N.; Comi, C.; Magistrelli, L.; Rasini, E.; Legnaro, M.; Bombelli, R.; Aleksic, I.; Blandini, F.; Minafra, B.; Riboldazzi, G.; et al. Parkinson's Disease Patients Have a Complex Phenotypic and Functional Th1 Bias: Cross-Sectional Studies of CD4+ Th1/Th2/T17 and Treg in Drug-Naïve and Drug-Treated Patients. *J. Neuroinflammation* **2018**, *15*, 205. [CrossRef]
59. Karaaslan, Z.; Kahraman, Ö.T.; Şanlı, E.; Ergen, H.A.; Ulusoy, C.; Bilgiç, B.; Yılmaz, V.; Tüzün, E.; Hanağası, H.A.; Küçükali, C.İ. Inflammation and Regulatory T Cell Genes Are Differentially Expressed in Peripheral Blood Mononuclear Cells of Parkinson's Disease Patients. *Sci. Rep.* **2021**, *11*, 2316. [CrossRef]
60. Subbarayan, M.S.; Hudson, C.; Moss, L.D.; Nash, K.R.; Bickford, P.C. T Cell Infiltration and Upregulation of MHCII in Microglia Leads to Accelerated Neuronal Loss in an α-Synuclein Rat Model of Parkinson's Disease. *J. Neuroinflammation* **2020**, *17*, 242. [CrossRef] [PubMed]
61. Nomura, T.; Watanabe, T.; Habu, S. *Humanized Mice*; Springer: Berlin/Heidelberg, Germany, 2008; ISBN 9783540756460.
62. Członkowska, A.; Kohutnicka, M.; Kurkowska-Jastrzebska, I.; Członkowski, A. Microglial Reaction in MPTP (1-Methyl-4-Phenyl-1,2,3,6-Tetrahydropyridine) Induced Parkinson's Disease Mice Model. *Neurodegeneration* **1996**, *5*, 137–143. [CrossRef]
63. Wu, D.C.; Jackson-Lewis, V.; Vila, M.; Tieu, K.; Teismann, P.; Vadseth, C.; Choi, D.-K.; Ischiropoulos, H.; Przedborski, S. Blockade of Microglial Activation Is Neuroprotective in the 1-Methyl-4-Phenyl-1,2,3,6-Tetrahydropyridine Mouse Model of Parkinson Disease. *J. Neurosci.* **2002**, *22*, 1763–1771. [CrossRef]
64. Giuliani, F.; Hader, W.; Yong, V.W. Minocycline Attenuates T Cell and Microglia Activity to Impair Cytokine Production in T Cell-Microglia Interaction. *J. Leukoc. Biol.* **2005**, *78*, 135–143. [CrossRef] [PubMed]
65. Sriram, K.; Matheson, J.M.; Benkovic, S.A.; Miller, D.B.; Luster, M.I.; O'Callaghan, J.P. Mice Deficient in TNF Receptors Are Protected against Dopaminergic Neurotoxicity: Implications for Parkinson's Disease. *FASEB J.* **2002**, *16*, 1474–1476. [CrossRef]
66. Barcia, C.; Ros, C.M.; Annese, V.; Gómez, A.; Ros-Bernal, F.; Aguado-Yera, D.; Martínez-Pagán, M.E.; de Pablos, V.; Fernandez-Villalba, E.; Herrero, M.T. IFN-γ Signaling, with the Synergistic Contribution of TNF-α, Mediates Cell Specific Microglial and Astroglial Activation in Experimental Models of Parkinson's Disease. *Cell Death Dis.* **2011**, *2*, e142. [CrossRef]
67. Gao, H.-M.; Hong, J.-S.; Zhang, W.; Liu, B. Synergistic Dopaminergic Neurotoxicity of the Pesticide Rotenone and Inflammogen Lipopolysaccharide: Relevance to the Etiology of Parkinson's Disease. *J. Neurosci.* **2003**, *23*, 1228–1236. [CrossRef]
68. Gao, H.-M.; Zhou, H.; Zhang, F.; Wilson, B.C.; Kam, W.; Hong, J.-S. HMGB1 Acts on Microglia Mac1 to Mediate Chronic Neuroinflammation That Drives Progressive Neurodegeneration. *J. Neurosci.* **2011**, *31*, 1081–1092. [CrossRef] [PubMed]
69. Klintworth, H.; Garden, G.; Xia, Z. Rotenone and Paraquat Do Not Directly Activate Microglia or Induce Inflammatory Cytokine Release. *Neurosci. Lett.* **2009**, *462*, 1–5. [CrossRef]
70. Gao, F.; Chen, D.; Hu, Q.; Wang, G. Rotenone Directly Induces BV2 Cell Activation via the p38 MAPK Pathway. *PLoS ONE* **2013**, *8*, e72046. [CrossRef]
71. Athanassiadou, A.; Voutsinas, G.; Psiouri, L.; Leroy, E.; Polymeropoulos, M.H.; Ilias, A.; Maniatis, G.M.; Papapetropoulos, T. Genetic Analysis of Families with Parkinson Disease That Carry the Ala53Thr Mutation in the Gene Encoding Alpha-Synuclein. *Am. J. Hum. Genet.* **1999**, *65*, 555–558. [CrossRef]
72. Polymeropoulos, M.H.; Lavedan, C.; Leroy, E.; Ide, S.E.; Dehejia, A.; Dutra, A.; Pike, B.; Root, H.; Rubenstein, J.; Boyer, R.; et al. Mutation in the Alpha-Synuclein Gene Identified in Families with Parkinson's Disease. *Science* **1997**, *276*, 2045–2047. [CrossRef] [PubMed]
73. Lesage, S.; Anheim, M.; Letournel, F.; Bousset, L.; Honoré, A.; Rozas, N.; Pieri, L.; Madiona, K.; Dürr, A.; Melki, R.; et al. G51D α-Synuclein Mutation Causes a Novel Parkinsonian-Pyramidal Syndrome. *Ann. Neurol.* **2013**, *73*, 459–471. [CrossRef]
74. Ross, O.A.; Braithwaite, A.T.; Skipper, L.M.; Kachergus, J.; Hulihan, M.M.; Middleton, F.A.; Nishioka, K.; Fuchs, J.; Gasser, T.; Maraganore, D.M.; et al. Genomic Investigation of Alpha-Synuclein Multiplication and Parkinsonism. *Ann. Neurol.* **2008**, *63*, 743–750. [CrossRef]
75. Singleton, A.B.; Farrer, M.; Johnson, J.; Singleton, A.; Hague, S.; Kachergus, J.; Hulihan, M.; Peuralinna, T.; Dutra, A.; Nussbaum, R.; et al. Alpha-Synuclein Locus Triplication Causes Parkinson's Disease. *Science* **2003**, *302*, 841. [CrossRef] [PubMed]
76. Krüger, R.; Kuhn, W.; Müller, T.; Woitalla, D.; Graeber, M.; Kösel, S.; Przuntek, H.; Epplen, J.T.; Schöls, L.; Riess, O. Ala30Pro Mutation in the Gene Encoding Alpha-Synuclein in Parkinson's Disease. *Nat. Genet.* **1998**, *18*, 106–108. [CrossRef]
77. Kim, W.S.; Kågedal, K.; Halliday, G.M. Alpha-Synuclein Biology in Lewy Body Diseases. *Alzheimers. Res. Ther.* **2014**, *6*, 73. [CrossRef]
78. Reynolds, A.D.; Stone, D.K.; Mosley, R.L.; Gendelman, H.E. Nitrated {alpha}-Synuclein-Induced Alterations in Microglial Immunity Are Regulated by CD4+ T Cell Subsets. *J. Immunol.* **2009**, *182*, 4137–4149. [CrossRef]
79. Benner, E.J.; Banerjee, R.; Reynolds, A.D.; Sherman, S.; Pisarev, V.M.; Tsiperson, V.; Nemachek, C.; Ciborowski, P.; Przedborski, S.; Mosley, R.L.; et al. Nitrated Alpha-Synuclein Immunity Accelerates Degeneration of Nigral Dopaminergic Neurons. *PLoS ONE* **2008**, *3*, e1376. [CrossRef] [PubMed]

80. Zhang, W.; Wang, T.; Pei, Z.; Miller, D.S.; Wu, X.; Block, M.L.; Wilson, B.; Zhang, W.; Zhou, Y.; Hong, J.-S.; et al. Aggregated Alpha-Synuclein Activates Microglia: A Process Leading to Disease Progression in Parkinson's Disease. *FASEB J.* **2005**, *19*, 533–542. [CrossRef] [PubMed]
81. Couch, Y.; Alvarez-Erviti, L.; Sibson, N.R.; Wood, M.J.A.; Anthony, D.C. The Acute Inflammatory Response to Intranigral α-Synuclein Differs Significantly from Intranigral Lipopolysaccharide and Is Exacerbated by Peripheral Inflammation. *J. Neuroinflammation* **2011**, *8*, 166. [CrossRef]
82. Su, X.; Maguire-Zeiss, K.A.; Giuliano, R.; Prifti, L.; Venkatesh, K.; Federoff, H.J. Synuclein Activates Microglia in a Model of Parkinson's Disease. *Neurobiol. Aging* **2008**, *29*, 1690–1701. [CrossRef]
83. Watson, M.B.; Richter, F.; Lee, S.K.; Gabby, L.; Wu, J.; Masliah, E.; Effros, R.B.; Chesselet, M.-F. Regionally-Specific Microglial Activation in Young Mice over-Expressing Human Wildtype Alpha-Synuclein. *Exp. Neurol.* **2012**, *237*, 318–334. [CrossRef]
84. Béraud, D.; Twomey, M.; Bloom, B.; Mittereder, A.; Ton, V.; Neitzke, K.; Chasovskikh, S.; Mhyre, T.R.; Maguire-Zeiss, K.A. α-Synuclein Alters Toll-Like Receptor Expression. *Front. Neurosci.* **2011**, *5*, 80. [CrossRef] [PubMed]
85. Daniele, S.G.; Béraud, D.; Davenport, C.; Cheng, K.; Yin, H.; Maguire-Zeiss, K.A. Activation of MyD88-Dependent TLR1/2 Signaling by Misfolded α-Synuclein, a Protein Linked to Neurodegenerative Disorders. *Sci. Signal.* **2015**, *8*, ra45. [CrossRef]
86. Gordon, R.; Albornoz, E.A.; Christie, D.C.; Langley, M.R.; Kumar, V.; Mantovani, S.; Robertson, A.A.B.; Butler, M.S.; Rowe, D.B.; O'Neill, L.A.; et al. Inflammasome Inhibition Prevents α-Synuclein Pathology and Dopaminergic Neurodegeneration in Mice. *Sci. Transl. Med.* **2018**, *10*. [CrossRef]
87. Pike, A.F.; Varanita, T.; Herrebout, M.A.C.; Plug, B.C.; Kole, J.; Musters, R.J.P.; Teunissen, C.E.; Hoozemans, J.J.M.; Bubacco, L.; Veerhuis, R. α-Synuclein Evokes NLRP3 Inflammasome-Mediated IL-1β Secretion from Primary Human Microglia. *Glia* **2021**. [CrossRef] [PubMed]
88. Hoenen, C.; Gustin, A.; Birck, C.; Kirchmeyer, M.; Beaume, N.; Felten, P.; Grandbarbe, L.; Heuschling, P.; Heurtaux, T. Alpha-Synuclein Proteins Promote Pro-Inflammatory Cascades in Microglia: Stronger Effects of the A53T Mutant. *PLoS ONE* **2016**, *11*, e0162717. [CrossRef] [PubMed]
89. Sánchez, K.; Maguire-Zeiss, K. MMP13 Expression Is Increased Following Mutant α-Synuclein Exposure and Promotes Inflammatory Responses in Microglia. *Front. Neurosci.* **2020**, *14*, 585544. [CrossRef]
90. Zhang, W.; Dallas, S.; Zhang, D.; Guo, J.-P.; Pang, H.; Wilson, B.; Miller, D.S.; Chen, B.; Zhang, W.; McGeer, P.L.; et al. Microglial PHOX and Mac-1 Are Essential to the Enhanced Dopaminergic Neurodegeneration Elicited by A30P and A53T Mutant Alpha-Synuclein. *Glia* **2007**, *55*, 1178–1188. [CrossRef]
91. Gasser, T. Usefulness of Genetic Testing in PD and PD Trials: A Balanced Review. *J. Parkinsons. Dis.* **2015**, *5*, 209–215. [CrossRef]
92. Gardet, A.; Benita, Y.; Li, C.; Sands, B.E.; Ballester, I.; Stevens, C.; Korzenik, J.R.; Rioux, J.D.; Daly, M.J.; Xavier, R.J.; et al. LRRK2 Is Involved in the IFN-Gamma Response and Host Response to Pathogens. *J. Immunol.* **2010**, *185*, 5577–5585. [CrossRef]
93. Hakimi, M.; Selvanantham, T.; Swinton, E.; Padmore, R.F.; Tong, Y.; Kabbach, G.; Venderova, K.; Girardin, S.E.; Bulman, D.E.; Scherzer, C.R.; et al. Parkinson's Disease-Linked LRRK2 Is Expressed in Circulating and Tissue Immune Cells and Upregulated Following Recognition of Microbial Structures. *J. Neural Transm.* **2011**, *118*, 795–808. [CrossRef]
94. Gillardon, F.; Schmid, R.; Draheim, H. Parkinson's Disease-Linked Leucine-Rich Repeat Kinase 2(R1441G) Mutation Increases Proinflammatory Cytokine Release from Activated Primary Microglial Cells and Resultant Neurotoxicity. *Neuroscience* **2012**, *208*, 41–48. [CrossRef]
95. Zhang, F.-R.; Huang, W.; Chen, S.-M.; Sun, L.-D.; Liu, H.; Li, Y.; Cui, Y.; Yan, X.-X.; Yang, H.-T.; Yang, R.-D.; et al. Genomewide Association Study of Leprosy. *N. Engl. J. Med.* **2009**, *361*, 2609–2618. [CrossRef] [PubMed]
96. Umeno, J.; Asano, K.; Matsushita, T.; Matsumoto, T.; Kiyohara, Y.; Iida, M.; Nakamura, Y.; Kamatani, N.; Kubo, M. Meta-Analysis of Published Studies Identified Eight Additional Common Susceptibility Loci for Crohn's Disease and Ulcerative Colitis. *Inflamm. Bowel Dis.* **2011**, *17*, 2407–2415. [CrossRef] [PubMed]
97. Van Limbergen, J.; Wilson, D.C.; Satsangi, J. The Genetics of Crohn's Disease. *Annu. Rev. Genomics Hum. Genet.* **2009**, *10*, 89–116. [CrossRef] [PubMed]
98. Weindel, C.G.; Bell, S.L.; Huntington, T.E.; Vail, K.J.; Srinivasan, R.; Patrick, K.L.; Watson, R.O. LRRK2 Regulates Innate Immune Responses and Neuroinflammation during Mycobacterium Tuberculosis Infection. *bioRxiv* **2019**, 699066. [CrossRef]
99. Goldwurm, S.; Zini, M.; Mariani, L.; Tesei, S.; Miceli, R.; Sironi, F.; Clementi, M.; Bonifati, V.; Pezzoli, G. Evaluation of LRRK2 G2019S Penetrance: Relevance for Genetic Counseling in Parkinson Disease. *Neurology* **2007**, *68*, 1141–1143. [CrossRef] [PubMed]
100. Tong, Y.; Yamaguchi, H.; Giaime, E.; Boyle, S.; Kopan, R.; Kelleher, R.J., 3rd; Shen, J. Loss of Leucine-Rich Repeat Kinase 2 Causes Impairment of Protein Degradation Pathways, Accumulation of Alpha-Synuclein, and Apoptotic Cell Death in Aged Mice. *Proc. Natl. Acad. Sci. USA* **2010**, *107*, 9879–9884. [CrossRef] [PubMed]
101. Li, X.; Patel, J.C.; Wang, J.; Avshalumov, M.V.; Nicholson, C.; Buxbaum, J.D.; Elder, G.A.; Rice, M.E.; Yue, Z. Enhanced Striatal Dopamine Transmission and Motor Performance with LRRK2 Overexpression in Mice Is Eliminated by Familial Parkinson's Disease Mutation G2019S. *J. Neurosci.* **2010**, *30*, 1788–1797. [CrossRef]
102. Moehle, M.S.; Webber, P.J.; Tse, T.; Sukar, N.; Standaert, D.G.; DeSilva, T.M.; Cowell, R.M.; West, A.B. LRRK2 Inhibition Attenuates Microglial Inflammatory Responses. *J. Neurosci.* **2012**, *32*, 1602–1611. [CrossRef]
103. Kim, B.; Yang, M.-S.; Choi, D.; Kim, J.-H.; Kim, H.-S.; Seol, W.; Choi, S.; Jou, I.; Kim, E.-Y.; Joe, E.-H. Impaired Inflammatory Responses in Murine Lrrk2-Knockdown Brain Microglia. *PLoS ONE* **2012**, *7*, e34693. [CrossRef]

104. Dzamko, N.; Inesta-Vaquera, F.; Zhang, J.; Xie, C.; Cai, H.; Arthur, S.; Tan, L.; Choi, H.; Gray, N.; Cohen, P.; et al. The IkappaB Kinase Family Phosphorylates the Parkinson's Disease Kinase LRRK2 at Ser935 and Ser910 during Toll-like Receptor Signaling. *PLoS ONE* **2012**, *7*, e39132. [CrossRef]
105. Kitada, T.; Asakawa, S.; Hattori, N.; Matsumine, H.; Yamamura, Y.; Minoshima, S.; Yokochi, M.; Mizuno, Y.; Shimizu, N. Mutations in the Parkin Gene Cause Autosomal Recessive Juvenile Parkinsonism. *Nature* **1998**, *392*, 605–608. [CrossRef] [PubMed]
106. Pickrell, A.M.; Youle, R.J. The Roles of PINK1, Parkin, and Mitochondrial Fidelity in Parkinson's Disease. *Neuron* **2015**, *85*, 257–273. [CrossRef]
107. Larsen, S.B.; Hanss, Z.; Krüger, R. The Genetic Architecture of Mitochondrial Dysfunction in Parkinson's Disease. *Cell Tissue Res.* **2018**, *373*, 21–37. [CrossRef]
108. Klein, C.; Djarmati, A.; Hedrich, K.; Schäfer, N.; Scaglione, C.; Marchese, R.; Kock, N.; Schüle, B.; Hiller, A.; Lohnau, T.; et al. PINK1, Parkin, and DJ-1 Mutations in Italian Patients with Early-Onset Parkinsonism. *Eur. J. Hum. Genet.* **2005**, *13*, 1086–1093. [CrossRef]
109. Dela Cruz, C.S.; Kang, M.-J. Mitochondrial Dysfunction and Damage Associated Molecular Patterns (DAMPs) in Chronic Inflammatory Diseases. *Mitochondrion* **2018**, *41*, 37–44. [CrossRef] [PubMed]
110. Zhou, R.; Yazdi, A.S.; Menu, P.; Tschopp, J. A Role for Mitochondria in NLRP3 Inflammasome Activation. *Nature* **2011**, *469*, 221–225. [CrossRef] [PubMed]
111. Nakahira, K.; Haspel, J.A.; Rathinam, V.A.K.; Lee, S.-J.; Dolinay, T.; Lam, H.C.; Englert, J.A.; Rabinovitch, M.; Cernadas, M.; Kim, H.P.; et al. Autophagy Proteins Regulate Innate Immune Responses by Inhibiting the Release of Mitochondrial DNA Mediated by the NALP3 Inflammasome. *Nat. Immunol.* **2011**, *12*, 222–230. [CrossRef] [PubMed]
112. Frank-Cannon, T.C.; Tran, T.; Ruhn, K.A.; Martinez, T.N.; Hong, J.; Marvin, M.; Hartley, M.; Treviño, I.; O'Brien, D.E.; Casey, B.; et al. Parkin Deficiency Increases Vulnerability to Inflammation-Related Nigral Degeneration. *J. Neurosci.* **2008**, *28*, 10825–10834. [CrossRef]
113. Zhong, Z.; Umemura, A.; Sanchez-Lopez, E.; Liang, S.; Shalapour, S.; Wong, J.; He, F.; Boassa, D.; Perkins, G.; Ali, S.R.; et al. NF-κB Restricts Inflammasome Activation via Elimination of Damaged Mitochondria. *Cell* **2016**, *164*, 896–910. [CrossRef]
114. Mouton-Liger, F.; Rosazza, T.; Sepulveda-Diaz, J.; Ieang, A.; Hassoun, S.-M.; Claire, E.; Mangone, G.; Brice, A.; Michel, P.P.; Corvol, J.-C.; et al. Parkin Deficiency Modulates NLRP3 Inflammasome Activation by Attenuating an A20-Dependent Negative Feedback Loop. *Glia* **2018**, *66*, 1736–1751. [CrossRef]
115. Tran, T.A.; Nguyen, A.D.; Chang, J.; Goldberg, M.S.; Lee, J.-K.; Tansey, M.G. Lipopolysaccharide and Tumor Necrosis Factor Regulate Parkin Expression via Nuclear Factor-Kappa B. *PLoS ONE* **2011**, *6*, e23660. [CrossRef] [PubMed]
116. Matheoud, D.; Sugiura, A.; Bellemare-Pelletier, A.; Laplante, A.; Rondeau, C.; Chemali, M.; Fazel, A.; Bergeron, J.J.; Trudeau, L.-E.; Burelle, Y.; et al. Parkinson's Disease-Related Proteins PINK1 and Parkin Repress Mitochondrial Antigen Presentation. *Cell* **2016**, *166*, 314–327. [CrossRef] [PubMed]
117. Clements, C.M.; McNally, R.S.; Conti, B.J.; Mak, T.W.; Ting, J.P.-Y. DJ-1, a Cancer- and Parkinson's Disease-Associated Protein, Stabilizes the Antioxidant Transcriptional Master Regulator Nrf2. *Proc. Natl. Acad. Sci. USA* **2006**, *103*, 15091–15096. [CrossRef] [PubMed]
118. Chien, C.-H.; Lee, M.-J.; Liou, H.-C.; Liou, H.-H.; Fu, W.-M. Microglia-Derived Cytokines/chemokines Are Involved in the Enhancement of LPS-Induced Loss of Nigrostriatal Dopaminergic Neurons in DJ-1 Knockout Mice. *PLoS ONE* **2016**, *11*, e0151569. [CrossRef] [PubMed]
119. Kim, J.-H.; Choi, D.-J.; Jeong, H.-K.; Kim, J.; Kim, D.W.; Choi, S.Y.; Park, S.-M.; Suh, Y.H.; Jou, I.; Joe, E.-H. DJ-1 Facilitates the Interaction between STAT1 and Its Phosphatase, SHP-1, in Brain Microglia and Astrocytes: A Novel Anti-Inflammatory Function of DJ-1. *Neurobiol. Dis.* **2013**, *60*, 1–10. [CrossRef]
120. Trudler, D.; Weinreb, O.; Mandel, S.A.; Youdim, M.B.H.; Frenkel, D. DJ-1 Deficiency Triggers Microglia Sensitivity to Dopamine toward a pro-Inflammatory Phenotype That Is Attenuated by Rasagiline. *J. Neurochem.* **2014**, *129*, 434–447. [CrossRef]
121. Nash, Y.; Schmukler, E.; Trudler, D.; Pinkas-Kramarski, R.; Frenkel, D. DJ-1 Deficiency Impairs Autophagy and Reduces Alpha-Synuclein Phagocytosis by Microglia. *J. Neurochem.* **2017**, *143*, 584–594. [CrossRef] [PubMed]
122. Ji, Y.-J.; Wang, H.-L.; Yin, B.-L.; Ren, X.-Y. Down-Regulation of DJ-1 Augments Neuroinflammation via Nrf2/Trx1/NLRP3 Axis in MPTP-Induced Parkinson's Disease Mouse Model. *Neuroscience* **2020**, *442*, 253–263. [CrossRef]
123. Volpato, V.; Webber, C. Addressing Variability in iPSC-Derived Models of Human Disease: Guidelines to Promote Reproducibility. *Dis. Model. Mech.* **2020**, *13*. [CrossRef]
124. Haenseler, W.; Zambon, F.; Lee, H.; Vowles, J.; Rinaldi, F.; Duggal, G.; Houlden, H.; Gwinn, K.; Wray, S.; Luk, K.C.; et al. Excess α-Synuclein Compromises Phagocytosis in iPSC-Derived Macrophages. *Sci. Rep.* **2017**, *7*, 9003. [CrossRef] [PubMed]
125. Trudler, D.; Nazor, K.L.; Eisele, Y.S.; Grabauskas, T.; Dolatabadi, N.; Parker, J.; Sultan, A.; Zhong, Z.; Goodwin, M.S.; Levites, Y.; et al. Soluble α-Synuclein-Antibody Complexes Activate the NLRP3 Inflammasome in hiPSC-Derived Microglia. *Proc. Natl. Acad. Sci. USA* **2021**, *118*. [CrossRef] [PubMed]
126. Lee, H.; Flynn, R.; Sharma, I.; Haberman, E.; Carling, P.J.; Nicholls, F.J.; Stegmann, M.; Vowles, J.; Haenseler, W.; Wade-Martins, R.; et al. LRRK2 Is Recruited to Phagosomes and Co-Recruits RAB8 and RAB10 in Human Pluripotent Stem Cell-Derived Macrophages. *Stem Cell Rep.* **2020**, *14*, 940–955. [CrossRef] [PubMed]

127. Panagiotakopoulou, V.; Ivanyuk, D.; De Cicco, S.; Haq, W.; Arsić, A.; Yu, C.; Messelodi, D.; Oldrati, M.; Schöndorf, D.C.; Perez, M.-J.; et al. Interferon-γ Signaling Synergizes with LRRK2 in Neurons and Microglia Derived from Human Induced Pluripotent Stem Cells. *Nat. Commun.* **2020**, *11*, 5163. [CrossRef]
128. Speidel, A.; Felk, S.; Reinhardt, P.; Sterneckert, J.; Gillardon, F. Leucine-Rich Repeat Kinase 2 Influences Fate Decision of Human Monocytes Differentiated from Induced Pluripotent Stem Cells. *PLoS ONE* **2016**, *11*, e0165949. [CrossRef]
129. Lancaster, M.A.; Renner, M.; Martin, C.-A.; Wenzel, D.; Bicknell, L.S.; Hurles, M.E.; Homfray, T.; Penninger, J.M.; Jackson, A.P.; Knoblich, J.A. Cerebral Organoids Model Human Brain Development and Microcephaly. *Nature* **2013**, *501*, 373–379. [CrossRef]
130. Kadoshima, T.; Sakaguchi, H.; Nakano, T.; Soen, M.; Ando, S.; Eiraku, M.; Sasai, Y. Self-Organization of Axial Polarity, inside-out Layer Pattern, and Species-Specific Progenitor Dynamics in Human ES Cell–derived Neocortex. *Proc. Natl. Acad. Sci. USA* **2013**, *110*, 20284–20289. [CrossRef]
131. Lin, Y.-T.; Seo, J.; Gao, F.; Feldman, H.M.; Wen, H.-L.; Penney, J.; Cam, H.P.; Gjoneska, E.; Raja, W.K.; Cheng, J.; et al. APOE4 Causes Widespread Molecular and Cellular Alterations Associated with Alzheimer's Disease Phenotypes in Human iPSC-Derived Brain Cell Types. *Neuron* **2018**, *98*, 1141–1154.e7. [CrossRef]
132. Pérez, M.J.; Ivanyuk, D.; Panagiotakopoulou, V.; Di Napoli, G.; Kalb, S.; Brunetti, D.; Al-Shaana, R.; Kaeser, S.A.; Fraschka, S.A.-K.; Jucker, M.; et al. Loss of Function of the Mitochondrial Peptidase PITRM1 Induces Proteotoxic Stress and Alzheimer's Disease-like Pathology in Human Cerebral Organoids. *Mol. Psychiatry* **2020**. [CrossRef]
133. Linkous, A.; Balamatsias, D.; Snuderl, M.; Edwards, L.; Miyaguchi, K.; Milner, T.; Reich, B.; Cohen-Gould, L.; Storaska, A.; Nakayama, Y.; et al. Modeling Patient-Derived Glioblastoma with Cerebral Organoids. *Cell Rep.* **2019**, *26*, 3203–3211.e5. [CrossRef]
134. Ogawa, J.; Pao, G.M.; Shokhirev, M.N.; Verma, I.M. Glioblastoma Model Using Human Cerebral Organoids. *Cell Rep.* **2018**, *23*, 1220–1229. [CrossRef]
135. Nickels, S.L.; Modamio, J.; Mendes-Pinheiro, B.; Monzel, A.S.; Betsou, F.; Schwamborn, J.C. Reproducible Generation of Human Midbrain Organoids for in Vitro Modeling of Parkinson's Disease. *Stem Cell Res.* **2020**, *46*, 101870. [CrossRef] [PubMed]
136. Kano, M.; Takanashi, M.; Oyama, G.; Yoritaka, A.; Hatano, T.; Shiba-Fukushima, K.; Nagai, M.; Nishiyama, K.; Hasegawa, K.; Inoshita, T.; et al. Reduced Astrocytic Reactivity in Human Brains and Midbrain Organoids with PRKN Mutations. *NPJ Parkinsons Dis.* **2020**, *6*, 33. [CrossRef] [PubMed]
137. di Domenico, A.; Carola, G.; Calatayud, C.; Pons-Espinal, M.; Muñoz, J.P.; Richaud-Patin, Y.; Fernandez-Carasa, I.; Gut, M.; Faella, A.; Parameswaran, J.; et al. Patient-Specific iPSC-Derived Astrocytes Contribute to Non-Cell-Autonomous Neurodegeneration in Parkinson's Disease. *Stem Cell Rep.* **2019**, *12*, 213–229. [CrossRef]
138. Rõlova, T.; Lehtonen, Š.; Goldsteins, G.; Kettunen, P.; Koistinaho, J. Metabolic and Immune Dysfunction of Glia in Neurodegenerative Disorders: Focus on iPSC Models. *Stem Cells* **2021**, *39*, 256–265. [CrossRef]
139. Brownjohn, P.W.; Smith, J.; Solanki, R.; Lohmann, E.; Houlden, H.; Hardy, J.; Dietmann, S.; Livesey, F.J. Functional Studies of Missense TREM2 Mutations in Human Stem Cell-Derived Microglia. *Stem Cell Rep.* **2018**, *10*, 1294–1307. [CrossRef] [PubMed]
140. Abreu, C.M.; Gama, L.; Krasemann, S.; Chesnut, M.; Odwin-Dacosta, S.; Hogberg, H.T.; Hartung, T.; Pamies, D. Microglia Increase Inflammatory Responses in iPSC-Derived Human BrainSpheres. *Front. Microbiol.* **2018**, *9*, 2766. [CrossRef]
141. Fagerlund, I.; Dougalis, A.; Shakirzyanova, A.; Gómez-Budia, M.; Konttinen, H.; Ohtonen, S.; Feroze, F.; Koskuvi, M.; Kuusisto, J.; Hernández, D.; et al. Microglia Orchestrate Neuronal Activity in Brain Organoids. *bioRxiv* **2020**. [CrossRef]
142. Ormel, P.R.; Vieira de Sá, R.; van Bodegraven, E.J.; Karst, H.; Harschnitz, O.; Sneeboer, M.A.M.; Johansen, L.E.; van Dijk, R.E.; Scheefhals, N.; Berdenis van Berlekom, A.; et al. Microglia Innately Develop within Cerebral Organoids. *Nat. Commun.* **2018**, *9*, 4167. [CrossRef]
143. Hosmane, S.; Tegenge, M.A.; Rajbhandari, L.; Uapinyoying, P.; Ganesh Kumar, N.; Thakor, N.; Venkatesan, A. Toll/interleukin-1 Receptor Domain-Containing Adapter Inducing Interferon-β Mediates Microglial Phagocytosis of Degenerating Axons. *J. Neurosci.* **2012**, *32*, 7745–7757. [CrossRef]
144. Park, J.; Wetzel, I.; Marriott, I.; Dréau, D.; D'Avanzo, C.; Kim, D.Y.; Tanzi, R.E.; Cho, H. A 3D Human Triculture System Modeling Neurodegeneration and Neuroinflammation in Alzheimer's Disease. *Nat. Neurosci.* **2018**, *21*, 941–951. [CrossRef]
145. Pediaditakis, I.; Kodella, K.R.; Manatakis, D.V.; Hinojosa, C.D.; Manolakos, E.S.; Rubin, L.L.; Hamilton, G.A.; Karalis, K. Modeling Alpha-Synuclein Pathology in a Human Brain-Chip to Assess Blood-Brain Barrier Disruption in Parkinson's Disease. *bioRxiv* **2020**. [CrossRef]
146. Ribecco-Lutkiewicz, M.; Sodja, C.; Haukenfrers, J.; Haqqani, A.S.; Ly, D.; Zachar, P.; Baumann, E.; Ball, M.; Huang, J.; Rukhlova, M.; et al. A Novel Human Induced Pluripotent Stem Cell Blood-Brain Barrier Model: Applicability to Study Antibody-Triggered Receptor-Mediated Transcytosis. *Sci. Rep.* **2018**, *8*, 1873. [CrossRef]
147. Bergmann, S.; Lawler, S.E.; Qu, Y.; Fadzen, C.M.; Wolfe, J.M.; Regan, M.S.; Pentelute, B.L.; Agar, N.Y.R.; Cho, C.-F. Blood-Brain-Barrier Organoids for Investigating the Permeability of CNS Therapeutics. *Nat. Protoc.* **2018**, *13*, 2827–2843. [CrossRef]
148. Subramaniam, S.R.; Federoff, H.J. Targeting Microglial Activation States as a Therapeutic Avenue in Parkinson's Disease. *Front. Aging Neurosci.* **2017**, *9*, 176. [CrossRef]
149. Teismann, P.; Ferger, B. Inhibition of the Cyclooxygenase Isoenzymes COX-1 and COX-2 Provide Neuroprotection in the MPTP-Mouse Model of Parkinson's Disease. *Synapse* **2001**, *39*, 167–174. [CrossRef]
150. Chen, H.; Zhang, S.M.; Hernán, M.A.; Schwarzschild, M.A.; Willett, W.C.; Colditz, G.A.; Speizer, F.E.; Ascherio, A. Nonsteroidal Anti-Inflammatory Drugs and the Risk of Parkinson Disease. *Arch. Neurol.* **2003**, *60*, 1059–1064. [CrossRef]

151. Ren, L.; Yi, J.; Yang, J.; Li, P.; Cheng, X.; Mao, P. Nonsteroidal Anti-Inflammatory Drugs Use and Risk of Parkinson Disease: A Dose-Response Meta-Analysis. *Medicine* **2018**, *97*, e12172. [CrossRef] [PubMed]
152. McCoy, M.K.; Ruhn, K.A.; Martinez, T.N.; McAlpine, F.E.; Blesch, A.; Tansey, M.G. Intranigral Lentiviral Delivery of Dominant-Negative TNF Attenuates Neurodegeneration and Behavioral Deficits in Hemiparkinsonian Rats. *Mol. Ther.* **2008**, *16*, 1572–1579. [CrossRef]
153. García, M.C.; Cinquina, V.; Palomo-Garo, C.; Rábano, A.; Fernández-Ruiz, J. Identification of CB_2 Receptors in Human Nigral Neurons That Degenerate in Parkinson's Disease. *Neurosci. Lett.* **2015**, *587*, 1–4. [CrossRef]
154. Javed, H.; Azimullah, S.; Haque, M.E.; Ojha, S.K. Cannabinoid Type 2 (CB2) Receptors Activation Protects against Oxidative Stress and Neuroinflammation Associated Dopaminergic Neurodegeneration in Rotenone Model of Parkinson's Disease. *Front. Neurosci.* **2016**, *10*, 321. [CrossRef]
155. Schwenkgrub, J.; Joniec-Maciejak, I.; Sznejder-Pachołek, A.; Wawer, A.; Ciesielska, A.; Bankiewicz, K.; Członkowska, A.; Członkowski, A. Effect of Human Interleukin-10 on the Expression of Nitric Oxide Synthases in the MPTP-Based Model of Parkinson's Disease. *Pharmacol. Rep.* **2013**, *65*, 44–49. [CrossRef]
156. Wang, J.; Wang, J.; Wang, J.; Yang, B.; Weng, Q.; He, Q. Targeting Microglia and Macrophages: A Potential Treatment Strategy for Multiple Sclerosis. *Front. Pharmacol.* **2019**, *10*, 286. [CrossRef] [PubMed]
157. Churchill, M.J.; Cantu, M.A.; Kasanga, E.A.; Moore, C.; Salvatore, M.F.; Meshul, C.K. Glatiramer Acetate Reverses Motor Dysfunction and the Decrease in Tyrosine Hydroxylase Levels in a Mouse Model of Parkinson's Disease. *Neuroscience* **2019**, *414*, 8–27. [CrossRef] [PubMed]
158. Zella, M.A.S.; Metzdorf, J.; Ostendorf, F.; Maass, F.; Muhlack, S.; Gold, R.; Haghikia, A.; Tönges, L. Novel Immunotherapeutic Approaches to Target Alpha-Synuclein and Related Neuroinflammation in Parkinson's Disease. *Cells* **2019**, *8*, 105. [CrossRef] [PubMed]
159. Games, D.; Valera, E.; Spencer, B.; Rockenstein, E.; Mante, M.; Adame, A.; Patrick, C.; Ubhi, K.; Nuber, S.; Sacayon, P.; et al. Reducing C-Terminal-Truncated Alpha-Synuclein by Immunotherapy Attenuates Neurodegeneration and Propagation in Parkinson's Disease-like Models. *J. Neurosci.* **2014**, *34*, 9441–9454. [CrossRef] [PubMed]
160. Bae, E.-J.; Lee, H.-J.; Rockenstein, E.; Ho, D.-H.; Park, E.-B.; Yang, N.-Y.; Desplats, P.; Masliah, E.; Lee, S.-J. Antibody-Aided Clearance of Extracellular α-Synuclein Prevents Cell-to-Cell Aggregate Transmission. *J. Neurosci.* **2012**, *32*, 13454–13469. [CrossRef]
161. El-Agnaf, O.; Overk, C.; Rockenstein, E.; Mante, M.; Florio, J.; Adame, A.; Vaikath, N.; Majbour, N.; Lee, S.-J.; Kim, C.; et al. Differential Effects of Immunotherapy with Antibodies Targeting α-Synuclein Oligomers and Fibrils in a Transgenic Model of Synucleinopathy. *Neurobiol. Dis.* **2017**, *104*, 85–96. [CrossRef]
162. Shin, J.; Kim, H.-J.; Jeon, B. Immunotherapy Targeting Neurodegenerative Proteinopathies: α-Synucleinopathies and Tauopathies. *J. Mov. Disord.* **2020**, *13*, 11–19. [CrossRef]
163. Alon, S.; Goodwin, D.R.; Sinha, A.; Wassie, A.T.; Chen, F.; Daugharthy, E.R.; Bando, Y.; Kajita, A.; Xue, A.G.; Marrett, K.; et al. Expansion Sequencing: Spatially Precise in Situ Transcriptomics in Intact Biological Systems. *Science* **2021**, *371*. [CrossRef]
164. Vickovic, S.; Eraslan, G.; Salmén, F.; Klughammer, J.; Stenbeck, L.; Schapiro, D.; Äijö, T.; Bonneau, R.; Bergenstråhle, L.; Navarro, J.F.; et al. High-Definition Spatial Transcriptomics for in Situ Tissue Profiling. *Nat. Methods* **2019**, *16*, 987–990. [CrossRef] [PubMed]
165. Chen, W.-T.; Lu, A.; Craessaerts, K.; Pavie, B.; Sala Frigerio, C.; Corthout, N.; Qian, X.; Laláková, J.; Kühnemund, M.; Voytyuk, I.; et al. Spatial Transcriptomics and In Situ Sequencing to Study Alzheimer's Disease. *Cell* **2020**, *182*, 976–991.e19. [CrossRef]
166. Clayton, K.; Delpech, J.C.; Herron, S.; Iwahara, N.; Ericsson, M.; Saito, T.; Saido, T.C.; Ikezu, S.; Ikezu, T. Plaque Associated Microglia Hyper-Secrete Extracellular Vesicles and Accelerate Tau Propagation in a Humanized APP Mouse Model. *Mol. Neurodegener.* **2021**, *16*, 18. [CrossRef] [PubMed]